Dosimetry and X-ray spectroscopy with the photon counting pixel detector Dosepix

Dosimetrie und Röntgenspektroskopie mit dem photonenzählenden Pixeldetektor Dosepix

der Naturwissenschaftlichen Fakultät
der Friedrich-Alexander-Universität Erlangen-Nürnberg
zur

Erlangung des Doktorgrades Dr. rer. nat.

vorgelegt von
Sebastian Schmidt
aus Hersbruck

Als Dissertation genehmigt
von der Naturwissenschaftlichen Fakultät
der Friedrich-Alexander-Universität Erlangen-Nürnberg

Tag der mündlichen Prüfung: 12.10.2021

Vorsitzender des Promotionsorgans: Prof. Dr. Wolfgang Achtziger

Gutachter: PD Dr. Thilo Michel
Prof. Dr. Ivor Fleck

Mündliche Prüfer: Prof. Dr. Uli Katz
PD Dr. Thilo Michel
Prof. Dr. Hanno Sahlmann

Abstract

Dosepix is a pixelated photon-counting detector designed for dosimetry tasks. It employs a silicon sensor to register the deposited energies from photon interactions. Each of its 16×16 pixels acquires events independently and can resolve energy. The pixelation of Dosepix ensures that the event rate per pixel is reduced. The deposited energies of registered events can directly be sorted in a configurable internal 16 bin histogram allowing for dead-time free measurements. These features make Dosepix a promising detector for dosimetry and X-ray spectroscopy applications.

These tasks are accomplished with systems of one or multiple Dosepix detectors in this thesis. The detectors are used with appropriate filters which attenuate and change the impinging photon spectrum. This increases the information and the ability to measure correctly for different angles of irradiation. The response of the Dosepix detector to photon fields of various energies is simulated for numerous setups and analysed in great detail. Conversion factors from registered photon events to personal dose equivalents, representing stochastic effects of radiation inducing health risks, are optimised and evaluated with measurements. Filters for Dosepix are designed to reduce the number of required detectors for dose estimation in clinical use. A fast energy calibration method for Dosepix is developed via deep learning methods. It only requires the measurement of a single calibration source and is able to work with data of low statistics. A convolutional neural network is developed, which reconstructs an X-ray tube's photon spectrum from measurements with a Dosepix detector system. Additional networks to estimate various characteristics of this spectrum, essential for quality assurance, are established. A detailed simulation of the inner workings of Dosepix at the hardware level is introduced. It describes a detector's behaviour for high photon flux conditions.

A system of three Dosepix detectors with different metal filters can measure the personal dose equivalents $H_\mathrm{p}(10)$ and $H_\mathrm{p}(0.07)$ within the required legal limits for an energy range of 12 keV to 1250 keV. The additional requirement of irradiation angles of up to 60° constraints the $H_\mathrm{p}(0.07)$ estimation capabilities to photon energies greater than 25 keV. Simulations of a single Dosepix with a PMMA filter optimised to $H_\mathrm{p}(10)$ show that the detector can measure dose within an energy range important for medical applications of 14 keV to 250 keV, for irradiation angles of up to 60°. With the same filter, the estimation of $H_\mathrm{p}(0.07)$ for energies greater 20 keV is possible. A Dosepix system for eye lens dosimetry is introduced in simulations. It can determine the personal dose equivalent $H_\mathrm{p}(3)$ for energies of up to 250 keV and irradiation angles of 70°. For photon energies above 15 keV, angles of up to 90° are possible. A three Dosepix detector system with flat metal filters is used for the quality assurance of X-ray tubes. A convolutional neural network can predict the photon spectra for X-ray tube voltages in a range of 40 kV to 120 kV from measurements. Additionally, characteristics of these spectra are estimated, including the kVp-value, the half-value layers (HVL) for aluminium and copper, conversion factors from photon fluence to

dose equivalents and air kerma, and the photon fluence. A reconstruction of X-ray tube spectra scaled with the number of emitted photons is possible for fast measurements by utilising the dead-time freeness of the detector and deep learning methods. All introduced methods and analyses validate the capabilities of Dosepix regarding dosimetry and quality assurance of X-ray tubes. These results allow for compact devices employing Dosepix as their main component for various applications in science and medical technology.

Kurzzusammenfassung

Dosepix ist ein pixelierter, photonenzählender Detektor, der für die Dosimetrie entwickelt wurde. Er verwendet einen Siliziumsensor, um deponierte Energien von Wechselwirkungen mit Photonen zu registrieren. Die 16×16 Pixel des Dosepix-Detektors erfassen Ereignisse unabhängig voneinander und sind in der Lage, Energie aufzulösen. Die Pixelierung stellt sicher, dass die Ereignisrate pro Pixel verringert ist. Registrierte deponierte Energien können direkt in ein aus 16 Bins bestehendes Histogramm gespeichert werden, was ein Messen ohne Totzeit ermöglicht. Die vorgestellten Eigenschaften machen Dosepix zu einem vielversprechenden Detektor für Anwendungen in der Dosimetrie und Röntgenspektroskopie.

In dieser Arbeit werden diese Aufgaben mit Systemen, die einen oder mehrere Dosepix-Detektoren umfassen, realisiert. Geeignete Filter für die Detektoren werden eingesetzt, um das einfallende Photonenspektrum abzuschwächen und zu verzerren. Dies erhöht den Informationsgehalt und die Fähigkeit, unter verschiedenen Einstrahlungswinkeln korrekt zu messen. Die Response des Dosepix-Detektors für Photonenfelder verschiedener Energien wird für zahlreiche Aufbauten simuliert und im Detail analysiert. Umrechnungsfaktoren von registrierten Photonenereignissen in Personendosen, die stochastische Gesundheitsrisiken durch Strahlung repräsentieren, werden optimiert und mit Messungen verglichen. Die Anzahl benötigter Dosepix-Detektoren für die Dosimetrie im klinischen Einsatz wird durch optimierte PMMA-Filter minimiert. Eine schnelle, auf Deep-Learning basierende Methode zur Energiekalibrierung für Dosepix wird entwickelt. Diese erfordert lediglich die Messung eines einzigen Prüfstrahlers und funktioniert mit Daten von geringer Statistik. Ein Convolutional Neural Network wird vorgestellt, das das Photonenspektrum einer Röntgenröhre mittels Messungen eines Dosepix-Detektorsystems rekonstruiert. Zusätzliche Netzwerke zur Vorhersage verschiedener wichtiger Messgrößen für die Qualitätssicherung werden entwickelt. Eine detaillierte Simulation, die die Funktion von Dosepix auf Hardware-Ebene beschreibt, wird präsentiert. Sie erlaubt es, Detektorprobleme, die bei hohen Photonenflüssen auftreten, zu beschreiben.

Ein System aus drei Dosepix-Detektoren mit unterschiedlichen Metallfiltern kann die Personendosen $H_\mathrm{p}(10)$ und $H_\mathrm{p}(0.07)$ innerhalb der geforderten gesetzlichen Grenzwerte für einen Energiebereich von 12 keV bis 1250 keV messen. Die Forderung von Bestrahlungswinkeln von bis zu 60° schränkt die korrekte Vorhersage von $H_\mathrm{p}(0.07)$ auf Photonenenergien über 25 keV ein. Simulationen eines einzelnen Dosepix-Detektors mit einem für $H_\mathrm{p}(10)$ optimierten PMMA-Filter zeigen, dass die Dosis in einem für medizinische Anwendungen wichtigen Energiebereich von 14 keV bis 250 keV und Bestrahlungswinkeln von bis zu 60° messbar ist. Mit dem selben Filter ist die Bestimmung von $H_\mathrm{p}(0.07)$ für Energien von über 20 keV möglich. Ein Dosepix-System für die Augenlinsendosimetrie wird mittels Simulationen vorgestellt. Dieses kann die Personendosis $H_\mathrm{p}(3)$ für Energien von bis zu 250 keV und Bestrahlungswinkeln von 70° bestimmen. Dosisbestimmung unter Winkeln von bis zu 90° ist für Photonenener-

gien über 15 keV möglich. Ein Detektorsystem aus drei Dosepix-Detektoren mit flachen Metallfiltern wird zur Qualitätssicherung von Röntgenröhren eingesetzt. Es kann über ein Convolutional Neural Network Photonenspektren für Röntgenröhrenspannungen in einem Bereich von 40 kV bis 120 kV aus Messungen rekonstruieren. Zusätzlich werden Charakteristika dieser Spektren mit hoher Präzision bestimmt. Diese umfassen den kVp-Wert, die Halbwertschichtdicken (HVL) für Aluminium und Kupfer, Umrechnungsfaktoren von Photonenfluenz zu Äquivalentdosen und Luftkerma, sowie die Photonenfluenz selbst. Die Totzeit-Freiheit des Detektors und Deep-Learning-Methoden ermöglichen die Vorhersage von Röntgenröhrenspektren, die mit der zugehörigen Photonenfluenz skaliert sind, mittels schneller Detektormessungen. Die vorgestellten Methoden und Analysen bestätigen die Fähigkeiten des Dosepix-Detektors hinsichtlich Dosimetrie und der Qualitätssicherung von Röntgenröhren. Dies ermöglicht die Entwicklung von kompakten Geräten mit Dosepix als Hauptkomponente für verschiedene Anwendungen in Wissenschaft und Medizintechnik.

Contents

CHAPTER 1

Introduction

X-radiation is applied in many different fields to improve our daily lives. It is used in medical imaging to check for fractured bones or to find dental issues or tumours. In radiotherapy, cancer is treated by locally applying high doses of radiation. For security, e.g. at airports, imaging is used to find prohibited objects inside packages or on persons. In industrial radiography, radiation is utilised to detect defects in materials via non-destructive testing. These are just a few examples that indicate the importance of X-ray applications to society.

However, all these benefits come at a cost. While X-radiation is helping people on one side, it is also dangerous. In general, human exposure should be minimised as ionising radiation is carcinogenic and damages organs and tissues. There is always a possibility for personnel working with X-ray sources to be exposed. Therefore, individual monitoring of the personal dose equivalent is legally required. Accredited dosemeters are employed for this task. They are usually read-out monthly and return information about the acquired dose. If thresholds are exceeded, measures to prevent exposure or temporary bans from working with X-ray sources are possible [1]. The long time between dosemeter read-outs might make people anxious, especially if an exposure may have occurred. An additional active dosemeter can be used to soothe its bearer. It always provides the current accumulated dose and is capable of warning if a limit is exceeded. Due to their poor performance, active dosemeters cannot be accredited for use with pulsed radiation fields in Germany [2]. If the dose rate is high, these devices underestimate dose or even miss exposures completely [3]. However, pulsed radiation fields are common in medical applications, like in interventional radiology and cardiology, and dosemeters working correctly under these conditions are demanded [4].

Active dosemeters often employ multiple silicon diodes for the detection of X-radiation. In this work, all measurements are performed with Dosepix [5], a pixelated photon-counting detector designed for dosimetry tasks. Due to its pixelated sensor, the detector corresponds to a compound of 256 single silicon diodes. Each pixel has its own electronics and works independently. A single pixel's workload is reduced

by distributing the total deposited energy in the detector's sensor to the pixels. This feature allows for applications involving high photon fluxes, for example, emitted by X-ray tubes. Dosepix digitally counts the number of registered events without introducing a dead-time while also resolving the energy of the events. Due to the detector's hardware design, proper counting is possible even for conditions of pulsed radiation fields. The detector has a practical size, employing a sensor with an area of about 13 mm^2. This allows building portable measurement systems that use one or multiple detectors as their main components. Dosepix, with its specified characteristics, is convenient for use in various applications. This thesis focuses on tasks related to dosimetry, X-ray spectroscopy, and quality assurance of X-ray tubes.

First, a method to simulate a setup involving Dosepix detectors and additional geometry is introduced. The simulation provides information about the detector responses for different initial photon energies and measurement setups. Dosimetry tasks with Dosepix detectors are covered. Based on simulations, conversion coefficients to transform registered photon events and their energies into dose equivalents are determined. These are evaluated and optimised via measurements. The simulation resembles the basis for all analyses within this thesis. The temperature dependence of Dosepix is analysed, and a method to correct dose acquisitions is introduced. A fast energy calibration method for Dosepix via the measurement of only a single radioactive source is established. A deep learning method is utilised to determine the conversion of the detector's energy measurand to corresponding deposited energy for all pixels at once. The introduction to dosimetry is based on an established setup consisting of three Dosepix detectors. The number of required detectors is minimised by optimising filter designs for a Dosepix detector in simulation. Corresponding conversion coefficients from registered events to dose equivalents are determined. Another application is X-ray spectroscopy with Dosepix, which is achieved via deep learning methods. An X-ray tube's photon spectrum is reconstructed from registered photon events of three differently filtered detectors. Multiple quantities that characterise a spectrum are additionally determined. This is important for the quality assurance of an X-ray tube. The employed deep learning models are trained on simulations and evaluated on measurements. An in-depth analysis of the functioning of the Dosepix hardware under high photon flux conditions is performed in the last chapter. The detector's behaviour is determined from measurements and implemented in simulations. Problems with high photon flux arise, and measures to reduce their influence are introduced.

CHAPTER 2

Theoretical background

Contents

This chapter presents an overview of the theoretical background relevant to the discussed topics of this thesis. The Dosepix detector and its working principle are

introduced. Since the detector is utilised to register photons, the different interaction types of photons with matter are described. A brief explanation about X-ray tubes is given as they are used in measurements with Dosepix. The detector is utilised for dosimetry tasks, and therefore an overview of important dosimetric quantities is provided. As some analyses in the thesis rely on deep learning, an introduction to the topic is presented.

2.1 The Dosepix detector

Dosepix is a hybrid pixelated photon counting and energy resolving detector. It was designed for photon dosimetry tasks by CERN [6], especially by W. Wong [5, 7], in cooperation with ECAP [8], and IBA dosimetry [9]. The layout and functioning of the detector are introduced in the following. A photograph of Dosepix is shown in figure 2.1.

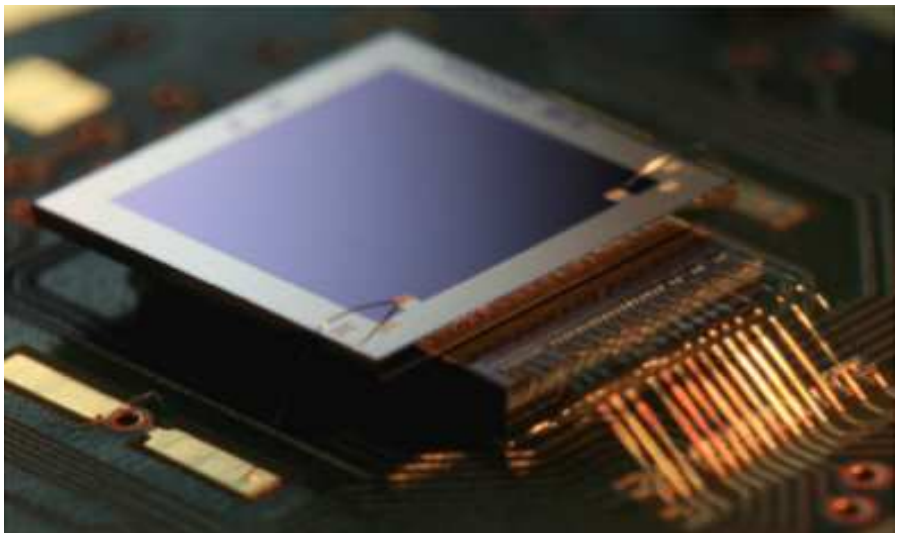

Figure 2.1.: A photograph of a Dosepix detector. The image is taken from [10].

The corresponding layout is depicted in figure 2.2. A hybrid design means that the detector consists of two main parts. First, a segmented semiconductor sensor used as sensitive material. Photons interact with it, and a charge signal is generated. The sensor is connected pixelwise, mechanically and electrically, via bump bonds to the second main part of the detector, an ASIC (application-specific integrated circuit). It handles the processing of the sensor's signals. For Dosepix, each pixel has its own readout electronics. The advantage of the hybrid approach is that the sensor design can be changed while the ASIC remains. The ASIC constrains the number of pixels which is 16×16 for Dosepix. For the sensor, multiple attributes can be changed, including its material and pixel sizes. In this thesis, Dosepix is used with a 300 µm

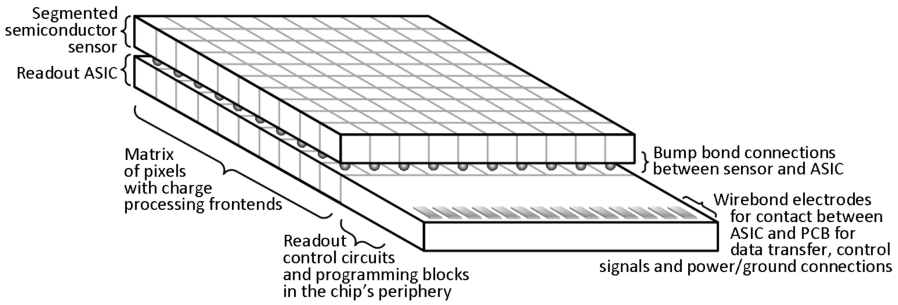

Figure 2.2.: Layout of the main components of a pixelated hybrid photon detector. The image is taken from [5].

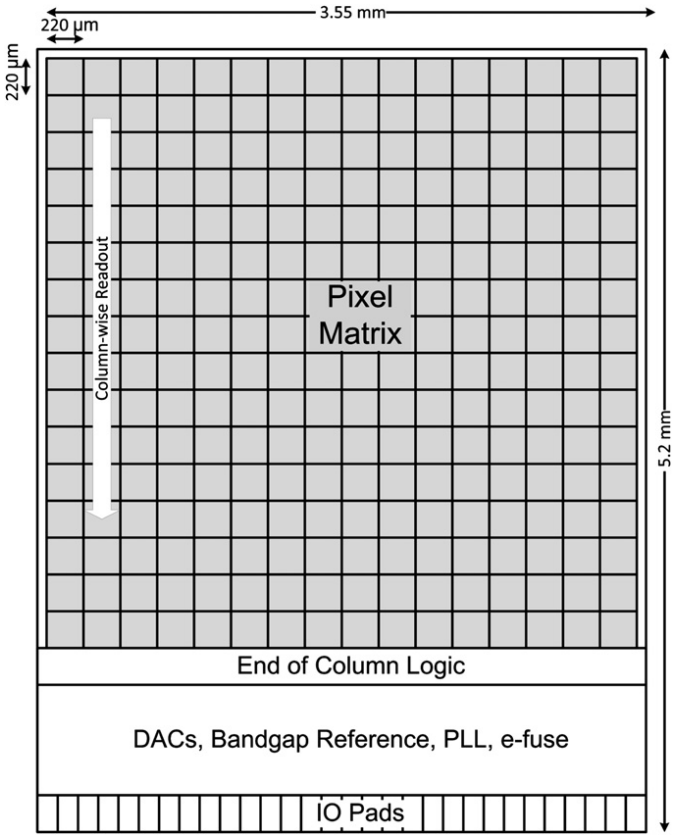

Figure 2.3.: Floorplan of the Dosepix detector. The image is taken from [7].

thick p-in-n silicon sensor. Figure 2.3 shows the floorplan of the detector. The pixel matrix of the sensor comprises two different pixel sizes. There are two rows of small pixels with a size of 55 µm × 55 µm at each end of the matrix. The remaining rows consist of large pixels with a size of 220 µm × 220 µm each.

The detector's readout is performed column-wise as indicated by the white arrow in figure 2.3. For one column, 4 small and 12 large pixels are read out. The image indicates the size of the detector of 3.55 mm × 5.2 mm. Due to the small size, Dosepix is easily applicable for various tasks involving X-radiation, especially in personal dosimetry. The total number of events induced in the detector's sensor is distributed to multiple pixels. If the event rate is too high, various problems arise, which are documented in chapter 7. The segmentation into pixels results in a reduced event rate for a single pixel, and therefore in a higher photon flux, the detector can handle. The event rate is further reduced by limiting a pixel's area, as done for the 4×16 small pixels.

2.1.1 Measurement procedure

The measurement procedure of Dosepix is illustrated in more detail in the following. Photons emitted from X-ray sources interact with the detector's sensor material, leading to the creation of ionising electrons, as will be described in section 2.2. These electrons then deposit their energy in the sensor and create electron-hole pairs. The required energy for the creation is 3.62 eV [11] for silicon. An electric field is present between the upper side of the sensor and the ASIC electrodes of Dosepix. Usually, a positive voltage of about 100 V for the used sensor is applied. The generated holes drift towards the electrodes and are collected at the ASIC's input for a pixel.

During the drift, the charge cloud expands due to diffusion. Under the assumption of an initial dot-like distribution, the cloud extends and gets normally distributed with a standard deviation σ depending on the duration t of the drift via equation [12]

$$\sigma = \sqrt{6Dt} \tag{2.1}$$

which corresponds to a random walk in 3D with D, the diffusion constant in silicon. The duration t depends on the applied electric field and the depth the energy deposition took place within the sensor, i.e. the drift distance. Additionally, repulsion occurs for which charges are separating during the drift in the applied electric field. Charges of the same sign are repelling each other. This effect leads to a broadening of the charge cloud. [13]

Figure 2.4 illustrates the charge sharing effect for a hybrid pixel detector explained in the following. The initial depositions are depicted via red dots. The resulting drifting charge clouds are reflected via the cones below the interaction points. For photon A, the deposition took place close to the centre of a pixel electrode. Therefore, all charges are collected by a single pixel. For photon B, the charge cloud is collected by 4 pixels, leading to the registration of multiple events. This effect is called charge sharing and leads to the distortion of a measured deposited energy spectrum. The larger the pixel sizes of a detector, the lower the probability for charge sharing to occur.

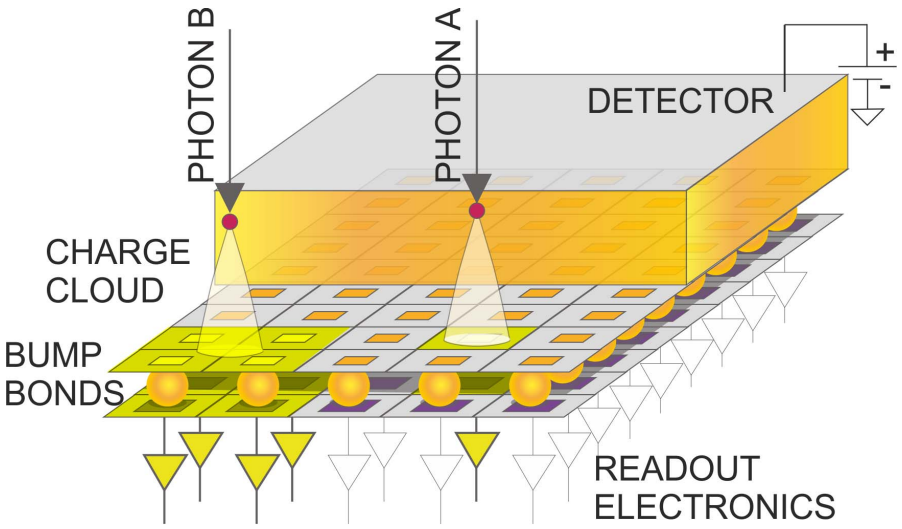

Figure 2.4.: Depiction of charge sharing effects in a hybrid pixelated detector like Dosepix. For photon A, an energy deposition takes place close to the centre of a pixel. The drifting charge cloud is registered by a single pixel only. For photon B, the energy deposition occurs close to the corner of four pixels, leading to the detection by multiple pixels. The image is taken from [14].

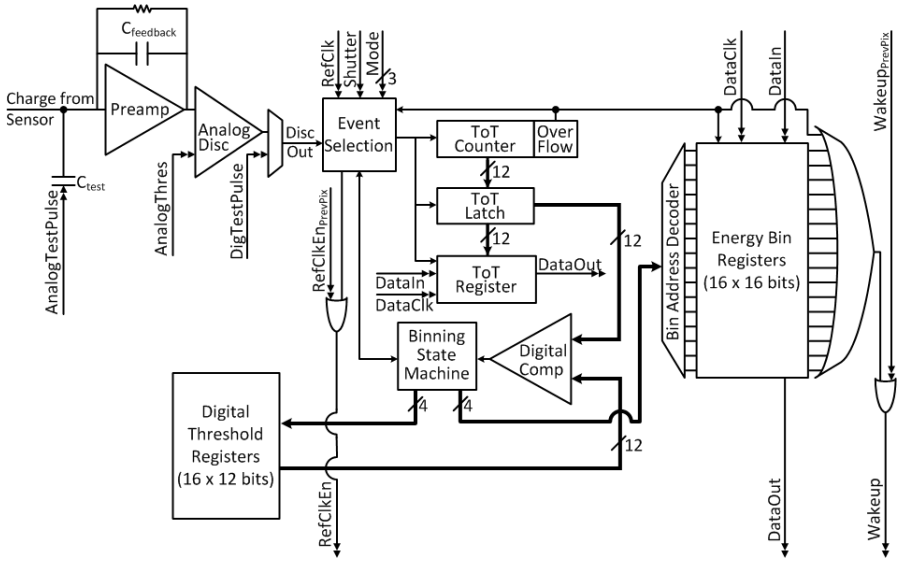

Figure 2.5.: A block diagram of the electronics of a single pixel of the Dosepix ASIC. The image is taken from [5].

Figure 2.5 depicts a block diagram of the electronics of a pixel. The input charge signal from the sensor is amplified using a charge sensitive amplifier. It returns an analogue signal, illustrated in figure 2.6. For an in-depth analysis of the analogue circuit of Dosepix, see chapter 7. The amplitude of each voltage pulse is proportional to the energy deposited within a pixel. Each pulse is decreased with a constant current proportional to an adjustable current I_{krum}. In summary, an initial pulse is amplified and stretched in time, as shown in the figure. By measuring the pulse duration, a statement about the deposited energy within the pixel is made.

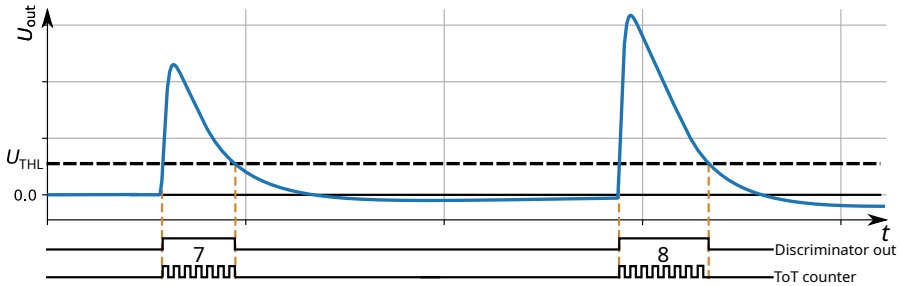

Figure 2.6.: The exemplary voltage signal U_{out} as a function of time at the output of the analogue electronics for a single pixel of Dosepix. Two interactions within a pixel of the sensor lead to the shown signal. A discriminator is used to check the amplitude of U_{out}. If the threshold voltage U_{THL}, indicated by the dashed line, is exceeded, the discriminator outputs a high signal. During this time, clock pulses are counted to provide a ToT value for each pulse. The image is based on [5].

The amplitude of the analogue signal U_{out} is compared to a threshold voltage U_{THL}, indicated by a dashed line in the figure, via a discriminator. The discriminator outputs a high signal if the threshold is exceeded. The ToT counter then counts the cycles of a permanently running clock signal. Here, ToT is the abbreviation for Time over Threshold. For high deposited energies and, as a consequence, high amplitudes of U_{out}, the relation to ToT is linear. For low energies, this relation no longer holds. Therefore, a calibration to convert measured ToT to deposited energy must be performed. The procedure utilised in this thesis is explained in detail in chapter 4.

The two important variables influencing the relation between ToT and deposited energy are the threshold voltage U_{THL} and the current I_{krum}. The threshold voltage is adjusted, so the noise present on the baseline level cannot exceed it. This ensures that Dosepix can perform noise-free measurements. It leads to a cut-off of low deposited energies that also cannot exceed this threshold. The adjustment of the threshold is performed for every pixel and is called equalisation. I_{krum} changes the slope of a pulse within the analogue electronics. Increasing the current leads to shorter pulses and lower values of ToT. A disadvantage is an increasing error on the deposited energy due to ToT being discrete, i.e. a single ToT value might reflect a large range of deposited energies. On the other hand, pile-up is suppressed, which is beneficial. This effect

represents multiple pulses within the analogue electronics taking place within a short time, leading to a superposition of the signals. See chapter 7 for more details. Within this thesis, multiple values for I_{krum} are used, depending on the application.

ToT can represent a measurand and a unit. In the former case, it represents a time and has a unit of 10 ns due to the used clock speed of 100 MHz. If ToT is treated as a unit, it represents the number of registered clock cycles.

2.1.2 Operation modes

Dosepix can be operated in multiple measurement modes. The following description is based on [5]. Since it was already partly introduced in the previous section, the ToT-mode is described first. When measuring with the detector, it counts the number of clock cycles an analogue pulse exceeds the threshold level. This number is called ToT and is stored in the ToT register as depicted in figure 2.5. Every time a new pulse is detected, the register value is overwritten. Therefore, the number of registered events depends on the detector's readout speed, which has a magnitude of about 10 Hz depending on the used hardware. This makes this mode unapplicable for dose measurements as there must be no dead-time as otherwise possible exposures might be missed. However, the mode has the best precision as it always returns exact ToT values. It is mostly used for the energy calibration of the conversion of ToT to deposited energy.

A second mode is the so-called photon-counting mode. As the name describes, photons are counted without any information about their energy being stored. A read-out returns the number of registered photons since the last data acquisition.

Another mode is the integration mode in which all registered ToT-values are added for a data frame. It provides a measure in ToT corresponding to the integrated deposited energy of a pixel.

Finally, the energy-binning mode is introduced. It is a speciality of Dosepix that makes the detector suitable for dosimetry tasks. Therefore, the mode is often called Dosi-mode. Again, the electronics of each pixel detect events and return their corresponding ToT values as described previously. Instead of providing these values directly, they are histogrammed via a binning state machine. Here, 16 bin edges are configured. They are stored in the digital threshold registers, as shown in figure 2.5. Once a ToT event is registered, its value is compared to these thresholds with a digital comparator. The binning state machine then decides which energy bin the event belongs to and increments the corresponding number of registered events. If a read-out is performed, the histogram of the energy bin registers is returned. For previous modes, a read-out meant that all pixels' values are returned at once by concatenating them and transferring them via a serial connection. In Dosi-mode, read-out is performed column-wise. This ensures the applicability to dosimetry tasks. There are 16 columns in total, and only a single column is read-out at a time while the remaining ones continue to count events. A read-out loop over the columns is performed in a

rolling shutter procedure, ensuring no dead-time. However, the detector's active area is reduced to $\frac{15}{16}$. Within the scope of this thesis, only ToT- and Dosi-mode are used.

2.1.3 Analogue test pulses

In the regular operation of Dosepix, the attached sensor is the input of the analogue electronics of each pixel. As illustrated in figure 2.5, this input can be configured to use an analogue test signal instead. Here, a brief summary is given, where the exact implementation is explained in more detail in [5]. A voltage pulse U_{TP} is generated and applied to a test capacitance C_{test}. The pulse corresponds to a charge Q_{test} at a pixel's preamplifier input. The charge is calculated via

$$Q_{\mathrm{test}} = U_{\mathrm{TP}} \cdot C_{\mathrm{test}}. \tag{2.2}$$

A capacitance of $C_{\mathrm{test}} = 7.3\,\mathrm{fF} \pm 2.1\%_{\mathrm{rms}}$ was determined via simulation in [5]. The injected charge can be calculated, utilising the equation. Due to the capacity's uncertainty, the value is impractical for real applications. Additionally, an error due to a design flaw in the analogue electronics exists. It influences the voltage level in the electronics and, therefore, the returned ToT values. However, the information from test pulse measurements is useful for some applications, as will be presented in this thesis.

2.2 Interactions of photons with matter

Dosepix uses a silicon sensor as sensitive material to register photons and their deposited energies. In the following, the interactions of photons with matter are described. Monoenergetic photons of intensity I_0 are impinging on a material with a thickness of d and a density of ρ. Via the exponential attenuation law [15]

$$I = I_0 \cdot \exp\left(-\mu \cdot \rho \cdot d\right), \tag{2.3}$$

the intensity I of the photons after passing the material is calculated. Here, μ represents the mass attenuation coefficient. The formula describes the reduction of photons due to various interactions with matter. Each time an interaction occurs, energy is transferred to electrons, depositing their energy in the sensor. Four types of photon interactions are explained in the following. They include

- photoelectric absorption
- coherent scattering
- incoherent scattering
- pair production

The corresponding mass attenuation coefficients of the interactions as a function of photon energy are depicted for silicon in figure 2.7. The following descriptions of the various photon interactions are based on [16].

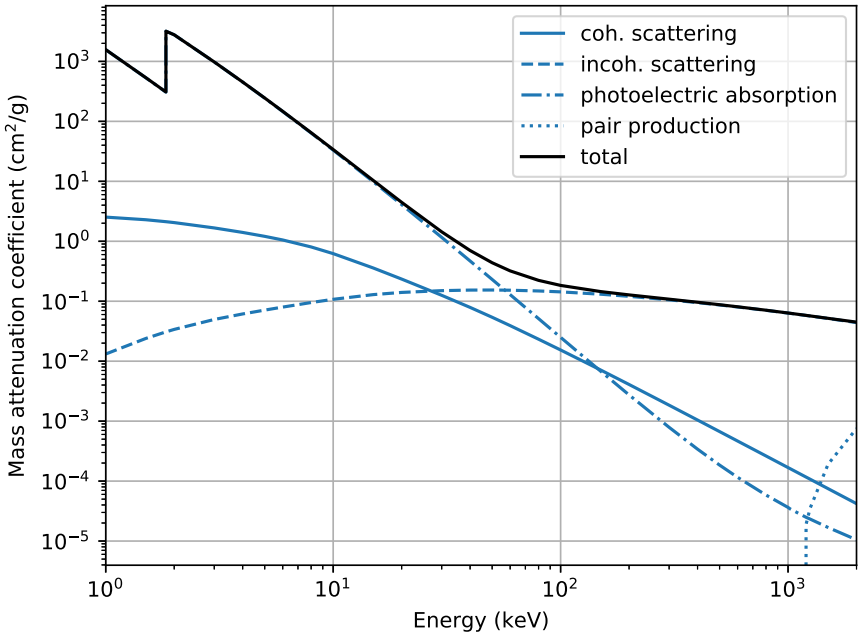

Figure 2.7.: Mass attenuation coefficients as a function of photon energy for different types of interactions according to the legend. The data is taken from [17].

2.2.1 Photoelectric absorption

In the case of photoelectric absorption, a photon transfers its total energy to an atom's electron. The kinetic energy of this electron then equals the energy of the emitted photon minus the binding energy. The probability for this process to occur is highest if the photon energy is equal or slightly greater than the corresponding binding energies. This leads to edges in the trend of the mass attenuation coefficient as a function of photon energy E, shown for silicon in figure 2.7. The edge of the K-shell is visible for an energy of 1.839 keV [17]. The relation between the mass attenuation coefficient and the photon energy is described by $\propto \frac{Z^{3-4}}{E^3}$, with the atomic number Z. The probability of the photoelectric effect to occur decreases with energy. However, up to energies of about 60 keV the process is dominant.

After the ejection of an inner shell electron in the process, the atom remains in an excited state. If an electron from a higher shell fills the vacancy, a fluorescence photon with a characteristic energy is emitted. Alternatively, an energy transfer to an outer

shell electron takes place. It is ejected if its energy exceeds the binding energy and is then called Auger electron.

2.2.2 Coherent scattering

In coherent scattering, a photon interacts with the whole atom and not just one of its electrons. This process is also called Rayleigh scattering. No energy is transferred to the atom. Instead, the photon only changes its direction. With increasing photon energy, the probability for the process to take place decreases. Since no energy is transferred to the sensitive material, Dosepix is not able to detect these photons. However, the effect is important for simulation purposes as photons scattering with the detector's surroundings might still reach the detector.

2.2.3 Incoherent scattering

In incoherent scattering, a photon scatters at a charged particle, here, an electron. This process is also referred to as Compton scattering. A photon scatters under an angle of θ and transfers a part of its energy to the electron. The energy E' of the scattered photon of initial energy E is calculated via [18]

$$E' = \frac{E}{1 + \frac{E}{m_e c^2}\left(1 - \cos\theta\right)}. \tag{2.4}$$

Here, m_e is the electron mass and c the speed of light. If the photon is scattering in the forward direction, i.e. for $\theta = 0$, no energy is transferred to the electron. For perfect backscattering, i.e. $\theta = 180°$, a maximum energy transfer occurs. The electron then deposits its energy into the sensor, leading to a signal for Dosepix. This determines the maximum depositable energy in the registered deposited energy spectrum, reflected by a Compton edge. Figure 2.7 shows the mass attenuation coefficients for silicon, where incoherent scattering becomes the dominant process for photon energies greater than about 60 keV. Since the emitted photon only transfers a part of its energy in Compton scattering, subsequent interactions might occur. As the energy of the photon decreases, the probability for photoelectric absorption increases with each incoherent scattering.

2.2.4 Pair production

Pair production can only occur if a photon's energy is greater than two times the rest mass of an electron, i.e. 1.022 MeV. Within the Coulomb field of an atom, there is a probability that the photon converts to an electron-positron pair. Since this thesis mostly considers photons with energies below the pair production threshold, the effect is neglected in the analyses.

2.3 X-ray tube

X-ray tubes are commonly used in medical applications and industry. They provide an easy measure to generate high energetic photons using electric energy. An introduction about the functioning of X-ray tubes and their produced photon spectra are given in the following. The description is based on [19].

The X-ray tube itself comprises a cathode and anode and is evacuated. Electrons are created at the cathode and accelerated towards the anode by applying a potential difference. This voltage is referred to as X-ray tube voltage U_{XRT}. It is often specified as kVp, corresponding to *kilovoltage peak*. Electrons reaching the target material of the anode lead to the emission of X-rays via bremsstrahlung or characteristic X-rays.

For bremsstrahlung, an electron comes close to an atomic nucleus of the anode material. Due to the nucleus's positive charge, the electron decelerates, gets deflected, and due to the decelaration releases a part of its energy via an X-ray. All measurements within this thesis are performed with a Siemens Megalix Cat angiography tube, using a tungsten anode [20]. Exemplary spectra for different voltages U_{XRT} are simulated via xpecgen [21] and illustrated in figure 2.8. An additional filter of 1.5 mm aluminium is applied to the X-ray tube, corresponding to the exit window of the Megalix Cat. The spectra's shapes reflect the bremsstrahlung spectra with filter applied, which attenuates low energy photons.

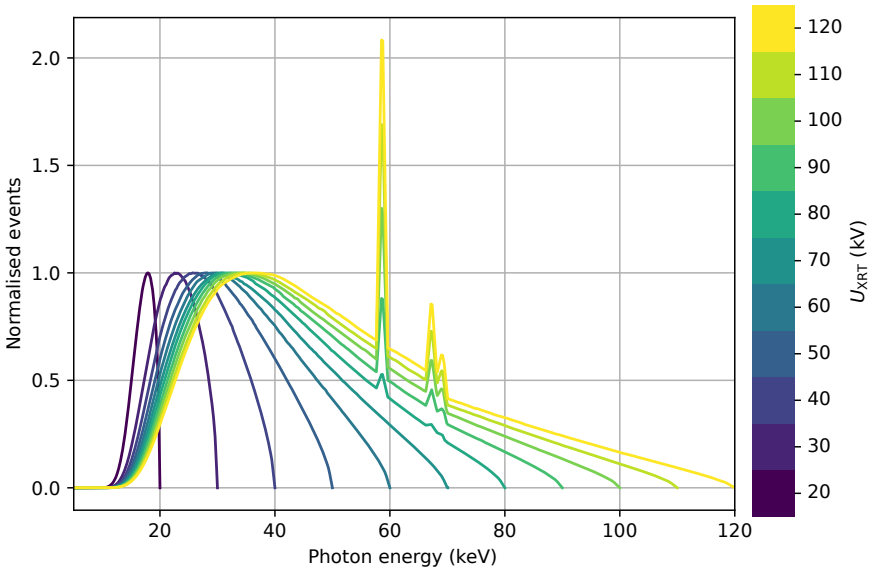

Figure 2.8.: Simulated X-ray tube spectra for various tube voltages U_{XRT} indicated by the colour bar. An additional Al-filter of 1.5 mm is applied to the X-ray tube.

All spectra show characteristic lines for energies within a range of 55 keV to 70 keV. They are created when an accelerated electron interacts with an inner shell electron of the target material. If the accelerated electron's energy is higher than the shell electron's binding energy, it may be ejected and leave a vacancy. An outer shell electron fills this vacancy, and an X-ray photon is emitted. An excerpt of dominant characteristic energies for tungsten are listed in table 2.1.

Transition	Energy (keV)
KL_1	57.4261(22)
KL_2	57.9819(19)
KL_3	59.3188(17)
KM_1	66.7069(33)
KM_2	66.9521(29)
KN_1	68.9320(43)
KN_2	69.0355(46)

Table 2.1.: An excerpt of the transition energies for tungsten. The data is taken from [22].

Often filters are used in front of an X-ray tube in applications. These attenuate photons of low energies and increase the mean photon energy of the emitted spectrum. Typical materials are aluminium, copper, tin, and lead. Depending on the material, characteristic edges reflected by a drop in photon fluence in the filtered spectrum are visible. At these K-edges, listed in the second column of table 2.2, there is a sharp jump towards high absorption in the trend of the attenuation coefficients introduced in 2.2.1. The coefficients of commonly used filters are depicted in figure 2.9. Additionally, their densities are listed in the third column of table 2.2.

Material	Energy (keV)	density ρ (gram/cm^3)
Al	1.56956	2.7
Cu	8.98796	8.92
Sn	29.20979	7.3
Pb	88.0128	11.34

Table 2.2.: The second column of the table reflects the theoretical energies of the K-edges for common filter materials of an X-ray tube. The data is taken from [22]. Additionally, the densities of these materials are listed in the third column, with the data taken from [23, 24].

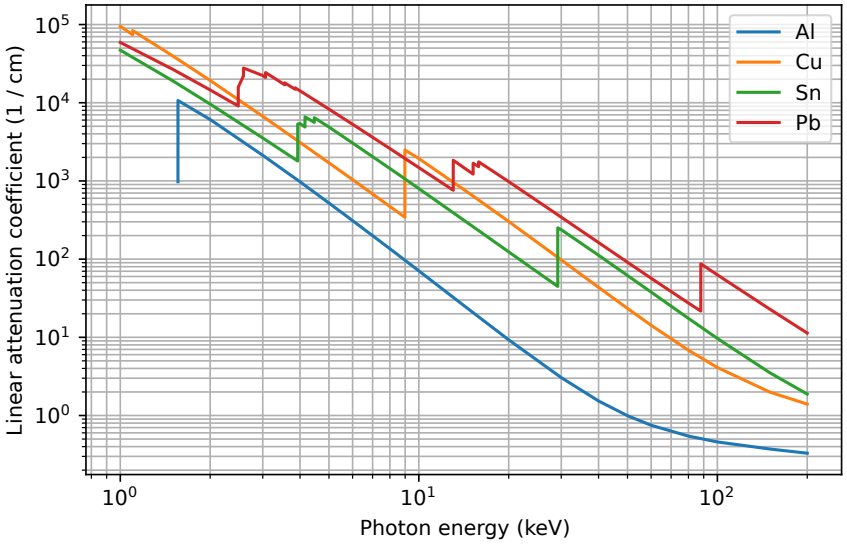

Figure 2.9.: The linear attenuation coefficients for commonly used filter materials of an X-ray tube according to the legend. The coefficients are the product of the mass attenuation coefficients from [17] and the densities of the materials in table 2.2.

2.4 Dosimetric quantities

A brief overview of relevant dosimetric quantities is given in the following. These are important for the described dosimetry applications with Dosepix within this thesis. The description of the quantities is based on [18].

First, physical dose quantities are introduced, starting with the **absorbed dose** D, defined as

$$D = \frac{\mathrm{d}E_{\mathrm{abs}}}{\mathrm{d}m}. \tag{2.5}$$

Here, $\mathrm{d}E_{\mathrm{abs}}$ is the energy that is locally absorbed by a material. It is divided by the irradiated mass $\mathrm{d}m$. The absorbed dose is given in units of Gy (Gray). The probability for photons to interact and, consequently, for energy depositions to take place depends on the material. Therefore, when specifying the absorbed dose, always the used material and its characteristics should be provided.

Another quantity is the **kerma** K. The word itself is an abbreviation for **k**inetic **e**nergy **r**eleased per **u**nit **m**ass [25]. K is described via

$$K = \frac{\mathrm{d}E_{\mathrm{trans}}}{\mathrm{d}m}. \tag{2.6}$$

The formula describes the kinetic energy dE_{trans} transferred by ionising radiation to secondary particles of first generation within a volume of mass dm. For photons, the secondary particles consist of electrons or positrons. Kerma is also given in units of Gy and depends on the used material. In this thesis, only the air kerma K_{air} is used.

Based on the physical quantities, operational quantities are introduced. They are represented in units of Sv (Sievert). These quantities are required for dosimetry tasks, i.e. for radiation protection of possibly exposed personnel. First, the **equivalent dose** H_T is described. It states the harmfulness of ionising radiation when impinging on a tissue or an organ T. H_T is calculated via

$$H_T = \sum_R w_R D_{T,R}. \tag{2.7}$$

A weighted sum over different types of ionising radiations R is performed. Radiation weighting factors w_R reflect the biological effectiveness of ionising radiation on the tissue or organ. The factors are multiplied with the corresponding absorbed doses $D_{T,R}$ in the sum. w_R equals 1 in the case of photon irradiation.

The **effective dose** D_E is the weighted sum over the equivalent doses for multiple tissues or organs T, i.e.

$$D_E = \sum_T w_T H_T. \tag{2.8}$$

Weighting factors w_T consider how harmful an equivalent dose of H_T is to a tissue T.

In this thesis, personal dose equivalents are most relevant. These are monitored in radiation protection and shall be determined via Dosepix. The measurands represent the equivalent dose at a certain depth within ICRU soft tissue, defined in [26]. The doses are represented via variables $H_p(x)$ where x corresponds to the depth in units of mm. Three commonly used depths and doses exist: the deep-dose equivalent $H_p(10)$, the eye dose equivalent $H_p(3)$, and the shallow dose equivalent $H_p(0.07)$. A dosemeter's quality is evaluated by attaching it to a phantom of ICRU soft tissue, performing measurements and comparing the results to the expectations. A phantom represents the bearer of the dosemeter. Often, simpler phantoms with approximately the same characteristics are used. These usually consist of PMMA and water. More information about them is given within chapters about dose simulations and measurements.

Additionally, ambient and directional dose equivalents $H^*(10)$ and $H'(0.07, \Omega)$ are relevant. They are defined according to [27]. The measurands are used in radiation protection to monitor external radiation. They represent the dose equivalent at a point within a distance d in the ICRU sphere, a spherical phantom with 30 cm radius made from ICRU soft tissue [26]. d corresponds to 10 mm and 0.07 mm. The ambient dose is independent of the direction of irradiation while the directional dose is not. For

the latter, Ω represents the direction. Since dosemeters for these dose equivalents are not carried by a person and are instead mounted at a fixed position within a room, performance tests are performed without a phantom.

2.5 Deep Learning

Various applications requiring predictions from measurements are introduced in this thesis. Systems are needed that provide condensed information from input data. Often, the underlying model is complicated as it is based on detector simulations. Classical methods might fail or are not efficiently applicable in this case. Deep learning methods are used for the predictions instead. All tasks within this thesis belong to the category of supervised machine learning. It means input and output data are matched. For every input sample, there is a corresponding label representing the output. In the following, neural networks and their training is explained. Additionally, different building blocks and terminology of neural networks are introduced. The implementation of neural networks within this thesis is realised in TensorFlow [28] and Keras [29].

2.5.1 Neural networks

The following introduction of neural networks is based on [30, 31]. The basic element of a network is a so-called neuron. A network itself is consisting of multiple layers, each comprising multiple neurons. The structure of a feedforward network is depicted in figure 2.10. It consists of an input layer i, several hidden layers h, and an output layer o.

In this thesis, only feedforward networks are used. For these, data flows directly from the input to the output, i.e. no recursions take place. The name deep learning originates from the fact that many layers are used for a network. The output z_j of a neuron j is described via

$$z_j = \phi\left(\sum_i w_{ji} \cdot z_i + b\right). \tag{2.9}$$

z_i refers to the inputs, w_i are the corresponding weights, and b is a bias added to the weighted sum. The input and output are both represented via z as the output of a neuron will be part of another neuron's input. A nonlinear function ϕ, called activation function, is applied to the sum, which allows a network to solve non-trivial problems. Various functions can be utilised. The most common one is the rectified linear unit, abbreviated as ReLU and defined as

$$\phi(z) = \max(0, z). \tag{2.10}$$

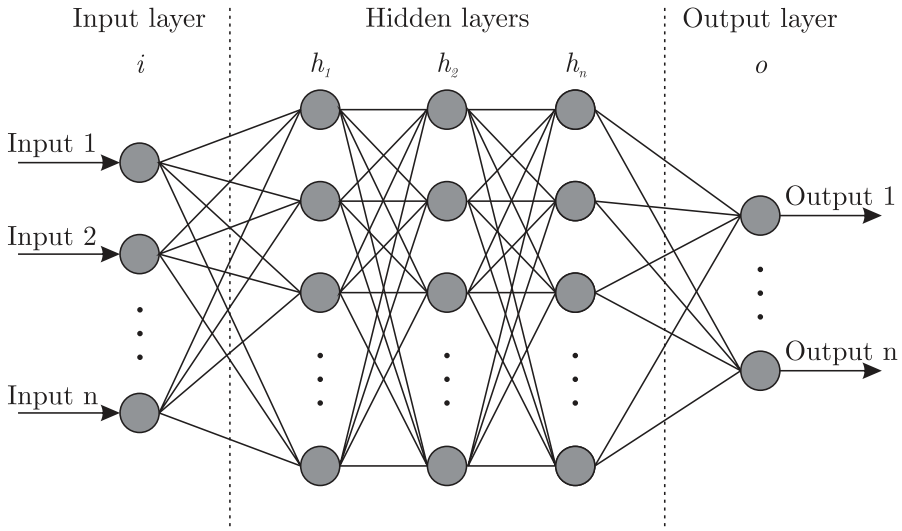

Figure 2.10.: The basic structure of a feedforward neural network of fully connected layers. It comprises an input layer i, multiple hidden layers h, and an output layer o. The image is taken from [32].

In the network depicted in figure 2.10, each output node of a first layer is connected to each input node of a second layer. This type of layer is called fully connected. The higher the number of neurons, the more weights exist and the longer the duration required to train a network. In later sections, different layer types with a reduced number of weights and other advantages are introduced.

Once the basic structure of a network is defined, its weights have to be adjusted. An optimisation of the weights using the training data has to be performed. An additional validation dataset is used to validate the functioning of the network. It is required since there is a probability that overfitting takes place, i.e. the network can make correct predictions for the training data but not for unknown data. If overfitting occurs, regularisation methods, like described in section 2.5.3, have to be implemented.

2.5.2 Learning via backpropagation

The algorithm for supervised learning is explained in the following. The optimisation is performed by minimising a loss function $\mathcal{L}$. A common choice is the mean squared error [30]

$$\mathcal{L} = \frac{1}{2n} \sum_s ||l(s) - o(s)||^2. \tag{2.11}$$

s represents a training sample, $l(s)$ the corresponding label, n the number of samples of the sum, and $o(s)$ the output value of the network for a sample s.

The optimisation is performed via backpropagation. Its description is based on [31]. The general idea is to understand how loss $\mathcal{L}$ changes when weight w_{ji} is varied. Then the weights can succesively be adjusted to optimise loss $\mathcal{L}$. First, a notation for the weighted sum of equation (2.9) is introduced as

$$a_j = \sum_i w_{ji} \cdot z_i. \tag{2.12}$$

Bias b_j is exchanged by an additional input with a fixed value of 1 to each layer of the network. This allows illustrating the backpropagation process without discussing biases explicitly. Index i represents the values within the sum, while index j corresponds to the neuron within the network. The activation of neuron j is then represented via

$$z_j = \phi(a_j). \tag{2.13}$$

The derivative of $\mathcal{L}$ in regards to w_{ji} is expressed via

$$\frac{\partial \mathcal{L}}{\partial w_{ji}} = \frac{\partial \mathcal{L}}{\partial a_j} \frac{\partial a_j}{\partial w_{ji}}, \tag{2.14}$$

where the chain rule for partial derivatives was applied. Two notations are introduced. First,

$$\delta_j = \frac{\partial \mathcal{L}}{\partial a_j}, \tag{2.15}$$

referred to as error in the following. Second,

$$\frac{\partial a_j}{\partial w_{ji}} = z_i, \tag{2.16}$$

where equation (2.12) is utilised. These expressions simplify equation (2.14) to

$$\frac{\partial \mathcal{L}}{\partial w_{ji}} = \delta_j z_i. \tag{2.17}$$

Using equation (2.15) in combination with expression (2.13) yields the error of the output neurons o as

$$\delta_k = \frac{\partial \mathcal{L}}{\partial a_k} = \phi'(a_k) \frac{\partial \mathcal{L}}{\partial o_k}, \tag{2.18}$$

where o_k is just another denotion of y_k. The error δ_j for a hidden neuron is evaluated by using the chain rule for partial derivatives to yield

$$\delta_j = \frac{\partial \mathcal{L}}{\partial a_j} = \sum_k \frac{\partial \mathcal{L}}{\partial a_k} \frac{\partial a_k}{\partial a_j} = \phi'(a_j) \sum_k w_{kj} \delta_k. \tag{2.19}$$

Here, the sum over k is performed for all neurons to which neuron j is connected. It finally illustrates the backpropagation formula to calculate the errors. The error of a hidden unit is calculated by propagating errors δ_k backwards in the network.

In summary, the process to determine the derivative of loss $\mathcal{L}$ to the weights is executed as follows:

- Apply the input to the network, forward propagate it, and determine the activations of the neurons
- Evaluate δ_k of the output neurons
- Backpropagate the errors δ_k via equation (2.19) to determine all errors δ_j of the hidden neurons
- Finally, use equation (2.17) to determine the derivatives $\frac{\partial \mathcal{L}}{\partial w_{ji}}$

With this information, the weights are adjusted to minimise loss $\mathcal{L}$. Gradient descent is applied by calculating [30]

$$w'_{ji} = w_{ji} - \eta \frac{\partial \mathcal{L}}{\partial w_{ji}} \tag{2.20}$$

where w'_{ji} is the updated weight, and η is the learning rate. In practical applications, training is proceeded in batches. An update of the weights is performed for multiple input samples instead of a single one. In this case, the mean of the partial derivatives $\frac{\partial \mathcal{L}}{\partial w_{ji}}$ of the different samples is used together with equation (2.20).

In the training of the network, the whole dataset is divided into batches. Once the network was trained on all batches, an epoch passed. For the next epoch, the batches within the dataset are shuffled and training proceeds as usual. The training of the networks within this thesis are performed using *Adaptive Moment Estimation*, better known as ADAM optimisation [33].

2.5.3 Overfitting and regularisation

Overfitting took place when a trained network is only able to predict well on training data. Then, the prediction accuracy for unknown data is significantly worse. Overfitting can be observed during network training when the losses for training and validation start to drift apart.

A straightforward method to prevent this behaviour is to increase the number of training samples. This is not always possible as, for example, data has to be generated in time-consuming simulations. However, other methods exist, called regularisation techniques. One of the most common is L2-regularisation. In its case, a sum is added to a loss $\mathcal{L}$ that has the form [30]

$$\frac{\lambda}{2n} \sum_i w_i^2, \tag{2.21}$$

where n is the number of weights w. This additional term ensures that small weights are favoured during optimisation. Factor λ provides a measure to adjust the importance of the introduced summand.

Within this thesis, mostly dropout is used for regularisation. The following explanation is based on [30]. For dropout, the loss function remains as is. Instead, the network itself is modified during training. Neurons within a layer are deactivated randomly, given a predefined probability. Weights are adjusted for a batch via backpropagation as described in the previous section. Afterwards, the whole process is repeated. First, all neurons are reactivated, neurons are randomly deactivated, and weights are adjusted again. One explanation why dropout is working as a regularisation method is described in the following according to [34]. By disabling neurons in the network, the remaining neurons cannot rely on the disabled ones anymore. For each new batch input to the network, a different network architecture is present. These all share the same weights, forcing remaining active neurons to rely on more robust features of the input data.

2.5.4 Convolutional neural networks

Convolutional neural networks are especially useful when dealing with data of grid-like topology. This is because they take the relation between neighbouring entries into account. Therefore, these networks are often used with image data. In this thesis, data will mostly consist of histograms of different dimensions which are comparable to images. [35] A convolutional neural network structure typically consists of multiple convolutional layers followed by multiple fully connected layers that provide the output.

Convolutional layers

In the following, the concept of convolutional layers is explained in detail. The description is based on [30]. Previously, for fully-connected layers, each neuron is connected to each neuron of a subsequent layer. For a convolutional layer, each neuron is only connected to a subset of an input layer's neurons. This region is called the local receptive field. This field is shifted over the network's inputs like depicted in figure 2.11. A local receptive field of 3×3 is used on a 4×4 input in blue (bottom). The shifting field illustrates how the neurons are connected. For each position, connections to a neuron are made, resulting in the 2×2 output neurons depicted in green (top). These connections resemble the underlying operation taking place. Input data is multiplied with a matrix of the same size of the receptive field, called the kernel. Additionally, a bias can be added. This results in a weighted sum to which a nonlinear activation function is applied like described in section 2.5.1. Each neuron of a convolutional layer is learning about a particular local receptive field of the input. This explains the origin of the name convolutional layer as the described operation resembles a convo-

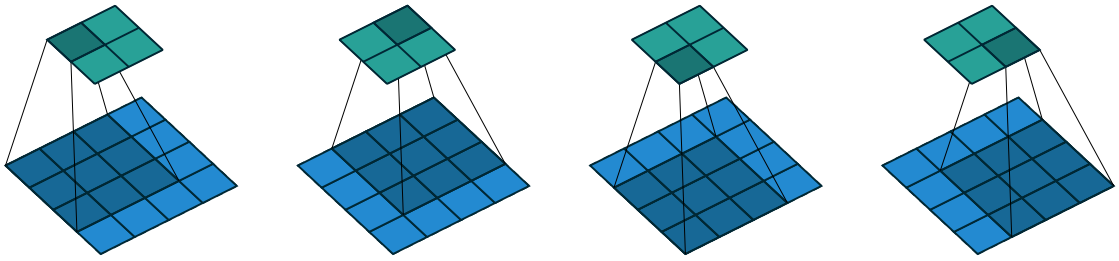

Figure 2.11.: Exemplary convolutional layer. The 4×4 input in blue (bottom) is convolved via a 3×3 kernel to provide the output in green (top). The image is taken from [36].

lution of the input. The kernel weights are shared, i.e. they are independent of the kernel position. All neurons detect the same feature of the input data, which introduces translation invariance. For example, a network might be able to detect which animal is depicted on an image independent from the animal's location within the image. When convolutional layers are combined with fully connected layers, the latter are able to additionally learn about the information from positions. A feature map of a convolutional network resembles the ability to detect certain features. The weights of a layer define the map. Multiple feature maps are required to detect a multitude of different features, which is achieved by adding an additional dimension to the layer.

The total number of weights of a convolutional layer is low compared to a fully connected layer due to the shared weights of the receptive field. Therefore, it provides an efficient method to detect features in multidimensional data.

Stride length and padding

In the example of figure 2.11, the kernel movement was performed with steps of 1. This step size is called stride length. The following description is based on [36]. Figure 2.12 shows an example with a stride length of 2.

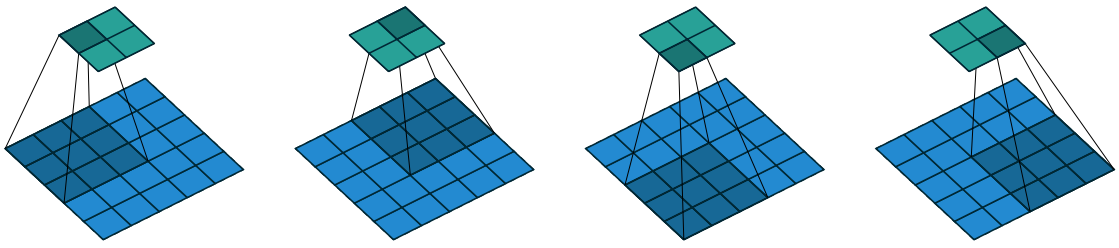

Figure 2.12.: Exemplary convolutional layer illustrating the use of stride lengths. The 5×5 input in blue (bottom) is convolved via a 3×3 kernel and a stride length of 2 to provide the 2×2 output in green (top). The image is taken from [36].

Here, the input dimension is larger than in figure 2.11, i.e. 5×5. Due to the stride length of 2, both layers have the same output size. Changing the stride reduces the layers' spatial dimension and, therefore, can be used to reduce the total number of weights within a network.

From one layer to another, the spatial size decreases. This might lead to information loss at the corners of the input. This size-reduction can be manipulated by so-called padding. Here, the input size is artificially increased by symmetrically extending the input's borders by filling them with new entries. Usually, zero-padding is used where the extension is performed with 0s.

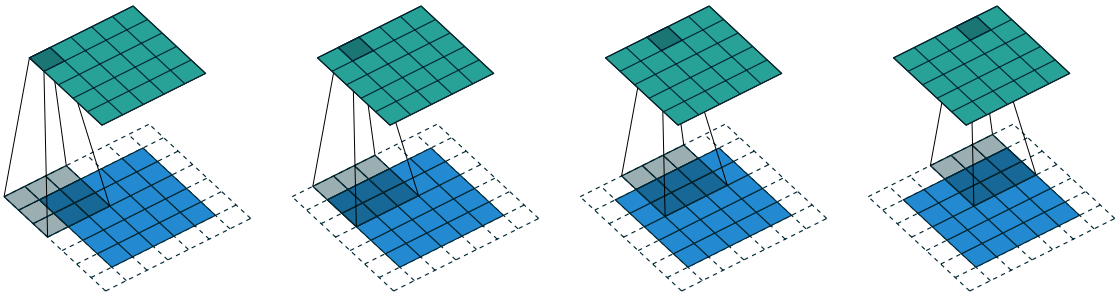

Figure 2.13.: Exemplary convolutional layer illustrating half padding. The 5×5 input in blue (bottom) is extended via zero padding. The result is convolved via a 3×3 kernel and a stride length of 1 to provide the 5×5 output in green (top). Input and output dimensions are identical. The image is taken from [36].

Figure 2.13 gives an example of half padding. It is also called same padding, as the input and output dimensions of the layer are the same. The dimension of the output size o of a convolutional layer is calculated via [36]

$$o = \left\lfloor \frac{i + 2p - k}{s} \right\rfloor + 1, \tag{2.22}$$

with the input dimension i, the kernel size k, and the stride length s.

2.5.5 Pooling layers

Pooling layers are often used in convolutional neural networks. Their following description is based on [30]. A kernel is shifted over the input with a specific stride length applied like previously described for the convolutional layers. For each step, an operation to the entries within the scope of the kernel is applied. For example, in max-pooling, the maximum is taken, and in average-pooling, the mean of the values is calculated. It leads to a reduction of the spatial size and, therefore, to a compression of the input data's information without introducing additional weights.

The dimension of the output o of the layer is calculated via [36]

$$o = \left\lfloor \frac{i-k}{s} \right\rfloor + 1, \tag{2.23}$$

with the input dimension i, the kernel size k, and the stride length s. As introduced before, convolutional layers often consist of multiple feature maps. When applying pooling layers, they act on each feature map separately, i.e. leave their dimension unchanged.

CHAPTER 3

Dosepix detector simulation and dosimetry applications

Contents

All analyses performed within this thesis rely on the simulation of the Dosepix detector. Therefore, a correct implementation of its hardware is crucial. The geometry of Dosepix and its surroundings are implemented. Simulations are evaluated by comparing them with measurements of a calibrated detector. More information about the calibration procedure is found in chapter 4. A first application is introduced by using a system of three detectors as a dosemeter. Simulations of the system are performed, and methods to calculate a dose value from the detectors' measured events are established. The results are compared to measurements. There is a temperature dependence for Dosepix leading to a distortion of the expected measurement outcomes. A method to correct ToT- and dose measurements for extreme temperatures is presented.

3.1 Dosepix detector simulation

The simulation of the Dosepix detector is essential for various analysis tasks. Measured spectra of radioactive sources are limited in their features. Calibration sources and fluorescence targets only emit specific photon energies with certain probabilities. These are also usually close to each other in energy, leading to peaks in the detector's deposited energy spectrum that are indistinguishable. Even with a filter applied, X-ray tubes always emit broad photon energy spectra with additional characteristic lines. Energy-dependent analyses are challenging as the spectra only allow to express a dependence regarding their mean photon energy. Since the interaction probability of photons with matter highly depends on energy, this leads to an error of the analysed characteristics. In simulations, there are no restrictions on the attributes of a radioactive source. These include the geometry of the source and the energies and directions of the emitted photons. Allpix^2 [37], a framework for the simulation of pixel-detectors based on GEANT4 [38] is used. Parts of the code are modified to fit the needs for a proper Dosepix simulation. These modifications include the import of CAD models to give a correct representation of the detector's readout electronics and its housing in the simulation's geometry. Additionally, accurate modelling of repulsion of charge carriers during drift within the sensor material is implemented according to [13]. This is required to consider charge sharing effects.

Since two pixel sizes for the sensor of Dosepix exist, two simulations are executed separately. For the large pixels, the sensor defined in the simulation corresponds to the real one, i.e. 12×16 pixels, each with a size of $220\,\mu m \times 220\,\mu m$. For the small pixels, due to their small active area of $55\,\mu m \times 55\,\mu m$, a modification is made. To maintain the same pitch, each small pixel is surrounded by a common guard electrode which is approximately at ground potential [39]. Deposited energies in this region create electron-hole pairs as usual but are not collected by a pixel electrode. In the simulation, an approximation is made by neglecting the mentioned gaps and placing the pixels next to each other. Also, their number is increased to 64×64 to provide

sufficient event statistics. The positioning of the pixels does not correspond to the real detector. However, this approach is adequate due to the small size of the Dosepix detector compared to its surroundings.

There is a correlation between the events of the pixels, independent of their size. If an extensive energy deposition within one pixel took place, the probability of charge sharing of neighbouring pixels increases due to many drifting charges and their repulsion (see section 2.1.1 for more details). Also, due to Compton scattering, multiple pixels might register an event for a single impinging photon. The described correlations only exist if the time of occurrence of the registered events is considered. This is not the case for Dosepix since time information is only available for single frames, i.e. the time resolution is highly dependent on the readout-speed of the hardware, which for the current setup has a magnitude of about 10 Hz in ToT-mode (see section for more information 2.1.2). Therefore, the time has no relevancy for measurements, the pixels are considered uncorrelated, and events of all pixels can be combined to increase event statistics.

3.1.1 Dosepix detector geometry

Figure 3.1 shows the implementation of the used Dosepix read-out hardware in Allpix^2 by importing its CAD-model. Due to the proximity of the hardware to the detectors, accurate modelling of geometry is crucial for a correct simulation of the detector system. Effects like absorption of photons or fluorescence at the surroundings have a considerable influence on the measured deposited energy spectrum of Dosepix. The printed circuit board, in green, has dimensions of 10 cm$\times$10 cm and mainly consists of FR-4 [40]. An additional layer of copper with a width of 50 µm, corresponding to the PCB's ground layer, is located at the backside. The holes at the PCB's top are designated as a perfboard for individual hardware designs. The grey volumes correspond to electrical components. They consist of various materials, while their true constituents are not well known and are only assumed. The chosen composition is 60% Sn, 30% BaTi, 7.5% Cu, and 2.5% Pb. The high amount of Sn is due to the used solder. BaTi is a main component of capacitors. The readout hardware has three slots for Dosepix detectors. Additionally, each detector is placed on a small PCB. This method is called chip on board (COB) where the Dosepix detector, consisting of a silicon ASIC with a height of 700 µm and a bump bonded silicon sensor of 300 µm, is electrically connected to the small PCB via wire bonds. The COBs in figure 3.1 are recognisable by the yellow ring-shaped copper layers with a height of 35 µm. Additionally, a layer of Ni with a width of 4 µm is present. The dark coloured cuboids in the centres of the ring structures represent the Dosepix detectors. The presented setup is the minimum of many simulations within this thesis. It is usually expanded by filters attached on top of the detectors and housing surrounding the whole system.

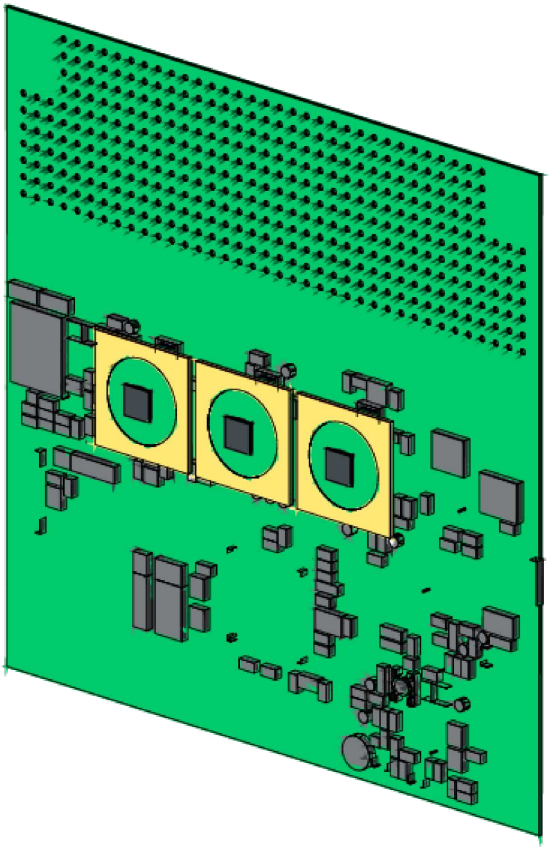

Figure 3.1.: Implementation of the readout hardware with three Dosepix detectors installed. The render represents the imported CAD model of the setup in Allpix^2. Yellow surfaces reflect copper and grey blocks electrical components.

3.1.2 MC agreement and detector resolution

Data from radioactive sources and fluorescences are analysed to evaluate the agreement of MC simulations and measurements with real hardware. Figure 3.2 illustrates exemplary setups of the readout hardware with three Dosepix detectors installed. (a) depicts a pyramidal beam that emits photons on the hardware's surface. This ensures that fluorescences of the hardware are present and that no computation time is wasted on simulating photons travelling through empty space. Within the pyramidal beam, the distributions of the photon directions are isotropic, which approximately corresponds to a radioactive source with a rectangular collimator. The beam geometry is used for the simulation of fluorescences. In measurements, the setup usually consists of an X-ray tube that emits photons at a target, leading to the emission of fluorescence photons. In an optimal setup, the detector should only be exposed to photons from

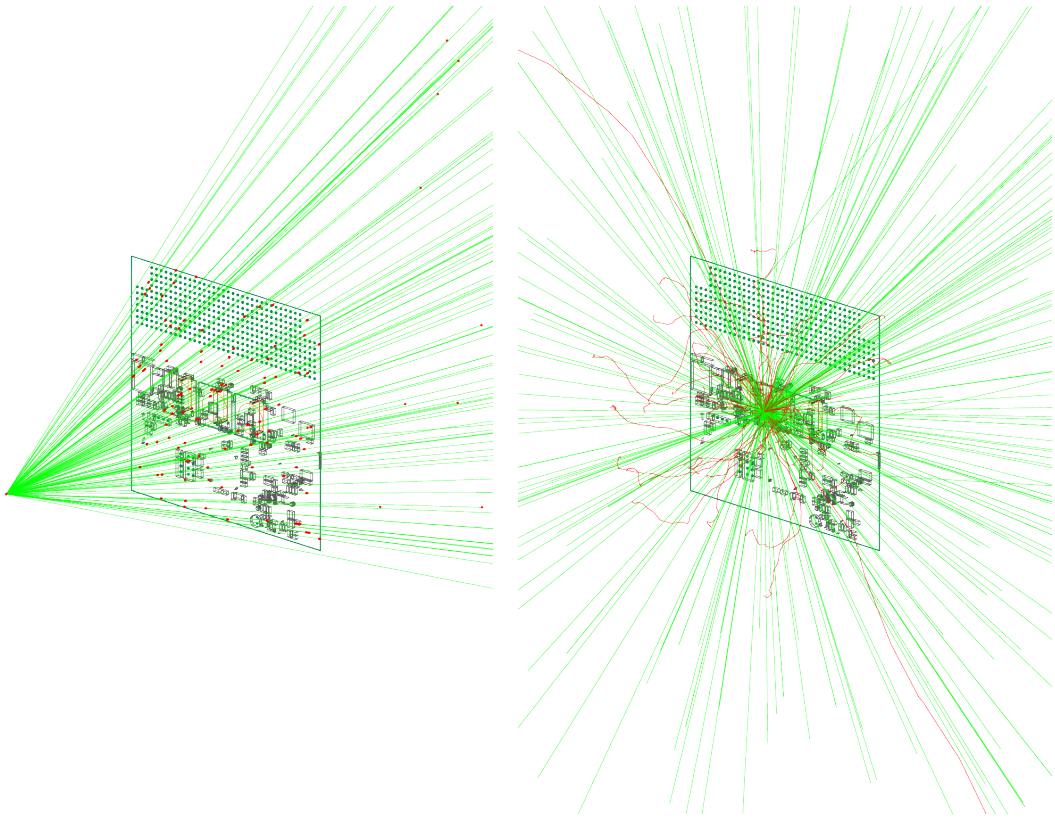

(a) Pyramidal radiation source (b) Isotropic radiation source

Figure 3.2.: Examples of different types of radiation sources used for the Dosepix detector simulation via Allpix^2. (a) illustrates a pyramidal source that isotropically emits photons on a previously defined area in space. Here, the PCB of the readout-electronics. (b) shows an exemplary radioactive source that is placed on top of the detector. Here, the decay of an ^{133}Ba source is simulated. Photons are indicated via green lines. Additionally, positrons are emitted, depicted by the red tracks.

these fluorescences. Therefore, it has to be shielded against the primary radiation of the X-ray tube. This kind of setup leads to a large reduction of the photon flux. A workaround is introduced to speed up the simulation.

The simulation process is split into two parts. First, a separate simulation natively implemented in Geant4 is used to emit monoenergetic photons on a fluorescence target as depicted in figure 3.3. The origin of the beam is the yellow dot on the left-hand side. 100 photons, indicated by green lines, are emitted on the target under an angle of 45°, similar to a real fluorescence setup. All yellow dots correspond to interaction points. Since the initial beam is entirely focused in simulation, the different photons

cannot be separated visually. A single photon interacting with the surrounding air is recognised as it changes its direction. However, interactions like these are not statistically relevant as the probability of their occurrence is low. The used primary photon energy is set higher than the target material's fluorescence energies as no excitation is possible otherwise. The target itself is visualised as blue block. Its thickness is set according to the exponential attenuation law of equation 2.3 that more than 99% of the photons interact with the target. A perfect detector is placed within the setup, represented by the white block. It is configured to let photons pass when irradiated directly. These photons interact with the target via the Compton effect or photoelectric effect, leading to fluorescence emission. These photons reach the detector, which registers their kinetic energies and kills off the event tracks. This information is then implemented in the second part of the simulation process. The previously determined kinetic energies of the fluorescences are sampled In Allpix^2 for a pyramidal source like previously described and depicted in figure 3.2.

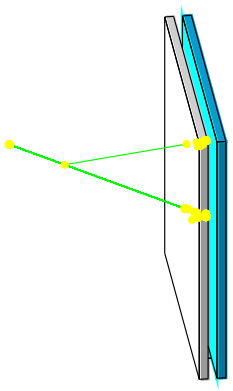

Figure 3.3.: The setup used for the simulation of X-ray fluorescences with Geant4. A perfect photon beam is emitted on a target represented by the light blue block. In front of this target, a perfect detector represented by the white block is placed. Emitted particles pass it without interaction while emission from the fluorescence target is registered, and the kinetic energies of the photons are stored.

Fluorescences are not the only important radiation sources for agreement analysis or energy calibration of the detector. Additionally, radionuclides are used. When their nuclei decay, photons with characteristic energies are emitted. Only a couple of photon energies dominate the spectra, leading to prominent peaks in the recorded deposited energy spectra. The source is placed, so each of the three Dosepix detectors of the readout hardware is well within the photon field. This corresponds to the setup in 3.2 (a).

If other particles are emitted from the source, like electrons or positrons, the setup has to be changed to one like depicted in (b), as the range the particles can travel in air is limited. In the example, a ^{133}Ba source is placed directly on top of the detector

at the readout electronics' central position. The source mainly undergoes electron capture and β^+-decays, which leads to the emission of photons, depicted in green, and positrons, indicated by the red tracks. A setup like this is suitable for radioactive sources with low activity. It is best to put the source close to the detector to maximise the photon flux for Dosepix.

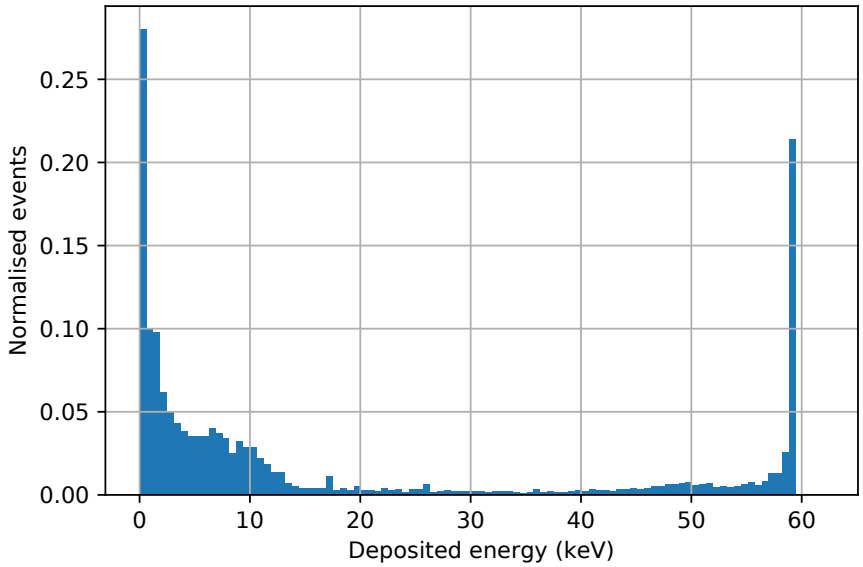

Figure 3.4.: The simulated deposited energy spectrum of a Dosepix detector irradiated with an ^{241}Am calibration source. The histogram is normalised to reflect the event density.

The Allpix^2 simulation of the detector does not include the signal processing of the ASIC of Dosepix. Instead, it returns the energy depositions within the attached sensor while considering the pixelation of the detector. Figure 3.4 shows a histogram of the deposited energies of a Dosepix detector for the irradiation with an ^{241}Am source. The histogram is normalised to reflect the density of the registered events. Since the detector's hardware is not simulated, there is no energy resolution. The spectrum mainly consists of sharp lines, indicating the characteristic photon energies of the source, located at 16.6 keV, 26.34 keV, and 59.54 keV [41]. Other lines originate from fluorescences of materials of Dosepix itself, the readout-hardware, or the housing of the Am-source, which mainly consists of tungsten and hard lead. Note that emitted and deposited photon energies are not identical as explained and analysed in section 3.1.3. The full energy peaks are skewed towards lower energies due to charge sharing and the Compton effect (see sections 2.1.1 and 2.2.3 for more details). Broader peaks in the spectrum are discernible at energies close to 11.25 keV, the Compton edge of the initial photon energy of 59.54 keV, and 48.54 keV, corresponding to the minimum energy of a scattered photon. The peak at low deposited energies originates from charge

sharing and Compton scattering. It includes events that contain only small fractions of the total deposited energy of interactions in the sensor. Being able to register these low energy events is an advantage of the simulation. In measurements, they cannot be detected since their energy is below the detector's energy threshold.

A deposited energy spectrum like in figure 3.4 cannot be directly compared to measurements due to the missing energy resolution of the detector. This resolution depends on various factors and has to be determined from measurements first. Each pixel has its own resolution, depending on the quality of the calibration from deposited energy to ToT. A spectrum measurement is usually made by combining all pixels, either all large or all small ones. Since there is a variation from pixel to pixel, it influences the detector's total resolution. Figure 3.5 depicts measurements of various radioactive sources with a Dosepix detector, represented by the blue curves. The plots in the figure comprise two calibration sources, ^{241}Am and ^{133}Ba, as well as two fluorescence-measurements of Gd and Sn targets. The used ^{133}Ba source is encapsulated in plastic, mostly absorbing all emitted positrons. For these sources, MC simulations are performed like previously described. As a result, sharp energy spectra are provided. These are broadened via a normal function whose standard deviation σ is described via

$$\sigma(E) = A \cdot \exp(-k \cdot E) + c \tag{3.1}$$

as a function of deposited energy E. The parameters of σ are optimised by broadening the MC spectra and calculating the distance in regards to the measurements. Here, both datasets use the same binning and are normalised to their maxima each. A Savitzky-Golay filter [42] is applied to smooth the data. A loss is introduced as

$$\mathcal{L} = \sum_{i=1}^{N_{\text{hist}}} \left| y_{\text{MC},i} - y_{\text{data},i} \right| \tag{3.2}$$

which is the sum over the differences of the entries y_i in the bins i of two histograms, one for MC simulation and one for measurement. Each histogram consists of N_{hist} bins. The four datasets depicted in figure 3.5 are optimised at once. This is achieved by calculating loss $\mathcal{L}$ for each dataset and taking the sum of all losses afterwards. This sum is the object of minimisation to determine the parameters of equation 3.1 via Nelder-Mead optimisation [43]. The results are listed in table 3.1.

A (keV)	k $\left(\frac{1}{\text{keV}}\right)$	c (keV)
2.735	0.092	1.197

Table 3.1.: Optimised parameters of equation (3.1) which describes the energy resolution σ of a Dosepix detector.

The corresponding curve of equation (3.1) as a function of deposited energy E is depicted in figure 3.6. Parameter c corresponds to the offset of the curve indicated

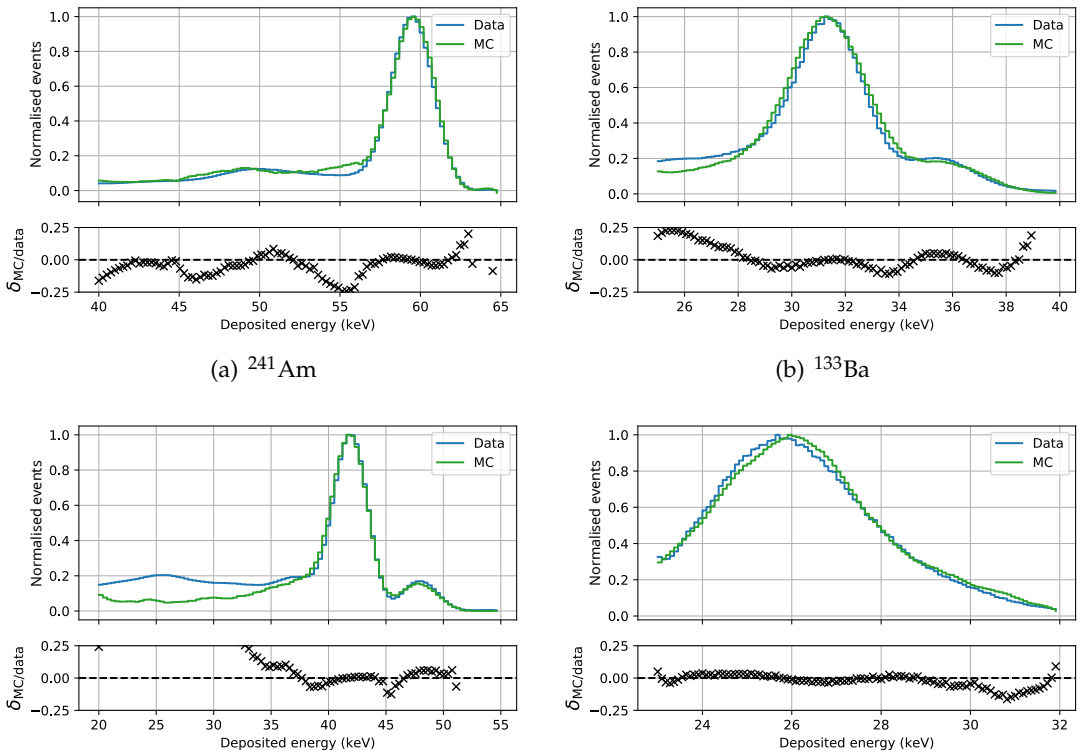

(a) ^{241}Am

(b) ^{133}Ba

(c) Gd-fluorescence

(d) Sn-fluorescence

Figure 3.5.: The measurements of various calibration sources and fluorescences, resembled by blue curves. Their corresponding MC simulations are depicted in green. All MC simulated curves have the same detector resolution according to equation 3.1 and the parameters in table 3.1 applied. The histograms are normalised to their maximum each. The bottom plots of the subplots show the deviation $\delta_{\mathrm{MC/data}}$ according to equation 3.3 of MC simulations and measurements.

by the black dashed line. $A - c$ describes the intercept with the y-axis at $E = 0$, and k represents the curve's shape. With the optimised parameters, the agreement of measurements and MC simulation is evaluated by calculating

$$\delta_{\mathrm{MC/data}} = \frac{y_{\mathrm{data}} - y_{\mathrm{MC}}}{y_{\mathrm{data}} + y_{\mathrm{MC}}}. \tag{3.3}$$

The corresponding values are depicted in the bottom plot of each subplot of figure 3.5. All curves generally agree well, with the absolute value of the deviation $\delta_{\mathrm{MC/data}}$ ranging within 0.25. The deviations are largest at energies two characteristic peaks are close to each other or at transitions from a full energy peak to the energies deposited via photoelectric effect by Compton-scattered photons. Even small deviations along

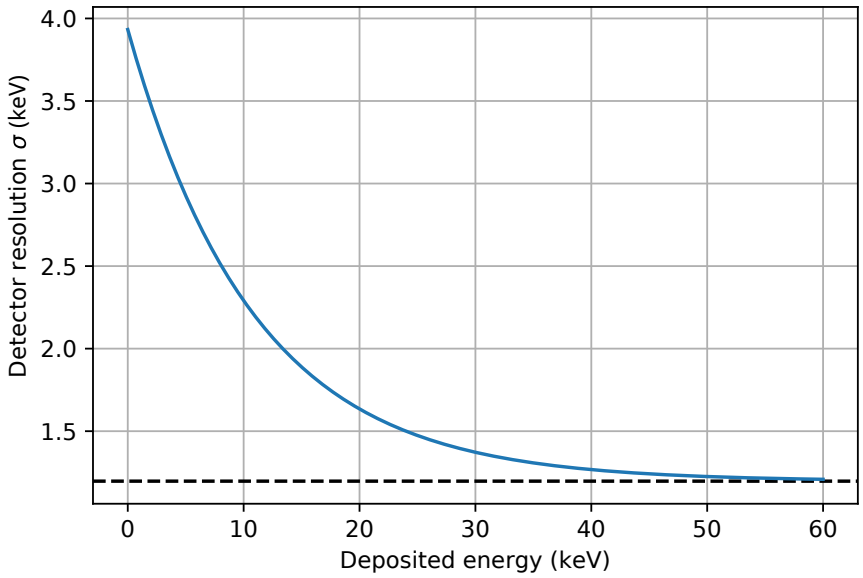

Figure 3.6.: The energy resolution σ in terms of standard deviation for a Dosepix detector. Equation (3.1), utilising the optimised parameters in table 3.1, is depicted as a function of deposited energy.

the energy-axis lead to large deviations for the number of registered events for these regions. All plots in the figure depict the important regions close to the features of a spectrum. Outside of these ranges, deviations like in 3.5 (c) show. At about 25 keV, the simulation underestimates events due to an incorrect modelling of the detector's surroundings and a resulting lack of fluorescence photons. These probably originate from antimony within hard lead blocks positioned close to the detector or the X-ray tube.

In conclusion, the optimisation of the energy resolution of MC simulations to measurements provides an excellent method to estimate a detector's characteristics. It additionally evaluates the quality of the simulation and justifies its later use in applications. Another method to determine the resolution is to take measurements and fit Gaussian functions to the full energy peaks to provide the corresponding standard deviations. This only works well if peaks are isolated, i.e. there are no overlaps of other peaks in the measured deposited energy spectrum. This seldomly is the case and might lead to a distortion of the estimated standard deviation. In the MC optimisation case, this is no issue since the simulation includes all characteristic lines of a spectrum.

3.1.3 Conversion of initial photon to deposited energy

Only a fraction of a deposited energy is registered by a single pixel. This is due to the limited volume of the silicon sensor and the pixelation of Dosepix. Charge sharing and Compton effect then distort the registered deposited energy spectrum.

In MC simulations, monoenergetic gamma sources with energy E_{init} emit photons on the detector, which registers a spectrum centred at the mean value of the deposited energy E_{dep}. E_{dep} is estimated by fitting an equation consisting of the sum of a normal distribution and an error function in the form of

$$\begin{aligned} f_{\text{erf}}(E, A, \mu_E, \sigma_E) &= \frac{A}{2} \cdot \left(\text{erf}\left(\frac{E - \mu_E}{\sigma_E} \right) + 1 \right), \\ f_{\text{norm}}(E, A, \mu_E, \sigma_E) &= A \cdot \exp\left(-\frac{(E - \mu_E)^2}{\sigma_E^2} \right), \\ f_{\text{norm+erf}}(A_1, A_2, \mu_E, \sigma_E, o) &= f_{\text{norm}}(E, A_1, \mu_E, \sigma_E) + f_{\text{erf}}(E, A_2, \mu_E, \sigma_E, d) + o \end{aligned} \tag{3.4}$$

to estimate the value of μ_E, corresponding to E_{dep}. All other parameters are used to describe the trend of the data but are neglected after the fit. The optimisation procedure is depicted in figure 3.7. Multiple simulations for different initial energies E_{init} and their deposited energy spectra are depicted. Before the fit, only the region about the peak is selected. Due to the skewness of a peak, the mean deposited energy is not identical to the mode. This discrepancy is especially noticeable for small pixels as the background contribution to the peaks is significantly large.

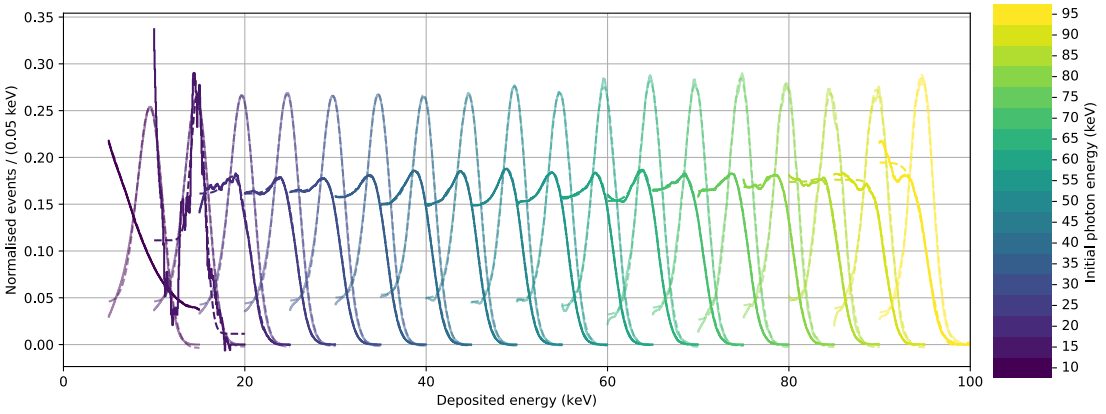

Figure 3.7.: The simulation of deposited energy spectra for different monoenergetic photon sources. A (normal + erf)-function (3.4), resembled by dashed lines, is fitted to each peak to estimate the mean deposited energy. The light-coloured curves represent large pixels and the saturated colours small pixels.

Figure 3.8 shows the ratio of deposited and initial energy $\frac{E_{\text{dep}}}{E_{\text{init}}}$ for different initial energies. For small pixels, the lower the initial energy, the noisier the determined fraction. The peak in the deposited energy spectrum gets closer to the low energy part of the spectrum until it merges with it completely. The low energy events, about 20 keV and less, are mostly charge sharing and Compton events, representing an approximately exponentially decreasing distribution. For initial photon energies of less than 20 keV, the fits for the small pixels as depicted in figure 3.7 fail. The conversion from initial to deposited photon energy is mainly performed to match peak positions to corresponding photon energies. Since no peaks are discernible for low initial energies of small pixels, this energy range is neglected.

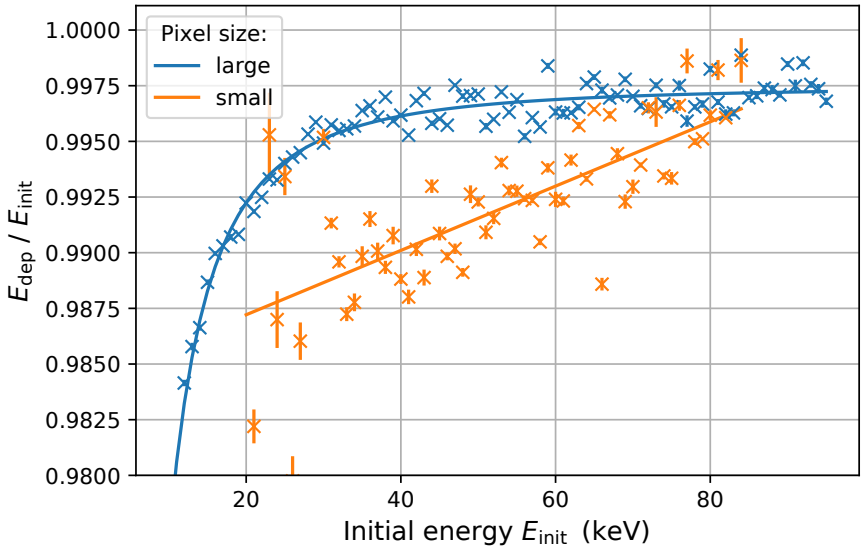

Figure 3.8.: The ratio of deposited and initial energy $\frac{E_{\text{dep}}}{E_{\text{init}}}$ as a function of initial energy. The error bars represent the fit errors of the mean deposited energies of the peaks. The data for the small pixels is depicted in orange, fitted with equation (3.6). The blue data points resemble the large pixels, fitted with equation (3.5).

For larger initial energies, the number of registered events in the peak decreases until it is no longer distinguishable from the remaining spectrum. This is due to the small effective size of the small pixels. With increasing initial energy, the probability of charge sharing increases and therefore, the peak ultimately disappears, which is discernible in figure 3.7.

The trend of the data for the large pixels is described via the hyperbolic function

$$f_{\text{dep/init}}(E_{\text{init}}) = \frac{a}{{E_{\text{init}}}^{b}} + c \tag{3.5}$$

$a(\mathrm{keV}^b)$	b	c	m (1 / keV)	t
-1.9 ± 0.5	1.96 ± 0.1	0.99749 ± 0.00016	0.000144 ± 0.000015	0.9843 ± 0.001

Table 3.2.: Optimised parameters of equations (3.5) and (3.6), for large and small pixels, describing the ratio of deposited and initial energy as a function of initial energy $f_{\mathrm{dep/init}}(E_{\mathrm{init}})$.

and via a linear function for the small pixels

$$f_{\mathrm{dep/init}}(E_{\mathrm{init}}) = m \cdot E_{\mathrm{init}} + t. \tag{3.6}$$

Table 3.2 shows the optimised values of the parameters of $f_{\mathrm{dep/init}}$ for small and large pixels. Finally, the conversion from initial to deposited energy is executed via

$$E_{\mathrm{dep}}(E_{\mathrm{init}}) = f_{\mathrm{dep/init}}(E_{\mathrm{init}}) \cdot E_{\mathrm{init}}. \tag{3.7}$$

3.2 Dosimetry with the Dosepix detector

The hardware features of Dosepix allow for measurements of personal dose equivalents [7]. This is vital for staff that is occupationally exposed to X-radiation. Typically, passive dosemeters are utilised to monitor this exposure. The accumulated dose is read-out in fixed intervals, usually once a month. Active personal dosemeters like the proposed Dosepix dosemeter are not allowed for legal radiation protection. This is mainly because most dosemeters show bad responses in pulsed radiation fields as they either underestimate the dose or fail to determine a dose at all [2]. This is not the case for Dosepix which can correctly work under such conditions as dead-time free data acquisition is possible. Active personal dosemeters give direct responses to the bearer of the system. The currently accumulated dose is shown at any time, and warning signals, like when exceeding a dose threshold, can be implemented.

Therefore, the performance of Dosepix in regards to the personal dose equivalents $H_{\mathrm{p}}(10)$ and $H_{\mathrm{p}}(0.07)$ (see section 2.4 for more details) is analysed in the following. The detector setup used to perform these measurements is introduced and implemented in MC simulations. A conversion from registered events and their deposited energies to dose values is determined using these results. The performance is finally evaluated via measurements.

3.2.1 Dosepix dosemeter setup

As established in [10, 44], the setup for a dosemeter according to figure 3.9 is chosen as it has proven to be promising for dosimetry applications. The setup consists of three Dosepix detectors with different types of filters installed in front of them. The first detector, depicted on the right-hand side of the image, is equipped with a hollow

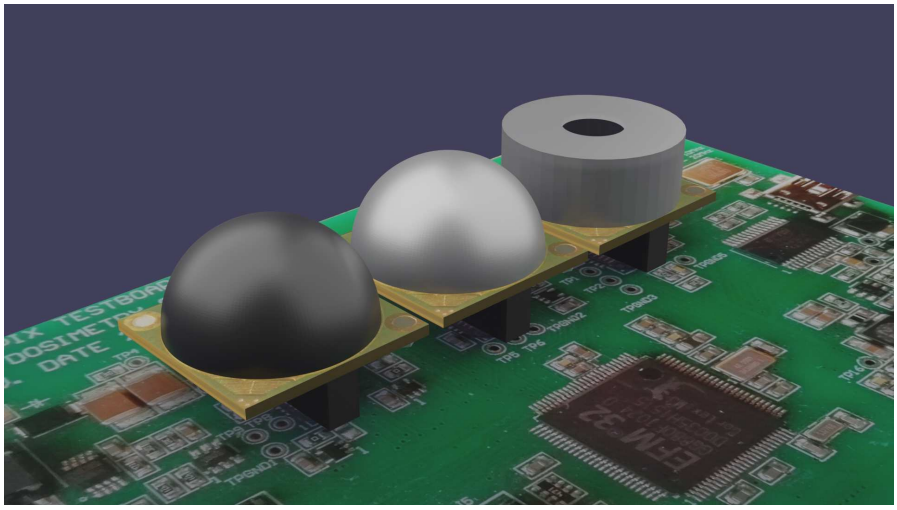

Figure 3.9.: Render of the setup used for personal dosimetry applications. It consists of three Dosepix detectors with different filters attached to them. These are a hollow aluminium cylinder (right) and two hollow hemispheres, one made of aluminium (centre) with a thickness of 2 mm and one of tin (left) and a thickness of 1 mm. Not shown in the picture is the PMMA-housing, usually surrounding the setup during measurements.

aluminium cylinder. Its top lid has a width of 0.25 mm. If the system is irradiated perpendicularly to the readout electronics' PCB, photons are not attenuated by this filter as it has a small opening at its top. Therefore, the detector is called *vacant* or in short *Vac* detector in the following. The second and third Dosepix, at the centre and left-hand side of the image, are both equipped with hollow hemispheres. One is made of aluminium and has a thickness of 2 mm, the other one consists of β-tin and has a thickness of 1 mm. These detectors are called *Al* and *Sn* in the following. The hemispherical shape is chosen to provide an attenuation almost independent of the irradiation angle of the applied photon field. The different filters change the initial photon spectrum via energy-dependent attenuation and Compton scattering to increase the information about the impinging photon spectrum. Not shown in figure 3.9 is the housing of the detector system, which has a PMMA lid of 1.5 mm at its top.

3.2.2 Slab phantom simulation

Phantoms are involved in evaluation measurements of the personal dose estimation capabilities of a dosemeter. These phantoms represent the body of a bearer of the dosemeter. In many applications, like for measurements of the personal dose equivalents of $H_\mathrm{p}(0.07)$ and $H_\mathrm{p}(10)$, the ISO water slab phantom defined in ISO 4037 [45, 46] is used. It consists of a hollow PMMA box with outer dimensions of 30 cm $\times$ 30 cm $\times$ 15 cm. The widths of the walls are 1 cm except for the frontal one that has

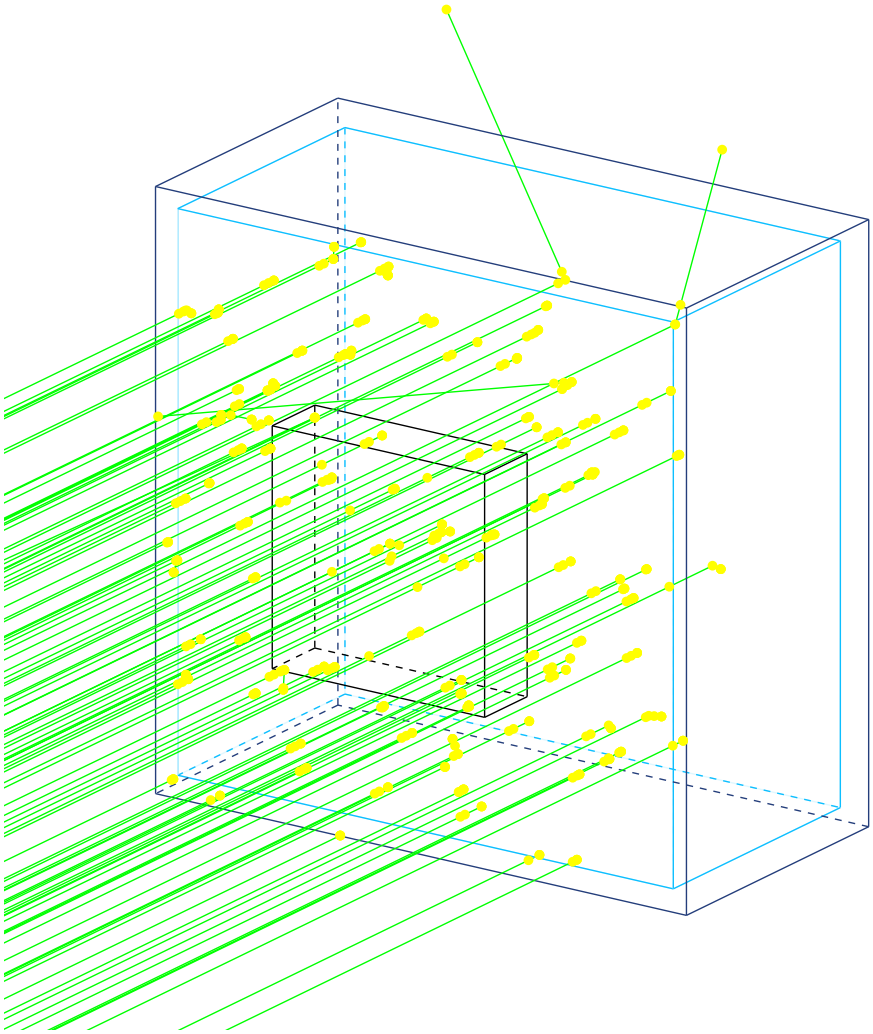

Figure 3.10.: Geant4 simulation for the determination of the characteristics of scattered photons from the ISO water slab phantom [45, 46]. The phantom is represented by the large blue box filled with water, indicated by the light-blue volume. Photons are perpendicularly emitted on the frontal surface of the phantom. The smaller black box directly attached to the phantom is a perfect detector. It is configured to only detect photons that previously had an interaction with the phantom.

a width of 0.25 cm. The characteristics of human tissue are reflected by additionally filling the box with water. The conversion factors from photon fluence to personal dose equivalents are calculated under the assumption of a parallel photon field. This approximately corresponds to measurements where the detector has a large distance to the radiation source. The whole surface of the phantom must be irradiated ho-

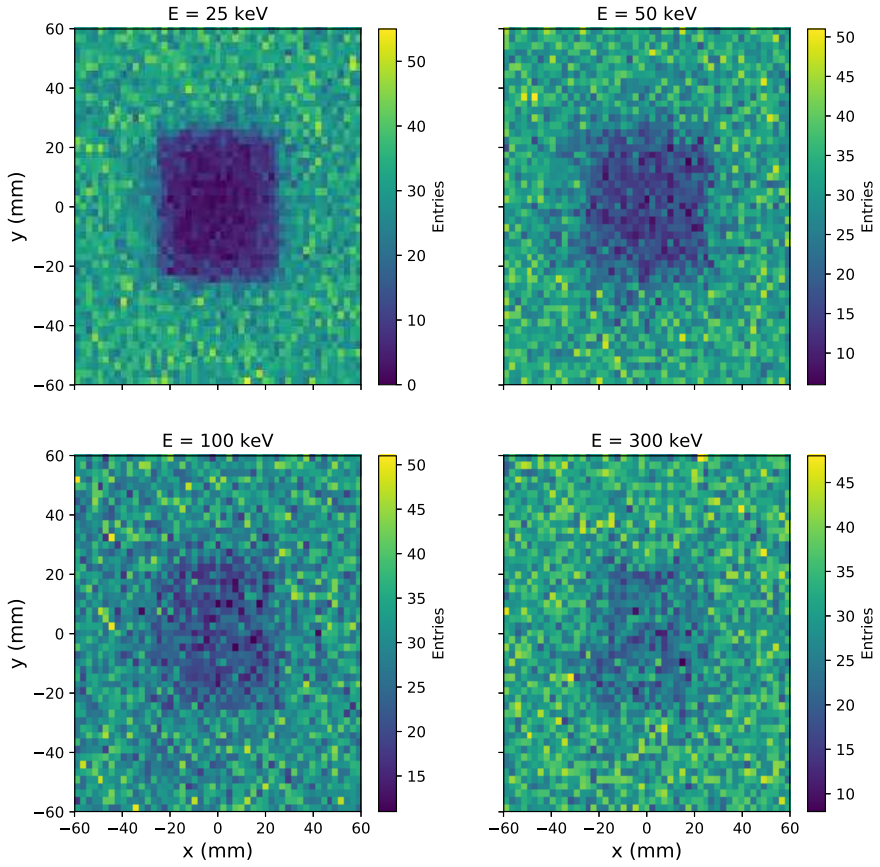

Figure 3.11.: The distribution of the x- and y-coordinates of photons scattered from the slab phantom and detected by the perfect detector. The setup is depicted in figure 3.10. The detector only detects photons that previously interacted with the phantom. Only x- and y- positions that lie within the detector's surface attached to the phantom are included. The titles of the individual plots denote the energy of the impinging photons.

mogeneously. The same requirements exist for the simulation. However, a problem regarding statistics exists. The photon flux must remain constant over the entire irradiated surface. The area of the Dosepix detectors in comparison to the area of the phantom is remarkably small. Photons directly emitted on the detectors have the highest probability to be detected. All photons emitted on the surroundings first have to undergo scattering processes to reach the detector. Therefore, a large number of particles has to be simulated to get sufficient statistics of registered events.

A method to speed up the simulation is introduced. A precalculation is performed as previously described for the simulation of the X-ray fluorescence setup. The whole process is divided into two stages. In the first stage, the characteristics of the photons

scattered from the phantom are analysed. In the second stage, the detector simulation, the phantom is replaced with the previously determined photon distributions. The whole process is described in detail in the following. The surface of the slab phantom is irradiated with monoenergetic photons to determine the characteristics of scattered photons as depicted in figure 3.10.

The source is parallel to the phantom's outer surface, so the direction of emitted particles is perpendicular to it. The surface of the radiation source is identical to the phantom's surface. The green tracks in the figure correspond to photon tracks. The yellow dots indicate either interactions with matter. A perfect detector is attached to the outer surface of the phantom, indicated by the black box. It has dimensions of $12\,\text{cm} \times 12\,\text{cm} \times 3.5\,\text{cm}$. The volume is chosen to be large enough to act as a placeholder for the Dosepix system. The perfect detector is configured to only register photons that previously interacted with the slab phantom and to kill tracks that are directly irradiated on it. Once a scattered photon reaches the detector, the event's characteristics are recorded. The x-y-plane of the coordinate system is parallel to the outer surface of the slab phantom as illustrated in figure 3.12 (a). The z-axis is perpendicular to the phantom's frontal surface and points away from it. The registered event characteristics include the kinetic energy E_{kin}, the cartesian coordinates the photons reached the perfect detector $\vec{x}$, and the angles in spherical coordinates, ϕ and θ, the particle entered the detector according to the coordinate system of figure 3.12 (b). The distributions of the detected events are presented in the following.

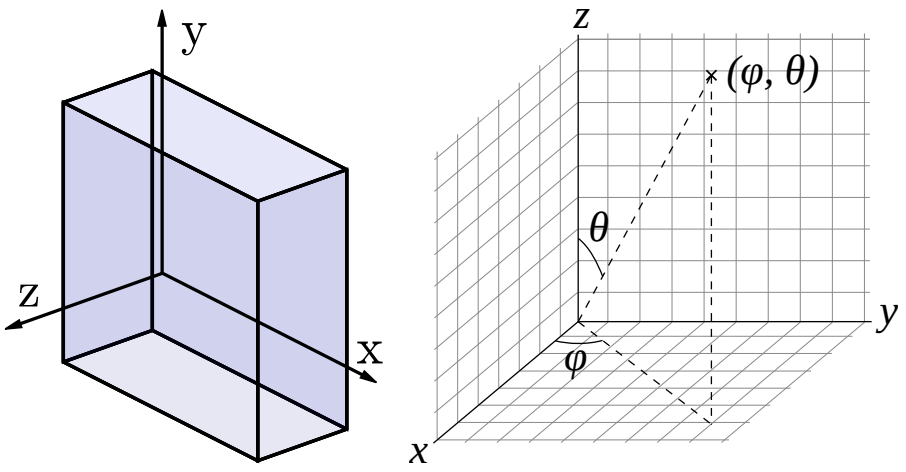

(a) Coordinates of the slab phantom (b) Spherical coordinates

Figure 3.12.: (a) depicts the coordinate system for the slab phantom. The origin is located at the centre of the frontal surface. (b) depicts the spherical coordinate system used to represent direction and position angles of photons. The image is a modified version of [47].

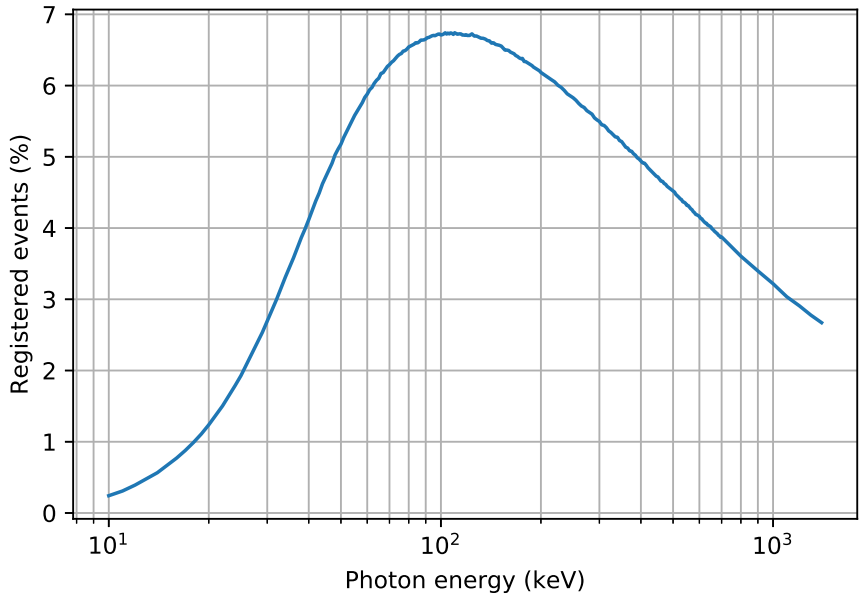

Figure 3.13.: The percentage of scattered photon events registered by the perfect detector sitting in front of the slab phantom as shown in figure 3.10. The calculations are performed for different initial photon energies. The percentage is determined in regards to the total number of events emitted on the phantom's surface.

Figure 3.11 shows a histogram of the x- and y-coordinates of $\vec{x}$. Only coordinates at the surface of the perfect detector attached to the phantom are included. The depicted x-y-plane is shielded from direct irradiation and only includes scattered photons. Four plots are shown, each corresponding to different energies of the emitted photons according to the titles. For low energies, a region with low statistics is deduced at the centre of the perfect detector. The region has a rectangular shape due to the shape of the detector. As energy increases, the probability for photons to reach the central part of the detector's surface increases, and the distributions get increasingly homogeneous.

A related distribution of registered events is depicted in figure 3.13. It shows the percentage of registered events of the perfect detector. The fraction is calculated in regards to the total number of photons emitted on the phantom's surface. With increasing photon energy, more scattered events are detected. The maximum is reached at about 100 keV. The number of registered events decreases for even higher energies as the interaction probability of a photon is reduced, and the particles can enter the phantom in greater depth. If scattering of a photon occurs, its energy reduces, and the probability to interact increases, and the photon may not be able to leave the phantom as photoelectric absorption may take place. Figure 3.14 depicts the energy spectra

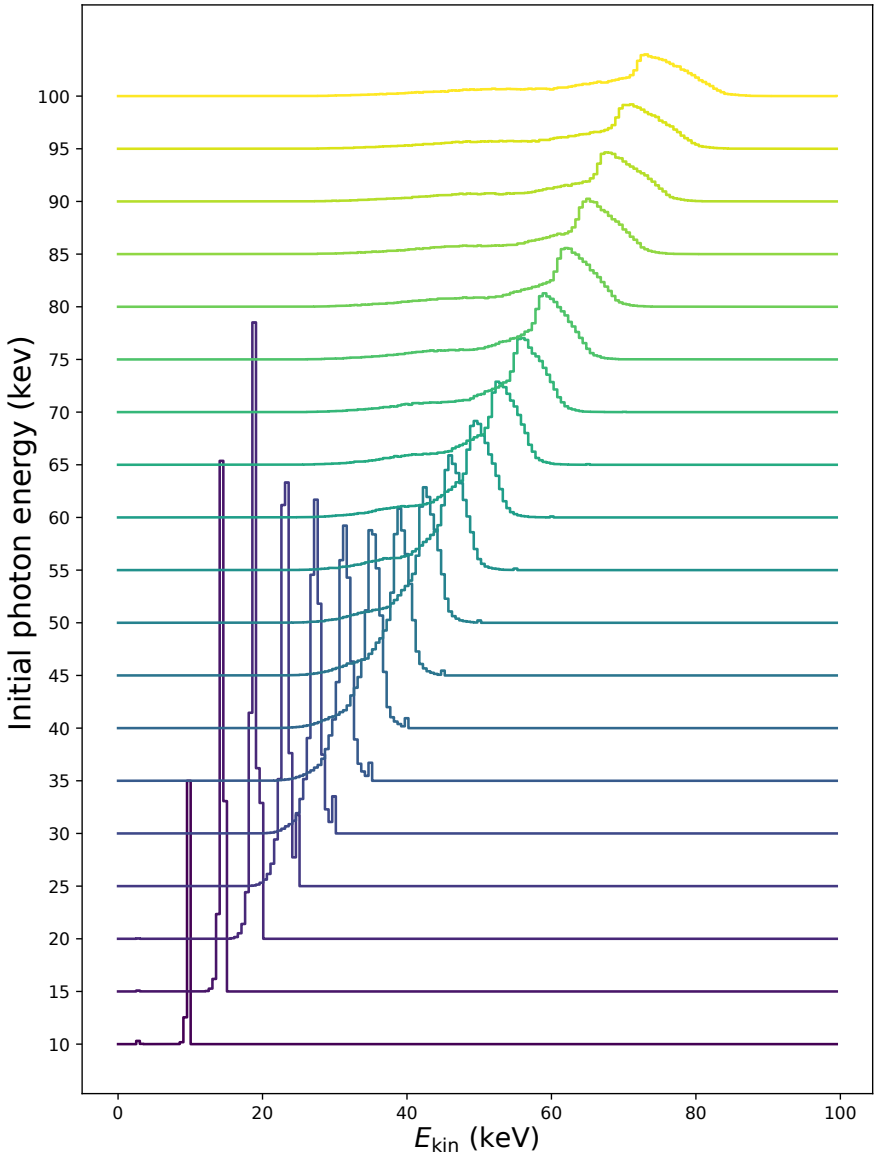

Figure 3.14.: The distributions of kinetic energies E_{kin} of photons scattered from the slab phantom and detected by the perfect detector of the setup in figure 3.10. The y-axis corresponds to the initial energy of the emitted photons.

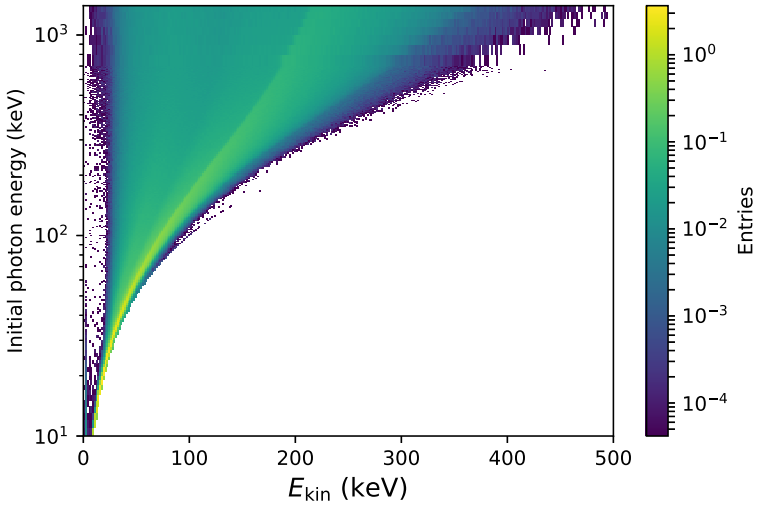

Figure 3.15.: The correlation of kinetic energies E_{kin} and initial energies of photons scattered from the slab phantom and registered by the perfect detector of the setup in figure 3.10. The number of registered events, indicated by the colours according to the colour bar, is scaled logarithmically.

as detected by the perfect detector mounted to the slab phantom's frontal surface for different initial photon energies.

Another perspective on these distributions, including even higher photon energies, is depicted in figure 3.15 in the form of a 2D-histogram. The number of registered events, indicated by the colours, is scaled logarithmically. The shapes of the energy spectra are explained via an example. The spectrum for an initial photon energy of 100 keV shown in figure 3.16 (a) is used. In (b), the correlation of kinetic energy E_{kin} to angle θ is depicted. θ describes the angle between the z-axis, perpendicular to the outer surface of the slab phantom, and the x-y-plane. The spectra always show the true photon energy as a perfect detector is utilised. Two dashed lines are included in (a). The line at the lower energy corresponds to the energy of a photon that interacted via perfect Compton-backscattering. The line at the high energy indicates the energy of a photon after Compton scattering under 90°. Since the perfect detector only detects events that previously interacted with the slab phantom, angles θ within a range of $[0°, 90°]$ are observed in (b). It seems impossible that energies greater than the right dashed line, corresponding to scattering under 90°, exist. However, this is possible if multiple scatterings take place in succession. For example, one scattering under 90° for primary energies of 100 keV results in a photon with 83.63 keV. When scattering twice, each time under 45°, the photon has an energy of 89.72 keV. The energy spectrum for energies lower than the left dashed line in (a) mainly corresponds to events scattered multiple times within the slab phantom. The description of the exact shape of the energy spectrum for multiple scatterings is complicated since also

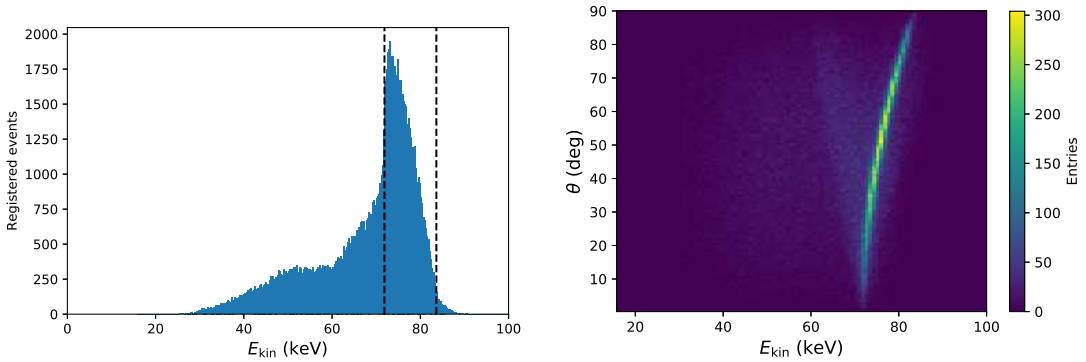

(a) Energy spectrum

(b) E_{kin} vs. θ

Figure 3.16.: (a) shows an exemplary energy spectrum of photons scattered from the slab phantom and detected by the perfect detector attached to the front of the slab phantom. An initial photon energy of 100 keV is used. The left dashed line corresponds to the energy of a photon after perfect Compton-backscattering, while the right one indicates the energy for a scattering under 90°. (b) depicts the corresponding correlation between the registered kinetic energy E_{kin} and scattering angle θ.

the distribution of the scattering angle, according to the Klein–Nishina formula has to be taken into account. However, the MC simulation considers all these influences. For low initial photon energies, another scattering process is visible, represented in figure 3.14 for initial energies of up to about 60 keV. Small but sharp peaks for E_{kin} of the scattered photons at approximately the initial energy are visible. These are due to coherent scattering where no energy transfer to an electron takes place.

Figure 3.17 depicts the correlation of the directions of photons scattered from the slab phantom and registered by the perfect detector as a function of the initial photon energy. All directions are given in spherical coordinates according to the coordinate system in figure 3.12 (b). The angles ϕ, shown in figure 3.17 (a), and θ in (b), only slightly depend on the initial energy of the primary photons.

The shape of the distribution in (a) is explained via an approximate description of the perfect detector's and the phantom's geometry. First, it is assumed that the frontal surface of the slab phantom is infinitely large. Photons are emitted perpendicularly on the surface but scatter isotropically from it. The sketch in figure 3.18 depicts a top view of the perfect detector's frontal surface. The arrowed line corresponds to the side of the effective surface A of the detector irradiated by photons scattering under an angle of ϕ. A is then proportional to

$$A \propto |\sin(\phi)| + |\cos(\phi)|. \tag{3.8}$$

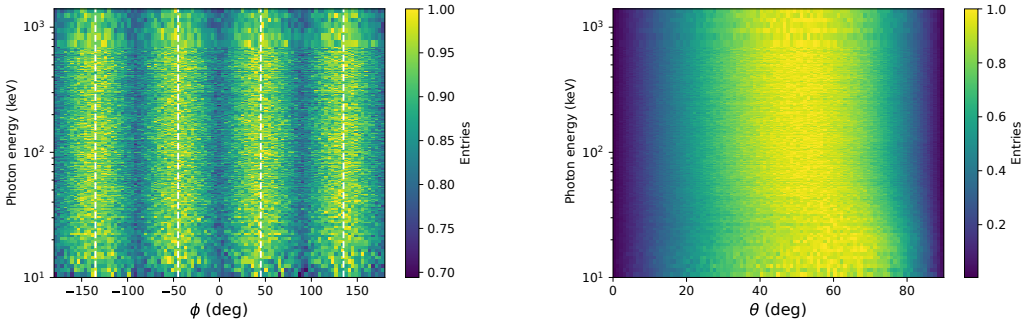

(a) ϕ-distribution (b) θ-distribution

Figure 3.17.: The figure shows the distributions of the directions photons' scattered from the slab phantom, detected by the perfect detector attached to its frontal surface. The directions are given in spherical coordinates according to the coordinate systems in figure 3.12. (a) shows the correlation of angle ϕ and (b) of angle θ in regards to the initial photon energy. In (a), white lines additionally indicate the maxima of the distribution.

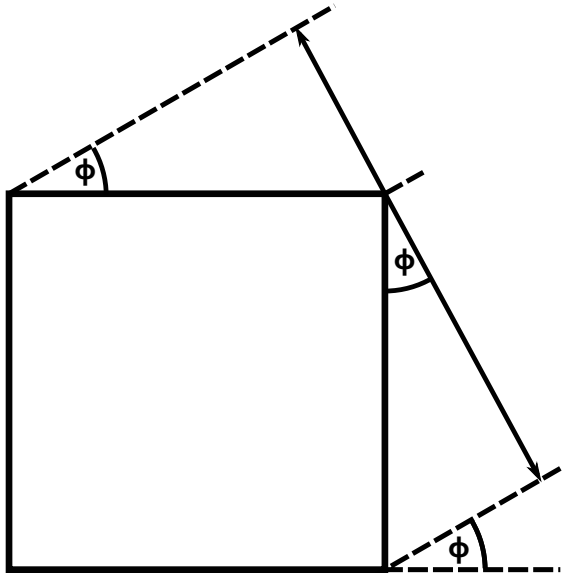

Figure 3.18.: Sketch of the top view of the frontal surface of the perfect detector attached to the slab phantom. ϕ corresponds to the angle of irradiation of the scattered photons. Under the assumption that the detector extends infinitely in the direction of z, the effective irradiated surface is proportional to the arrowed line's length in the sketch.

This function corresponds to the event density and position of maxima illustrated in figure 3.17 (a). The height of the perfect detector mostly explains the distribution shown in (b). Due to the detector's extension in z-direction, there is a higher probability to register events on its sides which is reflected by angles θ.

3.2.3 Dosepix detector simulation

In the second stage of the complete simulation, the previously described characteristics of photons scattered from the slab phantom are implemented in an Allpix^2 simulation. The percentage of registered events in figure 3.13 shows that only a small fraction of N emitted events leads to photons reaching the perfect detector, i.e. coming even close to the Dosepix detectors. The illustrated probability is called p_{pd} in the following, where the index represents „perfect detector". The remaining events are neglected and are not included in the Dosepix detector simulation. The photon field is parallel and its fluence constant. It is defined by $\Phi = \frac{N}{A_{\mathrm{ph}}}$, with A_{ph} the area of the frontal surface of the phantom, i.e. 30 cm $\times$ 30 cm. The index „ph" represents „phantom". The number of photons N_{dir} directly emitted on the area where previously the perfect detector was located is described via

$$N_{\mathrm{dir}} = A_{\mathrm{pd}} \cdot \frac{N}{A_{\mathrm{ph}}}. \tag{3.9}$$

Here, A_{pd} denotes the surface of this detector of 12 cm $\times$ 12 cm. The complete setup is used in the simulation, including the Dosepix detectors with filters installed, the readout electronics, and the housing. The slab phantom is still required since the perfect detector previously shielded it from photons.

In case of N_{dir}, events are generated and emitted on surface A_{pd}. The corresponding scattered photon events of the phantom N_{ph} are sampled from the precalculated distributions. Their number is described via

$$N_{\mathrm{ph}} = N \cdot p_{\mathrm{pd}}. \tag{3.10}$$

In total, only $N_{\mathrm{sim}} = N_{\mathrm{ph}} + N_{\mathrm{dir}}$ events have to be simulated. This results in a reduction of the number of generated events in the detector simulation by a factor of

$$p_{\mathrm{sim}} = \frac{1}{N}\left(N_{\mathrm{ph}} + N_{\mathrm{dir}}\right) = \frac{A_{\mathrm{pd}}}{A_{\mathrm{ph}}} + p_{\mathrm{pd}}. \tag{3.11}$$

Here, equations (3.9) and (3.10) are utilised. The first summand is 16% while the second one, i.e. p_{pd} according to figure 3.13, lies within a range of 0 to about 7%. This results in a reduction of simulated events by a factor of about 4 to 6, depending on the initial energy of the photons. This factor approximately corresponds to a speed-up of the calculation time required to perform the complete simulation.

Equation (3.11) is rearranged to

$$N = \frac{N_{\text{sim}}}{p_{\text{sim}}} \tag{3.12}$$

for practical reasons. This result allows providing the true number of photons N corresponding to N_{sim} simulated events. When performing the simulation, N_{sim} is split into directly emitted events N_{dir} and scattering events from the phantom N_{ph} via fraction

$$p_{\text{split}} = \frac{N_{\text{dir}}}{N_{\text{sim}}} = \frac{A_{\text{pd}}}{A_{\text{pd}} + (A_{\text{ph}} - A_{\text{pd}}) \cdot p_{\text{pd}}} \tag{3.13}$$

and the relations $N_{\text{dir}} = p_{\text{split}} \cdot N_{\text{sim}}$ and $N_{\text{ph}} = (1 - p_{\text{split}}) \cdot N_{\text{sim}}$. p_{split} lies in the range of 70% to 100%.

3.2.4 Dosepix dosemeter simulation

The setup of the Dosepix dosemeter is simulated as described in the previous section. The determined response spectra of the different detectors are depicted in figure 3.19. Only large pixels are considered in the following.

The number of registered events as a function of initial photon energy and registered deposited energy is shown. The number of emitted photons is the same for each initial photon energy. The colours are scaled logarithmically to reflect the features of the spectra better. The titles of the plots correspond to the filters of the detectors according to section 3.2.1. Dash-dotted lines indicate the energies of the Compton edge and the energy of a perfectly backscattered photon. The dashed line represents the full energy peaks in the spectra.

Figure 3.20 depicts the photon detection efficiency $\varepsilon = \frac{N}{\Phi}$ of the different Dosepix detectors determined via simulation. It corresponds to the fraction of registered events N and photon fluence Φ as a function of photon energy. The colours of the curves represent the Dosepix filters according to the legend.

The applied photon field is perpendicular to the frontal surface of the phantom. Photons are attenuated by the housing surrounding the detector system. For the *Vac* detector, no additional filter is present for photons from this direction. This is reflected by the number of registered events which is the highest compared to the other detectors, especially for low energies. For the *Al* and *Sn* detectors, the hemispherical filters additionally attenuate the photons. The attenuation is highest for the *Sn* detector, registering almost no events for initial energies below 40 keV. With increasing energy, the behaviour of the *Vac* and *Al* detectors begins to match and is almost identical once energies are greater than about 80 keV. The probability of a photon interacting with the detectors' filters via photoelectric effect is negligible for these energies. It effectively renders the attenuation of the filters ineffective. Only the filter of the *Sn* detector is attenuating photons for energies of up to about 200 keV. The detector responses are now utilised to perform analyses regarding dosimetry with the Dosepix detector system.

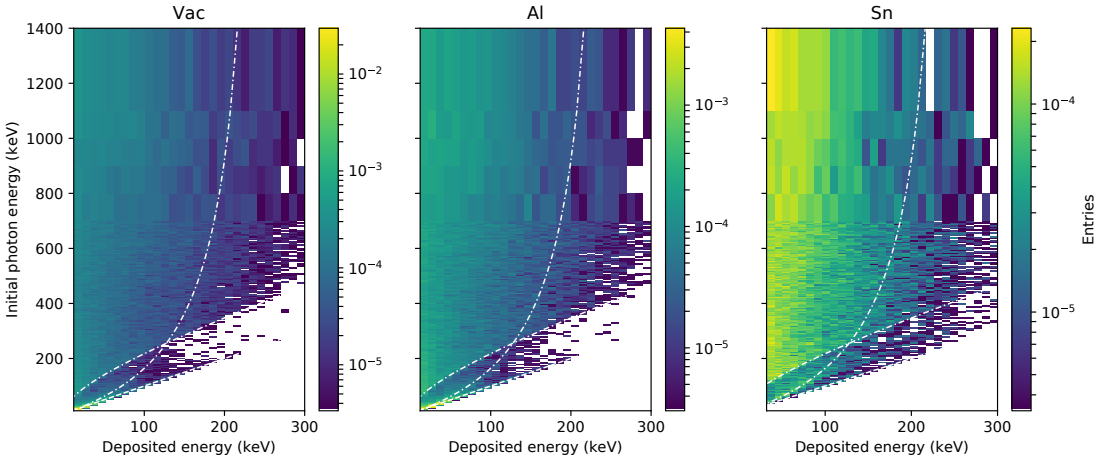

Figure 3.19.: Simulated response spectra for a monoenergetic photon field emitted perpendicularly on the slab phantom. The density maps show the number of registered events for the different Dosepix detectors as a function of initial photon energy and registered deposited energy. The number of events reflected by the different colours is scaled logarithmically. The labels of the plots correspond to the filters of the detectors according to section 3.2.1. Dashed-dotted lines indicate the Compton edge and the energy of a perfectly backscattered photon. Dashed lines represent the energies of the full energy peaks.

3.2.5 Dose reconstruction method

All measurements are performed with the Dosepix detectors operated in Dosi-mode (see section 2.1.2 for more details). The 16 bin edges b_i of each pixel of the histograms are set to the values listed in table A.1 of the appendix. These bins were determined heuristically. The last bin b_{16} counts all events of energies larger than its denoted value. The detector types correspond to the used filters of the detectors. The conversion from registered events $N_{d,i}$ per bin to dose equivalent H is performed according to [48, 49] via

$$H = \sum_{d} \sum_{i=1}^{16} k_{d,i} \cdot N_{d,i}, \tag{3.14}$$

where $d \in \{Vac, Al, Sn\}$ is the index corresponding to the filters of the detectors. $k_{d,i}$ denotes the conversion coefficients from registered events to dose for bin b_i of detector d. The error ΔH of H is estimated via

$$\Delta H = \sqrt{\sum_{d} \sum_{i=1}^{16} k_{d,i}^2 \cdot N_{d,i}}, \tag{3.15}$$

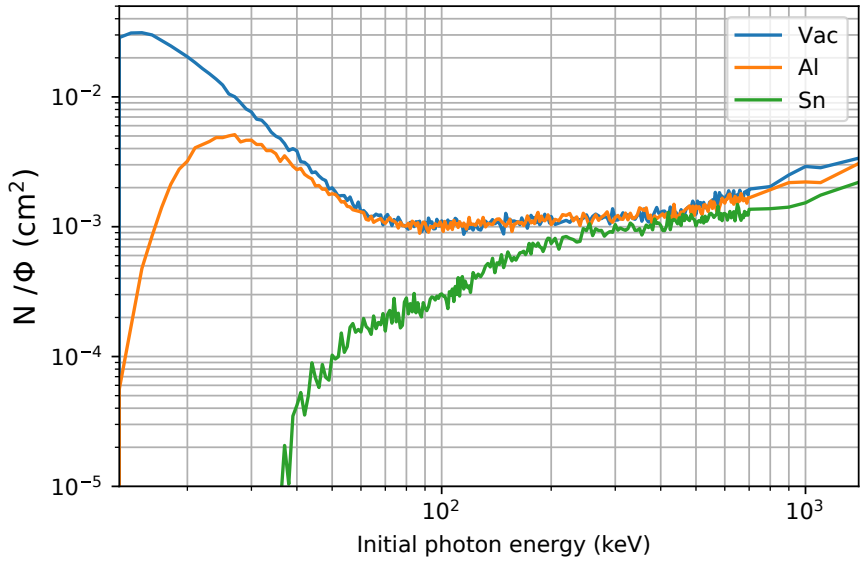

Figure 3.20.: The fraction of registered events N and fluence Φ of a parallel photon field emitted on the ISO water slab phantom [45, 46] as a function of initial energy. The colours correspond to the used filters in front of the Dosepix detectors, according to the legend.

where the assumption of $N_{d,i}$ being Poisson distributed is used. This is just an approximation effects like Compton scattering and charge sharing had to be considered (see [50] for a detailed description).

The dose response R is utilised to validate the performance of the detector system. It is calculated by taking the ratio of the measured personal dose equivalent H_{DPX} and the applied reference dose H_{ref}

$$R = \frac{H_{\mathrm{DPX}}}{H_{\mathrm{ref}}}. \tag{3.16}$$

A dosemeter shows a perfect performance if $R = 1$.

3.2.6 Simulation-based dose conversion coefficients

The conversion coefficients $k_{d,i}$ of equation (3.14) are optimised in regards to a perfect response according to equation (3.16) in the following. Only large pixels are considered. Photon spectra with different mean photon energies are required. If the spectrum is well known, the corresponding dose can directly be calculated via the photon fluence to dose conversion factors $\frac{H_{\mathrm{p}}}{\Phi}(E)$ depicted in figure 3.21. (a) shows the conversion to personal dose equivalent $H_{\mathrm{p}}(10)$, and (b) to $H_{\mathrm{p}}(0.07)$, both as a function of the initial photon energy. These factors represent a parallel photon field homogeneously emitted on the ISO water slab phantom [45, 46].

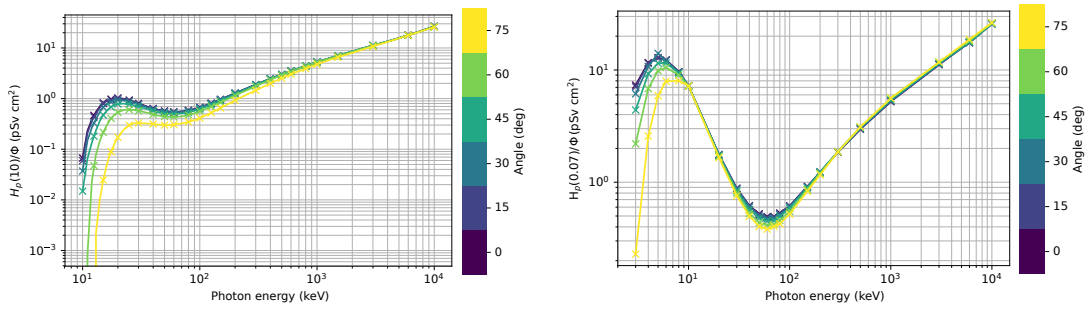

(a) $H_p(10)$ / Φ (b) $H_p(0.07)$ / Φ

Figure 3.21.: Conversion factors from photon fluence Φ of a monoenergetic parallel photon field emitted on a water slab phantom to personal dose equivalents. (a) shows the conversion to $H_p(10)$, (b) to $H_p(0.07)$. Different irradiation angles regarding the normal of the frontal surface of the slab phantom are given according to the colour bar. The data is taken from [45, 46].

Also included in the figure are the conversion factors for different irradiation angles. These are defined in relation to the normal of the frontal surface of the phantom. The curves of these datasets are coloured according to the colour bars, reflecting the irradiation angle. The photon fluence of a spectrum as a function of photon energy E is represented by $\Phi_{ir}(E)$, reflecting the number of emitted photons divided by the area of the slab phantom's frontal surface. The dose $H_{p,ir}$ corresponding to the spectrum is determined via

$$H_{p,ir} = \int dE\, \Phi_{ir}(E) \cdot \frac{H_p}{\Phi}(E). \tag{3.17}$$

In simulations, monoenergetic photons are used, i.e. equation (3.17) simplifies to a product. The reference doses for various initial energies are called $H_{ref,sim}$. The shapes of the registered deposited energy spectra for the different Dosepix detectors are determined via the previously introduced response spectra depicted in figure 3.19. These histograms are normalised to the number of emitted photons each. The number of registered events N_{DPX} for a mono-energetic photon spectrum of energy E with a corresponding photon fluence $\Phi_{ir}(E)$ is calculated via

$$N_{DPX} = \frac{N}{\Phi}(E) \cdot \Phi_{ir}(E), \tag{3.18}$$

with the photon detection efficiency $\frac{N}{\Phi}(E)$ according to figure 3.20. The simulated response spectra are then normalised so their sum reflects N_{DPX}.

The simulation provides deposited energy spectra that cannot be measured with a real Dosepix. The data has a dense binning, and there is no dead-time. This effectively

corresponds to Dosi-mode measurements with a large number of histogram bins instead of only 16. Therefore, to truly simulate the hardware, the binning according to the edges listed in table A.1 is applied. Figure 3.22 depicts this for the responses of an exemplary monoenergetic photon spectrum of 60 keV. The densely binned registered events are indicated by the y-axis on the left. The y-axis on the right resembles the rough binning of Dosi-mode. The different colours correspond to the filters used with the Dosepix detectors, according to the legend.

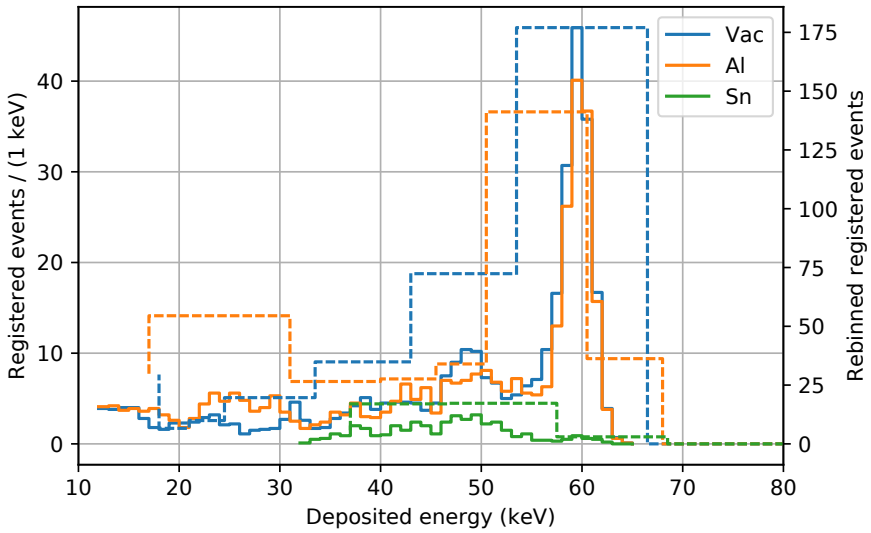

Figure 3.22.: The simulated respose of a 60 keV photon spectrum for the different Dosepix detectors of the dosemeter. The colours correspond to the filters of the detectors according to the legend. The y-axis on the left-hand side represents the densely binned histograms (solid) and the right-hand side the rebinned histograms (dashed). The rebinning is performed with the bin edge values of table A.1.

This binning process is applied to the whole simulation dataset of monoenergetic response spectra, providing the number of registered events $N_{d,i}$ for detector d and bin b_i each. The corresponding personal doses $H_{\mathrm{p,ir}}$ are calculated according to equation (3.17). Combining the values for the different photon energies results in three count matrices $\hat{N}_d$, and a dose vector $\vec{H}_{\mathrm{p}}$. Their relation is described by modifying equation (3.14) to

$$\vec{H}_{\mathrm{DPX,sim}} = \sum_d \hat{N}_d \cdot \vec{k}_d, \tag{3.19}$$

with d representing the different detectors of the dosemeter setup. Vector $\vec{k}_d$ describes the corresponding conversion coefficients from registered events to dose where each consists of 16 entries. This allows calculating a dose vector for the whole simulation

dataset directly. In an optimisation process, the coefficients $\vec{k}_d$ are adjusted until the loss

$$\mathcal{L} = \sqrt{\sum_j \left(\frac{H_{\mathrm{DPX,sim},j}}{H_{\mathrm{ref,sim},j}} - 1 \right)^2}, \tag{3.20}$$

where the sum over j iterates over the data for the different initial photon energies is minimised. The determined conversion coefficients are listed in table A.2 and are depicted in figure 3.23 for $H_\mathrm{p}(10)$ (a) and $H_\mathrm{p}(0.07)$ (b). The colours of the curves correspond to the filters of the detectors according to the legend. *Vac* and *Al* detectors show an increasing trend of the conversion coefficients as a function of deposited energy. The detection efficiency of the detectors decreases with increasing photon energy. If a photon of higher energy is detected, a compensation for photons that were not detected is made. This is achieved by applying a greater weight to the corresponding conversion factor. The trend of the factors is similar for both dose types, with only small variations in their values. This is because the conversion factors from fluence to dose equivalents, as depicted in figure 3.21, are very similar for most energies of the two dose types. Their biggest difference is for small energies, i.e. below about 40 keV.

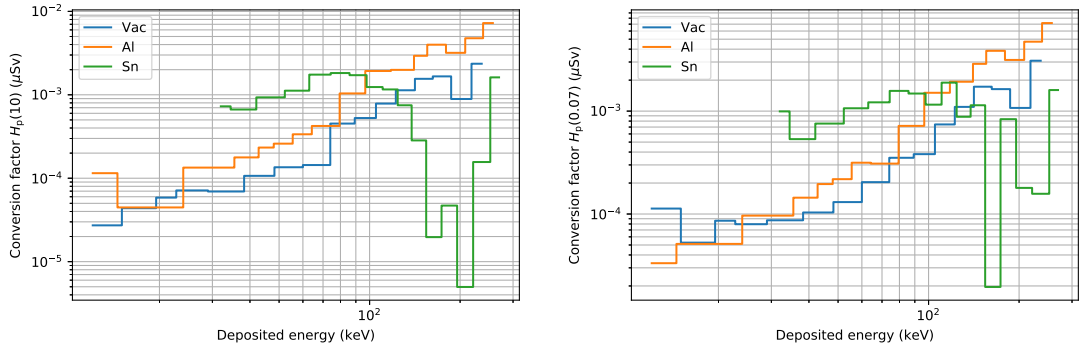

(a) $H_\mathrm{p}(10)$ (b) $H_\mathrm{p}(0.07)$

Figure 3.23.: Conversion coefficients from the number of registered events of the Dosepix detectors to personal dose equivalent. In (a), for $H_\mathrm{p}(10)$ and in (b), for $H_\mathrm{p}(0.07)$. The coefficients are optimised to simulation data only. The deposited energies correspond to the settings of the bin edges used in Dosi-mode.

This difference is also reflected in the trend of the conversion coefficients of figure 3.23. Generally, all curves are very smooth, which is favourable as the dose reconstruction process then is more robust against fluctuations in registered deposited energies. As will be shown in section 3.3, the measured ToT value varies with the temperature of the detector, leading to a discrepancy of the measured deposited energy and possibly

to the assignment to a wrong bin in Dosi-mode. If the conversion coefficients' trend is smooth, the error on the reconstructed dose is small as the deviation for neighbouring conversion coefficients is also small. This is only true for the *Vac* and *Al* detectors, whereas the *Sn* detector shows a jump at about 180 keV. However, this detector and especially this bin have a low contribution to the total dose due to the low probability of registering events compared to the other detectors and bins.

Applying the determined conversion coefficients $\vec{k}_d$ to data according to equation (3.19) provides the response of the dose depicted in figure 3.24. (a) corresponds to $H_\mathrm{p}(10)$, (b) to $H_\mathrm{p}0.07$. The blue curves resemble the MC simulations used in the optimisation. The orange curves represent measurements which were executed in collaboration with the national metrology institute of Germany (Physikalisch-Technische Bundesanstalt, PTB [51]) within the scope of a Master's thesis [52]. The used energy spectra are the so-called N-qualities N-15 to N-300 with mean photon energies ranging from 12 keV to 248.9 keV. These are narrow X-ray tube spectra, achieved by using different metal filters. Additionally, the radionuclides ^{137}Cs and ^{60}Co with mean energies of 662 keV and 1250 keV are used. The reference spectra are defined in [45, 46]. The N-qualities are referred to as N-series in the following. The dosemeter responses are required to lie within a range of 0.71 and 1.67 according to PTB [53]. These limits are indicated by the red dashed lines in figure 3.24. The evaluated MC responses are centred about a perfect response of 1. The data points deviate within a range of about ± 0.2 about the perfect response for $H_\mathrm{p}(10)$ and $H_\mathrm{p}(0.07)$ for photon energies above about 15 keV. For photon energies close to the minimum of 10 keV, the dose is underestimated for both dose types. This implies no solution for the conversion coefficients exists, which generally describes the dose for the complete energy range well.

The performance of the determined conversion factors is evaluated for measurements. Their responses are reflected via orange lines in figure 3.24. The corresponding means μ along with their standard deviations σ and minimum and maximum responses are listed in table 3.3.

Dose type	μ	σ	min	max
$H_\mathrm{p}(10)$	1.252	0.394	0.992	2.503
$H_\mathrm{p}(0.07)$	1.024	0.074	0.851	1.127

Table 3.3.: Means μ and standard deviations σ of the responses for the measurements depicted in figure 3.24 in orange. Additionally, minimum and maximum values are listed.

For $H_\mathrm{p}(0.07)$, simulations and measurements agree well as the statistical quantities show. Here, the maximum deviation of the response is 0.149. While the maximum deviation lies within 0.2 for mean energies greater than about 30 keV, there are discrepancies for low mean photon energies for $H_\mathrm{p}(10)$. Here, responses exceed the legal limits of 1.67 [53]. The deviations can be attributed to imperfections in the simula-

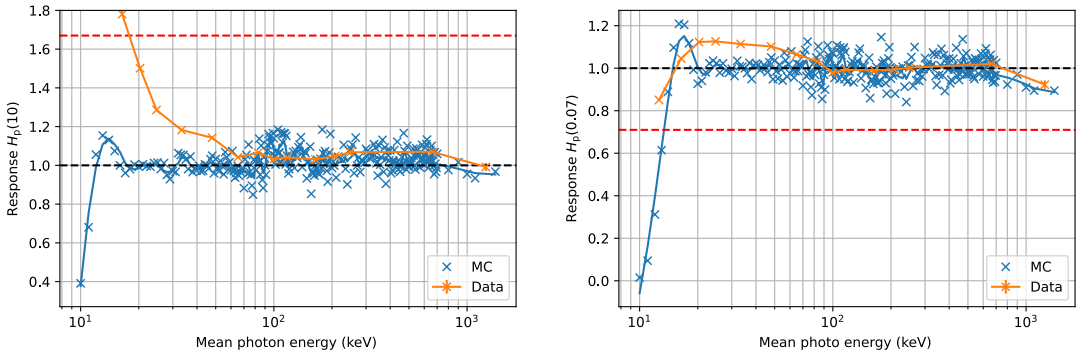

(a) $H_p(10)$ response

(b) $H_p(0.07)$ response

Figure 3.24.: Dose responses for MC simulation (in blue) and measurements (in orange). Error bars indicating the statistical error of the measurements are depicted but are too small to be discernible. The used conversion coefficients are optimised to simulation. Dashed red lines indicate the limits of the responses for a dosemeter to fulfil legal requirements according to PTB [53].

tion. For these low energies, the photoelectric effect is dominant. Slight deviations in material widths have a high influence on the attenuation of photons and also the fluorescence yield. Materials used for the readout electronics and housing of the dosemeter might have different characteristics than assumed. For example, PMMA is often dyed with pigments of higher density. A complex material analysis would be required to find the exact compositions of the used materials.

Figure 3.25 shows the response discrepancies in detail. According to the legend, the contributions to the total response for single detectors as indicated by the colours of the curves are depicted. The sum of the curves for all detectors equals the response of figure 3.24. Solid lines correspond to the MC simulation, while dashed lines with points reflect measurements. Since the MC simulation response is good for almost the whole energy range, simulations and measurements for the different detectors should also match well. In case of (b), for the personal dose equivalent $H_p(0.07)$ this is true while $H_p(10)$ (a) again shows discrepancies for low deposited energies.

The discrepancies can directly be attributed to the *Vac* detector. One issue could be the implementation of its filter or the housing in front of the detector in simulation. Again, it would require much work to understand the problem entirely. This effort cannot be justified at the current state of development as the dosemeter's housing is not in its final state. Therefore, every small change would require a repetition of the whole analysis process.

Another possibility for the discrepancy is depicted in figure 3.26. The number of registered events for the measurements are depicted as a function of mean photon en-

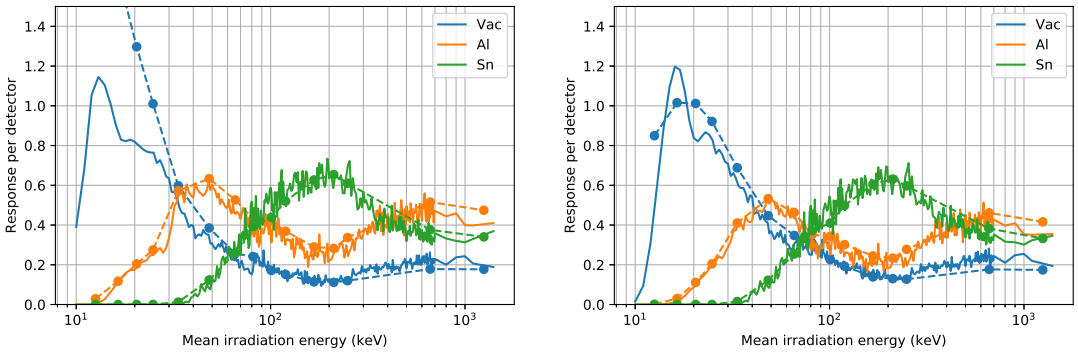

(a) $H_p(10)$ response per detector

(b) $H_p(0.07)$ response per detector

Figure 3.25.: Dose responses for MC simulation (solid lines) and measurements (data points and dashed lines). The curves correspond to the different detectors' response contributions as indicated by the colours and the legend. The sum of all curves corresponds to the response in figure 3.24. Error bars indicate the statistical error on the measurements but are too small to be discernible. The used conversion coefficients are optimised to MC data only.

ergy and deposited energy. The x-axis corresponds to the settings of the bin edges in Dosi-mode, the y-axis denotes the mean photon energies of the N-series and radionuclide spectra. The number of events is indicated by the colours, which are scaled logarithmically. The dashed lines represent the X-ray tube's voltage and, therefore, the highest possible photon energy. There should be no events in the measurements with deposited energies larger as indicated by these lines. These energies exist nevertheless, which is attributed to pile-up effects in the analogue electronics of the detector (see section 2.1.1 for more details). This is further proven as the *Vac* detector shows the highest number of these events while the *Sn* has the lowest number. This is due to the photon flux at the detector position, which is highest when no additional filter is used. There is no method to get rid of these pile-up events once a measurement has been made. Simply cutting them away does not give an appropriate representation. One pile-up event of high energy represents multiple single events of lower energy. Also, events with deposited energies below the detector's energy threshold have a possibility to be detected when pile-up takes place.

As stated in the legal requirements in [53], the minimum rated range of use is from 30 keV to 250 keV for $H_p(0.07)$ and 80 keV to 1250 keV for $H_p(10)$. The responses of the measurements fulfill the requirements for these energy ranges. Since these are only minimum requirements, an extension of the ranges is desirable which is performed in the following.

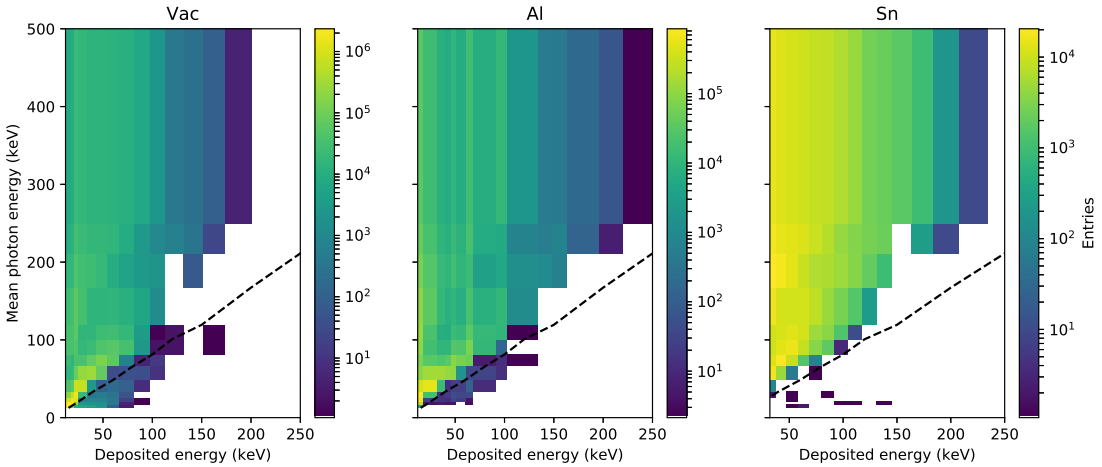

Figure 3.26.: The number of registered events from measurements with the Dosepix dosemeter. The y-axis represents the mean photon energies of the used N-series and radionuclide spectra. The x-axis indicates the settings of the bins in Dosi-mode for the different detectors. The number of registered events is represented by the logarithmically scaled colours. The plots correspond to the different detectors according to the labels in their titles. The black dashed lines indicate the maximum possible photon energy emitted by the X-ray tube.

3.2.7 Data-based dose conversion coefficients

A direct fit of data to determine the conversion coefficients from registered events to dose requires many measurements of photon spectra. This is due to the 16 dose conversion factors per detector and the resulting number of degrees of freedom. Photon spectra ideally should also be as narrow as possible, which is difficult to achieve when using a filtered X-ray tube. A tradeoff is made by extending the simulation dataset for the optimisation of dose conversion factors with measurements. This improves the dose-response while keeping the stability introduced by the simulation data. The loss $\mathcal{L}$ of equation (3.20) is extended, resulting in

$$\mathcal{L}_{\text{data}} = \sqrt{\sum_j \left(\frac{H_{\text{DPX,sim},j}}{H_{\text{ref,sim},j}} - 1 \right)^2} + w \cdot \sqrt{\sum_j \left(\frac{H_{\text{DPX},j}}{H_{\text{ref},j}} - 1 \right)^2}, \tag{3.21}$$

where j is the sum over the measured datasets, H_{DPX} is the dose calculated from detector data via equation (3.19), and H_{ref} is the reference dose measured directly via an ionisation chamber by PTB (see [52] for more details). The object of optimisation are the conversion coefficients $\vec{k}_d$ of equation (3.19), where d represents the different detectors. Factor w introduces a weighting of the measurement loss in comparison to the simulation loss. A value of $w = 10$ is chosen heuristically. The previously determined

conversion coefficients from fits to simulation data are used as start parameters for the optimisation which additionally increases the stability. The optimised coefficients are listed in table A.3 and depicted in figure 3.27 for $H_p(10)$ (a) and $H_p(0.07)$ (b). There are only small differences compared to the coefficients optimised to simulation data only, shown in figure 3.23. The coefficients are smooth as a function of the deposited energy and even got smoother when comparing the bin at about 180 keV for the *Sn* detector of the previous coefficients. These coefficients allow a correct dose reconstruction even when temperature changes result in shifts of the registered deposited energies.

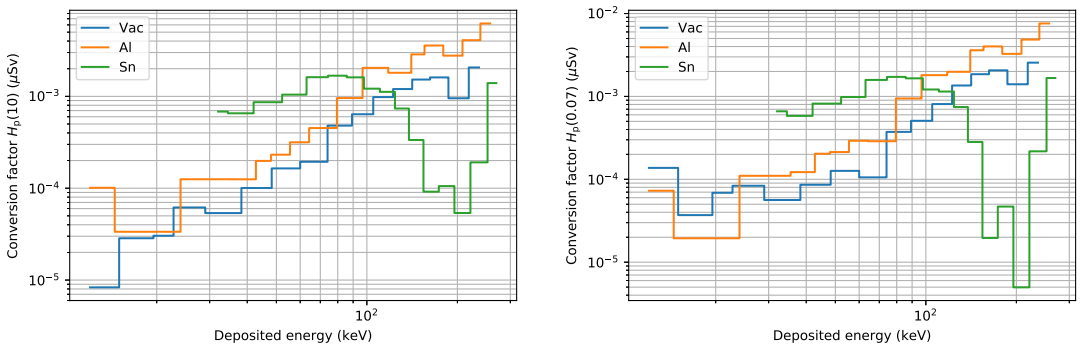

(a) $H_p(10)$ (b) $H_p(0.07)$

Figure 3.27.: Conversion coefficients from registered events of the Dosepix detectors to personal dose equivalent of table A.3. In (a), for $H_p(10)$ and in (b), for $H_p(0.07)$. The coefficients are optimised to simulation and measurement data. The deposited energies correspond to the settings of the bin edges used in Dosi-mode.

Applying the optimised conversion coefficients to MC and measurement data returns the responses depicted in figure 3.28. (a) represents the personal dose equivalent $H_p(10)$ and (b) $H_p(0.07)$. Also, measurements under different irradiation angles θ_{ir} of 30° and 60° are included. The statistical quantities of the responses of all mean photon energies are listed in table 3.4. The coefficients are optimised to measurements of 0° irradiation angle. The corresponding responses are flat and centred about a perfect response of 1.The MC simulation responses show a large deviation for small deposited energies for $H_p(10)$. The measurements under different irradiation angles match the expectations well. For 30°, the determined responses are similar to the ones of 0° except for the data point of lowest mean photon energy. As the value for 60° agrees well, this indicates difficulties during the measurement. Therefore, the 30° measurement has to be repeated to give a reliable statement about its quality. For $H_p(0.07)$, data responses decrease with decreasing mean photon energies. This deviation cannot be attributed to the conversion coefficients. The reason is the filter's shape for the *Vac*

Dose type	θ_{ir} (deg)	μ	σ	min	max
$H_p(10)$	0	0.998	0.012	0.963	1.033
	30	0.958	0.093	0.703	1.037
	60	1.074	0.059	0.956	1.135
$H_p(0.07)$	0	1.000	0.018	0.955	1.042
	30	0.891	0.190	0.371	1.015
	60	0.743	0.313	0.136	1.060

Table 3.4.: The means μ and corresponding standard deviations σ of the responses for the measurements depicted in figure 3.28. Additionally, minimum and maximum values are listed. θ_{ir} represents the irradiation angle of the photon field in the measurements.

detector. Here, a tradeoff between proper reconstruction of $H_p(10)$ and $H_p(0.07)$ is made, explained via the conversion factors from photon fluence to dose depicted in figure 3.21. The factors for $H_p(0.07)$ in (b) are almost independent of the irradiation angle for photon energies greater than 10 keV. The values for $H_p(10)$ in (a) show a strong dependence. This is corrected via the filter of the *Vac* detector whose thickness, and as a consequence, capability to attenuate photons, varies with the irradiation angle. As the conversion factors' angular dependence from fluence to dose shows, it is impossible to perfectly estimate both dose types simultaneously. Therefore, a focus on a correct reconstruction of $H_p(10)$ is present. This finally limits the range of use for the dosemeter for $H_p(0.07)$ reconstruction to mean photon energies above about 25 keV.

3.2.8 Dose conversion coefficients for small pixels

The analyses presented in the previous sections only concerned large pixels. Due to their large area, they perform well in regards to energy deposition measurements. Their high count statistics are advantageous if the photon flux is low but also disadvantageous if it is high. In the latter case, pile-up starts to dominate, leading to a distortion of the registered deposited energy spectrum and discrepancies in the estimated dose. Due to small pixels being 16-times smaller than large pixels, they show lower count statistics and less pile-up.

The introduced method to determine the personal dose equivalent from Dosepix measurements is independent of the pixel type. The used conversion coefficients from registered events to dose are different, as deposited energy spectra differ. Since a correct simulation of small pixels, due to their reduced area, is time-consuming, an optimisation method for the conversion coefficients only utilising measurements is desirable.

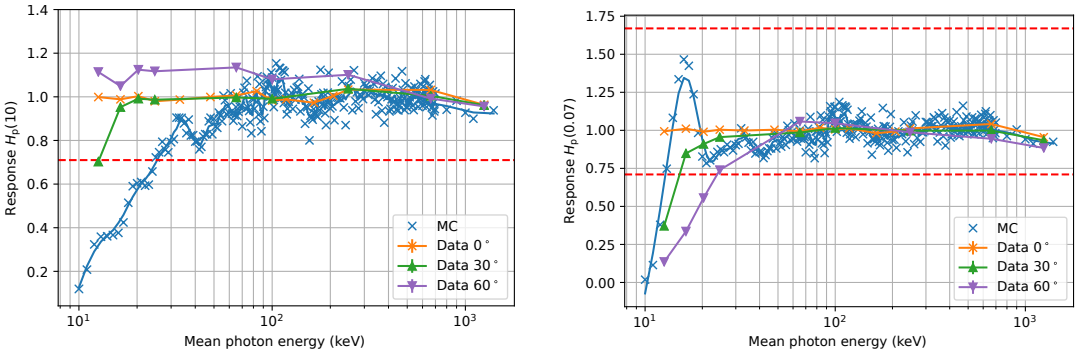

(a) $H_p(10)$ response

(b) $H_p(0.07)$ response

Figure 3.28.: Dose responses for MC simulation (in blue) and measurements for different irradiation angles as indicated by the legend. Error bars represent the statistical error but are too small to be discernible. The used conversion coefficients are optimised to MC simulations and measurements for 0° irradiation angle. The dashed red lines indicate the legal limits of the responses for a dosemeter according to PTB [53].

The requirement is a set of properly optimised coefficients for big pixels. The performance of small pixels is optimised to reflect the large pixels in the following. New measurements are made. Here, different X-ray tube spectra are utilised. They should be diverse in their mean photon energies, and the photon flux should be low to prevent pile-up. A large number of measurements is desirable as there are 16 conversion factors per detector. Various filter combinations are installed in front of the X-ray tube, and measurements under tube voltage variation are performed. The photon spectra's shape is not important as only the dose measured via the big pixels of the Dosepix dosemeter matters. The blue curves in the upper plots of figure 3.29 depict these doses. (a) reflects $H_p(10)$ and (b) $H_p(0.07)$. The dashed vertical lines indicate how the measurements were performed. In-between two lines, the same filter combination is installed in front of the X-ray tube. For the different measurements, only the tube's voltage is changed while keeping the time of irradiation approximately constant. The determined dose values of the large pixels are used as references H_{ref}. The corresponding doses for the small pixels, $\vec{H}_{DPX}$, are calculated for conversion coefficients $\vec{k}_d$ via equation (3.19). d represents the different Dosepix detectors of the dosemeter. The coefficients are then optimised so the response of $\frac{\vec{H}_{DPX}}{H_{ref}}$ is minimised according to the loss of equation (3.20).

The determined conversion coefficients for the small pixels are listed in table A.4 and depicted in figure 3.30 for $H_p(10)$ (a) and $H_p(0.07)$ (b). The same bin edges in Dosi-mode as for the large pixels listed in table A.1 are used. Since the optimisation process is now using measurement data only, the photon energy range is not

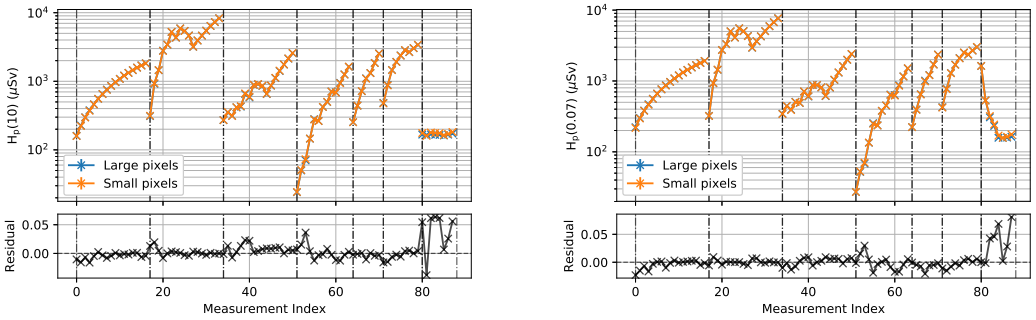

(a) $H_p(10)$ (b) $H_p(0.07)$

Figure 3.29.: Reconstructed personal dose equivalents for measurements with the Dosepix dosemeter. In (a), for $H_p(10)$ and in (b) for $H_p(0.07)$. Arbitrary photon spectra are utilised. In-between two vertical dashed lines, the same metal filter combination is applied to the X-ray tube. The voltage of the X-ray tube is varied between measurements. The curves in the upper plots indicate the doses for small and large pixels according to the legend. The bottom plots show the residuals of the curves for small and large pixels via equation (3.22).

as densely covered as previously. This results in conversion coefficients that are not as smooth in comparison to the large pixel ones. Therefore, also their robustness to temperature variation is limited.

The orange dose curves in figure 3.29 are determined by applying the conversion coefficients for the small pixels to the measurements used for optimisation. The agreement to the large pixel doses is evaluated by calculating the residuals

$$\frac{H_{\text{small}}}{H_{\text{large}}} - 1, \tag{3.22}$$

which are depicted in the bottom plots of the figure. These residuals, independent of dose type, are all centred about a value of 0 and only deviate slightly about it. Only a few measurements show worse agreement in comparison, having residuals of about 0.05. In conclusion, the small pixels can estimate the same doses as the large pixels for the measurements used in the optimisation.

The conversion coefficients for the small pixels are applied to the N-series, and radionuclide spectra measurements, performed at PTB (see [52] and section 3.2.5 for more details). The determined dose responses are shown in figure 3.31. The colours of the curves represent different irradiation angles θ_{ir} according to the legend. The red dashed lines reflect the legal response limits of 0.71 and 1.67 according to PTB [53]. The measurements are completely independent of the data utilised during the optimi-

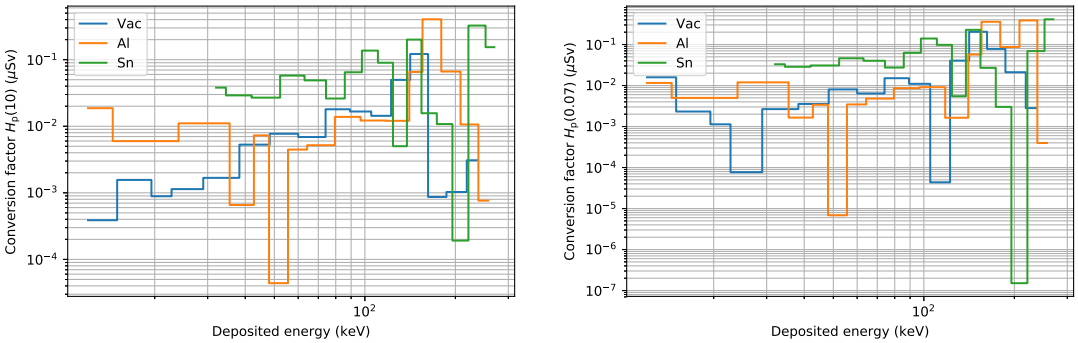

(a) $H_p(10)$ (b) $H_p(0.07)$

Figure 3.30.: Conversion coefficients from the number of registered events of the Dosepix detectors to personal dose equivalent for the small pixels. For $H_p(10)$ in (a) and $H_p(0.07)$ in (b). The coefficients are optimised so large and small pixels return the same dose. The colours of the curves reflect the different detectors of the dosemeter according to the legend. The deposited energies correspond to the settings of the bin edges used in Dosi-mode of the detectors.

sation of the dose conversion coefficients. The corresponding statistical quantities of the responses are listed in table 3.5.

Dose type	θ_{ir} (deg)	μ	σ	min	max
$H_p(10)$	0	0.993	0.079	0.811	1.091
	30	0.980	0.112	0.779	1.144
	60	1.123	0.186	0.805	1.436
$H_p(0.07)$	0	0.995	0.073	0.821	1.094
	30	0.914	0.140	0.652	1.131
	60	0.742	0.294	0.132	1.034

Table 3.5.: Means μ and standard deviations σ of the responses for the measurements depicted in figure 3.31. Additionally, minimum and maximum values are listed. θ_{ir} represents the irradiation angle of the photon field of the measurements. Only reconstructed doses via small pixels are included.

Overall, the dose reconstruction performance for small pixels is similar to the large pixels before. The small pixel responses are not as stable in comparison, which is mainly due to the reduced count rate and, as a consequence, larger statistical errors. For $H_p(10)$, the responses for irradiation angles θ_{ir} of 0° and 30° are very similar. The responses for 60° show larger deviations for mean photon energies below 100 keV.

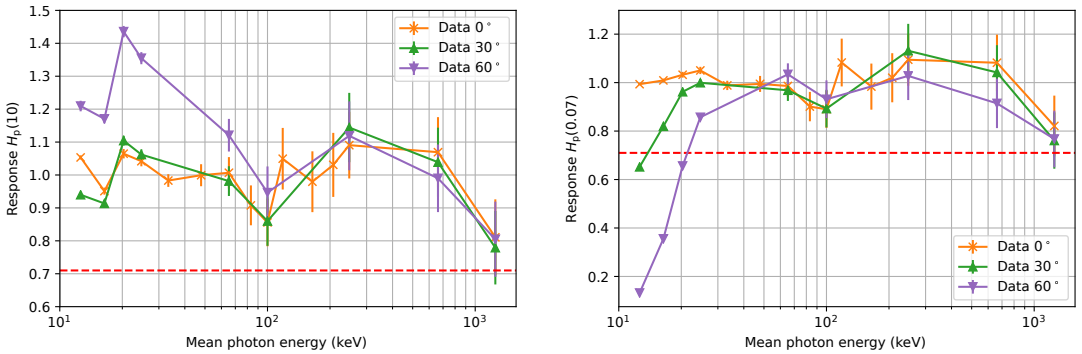

(a) $H_p(10)$ response

(b) $H_p(0.07)$ response

Figure 3.31.: Dose responses of the N-series and radionuclide measurements for different irradiation angles as indicated by the legend. Error bars represent the statistical error. Only the small pixels are used for the dose calculation. The dashed red lines indicate the limits of the legal requirements of the responses for a dosemeter according to PTB [53].

Nevertheless, these values are still within the legal limits. Therefore, $H_p(10)$ performance is concluded to be well for the whole evaluated energy range.

For $H_p(0.07)$, the responses for different irradiation angles θ_{ir} are similar for mean photon energies larger than about 80 keV. All responses are centred about a perfect response of 1. The last data point at a mean photon energy of 1250 keV is close to 0.8. Including its error, the value is below the limit of the legal requirements. Doses are underestimated for low mean photon energies and irradiation angles greater than 0°. Mean photon energies smaller than about 23 keV for irradiation angles of 60° lead to responses lower than the legal limit. As previously discussed for large pixels, this is not due to the used conversion factors and instead due to the shape of the Dosepix detectors' filters (see section 3.2.7 for more information).

In conclusion, small pixels provide results similar to large pixels and are suitable for dosimetry applications. Due to lower count statistics, the statistical error for the dose is increased. Therefore, dosimetry should mainly be performed with large pixels. Small pixels should only be used once photon fields of high dose rates are present and pile-up begins to occur for large pixels. A direct comparison of doses for small and large pixels tells if large pixels still work correctly for the present photon flux. If not, the result of the small pixels should be used instead.

3.2.9 Polynomial dose conversion coefficients for large pixels

A final method to determine conversion coefficients from registered events of the Dosepix detectors to dose equivalents is presented. Instead of attributing a single dose coefficient to each Dosi-mode bin, the coefficients are now sampled from a polynomial function. The function describing a conversion factor $k_d(E)$ at deposited energy E is defined as

$$k_d(E) = \left| \sum_{i=0}^{n_d-1} p_{d,i} \cdot E^i \right|. \tag{3.23}$$

Index d corresponds to the detector type, i.e. either *Vac*, *Al* or *Sn*, depending on the filter of Dosepix. n_d describes the degree of the polynomial for detector d. Parameters $p_{d,i}$ define the shapes of the polynomials. The absolute is applied for two reasons. First, it ensures that conversion factors are always greater than 0 as negative values might lead to negative doses. Second, it allows breaking the continuity of the conversion factors as a function of deposited energy, which increases the dose reconstruction abilities.

The bin edges for Dosi-mode defined in table A.1 are used. The values of the deposited energies E of the polynomial function of (3.23) correspond to the values of the left bin edges. Inserting the edge values for a detector d provides a vector of dose conversion factors $\vec{k}_d$. Calculation of the dose is executed as in the sections before, i.e. via

$$\vec{H}_{\mathrm{DPX}} = \sum_d \hat{N}_d \cdot \vec{k}_d. \tag{3.24}$$

Dose vector $\vec{H}_{\mathrm{DPX}}$ is calculated by taking the sum over the detector types d of the dot-products of the count matrices $\hat{N}_d$ and the conversion coefficient vectors $\vec{k}_d$. The rows of the matrices $\hat{N}_d$ consist of binned registered events of detector d for different photon spectra. The columns correspond to the bins used in Dosi-mode.

Instead of optimising the dose conversion coefficients directly, the constants of the polynomial function 3.23 $p_{d,i}$, and the degree of the polynomial n_d, are now varied during fit. The object of optimisation is the response of $\frac{H_{\mathrm{DPX}}}{H_{\mathrm{ref}}}$, i.e. the fraction of reconstructed and true dose. The loss of equation 3.21 is minimised. The datasets used in the fit are the simulated monoenergetic spectra, and the N-series and radionuclide measurements taken in [52]. In the following, only the large pixels are considered. The optimisation procedure for the small pixels is analogous. The final parameters of the polynomials for $H_{\mathrm{p}}(10)$ and $H_{\mathrm{p}}(0.07)$ according to equation 3.23, as a result of Nelder-Mead optimisation [43], are listed in table A.5 in the appendix. Not every detector type d has the same amount of parameters since the polynomial degree n_d is also optimised during the fit. The curves describing the conversion coefficients as a function of deposited energy are depicted in figure 3.32. For $H_{\mathrm{p}}(10)$ in (a), and

$H_p(0.07)$ in (b). The colours correspond to the detector types according to the legend. Solid lines represent the values of the polynomials for continuous energies. Steps correspond to the values of the conversion factors sampled for the used bin edges in Dosi-mode. The trend of the polynomials is smooth in general. However, the continuity is broken at certain energies.

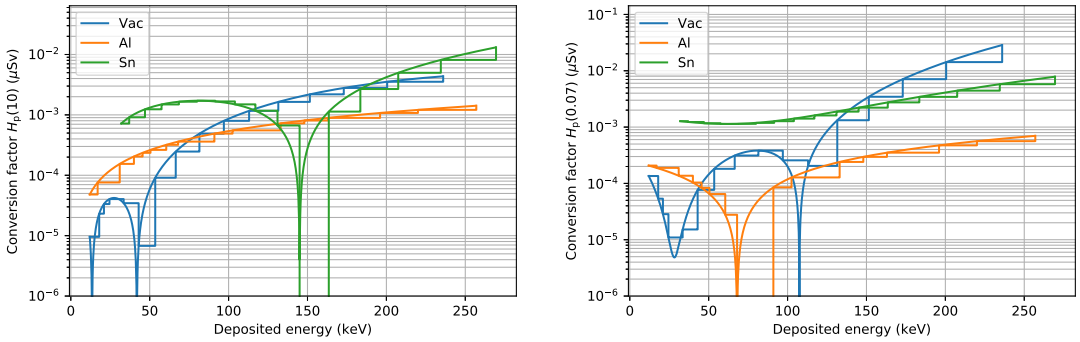

(a) $H_p(10)$ (b) $H_p(0.07)$

Figure 3.32.: Polynomial dose conversion coefficients from registered events of the Dosepix detectors to personal dose equivalent. For $H_p(10)$ in (a) and $H_p(0.07)$ in (b). The colours of the curves indicate the detector types according to the legend. The solid lines correspond to continuous deposited energies, while the steps represent the settings of the bin edges used in Dosi-mode of the detectors.

Figure 3.33 shows the responses for the reconstructed doses from MC simulations and N-series and radionuclide measurements from [52]. For $H_p(10)$ in (a) and $H_p(0.07)$ in (b). The datasets are the same as used in the direct optimisation of the large pixel dose conversion coefficients in section 3.2.7. The different curves correspond to various irradiation angles θ_{ir} according to the legends of the plots. The statistical quantities of these responses, i.e. their mean, the corresponding standard deviations and the minimum and maximum values, are listed in table 3.6. A focus on measurement data is set for the optimisation of the polynomial dose conversion coefficients, explaining the mismatch of the blue MC curve for low mean photon energies in case of $H_p(10)$ (a) and high energies for $H_p(0.07)$ (b). The dose reconstruction performance for measurements using the polynomial conversion coefficients is similar to the directly optimised coefficients' performance. The polynomial coefficients are only slightly worse for $H_p(10)$ data for 60° irradiation and small mean photon energies as well for the highest energies in case of $H_p(0.07)$.

In conclusion, there are some benefits of using 3 polynomials, one for each detector, instead of 16 conversion coefficients per detector. The polynomials inherit a smoothness, which otherwise is only achievable by including simulation data of various mean photon energies into the optimisation process. The parameters required for dose re-

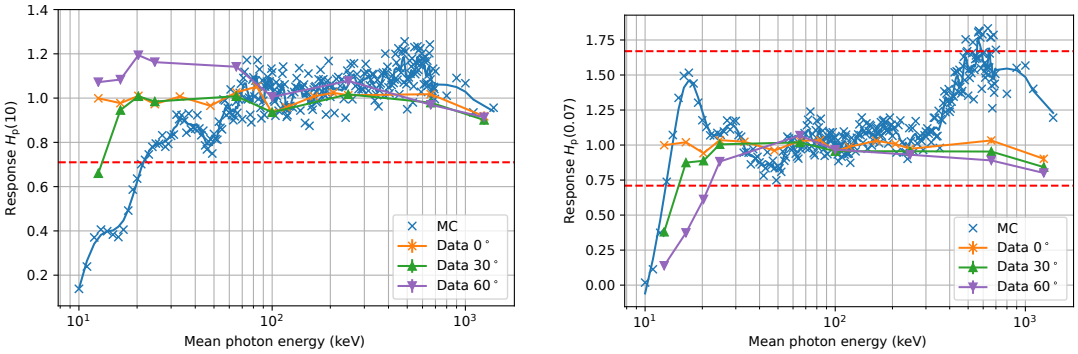

(a) $H_p(10)$ response

(b) $H_p(0.07)$ response

Figure 3.33.: Dose responses for N-series and radionuclide measurements under different irradiation angles as indicated by the legend. Error bars represent the statistical error of the measurements but are not discernible. Only large pixels utilising the polynomial dose conversion coefficients are reflected. The dashed red lines indicate the legal limits according to PTB [53].

Dose type	θ_{ir} (deg)	μ	σ	min	max
$H_p(10)$	0	0.992	0.036	0.918	1.052
	30	0.938	0.105	0.66	1.017
	60	1.069	0.087	0.913	1.194
$H_p(0.07)$	0	0.996	0.04	0.902	1.035
	30	0.875	0.183	0.38	1.019
	60	0.74	0.29	0.138	1.068

Table 3.6.: Means μ and standard deviations σ of dose responses for the measurements depicted in figure 3.33. Additionally, minimum and maximum values are listed. θ_{ir} represents the irradiation angle of the photon field used during measurements. Only responses reconstructed from large pixel data utilising the polynomial conversion factors are included.

construction is reduced from 48 to the sum of the polynomials' degrees, in this case, 9. Therefore, the amount of data required for the optimisation is reduced. The registered ToT values, and as a consequence, deposited energies of Dosepix are temperature dependent. A correction method whose functioning relies on the introduced polynomial dose conversion coefficients is described in the following.

3.3 Temperature dependence of Dosepix and its correction

One flaw of the Dosepix detector is its temperature dependence, i.e. registered ToT-values vary with temperature. The measure of ToT and its relation to deposited energy is explained in section 2.1.1. The easiest solution for the temperature dependence is to operate the detector under laboratory conditions, i.e. with a fixed temperature. This is no desirable method for most applications, especially in personal dosimetry. Here, the detector is a part of a dosemeter whose bearer is moving freely, and temperature conditions will change during the day. Several investigations are made to reduce the temperature dependence of Dosepix:

1. Measurements are made to show how the detector behaves for temperature variation
2. A method is developed to revert the undesired behaviour
3. The results are applied to dose measurements

3.3.1 Temperature dependence of Dosepix

There is no concluded explanation of why the registered ToT-value changes with temperature. There are indications this is a problem of the analogue electronics of the ASIC of Dosepix. Changing the attached sensor and, as a consequence, the input capacitance and the leakage current through the sensor might improve the temperature dependence. However, a software solution without changing the hardware is of interest.

The temperature dependence is measured and quantified. A sensor included in the ASIC of Dosepix is used to measure a voltage which is proportional to temperature. This voltage is converted via an analogue-to-digital converter to an integer number. Temperature values are represented in units of DAC, i.e. a digital number representing an analogue value. The conversion from DAC to °C is not known and has to be determined via calibration. For a calibration, stable environmental conditions with Dosepix being in thermodynamic equilibrium are required. The ambient temperature would be varied, and measurements taken. However, it is a sophisticated task that has to be performed for every detector since temperature to DAC conversions differ. However, a correct temperature calibration is unnecessary as it has no practical benefit when working with Dosepix. Everything described is therefore performed by utilising the temperature in DAC, where no additional error from DAC-to-°C conversion is introduced. Only rough temperature estimates will be given, which correspond to the measured DAC values.

The procedure to measure the temperature dependence of Dosepix is described in the following. The detector has a protective plastic cap installed and is put into a box.

Darkness is essential, as photons from light sources can generate a large number of charges in the sensor, which leads to the registration of ToT values. Inside the box, a heating resistor is placed close to the detector. Its heat dissipation is adjusted by varying the applied voltage and, therefore, the current. For the ToT measurements, no radioactive sources are required. Instead, the test pulse functionality of Dosepix is utilised, which is described in more detail in section 2.1.3. A fixed voltage is applied to the test pulse capacitor, and pulses are injected into the input of the analogue electronics. Only a single pixel column is active at a time, as injecting pulses to too many pixels at once leads to instabilities. If the temperature remains stable, the same ToT value should be measured on average. Statistical variations due to fluctuations in the test pulse capacitor's charging time and the ToT resolution are present. The influence of these fluctuations is reduced by performing many measurements in succession.

The plots of figure 3.34 depict measurements of test pulse energies in ToT under temperature variation for a single pixel column. Low test pulse energies are used in (a) and high energies in (b). All measurements in this chapter are performed with a setting of $I_{\mathrm{krum}} = 2\,\mathrm{nA}$. The left-hand sides of the plots depict the trend of the temperature as a function of time. The temperature in DAC is inverted in comparison to the measure in units of °C. High DAC values correspond to low temperatures and vice versa. The dashed lines indicate a reference temperature T_{ref}, set to 1615 DAC which corresponds to room temperature of about 20° C. The temperature trend in (a) indicates that the detector was already hot at the beginning. It was then cooling down for about 200 s when the heating resistor was switched on. It does not matter how the temperature variation is performed. It is most efficient to use both periods, the heating and the cool-down of the detector. The right-hand side of the plot of figure 3.34 (a) shows the ToT measurement of test pulses of constant energy for the pixels of the first pixel column. The colours of the datasets reflect the pixel index according to the colour bar. Pixels 1, 2, 15, and 16 are small pixels while the remaining pixels are large. Each data point describes the measurement of 10 test pulses performed in succession, providing the mean ToT value μ_{ToT} and the temperature. The error bars reflect the corresponding standard deviations. Taking the average is important as temperature data tends to be noisy. The relation between μ_{ToT} and temperature is considered to be linear. This trend's slope is determined via fit, as indicated by the solid lines in the plots. Once the detector has cooled down it is heated again in (a). Nevertheless, independent of how temperature is varied, the linear relation between ToT and temperature remains the same, and there is no hysteresis involved.

The right-hand side of figure 3.34 (a) shows that for low test pulse energies the mean ToT value increases with increasing temperature in °C. For high test pulse energies, shown in (b), it is vice versa, i.e. μ_{ToT} decreases with increasing temperature. To further analyse this behaviour, additional measurements for different test pulse energies are performed. The slope $m_{ToT/T}$ of the linear relation of μ_{ToT} as a function of temperature in DAC is determined via fit for each pixel. The intersections of the linear functions and the reference temperature T_{ref}, as illustrated by the dashed lines in the

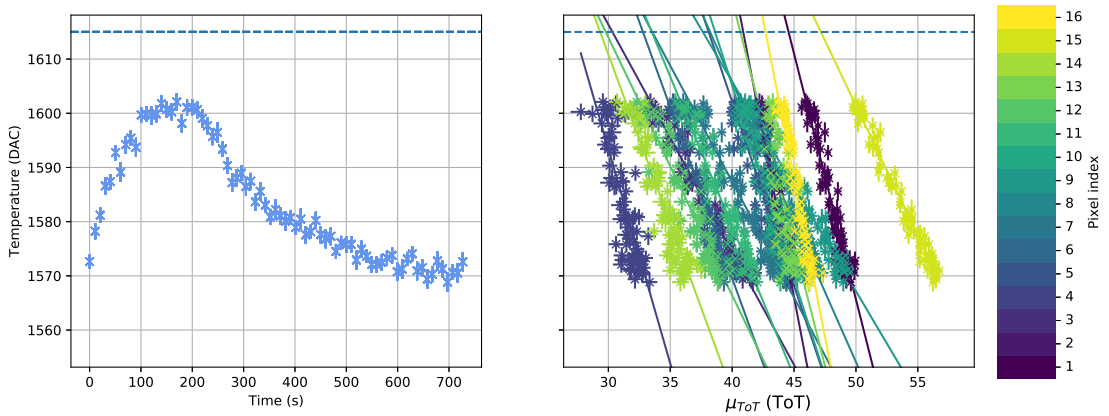

(a) Low test pulse energies

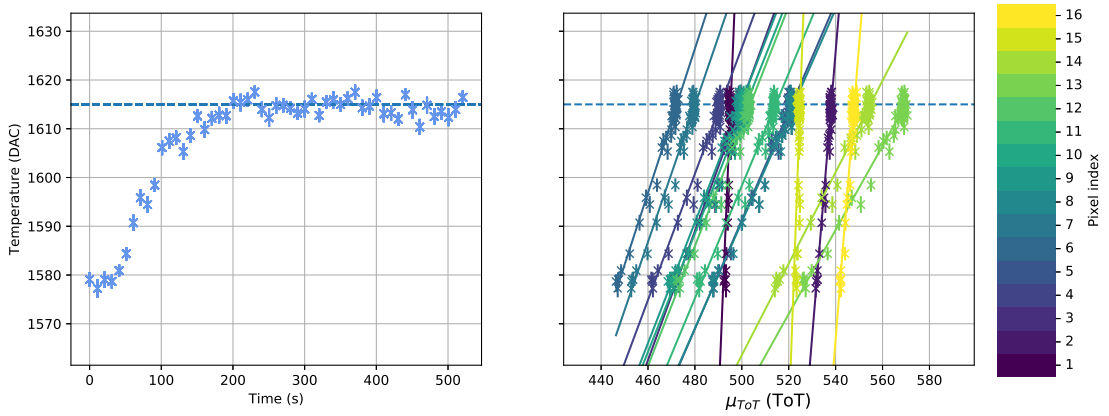

(b) High test pulse energies

Figure 3.34.: Test pulse measurements of a single pixel column under variation of temperature. The left-hand side of the plots shows the temperature as a function of time. The reference temperature T_{ref} is set to 1615 DAC and indicated by the dashed lines. The temperature in DAC is inverse to the temperature in °C. The plots on the right-hand side depict test pulse measurements for the pixels as a function of temperature. The colours represent different pixels, as indicated by the colour bars. Low test pulse energies are used in (a) and high energies in (b). Each data point represents 10 test pulse measurements. Their mean is taken, providing the mean temperature and corresponding ToT μ_{ToT}. The error bars reflect the corresponding standard deviations. Solid lines indicate the linear trend of μ_{ToT} as a function of temperature.

plots of figure 3.34, are determined for μ_{ToT} and are called ToT_{offset}. The values reflect what the detector would measure if there was no temperature dependence. Figure 3.35 depicts the determined slopes $m_{ToT/T}$ as a function of ToT_{offset} for the 16 pixels of the first pixel column. There is an approximately linear relation describing the slopes, which is fitted with equation

$$m_{ToT/T} = m_T \cdot ToT_{\text{offset}} + t_T, \tag{3.25}$$

where m_T and t_T are the parameters optimised during fit. Function (3.25) describes that the change of registered ToT does not only depend on temperature but also on the ToT value itself. The slopes $m_{ToT/T}$ describe the change of ToT with temperature. If the slope is positive, registered ToT values increase with decreasing temperature in °C. For negative slopes, it is vice versa. At $ToT_{\text{offset}} \approx 100\,\text{ToT}$, the slope is 0 and pixels show almost no temperature dependence. In general, the 4 small pixels have lower slopes than the large pixels and, in conclusion, a lower temperature dependence. Since the analogue electronics do not depend on the pixel size and the generation of the test pulses is identical, there is an indication that the different temperature behaviours are influenced by the attached sensor. This is probably due to the different coupling capacitances depending on the pixel sizes and, as a consequence, different leakage currents that affect the properties of the analogue electronics.

3.3.2 Temperature dependent ToT-correction

The behaviour of Dosepix under temperature variation is condensed in the parameters m_T and t_T of equation (3.25). The relation is used to determine slope $m_{\text{ToT/T}}$, the variation of ToT with temperature, for ToT_{offset}, the value which is measured at reference temperature T_{ref}. Multiplying $m_{\text{ToT/T}}$ with the temperature difference $\Delta T = T - T_{\text{ref}}$ yields the change in ToT in relation to the offset ToT value, i.e. $ToT - ToT_{\text{offset}}$, at a temperature T. Therefore, ToT is measured by Dosepix for an event represented by ToT_{offset} at temperature T via

$$ToT = ToT_{\text{offset}} + (T - T_{\text{ref}}) \cdot (m_T \cdot ToT_{\text{offset}} + t_T). \tag{3.26}$$

The temperature correction is determined by solving for ToT_{offset}, reflecting the value of ToT at the reference temperature T_{ref}

$$ToT_{\text{offset}}(ToT, T) = -\frac{(T - T_{\text{ref}}) \cdot t_T - ToT}{(T - T_{\text{ref}}) \cdot m_T + 1}. \tag{3.27}$$

The equation is applied to the data shown in the plots of the left-hand side of figure 3.36, corresponding to the uncorrected measurements used during the temperature calibration of the detector in figure 3.34. The plots on the right-hand side show the data after correction. Low test pulse energies are used in (a), and high test pulse energies in (b). The different colours correspond to the pixels according to the colour bar. After correction, the deviation as a function of temperature change is reduced.

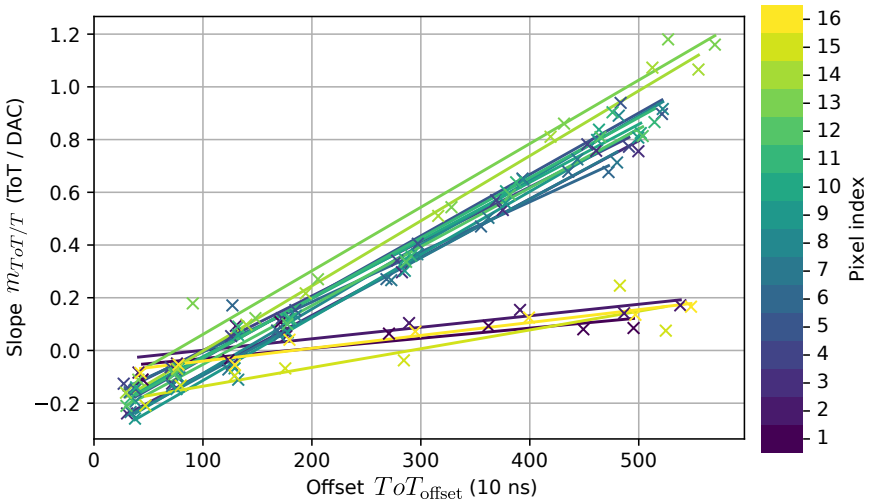

Figure 3.35.: Slopes $m_{ToT/T}$ of the plots on the right-hand side of figure 3.34 as a function of the offset ToT-value ToT_{offset}. Measurements for additional test pulse energies are included. The slope $m_{ToT/T}$ describes the change in mean ToT when the temperature in DAC is varied. Offset ToT_{offset} is the ToT value measured at the reference temperature T_{ref}, corresponding to room temperature of 20°C. The colours of the curves correspond to the various pixels as indicated by the colour bar. Here, pixels 1, 2, 15, and 16 are small pixels, the remaining pixels are large. Linear fits to the data points are performed to describe the slope's change as a function of ToT_{offset}.

A quantification of the improvement is depicted in figure 3.37. In the following, the information reflected by the data points is explained. The standard deviations σ_{ToT} along the μ_{ToT}-axis for the curves of figure 3.36 are calculated for each pixel. They represent a measure for the variation from the mean measured ToT values. These standard deviations are calculated within a fixed temperature range of $[1580, 1600]$ DAC, chosen as it is available for all measurements of different test pulse energies. The mean and the standard deviation for all pixel values are taken. The y-axis of figure 3.37 reflects the mean σ_{ToT}. The data points themselves denote the mean, and the error bars the corresponding standard deviations. The x-position and the related error bars reflect the mean offset ToT values ToT_{offset} and their corresponding standard deviations of all pixels, each for a measurement with a fixed test pulse energy. In total, an approximate description of how the pixels deviate under temperature variation as a function of their measured energy in ToT is depicted. Two curves are shown, illustrating the described deviation before and after temperature correction. Both curves have a minimum at a mean ToT_{offset} of about 135 ToT. The temperature dependence of Dosepix almost vanishes at these deposited energies. Corrected and uncorrected measurements provide approximately the same results. For all other mean ToT_{offset},

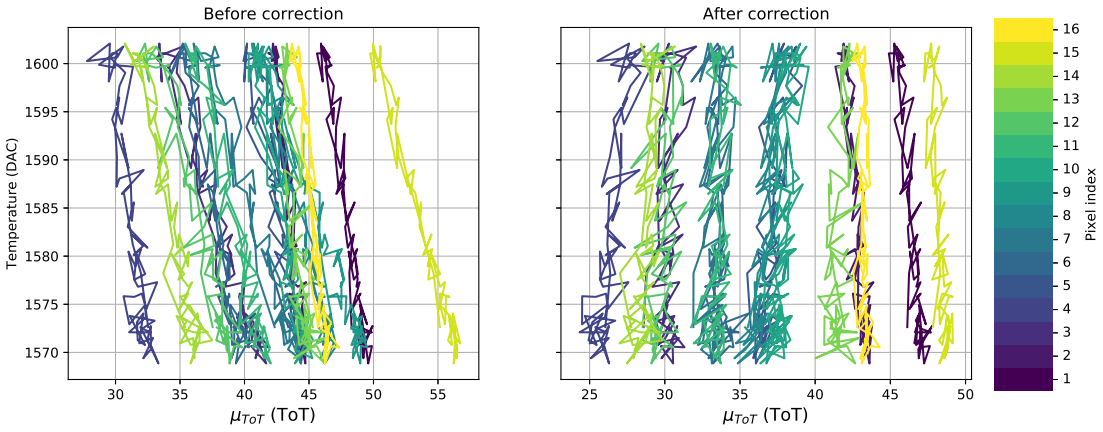

(a) Low test pulse energies

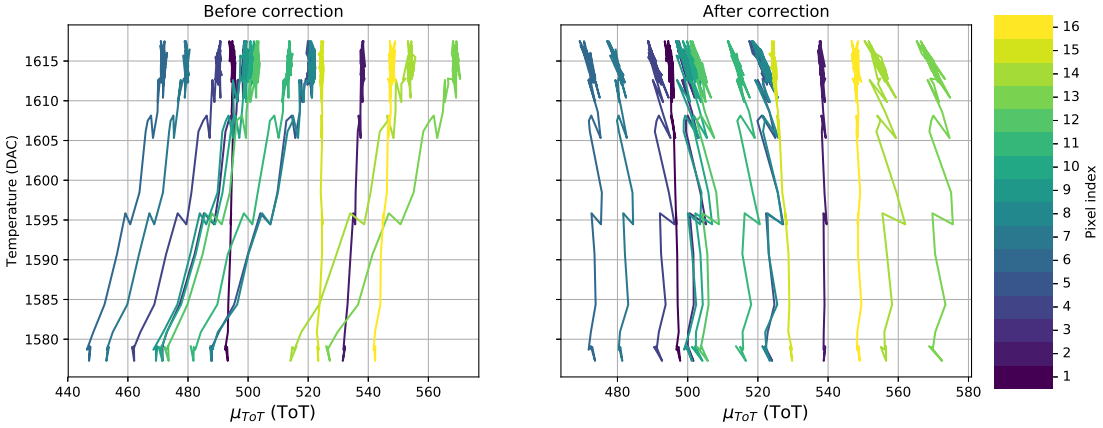

(b) High test pulse energies

Figure 3.36.: Test pulse measurements of a single pixel column under the variation of temperature. In (a), for low test pulse energies, and in (b), for high energies. The plots on the left-hand side depict the same data as the plots on the right-hand side of figure 3.34. These are the uncorrected measurements. The plots on the right-hand side of this figure resemble the data with the correction of equation (3.27) applied. The colours of the curves correspond to the pixels according to the colour bar.

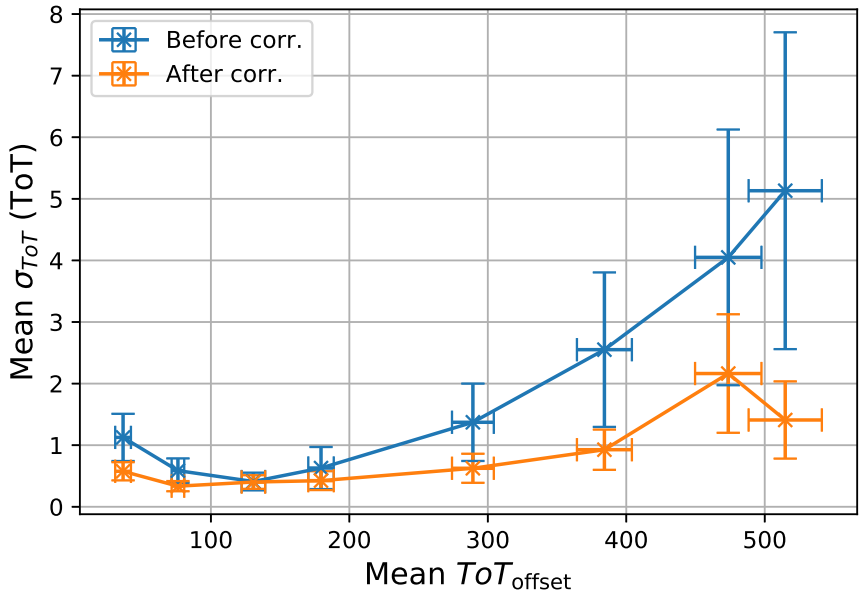

Figure 3.37.: The means of the standard deviations σ_{ToT} of the uncorrected and temperature corrected ToT measurements of figure 3.36. The error bars along the y-axis correspond to the standard deviation of the mean. Measurements for different test pulse energies are included. Their position along the x-axis is calculated by taking the mean of ToT_{offset} of all pixels. The error bar reflects the corresponding standard deviation. In conclusion, the deviations due to temperature changes are depicted as a function of ToT_{offset} for corrected and uncorrected measurements according to the legend.

the correction shows a considerable improvement. For a perfect correction, mean σ_{ToT} is independent of mean ToT_{offset}. This is not the case, mostly due to error propagation of inaccuracies introduced during the temperature calibration measurements and the model of the temperature dependence of Dosepix which is only an approximation. However, the correction procedure is considered to be successful, removing the temperature dependence for small ToT values almost completely. In the scope of a Bachelor's thesis [54], an analysis of the temperature dependence of Dosepix under a variation of I_{krum} was performed. It revealed that larger values of I_{krum} provide increased stability. The exact reason is not well understood, as the effects taking place in the analogue electronics under temperature variation are yet to be analysed in detail. One possible explanation can be found in figure 3.37. If I_{krum} is increased, the registered ToT values decrease (see section 2.1.1 for more details). For lower values of ToT, the mean deviation of the pixels σ_{ToT} is lower, and therefore temperature stability is higher. However, as all measurements presented in this chapter used a constant value of $I_{\text{krum}} = 2\,\text{nA}$, additional measurements under a variation of I_{krum} have to be

performed in the future. The value of I_{krum} is kept in the following. Larger variations in *ToT* occur when temperature changes, assisting to better visualise the temperature correction's performance.

3.3.3 Temperature corrected dose estimation

The previously described method of temperature correction can easily be applied to measurements performed in ToT-mode. Each readout provides the ToT-value per pixel, which can then be corrected and transformed into deposited energy (see chapter 4 for more information). However, this detector-mode is mostly used for an energy calibration of the detector. Therefore, laboratory conditions are present, and usually, no temperature correction is required. When using Dosepix detectors for dosimetry applications like described in sections 3.1.1 and 3.2, the situation is different since Dosi-mode is utilised. Bin edges in ToT are defined in hardware registers, and a binning state machine directly sorts registered ToT-events into a histogram. If temperature changes, the measured ToT-values change, and events might be attributed to the wrong bin. It leads to a distortion of the mean registered deposited energy and also the measured dose. The higher the temperature deviation, the larger the discrepancy of the registered dose. Since it is possible to perform a temperature correction for measured ToT-values, the bin edges utilised in Dosi-mode could be corrected while Dosepix is measuring. However, during a change of hardware settings, no events are correctly sorted into bins. Also, entries in the histogram might get corrupted. Therefore, a short dead-time is introduced which can have a large influence on dose estimation. Also, it would always lead to an underestimation of dose which should be avoided.

A different correction strategy is utilised in the following. Instead of changing the bin edges in hardware, the dose conversion coefficients from registered events to dose equivalents are varied. The polynomial conversion coefficients introduced in section 3.2.9 are used. These allow to directly sample coefficients from the defined polynomial functions for certain deposited energies E. The registered deposited energy spectrum in ToT deviates under temperature variation, while the bin edges in Dosi-mode, specified in ToT, stay the same. The deposited energy axis used to sample the conversion coefficients from the polynomial conversion factors must be scaled accordingly to correct temperature variation.

A measurement with an ^{241}Am calibration source is used to explain the procedure in detail. The Dosepix dosemeter consisting of three detectors with different filters (see section 3.2.1 for more details) and the radioactive source are put in a refrigerator. The air is cooled down to about $-20°$C, the refrigerator is turned off, and the dosemeter takes data until room temperature of about 20°C is reached. The trend of the temperature as recorded with the *Vac* Dosepix is illustrated in figure 3.38. Temperature is reflected in units of DAC, which is inverse to °C. The measurement duration is about 6 hours due to the insulation of the refrigerator. The information of the internal

temperature sensor of Dosepix is very noisy, reflected in blue, and therefore smoothing via a moving average over 10 frames is applied, resulting in the orange curve. This smoothing is reasonable for real applications as readout time is fast compared to the change in temperature.

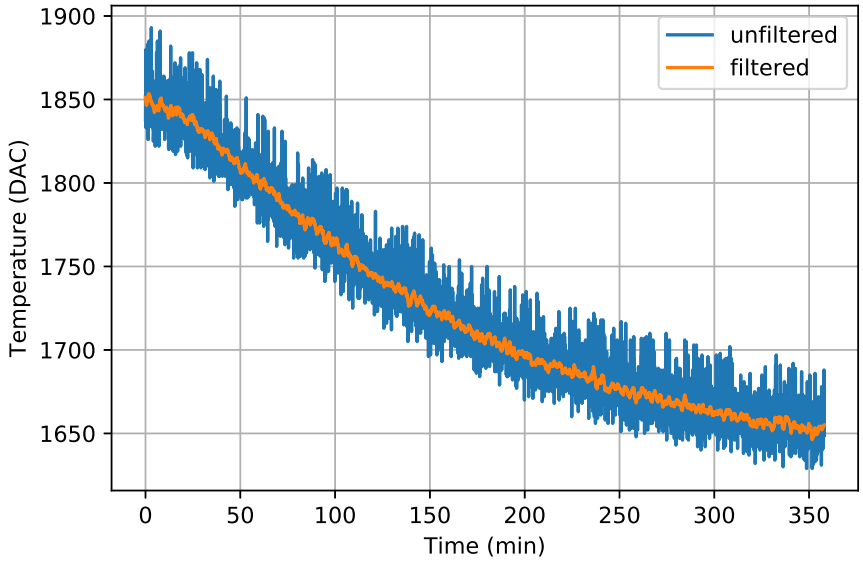

Figure 3.38.: Temperature variation for a measurement of an ^{241}Am calibration source. The Dosepix dosemeter described in section 3.2.1 is used. The setup is put in a refrigerator and cooled down to about $-20°$C. The measurement is started, the refrigerator turned off, and the temperature is recorded via the *Vac* detector in units of DAC. After about 6 hours, the temperature is about 20°C, and data acquisition is stopped. The unfiltered temperature data, shown in blue, is filtered by taking a moving average over 10 frames, resulting in the orange curve.

Measured frames at different temperatures are depicted in figure 3.39. These include the number of registered events for the specified bin edges used in Dosi-mode. The curves reflect the different Dosepix detectors of the dosimetry setup according to the legends.

The bottom right plot corresponds to a measurement performed at approximately room temperature, and therefore, calibration temperature. The other plots show measurements at cooler temperatures. For the top left plot, the temperature is approximately $-20°$C. The deposited energy spectrum of the *Vac* detector is broadening with decreasing temperature. The spectra of the other detectors only change slightly since their hemispherical metal filters insulate them. The cool-down via the refrigerator was too fast to reach a thermodynamic equilibrium of the air and the detectors. The temperature was only measured via the *Vac* detector due to limitations of the

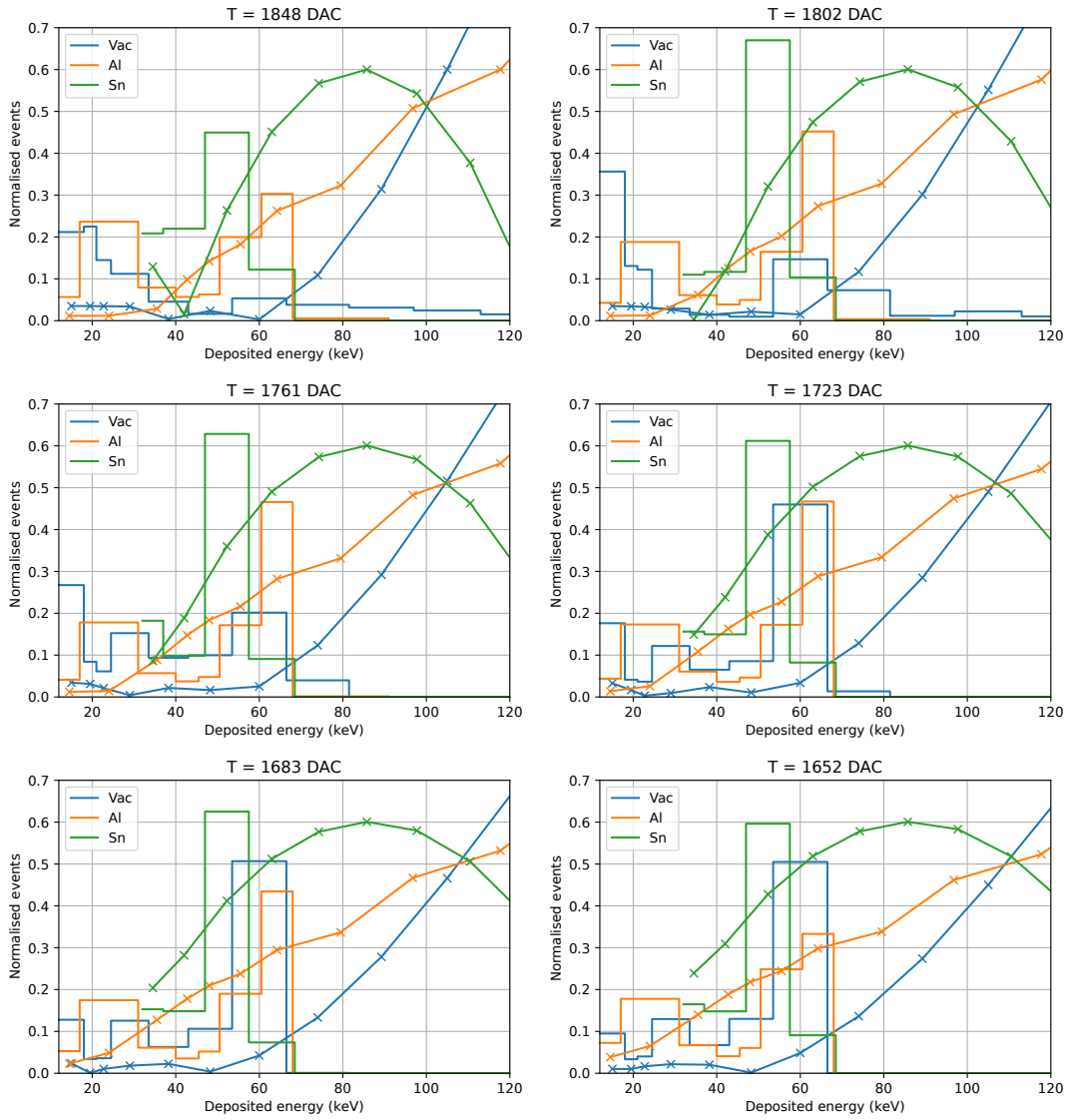

Figure 3.39.: The number of registered events in Dosi-mode for the measurements of an Am^{241} source under temperature variation. Each plot represents an excerpt of the dataset at certain temperatures as indicated by the titles. The plot on the top left corresponds to a temperature of about $-20°C$, the plot on the bottom right to a temperature of about $20°C$. The histograms indicate the normalised number of events for the different detectors according to the legend. The curves with markers indicate the values of the used conversion coefficients to calculate the dose from registered events.

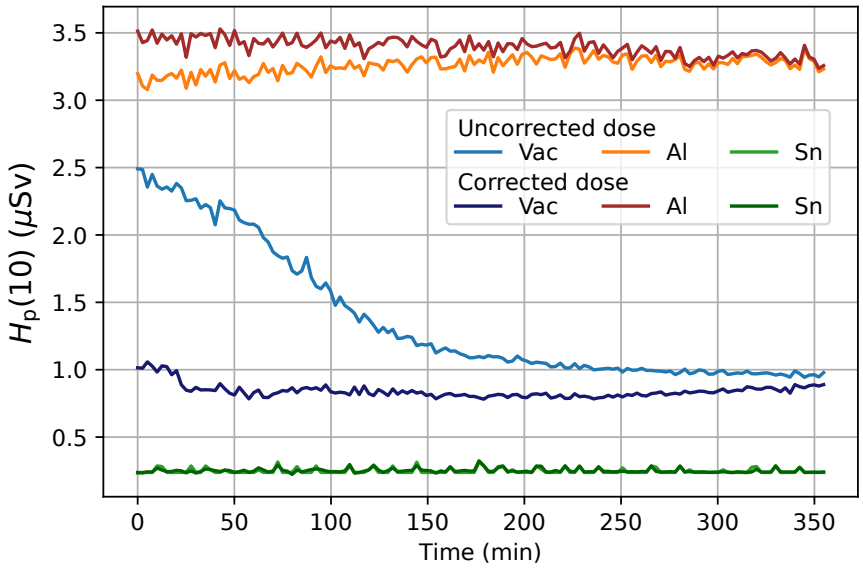

Figure 3.40.: The reconstructed dose $H_p(10)$ per detector of the Dosepix dosemeter setup for the measurement of ^{241}Am under temperature variation. The time information corresponds to the temperature plot of figure 3.38. The colours reflect the different detectors according to the legend. Light-coloured curves represent the doses before, dark-coloured curves after the temperature correction.

readout-hardware. In general, the temperature should be measured for each detector separately to achieve the best results.

For decreasing temperature in °C, the deposited energy spectra start to broaden and the dose conversion coefficients have to compensate this effect. A virtual deposited energy axis is introduced. It scales with the temperature correction of equation (3.26) and is afterwards applied to the polynomial functions of equation (3.23) to provide the dose conversion coefficients. The curves with data points in figure 3.39 reflect the values of these coefficients. The y-axis does not represent the actual values but is proportional to them and indicates the change of the coefficients. The points' positions along the x-axis correspond to the mean deposited energies of the bin edges. These indicate which coefficient is used for which bin in dose calculation. With changing temperature, also the dose conversion coefficients change. Due to the energy correction, the virtual deposited energies lead to a change in the histogram's effective bin widths. This effect is corrected by scaling the dose coefficients by fractions of the virtual and original bin widths.

The corrected conversion coefficients are used to reconstruct the dose. Only $H_p(10)$ is discussed, while the procedure is analogous for other dose types. Figure 3.40 shows the estimated dose as a function of time while the temperature changes as shown in

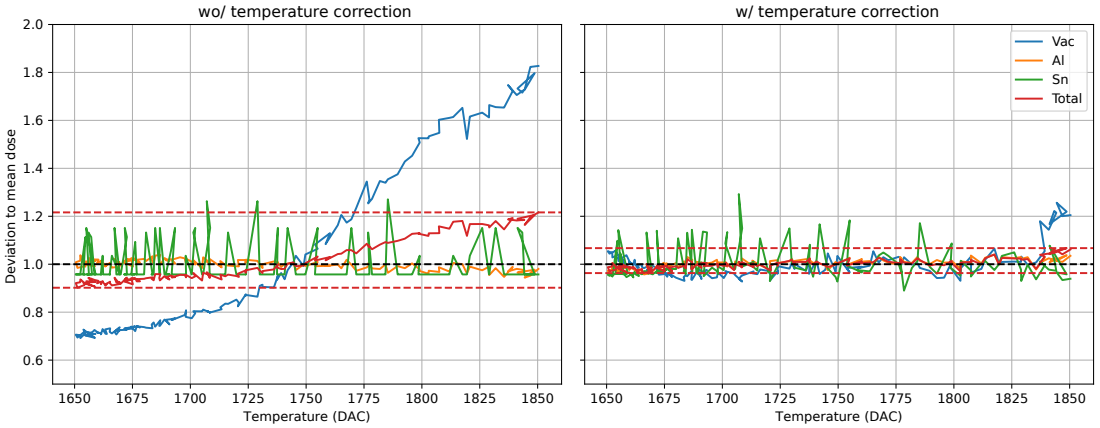

Figure 3.41.: The deviations to the means for the measured doses of $H_p(10)$ depicted in figure 3.40. The x-axis reflects the temperature variation of figure 3.38. The colours of the curves represent the different detectors, according to the legend. The solid red line corresponds to the total dose, i.e. the sum over the single detectors' doses. Red dashed lines indicate the minimum and maximum values of the red curves.

figure 3.38. The different colours of the curves correspond to the different detector types according to the legend. Light-coloured curves represent the doses before correction, dark-coloured curves after correction. Taking the sum of all detectors provides the total dose of $H_p(10)$. Since the temperature at the end of the measurement equals approximately the calibration temperature, these doses reflect the reference values. The applied temperature correction has only a small effect on the registered doses of the *Al* and *Sn* detectors due to the insulation of the filters. For the *Vac* detector without correction, the dose deviates about 2.5 at maximum compared to the reference calibration temperature. This deviation is much smaller after correction, and the trend of the dose corresponding to the change of temperature is no longer visible.

3.41 additionally shows the improvement due to the temperature correction. The plots depict the doses for the dosemeter's detectors and their sum, the total dose. Every curve is normalised to reflect the deviation from the mean. The x-axis indicates the temperature present during measurements. The higher its value, the lower the temperature in °C. The colours of the curves correspond to the detectors as indicated by the legend. The left-hand side plot shows the dose without temperature correction, the right-hand side plot with correction applied. For the uncorrected doses, *Al* and *Sn* show only slight variations while *Vac* varies within a range of about $[0.7, 1.8]$. After correction, these deviations are almost completely gone. The *Sn* detector in general shows large fluctuations about a value of 1, which is due to the low count statistics compared to the other detectors.

The solid red curves in the plots of 3.41 reflect the total dose measured with the Dosepix dosemeter. The dashed lines indicate the corresponding minimum and maximum values. The statistical quantities for the total doses illustrated in figure 3.40 are listed in table 3.7. They include the mean μ, the related standard deviations σ, and the minimum and maximum doses. Additionally, the extreme values of the curves normalised to the mean depicted in figure 3.41 are listed. The first column indicates if temperature correction is applied to the data of a row. The last row shows the fraction of uncorrected and corrected values. Under the assumption that corrected measurements more closely resemble the actual dose values, the fractions show that uncorrected measurements on average overestimate the dose. The corresponding standard deviation is almost 5 times higher for the whole temperature range. The deviation is highest for cold temperatures in °C as indicated by comparing the mean and maximum of the uncorrected dose. Here, the dose is overestimated by about 22%. After correction, the overestimation drops to 7%. The standard deviation σ shows an improvement of about 80% after correction.

Corrected	μ (µSv)	σ (µSv)	min (µSv)	max (µSv)	min (norm)	max(norm)
no	4.87	0.44	4.39	5.93	0.9	1.22
yes	4.49	0.09	4.32	4.79	0.96	1.07
no / yes	1.08	4.89	1.02	1.24	0.94	1.14

Table 3.7.: The statistical quantities of the total measured doses, corresponding to the sum of all detectors and therefore curves depicted in figure 3.40. These include the means μ, the standard deviations σ, and the minimum and maximum values. Additionally, the extreme values for the normalised total doses of figure 3.41 are listed. The rows represent the corrected and uncorrected data according to the first column. The fraction of uncorrected and corrected statistical values are resembled by the last row.

In conclusion, temperature correction is improving the estimated doses. All deviations, also uncorrected ones, are within the legal limits for the dose response of 0.71 and 1.67 according to PTB [53]. However, there might be individual photon spectra for which this is no longer the case. Also, temperature always remained within limits of -20°C to 20°C for the discussed data. Varying the temperature further will lead to an increased dose variation which requires additional measurements and analysis. The introduced method of temperature calibration improves the dose estimation capabilities of a Dosepix dosemeter and increases the system's quality.

3.4 Conclusion

The main goal of this chapter was to establish a proper implementation of Dosepix in simulation. It allows generating detector responses for the irradiation with various

photon fields. Measurement setups can be included in the geometry of the simulation to accurately model reality. The proper functioning of the simulation was validated by comparing its results with measurements. A good performance was achieved, and the energy resolution of the detector was determined. Both are requirements to perform simulations of a dosemeter consisting of three Dosepix detectors. The setup for a measurement of $H_\mathrm{p}(0.07)$ and $H_\mathrm{p}(10)$ personal dose equivalents, including a phantom, was implemented in simulation. Via the generation of response spectra for the irradiation with monoenergetic photons, the optimisation of conversion factors from registered events to dose was executed. These factors were applied to measurements and compared to simulations, which showed a good agreement. However, there are discrepancies for lower photon energies. A method was introduced to include measurements into the optimisation of the dose conversion factors. The method leads to responses that only slightly deviate from the perfect response of 1 for $H_\mathrm{p}(10)$ and irradiation angles of up to 60°. $H_\mathrm{p}(0.07)$ dosimetry is well for initial photon energies greater than about 25 keV as the performance is limited by high irradiation angles. Based on the methods established in this thesis to determine dose conversion coefficients, additional measurements regarding legal requirements were executed in cooperation with PTB and published in [55]. Additionally, the coefficient of variation was analysed, reflecting the fraction of the standard deviation and mean of multiple dose measurements. The results are well within the legal limits and further approve the applicability of the Dosepix dosemeter for measurements of $H_\mathrm{p}(10)$ and $H_\mathrm{p}(0.07)$. By combining simulation and measurement data, smooth dose conversion factors were determined which resulted in a smoothness corresponding to increased stability of dose estimation of the dosemeter.

A method was introduced to determine dose conversion factors for the small pixels of Dosepix. It utilises measurements and the fact that small and large pixels should always return the same dose. For the previous methods, discrete conversion factors were used. However, an approach to describe their trend via polynomial functions was introduced, which provided similar performance. The benefit is that the function's number of parameters is reduced, and generally smooth trends as a function of deposited energy are achieved. The method also is a requirement to perform a temperature-dependent correction of the dose. The behaviour of Dosepix under temperature variation was analysed and a method to correct this dependence was introduced. It allows performing proper dose reconstruction even for extreme temperatures.

In conclusion, simulations of the detector were established and evaluated with measurements. A first application in regards to dose estimation was introduced. Everything established in this chapter is essential and the represents the foundation for the following chapters.

CHAPTER 4

Energy calibration of Dosepix via deep learning

Contents

The energy calibration of pixelated photon-counting detectors usually involves measurements with radioactive sources over extended periods. This is due to small pixel sizes and resulting low event rates. Only the parts of measured energy spectra containing peaks are used in these established calibration methods. Therefore, a possible improvement is to use entire recorded energy spectra to calibrate a Dosepix detector.

This is achieved via deep learning, which provides a fast method to process information of all pixels of a detector at once. Simulation data is generated and used to train a convolutional neural network. Calibration measurements with the detector are performed for various hardware settings of Dosepix. The neural network provides the corresponding calibration coefficients to convert the registered ToT spectra to deposited energy. These spectra are analysed and used to evaluate the method.

4.1 Standard energy calibration

A commonly used calibration approach is called standard calibration in the following. Here, a brief introduction of the method is provided. See for example [52, 56] for a more detailed description.

4.1.1 Calibration measurements

In the standard calibration procedure, detector measurements with various gamma calibration sources are required. The emitted spectra of these sources should consist of mono-energetic lines that are not too close to each other in energy. Additionally, high activity, and therefore photon flux, is desirable as this leads to a higher number of registered events within a short time. Usually, an X-ray tube with different fluorescence targets is used. The energy depositions in the sensor lead to broad peaks in the ToT-spectra registered by the detector. Figure 4.1 depicts this for X-ray tube measurements of various fluorescence targets and a measurement of an ^{241}Am-source. Only data of an exemplary large pixel is depicted. The rough positions of the peaks in the ToT-spectra are determined by applying a peak finder. Only the regions centred about the peak are kept. Gaussian fits are used to get estimations of the mean peak energies. The energies of the various fluorescences are well known (they can be looked up at e.g. [41]). These energies have to be converted into their corresponding deposited energies via equation (3.7). Afterwards, the values are matched to the estimated peak positions in the ToT-spectra as depicted in figure 4.2.

4.1.2 Calibration function

A calibration curve has to be fitted to the dataset consisting of deposited energies and corresponding measured ToT values to convert deposited energies into ToT. Most publications working with pixel detectors similar to Dosepix or Dosepix itself use a function of the form [57]

$$ToT(E) = aE + b + \frac{c}{E - t}. \tag{4.1}$$

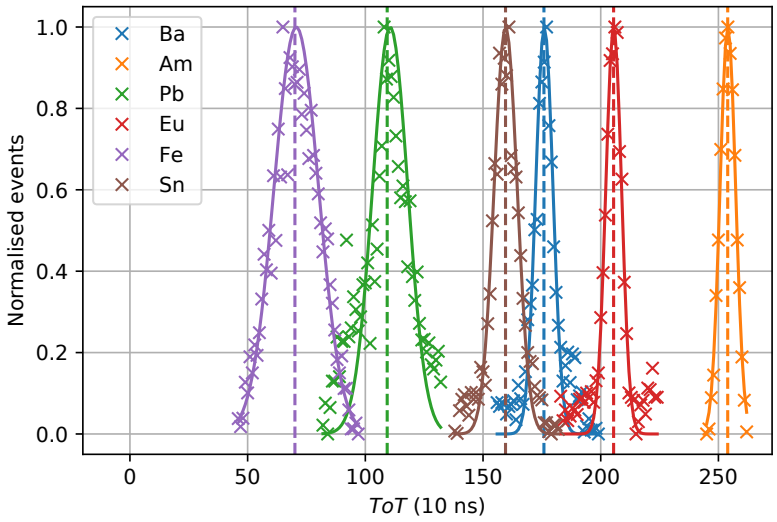

Figure 4.1.: Measurements of fluorescence targets irradiated with an X-ray tube and of an ^{241}Am-source according to the legend. The data registered by an exemplary large pixel is depicted. Only the regions about the peaks are kept to estimate the mean peak positions. These are determined from Gaussian fits and indicated by the dashed lines.

This function is invertible, i.e. the conversion from deposited energy into ToT is possible via

$$E(ToT) = \frac{1}{2a} \cdot \left(a \cdot t + ToT - b + \sqrt{(b + a \cdot t - ToT)^2 - 4 \cdot a \cdot c} \right). \tag{4.2}$$

Solving this equation for $E(ToT = 0)$ provides the threshold energy E_{THL}

$$E_{\mathrm{THL}} = \frac{1}{2a} \cdot \left(a \cdot t - b + \sqrt{(b + a \cdot t)^2 - 4 \cdot a \cdot c} \right). \tag{4.3}$$

This energy resembles the lowest deposited energy the detector can measure. Figure 4.2 shows fits to deposited energy and ToT pairs via equation 4.1 for 12 exemplary large pixels. If not specified otherwise, equation (4.1) and its inverse (4.2) are used for the conversion of ToT to energy and vice versa in this thesis. Equation (4.1) will be referred to as calibration function.

4.1.3 Calibration function parameters

A detailed analysis of the parameters a, b, c, and t of calibration function (4.1) is illustrated in figure 4.3. Each parameter, as indicated by the title, is scaled according

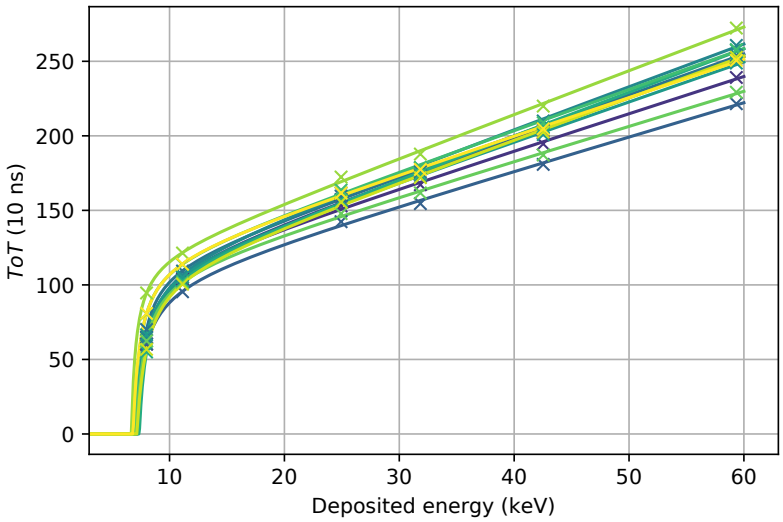

Figure 4.2.: Peak positions of ToT spectra of calibration measurements as a function of corresponding deposited energy. The positions are determined by fitting Gaussians to the peaks of the registered ToT spectra. Error bars indicate the fit error but are too small to be discernible. 12 large pixels of an exemplary pixel column are depicted. Calibration function (4.1) is used to describe the trend of the data points.

to the colour bar while the remaining parameters stay constant. Here, constant values of $a = 2.15$, $b = 150$, $c = -275$, and $t = 7.5$ are used.

Each parameter attributes to a certain characteristic of the calibration curve:

- a: describes the slope of the linear part of the curve and is therefore representing I_{krum}
- b: shifts and scales the curve along the ToT-axis
- c: changes the hardness of the knee of the curve
- t: shifts and scales the curve along the deposited energy axis

4.1.4 Analogue test pulse calibration function

The trend of ToT as a function of charges at the input of a pixel's analogue electronics is approximated utilising the test pulses of Dosepix (see section 2.1.3 for more information). Voltage U_{TP} of equation (2.2) is varied, multiple test pulses are created, and a spectrum in ToT-mode is taken. Afterwards, the mean and the standard deviation for each spectrum are calculated. This provides the blue data points depicted in the

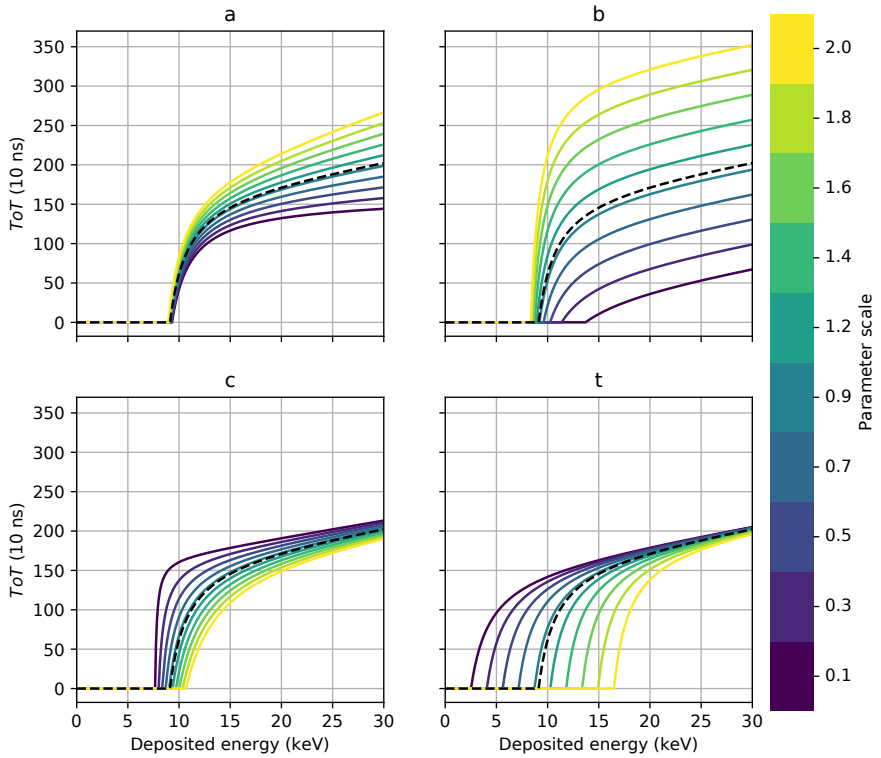

Figure 4.3.: The variation of the parameters of calibration function (4.1). The parameter shown in the title of each plot is scaled according to the colour bar while the remaing parameters stay constant. The dashed line represents the calibration curve for the initial calibration parameters of $a = 2.15$, $b = 150$, $c = -275$, and $t = 7.5$.

top plot of figure 4.4. The x-axis reflects test pulse energies, resembling an arbitrary measurand proportional to the injected charge at the input of the analogue electronics. The illustrated data is for an exemplary pixel. However, all pixels show a similar trend and no difference between large and small pixels exists as charges are injected directly into the electronics' input, neglecting the sensor.

A calibration curve is fitted to the data, resembled by the black dashed line. The bottom plot shows the relative deviation of ToT_{pulse} from measurements and ToT_{fit} from fit by calculating

$$1 - \frac{ToT_{\text{pulse}}}{ToT_{\text{fit}}}. \tag{4.4}$$

The deviation shows that the used calibration function does not entirely match the trend of the data. Test pulses provide an easy method for this evaluation. The same can be achieved using measurements with radioactive sources. However, their mean

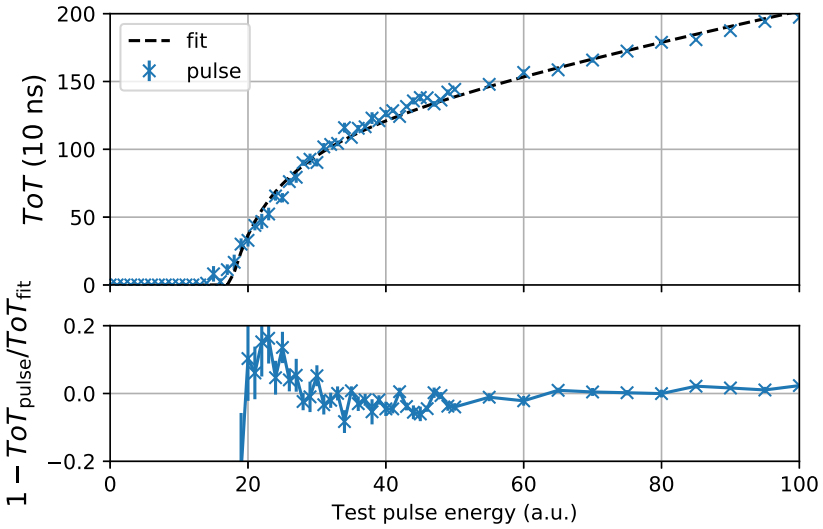

Figure 4.4.: The top plot depicts the registered mean *ToT* values for different test pulse energies in blue. Error bars reflect the corresponding standard deviations for each data point. The energy-axis is scaled arbitrarily. The dashed black line represents a fit with the calibration function. The bottom plot depicts the relative deviation of the curves of the top plot. Error bars are determined via error propagation.

photon energy cannot be controlled like it is possible for the test pulses. Despite the deviation, the previously defined calibration function is used. Its formulation is easy and only involves 4 parameters. The actual trend is too complex to be described with an analytical function. Instead, an interpolated function would be required. However, in most applications, there is no requirement for this high precision. In dosimetry applications, the loss of accuracy due to the standard calibration function is neglectable.

4.1.5 Disadvantages

The standard calibration method requires radioactive sources with a high photon flux. This provides a reasonably large number of registered events per pixel to estimate the peak positions in the ToT-spectra. Multiple measurements with various sources are necessary. At least five measurements are required, but the more, the better the final calibration.

For deposited energies close to the detector's threshold, mistakes are made easily as many events due to effects like charge sharing and Compton scattering are present. If a peak of a deposited fluorescence energy is located in this regime, it superimposes with it and is not identifiable anymore. Converting this spectral shape into ToT leads

to a broad peak in the spectrum, often misidentified for a fluorescence energy. This misidentification then leads to a matching to a too-small ToT value. Fitting the calibration curve to the mean peak energies will then result in an underestimated energy threshold.

4.2 Energy calibration via deep learning

The standard calibration approach requires multiple measurements with various sources to determine proper calibration parameters for the pixels of the detector. Only a small region of the ToT spectra is used to gain information about the conversion from ToT to deposited energy in each measurement, while the remainder is discarded. An improved approach to calibration should consider the spectrum as a whole. Instead of taking multiple measurements, only a single calibration source and a short measurement duration should be required. In the following, a convolutional neural network (CNN) is utilised for this task. See section 2.5 for more information about deep learning.

4.2.1 Network design

The network takes a ToT spectrum of a single pixel, binned to 400 values with its left bin edges ranging from 0 to 400, as its input and outputs the corresponding 4 calibration parameters of equation (4.1) to convert the input ToT spectrum into deposited energy.

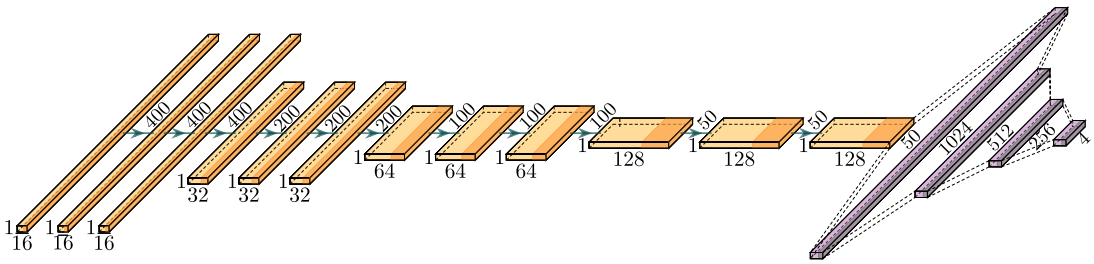

Figure 4.5.: Convolutional neural network for the conversion of ToT to deposited energy for Dosepix. It takes a ToT spectrum at its input and provides the corresponding conversion parameters of equation (4.1) as its output. Yellow blocks correspond to convolutional layers, purple blocks to fully connected layers. The dark regions within the blocks indicate the use of a ReLU activation function. The image is created using [58].

The design of the network is depicted in figure 4.5. The network consists of four major groups of three successively stacked convolutional layers of the same filter size each. Average pooling layers halve each group's input size while the filter sizes are

doubled, with an initial size of 16. The last convolutional layer's output is flattened to one dimension and reduced via fully connected layers to the desired output size of 4, corresponding to the number of conversion parameters. In-between these layers, dropout of 20% is used to prevent overfitting. All layers use a ReLu-activation function except for the output layer, which has no activation. Additionally, a custom layer that is only active during training provides additional regularisation via data augmentation. This layer is placed directly after the input and applies Gaussian noise with a random standard deviation to the input ToT spectrum parts that are not 0. The standard deviation is sampled from a uniform distribution ranging from 0 to 0.3 per input spectrum. The corresponding noise $\tilde{X}$ is sampled and the initial spectrum is multiplied with $1 + \tilde{X}$. An example of the functioning of the layer is depicted in figure 4.6. As a whole, the design of the network corresponds to an encoder. It compresses the complex input data and represents it on a simple latent space, represented by the four calibration parameters.

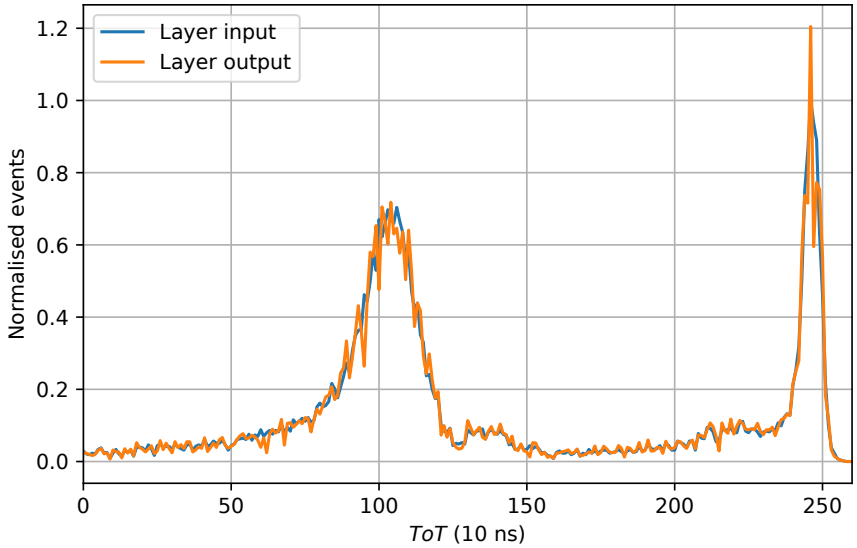

Figure 4.6.: The input (blue) and output (orange) spectra of a custom layer which adds Gaussian noise with a random standard deviation to the non-zero parts of the input ToT spectrum during training.

4.2.2 Training and validation data generation

Only one type of source should be used for the calibration of the detector. Therefore, the measured deposited energy spectrum has to be diverse in its shape, i.e. it should consist of various characteristic peaks and edges. It should also contain high deposited energies as this allows an accurate modelling of the linear part of the calibration function. Although X-ray tubes have a high photon flux, they wear off when permanently used and are expensive in purchase and maintenance. Therefore, an ^{241}Am calibration source with high activity is used instead. To further extend the photon spectrum's features, a molybdenum fluorescence target is placed directly in front of the source. The readout hardware with detectors attached is placed in front of the assembly of calibration source and target. A short test if all detectors show a reasonable event rate is made. The rate is adjusted by moving the detectors or the source until an optimal position is found. The central detector, sitting directly in front of the source's opening, will show the highest event rate and a slightly differently shaped spectrum compared to the neighbouring detectors. These effects have to be considered when creating training data for the network.

The buildup of the used calibration source is resembled via simulated spectra. Multiple sources are combined randomly to gain robustness for variations of the setup and its surroundings. Detector responses for ^{241}Am, Mo- and Sb-fluorescences of a Dosepix detector are simulated separately first. Antimony is found in many lead alloys to harden the material. This includes lead bricks for radiation shielding and housings of calibration sources like for the Am-source.

The different simulated spectra are combined with specified shares. Americium represents the reference amount, called f_{Am} and is set to 1. The amounts of molybdenum and antimony are called f_{Mo} and f_{Sb}. The combination of spectra is done as follows. First, various parameters are chosen randomly and uniformly from specified ranges. These include the total number of events N in the final spectrum, the shares of Mo and Sb in comparison to Am, and the calibration parameters a, b, c, and t of the calibration function (4.1). The ranges of the used values for small and large pixels are listed in table 4.1. The simulated spectra are provided as unbinned data. N_i events are chosen randomly via the determined fraction f_i according to

$$N_i = N \cdot \frac{f_i}{\sum_j f_j},$$

where $i \in \{\mathrm{Am}, \mathrm{Mo}, \mathrm{Sb}\}$.

1024 exemplary deposited energy spectra for large pixels are depicted in figure 4.7. The deposited energies of the events are converted into ToT via the selected random calibration parameters and calibration function (4.1). The values are combined into a ToT histogram which is stored together with its label, represented by the parameters a, b, c, and t, in a training and validation dataset. The histograms are normalised to

parameter	lower limit	upper limit
a	0.3	4
b	100	200
c	-500	-50
t	5	10
N	5000	100000
f_{Mo}	0.6	0.8
f_{Sb}	0	0.05

Table 4.1.: The ranges for the randomly and uniformly distributed parameters of equation (4.1) to convert deposited energy spectra into ToT spectra for training and validation data generation.

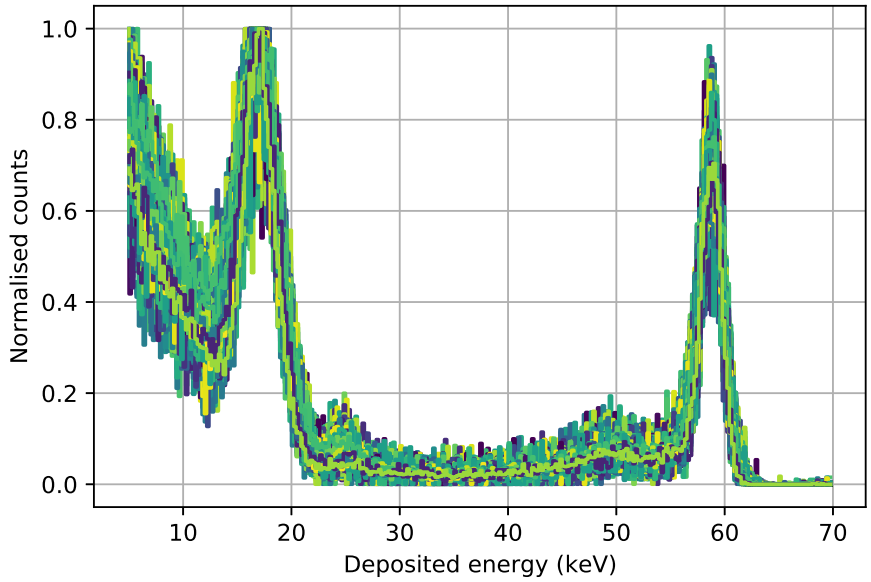

Figure 4.7.: 1024 deposited energy spectra generated by combining large pixel simulations of an ^{241}Am-source, and Mo- and Sb-fluorescences. More information about the generation procedure is given in the text.

their maximum each and the parameters to the mean values of the defined parameter ranges in table 4.1.

Figure 4.8 shows the calibration curves for 1024 randomly chosen calibration parameter sets of the validation dataset. The curves are overlayed on top of each other in (a). The density of the curves is depicted in (b), which indicates the influence of the calibration parameters on the resulting deposited energy to *ToT* conversion. Since large and small pixels use the same conversion parameter ranges, the distributions of the calibration curves look similar. The deposited energy spectra for the different

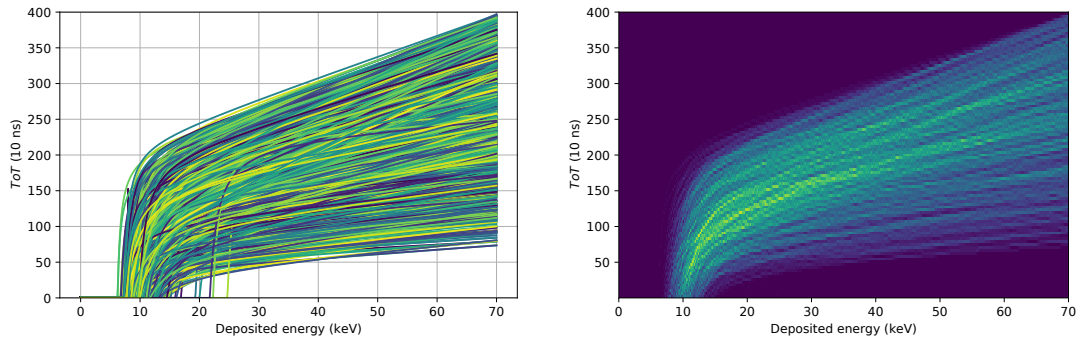

(a) Generated calibration curves

(b) Density of generated calibration curves

Figure 4.8.: (a) shows the calibration curves of 1024 randomly chosen calibration parameter sets from the validation dataset. The density of the curves is illustrated via a 2D histogram in (b). Only data of large pixels is used.

pixel sizes look significantly different. Therefore, the conversion from the constructed deposited energy spectra to ToT has to be processed separately.

4.2.3 Loss definition

Two losses are used during the trainings of the networks. Both are used for the large pixels, only the first is used for the small pixels. The loss is a regular mean squared error of the form

$$L_{\text{MSE}} = \frac{1}{4}\sum_{i=1}^{4}(y_{\text{pred},i} - y_{\text{true},i})^2, \tag{4.5}$$

where $\vec{y}_{\text{pred}}$ and $\vec{y}_{\text{true}}$ are vectors containing the four predicted and target calibration parameters.

The second loss is called peak-loss L_{peak} and is only used for the large pixel network. It describes how well peak positions of a ToT spectrum fit the expected values. This is achieved by using a second set of labels that contains the peak positions in ToT. These are determined via peak finding and fitting of a scaled normal distribution to the training data's ToT spectra. During loss evaluation, these peak values are converted from ToT to predicted deposited energy E_{pred} via the calibration parameters in $\vec{y}_{\text{pred}}$ and the calibration function (4.1). The peak-loss also includes the mean squared error L_{MSE} and is defined as

$$L_{\text{peak}} = \frac{1}{2}\sum_{i\in\{\text{Am,Mo}\}}(E_{\text{pred},i} - E_{\text{true},i})^2 + L_{\text{MSE}}, \tag{4.6}$$

source	E_{init} (keV)	E_{dep} (keV)
Am	59.54	59.35
Mo	17.44	17.27

Table 4.2.: Initial and deposited energies for an ^{241}Am-source and a Mo-fluorescence target. Only dominant energies are listed and used. The initial energies are taken from [41].

where the sum of i iterates over the peak energies of the Am-source and Mo-fluorescences. The Sb-fluorescence is not considered, as it does not create a dominant peak in the spectrum.

The important energies for Am and Mo are listed in table 4.2 which includes the initial energies E_{init} and the corresponding deposited energies for large pixels E_{dep}. The deposited energies are calculated using the method introduced in 3.1.3. Data of the initial energies are taken from [41]. The value for Mo is the weighted sum of multiple energies. Deposited energies are only stated for large pixels as loss L_{peak} is only used for the large pixel network. When the losses are evaluated, they are calculated for each sample of the batch first and the average of all samples of a batch is provided. In the following section about the network's training, more details about when which loss is used is described.

4.2.4 Training process

Since the deposited energy spectra for large and small pixels are significantly different, each pixel type requires a network that is trained separately. The network for the large pixels is trained on 120k samples and validated on 20k samples. The training is divided into two stages to achieve a higher precision. First, the mean squared error loss L_{MSE} is used. The training progress is depicted for the first 100 epochs in figure 4.9 (a). Once a good performance of the network is reached, the loss function is switched to L_{peak}. This allows the CNN to further increase its ability to match the peak ToT values to their corresponding deposited energies. The training process is illustrated in figure 4.9 (b). Both losses in the two training stages show an offset between training and validation due to the additional error introduced by dropout during training (see section 2.5.3 for more information). Nevertheless, the training is considered successful as the loss converges properly, and there is no indication of overfitting.

The network for the small pixels is trained on 60k samples and validated on 10k samples. The training now only uses the mean squared error loss L_{MSE}. The peak-loss is neglected since peak fitting in the training data is not precise due to low event statistics and the resulting non-dominant shapes of the peaks. This is especially noticeable for the Mo-fluorescence peak, which is close to the low energy part of the spectrum and might even blend with it. The trend of the loss during training is depicted in

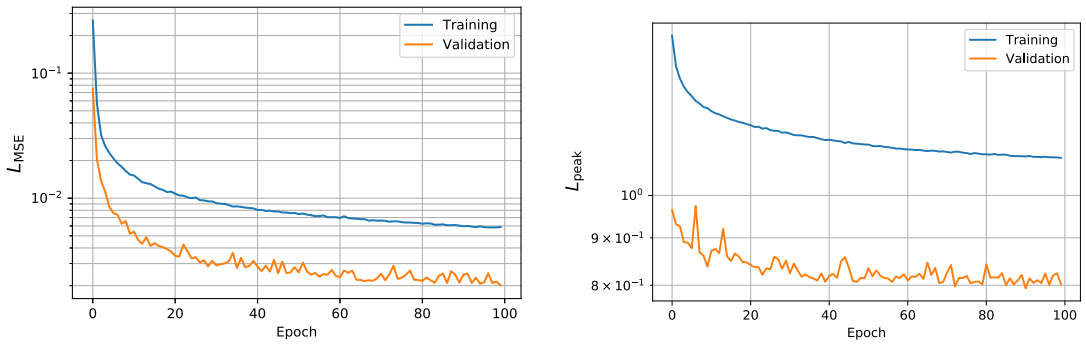

(a) Mean squared error loss L_{MSE}

(b) Peak-loss L_{peak}

Figure 4.9.: The training of the large pixel network is performed in two stages. First, using the mean squared error loss L_{MSE} (a) and afterwards using the peak-loss L_{peak} (b). The minimisation of the losses as a function of epoch is shown. An epoch describes 120k samples for training and 20k samples for validation.

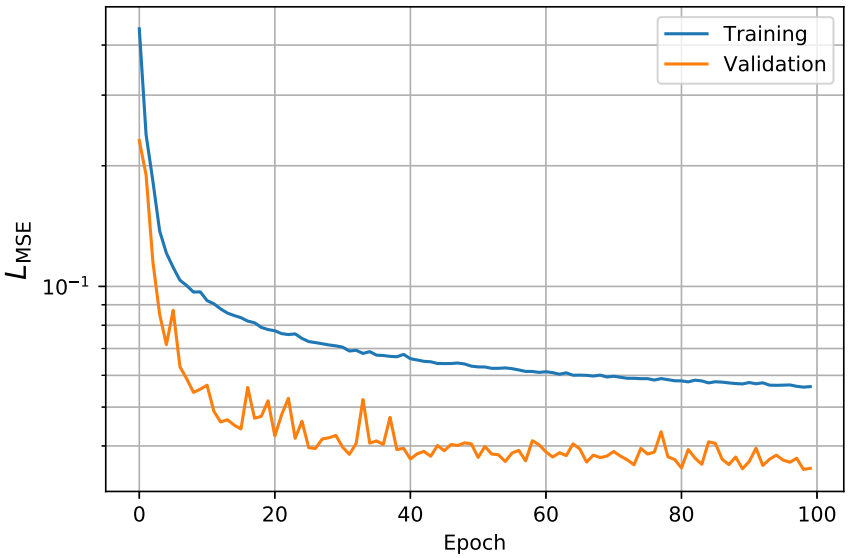

Figure 4.10.: The small pixel CNN training is performed in a single stage using the mean squared error loss L_{MSE}. The minimisation of this loss is depicted as a function of epoch. One epoch represents 60k samples in training and 10k samples in validation.

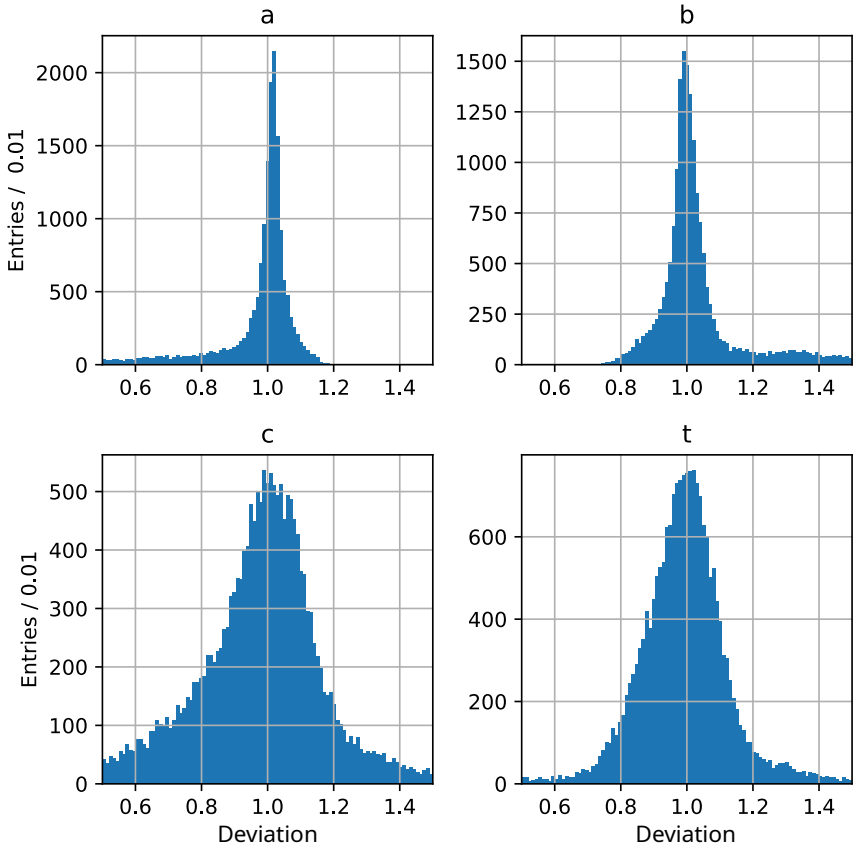

Figure 4.11.: Histograms of deviations X of actual and predicted values, according to equation 4.7, for the validation dataset's calibration parameters for large pixels. The histograms correspond to the parameters according to their titles.

figure 4.10. Like before for the large pixels, the discrepancy for training and validation is due to the used dropout during training. After the trainings for the large and small pixel networks, predictions on the validation datasets are performed. The predicted and true values for the calibration parameters a, b, c, and t are combined into vectors $\vec{y}_{\text{pred}}$ and $\vec{y}_{\text{true}}$. The deviation in regards to their target values are calculated via

$$X_i = \frac{y_{\text{pred},i}}{y_{\text{true},i}}, \tag{4.7}$$

where i is an index over $\{a, b, c, t\}$. Histograms for these fractions are depicted in figure 4.11 for large and in figure 4.12 for small pixels. Table 4.3 shows the statistical quantities of the distributions of the deviations for large (a) and small pixels (b).

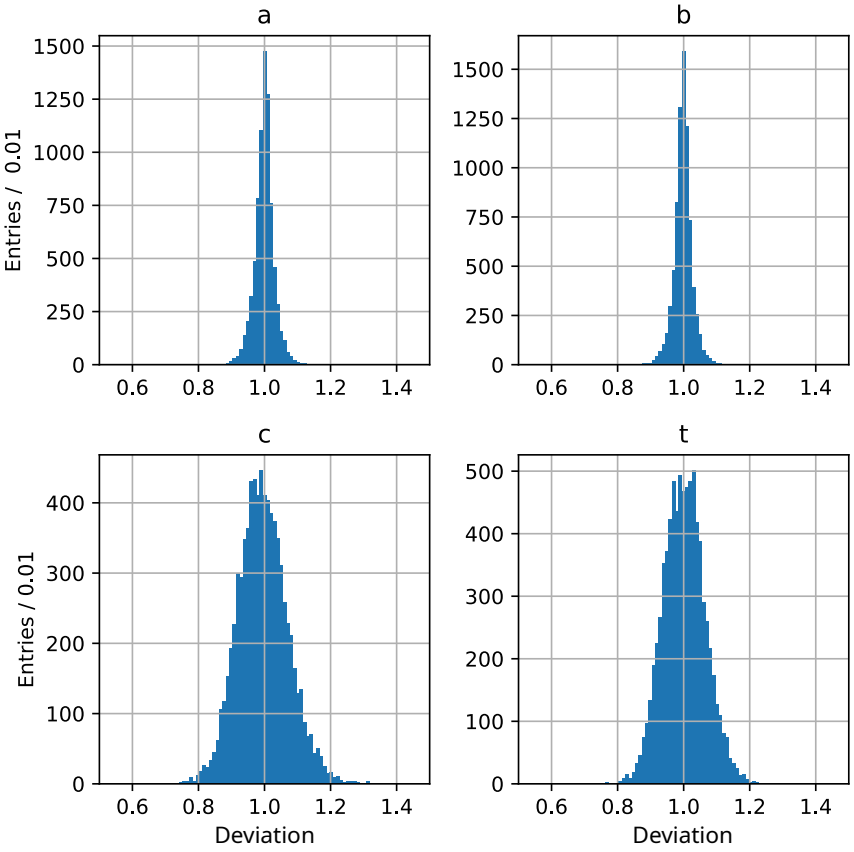

Figure 4.12.: Histograms of deviations of actual and predicted values for the validation dataset's calibration parameters for small pixels. The histograms correspond to the parameters according to their titles.

They include the median $\mu_{1/2,\mathrm{dev}}$, the mean value μ_{dev}, the corresponding standard deviation σ_{dev}, and an additional measure of the width of the distributions

$$s_{\mathrm{dev}} = \mu(|X - 1|), \tag{4.8}$$

i.e. the mean of the absolute of deviation X about 1. s_{dev} gives a more accurate measure for the width of the deviation than the standard deviation σ_{dev} as the distributions are not normally distributed.

All histograms of deviations X are centred at a value of about 1 in regards to their median $\mu_{1/2,\mathrm{dev}}$. This indicates a correct prediction of the networks for the calibration parameters. The mean values μ_{dev} agree well to the median for small pixels but show deviations for large pixels. The same is reflected by the measures of σ_{dev} and s_{dev}. The reason is an introduced bias in the second training stage for the large pixels where the peak-loss is optimised. It emphasised the peak reconstruction ability of

the network while slightly overriding the calibration parameter estimation. This may negatively influence the prediction of simulation data but will significantly enhance the prediction for real measurements as it is impossible to generate simulated training data which perfectly describes the measurements.

parameter	$\mu_{1/2,\mathrm{dev}}$	μ_{dev}	σ_{dev}	s_{dev}
a	0.999	0.808	0.383	0.227
b	1.011	1.166	0.423	0.207
c	1.000	1.060	0.712	0.272
t	0.990	0.982	0.155	0.107

(a) Large pixel statistical quantities

parameter	$\mu_{1/2,\mathrm{dev}}$	μ_{dev}	σ_{dev}	s_{dev}
a	1	1	0.0230	0.022
b	0.999	0.998	0.028	0.02
c	0.992	0.996	0.076	0.06
t	1.000	1.001	0.063	0.05

(b) Small pixel statistical quantities

Table 4.3.: The medians $\mu_{1/2,\mathrm{dev}}$, means μ_{dev}, standard deviations σ_{dev}, and deviations s_{dev} (see equation (4.8)) of the deviations X of equation 4.7 of the predicted and target calibration parameters of the validation dataset for large (a) and small pixels (b).

Figure 4.13 shows 1024 randomly chosen ToT spectra from the validation dataset which are converted into deposited energy via the corresponding predicted calibration parameters. The resulting calibration curves overlayed on top of each other are depicted for large pixels in (a) and small pixels in (c). (b) and (d) illustrate the corresponding densities of these curves. The full energy peaks of the Mo-fluorescences and the Am are matched well for the large pixels, due to the optimisation via the peak-loss. Features like the edge of backscattered photons corresponding to the full energy peak and the Sb-fluorescence are discernible. Their visibility is a result of the optimisation via the mean squared error. In (a), two deposited energy spectra are present, which do not agree well with the expectation. This is possibly due to the sampled calibration parameter combinations, which lead to ToT spectra challenging to predict from. Nevertheless, this is seldomly occurring and therefore considered statistically insignificant. For the small pixels in (d), a high density in the region of the Am photopeak is noticeable. Other features are hardly discernible, especially the Mo-fluorescence, which merges with the spectrum's low energy part consisting of charge sharing and Compton events.

4.2.5 Results

The trained networks are used to predict the calibration parameters for all pixels of an exemplary Dosepix detector. A calibration measurement in ToT-mode with an Am-source and an additional Mo-fluorescence target is made. This measurement's duration was about 10 minutes for the large pixels and about 60 minutes for the small pixels. Small pixels need to be irradiated longer since the event rate per pixel is reduced due to their size. The input of a network consists of a concatenation of the ToT

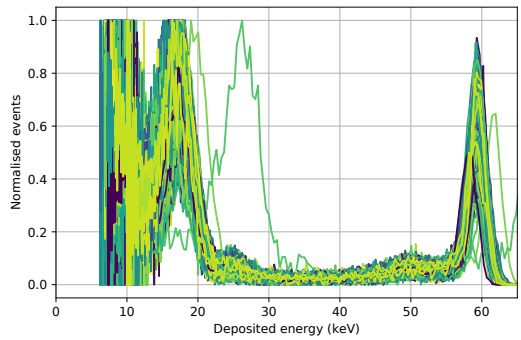

(a) Predicted deposited energy spectra (large pixels)

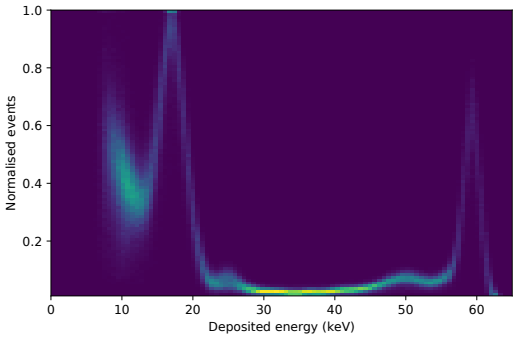

(b) Density of predicted deposited energy spectra (large pixels)

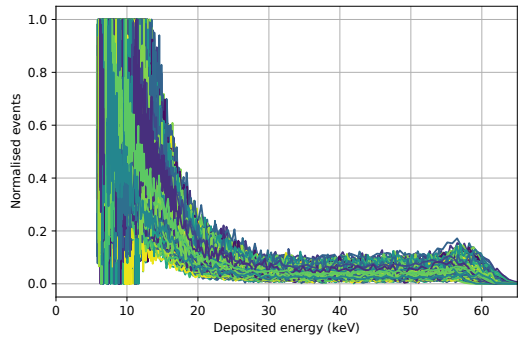

(c) Predicted deposited energy spectra (small pixels)

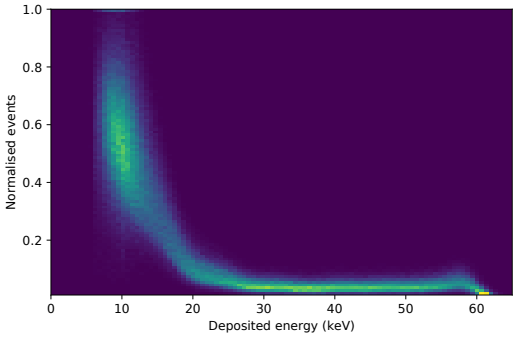

(d) Density of predicted deposited energy spectra (small pixels)

Figure 4.13.: The deposited energy spectra converted from 1024 randomly chosen ToT spectra of the validation dataset via the predicted calibration parameters are shown for large (a) and small pixels (c). The densities of the spectra are illustrated via 2D histograms for large pixels in (b) and small pixels in (d).

spectra for all pixels. Different networks for large and small pixels are used. Figure 4.14 shows an excerpt of this data with 12 large pixels of a single detector column (a) and 16 small pixels of four detector columns (c). The outputs of the networks, i.e. the provided conversion parameters, are then utilised to transform the measured spectra from ToT into deposited energy which are depicted in figure 4.14 for large (b) and small pixels (d).

The average of the deposited energy spectra for all pixels is illustrated in figure 4.15 for large (a) and small pixels (b). The resulting spectrum is noisy for the large pixels, which is due to the short measurement time. However, it is noticeable that low event statistics are no issue for the networks as they can still determine the calibra-

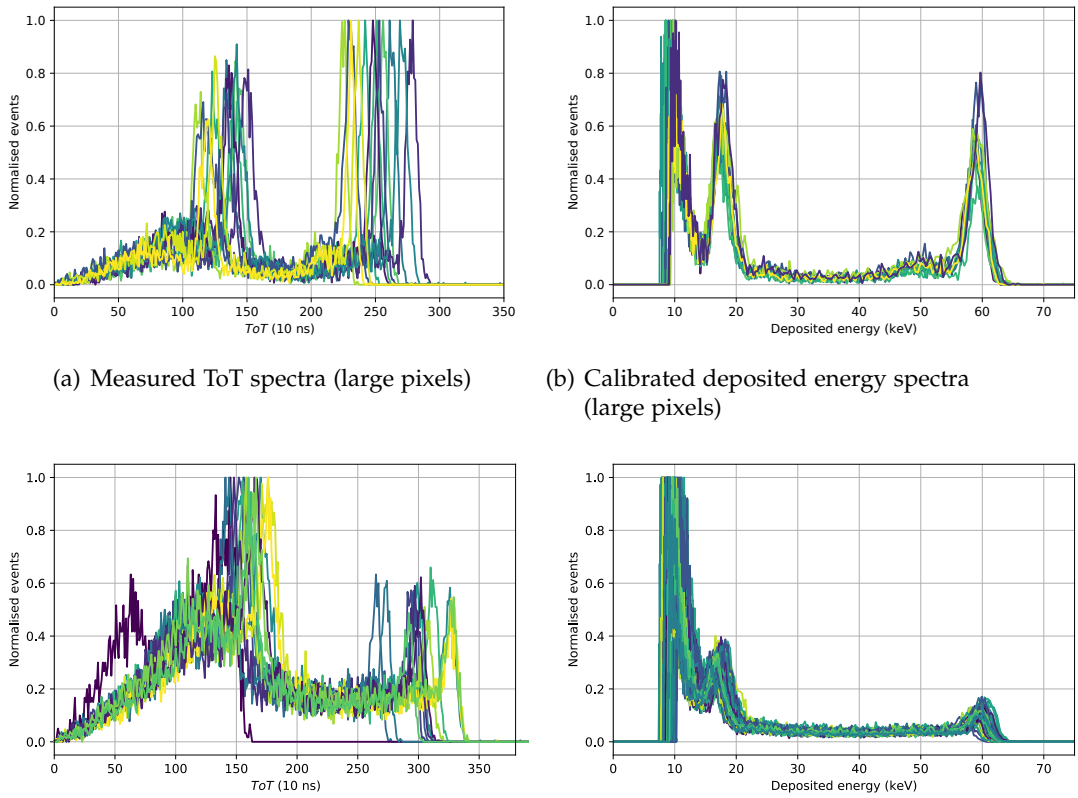

(a) Measured ToT spectra (large pixels)

(b) Calibrated deposited energy spectra (large pixels)

(c) Measured ToT spectra (small pixels)

(d) Calibrated deposited energy spectra (small pixels)

Figure 4.14.: (a) shows measured ToT spectra for 12 large pixels of a single column of Dosepix, (c) for 16 small pixels of four columns. The spectra are used as inputs of the calibration networks to determine the corresponding calibration parameters. These are utilised to convert the ToT spectra into the deposited energy spectra depicted in (b) for large and in (d) for small pixels.

tion parameters successfully. This allows for a faster calibration of detectors which is especially useful if many calibrated detectors are required. In the average spectrum of the large pixels, features like the Sb-fluorescence or the edge of backscattered photons corresponding to the Am full energy peak are also discernible. No significant broadening of the peaks is observed for both pixel sizes, which corresponds to a good quality of the conversion from *ToT* to deposited energy. The number of events in the spectrum at low deposited energies mainly consists of events from charge sharing and the Compton effect. This part of the spectrum decreases approximately exponentially for increasing deposited energy.

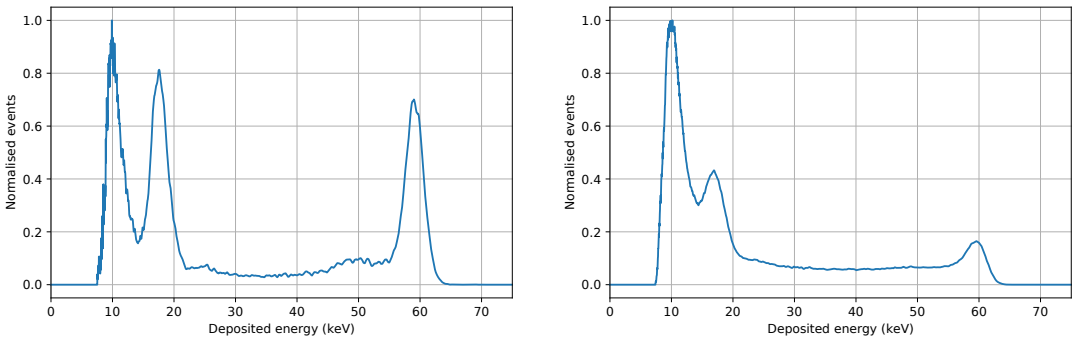

(a) Large pixels (b) Small pixels

Figure 4.15.: The normalised average deposited energy spectra of the large (a) and small pixels (b) of an exemplary calibrated detector.

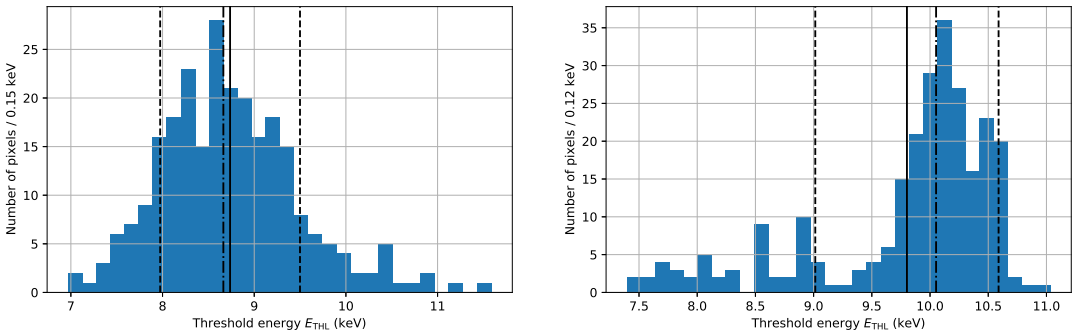

(a) Large pixels (b) Small pixels

Figure 4.16.: Histograms of the threshold energy E_{THL} for large pixels (a) and small pixels (b) of an exemplary calibrated detector. The solid vertical lines represent the mean values, the dashed lines the corresponding standard deviations, and the dash-dotted lines the medians.

There are no detected events below a certain threshold energy E_{THL}, resulting in hard cut-offs of the averaged spectra. E_{THL} is evaluated using the calibration parameters in connection with equation (4.3). A histogram of the values is depicted in figure 4.16 for large (a) and small pixels (b). The mean energy threshold μ_{THL} and the corresponding standard deviation σ_{THL} for all pixels of different pixel sizes are listed in table 4.4. These numbers depend on the detector and the equalisation of the pixel thresholds (see section 2.1.1 for more details). Here, large and small pixels show similar threshold energies.

pixel size	μ_{THL} (keV)	σ_{THL} (keV)
large	8.7	0.8
small	9.8	0.8

Table 4.4.: Mean energy threshold μ_{THL} and corresponding standard deviation σ_{THL} for the distributions of figure 4.16 for large and small pixels of an exemplary calibrated detector.

Threshold variation

Calibration measurements under variation of the global threshold (THL) are performed. The value of the THL is shifted in digital units, called DAC in the following, in the hardware register of Dosepix, resulting in a change of the threshold energy E_{THL}. A THL shift of 0 corresponds to the value determined in the equalisation of the detector (see section 2.1.1 for more details). Increasing the THL shift leads to an increase of E_{THL} and therefore to a shift of the cut-off energy in the deposited energy spectrum. This analysis is performed for large pixels only. All measured ToT spectra for different THL shifts are evaluated via the CNN and converted into deposited energy via the predicted calibration parameters. The determined calibration curves and the deposited energy spectra are depicted in figure 4.17.

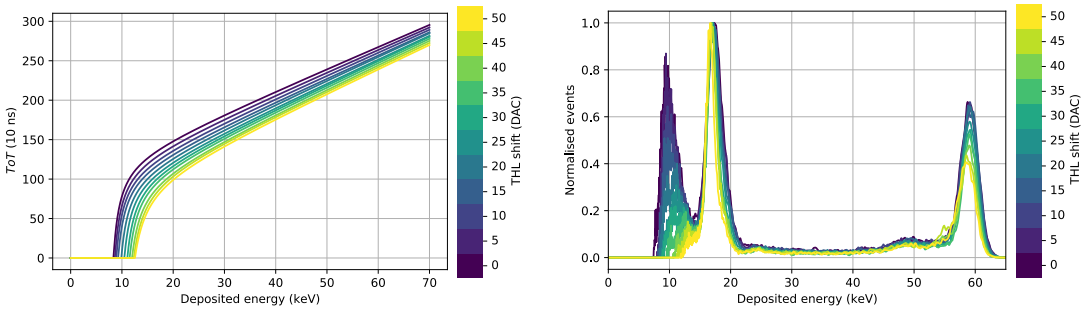

(a) Calibration curves

(b) Calibrated deposited energy spectra

Figure 4.17.: Mean calibration curves (a) and deposited energy spectra after calibration (b) for different THL shifts as indicated by the colour bars. A shift of 0 corresponds to the THL determined in the equalisation of the detector. Increasing the shift corresponds to an increase in threshold energy E_{THL}.

With increasing THL shift, the calibration curves are increasingly offset towards higher deposited energies. The shapes of the converted deposited energy spectra are almost independent of the THL shift. The dominant peaks and the spectra's features keep their positions and do not increase their width. This further approves the CNN's prediction abilities in regards to the set THL value as long as the deposited energy

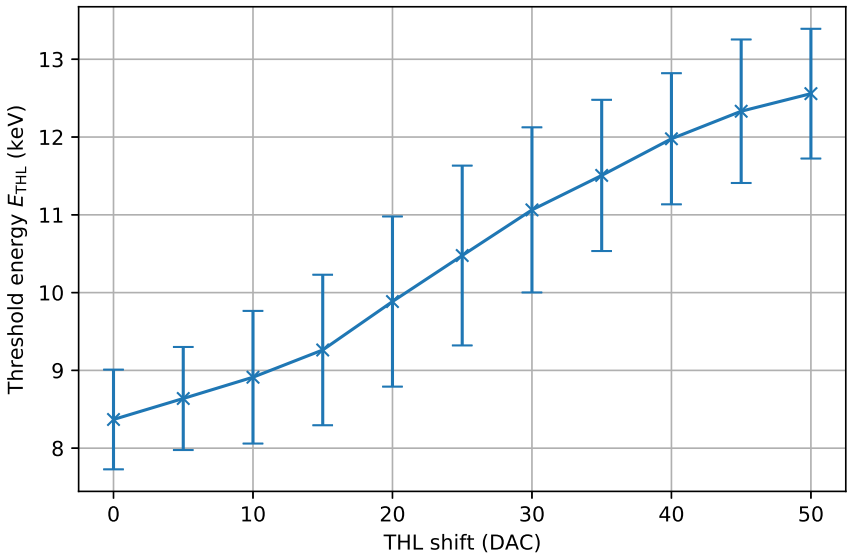

Figure 4.18.: Predicted energy threshold E_{THL} as a function of THL shift. The values and error bars correspond to the means and standard deviations of all large pixels.

threshold is lower than the energy of the Mo-fluorescence peak in the spectrum. The predicted calibration parameters are used to calculate the threshold energy E_{THL} via equation (4.3) for each pixel and value of THL shift. Figure 4.18 depicts the mean value of E_{THL} and the corresponding standard deviation of all pixels for each measurement. The curve shows an approximately linear correlation between the energy threshold E_{THL} and THL shift which agrees well with the expectation. The voltage amplitude of the pulses in the analogue electronics of the detector is proportional to the deposited energy, and the voltage of the threshold discriminator linearly depends on the set THL DAC value.

The deviation of the mean values of the predicted calibration parameters regarding their means at a THL shift of 0 is depicted in figure 4.19. Parameter a, which mostly represents the characteristics of I_{krum} remains almost independent from THL shift. It corresponds to the detector's hardware settings since I_{krum} remained the same for all measurements. b and t decrease and increase as a function of increasing THL shift. According to the behaviour of the calibration parameters, stated in section 4.1.3, this resembles a shift of the calibration curve towards higher deposited energies and an increase of E_{THL}. Figure 4.19 shows that all parameters change smoothly with THL shift, approving the networks' continuity regarding its input.

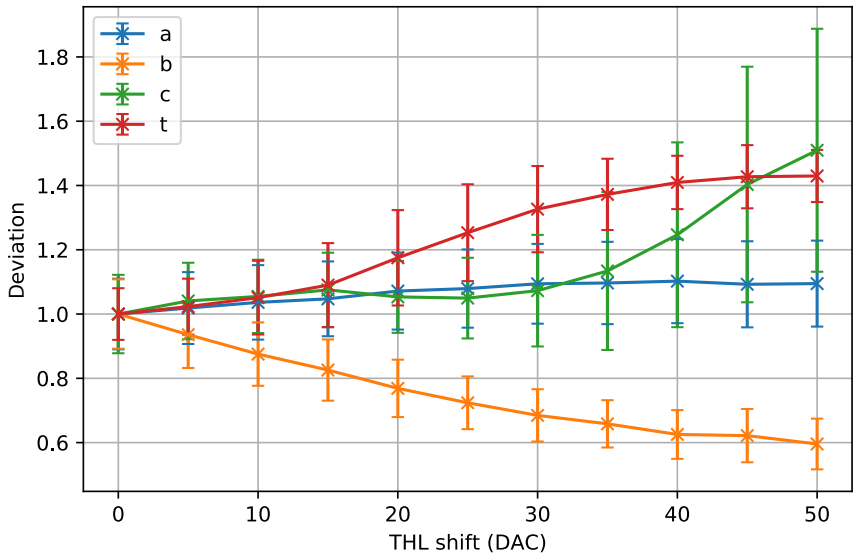

Figure 4.19.: Deviations of the means for the large pixels of the predicted calibration parameters regarding the means at a THL shift of 0. The error bars represent the corresponding standard deviations.

I_{krum} variation

The threshold is now kept constant and I_{krum} (see section 2.1.1 for more details) is changed between measurements. The variation of the current is performed in units of DAC where one DAC represents 0.2 nA. Figure 4.20 (a) shows the predicted mean calibration curves and (b) the corresponding deposited energy spectra.

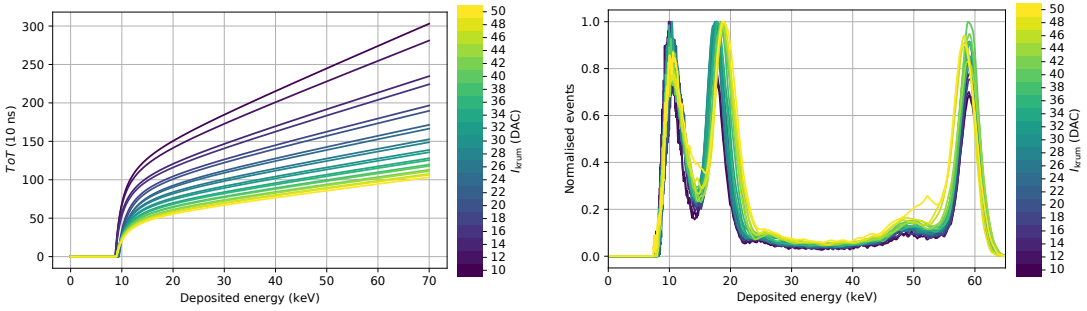

(a) Calibration curves

(b) Calibrated deposited energy spectra

Figure 4.20.: Mean calibration curves (a) and deposited energy spectra after calibration (b) for different values of I_{krum} whose values are indicated by the colour bars.

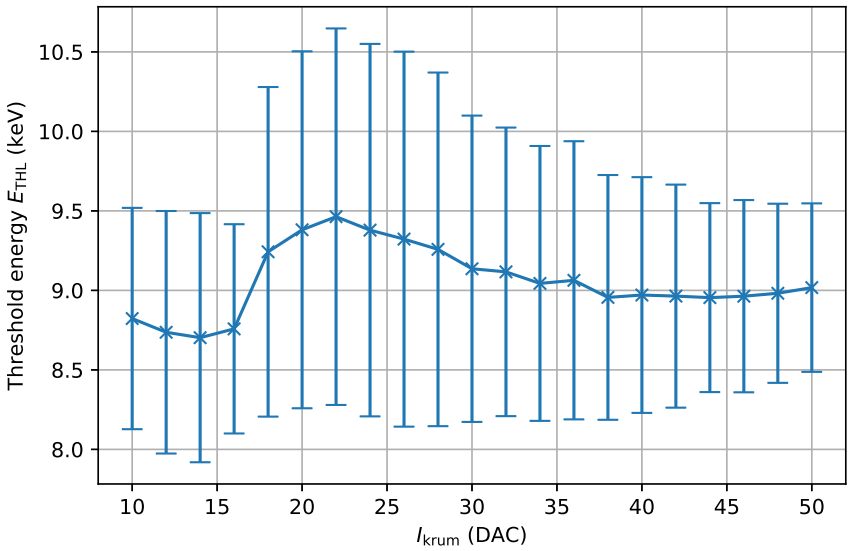

Figure 4.21.: Predicted energy threshold E_{THL} as a function of I_{krum}. The values and error bars correspond to the mean and standard deviation of the large pixels.

The calibration curves show decreasing slopes of their linear parts as a function of increasing I_{krum}. The threshold energy E_{THL} remains almost constant, depicted in figure 4.21. The deposited energy spectra indicate a correct working of the network as peaks do not change their position significantly, and the spectra's features are discernible. There is a slight mismatch between the target peak energies and the predicted energies towards larger values of I_{krum}. Since ToT is discrete, a bin in ToT corresponds to a bin of increasing width in deposited energy for increasing I_{krum}, leading to an increasingly discrete deposited energy spectrum. This effect is reduced by taking the average of all large pixels of the detector.

Figure 4.22 depicts the deviations of the means for large pixels of the predicted calibration parameters as a function of I_{krum} regarding the means for $I_{\mathrm{krum}} = 10\,\mathrm{DAC}$. The error bars represent the corresponding standard deviations. Here, t remains almost constant due to the constant threshold energy E_{THL}. The deviation of a is proportional to I_{krum}^{-1} which agrees with the expectation. This is explained by considering a simplified version of the pulse shapes in a pixel's analogue electronics (see section 2.1.1 for more details). The rise time is neglected, and the peaks are assumed to be shaped like a right-angled triangle where the x-axis represents time, and the y-axis represents voltage. The pulse is describing the discharge of a capacitor with a constant current $I \propto I_{\mathrm{krum}}$, i.e. the voltage as a function of time is

$$U(t) = \frac{1}{C} \cdot I \cdot t + U_0, \tag{4.9}$$

where U_0 is the height of the pulse, which is proportional to the energy deposited in the detector's sensor, C is the capacity of the charge sensitive amplifier in the circuit, and I is the constant current used for the discharge. The ToT value provided by the electronics is proportional to the time t, i.e.

$$ToT \propto t = C \cdot \frac{U_0 - U(t)}{I}. \tag{4.10}$$

This directly reveals the inverse proportionality of the determined ToT values and I_{krum}. Again, all parameters change smoothly when varying I_{krum}, which proves the network's continuity when changing its input ToT spectra.

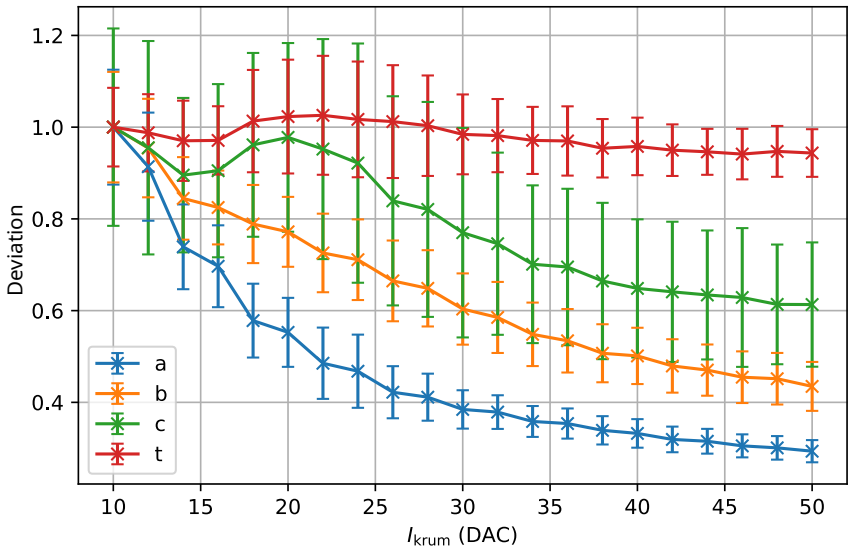

Figure 4.22.: Deviations of the means for large pixels of the predicted calibration parameters regarding $I_{\text{krum}} = 10\,\text{DAC}$. The error bars represent the corresponding standard deviations.

4.3 Conclusion

Standard and CNN energy calibration approaches should, in principle, produce the same calibration parameters for each pixel. However, some disadvantages for the standard calibration exist. Multiple measurements with various calibration sources have to be performed. It is time-consuming, especially if many detectors need to be calibrated. This duration can be reduced by using an X-Ray tube, providing high photon flux, in combination with fluorescence targets. But, this increases the cost of the calibration. Once the measurements are done, algorithms are required to estimate the mean peak positions in the ToT-spectra for each pixel which is a possible source

for human-biasing as the algorithm usually includes a manually trimmed peak-finder to give a first estimation of the peak position.

The networks only use single measurements as their inputs. The prediction is fast since the measurement data of all pixels are evaluated at once. The network does not rely on manual adjustments since it only relies on the simulation of the calibration source and the detector system. This can also be considered a flaw of the network since its output highly depends on the quality of the simulation. Therefore, a good simulation agreement is a requirement for the method.

The results in this chapter show that the trained networks are able to predict calibration parameters from measurements well. Additionally, the networks proved to be robust against changes in Dosepix hardware settings. Varying the global threshold (THL) and I_{krum} changed the predicted calibration curves as expected. Since different buildups of the calibration source were included in the simulation, it is possible to take measurements with many detectors at once. This increases the calibration efficiency and provides a straightforward procedure that does not require an exact measurement setup.

CHAPTER 5

Optimisation of Dosepix filters for medical dosimetry

Contents

Dosepix has excellent characteristics for a usage in dosimetry applications as shown in section 3.2. A setup of three detectors was utilised to determine the personal dose equivalents $H_p(10)$ and $H_p(0.07)$ from measurements. Each of the Dosepix detectors has a different filter in front of it. These are required to change the initial photon spectrum to increase the information provided by the detectors. The design of the filters was established in [10, 44]. However, the filters were chosen mostly based on experience and experimentation. The determination of filter designs presented in this chapter is based entirely on simulations. An optimisation of a filter for a Dosepix is made in regards to the response. An additional goal is to reduce the number of required Dosepix detectors. This helps to reduce the cost and size of possible future experiments or dosemeter devices. The range of applications is also expanded to eye-lens dosimetry, briefly introduced in the first section. Afterwards, a description of the simulation methods for the different dose types is presented. These are finally used to optimise the filters of the Dosepix detectors and to find corresponding conversion coefficients from registered events to dose. All analyses are focused on an energy range of up to 250 keV which is important for medical applications, where X-ray tube voltages typically do not exceed 150 keV (see for example [59]).

5.1 Eye lens dosimetry

The harm of radiation in regards to the eye-lens has been underestimated in the past. With an exposure, a risk for the formation of cataracts arises. Therefore, the annual limit for the equivalent dose for the eye lens has been reduced from 150 mSv to 20 mSv per year for occupationally exposed staff in Germany according to the guidelines of EURATOM [60]. The ORAMED project (**o**ptimization of **ra**diation protection of **med**ical staff) included analyses of procedures in interventional radiology and cardiology in regards to eye lens dosimetry [61]. It showed that the new dose limit is exceeded by exposed staff if no proper protective equipment is used, making monitoring important. It revealed that the tested active personal dosemeters do not work well for low photon energies and pulsed photon fields. In these aspects, an application of Dosepix seems promising.

In eye-lens dosimetry, the $H_p(3)$ personal dose equivalent is determined (see section 2.4 for more details). Currently, no filter design for Dosepix exists to measure this quantity. Additionally, the number of required detectors per eye should be minimised as a future dosemeter has to be placed close to its bearer's eye-lens. Therefore, the device should be as small as possible. A first conceptual design depicted in figure 5.1 is introduced, which takes these requirements into account. The person is wearing protective glasses, which attenuate possible X-radiation and therefore protect the eyes. However, there remains harm due to the backscattering of photons within the head, which might reach the eye lens. The dark-grey squares indicate Dosepix detectors placed directly above the eyes of the person. Here, each detector is designated to measure only the dose of the eye it is close to. The detectors are fixed on a curved

metal plate mounted via a head strap to the bearer's head. Readout electronics have to be placed either close to the detectors or have to be attached to the person's head. The distance between the detectors should approximately correspond to the distance between the eyes of the system's bearer. The introduced concept only gives an idea of how the detectors should be placed.

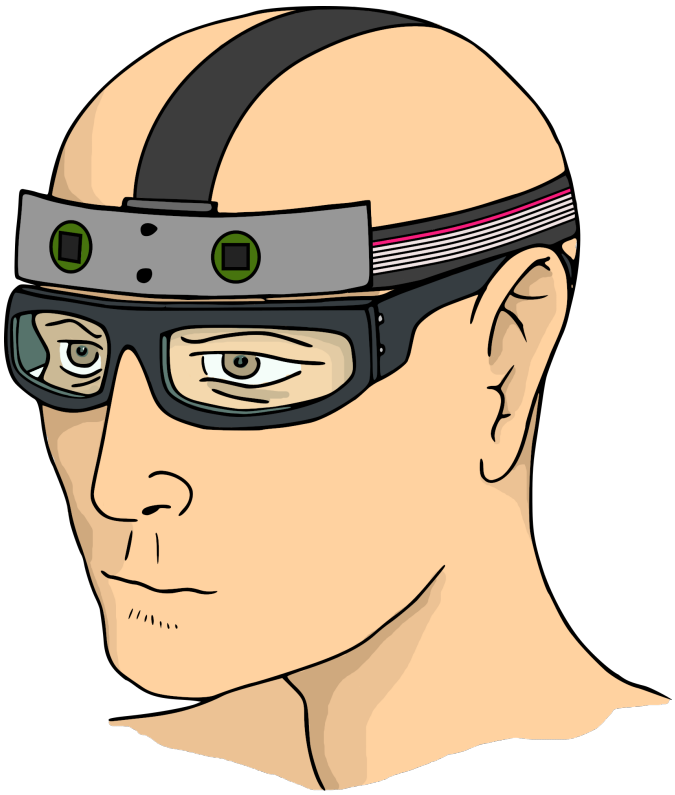

Figure 5.1.: Concept of an eye-lens dosemeter. It consists of two Dosepix detectors placed directly above the eyes of the bearer. Original version of the image in [62].

No head model is going to be used in measurements and simulations. Instead, a cylinder phantom is utilised, which approximates the shape of a human head. Its dimensions and materials are specified in ISO 4037 [45, 46] and are briefly described in the following. The phantom has a diameter of 20 cm, the identical dimension in height and is made of PMMA. Its outer wall and the end faces have a width of 5 mm. Additionally, the phantom is filled with water.

Figure 5.2 depicts the conversion factors from photon fluence of a monoenergetic parallel photon field emitted on the water cylinder phantom to personal dose equivalent $H_p(3)$ [45, 46]. The different curves correspond to different irradiation angles according to the colour bar. The angle is varied about the axis of rotational symmetry of the phantom. The conversion factors represent the dose per fluence for an

infinitesimal thin dosemeter placed at an angle of 0° within a depth of 3 mm. Later in simulations, the factors are used to determine the applied dose from the fluence of the emitted parallel photon field.

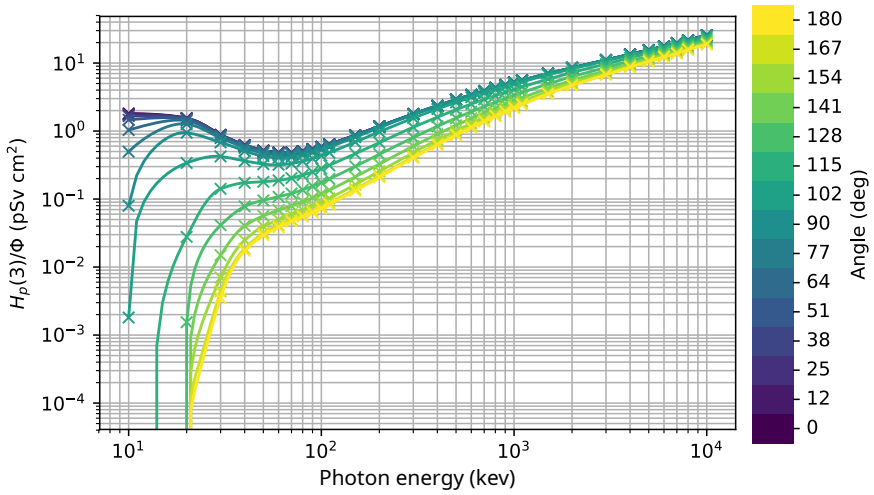

Figure 5.2.: Conversion factors from photon fluence of a monoenergetic parallel photon field emitted on a cylinder phantom to personal dose equivalent $H_\mathrm{p}(3)$. The colours of the curves correspond to different irradiation angles according to the colour bar. The data is taken from [45, 46].

5.2 Dosepix detector simulation

Simulations are required to perform an optimisation of a filter in front of a Dosepix detector. The requirements of the dosemeter include a good performance under an extensive range of photon energies and angles of irradiation. The best results for a filter optimisation are achieved in the following way. The filter geometry is directly manipulated in simulation, the simulation process for different irradiation angles and photon energies is performed, and a loss on the resulting dose reconstruction performance is evaluated. Judging by this loss, the filter geometry is adjusted, and the next iteration of the optimisation begins. The computational effort and time required for this method are high as the examined irradiation angles and energies have to be simulated for each iteration.

Therefore, a more practical approach is utilised. Various assumptions and approximations have to be made. There are two types of detector irradiation that are assumed to be independent of each other. First, photons that are directly impinging on the detector and its filter in front of it. Second, irradiation from backscattering, i.e. photons that previously interacted with the phantom used in dosimetry measurements. While the direct irradiation does not depend on the dose type, the backscattering does. This

is because for measurements of $H_p(10)$ and $H_p(0.07)$, a slab phantom is used while $H_p(3)$ uses a cylinder phantom. On the other hand, the backscattering simulation is assumed to be independent of the filter applied in front of Dosepix. The following sections describe how the different irradiation types are implemented in simulation. They also illustrate the measures taken to keep computational effort as low as possible. Direct irradiation and backscattering are finally added to give an approximate representation of reality.

5.2.1 Slab phantom backscattering

The ISO water slab phantom [45, 46] as previously described in section 3.2.2 is included when simulating Dosepix setups for dosimetry of the dose equivalents of $H_p(10)$ and $H_p(0.07)$. The simulation is performed in two stages. First, only the backscattering characteristics of the slab phantom are processed. In a second stage, the relevant events of stage one are emitted on Dosepix to determine the corresponding detector response.

Slab phantom simulation

The geometry of the slab phantom simulation is depicted in figure 5.3. At the centre of the frontal surface of the phantom, the PCB of the readout hardware described in section 3.1.1 is attached. The PCB has a total surface of 10 cm×10 cm. At the current state of development, the electronics of a future possible dosemeter is not known and therefore, this PCB serves as a placeholder. Also, there is no housing at the backside of the readout hardware for the same reason. When designing housing at a later stage of development, many factors have to be considered. These include, for example, the method of production, shape and material. The housing will probably consist of plastic with a thickness of about 1 mm to 3 mm. It will mostly absorb photons in the low energy range, i.e. with energies below about 40 keV. But since the share of backscattered photons on the total number of registered photons is relatively small and exact properties are unknown, no housing is installed for the approximative backscattering simulation. Additionally, the assumption that the later used filter and the Dosepix detector itself are small in comparison to the irradiated surface of the phantom is made, i.e. their shielding of photons is neglectable.

The small box on top of the readout electronics represents a perfect detector as illustrated in figure 5.3. It is placed to act as a bounding volume of the location the three detectors of the PCB are usually positioned. The perfect detector registers only photons that scattered from the slab phantom. The green lines in the figure depict the primary photons. The photon source is a square plane parallel to the phantom's frontal surface and has the same dimensions. Photons are emitted perpendicularly on the surface. The used coordinate system is reflected in figure 3.12. (a) depicts the Cartesian coordinates of the phantom. The x-y-plane lies within its frontal surface,

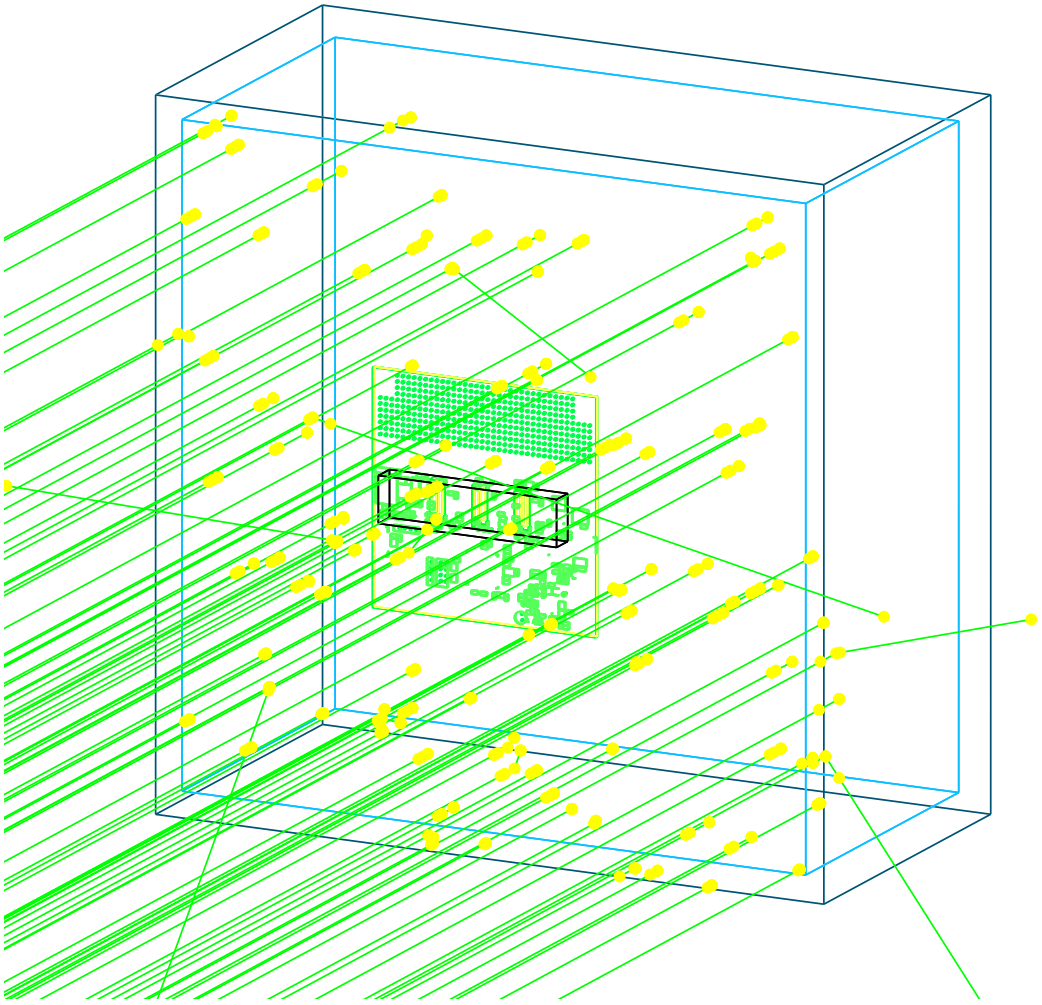

Figure 5.3.: Simulation of backscattering events for the slab phantom. Photons are emitted perpendicularly on the frontal surface of the phantom. Their tracks are indicated in green. Yellow dots represent positions interactions took place. Attached to the frontal surface of the phantom are the readout electronics. No Dosepix detectors are implemented in the geometry. Instead, a perfect detector, indicated by the black box, is placed at their usual position. It is used to register the characteristics of photons scattered from the slab phantom.

and the z-axis is perpendicular to it. The irradiation angles are given in spherical coordinates, as illustrated in (b). θ_{ir} denotes the angle between the normal of the phantom's frontal surface and irradiation direction. ϕ_{ir} rotates within this surface. Yellow dots in the figure represent the positions interactions took place. If a photon track intersects with the perfect detector, its energy, the position of the intersection, and the direction of the track are stored.

In the simulation of the phantom, N_{ph} photons are generated and emitted on the phantom's effective surface area of A. A depends on the irradiation angles and is calculated by performing a projection of the phantom's surface onto the planar source's surface. The dimensions of the source have to be adjusted so A is completely irradiated. For an emission perpendicular to the phantom's frontal surface, A corresponds to 30 cm×30 cm. The irradiation with N_{ph} photons results in a corresponding photon fluence $\Phi_{ph} = \frac{N_{ph}}{A}$. N_{det} events are registered per fluence Φ_{ph} by the perfect detector, resulting in an efficiency p of

$$p = \frac{N_{det}}{\Phi_{ph}}. \tag{5.1}$$

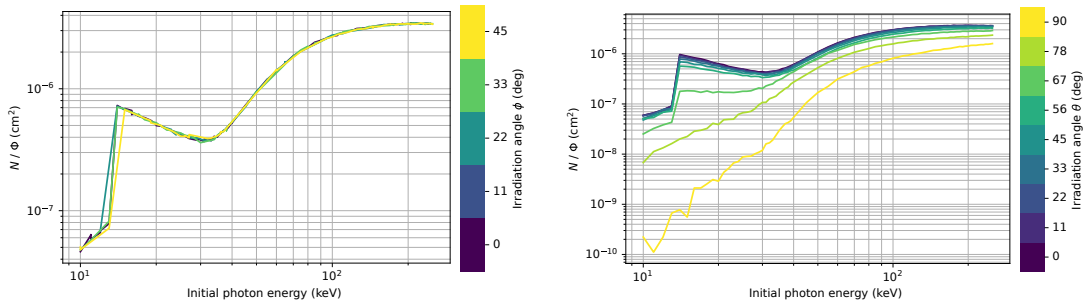

(a) $\theta_{ir} = 45°$, ϕ_{ir} is varied

(b) $\phi_{ir} = 0°$, θ_{ir} is varied

Figure 5.4.: Photons are emitted on the slab phantom for various irradiation angles. Scattered events are registered by the perfect detector illustrated in figure 5.3. The plots represent the number of registered photons per photon fluence as a function of the initial photon energy. In (a), for a fixed angle of $\theta_{ir} = 45°$ under variation of angle ϕ_{ir} as indicated by the colour bar. In (b), for a fixed ϕ_{ir} of 0° while θ_{ir} is varied as shown by the colour bar.

The trend of this efficiency as a function of initial photon energy is depicted in figure 5.4. The irradiation angle θ_{ir} is fixed to a value of 45° while ϕ_{ir} is varied according to the colour bar in (a). It is sufficient to vary the angle up to 45° due to the symmetry of the slab phantom. There is almost no dependence on angle ϕ_{ir} as all curves are approximately identical. They all show a large jump in the number of

registered events at photon energies of about 12 keV. This is due to the readout hardware's PCB, mainly consisting of FR-4 [40] which usually includes bromine. Bromine has dominant fluorescence energies of 11.879 keV, 11.925 keV and about 13.3 keV [41]. These fluorescences only take place once the primary photon's energy is larger than the specified energies, explaining the jumps in the efficiency curves. With increasing initial photon energy, the number of registered events reduces as the probability for the photoelectric effect is decreasing. Fewer interactions with the material of the PCB take place, and fewer fluorescence photons are emitted. At energies larger than about 35 keV Compton effect dominates, and fluorescences have almost no importance. The number of registered events increases with increasing initial energy and reaches its maximum at about 200 keV. The highest simulated initial energy is 250 keV. If the energy was increased further, the trend of the registered events would decrease as the primary photons can penetrate the slab phantom deeper before they interact. Afterwards, there is a long distance to leave the phantom again. If Compton interactions take place, the direction of the photon changes and the energy is reduced. Therefore, with each additional interaction, the probability for photoelectric effect increases and the probability to leave the phantom decreases.

In Figure 5.4 (b), ϕ_{ir} is fixed to 0° while θ_{ir} is varied from 0° to 90° according to the colour bar. The general trend as a function of initial photon energy is similar to the one described for (a). There is a jump in registered events when bromine fluorescences take place. With an increasing angle of θ_{ir}, the number of registered photons decreases due to the source's fixed photon fluence. The highest photon yield for the detector is present if photons are directly emitted on the phantom's frontal surface, i.e. for $\theta_{\mathrm{ir}} = 0^\circ$. Once the angle increases, the effective irradiated area A is decreasing. A is minimised for an angle of $\theta_{\mathrm{ir}} = 90^\circ$ where the probability to register scattered photons is lowest. See section 3.2 and figure 3.14 for a description of the registered energies of the perfect detector. A differently shaped perfect detector is used, and the irradiation angle is not varied. Nevertheless, these variations only have a small influence on the resulting energy distributions. No bromine fluorescences exist as there is no PCB in the simulation.

Finally, figure 5.4 (a) illustrates that there is almost no dependence on irradiation angle ϕ_{ir}. Therefore, only the variation of θ_{ir} shown in (b) is considered and $\phi_{\mathrm{ir}} = 0^\circ$ is used.

Detector simulation

The determined simulation data, i.e. the characteristics of the registered events of the perfect detector, are now implemented in the Allpix^2 [37] simulation of the Dosepix detector (see chapter 3 for more details). Only a single Dosepix detector is placed in the simulation's geometry, located at the central slot of the readout electronics as this is the best detector position considering symmetry. There must be no filter in front of the detector as this is handled by the simulation of direct irradiation later. The readout

electronics and the slab phantom are not present in the geometry and are exchanged by a source representing the recorded photons and their characteristics of the perfect detector.

In the detector simulation, N_{DPX} events are sampled from the phantom simulation. Considering the previously defined phantom efficiency p, described via equation (5.1) and shown in figure 5.4, this corresponds to a fluence of the emitted photon field of

$$\Phi_{\mathrm{DPX}} = \frac{N_{\mathrm{DPX}}}{p}. \tag{5.2}$$

All generated response spectra will be normalised with this fluence. The responses of direct irradiation are normalised in the same manner. This way, the spectra can easily be sampled and added. The introduced method of backscattering precalculation allows for a reduction of the computation time. Multiple simulations are performed for different photon energies and angles of θ_{ir}. A linear interpolation of the histogrammed response spectra is performed to increase the applicability of the dataset. A function is provided which depends on the initial energy E, the irradiation angle θ_{ir} and the deposited energy E_{dep}. It returns the corresponding number of registered events per photon fluence.

5.2.2 Cylinder phantom backscattering

For $H_{\mathrm{p}}(3)$ dosimetry, regarding the eye lens, the cylinder phantom is utilised. Like for the slab phantom, the whole simulation process is divided into two stages. In the first stage, the characteristics of the scattered photons are calculated. In the second stage, the simulation of the Dosepix detectors is made utilising the precalculated phantom simulation.

Cylinder phantom simulation

In the first simulation stage, only the cylinder phantom is implemented. A planar photon source of dimensions 20 cm×20 cm emits photons directly on the curved surface of the cylinder phantom depicted in figure 5.5. The photon tracks are illustrated as green lines. Yellow dots indicate interactions. A perfect detector is located at the central height of the phantom. It is ring-shaped and depicted in black. The detector has a height of 3.6 cm and a width of 1 cm. The detector's dimensions are chosen so Dosepix detectors with their small PCB attached (see section 3.1.1 for more details) fit within its volume. For the simulated setup, the Dosepix detectors are put close to the phantom, which corresponds to a positioning of the detectors close to the eyes of the bearer of the dosemeter. The perfect detector only registers photons that previously interacted with the cylinder phantom. The detector registers all important characteristics of the photons, i.e. their energies, the positions their tracks intersected with the detector, and the corresponding directions.

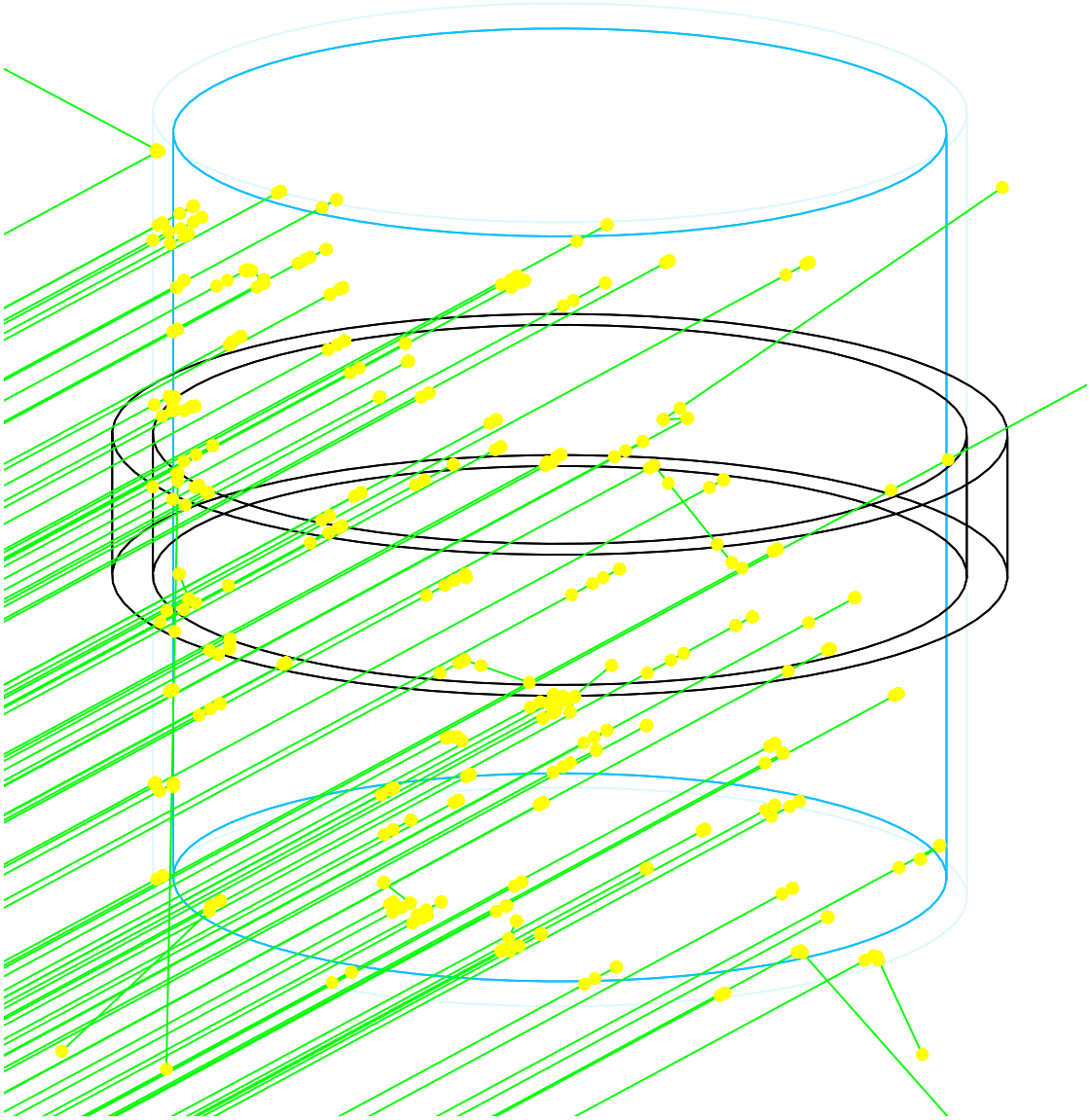

Figure 5.5.: Simulation of backscattering events for the cylinder phantom. A parallel photon field is emitted on the curved surface of the phantom. The photon tracks are indicated in green. Yellow dots represent the positions interactions took place. A perfect detector, represented by the black ring, is placed where later Dosepix detectors are located. The detector is used to register the characteristics of photons that scattered from the cylinder phantom.

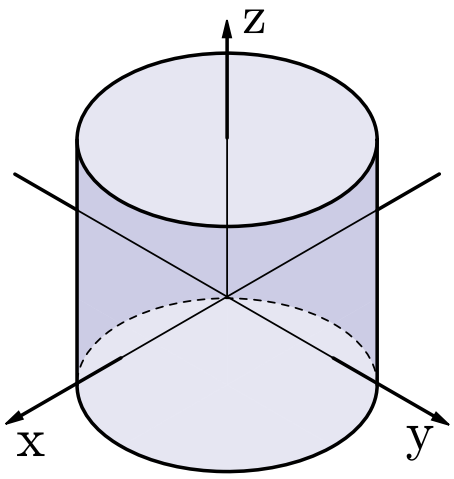

Figure 5.6.: Cartesian coordinate system for the cylinder phantom. The x-y-plane is located at the central height of the phantom. The image is a modified version of [63].

The Cartesian coordinate system of the cylinder phantom is depicted in figure 5.6. Additionally, a spherical coordinate system according to figure 3.12 (b) is used. The angles ϕ and θ represent the positions of intersections of photons with the perfect detector. The angles ϕ_{dir} and θ_{dir} reflect the direction of these photon tracks. For dose estimations, only photons emitted perpendicularly on the surface of the cylinder phantom are relevant. Therefore, using the symmetry of the setup, only a single irradiation direction is considered.

The characteristics of the backscattering events registered by the perfect detector are presented in the following. Figure 5.7 illustrates the intersections of the photon tracks and the boundaries of the detector. The radial components of the coordinates are neglected due to the small width of the detector of 1 cm. All histograms are normalised to the number of registered events and employ the same binning. The colours represent different initial photon energies ranging from 10 keV to 100 keV according to the colour bar. Figure (a) shows the event distributions for angle ϕ for different initial energies. They are centred about a mean of $\phi = 0°$, independent of the energy. At this angle, the most photons are scattering back from the phantom, reflected by small peaks in the distributions.

The main reason is the constant photon fluence of the photon source. For an explanation, the slope of the phantom's curved surface concerning the position angle ϕ is considered in the sketch in figure 5.8. A parallel photon field is emitted from bottom to top. The red circle fragments correspond to an angle range of $\Delta\phi$. The distances d are projections of the curvature in direction of irradiation. Their index resembles position angle ϕ. The more ϕ deviates from $0°$, the smaller the effective irradiated area, which is proportional to d, for an angle segment $\Delta\phi$. Since photon fluence is constant,

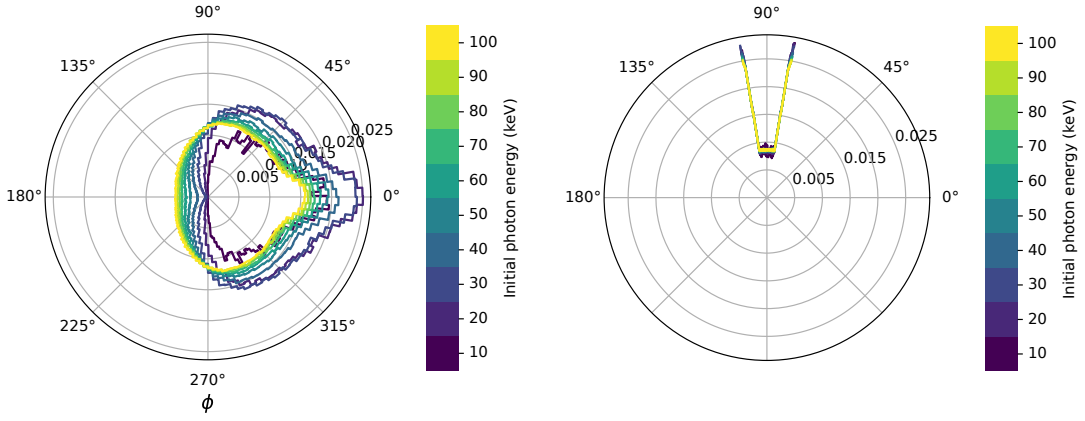

(a) ϕ-distribution (b) θ-distribution

Figure 5.7.: Position distribution of backscattering photons reaching the perfect detector for a direct emission of photons on the cylinder phantom depicted in figure 5.5. The positions are represented in spherical coordinates via angles ϕ (a) and θ (b). Each histogram is normalised to its number of registered events.

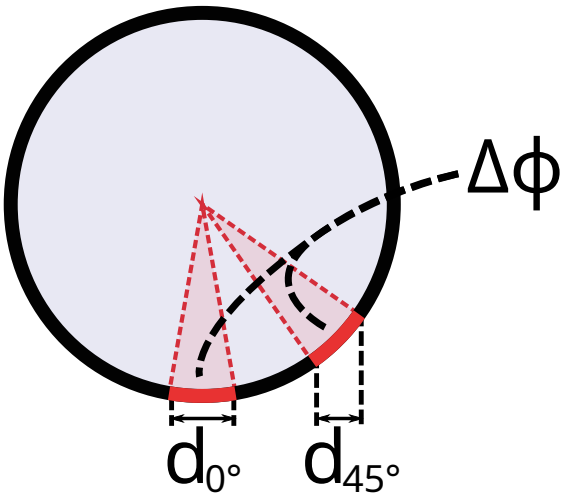

Figure 5.8.: The curvature of the cylinder phantom. It is irradiated from bottom to top. The red circle fragments illustrate an angle range of $\Delta\phi$. The distances d reflect the projections of the curvature in direction of irradiation. The indices resemble the position angle ϕ.

the number of emitted photons for the segment decreases. Consequently, the number of backscattered photons also decreases, as reflected by the trend of the distributions in (a) for small initial photon energies. Photons can penetrate the cylinder phantom deeper for higher initial energies, leading to a smoothing of the distribution. Additionally, more events for angles of ϕ between 90° and 270° are registered as photons can pass the phantom and are registered by the perfect detector on the opposite side.

The distributions of the position angle θ are depicted in figure 5.7 (b). All distributions are similar, independent of the energy of the emitted photons, as the height of the perfect detector limits θ. The smallest fraction of events is registered for values close to $\theta = 90°$, which corresponds to event positions in the x-y-plane. The number of registered events stays at about this level for small deviations from 90° but shows a huge jump at certain angles. At these positions, the top and bottom rings of the perfect detector are located. Here, the highest number of events are registered as many scattered photons can reach those detector surfaces since the whole surface of the phantom is irradiated.

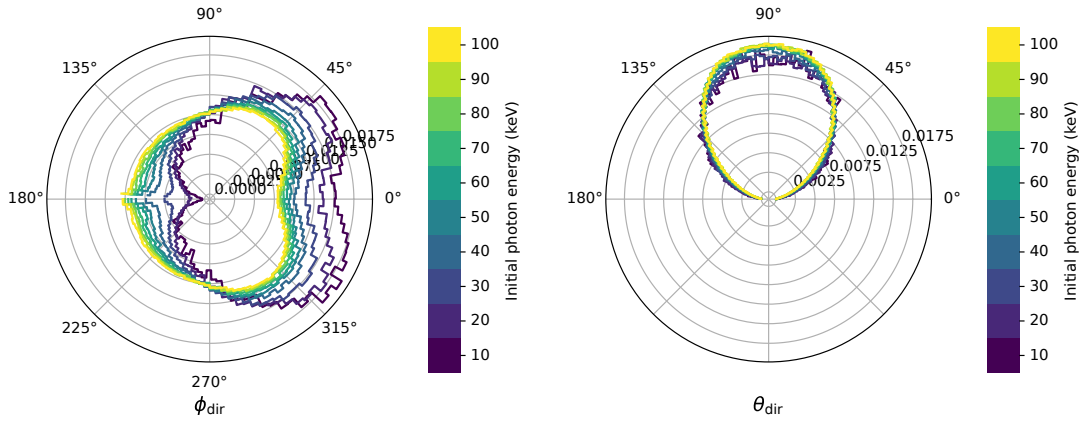

(a) ϕ_{dir}-distribution

(b) θ_{dir}-distribution

Figure 5.9.: Direction distribution of backscattering events reaching the perfect detector for the emission of photons on the cylinder phantom depicted in figure 5.5. The directions are represented via angles ϕ_{dir} (a) and θ_{dir} (b) in spherical coordinates. Each histogram is normalised to its number of registered events.

Figure 5.9 shows the direction distributions of backscattering events, represented by the spherical angles ϕ_{dir} (a) and θ_{dir} (b). All histograms are normalised to their number of registered events and have an equal binning. The colours correspond to different initial photon energies according to the colour bar. (a) shows that the direction represented by ϕ_{dir} is symmetrical about 0°, pointing in the direction of the

source. However, it does not correspond to the most common scattering directions, which are approximately 45° and 315°.

These scattering directions are described via figure 5.10. The exemplary emission of a photon is illustrated in (a). The photon enters the phantom at a position denoted by angle ϕ. The thick dashed line is perpendicular to the surface of the phantom at the previously described position. If Compton scattering takes place, a scattering in forward direction is favoured according to the Klein-Nishina formula. If the photon is travelling within the phantom afterwards, the probability of leaving it and being detected by the perfect detector decreases. If multiple scattering processes occur in succession, the photon's direction when leaving the phantom is arbitrary. These effects are resembled in figure 5.10 (b) which illustrates the correlation of the position angle ϕ and direction ϕ_{dir} for scattered of an initial energy of 100 keV. The dash-dotted line represents the case $\phi_{\text{dir}} = \phi$. The dashed lines resemble $\phi_{\text{dir}} = \phi + \text{sgn}(\phi) \cdot 90°$, where the periodicity of ϕ_{dir} is taken into account. This illustrates the favoured region as previously described via (a). The projection of the data on the axis of ϕ_{dir} in plot (b) resembles the symmetrical plot of figure 5.9 (a).

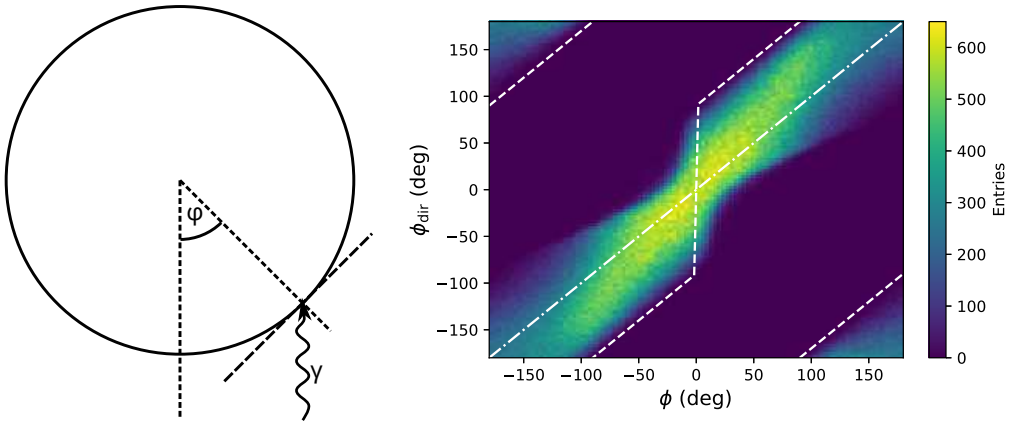

(a) Sketch of photon-cylinder phantom interaction

(b) ϕ_{dir}-ϕ distribution

Figure 5.10.: (a) shows the exemplary interaction of a photon with the cylinder phantom. Its track enters the phantom at a position resembled by angle ϕ. The dashed line at the intersection point describes the tangent to the outer surface of the phantom. (b) shows the correlation of position angle ϕ and direction angle ϕ_{dir} of the registered events of the perfect detector for photons of 100 keV initial energy is shown. A dash-dotted line indicates the relation $\phi_{\text{dir}} = \phi$ and dashed lines $\phi_{\text{dir}} = \phi + \text{sgn}(\phi) \cdot 90°$.

With increasing energy of the photons, higher direction angles ϕ_{dir} are registered. More photons can cross the cylinder phantom with no or only a few interactions, especially at the edges of the phantom. In 5.9 (b), the distribution of the direction of θ_{dir} is

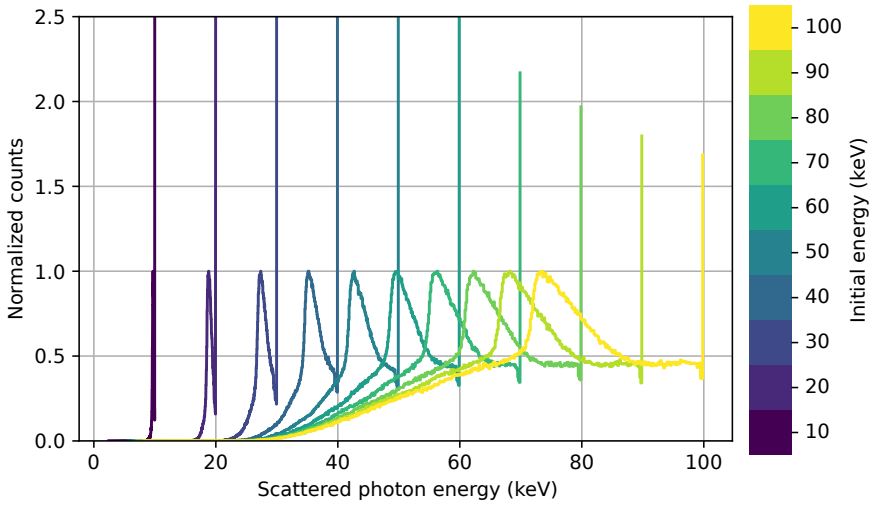

Figure 5.11.: Energy distributions of backscattered photons registered by the perfect detector for different initial energies. The colours of the curves reflect the energies according to the colour bar. All histograms are normalised to their maximum, excluding the highest energy bin.

illustrated. Almost no dependence on the initial energy is noticeable. The distribution itself is centered at an angle of $\theta_{\text{dir}} = 90°$. This corresponds to the position distribution of θ of figure 5.7 (b). Most of the registered events leave the phantom within the region close to the perfect detector. Since also the top and the bottom surfaces of the ring-shaped detector register events, this results in the broad distribution of θ_{dir}.

Figure 5.11 depicts the energy distribution of the scattered photons registered by the perfect detector for different initial energies. The colours of the curves reflect these energies according to the colour bar. All curves are normalised to their maximum, excluding the highest energy bin. The number of events within this bin is due to coherent scattering processes (see section 2.2.2 for more details). A scattering photon changes its direction but keeps its energy. This effect is highest for small initial energies. With increasing energies, the entries in the highest energy bin are originating from forward scattering at the cylinder's edges. The shapes of the energy spectra can mainly be described via single and multiple Compton scattering processes. A detailed description of the model is complicated and therefore resembled via the shown MC simulation.

Detector simulation

The simulated backscattering events from the cylinder phantom are implemented in the detector simulation. The geometry now only consists of Dosepix detectors while the phantom is exchanged with a photon source emitting photons with the precalcu-

lated characteristics. Like previously for the slab phantom, N_{DPX} events are sampled from the phantom's event distribution. The corresponding true photon fluence Φ_{DPX} is calculated via equation (5.2). The projected surface of the phantom projected on the planar source A (20 cm×20 cm) is used. The efficiency p of the phantom is required. It describes the fraction of registered events of the perfect detector N_{det} and the photon fluence Φ_{ph} according to equation (5.1).

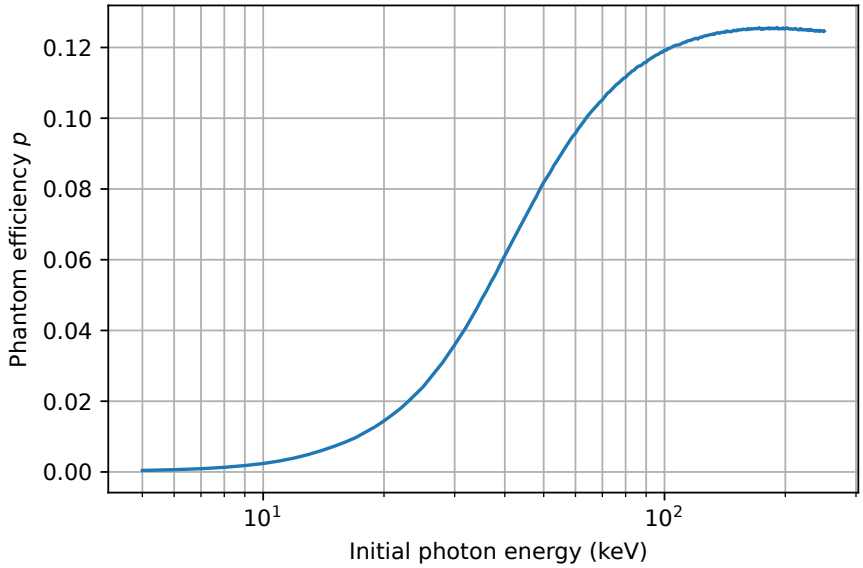

Figure 5.12.: The cylinder phantom efficiency as a function of initial photon energy. It describes the fraction of events detected by the ring-shaped perfect detector N_{det}, and the photon fluence Φ_{ph}, according to equation (5.1).

The trend of this efficiency as a function of initial energy is depicted in figure 5.12. For low energies, almost all photons are absorbed by the phantom and cannot reach the perfect detector. With increasing energy, the probability for photoelectric effect decreases and Compton scattering becomes more probable, leading to an increased number of registered events. The efficiency p for the cylinder phantom is higher than the slab phantom's as the perfect detector extends to the cylinder phantom's backside. Therefore, photons traversing the phantom still have a chance to be registered. The previously described detector simulations are performed under the assumption that Dosepix detectors and their PCBs are so small they do not shield the direct irradiation of the phantom.

In the following, the placement of the detectors concerning the cylinder phantom is considered. The setup is illustrated in figure 5.13. It shows an excerpt of the top-down view of the cylinder phantom, resembled by the circle with a radius of 10 cm. The green lines indicate the locations and orientations of the Dosepix detectors. The two main detectors, one for each eye, are located where the dashed and dashed-dotted

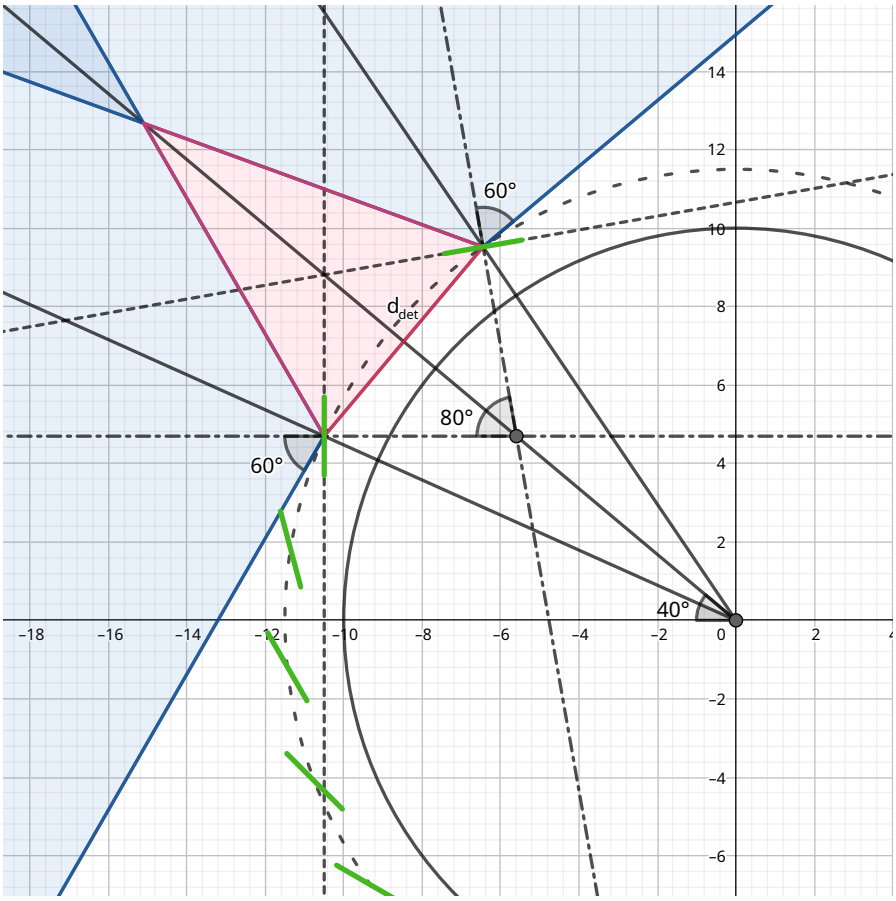

Figure 5.13.: Dosepix detector placement in relation to the cylinder phantom in a top-down view. The solid black circle indicates the phantom. Green lines correspond to the positions and orientations of the Dosepix detectors. The two main detectors are centred at the intersection points of the dashed and dash-dotted lines. The detectors are assumed to have a half opening angle of 60°. This results in a field of view as represented by the blue shaded region. The red shaded region indicates the source positions at which no proper dose estimation is possible. Additional Dosepix detectors are placed within the geometry corresponding to different irradiation angles, as explained in the text. The image is made with [64].

lines intersect. Their centres are separated by a distance of $d_{\mathrm{det}} = 6.3\,\mathrm{cm}$ which approximately corresponds to the average pupillary distance of adults, i.e. the distance from one eye's pupil to the other [65]. The centres of the detectors have a distance to the outer wall of the phantom of 1.5 cm and are indicated by the loosely dashed circle. Each detector is tilted by an angle of 40° in regards to the symmetry axis of the setup. The blue shaded region illustrates a detectors' field of view under the assumption that it can estimate dose for a half opening angle of 60°. However, this has to be evaluated via simulations. This region indicates directions of photon emission the dosimetry setup might be able to correctly estimate dose. Due to the tilting of the detectors, the red region is created. Here, reduced dose-response is present. However, this is only the case for sources that lie within the indicated region. This placement is unlikely in real applications and should also be avoided at all costs.

By exploiting the cylinder phantom's rotational symmetry, different irradiation angles are simulated via detector placement. This is indicated by the additional detectors reflected by green lines in the figure. These correspond to a rotated version of the detector located at the bottom corner of the red triangle. The rotation is executed about the centre of the phantom. An irradiation angle of ϕ_{ir} is introduced. For $\phi_{\mathrm{ir}} = 0°$, photon tracks are parallel to the symmetry axis of the two main detectors. The tracks point from the outside to the inside of the phantom. At $\phi_{\mathrm{ir}} = 40°$, photons are emitted perpendicularly on one of the main detectors. In the phantom simulation, only a fixed irradiation angle is utilised. A rotation of a main detector by an angle of ϕ_{det} then directly corresponds to an irradiation angle of $\phi_{\mathrm{ir}} = \phi_{\mathrm{det}}$. This way, multiple detectors, each reflecting a different irradiation angle, are placed within the geometry of the detector simulation. Also, the detector system's symmetry is utilised, and only one half of the setup is simulated while the other half is provided by mirroring at the symmetry axis.

Figure 5.14 shows the implementation of the detectors in simulation. Their response spectra are taken, and the corresponding irradiation angles ϕ_{ir} are attributed afterwards. The responses are normalised using the photon fluence, and a linear interpolation of the spectra is made. This provides a function that returns the number of events registered by Dosepix per photon fluence for the arguments of initial photon energy, irradiation angle ϕ_{ir}, and deposited energy.

5.2.3 Direct irradiation for different filter thicknesses

For backscattering simulations, a distinction between the different dose types and the used phantoms is made. When dealing with direct irradiation of the detectors, this is not the case. Instead, the effect of different filters in front of the detectors is analysed. Multiple measures can be varied in simulation. These include the material and thickness of the filter and the orientation in regards to the detector.

The simulation's main goal is to reflect the response of Dosepix for an arbitrarily shaped filter in front of it. An example is illustrated in figure 5.15. Photons, indicated

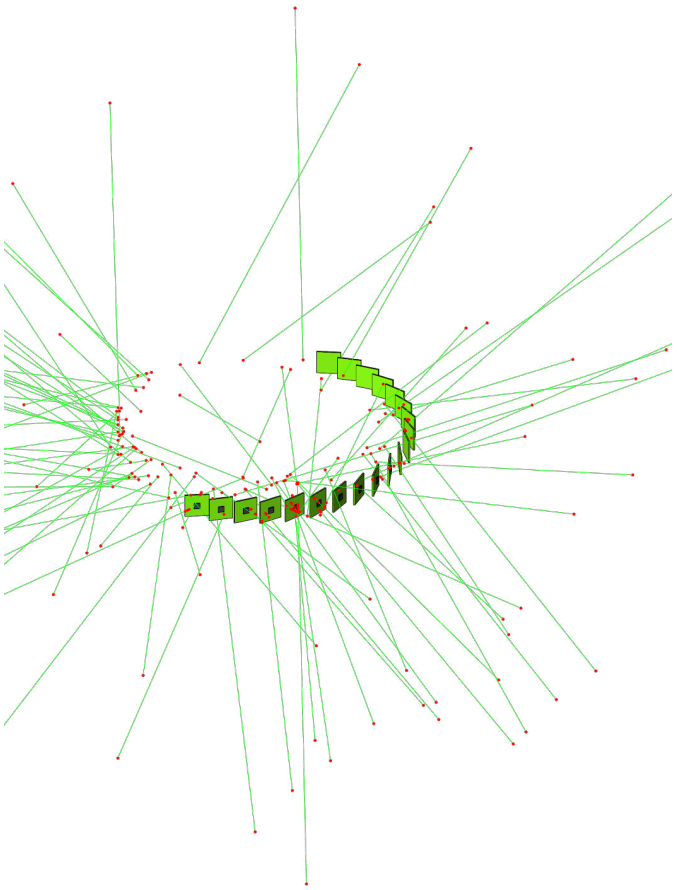

Figure 5.14.: Detector simulation of the cylinder phantom backscattering. Multiple Dosepix detectors, each attached to a small green PCB, are implemented in geometry. The cylinder phantom is exchanged with the pre-calculated photon characteristics registered by the perfect detector in an independent phantom simulation. Green lines indicate the photon tracks and red dots either start, end, or interaction points. Each Dosepix represents a different angle of irradiation on the phantom. Their positioning resembles the one of figure 5.13.

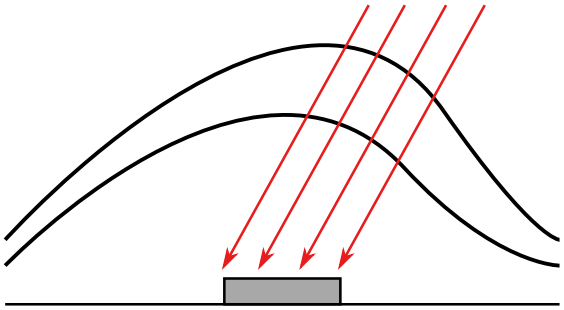

Figure 5.15.: Irradiation of Dosepix with an arbitrarily shaped filter in front of it. The red arrows resemble photons that are emitted on the detector represented by the grey block. The two black lines represent the shape of the filter.

by red arrows, are impinging on Dosepix, reflected by the grey block. The two curved lines represent the arbitrarily shaped filter. The irradiated part is exchanged with a flat filter of the same thickness to approximate the arbitrary filter's behaviour. Additionally, the direction of irradiation is important as the response of Dosepix depends on it. This way, the arbitrary shape can be represented by flat filters of different thicknesses and for different irradiation angles. This approximation is only valid if the distance between the detector and the arbitrary filter's inner walls is large. Otherwise, an error due to the variation of the filter's thickness with irradiation angle is made.

An exemplary simulation for a flat filter of a certain thickness is illustrated in figure 5.16. Instead of changing the direction of emission of a photon source, a fixed direction is utilised, and the detectors are rotated. 36 Dosepix detectors are implemented, each representing a different irradiation angle. In front of the detectors, a planar filter is placed perpendicularly to the photon field. Simulations for different filter thicknesses are made. When the responses are combined to reflect the response of Dosepix for an arbitrary filter, an error regarding Compton scattering is introduced. Under the assumption that the detector is small in comparison to the filter, this error is neglectable. Additionally, as previously stated, the alternative is to simulate the complete filter shape for each iteration of an optimisation process. Whereas now, the precalculation is only made once and is used to approximate the response of Dosepix for different angles of irradiation and arbitrary filter shapes in a fast manner.

5.3 Dosepix response spectra

The responses of Dosepix as a result of the previously described simulations are presented in the following. Irradiation angles for $H_p(3)$ dosimetry, involving the cylinder phantom, are specified as shown in figure 5.17, depicting a top-down view of the phantom and Dosepix detector (in green), responsible for dose measurements of the right eye of a person wearing the dosemeter.

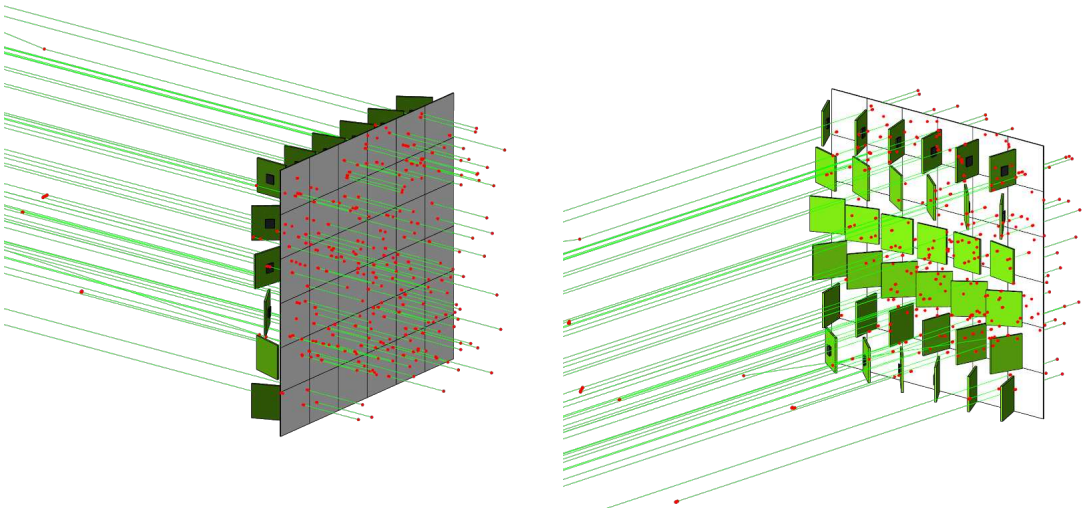

(a) Frontside view (b) Backside view

Figure 5.16.: Simulation of direct irradiation of Dosepix. (a) shows the setup in frontside view, (b) depicts the same setup but in backside view. 36 Dosepix detectors, including their small PCBs, are implemented. Each detector resembles a different direction of photon emission. In front of the detectors, a filter plate of fixed thickness is installed. The simulated photons, whose tracks are resembled by the green lines, are directly emitted on the filter. Red dots indicate start and interaction points of the photons.

The image corresponds to figure 5.14 but is rotated about the phantom's centre until the upper surface of the Dosepix detector is parallel to the y-axis and points in the negative direction of the x-axis. For a dosemeter, a preferential direction has to be chosen. It corresponds to the normal of the detector indicated by the blue arrow in the figure. The irradiation angle ϕ is given in regards to this direction. ϕ is represented by a single photon in the figure but corresponds to a parallel photon field. Since direct irradiation leads to the highest number of registered events, the filter design will be more symmetric. If a detector is used for each eye, the field of view of the dosemeter is expanded. Often, it is beneficial to combine the data of multiple detectors to estimate dose from registered events. However, this only works if the detectors use different filters. The detectors will then provide various representations of an input photon spectrum. Using identical detectors only increases the statistics of registered events. The symmetry of the detectors cannot be broken for an eye lens dosemeter as it leads to a loss of the ability to estimate dose per eye.

Figure 5.17 includes dash-dotted lines indicating the range of the irradiation angles the cylinder phantom shields direct irradiation for the detector. Under the assumption that Dosepix is small and described by a single point in space, this range is reflected

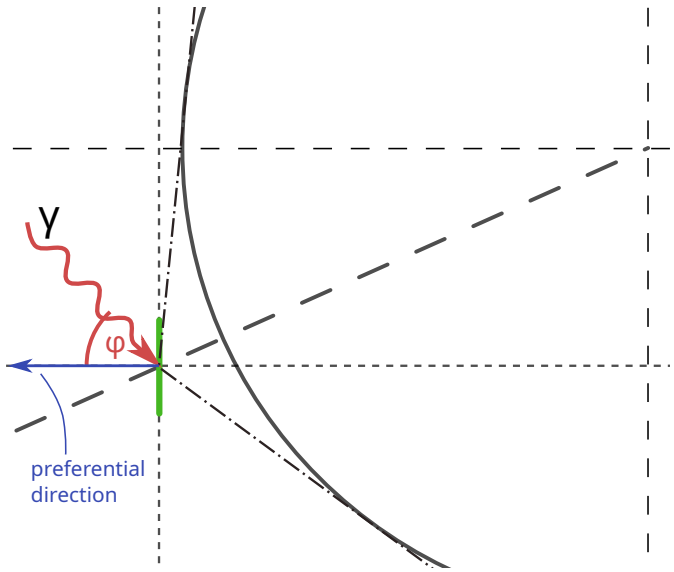

Figure 5.17.: The definition of the irradiation angle ϕ of primary photons. The circle indicates the top-down view of the cylinder phantom. The Dosepix detector responsible for dose measurements of the right eye of the bearer of the dosemeter is depicted in green. The irradiation angle is defined about the normal of the frontal surface of the detector. An additional dash-dotted lines indicate the irradiation angle region the cylinder phantom shields direct irradiation.

by angles larger than 107.68° and smaller than −138.32°. Due to the shielding in this regime, only backscattering is considered. For the remaining angles of irradiation, the sum of direct irradiation and backscattering is considered.

The irradiation angle in case of the slab phantom, used for $H_p(10)$ and $H_p(0.07)$ dosimetry, is defined relative to the normal of the frontal surface of the phantom. The normal corresponds to the z-axis depicted in figure 3.12 (a). An angular range of 0° to 60° is used as it corresponds to the minimum legal requirements of a dosemeter, according to PTB [53]. Due to the symmetry of the setup, it is sufficient to evaluate positive irradiation angles only.

The following sections illustrate the simulated deposited energy spectra and their integrals of registered events for a Dosepix detector. Only deposited energies greater than 10 keV are considered. All response spectra are normalised to the fluence of the simulated parallel photon field in simulation.

5.3.1 Backscattering

The Dosepix responses for the backscattering simulation are presented. The deposited energy spectra are illustrated in figure 5.18 for the slab phantom (a) and the cylinder

phantom (b). The spectra are shown for emitted photons of 40 keV. The colours of the curves represent different irradiation angles according to the colour bars. A diverging colour scale centred about 0° is chosen in (b) as the deposited energy spectra are not symmetrical to this angle. For the slab phantom in (a), the spectra's shapes are similar for all irradiation angles. There is a primary peak centred at about 35 keV. It includes photons that previously underwent Compton backscattering in the phantom or the hardware attached to the detector, resulting in a minimum photon energy of 34.59 keV. For certain irradiation angles, a second peak centred at about 29 keV is visible. It corresponds to photons that scattered twice, reflected by a minimum photon energy of 30.47 keV. Compton scatterings of higher order are not discernible as the probability for photoelectric absorption in the phantom increases with decreasing photon energy.

The shapes of the deposited energy spectra in 5.18 (b) for the cylinder phantom are similar to the spectra for the slab phantom in (a). There is no symmetry about the irradiation angle of 0° as shown for the setup in figure 5.17. Here, the Dosepix detector is shifted in regards to the centre of the cylinder phantom along the y-axis. The deposited energy spectra consist of a broad peak each. This peak is the superposition of full energy peaks of photons scattered multiple times in the phantom. The resulting peak is broader for the slab phantom, due to the curved shape of the cylinder phantom. When comparing the scales of the spectra in (a) and (b), the cylinder phantom shows more registered events. This is mainly due to the implementation of the readout electronics for the slab phantom, which shields photons of low energies.

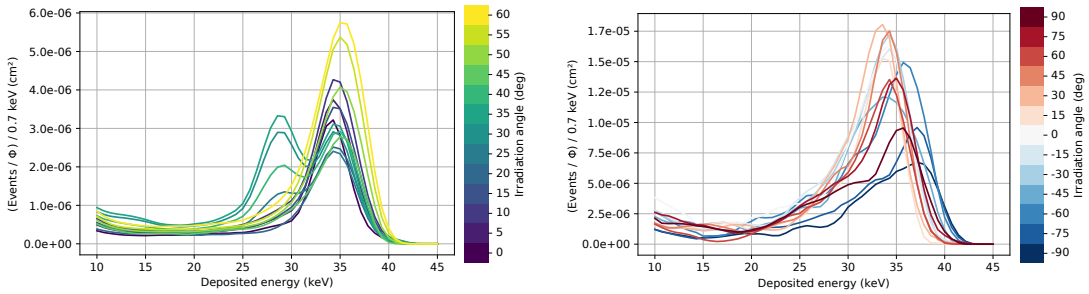

(a) Slab phantom

(b) Cylinder phantom

Figure 5.18.: Deposited energy spectra for an initial photon energy of 40 keV. For the slab phantom in (a) and the cylinder phantom in (b). The colours of the curves correspond to different irradiation angles according to the colour bars. The numbers of registered events are normalised to the simulated photon fluence Φ.

Figure 5.19 shows the total number of registered backscattering events as a function of the irradiation angle for the slab phantom (a) and the cylinder phantom (b). The colours of the curves correspond to the initial photon energy according to the colour bars. The energies are varied within a range of 10 keV to 40 keV since here,

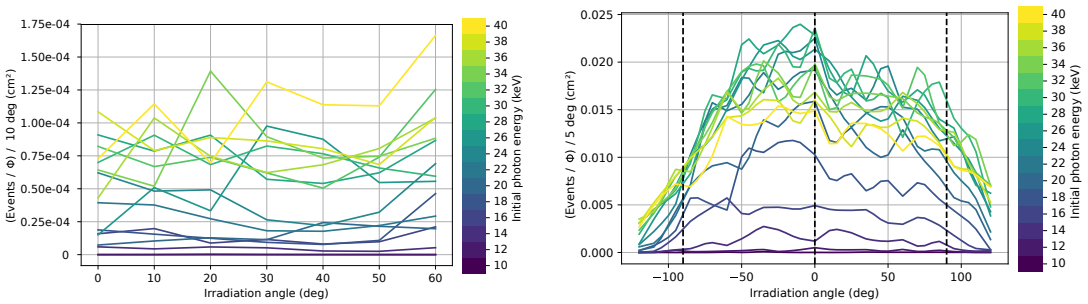

(a) Slab phantom

(b) Cylinder phantom

Figure 5.19.: The total number of registered backscattering events for the slab phantom (a) and the cylinder phantom (b) as a function of the irradiation angle. The colours of the curves represent the initial photon energies according to the colour bars. Each data point reflects the integral of a deposited energy spectrum normalised to fluence Φ like shown in figure 5.18. Only deposited energies $\geq 10\,\mathrm{keV}$ are considered.

the total number of registered events shows the most significant changes. In general, the number of registered events is low, leading to strong statistical fluctuations for different irradiation angles. The dependence on the irradiation angle is low for the slab phantom in (a). For the cylinder phantom in (b), a larger range of the irradiation angle is analysed. The number of registered events is approximately stable for irradiation angles within about -50° to 80°, and decreases steadily for angles outside of this range. This unsymmetric behaviour is denoted to the shifted position of the detector concerning the cylinder phantom. When comparing the phantoms, the total number of registered events for the slab phantom is generally lower than for the cylinder phantom due to the additional shielding of the readout electronics like previously mentioned.

5.3.2 Direct irradiation

The characteristics of the response spectra for the direct irradiation simulations are illustrated in the following. No separation between the phantoms is required. Figure 5.20 shows the deposited energy spectra for a Dosepix detector without additional filter for an initial photon energy of 20 keV (a) and 40 keV (b). The different colours of the curves represent the irradiation angles according to the colour bar. These angles lie within a range of 0° to 90°. For 0°, the photons impinge perpendicularly to the frontal surface of the sensor of the detector. In this case, the mean deposited energies of the peaks in the spectra are closest to the corresponding initial photon energies. There is a slight offset between initial and registered deposited energy as described in section 3.1.3. With increasing irradiation angles, the peaks in the deposited energy spectra

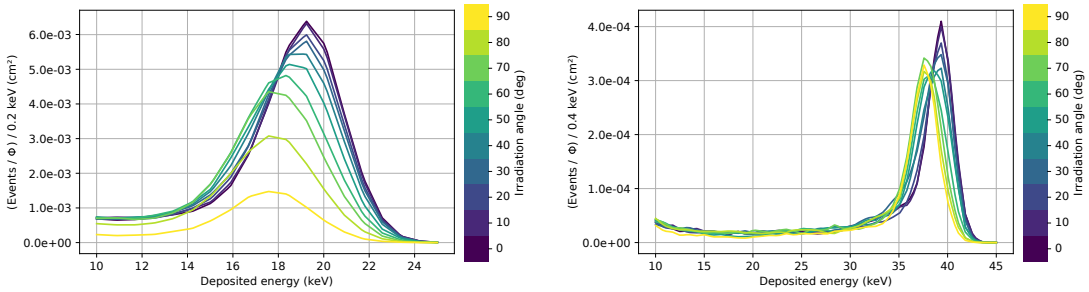

(a) Initial energy of 20 keV

(b) Initial energy of 40 keV

Figure 5.20.: Deposited energy spectra for the simulation of direct irradiation on a Dosepix detector. For a photon energy of 20 keV in (a) and 40 keV in (b). The colours of the curves represent the irradiation angles according to the colour bars. All spectra represent the number of registered events per photon fluence.

shift towards lower energies. The peaks' shapes are described by a superposition of a full energy peak and a peak of events from Compton scattered photons. Due to the detector's energy resolution, these peaks cannot be separated and appear as a single peak, shifted in deposited energy depending on the probabilities of the different processes to take place. The trend of the number of registered events N as a function of irradiation angle θ_{ir} is approximately described via

$$N(\theta_{\mathrm{ir}}) \propto \cos\theta_{\mathrm{ir}} \cdot (1 - \exp(\mu \cdot \rho \cdot d(\theta_{\mathrm{ir}}))) \,, \tag{5.3}$$

where the exponential attenuation law introduced in section 2.2 is used. $d(\theta_{\mathrm{ir}})$ reflects the effective thickness of the sensor material for an irradiation angle θ_{ir}, i.e.

$$d(\theta_{\mathrm{ir}}) = \frac{d_0}{\cos\theta_{\mathrm{ir}}}, \tag{5.4}$$

This thickness corresponds with $d_0 = 300\,\mu\mathrm{m}$ the thickness for $\theta_{\mathrm{ir}} = 0$. μ is the mass absorption coefficient and $\rho = 2.33\,\frac{\mathrm{g}}{\mathrm{cm}^3}$ the density of silicon [23]. The first factor $\cos(\theta_{\mathrm{ir}})$ considers the effective irradiated area of the detector for a homogeneous photon fluence. It deceases with θ_{ir} as the photon fluence is constant in the simulation.

Figure 5.21 shows the fraction of registered events $N(\theta_{\mathrm{ir}})$ and $N(\theta_{\mathrm{ir}} = 0)$ as a function of θ_{ir}. The initial photon energy is 20 keV and the mass absorption coefficients for photoelectric absorption and Compton scattering for silicon are used [17] in (a). While Compton scattering is almost independent of the irradiation angle θ_{ir}, the number of registered events due to photoelectric absorption decreases steadily. Note, that Compton-scattered photons also have to interact with the sensor of the detector via photoelectric effect. However, due to their reduced energy, the probability to interact

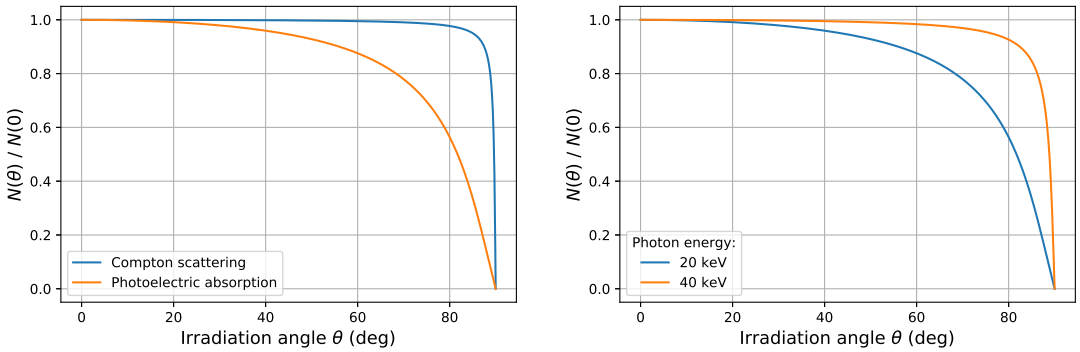

(a) Interaction type dependence

(b) Photon energy dependence

Figure 5.21.: Approximative description of the fraction of the number of registered events $N(\theta_{\mathrm{ir}})$, for an irradiation angle θ_{ir}, and $N(\theta_{\mathrm{ir}} = 0)$. The trends are described via equation (5.3). (a) uses a photon energy of 20 keV and shows the dependence for the different interaction processes according to the legend. (b) considers photoelectric absorption only and takes different initial photon energies according to the legend into account.

is increased. This corresponds to the peak shifting towards lower energies in the deposited energy spectra of figure 5.20 (a). In figure 5.21 (b), photoelectric absorption for initial photon energies of 20 keV and 40 keV according to the legend is considered. With higher photon energies, the dependence of the number of registered events on the irradiation angle θ_{ir} decreases.

This is further illustrated by figure 5.22, which shows the total number of registered events as a function of the irradiation angle. The different colours of the curves indicate the initial energy according to the colour bar. The depicted irradiation angles are limited to a range of $-110°$ to $110°$. (b) shows the same data as (a), but each curve is normalised to its maximum. (a) shows that with increasing initial photon energy, the amplitude of the curves first increases, reaches its maximum at about 12 keV, and afterwards decreases steadily. This trend corresponds to the energy dependence of the photoelectric absorption in silicon. In (b), the trend of the curves as a function of the irradiation angle is shown. All curves reflect that the number of registered events decreases rapidly for absolute irradiation angles close to $90°$. This decrease corresponds to figure 5.21. Figure 5.22 (b) shows that the number of registered events increases for irradiation angles greater than $90°$. This increase is due to the effective area of the sensor, which also increases. However, photons are attenuated because they first have to cross the sensor's underside to reach it.

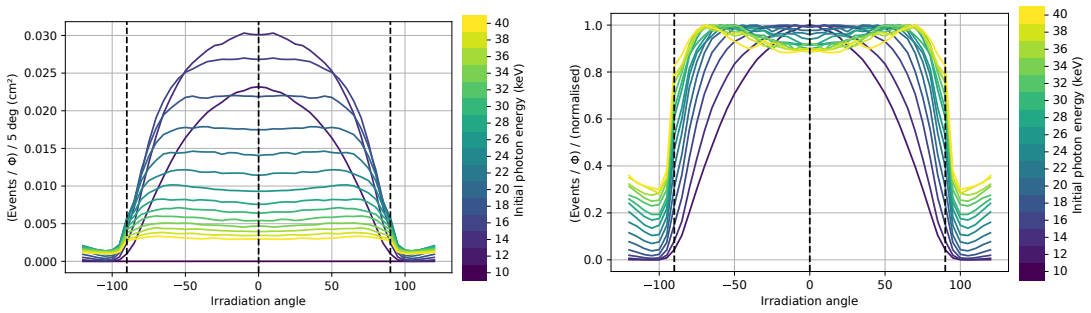

(a) Original

(b) Normalised to maximum

Figure 5.22.: The total number of registered events as a function of irradiation angle. All data points are normalised to the photon fluence Φ in simulation in (a). The colours of the curves correspond to the initial energies of the photons according to the colour bars. (b) depicts the data of (a), with each curve normalised to its maximum. Dashed lines indicate irradiation angles of $-90°$, $0°$, and $90°$.

5.3.3 Direct irradiation with filter

In the following, flat PMMA filter's are added in front of Dosepix, and the detector's behaviour for direct irradiation is analysed. The setup of figure 5.16 is used. Due to the low density of PMMA of about $1.15\,\frac{\mathrm{g}}{\mathrm{cm}^3}$ [66], the material has low photon attenuation capabilities. Thicknesses of up to 20 mm are simulated to compensate for this. Materials with higher densities allow for thinner filter designs. However, the material has to be easily machinable to get it into the desired shape. PMMA and plastics are a good choice since they can be 3D-printed. Also, since the housing of a dosemeter will probably be made from a similar material, the filter design can directly be implemented as a part of it. Figure 5.23 illustrates the total number of registered events as a function of the irradiation angle. The colours of the curves correspond to the thicknesses of the used planar filter according to the colour bar. The initial photon energy is 20 keV in (a) and 40 keV in (b).

The shapes of the curves as a function of irradiation angle are described in the previous section. With increasing thickness of the PMMA-filter the number of registered events, and as a consequence, the amplitudes of the curves decrease. This trend is evident in (a) and visible to a lower degree in (b). It shows that the ability of the filter material to attenuate photons mainly depends on photoelectric absorption. For higher photon energies, the Compton effect is increasingly dominant. Photons scatter at the filter, lose a part of their energy, and change their direction. Nevertheless, they might still be able to reach the sensor of the detector to be eventually detected. Therefore, the ability of a filter to attenuate photons is decreasing with increasing initial energy.

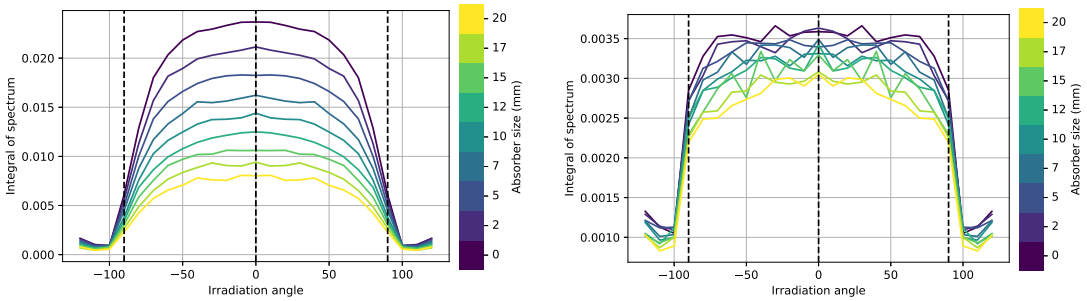

(a) Initial energy of 20 keV

(b) Initial energy of 40 keV

Figure 5.23.: The total number of registered events as a function of irradiation angle. All data points are normalised to fluence Φ of the simulated photon field. The energy of the primary photons is 20 keV in (a) and 40 keV in (b). Flat PMMA-filters with different thicknesses are implemented in simulation. The colours of the curves represent these thicknesses according to the colour bars.

5.3.4 Fraction of backscattering and direct irradiation

Finally, the fraction of the number of registered backscattering events N_{back} and events from direct emission N_{dir} is analysed. It indicates the influence of the phantoms on measurements. First, only direct irradiation without a filter is considered. Figure 5.24 shows the fraction $N_{\text{back}}/N_{\text{dir}}$ as a function of the irradiation angle, for the slab phantom in (a) and the cylinder phantom in (b). The colours of the curves represent the initial photon energy according to the colour bar, which range from 10 keV to 100 keV.

There is almost no dependence on the irradiation angle for the slab phantom in (a). The fraction of backscattering and direct irradiation events increases with increasing initial photon energy. This trend is due to the photon detection efficiency of Dosepix, which decreases for increasing energy. The same trend is visible for the cylinder phantom in (b) for an irradiation angle range of $-90°$ to $90°$. Dashed lines in the plot represent these angles, together with $0°$ and $107.68°$. $107.68°$ corresponds to the angle the cylinder phantom shields direct irradiation for the detector illustrated in figure 5.17. For absolute irradiation angles greater than $90°$, the influence of direct irradiation is reduced due to the constant photon fluence and decreased effective irradiated area of the detector's sensor. Events from backscattering are not influenced by this issue, leading to an increased ratio of backscattering and direct irradiation events.

Figure 5.25 illustrates the fraction of registered events from backscattering and direct irradiation as a function of the PMMA-filter thickness. (a) shows the data for the slab phantom and (b) for the cylinder phantom. The colours of the curves correspond

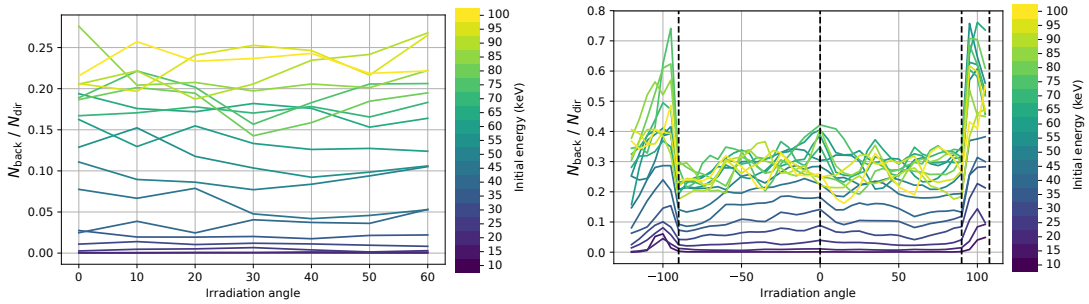

(a) Slab phantom

(b) Cylinder phantom

Figure 5.24.: The fraction of registered events from backscattering N_{back} and direct irradiation N_{dir} as a function of the irradiation angle, for the slab phantom in (a) and the cylinder phantom in (b). The colour of the curves represents different initial energies according to the colour bar. The dashed lines for the cylinder phantom in (b) represent irradiation angles of $-90°$, $0°$, $90°$ and the shielding angle $107.68°$ according to figure 5.17.

to different photon energies according to the legend. The illustrated change describes the fraction of the value of $\frac{N_{back}}{N_{dir}}$ for a certain filter thickness and the corresponding value if no filter is present. The higher this change, the higher the share of registered events from backscattering. The curves for the plots in (a) and (b) are similar but differ in their magnitudes. With increasing filter thicknesses, fewer photons from direct irradiation reach the sensor of Dosepix. For increasing photon energy, the filter's attenuation decreases, leading to curves for which the change of $\frac{N_{back}}{N_{dir}}$ is close to 1 independent of the filter thickness. This illustrates that for photon energies above about 60 keV the attenuation of the PMMA filter becomes almost ineffective to photons.

5.4 Filter shape optimisation

The data for optimising the shape of a PMMA-filter in front of a Dosepix detector regarding dose estimations were introduced in the previous sections. Simulations for different settings are precalculated, and the resulting detector responses are linearly interpolated for different irradiation angles, filter thicknesses, and initial photon energies. The interpolated data can be sampled during an optimisation process. This removes the necessity for additional computations and ultimately leads to a speed-up. The used range of initial photon energies is $[10, 40]$ keV in steps of 1 keV and $[45, 250]$ keV in steps of 5 keV. The values are chosen to optimise the dose reconstruction abilities for typical photon energies found in medical applications (see for example [59]) and to fulfill the minimum requirements for a $H_p(0.07)$ and $H_p(3)$ dosemeter according to PTB [53, 67]. For $H_p(10)$, the minimum energy range is from 80 keV

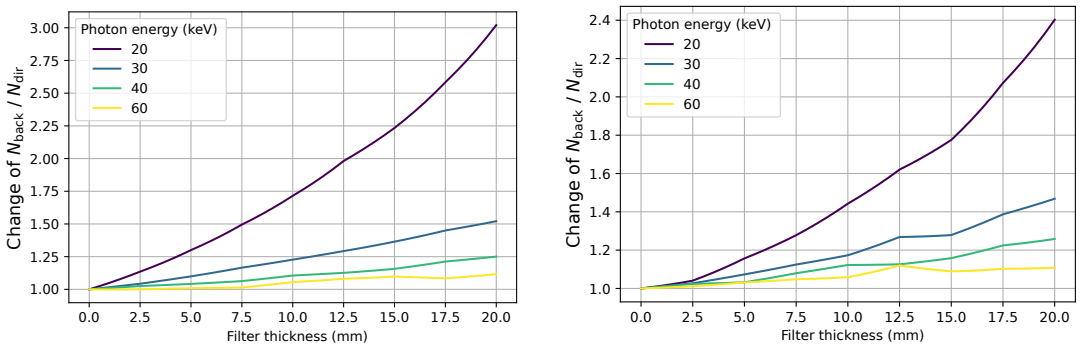

(a) Slab phantom

(b) Cylinder phantom

Figure 5.25.: Change of the fraction of registered events from backscattering and direct irradiation $\frac{N_{back}}{N_{dir}}$ as a function of the thickness of the PMMA-filter in front of a Dosepix detector. The data points are normalised to the fraction without filter. (a) depicts the data for the slab phantom, (b) for the cylinder phantom. The colours of the curves represent different initial photon energies according to the legend.

to 1250 keV. However, only the previously defined energy range is used to focus on medical applications. First, the thickness for the filter at an irradiation angle of 0° is of interest. It is later used to determine the filter thickness for the remaining irradiation angle range.

5.4.1 Filter thickness for perpendicular irradiation

The determination of the filter thickness for an irradiation angle of 0° is essential. This angle is used as a reference, i.e. the detector should estimate doses as best as possible for it. Dose conversion coefficients for registered events of the detector to dose are determined for this reference angle only. All other irradiation angles use the same coefficients since a determination of the irradiation angle from measurement data is not possible.

The interpolated response spectra for the irradiation with monoenergetic photons for direct irradiation and backscattering are sampled in the following. These responses are normalised to the applied photon fluence Φ each. The spectra differ in their backscattering contributions depending on the used phantom type. Since all dose measurements are performed in Dosi-mode, the deposited energy spectra are binned accordingly. For the determination of the filter thicknesses for 0° irradiation angle, start values of the bin edges are chosen heuristically. The 16 left edges of the bins are distributed uniformly within $[10, 180]$ keV. The last bin counts all registered deposited energies greater than 180 keV.

First, the start values of the bin edges are used to bin the response spectra for all discussed initial photon energies. The result is a matrix $\hat{N}$ with its rows representing the different energies and its columns containing the binned number of registered events. Performing a matrix multiplication with a vector containing the conversion coefficients from events to dose $\vec{k}$ results in the dose vector $\vec{H}_{\mathrm{DPX}}$ according to

$$\vec{H}_{\mathrm{DPX}}(\vec{k}) = \hat{N} \cdot \vec{k}. \tag{5.5}$$

See section 3.2.6 for more information. Dose vector H_{DPX} is compared with the target dose vector $\vec{H}$ to optimise vector $\vec{k}$. $\vec{H}$ is determined by taking the conversion factors $\frac{D}{\Phi}(E)$ from fluence to personal dose equivalents D for photon energies E and multiplying them with the photon fluence Φ. For simplicity, a unit fluence of $\Phi = \frac{1}{\mathrm{cm}^2}$ is used. The same fluence then also has to be used for the response spectra of the detector. qualityThe conversion factors $\frac{D}{\Phi}(E)$ are illustrated in figure 3.21 for $\vec{H}_{\mathrm{p}}(10)/\Phi$ (a) and $H_{\mathrm{p}}(0.07)/\Phi$ (b), and in figure 5.2 for $H_{\mathrm{p}}(3)/\Phi$. To optimise $\vec{k}$, the loss function

$$\mathcal{L}(\vec{k}) = \sqrt{\sum_{i=1}^{N_E} \left(1 - \frac{H_{\mathrm{DPX},i}(\vec{k})}{H_i}\right)^2} \tag{5.6}$$

is minimised. The sum of index i is over the N_E initial photon energies. $\mathcal{L}$ describes the mean squared error of the dose responses $\frac{H_{\mathrm{DPX},i}}{H_i}$ concerning the perfect response of 1. The optimisation of the conversion coefficients $\vec{k}$ is repeated for different thicknesses to find the PMMA filter's shape in front of the Dosepix detector. The thicknesses are varied within a range of $[0, 20]$ mm with a step size of 1 mm. A first evaluation using the initial values of the bin edges shows that filter thicknesses of 1 mm ($H_{\mathrm{p}}(3)$), 7 mm ($H_{\mathrm{p}}(10)$) and 1 mm ($H_{\mathrm{p}}(0.07)$) provide the best conversion coefficients. These preliminary results are used to optimise the bin edges of Dosi-mode. Their optimisation is executed under the assumption that the best filter thicknesses do not change when the bin edges are varied.

In bin edge optimisation, their values are varied via a genetic algorithm. It is implemented in the DEAP framework [68]. In the beginning, an initial population of edges is created. These are randomly varied versions of the start edges. The performance of each individual of the population is evaluated. This evaluation corresponds to the previously introduced optimisation of the conversion coefficients for 0° irradiation angle and the determination of loss $\mathcal{L}$. In a new generation, the individuals of the population are modified or exchanged according to fixed rules. These include mutations, i.e. the random modification of bin edges of an individual, crossovers, i.e. the splitting and recombination of multiple individuals at a random point, or selection, i.e. the discarding of flawed individuals and the introduction of random new ones. Finally, the procedure leads to individuals within the population with increasingly better performance from generation to generation. The algorithm is executed until the evaluated loss $\mathcal{L}$ converges. The determined bin edges b_i are listed in table A.6 of the appendix.

They only slightly vary from the initial values, approving the quality of the start parameters. The following analyses use these optimised bin edges. Figure 5.26 shows the corresponding dose responses, i.e. the fraction of estimated and true dose, as a function of initial photon energy. Different filter thicknesses according to the colour bar are evaluated. For each filter thickness, a new set of dose conversion factors is optimised. (a) depicts the results for $H_\mathrm{p}(3)$, (b) for $H_\mathrm{p}(10)$, and (c) for $H_\mathrm{p}(0.07)$.

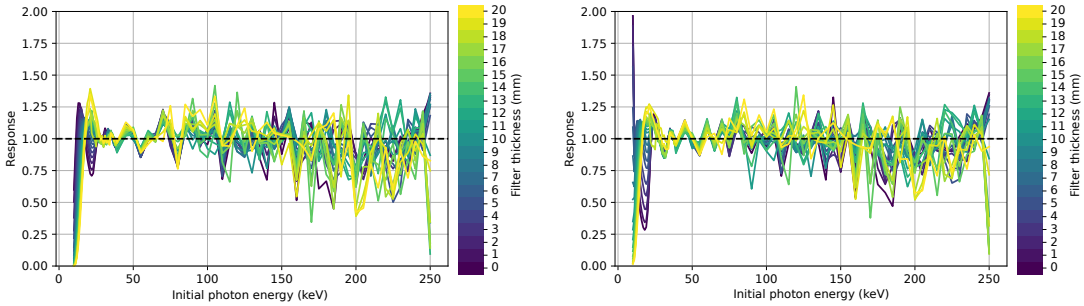

(a) $H_\mathrm{p}(3)$

(b) $H_\mathrm{p}(10)$

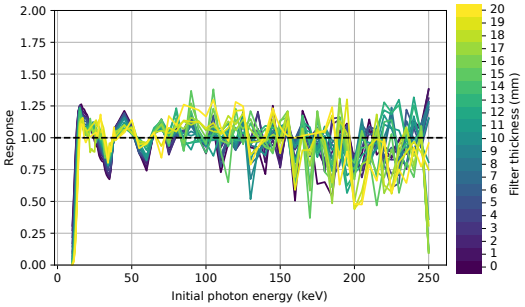

(c) $H_\mathrm{p}(0.07)$

Figure 5.26.: Dose response, i.e. the fraction of the reconstructed dose via Dosepix and the target dose, as a function of initial photon energy. (a) shows the results for $H_\mathrm{p}(3)$, (b) for $H_\mathrm{p}(10)$, and (c) for $H_\mathrm{p}(0.07)$. The used dose conversion coefficients are optimised via a fit to the target dose. Dashed lines indicate the perfect response of 1. The colours of the different curves correspond to different thicknesses of the PMMA filter in front of Dosepix according to the colour bar.

All response curves show fluctuations that increase with increasing initial photon energies. The reason is a decreasing photon detection efficiency of Dosepix and, as a consequence, decreasing event statistics. Due to the simulations' complexity, a high computational effort is required to increase statistics. Instead, a focus on the mean values of the response curves is set in this analysis. It is represented by the MSE loss $\mathcal{L}$ of equation (5.6). The loss as a function of filter thickness is illustrated in figure 5.27

for different filter sizes. The different curves are analysed to provide the best filter thickness. The curves of $H_p(3)$ and $H_p(0.07)$ show an almost identical trend, differing mostly in their magnitudes. A minimum loss is achieved for 1 mm for both dose types. These values are used for the filter thickness for 0° irradiation angle. The dashed line in the plot indicates their values.

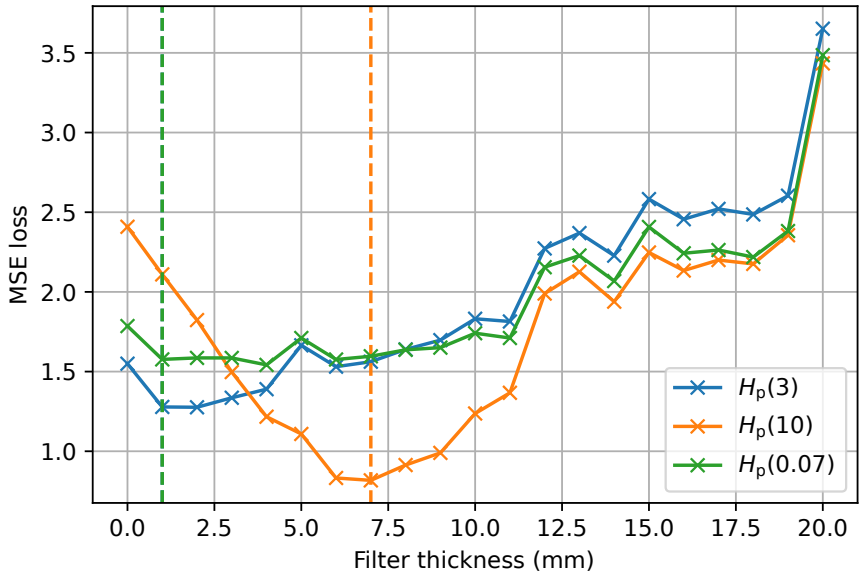

Figure 5.27.: MSE loss $\mathcal{L}$, calculated according to equation (5.6), as a function of the PMMA filter thickness. The curves represent different dose types according to the legend. Dashed vertical lines indicate the final choices of the filter thicknesses for an irradiation angle of 0°.

For $H_p(10)$, the trend of loss $\mathcal{L}$ as a function of filter thickness is different. Here, the performance of the dose reconstruction increases with increasing filter thickness at first. The loss reaches its minimum at about 7 mm and increases for larger thicknesses. Lower event statistics and greater fluctuations in the response additionally contribute to this worsening. A value of 7 mm is chosen for the filter thickness at 0° irradiation angle, which is indicated by the dashed line.

The corresponding conversion coefficients from registered events to dose are calculated for the chosen filter thicknesses. Their values are listed in table A.6 and depicted as a function of deposited energy in figure 5.28 (a) for the different dose types according to the legend. All curves look similar due to the similarity of the conversion factors from photon fluence to dose equivalents of the different dose types. The dose conversion coefficients approximately increase exponentially with linearly increasing deposited energy. Registered events with higher deposited energies are given a higher weight for dose calculation to compensate the detector's lower photon detection efficiency.

The dose coefficients of figure 5.28 (a) are used to calculate the optimised dose responses shown in (b). The colours correspond to the different dose types according to the legend. All response curves are similar as they employ the same simulation data.

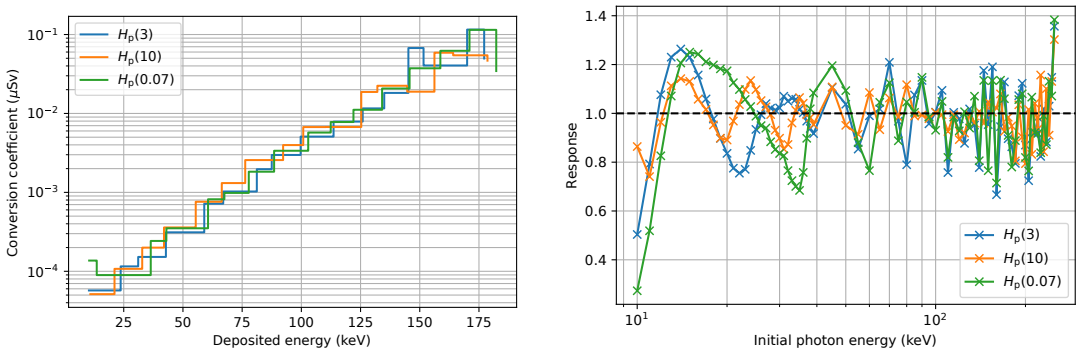

(a) Dose onversion coefficients

(b) Response curves

Figure 5.28.: (a) shows the optimised dose conversion coefficients as a function of deposited energy of table A.6. The bins correspond to the settings in Dosi-mode of the Dosepix detector. (b) depicts the dose responses corresponding to a calculation with the coefficients of (a). The curves represent the performance of dose reconstruction for the detector for an irradiation angle of 0°. The different colours of the curves in (a) and (b) represent the different types of personal dose equivalents according to the legends of the plots.

If there are statistical fluctuations in data, they are present in the responses also. These fluctuations increase with increasing photon energy since the number of registered events decreases. The main difference between the different dose types is noticeable for low initial energies, i.e. less than about 30 keV. The trend of the curves indicates there is no solution for the conversion coefficients $\vec{k}$, providing good dose estimation abilities for high and low photon energies simultaneously. According to PTB [53, 67], the requirements for a dosemeter are dose responses within a range of 0.71 and 1.67. This limits the energy range to photon energies greater than about 14 keV. Within the dose response curves, some values are close to 0.7. Also, the curves show a sawtooth-like trend due to the limited number of bins in Dosi-mode. For real measurements, the responses are smoother, as the photon spectra are usually broader. The response's shown features can probably be compensated when combining measurement data of multiple detectors employing different filter designs. However, the objective is to optimise filters for a single detector to reduce the number of required detectors.

5.4.2 Filter optimisation for complete irradiation angle range

The determined dose conversion coefficients $\vec{k}$ for 0° irradiation angle are now utilised to optimise the complete shape of a PMMA filter. In the following, different methods for $H_\mathrm{p}(3)$, and $H_\mathrm{p}(10)$ and $H_\mathrm{p}(0.07)$ are used. For $H_\mathrm{p}(3)$, only one irradiation angle is important. It rotates about the symmetry axis of the cylinder phantom. Therefore, also the filter design has to be optimised for one dimension only. For the other dose types, the direction of irradiation is described by two angles.

Filter optimisation for $H_\mathrm{p}(3)$

The filter thickness optimisation for $H_\mathrm{p}(3)$ is performed as a function of the irradiation angle rotating about the cylinder phantom's rotational symmetry axis. The resulting filter design is described by this angle alone. The shape has to be stretched along the height-dimension of the phantom afterwards. In the following, the approximation that Dosepix is tiny compared to the filter is used, i.e. the walls of the filters are far away from the detector itself, and each irradiation angle is considered individually. For more details, see section 5.2.3.

The fit procedure consists of a loop over a range of irradiation angles. Within each iteration, the loss $\mathcal{L}$ according to equation (5.6) is optimised. Previously, the actual dose $\vec{H}$ was fixed while the estimated dose $\vec{H}_\mathrm{DPX} = \hat{N} \cdot \vec{k}$ was varied with $\vec{k}$. Now, $\vec{k}$ stays fixed, and the filter thickness is varied instead. In each iteration of the optimisation process, the count matrix $\vec{N}$ is sampled from the interpolated simulations for the current filter thickness. The true dose vector $\vec{H}$ is determined from the conversion coefficients from fluence to dose of figure 5.2 for the current irradiation angle. The results of the filter shape optimisation are illustrated in figure 5.29.

(a) shows the MSE loss $\mathcal{L}$ as a function of the irradiation angle. (b) depicts the results of the determined filter thicknesses for different angles. The curves illustrate a possible final design. The inner surface is set to a radius of 5 mm and is indicated by the blue curve. The sensor of Dosepix is located at a radius of 0 mm. The orange line corresponds to the curvature of the outer surface of the optimised filter. The dashed line at a fixed radius of 6 mm indicates the start value of the filter thickness of 1 mm. Two dashed lines at $-70°$ and $70°$ are included to indicate the irradiation angles the thickness of the optimised filter increases strongly. Since the used simulation data underlies statistical fluctuations, their influence is also present in the orange curve. The filter shape stays constant at about 1 mm within an irradiation angle range of $-70°$ and $70°$. In (a), the loss remains almost stable and low within this angle range. The filter thickness gets large for greater angles and reaches its peak at about $-90°$ and $90°$. Even larger angles are excluded since no proper dose reconstruction is possible for them.

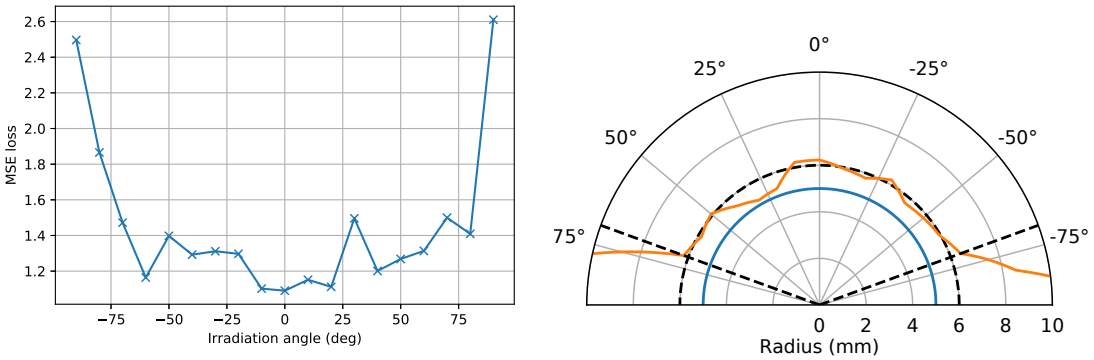

(a) MSE loss $\mathcal{L}$ (b) Filter shape

Figure 5.29.: (a) shows the MSE loss $\mathcal{L}$ after the optimisation of the filter thicknesses for different irradiation angles. (b) shows the corresponding shape of the filter as a function of the irradiation angle. The blue curve describes the filter's inner shape. The sensor of a Dosepix detector is centred at a radius of 0 mm. The sensor's surface points in the direction of 0°. The orange line illustrates the outer shape of the optimised filter. A dashed line indicates the start parameter of the thickness of 1 mm. The other dashed lines at irradiation angles of $-70°$ and $70°$ represent the angles the thickness of the filter begins to increase strongly.

The corresponding dose responses after the optimisation are illustrated in figure 5.30. (a) shows the curves for different irradiation angles according to the colour bar. (b) depicts the average of the curves in (a). The error bars correspond to the standard deviations. The shaded region reflects the minimum and maximum responses of (a). All responses are centred about a perfect response of 1. Again, fluctuations at high photon energies are present. However, the mean response in (b) shows that the actual deviation is not as high. As before for the optimisation of conversion coefficients for 0° irradiation angle, the performance of dose estimation is worst for small initial photon energies. This is especially the case for an angle of 90°. Here, dose reconstructed with the detector overestimates the true dose. However, dose reconstruction is difficult for these energies, and irradiation angles since the conversion coefficients from fluence to dose are close to 0 as figure 5.2 shows.

In summary, the performance for dose reconstruction is best for a PMMA-filter with a thickness of about 1 mm within an irradiation angle range of $-70°$ and $70°$. The individual response curves show that performance is just slightly worse for larger angles. There is an indication that the dose estimation abilities do not depend much on the filter's thickness. This is reflected in figure 5.27 where the MSE loss $\mathcal{L}$ remains almost stable within a filter thickness range of 0 mm to 10 mm.

Considering the trend of the loss, a simpler filter design that is easier to use in real applications is tested. Its shape is depicted in figure 5.31 (a). The blue curve describes

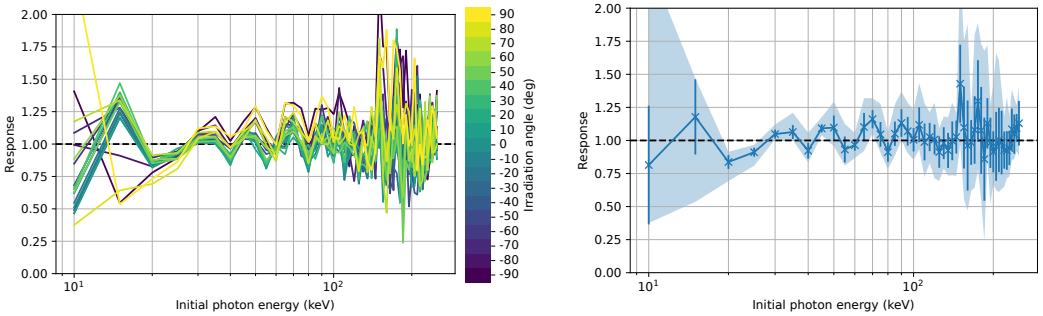

(a) Individual response curves

(b) Average of response curves in (a)

Figure 5.30.: (a) shows the dose responses for the optimised filter depicted in figure 5.29 (b) as a function of initial photon energy. The colours of the curves correspond to different irradiation angles according to the colour bar. (b) shows the average of the curves in (a). The error bars indicate the corresponding standard deviations. The light shaded region reflects the minimum and maximum responses.

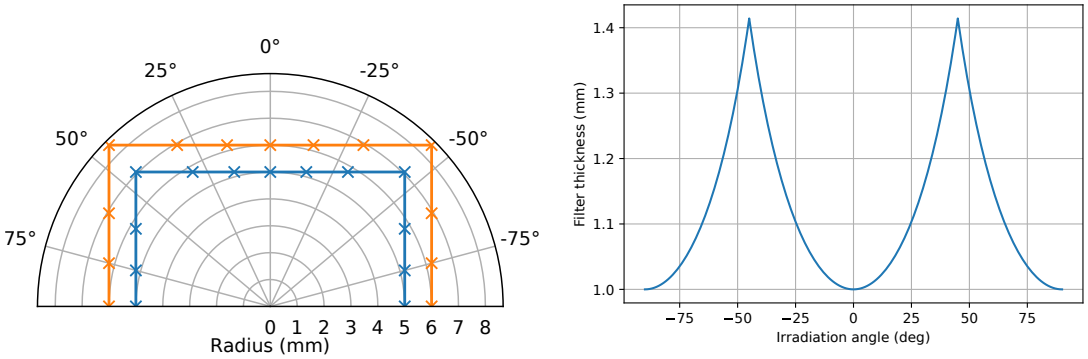

(a) Filter shape

(b) Filter thickness

Figure 5.31.: Simplified PMMA filter design for $H_p(3)$ dose measurements. In (a), the shape of the filter is illustrated. The blue curve describes the trend of the inner surface, the orange curve the trend of the outer surface. (b) reflects the thickness of the filter as a function of the irradiation angle.

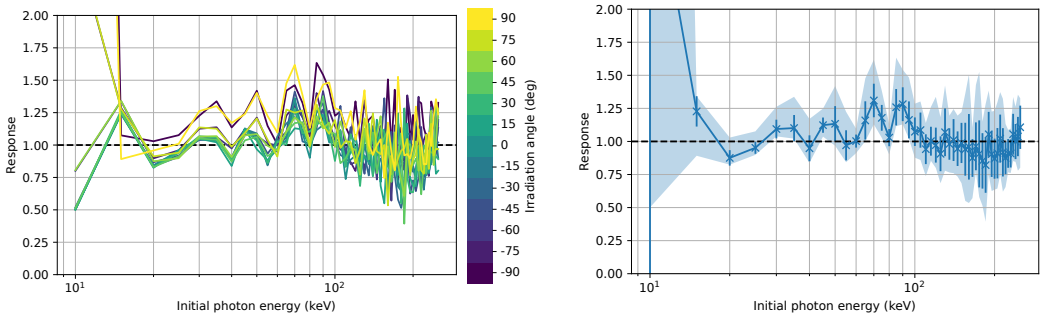

(a) Individual curves

(b) Average of curves in (a)

Figure 5.32.: (a) shows the dose responses for the filter depicted in figure 5.31 (a) as a function of initial photon energy. The colours of the curves correspond to different irradiation angles according to the colour bar. (b) shows the average of the curves in (a). The error bars indicate the corresponding standard deviations. Additionally, the light shaded region reflects the minimum and maximum responses.

the inner, the orange curve the outer shape of the filter. It resembles a housing made of flat planes with thicknesses of 1 mm. At absolute angles of 45°, the edges of two walls are located. The resulting thickness of the filter as a function of the irradiation angle is illustrated in (b). The maximum thickness is $\sqrt{2}\,\mathrm{mm} \approx 1.41\,\mathrm{mm}$. Therefore, the thickness varies within a small region only. The shape of the filter is evaluated by calculating the corresponding responses, presented in figure 5.32. (a) shows the individual curves as a function of initial photon energy. Their colour corresponds to the irradiation angle according to the colour bar. (b) shows the mean of the curves of (a). The error bars represent the corresponding standard deviations. Via the lightly shaded region, the minimum and maximum responses are indicated.

The determined responses show that the detector's dose reconstruction capabilities with the simple cap design are also well. The mean responses are within the required range of 0.71 and 1.67 [53]. In comparison to the fully optimised filter, the simple filter shows deficiencies for low initial photon energies and in the region of about 80 keV to 100 keV. For the low energies, only absolute irradiation angles greater than 70° are affected, while within the other region, all angles are affected, with the responses still being reasonable. This finally shows that the shape of the filter in front of Dosepix is not that important to measure $H_\mathrm{p}(3)$. However, measurements are required to validate the results.

Filter optimisation for $H_\mathrm{p}(10)$

For $H_\mathrm{p}(10)$, which utilises the slab phantom, a different filter optimisation approach is used. Here, a correct filter thickness is more important than for $H_\mathrm{p}(3)$. It is reflected

by the loss from the optimisation of the filter thickness at an irradiation angle of 0° as depicted in figure 5.27. For the other dose types, this loss remains almost stable within a range of up to 10 mm filter thickness, but it varies strongly for $H_p(10)$. The direction of the irradiation for the slab phantom is described in spherical coordinates with two angles ϕ and θ according to figure 3.12. An improved optimisation algorithm now also considers the pixelation of the Dosepix detector. First, a filter is placed in front of the detector. It should be describable with only a few parameters since its shape is to be optimised. A superquadrics model is used to represent the inner and outer surface of the filter. The height of the surface, resembled by the z-coordinate, is determined via the following function which depends on the coordinates within the plane, x and y [69]

$$z(x,y) = C \cdot \left(1 - \left|\frac{x}{A}\right|^r - \left|\frac{y}{A}\right|^r\right)^{\frac{1}{t}}. \tag{5.7}$$

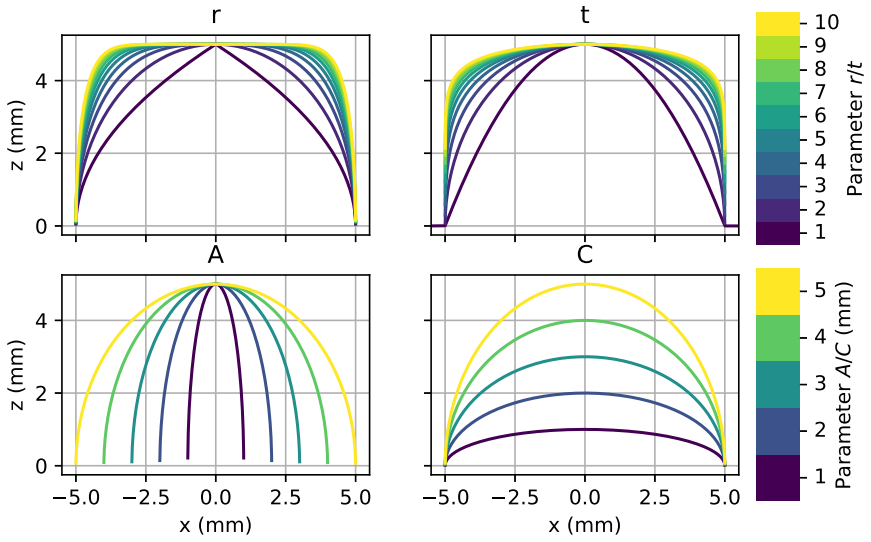

Figure 5.33.: Description of the shapes of a filter via the superquadrics equation (5.7). The projections for $y = 0$ are illustrated. Initial parameters are fixed to $\{r, t, A, C\} = \{2, 2, 5\,\text{mm}, 5\,\text{mm}\}$. The curves represent evaluations of the function where only the parameters in the titles of the plots are varied according to the values indicated by the colour bars.

The shape is described by four parameters r, t, A, and C. Their influence on the shape of the filter is illustrated in figure 5.33. Initial values are chosen for the parameters corresponding to a half-sphere with a radius of 5 mm: $\{r, t, A, C\} = \{2, 2, 5\,\text{mm}, 5\,\text{mm}\}$. For each subplot, only the parameter specified in the title varies according to the corresponding colour bar. The profiles of the resulting filter shapes

for $y = 0$ are depicted. The surface is not rotationally symmetric about the z-axis. Instead, it is symmetric along the surfaces defined by the diagonals of the x- and y-axis, and the z-axis. This symmetry corresponds to the quadrangular shape of the surface of the Dosepix detector and is therefore preferential. Parameters r and t manipulate the curvature of the filter design. If both have a value of 2, the shape is an ellipsoid. Parameter A corresponds to the radius along the x-axis, while C describes the radius in z-direction. If $C = A$ and $r = t = 2$, the shape is a half-sphere. To reduce the number of parameters for optimisation, the inner surface is fixed to $\{r, t, A, C\} = \{2, 2, 8\,\text{mm}, 8\,\text{mm}\}$. This provides enough space for the Dosepix detector to fit inside the filter. The optimisation of the filter thickness for an irradiation angle of 0° determined a thickness d_0. It corresponds to the width the new filter should have at its centre. Therefore, the parameter C, describing the radius in z-direction, of the filter design's outer surface is set to $8\,\text{mm} + d_0$.

A Nelder-Mead algorithm [43] is used to optimise parameters r, t, and A of the previously described outer shape of the filter while the inner shape stays fixed. The contribution of the pixelation of the detector is taken into account. Here, an approximation is made. Instead of dividing the sensor's surface into 12×16 large pixels like in real hardware, a lower amount of pixels, here 7×7, is used. This leads to a small loss in precision but speeds up the calculation. A brief description of the steps performed in each iteration of the optimisation algorithm is given in the following:

- Start the iterations over different irradiation directions. Angles of ϕ at 0° and 45° are considered. For each ϕ, θ is varied within 0° to 60° in steps of 15°. These steps are performed for each direction:
  - Cast rays for the current direction from the centre of each pixel and evaluate the intersections with the inner and outer filter surfaces
  - Use the distances between the intersection points to determine the filter thicknesses
  - Sample the corresponding simulated Dosepix response spectra for each pixel
- Optimise the conversion factors from registered events to dose for a perpendicular irradiation direction
- Calculate the dose for every irradiation direction and evaluate the corresponding dose loss of equation (5.6)
- Calculate the total loss by taking the average of the losses for different irradiation directions
- The optimisation of the filter shape ends when the loss converges

The optimisation algorithm is described in detail in the following. The first step of each iteration is the variation of the parameters of the outer surface of the filter.

Corresponding response spectra for all irradiation angles of all pixels of the detector are sampled. For each pixel, a ray is cast in the negative direction of each irradiation angle. A ray intersects twice with the surfaces of the filter. This is illustrated in figure 5.34 for the start parameters of the outer shape of the filter of $\{r, t, A, C\} = \{2, 2, 15\,\text{mm}, 15\,\text{mm}\}$. Five rays with an irradiation direction of $\phi = 0°$ and $\theta = 45°$ are shown. The intersections with the inner surface are highlighted in orange and with the outer surfaces in blue.

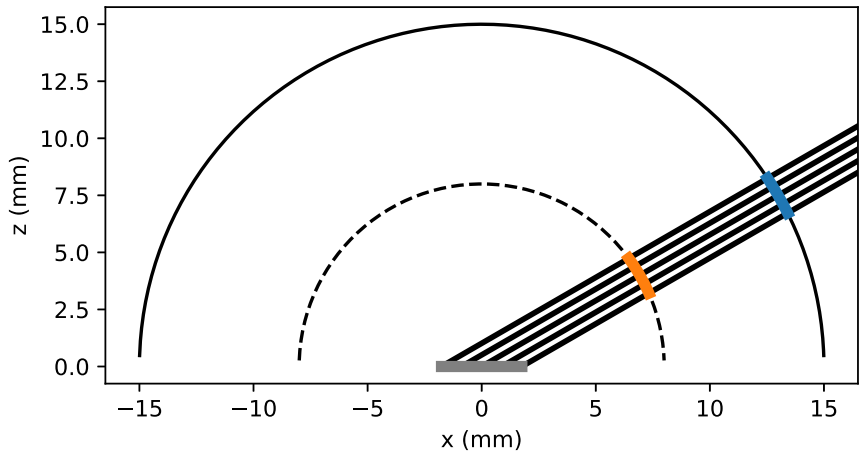

Figure 5.34.: Start shape of the filter for $H_p(10)$ dose estimation. Parameters $\{r, t, A, C\} = \{2, 2, 15\,\text{mm}, 15\,\text{mm}\}$ are used with equation (5.7) to describe the height of the outer surface. Only the slice for $y = 0$ is depicted. The sensor is illustrated as a grey block at the centre. Its width corresponds to a real Dosepix sensor. Five rays are casted from the sensor in direction of $\phi = 0°$ and $\theta = 45°$. Their intersections with the inner surface are highlighted in orange and with the outer surface in blue.

The intersections are calculated using a ray-marching algorithm utilising the midpoint method, according to [70]. The casted ray has the form of

$$\vec{r} = \lambda \begin{pmatrix} \sin\theta \cdot \cos\phi \\ \sin\theta \cdot \sin\phi \\ \cos\theta \end{pmatrix} + \vec{p} \tag{5.8}$$

where ϕ and θ describe the direction of the ray and $\vec{p}$ resembles the central position of a pixel. λ is varied by a fixed amount, and the values of $\vec{r}$ are determined. The x- and y-coordinates are used to evaluate the height of the filter's shape at this location by evaluating equation (5.7). If the z-coordinate of the ray is less than the filter's height, another step is performed by increasing λ. This procedure is repeated until the ray's z-coordinate exceeds the evaluated filter height. Afterwards, the midpoint-method is used.

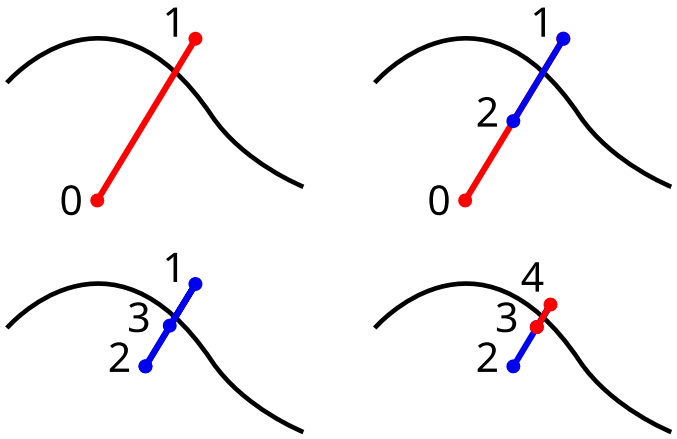

Figure 5.35.: Example of the midpoint-method to find the intersection of a ray and an arbitrary surface. The ray is cast from point 0 to point 1 in the first image. The black lines illustrate the shape of the filter surface. The ray's colour corresponds to the position of the last evaluated point. If its z-coordinate is greater than the height of the surface, it is coloured red. If the point lies below the surface, it is coloured blue. This colour represents the direction the next step is taken. Red means in the opposite direction of the initial ray, blue in the same direction . For each new step, the previous step width is halved.

Its processing is depicted in figure 5.35 and explained in the following. From point 0 to 1, the ray crosses the filter's surface, represented by the black line. Since the z-coordinate of point 1 is greater than the surface's height, the ray is depicted in red. If it is below, it is coloured in blue. The point of intersection has to be between points 0 and 1. Therefore, a step in the direction of 0 via the midpoint-method is made. The new point 2 will be at the centre of points 0 and 1. The resulting point is below the surface, and the next step is made in the initial direction of the ray. For each new step, the step length is halved. After point 3, another step in the initial ray direction is made, resulting in point 4 that now lies above the filter's height, as indicated by the red line. Therefore, the next step is made in the negative ray direction again. The procedure is repeated until a pre-defined accuracy is achieved. This way, the intersections of the casted rays with the filter's inner and outer surfaces for each pixel of the matrix are calculated. The thickness of the PMMA filter a photon has to traverse is provided by taking the distance between the intersection points. Afterwards, the direction of irradiation, as well as the filter thickness, are available. These measures are used to sample the corresponding response spectra of Dosepix from the precalculated and interpolated simulation data. These simulations were previously performed for the whole detector, and therefore the number of registered events is scaled to the utilised pixel size. Finally, for the optimisation algorithm's current iteration, the re-

sponse spectra for each pixel corresponding to the currently evaluated filter design are provided.

The conversion factors from registered events to dose are optimised for an irradiation direction perpendicular to the slab phantom's frontal surface. This optimisation is analogous to section 5.4.1. Now, each pixel has a response spectrum attributed. Therefore, dose is calculated per pixel, and the sum over the pixels is taken afterwards. It corresponds to the method used for measurement data. The determined conversion factors are used to evaluate the dose responses for all simulated irradiation directions. The loss per direction is calculated according to equation (5.6). The total loss, which is the optimisation algorithm's value to evaluate the results, is finally calculated by taking the mean of the direction-losses.

The optimisation finally provides a parameter set of

$$\{r, t, A, C\} = \{1.856, 2.460, 27.175\,\text{mm}, 15\,\text{mm}\}$$

for the outer surface of the filter. The shape for $y = 0$ is illustrated in figure 5.36. The radius along the x- and y-axes is 27.175 mm for $z = 0$. Since the inner radius of the filter is 8 mm, this corresponds to a thickness of 19.175 mm This rather large shape is required due to the low density of the used PMMA and, as a consequence, low capability to attenuate photons. The response spectra for all pixels are calculated for

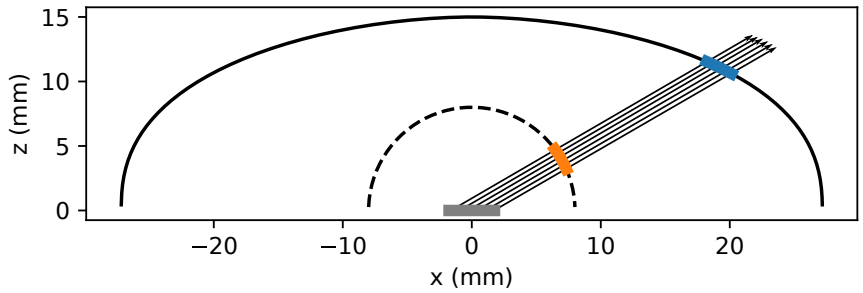

Figure 5.36.: Optimised shape of the filter for $H_p(10)$. Parameters $\{r, t, A, C\} = \{1.856, 2.460, 27.175\,\text{mm}, 15\,\text{mm}\}$ are used with equation (5.7) to describe the height of the outer surface. Only the section for $y = 0$ is depicted. The detector is illustrated as a grey block at the centre. Its width corresponds to a real Dosepix sensor. Five rays are casted from the sensor in direction of $\phi = 0°$ and $\theta = 45°$. Their intersections with the inner surface are highlighted in orange and with the outer surface in blue.

different irradiation directions to provide a final set of conversion coefficients from registered events to dose equivalent $H_p(10)$. The procedure is analogous to the one used in the optimisation algorithm. The number of registered events per pixel is illustrated in figure 5.37. The rows of the plots resemble different angles of ϕ, the columns different angles of θ. ϕ has values of 0° and 45° where for each angle, θ

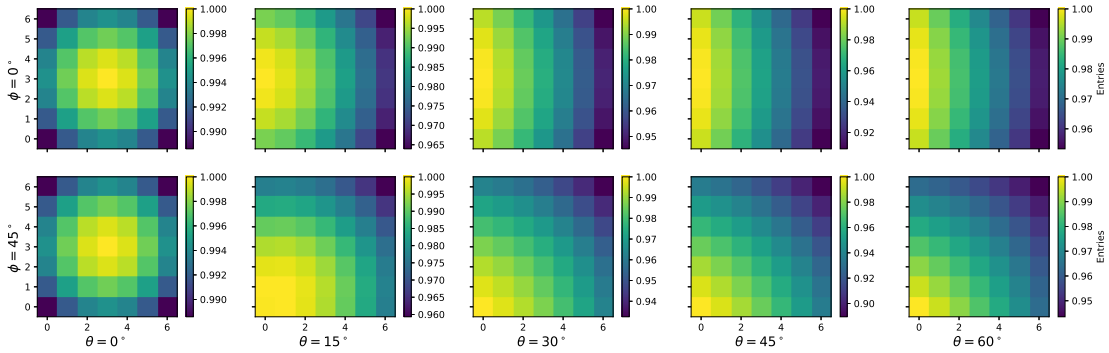

Figure 5.37.: Count distributions of the simulated pixel matrices for different irradiation directions. The initial photon energy is set to 20 keV. The plots on the y-axis correspond to different values of ϕ. θ is varied according to the x-axis. Each plot is normalised to its maximum.

is varied within 0° to 60° in steps of 15°. An exemplary photon energy of 20 keV is used. The gradients directly reflect the shape of the optimised filter in front of the detector depicted in figure 5.36. For irradiation perpendicular to the sensor's surface, the central part of the filter is thinnest. The width increases when moving away from the centre. Once the irradiation direction is tilted, i.e. for $\theta > 0°$, the gradient in registered events is from one sensor edge to the other for $\phi = 0°$, and from one corner to the diagonally opposing one for $\phi = 45°$. For $\phi = 0°$, photons are emitted from direction of positive x. This is illustrated for $\theta = 45°$ in figure 5.36. For pixels with a larger x-position, the rays have to pass a larger thickness of the filter, leading to an increased attenuation of photons.

Figure 5.38 depicts the number of events for different irradiation angles. Two curves are depicted, one for each setting of ϕ, while the x-axis reflects θ. Each curve is normalised to the case of $\theta = 0°$. There is only a slight dependence on angle ϕ. With increasing tilting angle θ, the number of registered events decreases and the filter thickness increases. This behaviour is favourable as $H_\mathrm{p}(10)/\Phi$ decreases for increasing irradiation angles, reflected in figure 3.21 (a). This is because dose is measured within a depth of 10 mm for $H_\mathrm{p}(10)$. For large angles, the attenuation distance for photons increases. Since the shapes of the spectra of deposited energies as measured with Dosepix do not depend much on the irradiation angle, reducing the number of registered events via the optimised filter helps to estimate the dose.

The final dose conversion coefficients for $H_\mathrm{p}(10)$ are optimised by minimising the response loss, as explained before. The factors are only optimised for an irradiation perpendicular to the sensor of the detector resulting in the dose conversion coefficients listed in table A.7, which are depicted in figure 5.39. Two curves are presented. One represents the new factors, labelled *optimised*, while the other one corresponds to the dose conversion coefficients previously optimised for the flat filter thickness

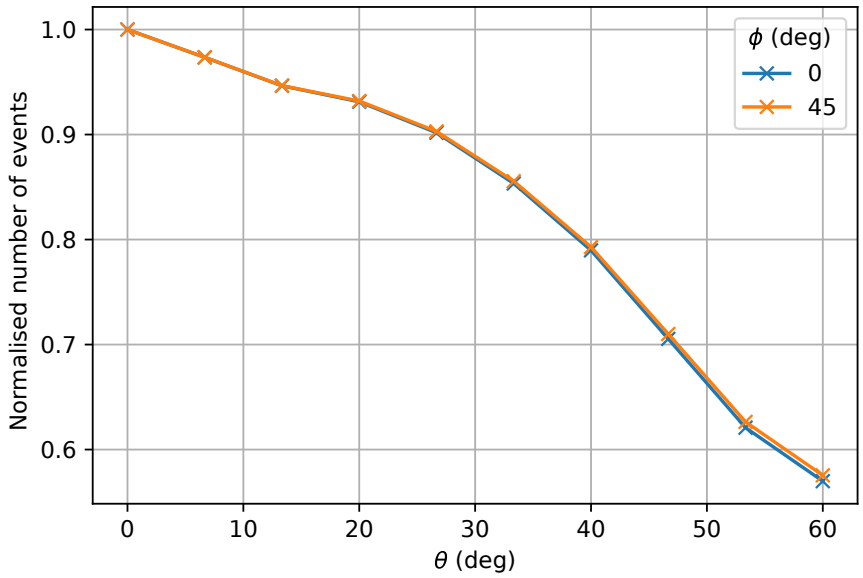

Figure 5.38.: The normalised number of registered events for the simulated Dosepix detector with the optimised $H_p(10)$ filter installed. Two curves for different irradiation angles of ϕ according to the legend are depicted. For these, angle θ is varied according to the x-axis.

for perpendicular irradiation in section 5.4.1, labelled as *flat*. Both curves show an exponential trend as a function of deposited energy. There is a difference between the factors due to the definitions of the shapes. In the latter case, the filter's thickness increases when moving in direction of x and y. This shows that the dose conversion coefficients are very sensitive. When actual dose measurements are made with the detector, it is beneficial to recalculate the conversion coefficients by combining data from measurements and simulations as introduced in section 3.2.7. For this set of dose conversion coefficients and the optimised filter, the responses are depicted in figure 5.40 (a) and (b). (c) and (d) show the responses for the start shape of the filter in figure 5.34. All curves are resembled as a function of the initial photon energy. In (a) and (c), the colours of the curves correspond to different irradiation angles θ according to the colour bars. In (b) and (d), the mean values of the curves in (a) and (c) are depicted. The error bars correspond to the standard deviations. Shaded regions indicate the minimum and maximum values of the responses.

(a) and (b) reflect the dose reconstruction abilities of the detector with the optimised filter installed. All response curves are centred about the perfect response at 1. Higher photon energies show statistical fluctuations, which are indicated by the error bars in (b). For lower photon energies, a fluctuation as a function of initial photon energy is visible. Its shape is mostly due to the binning in Dosi-mode. When measuring broad irradiation spectra, this effect will cancel out. For the largest irradiation angle

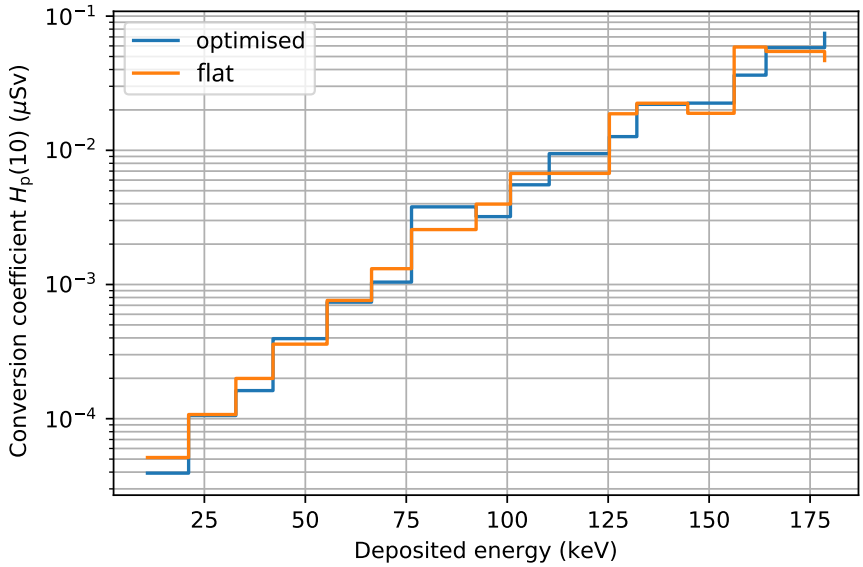

Figure 5.39.: $H_p(10)$ dose conversion coefficients. The blue curve, labelled *optimised*, shows the values for the optimised PMMA filter. The orange curve, labelled *flat*, representing the coefficients previously determined in the optimisation of the flat filter's thickness for perpendicular irradiation. Both curves use the bin edges of table A.7 on the deposited energy axis.

of $\theta = 60°$, a large deviation is present for low initial energies due to the conversion factors from fluence to dose $H_p(10)$ which are very low in this energy region. At about 100 keV an underestimation of the dose is visible for larger irradiation angles. This is mostly a statistical problem of the precalculated simulation and does not resemble the detector's true dose reconstruction abilities.

The importance of the optimised PMMA filter shows when comparing the responses of (a) and (b) to corresponding responses of the start shape of the filter in (c) and (d). Mainly low initial energies are affected by the filter, especially under large irradiation angles. For the start-filter, the dose is always overestimated. Dose estimation for low initial energies and large angles is too imprecise. For higher initial energies, overestimation takes place, but to a lesser extent. In this energy regime, the attenuation capabilities of the PMMA filter are low. However, this shows that by choosing proper dose conversion coefficients, a correct dose reconstruction is possible.

5.4.3 $H_p(10)$ optimised filter validation

Due to the complexity of the optimisation process of the PMMA filter, a validation is made. The shape of the filter is now implemented in the Allpix^2 [37] simulation of the measurement setup. The geometry includes the slab phantom, the readout electronics

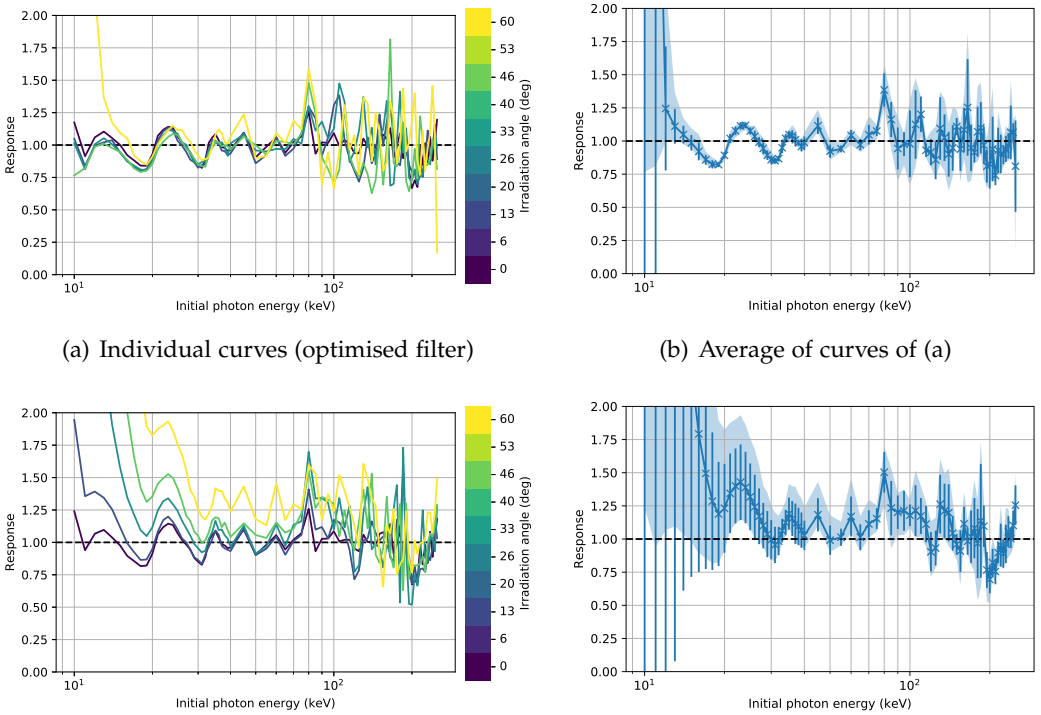

(a) Individual curves (optimised filter)

(b) Average of curves of (a)

(c) Individual curves (start filter)

(d) Average of curves of (c)

Figure 5.40.: The dose responses for $H_p(10)$ for the optimised (a) and the start filter (c) as a function of the initial photon energy are shown. The colours of the curves correspond to different irradiation angles according to the colour bars. (b) and (d) show the averages of the curves in (a) and (c). The error bars indicate the corresponding standard deviations and the light shaded regions the minimum and maximum responses.

at the phantom's centre, and a Dosepix detector with the optimised filter installed plugged in at the readout electronics' central slot.

Figure 5.41 shows the readout electronics, the installed Dosepix and the optimised filter. The geometry of the filter is opaque in (a), showing its full outer shape. The filter is half-transparent in (b) to present the filter's inner and outer surfaces. The grey block at the centre represents the Dosepix detector. It has just enough space to fit under the filter. Not depicted are the wire bonds which connect the detector with its PCB. These wires are shaped in small arcs extending beyond the upper edge of the detector's sensor. Therefore, sufficient space in front of the detector is required.

With the described setup, the simulation is performed for initial photon energies in a range of 10 keV to 250 keV. For each energy, irradiation angle θ is varied within 0° to 60° in steps of 15°. ϕ remains fixed at 0°. The simulation results are deposited

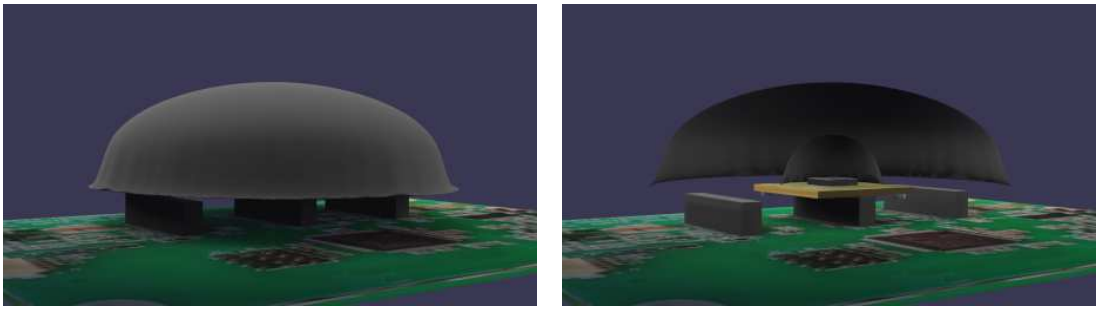

(a) Opaque filter (b) Half-transparent filter

Figure 5.41.: The optimised PMMA filter installed to a Dosepix detector located at the central slot of the readout-electronics. In (a), the geometry is opaque, illustrating the outer shape of the filter. In (b), the geometry is half-transparent to represent the inner surface of the filter. Within the filter, the Dosepix detector, resembled by the small grey block, is present.

energy spectra used to calculate the corresponding personal dose equivalents $H_p(10)$. Dose conversion coefficients are optimised for an irradiation angle of 0° like described in section 5.4.1. The determined factors are listed in table A.7 and depicted in figure 5.42, labelled *reoptimised*. Additionally, the factors previously optimised with the approximative simulation are included and labelled *optimised*. Since both curves use the same binning, the data is directly comparable. The trends of the curves are similar, with only slight variations between them. These are attributed to different statistical fluctuations in the simulations. Also, the simulation for the *optimised*-curve is only an approximation. However, since the differences are small, this approves the approximative simulation's usability to determine the PMMA filter's shape.

The corresponding responses for the *reoptimised*-curve, for the Allpix^2-simulated data, are shown in figure 5.43. (a) depicts single curves for different irradiation angles θ. (b) depicts the mean of the curves in (a). The error bars reflect the corresponding standard deviations, and the shaded region the minimum and maximum responses. In comparison, the responses determined from the approximated simulation are included in figure 5.40 (a) and (b). Both methods, the approximated and the complete Allpix^2 simulation provide similar response curves. The biggest difference is in their fluctuations for high initial photon energies. The number of emitted photons is increased for the complete simulation, leading to higher count statistics of the registered events. This is shown in figure 5.43 (b) where the error bars and the shaded region are now smaller. Again, there is a mismatch for an irradiation angle of $\theta = 60^\circ$ for low initial energies due to the small conversion factors from photon fluence to dose. For energies greater than 14 keV, the responses only show slight deviations about the perfect response of 1.

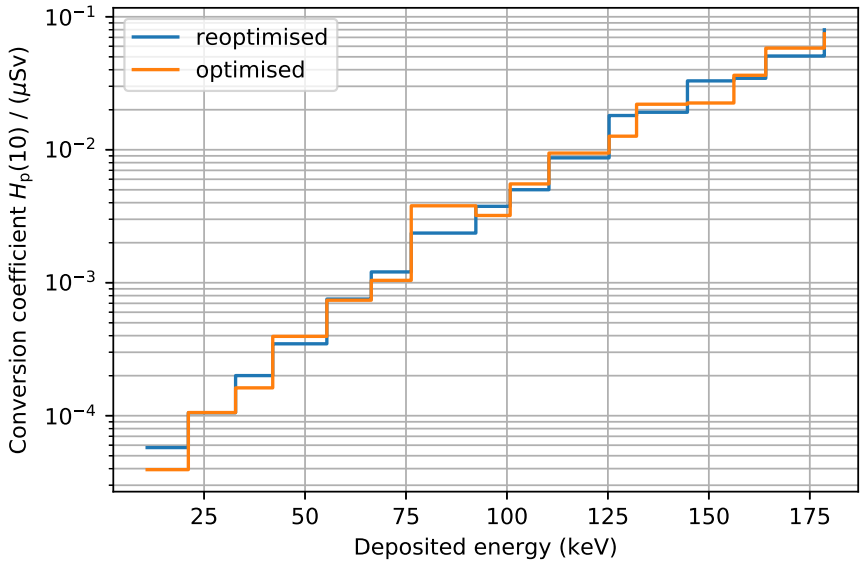

Figure 5.42.: Conversion coefficients from registered events to dose equivalent $H_p(10)$. Both curves utilise the optimsed PMMA filter of Dosepix. The blue curve, labelled *reoptimised*, shows the factors optimised to the Allpix^2 simulation. The orange curve, labelled *optimised*, depicts the factors optimised in section 5.4.2 via the approximated simulation. Both curves use the bin edges of table A.7 on the deposited energy axis.

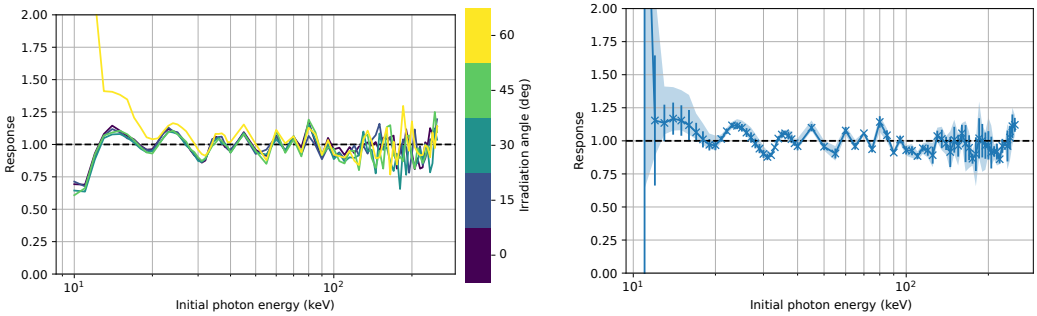

(a) Individual curves

(b) Average of curves in (a)

Figure 5.43.: (a) shows dose responses for the optimised filter of figure 5.31 (b) as a function of initial photon energy. The responses are based on Allpix^2 simulations. The colours of the curves correspond to different irradiation angles according to the colour bar. (b) shows the average of the curves in (a). The error bars indicate the corresponding standard deviations. Additionally, the light shaded region reflects the minimum and maximum responses.

In conclusion, the optimisation regarding $H_p(10)$ of the PMMA filter in front of Dosepix is successful. Simultaneously, the simulation of the complete system validates the approximative simulation used during optimisation. The described setup allows to measure $H_p(10)$ for an initial photon energy range of about 14 keV to 250 keV corresponding to photon energies usually found in medical applications. A test is made if the range can be extended to up to 1400 keV. Therefore, the initial photon energies in the Allpix^2 simulation are extended, new conversion coefficients from registered events to dose are optimised, and corresponding responses are calculated, which are depicted in figure 5.44.

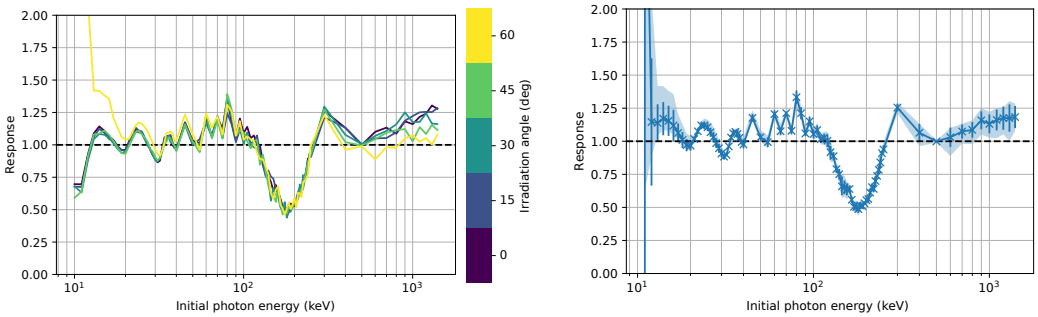

(a) Individual curves

(b) Average of curves of (a)

Figure 5.44.: (a) shows the dose responses for the optimised filter depicted in figure 5.31 (b) as a function of initial photon energy. The responses are based on Allpix^2 simulation data. In comparison to figure 5.43, the range of initial photon energies is extended. Also, responses are calculated using independently optimised conversion coefficients from registered events to dose equivalent. The colours of the curves correspond to different irradiation angles according to the colour bar. (b) shows the average of the curves in (a). The error bars indicate the corresponding standard deviations. Additionally, the light shaded region reflects the minimum and maximum responses.

There is a large deviation for the energy range of about 100 keV to 300 keV. With the shape of the filter, optimised for initial photon energies of up to 250 keV, there are no dose conversion coefficients for $H_p(10)$ which properly reconstruct doses for the whole energy range. The performance, indicated by the responses, only varies slightly when changing the bin edges in Dosi-mode. Therefore, at least one additional detector is required for the reconstruction. It requires an additional filter, made of a different material than PMMA. The methods presented in this thesis can easily be extended to utilise an increased number of detectors and by including higher initial energies. However, this is an object of future analyses. Here, the focus will remains on optimising the filters for initial photon energies relevant for medical use to keep the number of utilised Dosepix detectors as low as possible.

5.4.4 Dose response for $H_p(0.07)$

Previously, the personal dose equivalents for $H_p(3)$ and $H_p(10)$ were analysed. While it was shown that $H_p(10)$ requires a more complex filter shape to perform proper dose measurements, $H_p(3)$ has no strong dependence on the filter's shape. The loss in figure 5.27 indicates that $H_p(0.07)$ also only slightly depends on the thickness of the filter for perpendicular irradiation. This is evaluated by performing the Allpix^2 simulation for the setup similar to the one used for $H_p(10)$ before. The readout hardware with Dosepix detector is placed at the centre of the slab phantom. Two approaches are tested. First, no filter is used. Second, the filter optimised for $H_p(10)$ is used. The motivation of the latter approach is to evaluate the dose estimation abilities regarding $H_p(0.07)$ for a single detector system optimised to $H_p(10)$. Therefore, the bin edges in Dosi-mode for $H_p(10)$ are used in the following.

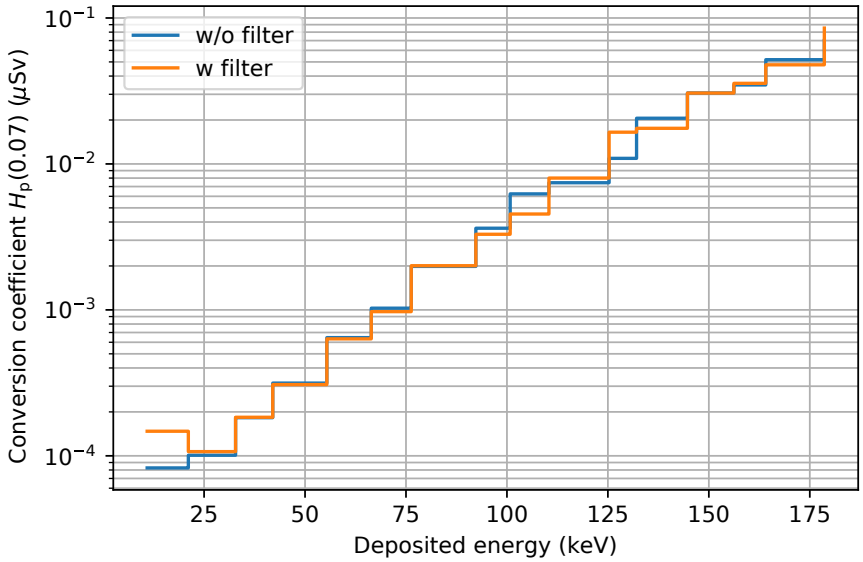

Figure 5.45.: Conversion coefficients from registered events to dose equivalent $H_p(0.07)$. Two curves are presented, one for the detector without filter and one with the filter optimised for $H_p(10)$. Both curves use the bin edges of table A.8 for $H_p(10)$ on the deposited energy axis.

The optimised conversion coefficients are listed in table A.8 and are shown in figure 5.45. Both curves, one corresponding to the data without filter and one to the data with filter, show a similar trend as a function of deposited energy. The main difference is the lowest energy bin. Since the PMMA filter is absorbing photons of low energies, the number of registered events for these energies is reduced, which is compensated by the conversion coefficients.

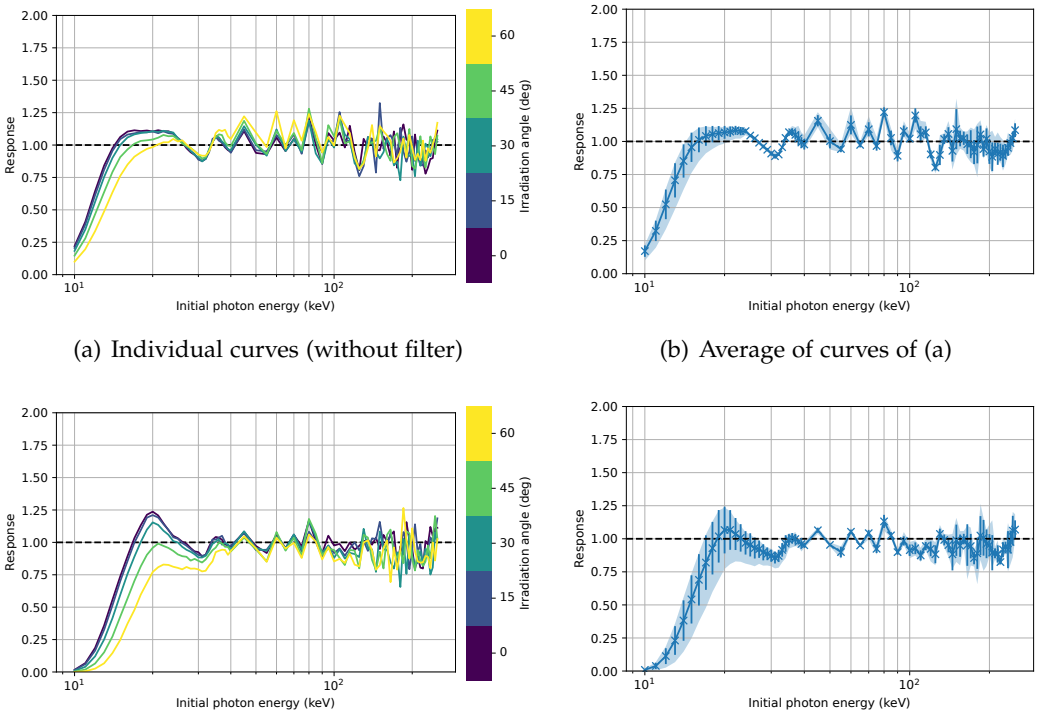

(a) Individual curves (without filter)

(b) Average of curves of (a)

(c) Individual curves ($H_p(10)$ optimised filter)

(d) Average of curves of (c)

Figure 5.46.: Dose responses for $H_p(0.07)$ as a function of initial photon energy. (a) shows the data without filter and (c) with the $H_p(10)$ optimised filter. The colours of the curves correspond to different irradiation angles according to the colour bars. (b) and (d) depict the averages of the curves in (a) and (c). The error bars indicate the corresponding standard deviations. The light shaded regions reflect the minimum and maximum responses.

The optimised responses corresponding to the factors are depicted in figure 5.46. (a) shows the data for the setup without filter and (b) for the filter previously optimised for $H_p(10)$. The colours of the curves indicate different irradiation angles θ according to the colour bar. (b) and (d) depict the average of the curves in (a) and (c). Additionally, error bars indicate the corresponding standard deviations, and shaded regions the minimum and maximum values of the responses. For initial photon energies greater than about 30 keV, the responses only slightly depend on the used filter. All responses are centred about a perfect response of 1 and only show a slight deviation from it. Fluctuations are again due to the low number of bins in Dosi-mode. For low initial energies, a small difference between the approaches becomes noticeable. In the case of no filter, the responses are slightly closer to 1 than for the optimised filter. Responses greater than 0.69 are required according to PTB [53]. Considering the different initial energies leads to an energy threshold of about 15 keV for no filter and

about 20 keV with filter. Both methods show an underestimation of dose for low initial energies. It reflects that the detector is not able to measure corresponding doses independent of the used filter accurately. In real measurements, the issue of low responses for low photon energies is not as relevant. X-ray spectra are broad, and although their mean energies are low, they have large contributions of higher energies.

5.5 Conclusion

An efficient method for the optimisation of filter designs for a Dosepix detector in regards of dose was established. The required calculation time was reduced by precalculating various setups in simulations. Direct irradiation and back-scattering were separated. These simulations were linearly interpolated for different photon energies, irradiation directions, and filter thicknesses. Dosepix response spectra for specific photon field characteristics and used filter can be determined fast by sampling data from the interpolated functions. It allowed performing optimisations of PMMA filter designs without a need to resimulate the whole complex setup. Simulations showed that a detector with a filter for $H_\mathrm{p}(10)$ is able to estimate dose for photon energies in the range of 14 keV to 250 keV and angles of up to 60°. For $H_\mathrm{p}(3)$, the exact shape of the filter is not important as long as the thickness is not too large, i.e. about less than 10 mm. For a filter with a thickness of about 1 mm, $H_\mathrm{p}(3)$ estimation is possible for energies up to 250 mm and angles of 90°. However, for angles greater than 70° deviations for photon energies below about 15 keV manifest. For a future dosemeter system, this result is important since it shows that a detector can be placed directly behind housing walls, and that the conversion coefficients from registered events to dose equivalent can adapt to the filter's shape. For $H_\mathrm{p}(10)$, this is not as easy and a more complex filter shape is required to estimate doses correctly. While the determined PMMA filter is large, a possible future optimisation with a different material like aluminium or tin will lead to smaller filters. A simulation of direct irradiation has to be repeated for the new material first. For $H_\mathrm{p}(0.07)$, the importance of a filter's shape is similar to $H_\mathrm{p}(3)$. The detector performs best if there is no or only a filter of small thickness. However, the optimised $H_\mathrm{p}(10)$ filter can also be used to measure $H_\mathrm{p}(0.07)$. The only disadvantage is an increase of the minimum photon energy the detector estimates dose accurately from about 15 keV to about 20 keV. If higher initial energies than 250 keV are required to measure $H_\mathrm{p}(10)$, additional detectors are needed. Each detector then has to use its own filter. The presented algorithms can be adopted to optimise two or more detectors at the same time without much additional computing effort. Simulations have to be precalculated for higher initial photon energies. However, this is a topic for future works. The tested energy ranges are sufficient for medical applications, and dose estimation is possible with a single detector. Everything presented in this chapter is based on simulations. The optimised filter shapes have to be manufactured and tested in measurements with radiation sources in the future. Different photon spectra have to be utilised, and also irradiation directions

have to be varied accordingly. The conversion coefficients from registered events to dose determined via simulations might not be directly applicable to data. However, by reoptimising the factors using a combination of measurements and simulations, the system will be able to measure the dose with responses close to the optimum.

CHAPTER 6

Spectroscopy and quality assurance of X-ray tubes

Contents

Dosepix detectors can be applied in other fields than dosimetry. For the large pixels with an area of 220 µm × 220 µm, the probability for effects like charge sharing to occur and distort the registered deposited energy spectrum is relatively low. Due to this, large pixels are suitable for spectroscopy tasks. The main goal of this chapter is to reconstruct the initial photon spectrum from measurements with Dosepix detectors.

The Dosi-mode of the detector allows for dead-time free measurements. Registered deposited energies are directly sorted in 16 bins per pixel. The histograms of the pixels are combined in a special way to benefit from the energy resolving abilities and the dead-time freeness. This combination method is presented in the first section of this chapter. A measurement setup is introduced consisting of three detectors, two equipped with different metal filters. Measurements and corresponding simulations are made with the setup, and their agreement is evaluated.

The simulations are the foundation to train and validate a convolutional neural network to reconstruct an initial photon spectrum from measurements. This operation resembles a deconvolution of the input data. The procedure is executed for various photon spectra of an X-ray tube with different filters and settings applied.

Additional networks are developed to reconstruct characteristics of an input spectrum. These include the kVp-value, the half-value layer, factors to convert photon fluence to various dose equivalents, and the photon fluence. Combining the methods, the goal of this chapter is to determine the initial photon spectrum, correctly scaled with the photon fluence, and additional characteristics from measurements. This allows quality assurance of an X-ray tube to ensure the proper working of a system. This is important for imaging tasks like in interventional radiology and cardiology to guarantee the quality of recorded images and to reduce the exposure of a patient. Additionally, the features of a sources can be characterised for scientific purposes.

6.1 Shifted bins in Dosi-mode

The choice of operation mode of Dosepix depends on the application. ToT-mode allows for precise measurements of energy spectra as the hardware provides ToT-data of single events. The downside is that the most recent event continuously overwrites the value of the ToT-register. Only the current value of the register is provided during

the read-out of a frame. Since read-out speed is relatively slow (about a magnitude of 10 Hz), event statistics are low. Dosi-mode directly sorts events via a binning state machine into a histogram with user-defined bins. This ensures that no events are missed which is especially important for dosimetry applications. Bin edges in energy are usually chosen to be identical for all pixels. This provides enough spectral information for dose estimation and keeps the required dose factors for the conversion from events to dose low. The best features of ToT- and Dosi-mode are combined to perform spectroscopy with Dosepix. These are the precision of the ToT-mode and the high count statistics of Dosi-mode.

6.1.1 Description of the method

The Dosepix detector can utilise the pixels' freely adjustable bin edges to measure a deposited energy histogram in Dosi-mode with high precision. While the first 15 bins of a pixel count events with energies in-between two neighbouring edges, the last bin is an overflow-bin for all higher energies. The content of this bin is neglected for each pixel in the analysis since its upper limit cannot be adjusted. The bin edges are set uniformly within a pre-defined energy range of E_{min} to E_{max}, resulting in a bin width of $E_{\mathrm{bw}} = \frac{E_{\mathrm{max}} - E_{\mathrm{min}}}{15}$. A small energy offset in the edges is introduced from pixel to pixel to ultimately increase the precision of the histogram, which is defined as

$$\Delta E_{\mathrm{p2p}} = \frac{E_{\mathrm{bw}}}{N_{\mathrm{px}}} \tag{6.1}$$

with the number of used pixels N_{px}. Mixing small and large pixels for this application is impossible as their areas and, consequently, count rates and registered spectra differ significantly. Therefore, only the large pixels are considered in the following, i.e. $N_{\mathrm{px}} = 16 \cdot 12 = 192$. The energy $E_{\mathrm{be},(i,j)}$ of a left bin edge j of pixel i is defined via

$$\begin{aligned} E_{\mathrm{be},(i,j)} &= E_{\mathrm{min}} + j \cdot E_{\mathrm{bw}} + i \cdot \Delta E_{\mathrm{p2p}} = \\ &= E_{\mathrm{min}} + E_{\mathrm{bw}} \cdot \left(j + \frac{i}{N_{\mathrm{px}}} \right) \end{aligned} \tag{6.2}$$

with $i \in [0, N_{\mathrm{px}} - 1]$ and $j \in [0, 15]$. The bin edges are combined for all pixels as depicted in figure 6.1 and described in the following. New bin edges are introduced at the intersection energies of overlapping bins. These rebinned bins consist of $192 \cdot 16$ edges which span a range from E_{min} to $E_{\mathrm{be},(191,15)} = E_{\mathrm{max}} + E_{\mathrm{bw}}$. Under the assumption of uniformly distributed events per bin in the original histogram, the bin contents are evenly distributed to the new bins. Since the rebinned histograms share the same bin edges, the contents of the bins of all pixels can be added. The combination of pixels provides a method to measure a deposited energy spectrum with increased precision compared to the standard 16 bin measurements. Figure 6.2 shows an exemplary measurement with an ^{241}Am source with Mo-fluorescence target. The energy range

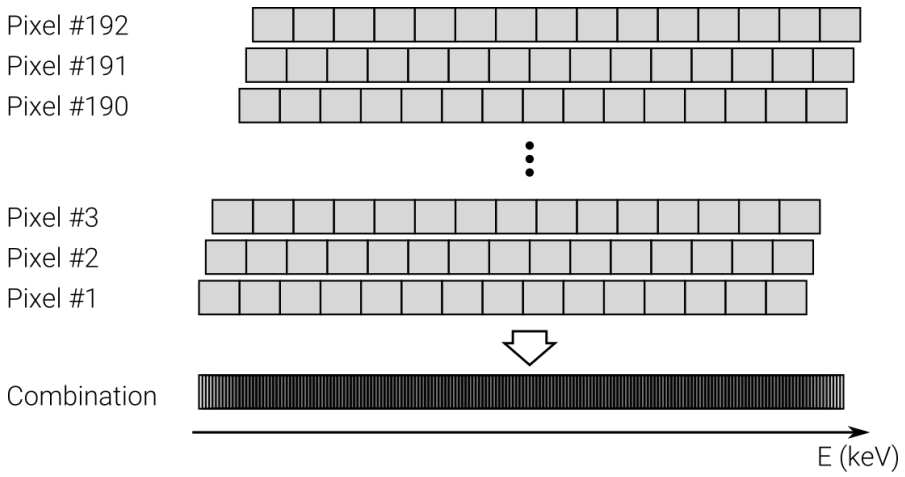

Figure 6.1.: The deposited energy histograms of all large pixels are combined to increase the energy precision for measurements in Dosi-mode. There is an offset of ΔE_{p2p}, according to equation (6.1), for the uniformly distributed energy bin edges between neighbouring pixels. Further explanation is given in the text.

of the bins is set to $E_{\mathrm{min}} = 10\,\mathrm{keV}$ and $E_{\mathrm{max}} = 120\,\mathrm{keV}$. The figure's left-hand side depicts a 2D histogram of all large pixels and their registered events per bin. With increasing pixel index, the regions with many events in the histograms shift towards lower energy bin indices. This directly indicates the hardware settings of the shifted bin edges. The entries of all pixels are then combined like previously described to create the deposited energy spectrum on the right-hand side of the figure.

6.1.2 Distortion effects

The combination of the histograms for the shifted bins per pixel increases the precision compared to regular operation in Dosi-mode. However, this method is not comparable to a measurement in ToT-mode as a distortion is introduced. Figure 6.3 illustrates this for an exemplary measurement of a mono-energetic photon source and a simplified perfect detector consisting of 6 pixels. All pixels detect photons of energy E_0 from the source, which are sorted into their corresponding energy bins as sketched in the upper half of the figure. Each bin is divided into 6 new bins with the previously explained rebinning method. The number of events is distributed uniformly to these bins. Via a combination of the entries of the new bins of all large pixels, a more precise histogram depicted in the bottom half of the figure is obtained. The resulting shape from rebinning is described by a triangular window function

$$\Lambda(E) = \frac{N_0}{\tau}\left(1 - \frac{|E - E_0|}{\tau}\right), \tag{6.3}$$

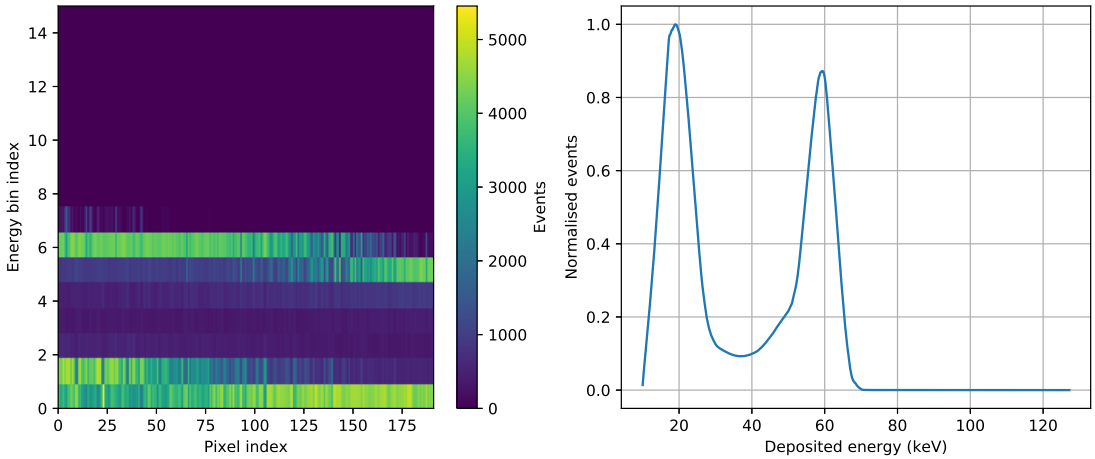

Figure 6.2.: 2D-histogram for all large pixels and their energy bins in Dosi-mode for the measurement of an ^{241}Am source with additional Mo-fluorescence target. The bin edges of the pixels are set according to equation (6.2). The entries of the histograms are combined to the deposited energy spectrum on the right-hand side.

centered at E_0 and with a half-width of τ. The width corresponds to $\tau = E_{\text{bw}} - \frac{1}{2}\Delta E_{\text{p2p}}$. The sum of all events covered by the triangular window is N_0 which corresponds to the number of registered events. The amplitude of the triangular window is $\frac{N_0}{\tau}$.

The measurement of a continuous energy spectrum is assumed in the following. Since the number of used pixels is large (192), the deposited energy spectrum after rebinning is assumed to be also continuous. The broadening due to the rebinning compared to measurements in ToT-mode is described by a calculation of the convolution of the true deposited energy spectrum and the triangular window function $\Lambda(E)$ of equation (6.3). This is illustrated in figure 6.4. Measurements of the same radiation source are performed in ToT- and Dosi-mode. The source consists of ^{241}Am with an additional Mo-fluorescence target. The measurement in ToT-mode corresponds to the deposited energy spectrum of a large pixel. Convolving it via the triangular window function results in a spectrum almost identical to the measurement performed in Dosi-mode with shifted bin edges.

There is an additional effect distorting the rebinned energy spectrum close to the energy limits of E_{min} and E_{max}. Since there is an energy offset between the bins of neighbouring pixels, only the first pixel measures in the specified range. The edges of the other pixels are calculated via equation (6.2) and depend on the index of the pixel and the number of the bin. For the first bin of the last pixel this yields $E_{\text{be},(191,0)} = E_{\text{min}} + \frac{191}{192}E_{\text{bw}}$. The linear behaviour of the first energy bins of the pixels leads to a triangular shape of the spectrum after rebinning and combining the pixel histograms. For the low energy edge, this results in a distortion in the range of E_{min} and $E_{\text{min}} + E_{\text{bw}}$.

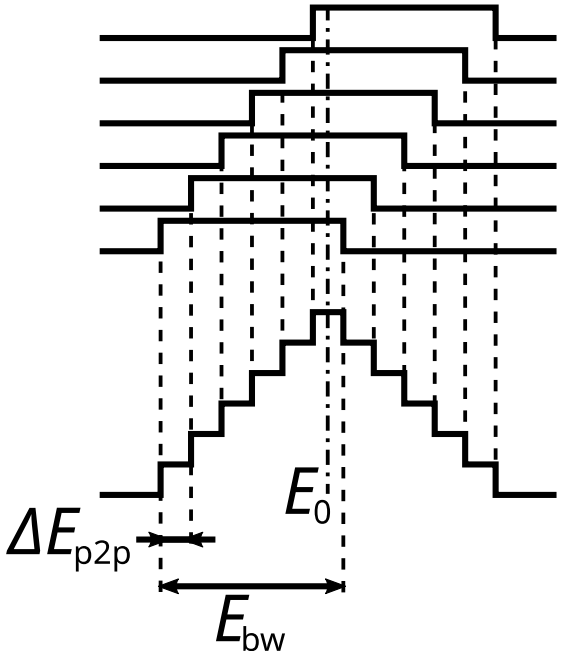

Figure 6.3.: The setup of a simplified perfect detector consisting of 6 pixels. The top half shows the bins which registered events from a mono-energetic photon source of energy E_0 indicated by the dash-dotted line. The bins are rebinned and combined to the histogram depicted at the bottom half.

For the high energy edge, the distortion takes place between E_{max} and $E_{\mathrm{max}} + E_{\mathrm{bw}}$. Therefore, when using the Dosi-mode with shifted bin edges, these effects must be considered and are implemented in the simulations of deposited energy spectra.

6.1.3 Deconvolution of measurements

The resolution of spectra measured with shifted bins in Dosi-mode can be increased by applying deconvolution. Measurements underlie statistical fluctuations depending on the measurement duration and a have a systematic error due to the shifting of bins which depends on the accuracy of the energy calibration. Due to this, a direct deconvolution is not applicable and a Wiener filter is used in the process, taking place in the frequency domain. The filter is described according to [71]. Multiple parameters are defined first. The original signal corresponds to the true deposited energy spectrum, which is the desired output of the deconvolution and is called $s(E)$ with its Fourier transform $S(\tilde{E})$. $x(E)$ and $X(\tilde{E})$ are the measured spectrum with shifted bins in Dosi-mode and its representation in the frequency domain. $H(\tilde{E})$ describes the triangular window function $\Lambda(E)$ of equation (6.3) in Fourier domain used as the deconvolution kernel. $P_{\mathrm{s}}(\tilde{E})$ and $P_{\mathrm{n}}(\tilde{E})$ are the power spectra of the original signal $s(E)$ and its noise $n(E)$. They are determined by taking the Fourier transform of the

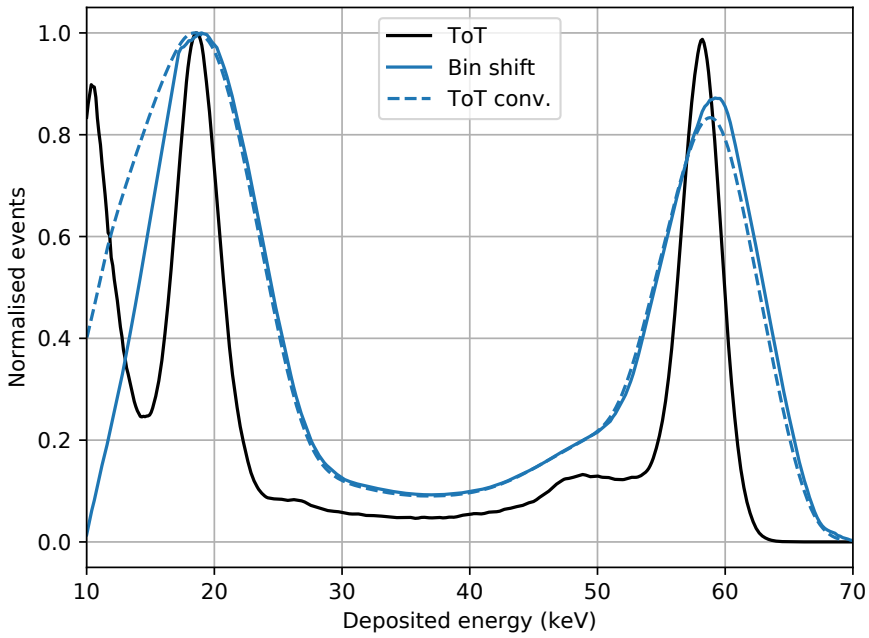

Figure 6.4.: Measurements of an ^{241}Am source with Mo-fluorescence target in ToT- and Dosi-mode with shifted bins. The average of the spectra of all pixels is taken. The Dosi-mode measurement shows additional broadening due to the rebinning of the histograms described via a convolution of the triangular window function (6.3). This is illustrated by the convolved ToT spectrum as represented by the blue dashed line.

autocorrelation. The deconvolution is then described by

$$S(\tilde{E}) = \frac{H^*(\tilde{E})}{|H(\tilde{E})|^2 + \lambda^2} \cdot X(\tilde{E}), \tag{6.4}$$

where the asterisk operator denotes the complex conjugate and λ^2 corresponds to the inverse of the signal to noise ratio, i.e. $\frac{P_\mathrm{n}(\tilde{E})}{P_\mathrm{s}(\tilde{E})}$. Finally, the original signal $s(E)$ is obtained by taking the inverse Fourier transform of $S(\tilde{E})$.

The deconvolution process is illustrated based on the exemplary input signal $s(E)$ of figure 6.5. The signal is convolved via the triangular window function $\Lambda(E)$. Gaussian noise is applied to simulate a measurement. The convolved input signal is deconvolved via the same kernel $\Lambda(E)$ using the described method of applying a Wiener filter. The parameter λ is varied according to the colour bar. The lower λ, the better the features of the spectrum are discernible. For high λ, the output becomes noisy and includes artefacts, i.e. features that are not present in the original signal. Therefore, a tradeoff in regards to stability and precision has to be made for λ, depending on the application.

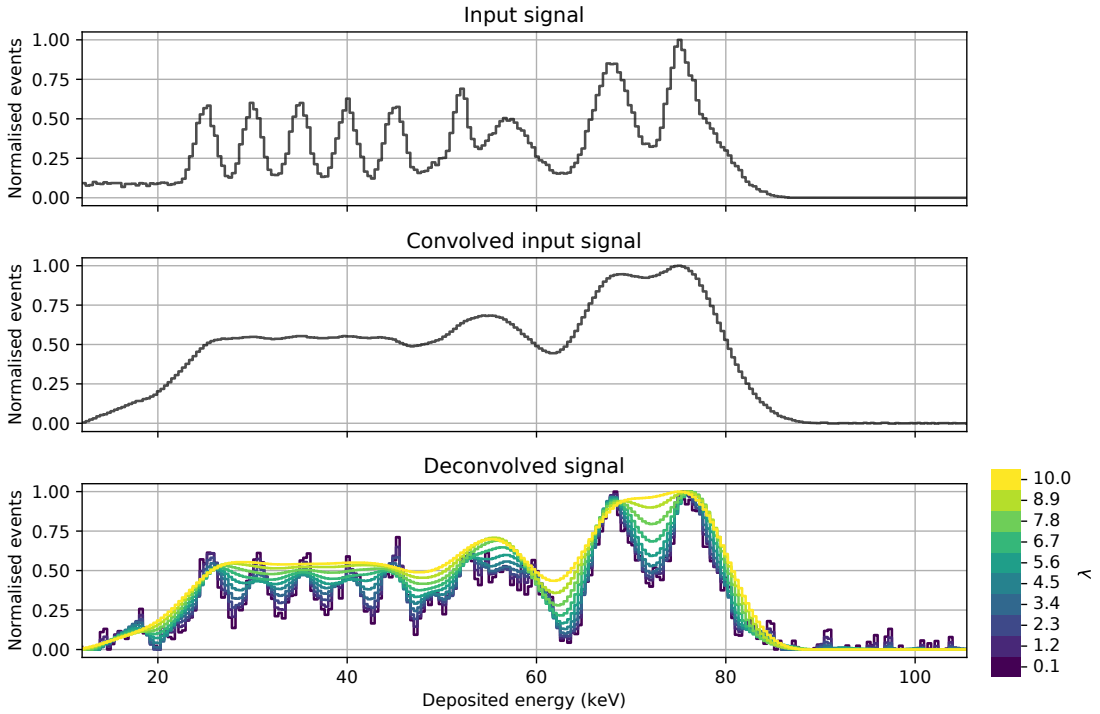

Figure 6.5.: The figure shows an exemplary input signal corresponding to a measurement of deposited energy in ToT mode. The signal is convolved with the triangular window function Λ of equation (6.3). The spectrum is deconvolved using the Wiener filter method with Λ as the kernel. Parameter λ, whose value is indicated by the colour bar, describes the inverse of the signal to noise ratio used by the deconvolution.

Figure 6.6 depicts the deconvolution process applied to a measurement of an ^{241}Am source with an additional Mo-fluorescence target. λ is set to a value of 5 for the Wiener filter. The deconvolved spectrum reveals features of the deposited energy spectrum like the backscatter peak corresponding to the full energy peak of Am and fluorescence peaks for Sb and Sn close to 29 keV. However, there is a slight mismatch for this peak energy which ideally should have its maximum at about 26 to 27 keV, depending on the accuracy of the detector calibration.

6.1.4 Extension of the method

The previously described method of combining the histograms for shifted bins of pixels is extended to improve the precision. The deposited energy range the spectrum is recorded in is defined by the limits E_{min} and E_{max}. Previously, each pixel's bin edges were assigned to span this range, with neighbouring pixels having an offset of ΔE_{p2p}. Instead of using single pixels to represent these energy ranges, a split factor

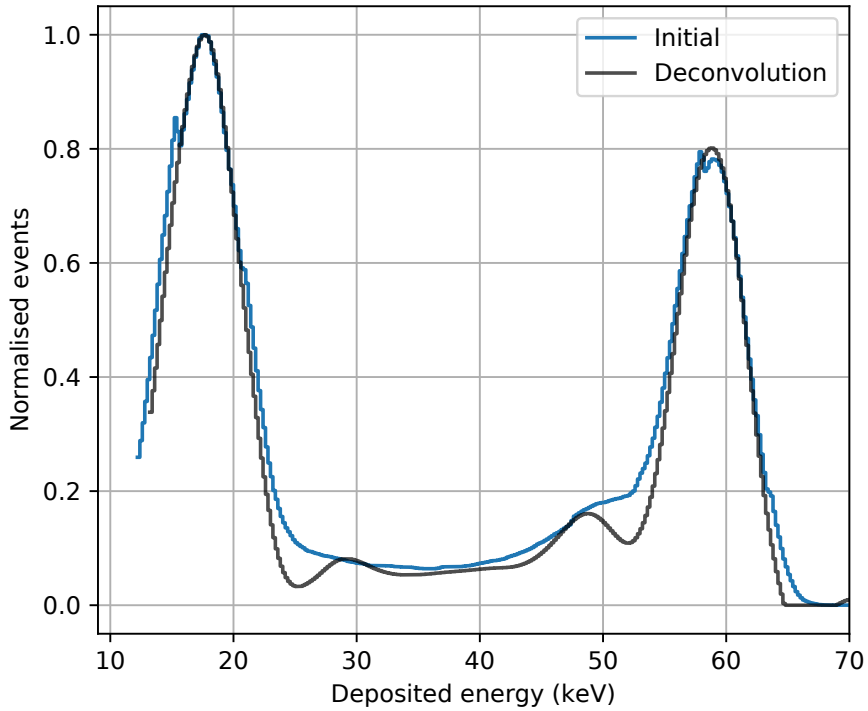

Figure 6.6.: The measurement of an ^{241}Am source with Mo-fluorescence target with shifted bins in Dosi-mode. The initial deposited energy spectrum is deconvolved via the method of Wiener filtering.

s is introduced. The combination of the pixels' bins is illustrated in figure 6.7 and explained in the following.

The energy ranges, previously resembled by single pixels, are now split to be represented by s pixels. Virtual pixels are introduced, each consisting of the concatenation of the bins of s real pixels. The total number of virtual pixels is $N'_{\mathrm{px}} = \frac{N_{\mathrm{px}}}{s}$, with N_{px} the number of real pixels. This indicates that N_{px} and s have to be divisible. The descriptions of the histogram combination method of section 6.1.1 still holds but is applied to virtual pixels now. The bin width of a virtual pixel is $E'_{\mathrm{bw}} = \frac{E_{\mathrm{max}} - E_{\mathrm{min}}}{15 \cdot s}$, the width parameter of the triangular window function Λ is $\tau' = \frac{\tau}{s}$. The precision of a registered deposited energy spectrum increases as the convolution window's width decreases with increasing s. However, this benefit comes at a cost. Since the whole energy range is split into s parts, the total number of registered events, i.e. the sum of all pixels, is also divided by a factor s. Previously, it was assumed that the rebinned histogram is continuous since the number of pixels is large. If s is set too high, the number of virtual pixels is lowered to a point where this assumption does not hold anymore. In this case, additional binning artefacts come into play. Therefore, s is never set higher than 4 in the following.

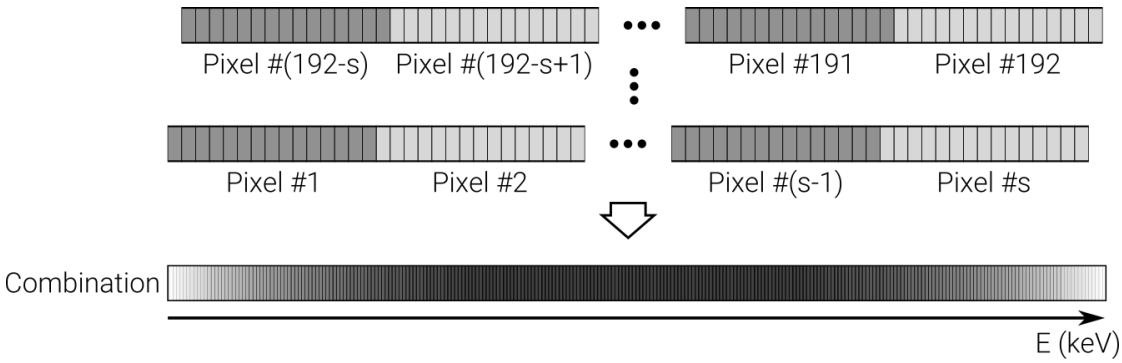

Figure 6.7.: The combination of histograms for pixels with shifted bin edges. The whole energy range is split into s parts and is described via virtual pixels, where each consists of s true pixels. After the combination of the virtual pixels, the energy resolution of the histogram and the number of registered events is decreased by a factor of s.

A measurement with ^{241}Am and Mo-fluorescence target is made to demonstrate the improved method. The results are depicted in figure 6.8 where the split parameter s is set to 4. On the left-hand side, a 2D-histogram of the registered events of the real pixels is shown. The virtual pixel index i' corresponds to the concatenation of true large pixels with indices of $i = n \cdot \frac{192}{s} + i'$ where $n \in [0, s]$. Virtual pixels are combined like previously described. The result is shown on the right-hand side of the figure. The black line represents the case for $s = 4$. For comparison, the spectrum for $s = 1$ of figure 6.2 is present as dashed blue line. This directly reveals the improvement in precision due to the extended method.

6.2 Detector setup

The detector setup used for the X-ray tube spectra measurements is depicted in figure 6.9. It consists of three Dosepix detectors where each has a plastic cap installed to protect from mechanical damages. The detector on the left has a filter of 2 mm aluminium, the one at the centre of 1 mm tin. All measurements are performed with the detector at the central position of the readout hardware moving along an imaginary line through the X-ray tube's focal point. The distance of the detectors in regards to the X-ray tube is increased to get an approximately parallel photon field. This implies that flat filters for the Dosepix detectors are sufficient. These filters are used to gain different interpretations of the emitted photon spectrum. The filters attenuate photons of low energies which increases focus on the higher energetic part of a spectrum. Also, Compton effect takes place, and fluorescences are emitted. With the introduced variety, the information about a photon spectrum is increased.

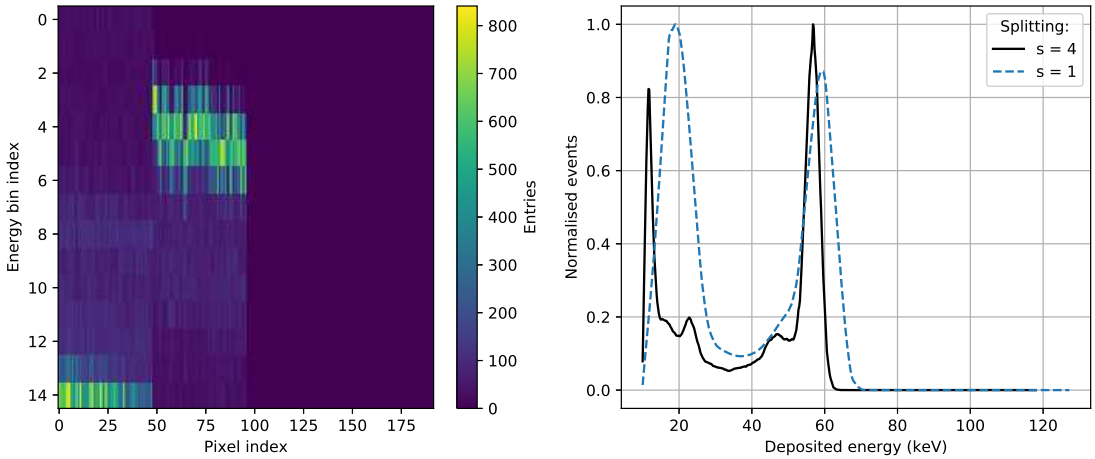

Figure 6.8.: The 2D-histogram of all pixels and their bins in Dosi-mode for the measurement of an ^{241}Am source with an additional Mo-fluorescence target. The split parameter s is set to 4, i.e. a virtual pixel consists of 4 real pixels. The entries of the histograms are combined to determine the deposited energy spectrum in black on the right-hand side. The dashed blue line additionally represents the same spectrum for $s = 1$.

6.3 Spectrum deconvolution

The spectrum of a radioactive source and the registered deposited energy spectrum of Dosepix differ a lot. This difference is due to the energy dependence of photon interactions with the sensor, and effects like Compton scattering and charge sharing (see section 2.2 for more details) and the resulting photon detection efficiency of Dosepix. These distortions make it impossible to reconstruct the impinging energy spectrum from measurements directly. The response spectra for the irradiation of a Dosepix detector with mono-energetic parallel photon fields are known from simulations. The response to a continuous input spectrum is the weighted superposition of individual responses. Therefore, a spectrum measured with Dosepix carries information about the emitted photons. It can be reconstructed by applying deconvolution methods like matrix inversion, spectrum stripping or Bayesian deconvolution (see e.g. [72, 73]). These approaches are often not particularly stable and require high events statistics to work correctly. This chapter introduces a new method, utilising a convolutional neural network (CNN). The priorities are stability and applicability in single-shot spectroscopy where an X-ray tube with optional filters is active for a short duration only. The Dosepix setup consisting of three filtered detectors takes events in Dosi-mode with shifted bin edges for a split of $s = 4$. The energy resolution is improved by a factor of 4, while count statistics are reduced by a factor of 4. This is accounted for by scaling the registered spectra with this factor. The energy limits in the measurements

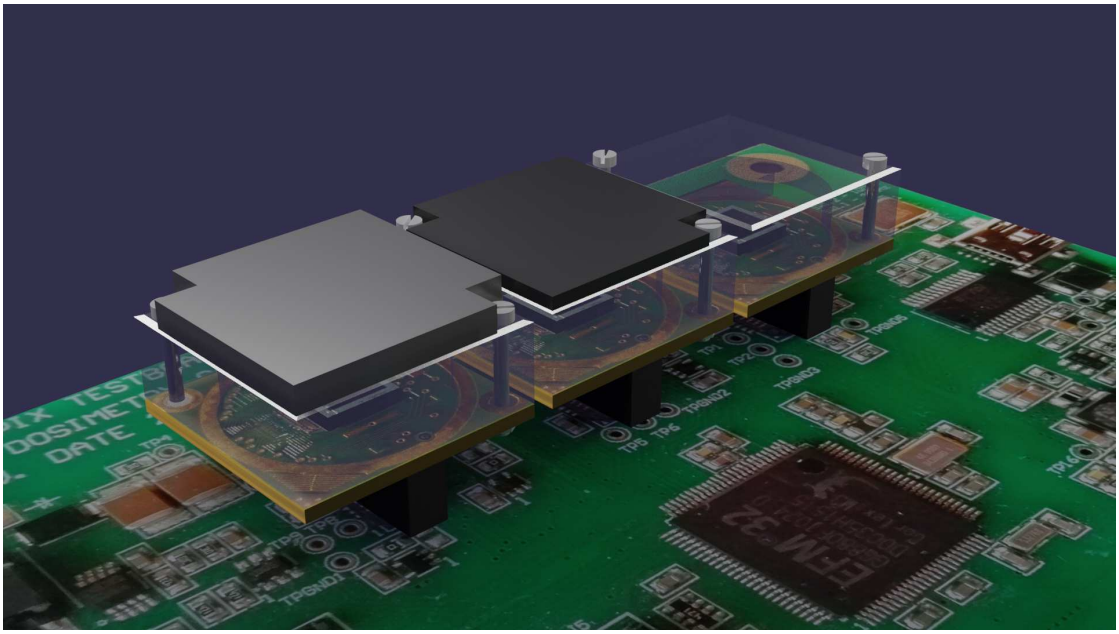

Figure 6.9.: A render of the Dosepix setup used for the measurements of X-ray tube spectra. All detectors have protective plastic caps installed. The detector at the central position has a filter of 1 mm tin and the detector on the left side of 2 mm aluminium.

are set to $E_{\text{min}} = 10\,\text{keV}$ and $E_{\text{max}} = 120\,\text{keV}$. A description of the network and its application to measurements is introduced in the following.

6.3.1 Network design

The convolutional neural network design for the deconvolution of Dosepix measurements is illustrated in figure 6.10. It takes the concatenation of three registered spectra as its input, each consisting of 100 bins. After concatenation, the data has two dimensions and a shape of 3×100. The network's output corresponds to the emitted photon spectrum from 0 to 120 keV, sampled in bins of 1 keV. Directly after the input, a layer that applies Gaussian noise with a random standard deviation to the data is present (see section 4.2.1 for more details). This layer is used for regularisation and is only active during training. Four convolutional layers follow. Each has a kernel size of 3×3 and employs same-padding. The numbers of filters are 32, 64, 128, and 256. In between convolutions, average pooling with a kernel size of 3 and a stride of 2 is used to reduce the data in lateral dimensions (see section 2.5.5 for more information). The activations are flattened to one dimension after the convolutions and gradually reduced to the desired output size of 121 by 4 dense layers. All layers of the network use a ReLU activation function (see section 2.5.1 for more information). The exception

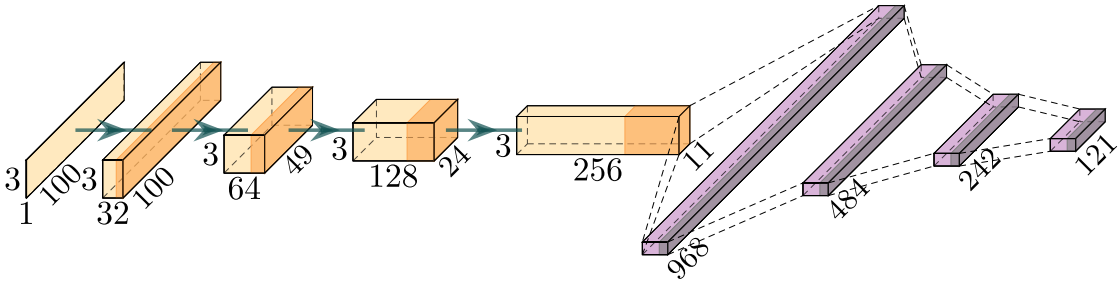

Figure 6.10.: The convolutional neural network for the deconvolution of three measured Dosepix spectra to reconstruct a corresponding initial photon spectrum. Yellow blocks resemble convolutional layers, purple blocks dense layers. The dark regions within the blocks indicate the use of an activation-function. The image is created using [58].

is the output, which uses an absolute function to ensure positive values. By taking the convolutions of the three measured spectra, correlations between the spectra of the detectors are taken into account.

6.3.2 Training and validation data generation

The network's input data consists of three Dosepix spectra where each detector has filters applied as described in section 6.2. The network's output is the deconvolution of these spectra, which corresponds to an initial photon spectrum. The generation of the X-ray tube spectra and the corresponding responses of the Dosepix detectors are described in the following.

X-ray tube spectrum generation

The training data consists of tungsten X-ray tube spectra. The python package xpecgen [21] is used for their generation. It employs the models defined in [74]. Via a variation of the free parameters of the X-ray tube, a dataset is generated. These parameters include the applied voltage and the thicknesses of one or multiple filters applied in front of the X-ray tube. The filter materials used are Al, Cu, Sn, and Pb. The tube voltage U_{XRT} is sampled from a uniform distribution of range 20 kV to 120 kV. The filter thicknesses are sampled from an exponential distribution with the probability density function

$$f(w, \beta) = \frac{1}{\beta} \exp\left(-\frac{w}{\beta}\right), \tag{6.5}$$

where w is the filter thickness and β the expected value. w itself has no unit but corresponds to cm. Smaller filter thicknesses are sampled with a higher probability. The distribution is chosen to resemble real-life situations, where small filters are used

more often than large ones. To properly scale the distribution along the thickness-axis, the expected value β_0 is set so the probability p to sample w_0 is

$$f(w_0, \beta_0) = p. \tag{6.6}$$

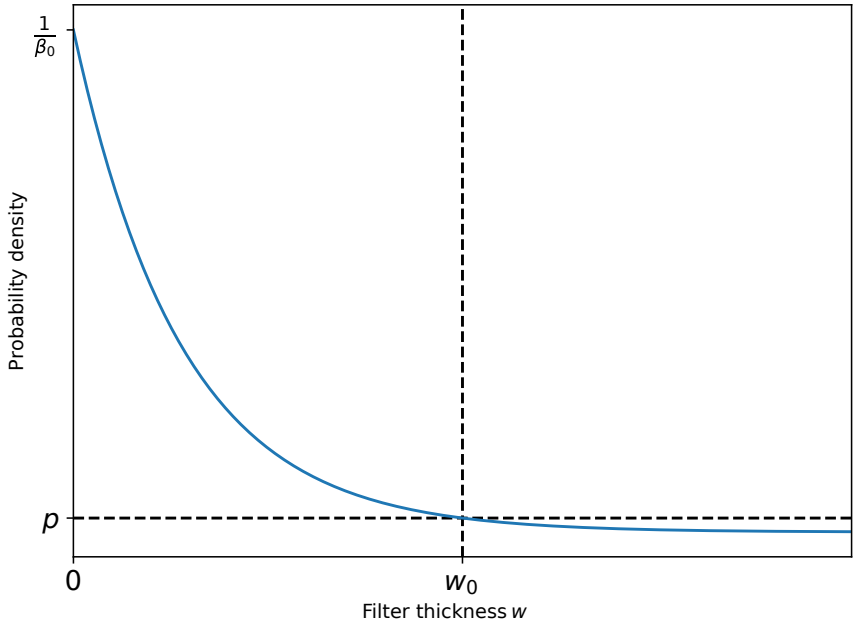

Figure 6.11.: A visualisation of the parameters of the exponential distribution $f(w, \beta_0)$ defined via equation (6.5). w_0 resembles the filter thickness the probability density equals p. β_0 corresponds to the expected value of the distribution and is chosen to fulfil $f(w_0, \beta_0) = p$.

The shape of distribution (6.5) and a visulisation of its parameters are illustrated in figure 6.11. The parameters are chosen heuristically. Probability p is set to 0.01 for all materials. Thicknesses w_0 specified in table 6.1 for different filter materials are used, resembling typical filter thicknesses in applications. w_0 has no units but corresponds to cm. To use distribution (6.5) to randomly generate filter widths via $f(w, \beta_0)$, equation (6.6) is solved for β_0 which yields

$$\beta_0 = -\frac{w_0}{W_{-1}(-w_0 \cdot p)}, \tag{6.7}$$

where W_{-1} is the -1st branch of the Lambert W function.

An additional random decision to use a filter is made. In real applications, filters are often stacked to achieve a desired X-ray tube spectrum. Each material has the same probability of $p_\mathrm{f} = \frac{1}{2}$ to be used. Therefore, the number of filters of different materials

Material	w_0
Al	1.
Cu	0.8
Sn	0.6
Pb	0.4

Table 6.1.: Thicknesses w_0 of the filters of the X-ray tube the distribution of equation (6.5) equals $p = 0.01$. Values for different filter materials are provided. w_0 itself has no unit but corresponds to cm.

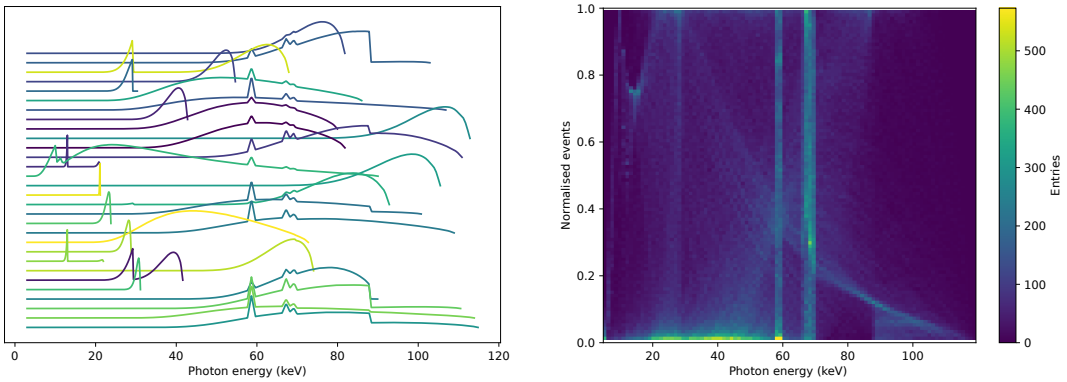

(a) 30 random XRT spectra

(b) Density histogram of 5k random XRT spectra

Figure 6.12.: (a) depicts the distributions of 30 random tungsten X-ray tube spectra with additional filters of Al, Cu, Sn, and Pb applied. (b) shows the density distribution of 5k random spectra.

is distributed according to a Binomial distribution of $B(n = 4, p_f = \frac{1}{2})$, where n is the number of available materials.

The sampled characteristics of an X-ray tube and its filters are used to generate the corresponding photon spectra via xpecgen [21]. Figure 6.12 (a) shows 30 random X-ray tube spectra. (b) shows the density of 5k normalised random spectra. Features shared by the spectra are discernible. See section 2.3 for a detailed explanation. The dominant peak in the region of about 20 keV to 30 keV is due to the shape of the bremsstrahlung spectrum. Also, characteristic lines of the tungsten anode are present. Drops in photon fluence at certain energies in the spectra correspond to the K-edges of the used filter materials.

Random spectra are generated according to the previously described rules. They are rebinned from 0 to 120 keV in steps of 1 keV to coincide with the output of the network. The determined histograms are stored as the labels of the training dataset.

Dosepix response spectra generation

The previously generated random spectra of the filtered X-ray tube are used to create the corresponding responses of the Dosepix detectors. These later reflect the input data of the network. The Dosepix detector setup described in section 6.2 is used. The responses to monoenergetic photon fields for each detector are simulated as discussed in chapter 3, with the difference that no phantom is involved now.

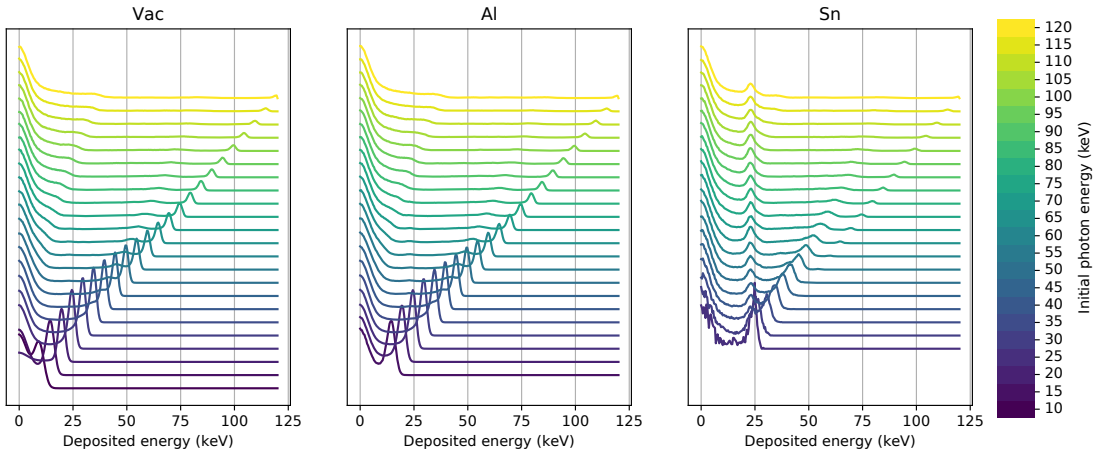

Figure 6.13.: The responses of the Dosepix detectors to an irradiation with monoenergetic parallel photon fields. The colour bar indicates the initial photon energies. The titles of the three plots correspond to the filters of the detectors according to section 6.2.

The resulting deposited energy spectra are depicted in figure 6.13. The colour bar represents the initial energy of the photon field. The titles of the plots correspond to the filters of the detectors. *Vac* is the abbreviation of vacant and represents the detector without a metal filter. Each deposited energy spectrum is normalised to the number of simulated events. Peaks at deposited energies close to the initial photon energy are discernible. There is a small difference between deposited and photon energy due to effects like Compton scattering and charge sharing, described in detail in section 3.1.3. The amplitudes of these peaks decrease with increasing photon energy due to the declining probability of photoelectric absorption to occur (see section 2.2.1 for more details).

Figure 6.14 illustrates a density representation of the spectra in figure 6.13. The data reflects response matrices for the different detectors. The colour indicates the probability a deposited energy is provided by the detector for a specific initial photon energy. The probability dimension is scaled logarithmically to emphasise the features of the spectra. White dashed lines represent the full energy peaks, dash-dotted lines the Compton edge and the backscatter peak, and dotted lines the Sn-fluorescences. The responses for the *Vac* and *Al* detectors look very similar. They mostly differ for

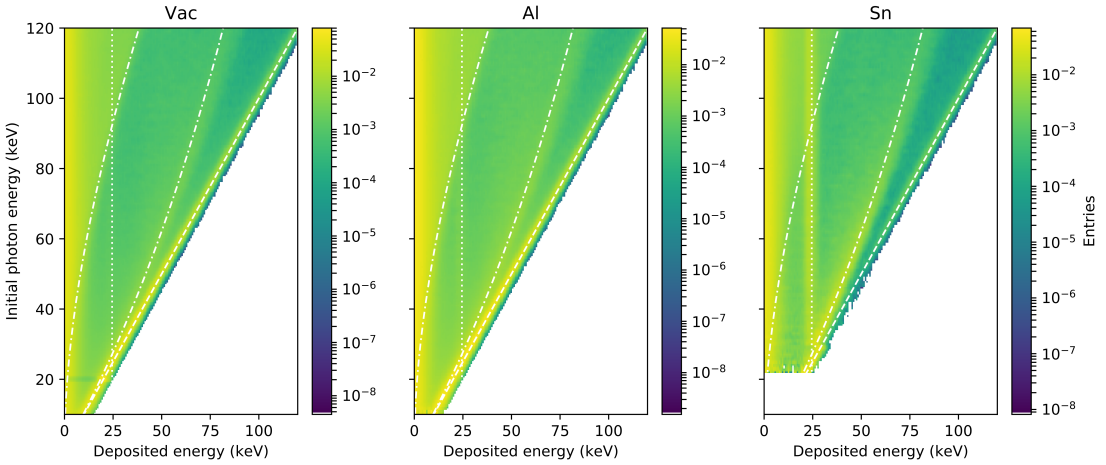

Figure 6.14.: The colours of the plots reflect the probability Dosepix registers a deposited energy for a certain photon energy. The axis of the probability is scaled logarithmically. White dashed lines indicate the full energy peaks, dash-dotted lines the corresponding Compton edges and backscatter peaks, and dotted lines the Sn-fluorescences. The titles of the plots correspond to the filter of the detectors according to section 6.2.

low initial photon energies. The *Sn* detector shows almost no registered events for these lower initial energies, due to the tin's strong attenuation capabilities. This is further illustrated in figure 6.15 which shows the detectors' efficiencies to register events for photons of different initial energies. The efficiency is defined as the ratio of detected events and the fluence of the simulated parallel photon field.

The efficiencies of the detectors differ for low initial energies. At about 60 keV, the *Vac* and *Al* detectors provide an almost identical number of events. The *Sn* detector with its strongly attenuating filter stays different for almost the whole energy range and starts to approach similar count rates at about 120 keV. The trend of the detection efficiencies further emphasises the task of the filters of the Dosepix detectors. They attenuate photons, emit fluorescences, and Compton scattering takes place. The probabilities for these processes to occur strongly depend on the material as indicated by the efficiencies. The spectra impinging on the different detectors then differ, leading to a variety of information at the input of the network, and as a consequence, to an improvement of its reconstruction abilities.

The response of a Dosepix detector as a function of deposited energy E for a monoenergetic parallel photon field of energy E' is called $R(E', E)$ (see figure 6.14). Responses are combined for the previously generated X-ray tube spectra of the labels, described by $f(E')$. $f(E')$ corresponds to a probability distribution that provides the weights in a superposition of the monoenergetic detector responses. Here, a correct normalisation is important. Responses $R(E, E')$ are normalised to their sum and there-

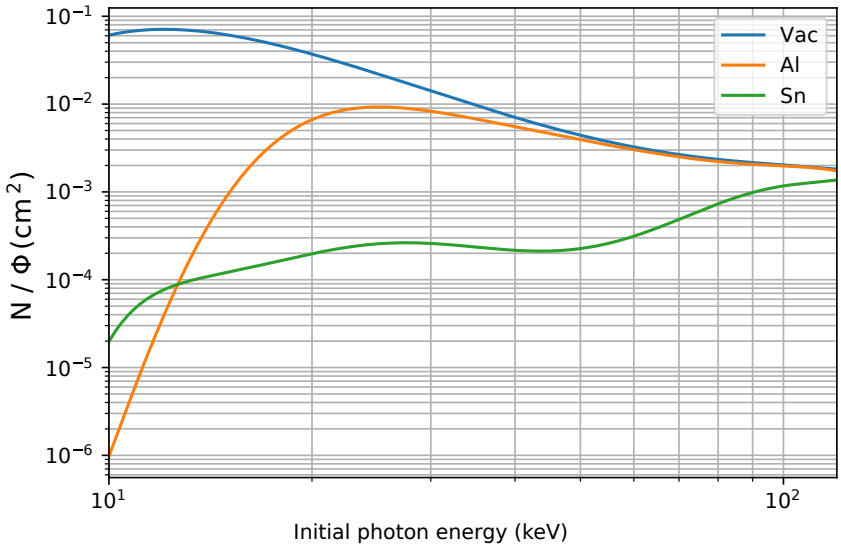

Figure 6.15.: The ratio of registered events N and fluence Φ of the parallel photon field as a function of its energy. The curves represent the Dosepix detectors with filters installed according to the legend.

fore have to be scaled with the efficiency, now called $\varepsilon(E')$ and shown in figure 6.15. In summary, the detector response $R_f(E)$ for a photon spectrum $f(E')$ is described via

$$R_f(E) = \int_0^\infty \mathrm{d}E' R(E', E) \cdot \varepsilon(E') \cdot f(E'). \tag{6.8}$$

$R_f(E)$ for the differently filtered detectors is provided by using the corresponding distributions of $R(E', E)$ and $\varepsilon(E')$.

Responses $R_f(E)$ for a corresponding exemplary photon spectrum $f(E')$ are depicted in figure 6.16. Since the voltage of the X-ray tube is high, the responses of the *Vac* and *Al* detector are similar. They only differ in their number of events for deposited energies below 60 keV while their shape is almost identical. The *Sn* detector registers a spectrum that completely differs from the other detectors. The total number of events is lower due to the strong attenuation, and there is a dominant peak at about 25 keV due to Sn fluorescences. A common feature of the *Vac* and *Al* spectra is a decreasing number of events for increasing deposited energies, which is due to the trend of the efficiency $\varepsilon(E)$. This example illustrates that there is no simple relation between the measured spectra and the initial photon spectrum. This further emphasises the requirement for a deconvolution.

Dosepix response spectra for all filtered X-ray tube spectra of the labels are generated. Each response is rebinned to 100 bins within the deposited energy range of

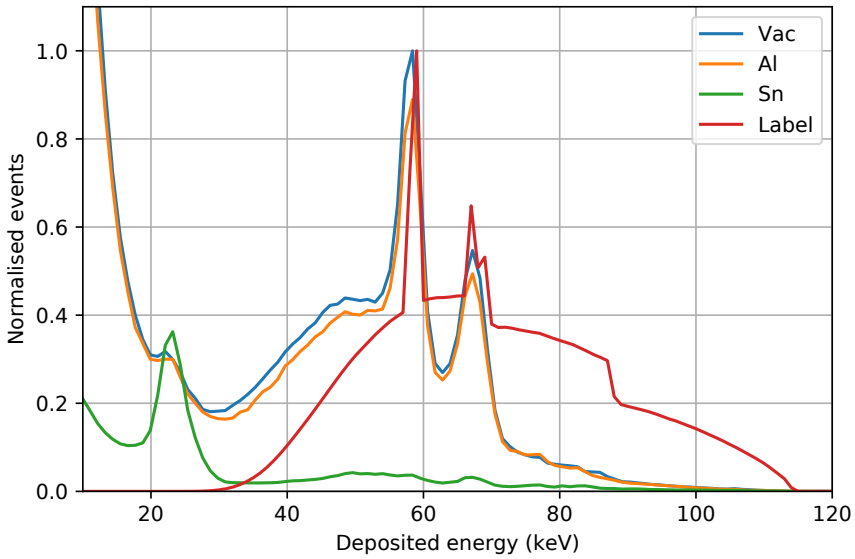

Figure 6.16.: The plot shows the initial photon spectrum in red („Label“) and the corresponding responses of the Dosepix detectors with filters applied according to the legend. The response spectra are normalised to the maximum value of the *Vac* spectrum for deposited energies greater than 20 keV.

10 keV to 120 keV. The responses are concatenated to a shape of 3×100 and stored as training data to represent the network's input.

6.3.3 Training process

The training process of the deconvolution network is explained in the following. Training is performed on 800k samples, validation on 150k samples. The order of the samples is reshuffled after each training epoch. The response spectra, reflecting the input of the network, are normalised to their sum each. Each spectrum of the labels is normalised to its maximum value. The batch size during training and validation is 1024. The metric used for the loss is the mean squared error L_{MSE} (see section 2.5.2 for more information). This loss is chosen as it considers a spectrum's exact shape, including characteristic lines. Figure 6.17 depicts the trend of this loss for five epochs. There is no indication of overfitting, i.e. the loss converges properly for training and validation.

Predictions on the validation dataset are made to prove the quality of the deconvolution network. Figure 6.18 shows two examples. The tops of the plots show simulated Dosepix detector responses provided as input to the network. The labels of the curves correspond to the filters of the detectors according to the legend. The bottoms of the

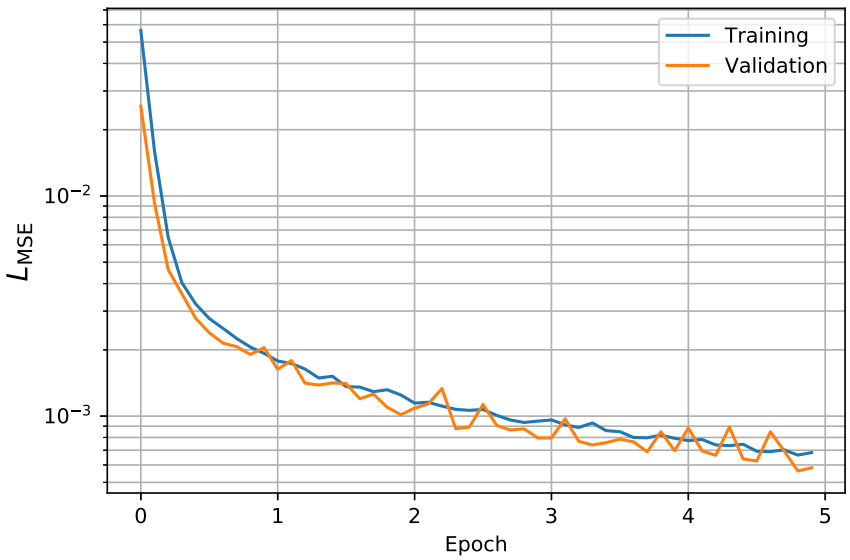

Figure 6.17.: The mean squared error L_{MSE} as a function of epochs for the training and validation of the deconvolution network. The trends of the curves indicate no overfitting.

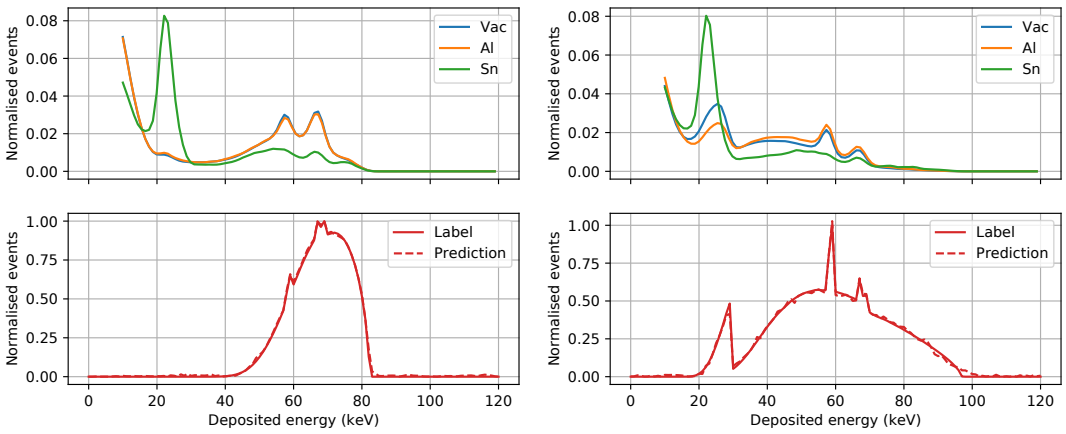

Figure 6.18.: Two examples of the deconvolution network are shown. The top plots depict the three Dosepix responses with the filters of the detectors according to the legend. The bottom plots show the corresponding photon spectra („Label“) as solid lines. The Dosepix responses constitute the input of the deconvolution network, providing the output „Prediction“, represented by a dashed line.

plots depict the corresponding predictions of the network, represented by a dashed line and the target spectrum via a solid line. Predicted and target curves are almost identical. The prediction shows small noise contributions in regions where no events are present in the target spectrum, e.g. for deposited energies higher than the maximum possible energy limited by the X-ray tube voltage.

Each of the Dosepix responses is normalised to its sum. This neglects the differences in registered events of the detectors. As the deconvolution via the network works sufficiently well, the normalisation is kept in the following. This way, additional robustness is gained when applying the network to real measurements. Possible discrepancies introduced by the simulation regarding the detectors' photon detection efficiencies will then have a decreased influence.

6.3.4 Results

The previous section shows that the deconvolution network works well with simulations. One desired quality of the network is robustness to discrepancies between simulated and measured input data. Therefore, the performance of the network is evaluated on real measurements in the following.

Weakly filtered X-ray tube spectra

Measurements with a Siemens Megalix Cat X-ray tube [20] (see section 2.3 for more details) without additional filters are made in the following. However, the exit window cannot be removed. It corresponds to an Al-filter of 1.5 mm. The acquired response spectra of the Dosepix detectors are depicted in figure 6.19. The voltage U_{XRT} of the X-ray tube is varied in a range of 40 kV to 120 kV in steps of 10 kV, indicated by the colour bar. The titles of the plots correspond to the filters of the detectors. The y-axis is scaled linearly in (a) and logarithmically in (b). See section 2.3 for more information about the features of the photon spectra of the X-ray tube. All Dosepix responses show a peak in the region of 20 keV to 30 keV, corresponding to the shape of the filtered bremsstrahlung spectrum, whose shape for low energies only slightly depends on the tube voltage. Once the voltage exceeds the transition energies for tungsten, the anode material of the X-ray tube, small peaks in the region of 50 keV to 70 keV emerge. These are most distinct for the *Vac* and *Al* detectors, whereas the number of registered events for the *Sn* detector is too low to separate the peaks from the bremsstrahlung spectrum. However, the *Sn* detector shows prominent Sn-fluorescence peaks. In figure 6.19 (a), where a linear scale is used, all spectra seem to cut off at about 80 keV. This is due to the low photon detection efficiencies of the detectors for higher photon energies. For the logarithmically scaled curves of (b), entries of higher energies are still discernible. The number of registered events decreases approximately exponentially with the deposited energy.

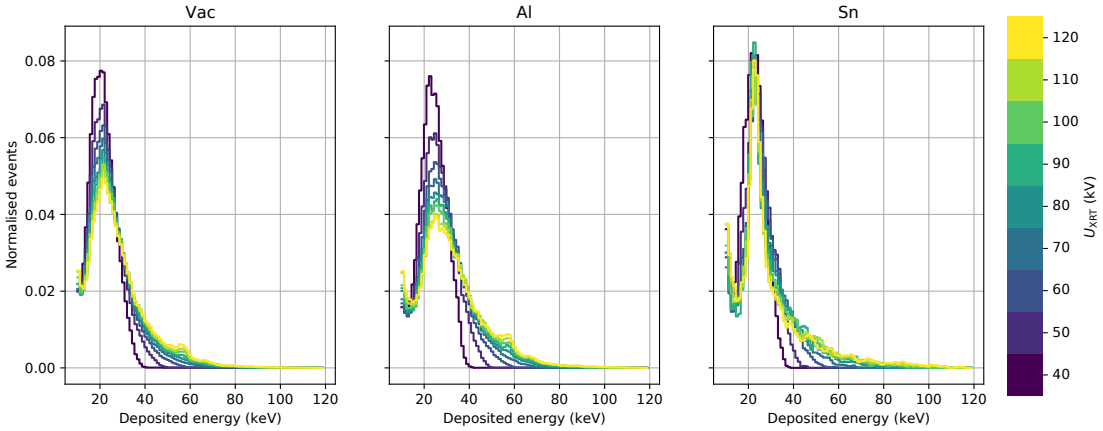

(a) Linear scale

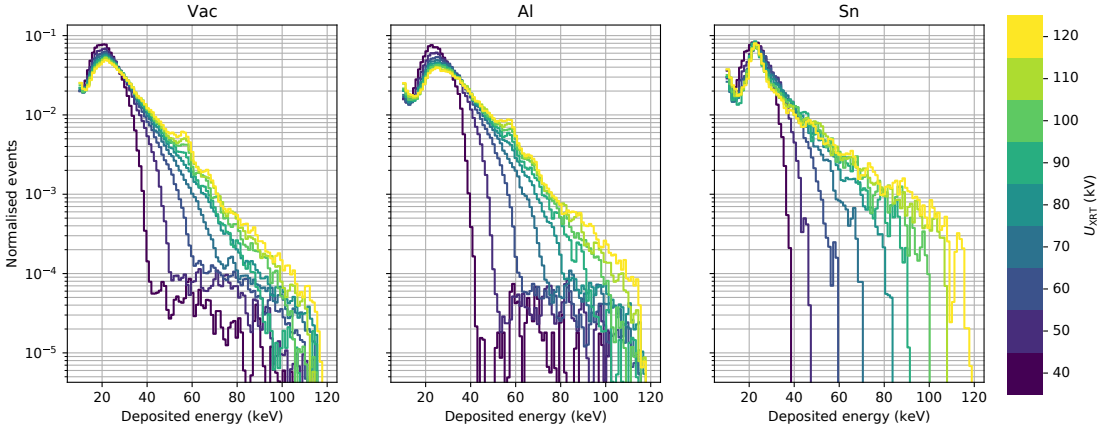

(b) Logarithmic scale

Figure 6.19.: The measurements of an X-ray tube with 1.5 mm Al-filter. The voltage of the tube is indicated by the colour bar. The responses of three Dosepix detectors with filters according to the titles of the plots are illustrated. All spectra are normalised to the sum of their registered events. The y-axis is scaled linearly in (a) and logarithmically in (b).

The measurements are used as input to the deconvolutional network, which predicts the corresponding photon spectra. The output is depicted in figure 6.20 (a) via solid lines. Dashed lines correspond to the simulated X-ray tube spectra. The colour bar indicates the tube voltage U_{XRT}. Dash-dotted vertical lines further illustrate the maximum possible photon energies.

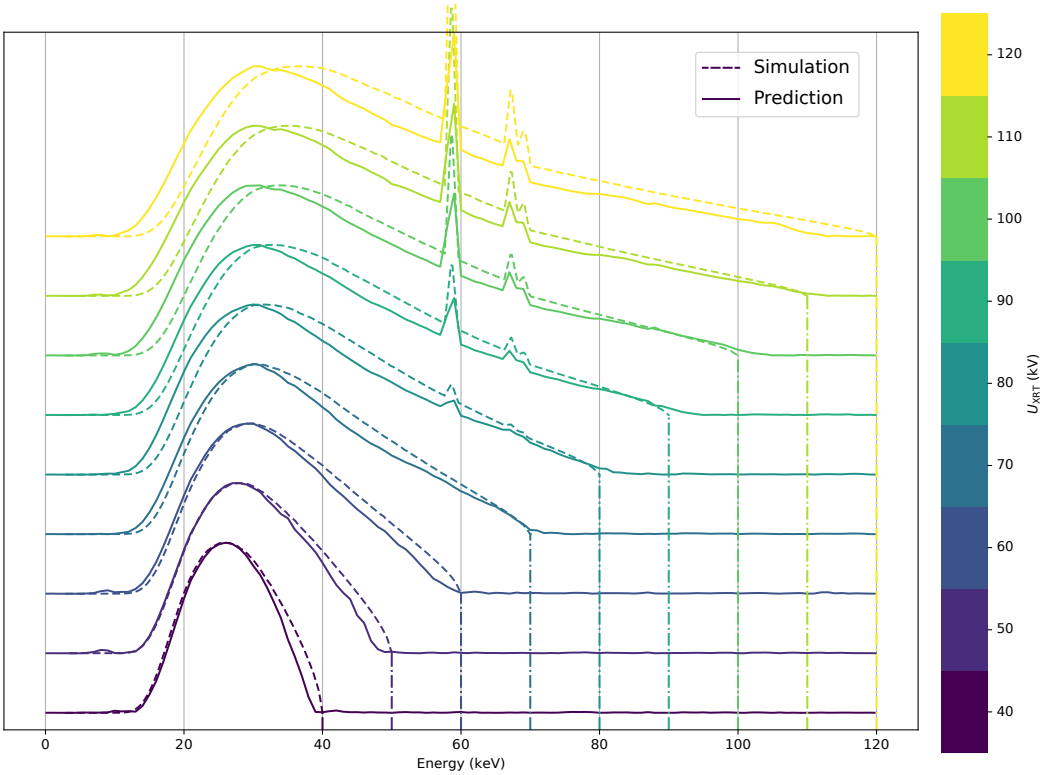

(a) Prediction and simulation of irradiation spectra

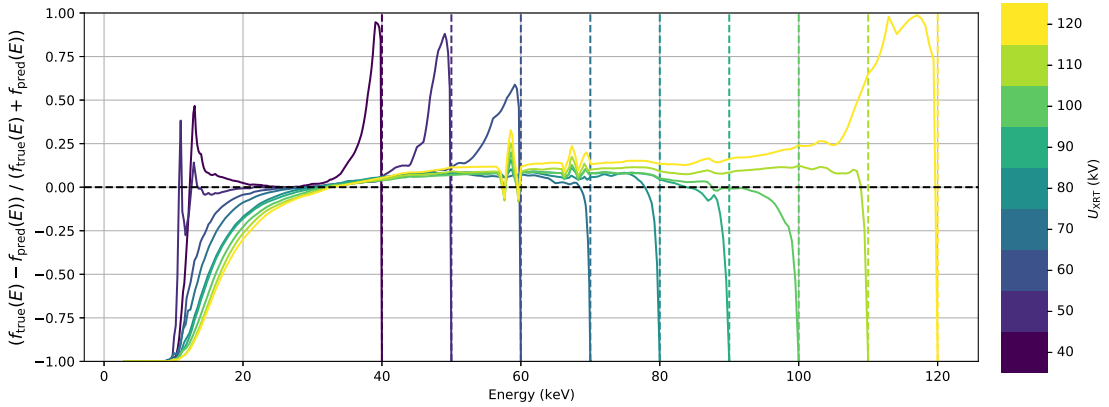

(b) Relative deviation of prediction and simulation

Figure 6.20.: The plot in (a) depicts the prediction (solid lines) and simulation (dashed lines) of the photon spectrum of an X-ray tube with 1.5 mm Al-filter. The colour bar indicates the used tube voltages. Additional vertical dash-dotted lines represent the maximum possible photon energies. (b) reflects the relative deviations of the predicted spectra $f_{\text{pred}}(E)$, and simulated spectra $f_{\text{true}}(E)$ according to equation (6.9).

Figure 6.20 (b) illustrates the relative deviations of the predicted spectra $f_{\text{pred}}(E)$, and simulated spectra $f_{\text{true}}(E)$ in (a) according to

$$\frac{f_{\text{true}}(E) - f_{\text{pred}}(E)}{f_{\text{true}}(E) + f_{\text{pred}}(E)}. \tag{6.9}$$

The mismatch of the low energy parts of the simulated and predicted spectra increases with increasing X-ray tube voltage. The discrepancy corresponds to an underestimation of the attenuation of the filter of the X-ray tube. For tube voltages in the range of 40 kV to 60 kV and for 120 kV the maximum energies in the spectra are underestimated. The energies are overestimated for the remaining voltages. The deviations according to equation (6.9) for energy ranges between the dominant peaks of the spectra up to close to the maximum energies, corresponding to the set tube voltages, are small and almost constant. There are only slight fluctuations at the transition energies of tungsten noticeable. The Dosepix responses for the measurement with a tube voltage of 120 keV have the problem of low statistics for high deposited energies, leading to an underestimation of events in the prediction for this region.

The discrepancies can mainly be attributed to imperfections in the detectors' calibrations from ToT to deposited energy (see chapter 4 for a description of the procedure). The simulation does not rely on this calibration since it directly works with deposited energies. Discrepancies are introduced by the used calibration function, which is only an approximation, as shown in section 4.1.4. This mostly leads to inaccuracies at lower deposited energies. Also, measurements with Dosepix depend on temperature, as is illustrated in section 3.3. Since no temperature correction is applied, a mismatch of registered ToT, and as a consequence, of deposited energy, is possible. However, the temperature during the measurements only slightly differed from the calibration temperature, leading to only a small error contribution. The calibration was performed via an ^{241}Am source which emits photons with energies of up to about 60 keV. Higher photon energies are not included in the calibration. The calibration function (see section 4.1.2 for more details) for the conversion from ToT to deposited energy describes higher deposited energies with a linear relation. Therefore, a small inaccuracy introduced in the calibration of low energies leads to an increased inaccuracy for high energies. This is the main contribution of the introduced error sources. When using the network for the prediction, its input spectra's inaccuracies are transferred to its output.

Additionally, a two-sample Kolmogorov-Smirnov test is performed to evaluate the agreement of predicted and simulated X-ray tube spectra. The description of the test is based on [75]. The Kolmogorov-Smirnov statistic is calculated via

$$D = \max \left| \hat{F}_{\text{pred}} - \hat{F}_{\text{sim}} \right|, \tag{6.10}$$

which describes the maximum distance between the empirical distribution functions $\hat{F}_{\text{pred}}$ and $\hat{F}_{\text{sim}}$, corresponding to the predicted and simulated spectra. A null hypoth-

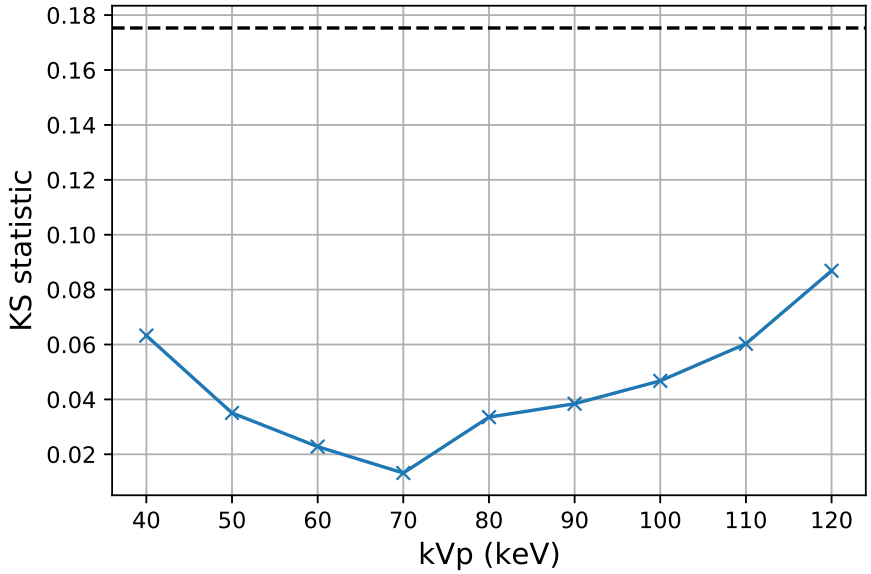

Figure 6.21.: Kolmogorov-Smirnov statistic according to equation (6.10) for the simulated and predicted weakly filtered X-ray tube spectra of figure 6.20 as a function of their kVp-value. The dashed line indicates D_α for $\alpha = 5\%$, the limit the null hypothesis of two samples from the tested distributions being from a common distribution is neglected.

esis is stated that two samples, one from the predicted and one from the simulated distribution, are drawn from a common distribution. The sample sizes of $\hat{F}_{\text{pred}}$ and $\hat{F}_{\text{sim}}$ are identical, i.e. $n = 121$. The critical value of the Kolmogorov-Smirnov is calculated via [75]

$$D_\alpha = K_\alpha \sqrt{\frac{2}{n}}. \tag{6.11}$$

α is the level the null hypothesis is rejected. Here, $\alpha = 5\%$ is used. The corresponding value of K_α is 1.36 [75], resulting in $D_\alpha = 0.175$. Figure 6.21 shows the Kolmogorov-Smirnov statistic according to equation (6.10) for the predicted and simulated photon spectra of figure 6.20 as a function of the kVp-value. The dashed line indicates the rejection limit of the null hypothesis, D_α. D indicates that the agreement of simulation and prediction is best for kVp $= 70\,$keV. All values are less than D_α, i.e. the null hypothesis for $\alpha = 0.05$ is accepted. In conclusion, despite the inaccuracies for low and high photon energies, the network is able to predict the weakly filtered X-ray tube spectra from measurements correctly.

Strongly filtered X-ray tube spectra

Since the deconvolution network's performance on X-ray tube spectra with weak filtration is well, the test is also made with filters of different materials of varying thicknesses. 21 spectra are measured, called R-series in the following [76]. The spectra's mean photon energies cover the whole energy range, making them well suited for evaluation tasks. Also, due to the different filter combinations, the shapes of the photon spectra vary. The used tube voltages and filter sizes are listed in table 6.2.

Code	kVp	Al (mm)	Cu (mm)	Sn (mm)	Mean energy (keV)
R0	40	3.5	0	0	29.7
R1	50	3.5	0	0	34.19
R2	45	3.5	0.3	0	37.21
R3	55	3.5	0	0	42.73
R4	55	5	0.9	0	47.12
R5	60	5	0.9	0	50.21
R6	65	5	0.9	0	53.14
R7	70	5	0.9	0	56.45
R8	70	6	2	0	60.54
R9	75	6	2	0	63.5
R10	80	6	2	0	65.99
R11	85	6	2	0	68.39
R12	90	6	2	0	70.73
R13	95	6	2	0	73.00
R14	100	8	5	0	83.94
R15	105	8	5	0	87.05
R16	110	8	5	0	90.04
R17	115	8	5	0	92.81
R18	120	8	5	0	95.59
R19	115	8	5	0.5	96.07
R20	120	8	5	0.5	99.04

Table 6.2.: The filters and tube voltages for R-series X-ray tube spectra [76]. Al, Cu, and Sn are used as filter materials. The values for Al include the internal filter of the Siemens Megalix Cat X-ray tube. Additionally, the mean energy of each spectrum is shown.

The simulated R-series photon spectra are depicted in figure 6.22 (a). (b) shows the corresponding mean energies as a function of the spectra's codes as described in the table. The mean energies reflect how the spectra cover the available energy range of the used Megalix X-ray tube.

The measurements with the X-ray tube and the specified filters are made for all codes of the R-series. The responses of the Dosepix detectors are illustrated in figure 6.23.

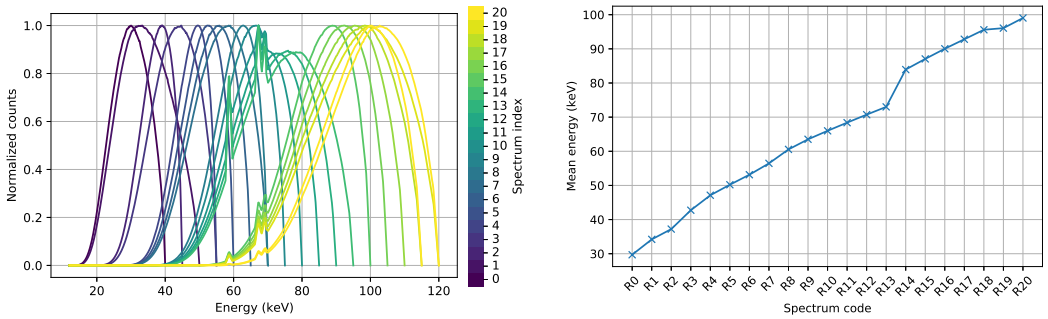

(a) Simulated spectra

(b) Mean energies of the spectra

Figure 6.22.: (a) shows the simulation of R-series spectra with the filters and tube voltages applied according to table 6.2. Each spectrum is normalised to its maximum. The index indicated by the colour bar corresponds to the code in table 6.2. (b) shows the mean energies of the spectra in (a).

All spectra are normalised to their number of registered events. The titles of the plots indicate the different detectors. The colours of the curves correspond to the codes of the R-series.

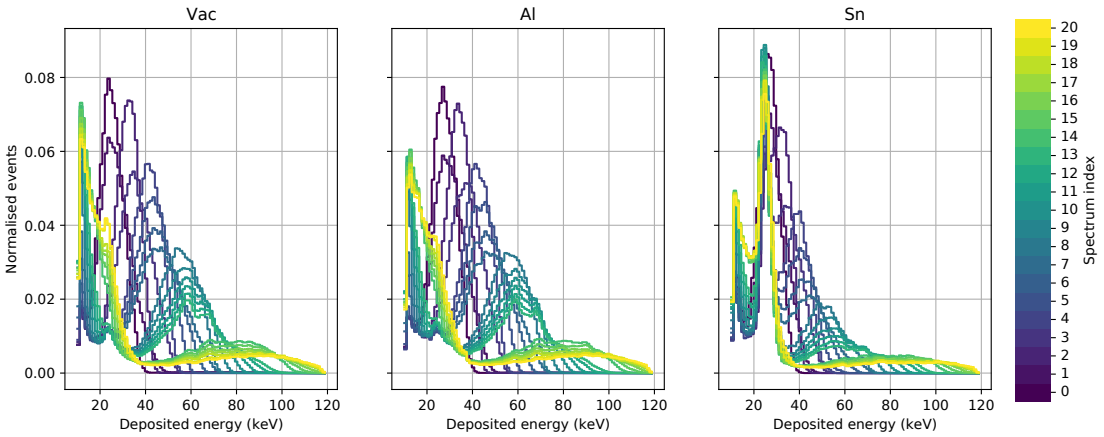

Figure 6.23.: Dosepix responses for the measurements of the R-series spectra. The titles of the plots correspond to the filters of the detectors. The colour bar indicates the code of the spectrum according to table 6.2.

Like in the measurements of the weakly filtered spectra before, the spectra of the *Vac* and *Al* detectors are similar, except for energies less than about 40 keV. In this region, the number of entries decreases approximately exponentially with the photon energy. The *Al* detector shows fewer entries than the *Vac* detector due to its filter's attenuation. The Sn-fluorescences in a region of about 25 keV are discernible for all detectors but

are most prominent for the *Sn* detector. Small peaks in the energy region of 50 keV to 70 keV show once the tube voltage exceeds the excitation energies of tungsten. All Dosepix detectors' responses, independent of the used filter, are broader the higher the voltage of the X-ray tube. All spectra show a similar trend for low deposited energies due to effects like Compton scattering and charge sharing (see section 2.1.1 for more details).

Figure 6.24 (a) shows the simulated spectra (dashed lines) and the predictions from measurements (solid lines) for the R-series spectra. The colour bar indicates the code of the spectra according to table 6.2. (b) depicts the relative deviation of prediction $f_{\text{pred}}(E)$, and simulation $f_{\text{true}}(E)$ according to equation (6.9). There is a mismatch in prediction and simulation for all spectra in the region close to the energy corresponding to the highest possible photon energies emitted by the X-ray tube. For tube voltages of up to 60 kV, the simulation overestimates the prediction. For higher voltages, it is vice versa. This discrepancy increases with increasing tube voltage, which is another indication of inaccuracies in the calibrations of the three detectors. The characteristic lines of tungsten are properly predicted. An adjustment of the calibration might resolve the observed discrepancies. This is analysed in section 6.5.

6.4 Spectrum characteristics

In addition to the shape of a photon spectrum, other characteristics help to assure the quality of an X-ray system. Via regular service measurements of medical X-ray tubes, image quality in imaging is ensured, and patients are protected from possible malfunctions and high exposures. The following 6 attributes of a photon spectrum are determined:

- kVp-value
- Half-value layer (HVL) for aluminium and copper
- Conversion factor from fluence to air kerma K_{air}/Φ
- Conversion factors from photon fluence to ambient dose equivalent $H^*(10)/\Phi$ and directional dose equivalent $H'(0.07, 0^\circ)/\Phi$

A detailed description of the characteristics and an explanation of their calculation from spectra is given in section 6.4.2. These parameters can also be calculated from a photon spectrum predicted by the deconvolution network. However, an approach to predict these measures directly is made. This way, possible errors introduced by the deconvolution network are circumvented. First, the architecture of the characteristics network is introduced in the following.

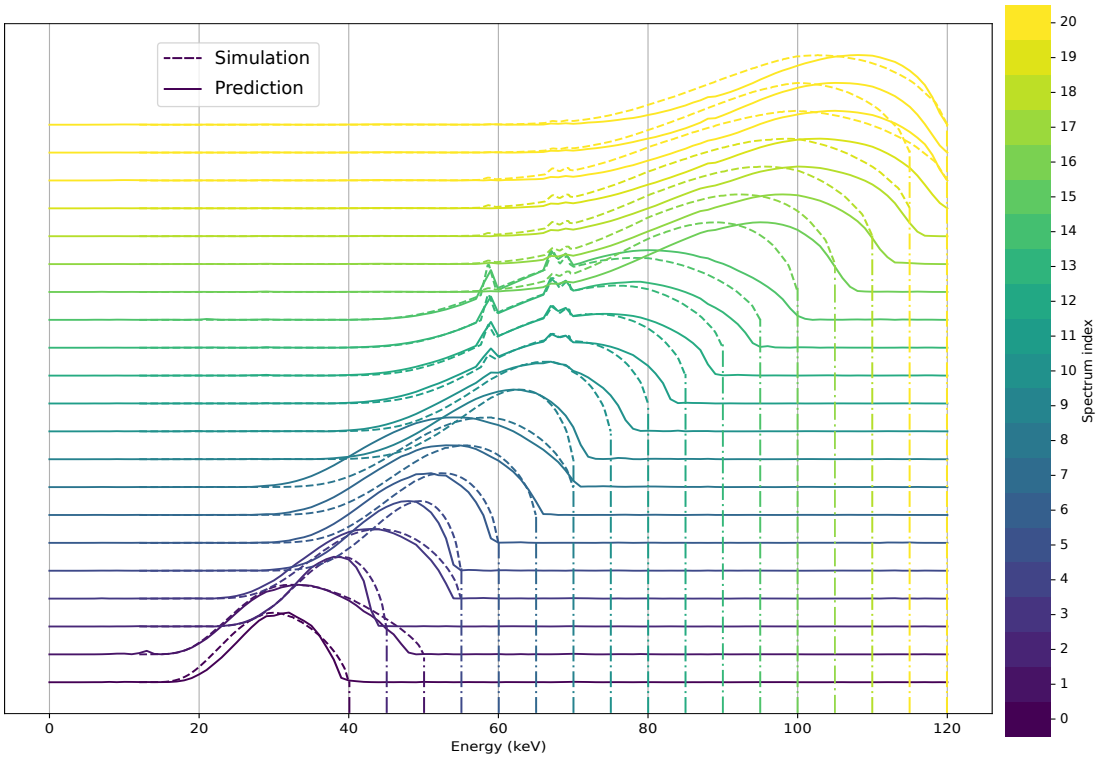

(a) Prediction and simulation of photon spectra

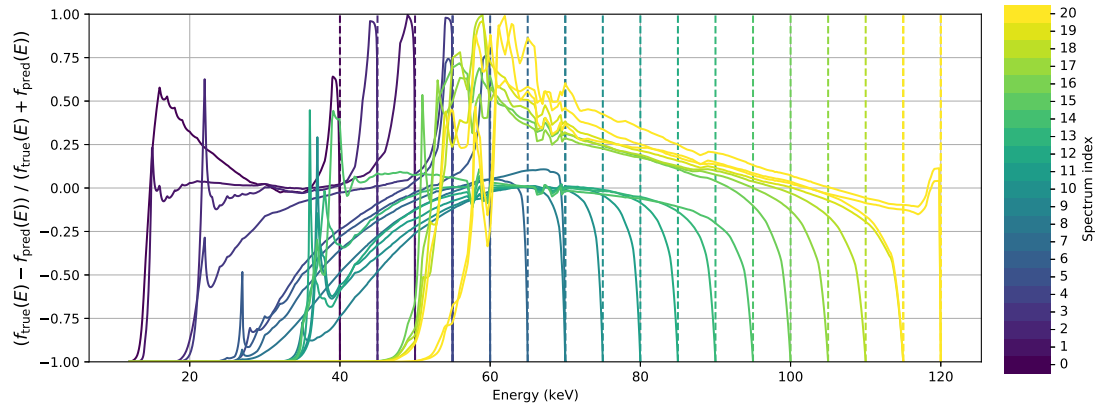

(b) Relative deviation of prediction and simulation

Figure 6.24.: (a) shows the prediction (solid lines) and simulation (dashed lines) of the R-series spectra. The index of the code according to table 6.2 is indicated by the colour bar. Dash-dotted lines represent the maximum possible photon energies. (b) depicts the relative deviation of prediction $f_{\text{pred}}(E)$, and simulation $f_{\text{true}}(E)$.

6.4.1 Network design

Figure 6.25 depicts the convolutional neural network's design to predict the characteristics of an X-ray tube spectrum. Its architecture is similar to the deconvolution network in section 6.3.1. The input shape of 100×3 is the same while the output size is reduced to 6, corresponding to the number of characteristics. After the input,

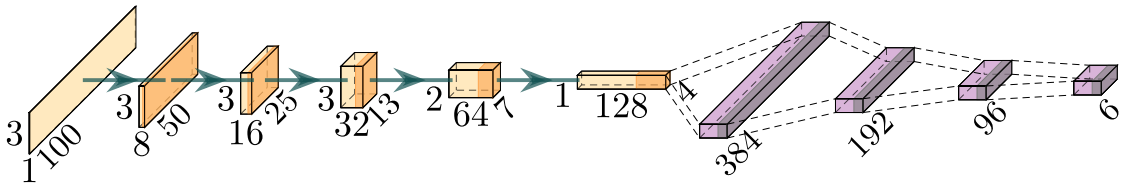

Figure 6.25.: The convolutional neural network for the prediction of 6 characteristics of an X-ray tube spectrum. It takes three Dosepix response spectra as input. Yellow blocks correspond to convolutional layers, purple blocks to dense layers. Dark regions at the ends of the blocks indicate the usage of activation functions. The image is created using [58].

a layer applying Gaussian noise with a random standard deviation to the spectra is present (see section 4.2.1 for more details). It is used for regularisation and is only active during training. 5 convolutional layers follow, the first 3 with a kernel size of 3×3, the following with a kernel size of 2×2. The layers' stride size reduces the detector dimension gradually from 3 to 1. For each convolutional layer, the number of filters is doubled in relation to the preceding layer. This results in filter sizes of 8, 16, 32, 64, and 128. Afterwards, the activations are flattened and reduced to the desired output size of 6 units via 4 dense layers. All network layers use a ReLU-activation function except the last one, which uses a linear activation.

The network is designed to compress the information of the three Dosepix response spectra at its input to 6 characteristic values of the corresponding X-ray tube spectrum. This is achieved via convolutional layers which consider correlations within the response spectra of the detectors.

6.4.2 Training and validation data generation

The training dataset is similar to the deconvolution network in section 6.3.2. The input data of the Dosepix responses are kept unchanged. The corresponding X-ray tube spectra previously used as label are now replaced with their characteristics. The methods used to extract the different characteristics from an X-ray tube spectrum are described in the following.

kVp-value

The kVp-value (kilovoltage peak) of an X-ray tube spectrum is known from its simulation. Here, the X-ray tube's voltage is set, which directly corresponds to the kVp-value of the spectrum. The voltages are chosen uniformly within a range of 40 kV to 120 kV.

Conversion factors from fluence to air kerma and dose equivalents

The conversion factors from fluence to air kerma, ambient dose equivalent $H^*(10)$, and directional dose equivalent $H'(0.07, 0°)$ compress the information of a photon spectrum to single numbers. These contain information about the possible harm to an exposed human. The ambient and directional dose equivalents instead of personal dose equivalents are chosen as there is no phantom in spectroscopy measurements. For a detailed description of the dosimetric quantities, see section 2.4. Only an irradiation angle of 0° is considered, which is ensured by a proper detector alignment during measurements. Figure 6.26 shows the trend of the conversion factors from photon fluence to dose factors as a function of energy, i.e. $\frac{D}{\Phi}(E)$.

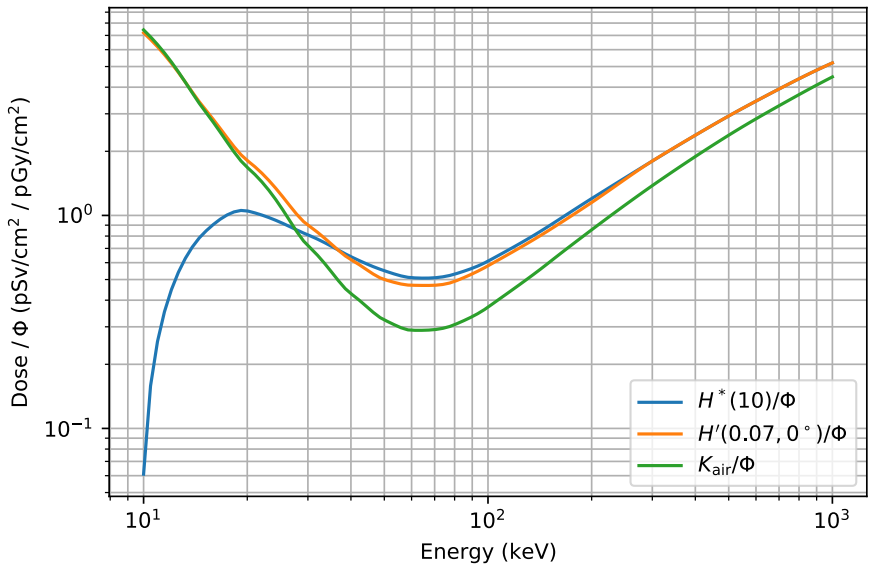

Figure 6.26.: Conversion factors from photon fluence Φ to air kerma (in pGy cm^2) and to dose equivalents $H^*(10)$ and $H'(0.07, 0°)$ (in pSv cm^2) as a function of initial photon energy. The data is taken from [45, 46, 77].

The conversion factors $\frac{D}{\Phi}$ corresponding to photon spectra $f(E)$ of the labels of the training data are calculated via

$$\frac{D}{\Phi} = \frac{\int \mathrm{d}E\, f(E) \cdot \frac{D}{\Phi}(E)}{\int \mathrm{d}E\, f(E)}, \tag{6.12}$$

where $\frac{D}{\Phi}(E)$ according to figure 6.26 for the different dose types is used. Spectra $f(E)$ represent the label data previously used for the deconvolution network.

Half-value layer (HVL)

The half-value layer (HVL) characterises the photon attenuation ability of an X-ray tube spectrum. It is reflected by the thickness of a specific material attenuating 50% of the incident energy, corresponding to a halving of the air kerma rate [78]. The attenuated dose D due to a filter of thickness d is calculated via

$$D(d) = \int_0^\infty \mathrm{d}E \; f(E) \cdot \frac{K_{\mathrm{air}}}{\Phi}(E) \cdot \exp\left(-\mu \cdot \rho \cdot d\right) \tag{6.13}$$

where $f(E)$ is the fluence of a photon spectrum as a function of energy E, $\frac{K_{\mathrm{air}}}{\Phi}(E)$ is the conversion from fluence Φ to air kerma according to figure 6.27, μ is the mass attenuation coefficient and ρ the density of the filter material. The half-value layer d_{HVL} reflects the thickness of the filter which fulfills the condition

$$D(d_{\mathrm{HVL}}) = \frac{D(d=0)}{2}. \tag{6.14}$$

Aluminium and copper are chosen as materials. Equation (6.14) is solved for d_{HVL} numerically. The new training data labels are calculated by using the photon spectra $f(E)$ of the label data previously used for the deconvolution network.

6.4.3 Training data distribution

The distributions of the X-ray tube characteristics in the training dataset are shown in figure 6.27. In general, uniform distributions are desirable as other shapes might lead to a network bias. However, the photon spectra previously generated for the deconvolution network are used to calculate the characteristics. These spectra are distributed uniformly in their tube voltages, which is reflected by the uniformity of the kVp-distribution. The distributions of the HVL values and dose conversion factors strongly depend on the shapes of the X-ray tube spectra, resulting in non-uniform distributions.

It is possible to sample characteristics uniformly from their distributions by neglecting a fraction of the dataset. However, since the parameters are correlated, sampling one parameter would produce a bias in the distributions of the remaining parameters. In conclusion, instead of adjusting the training dataset, possible bias effects are considered for the analysis of the measurement data.

6.4.4 Training process

The training dataset of the characteristics network is based on the dataset of the deconvolution network. Consequently, both share the same number of samples, i.e. 800k

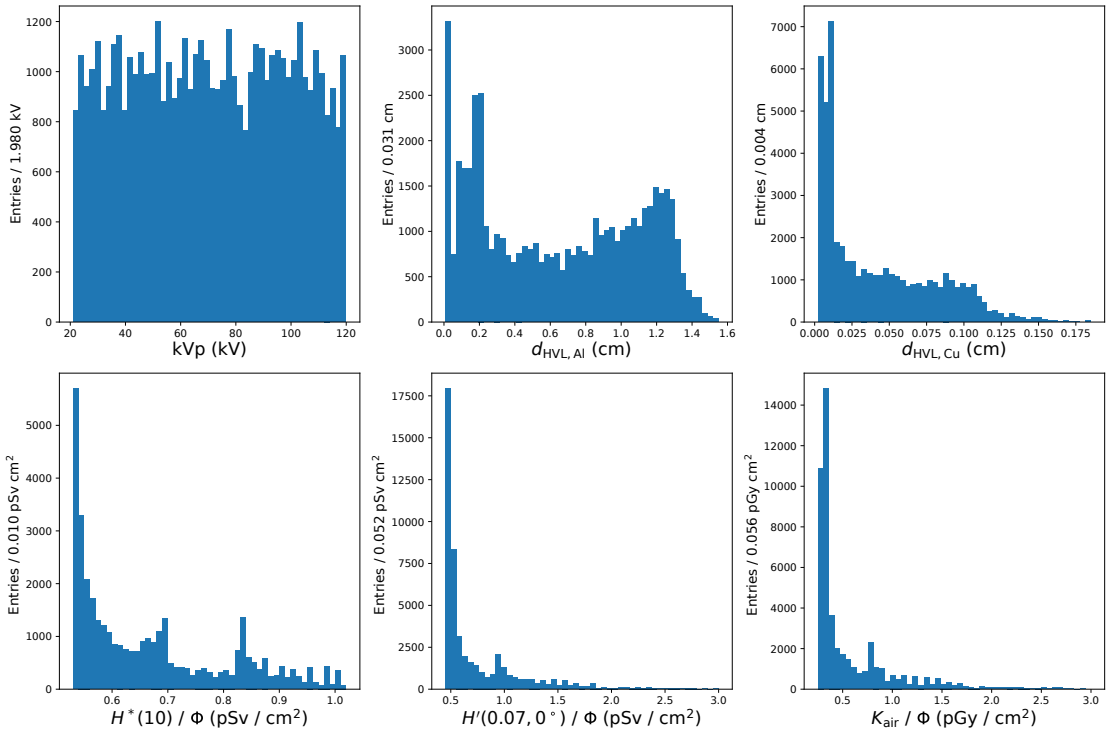

Figure 6.27.: The distributions of the X-ray tube characteristics of the training dataset for 50k exemplary samples. These parameters include the kVp-value, the half-value layers d_{HVL} for Al and Cu, and the conversion factors from fluence to air kerma, to $H^*(10)$ and $H'(0.07, 0^\circ)$.

for training and 150k for validation. The response spectra of Dosepix, representing the network's input, are normalised to their sum each. The characteristic parameters of the photon spectra, representing the output, are normalised to the mean values of their distributions, listed in table 6.3.

The batch size for training and validation is 1024. The mean squared error is used as the loss function. The trend of this loss L_{MSE} for the training of 5 epochs is depicted in figure 6.28. There is no indication of overfitting, and the loss is converging as expected. The performance of the network after training is validated on 50k samples. Figure 6.29 (a) depicts the ratio of predicted and true values $X = \frac{x_{\mathrm{pred}}}{x_{\mathrm{true}}}$. (b) reflects the relative deviation according to

$$X_{1/2} = |X - \mu_{1/2}|, \tag{6.15}$$

i.e. the absolute value of the difference of the ratio X and its distribution's median $\mu_{1/2}$. For the ratios X in (a), the dashed lines represent the distributions' means, and the dash-dotted lines the corresponding standard deviations. These values and the medians $\mu_{1/2}$ are listed in table 6.4. The means and medians are approximately

Parameter	mean value
kVp	70 kV
$d_{\mathrm{HVL,Al}}$	0.606 cm
$d_{\mathrm{HVL,Cu}}$	0.0253 cm
$H^*(10)/\Phi$	0.576 pSv cm^2
$H'(0.07, 0°)/\Phi$	0.549 pSv cm^2
K_{air}/Φ	0.36 pGy cm^2

Table 6.3.: The means of the distributions of the characteristics of the simulated photon spectra of the training dataset. Prior to the training of the network, the distributions are normalised to the corresponding means.

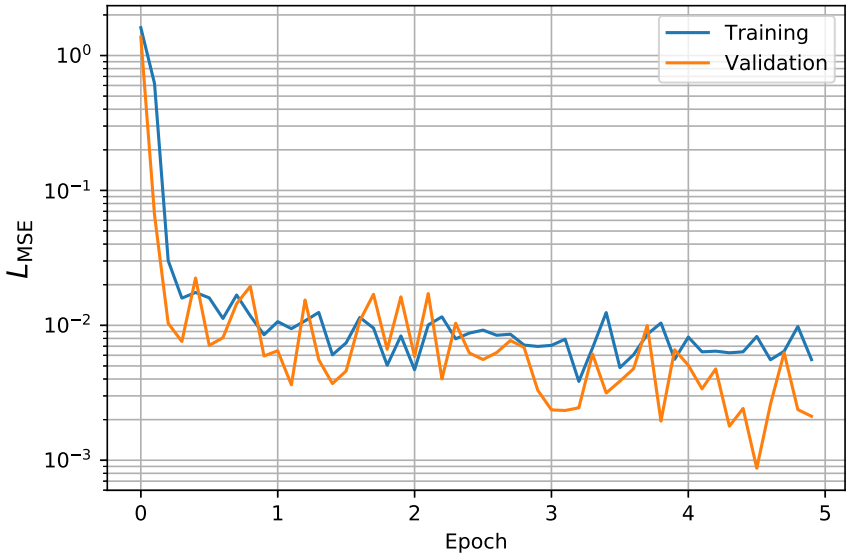

Figure 6.28.: Mean squared error L_{MSE} as a function of epochs for the training and validation of the characteristics network. There is no indication of overfitting.

1, proving the network's correct working regarding validation data. However, the distributions of the ratio of predicted and true values of kVp and the half-value layers show a slight positive skewness towards lower values. Nevertheless, the mean values are approximately 1, but the standard deviations are increased. Since the distributions are not normally distributed, the standard deviation is not the optimal measure for the uncertainty. Figure 6.29 (b) shows that the relative deviation can be described with a scaled exponential distribution via

$$g(x, \lambda) = N \cdot \exp\left(-\lambda \cdot x\right), \tag{6.16}$$

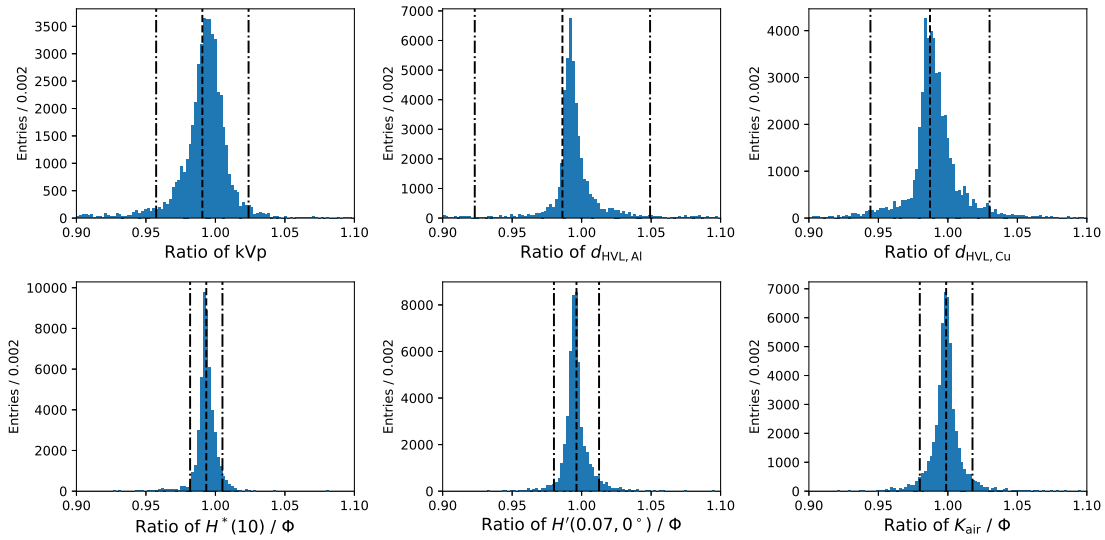

(a) Ratio X of predicted and true values

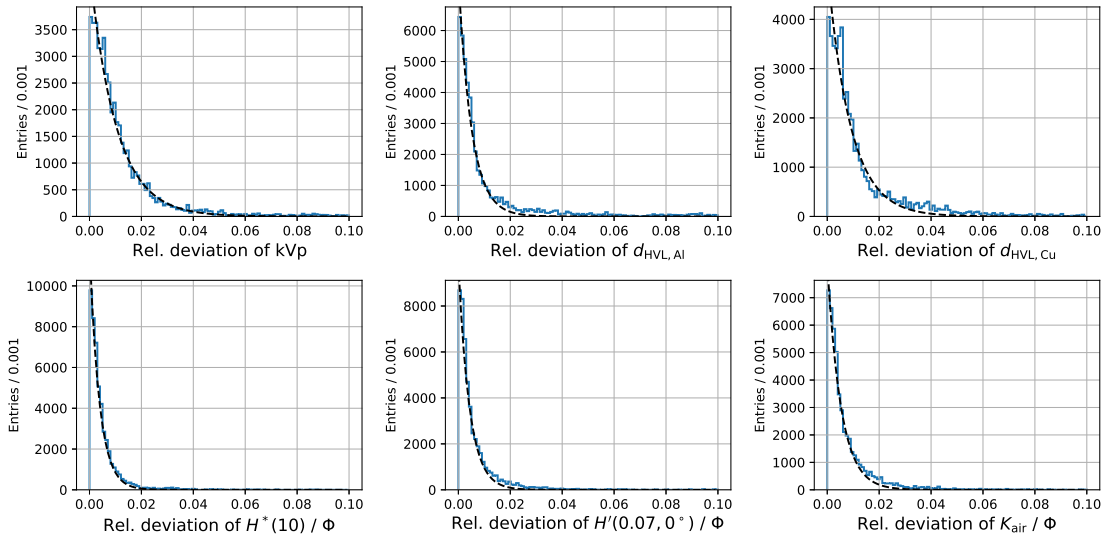

(b) Relative deviation $X_{1/2}$ of predicted and true values

Figure 6.29.: (a) depicts the ratio of predicted and actual values of the characteristic parameters for 50k samples of the validation dataset. The dashed lines indicate the mean values of the distributions, the dash-dotted lines the corresponding standard deviations. (b) shows the relative deviation $X_{1/2}$ according to equation (6.15). The dashed lines represent fits with equation (6.16).

Parameter	mean	median	standard deviation	$\frac{1}{\lambda}$
kVp	0.991	0.994	0.033	0.01013 ± 0.00020
$d_{\mathrm{HVL,Al}}$	0.986	0.993	0.063	0.00506 ± 0.00014
$d_{\mathrm{HVL,Cu}}$	0.987	0.989	0.043	0.00885 ± 0.00032
$H^*(10)$	0.993	0.993	0.012	0.00378 ± 0.00005
$H^*(0.07)$	0.996	0.995	0.016	0.00428 ± 0.00010
K_{air}	0.999	0.999	0.019	0.00528 ± 0.00012

Table 6.4.: Medians, means, and corresponding standard deviations of the ratio of predicted and true values X of the characteristic parameters for 50k samples of the validation dataset. The last column of $\frac{1}{\lambda}$ lists the uncertainty for the distributions of the relative deviation $X_{1/2}$ according to equation (6.15). $\frac{1}{\lambda}$ is determined by fitting the curves in figure 6.29 (b) with a scaled exponential distribution (6.16), where $\frac{1}{\lambda}$ corresponds to the mean.

where x reflects the bins of the histogrammed relative deviation of predicted and true values, and λ is the parameter characterising the exponential distribution. N corresponds to the number of entries in the histogram for which the relative deviation is 0. The values of $\frac{1}{\lambda}$, corresponding to the mean of the exponential distribution estimated via the fit, are listed in the last column of table 6.4 for the different parameters of the characteristics. $\frac{1}{\lambda}$. Therefore, $\frac{1}{\lambda}$ resembles the mean deviation for the ratio of predicted and true values of the characteristic parameters of figure 6.29 (b). Since the values are within a region of 1%, the training and validation of the characteristics network is considered successful.

6.4.5 Results

The R-series spectra's measurements (see section 6.3.4 for more details) are used to evaluate the performance of the characteristics network.

kVp-value and energy recalibration

The kVp-value of an X-ray tube spectrum resembles the voltage applied to the X-ray tube. It corresponds to the highest possible photon energy within the emitted spectrum. The errors on the voltages of the X-ray tube are assumed to be neglectable. All R-series measurements are used as input to the characteristics network to predict the corresponding kVp-values. Their true values are listed in table 6.2. The blue curve of figure 6.30 illustrates the relative deviation of the predicted voltages $U_{\mathrm{kVp,pred}}$, and true voltages $U_{\mathrm{kVp,true}}$ via

$$\frac{U_{\mathrm{kVp,pred}}}{U_{\mathrm{kVp,true}}} - 1, \tag{6.17}$$

as a function of the mean energy of the initial spectra.

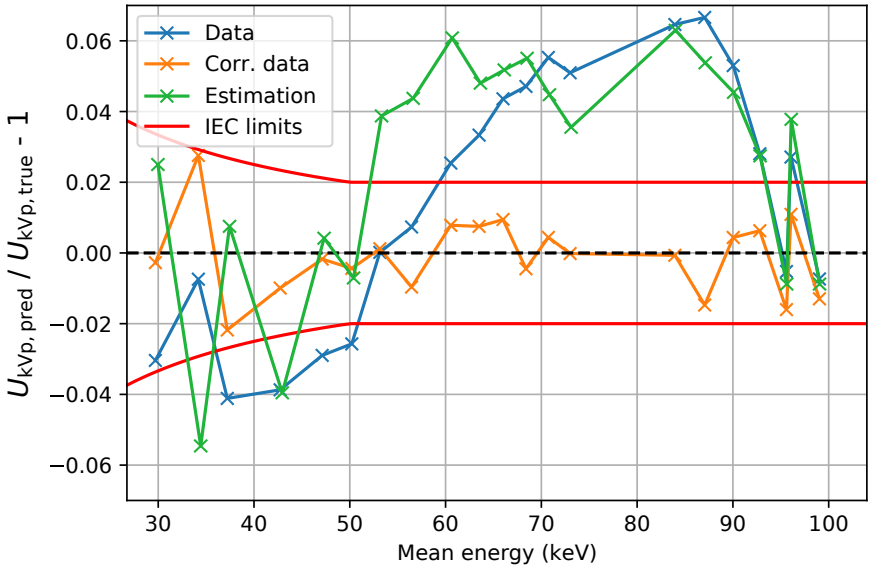

Figure 6.30.: The relative deviation of predicted and true kVp-values of the R-series spectra. The x-axis represents the mean energies of these spectra according to table 6.2. The green line corresponds to the directly estimated kVp values from data. The blue line shows the deviation for the predictions of the characteristics network from measurements. The orange curve resembles the predictions for the data corrected via equation (6.18). The red borders indicate the requirements of a kVp-meter according to IEC 61676 [79].

For mean energies below about 55 keV, the prediction underestimates the kVp-value. For higher mean energies, an overestimation is present. The deviations lie within a range of $[-4.1, 6.7]$ %. Under the assumption of a properly working characteristics network, an issue with the detectors' energy calibrations becomes apparent. The energy region and trends of the deviations correspond to the discrepancies observed for the deconvolution network in section 6.3.4. Here, also the reasons for the deviations are introduced.

A simple method to estimate the deviation of the energy calibration is introduced in the following. The data of the *Al* detector shown in the centre of figure 6.23 is compared to a threshold of $5 \cdot 10^{-4}$. Intersections with the threshold and the R-series measurements are determined. The threshold is not exactly 0 to neglect statistical noise. Under the consideration of a detector resolution σ of about 1.2 keV (see section 3.1.2 for more details), the intersections correspond to kVp-values $U_{\mathrm{kVp,data}}$. These values are compared to the true values $U_{\mathrm{kVp,true}}$ by taking their relative fraction, resembled by the green curve of figure 6.30. The deviation's trend closely resembles the

blue curve in figure 6.30. This approves that observed discrepancies in kVp are due to the energy calibration and are not introduced by the deconvolution network. The difference between the simple and the network method to determine the kVp-values is the available information. While the network employs all three detectors, leading to increased stability, only a single detector is used in the simplified approach. The red lines in figure 6.30 indicate the requirements for a kVp-measurement device according to IEC 61676 [79]. These limits are $\pm 1\,\mathrm{kV}$ for voltages greater than 50 kV and $\pm 2\%$ for voltages below. The predicted values of the characteristics network are not within these ranges. Under the premise that the detector simulation is accurate, the detectors' calibrations are corrected or refined in the following. This might additionally improve the prediction capabilities of the deconvolution network.

The goal of the recalibration is to scale the measurement spectra along their deposited energy axis to optimise the performance of kVp-prediction. The blue curve of figure 6.30 indicates three regions in mean energy where the relative deviations approximately follow linear trends. Carrying this over to the kVp-values, a correction function of the shape

$$E_{\mathrm{corr}}(E) = \begin{cases} A \cdot E & E < a \\ (E-a) \cdot B + A \cdot a & E \geq a \text{ and } E < b \\ (E-b) \cdot C + (b-a) \cdot B + A \cdot a & E \geq b \end{cases} \tag{6.18}$$

is defined. It describes the conversion from deposited energy E to corrected deposited energy E_{corr}. In a Nelder-Mead optimisation [43], energy corrections according to equation (6.18) are performed on the R-series measurements. kVp-predictions with the determined spectra are made, and the mean squared error of predicted and true kVp-values is minimised. This results in the parameters listed in table 6.5.

Parameter	Value
a	58.199 keV
b	114.127 keV
A	1.030
B	0.814
C	3.914

Table 6.5.: The parameters of the energy correction function (6.18) depicted in figure 6.31. The parameters were optimised via Nelder-Mead [43], which minimised the relative deviation of predicted and true kVp-values for the R-series measurements.

Inserting the optimised parameters in equation (6.18) provides the conversion curve from measured deposited energy to corrected deposited energy of figure 6.31. The parameters A, B, and C describe the slopes of the energy correction, indicating the quality of the detectors' energy calibrations. The closer the parameters are to 1, the

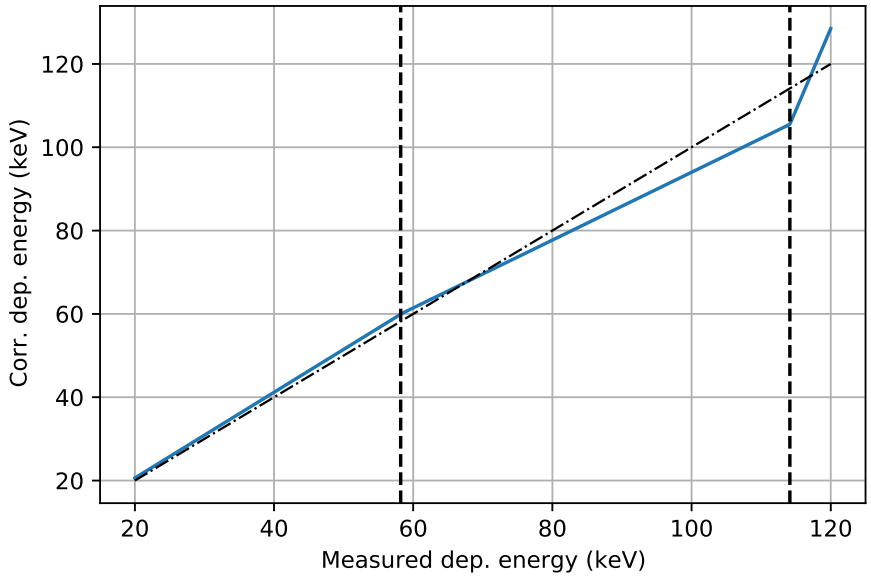

Figure 6.31.: The energy correction function (6.18) for the optimised parameters listed in table 6.5. The dashed lines are located at the parameter values a and b. These indicate the three regions of linear conversion with slopes of A, B, and C. The dash-dotted line represents a perfect calibration.

better. Since A fits well while B and C do not, it is apparent that calibration was only performed within a range of 60 keV. Within the energy region $E \geq a$ and $E < b$, the deviations between correction and measurement increases with the measured deposited energy E. The deviation in the calibration introduced in region $E < a$ is propagated and amplified for higher energies due to the linear part of the calibration function. The large deviation of C, describing the conversion for deposited energies greater than b, is due to the measurement's binning artefacts for shifted bins in Dosi-mode. A triangular cutoff close to the maximum energy of 120 keV is introduced as discussed in section 6.1.

The application of energy correction to the measurements of R0 to R19 spectra is depicted in figure 6.32. The colours of the curves indicate the filters of the detectors according to the legend. All spectra are normalised to their maximum each. The event-axis is scaled logarithmically to indicate the highest deposited energies of the spectra better. Solid lines represent the uncorrected spectra while dashed lines correspond to the corrected ones.

The orange curve in figure 6.30 shows that after energy correction, the prediction of the kVp-values of the measured R-series spectra is well within the limits of the IEC 61676 [79]. Since the recalibration is based on the optimisation of the kVp-prediction abilities of the network, an additional analysis with independent measurements is required in the future. A correctly scaled deposited energy axis is a necessity

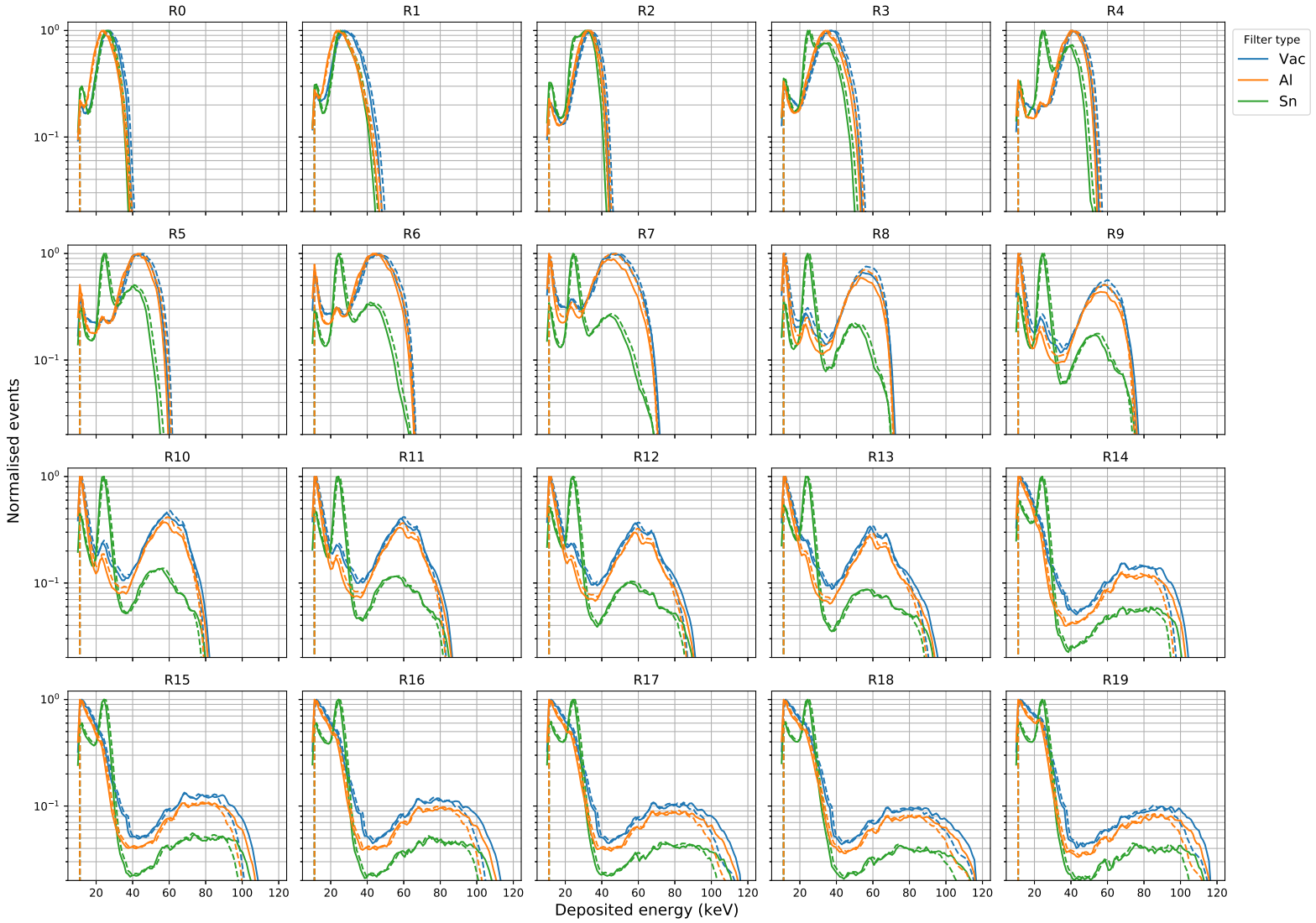

Figure 6.32.: Measurements of R-series spectra. The titles of the plots correspond to the codes according to table 6.2. The colours of the lines represent the filters of the Dosepix detectors, indicated by the legend. Solid lines represent uncorrected measurements and dashed lines the spectra after energy correction via equation (6.18). The y-axis, reflecting the number of registered events, is scaled logarithmically to visualise the curves' trends for high energies better.

when using the detectors for an application like spectroscopy. The determined energy correction function is also used in the following for the analysis of the remaining predicted characteristics of the X-ray tube spectra.

Half-value layer

The half-value layer describes the required thickness of a filter for the X-ray tube to reduce the photon spectrum's energy by 50%. Predictions of the HVL values d_{HVL} for Al and Cu are made for the R-series measurements via the characteristics network.

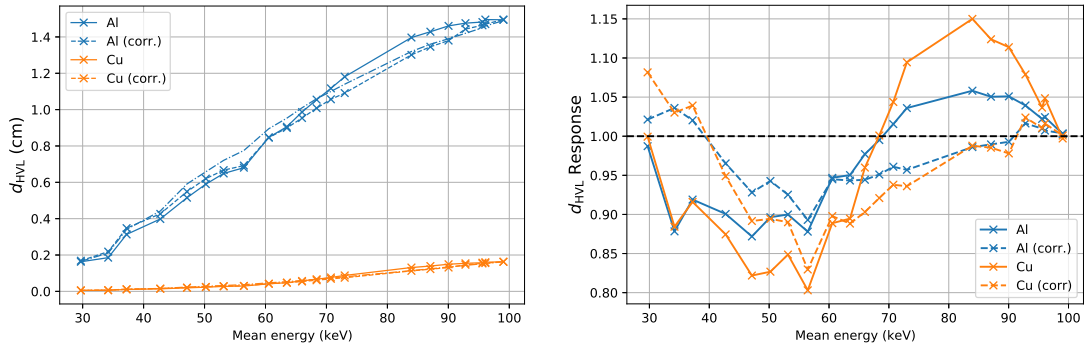

(a) Predicted and true half-value layer values

(b) Response of predicted and true half-value layer values

Figure 6.33.: (a) shows the actual and predicted values of the half-value layer d_{HVL} for Al and Cu for the R-series measurements. The x-axis corresponds to the mean energies of the spectra. (b) depicts the corresponding response, i.e. the fraction of predicted and actual values of the data in (a). Solid lines resemble original measurements, while dashed lines represent energy corrected data. A dash-dotted line indicates the actual half-value layer thickness in (a).

The determined values and their corresponding true values are depicted in figure 6.33 (a). (b) shows the response, i.e. the fraction of predicted and true values for the data in (a). The colours of the curves correspond to the filter materials according to the legend. Solid lines represent the original measurements' predictions and dashed lines the energy corrected measurements. The energy correction is executed as described in the previous section. Additionally, a dash-dotted line indicates the true values in (a). The uncorrected response curves in (b) show a similar trend to the kVp-values before. This indicates that the HVL is also affected by the discrepancies in the calibration of the detectors. The responses are flat after energy correction, especially for higher mean energies. Table 6.6 lists the mean value of all responses μ, the corresponding standard

deviation σ, and the root mean squared error in regards to the perfect response of 1

$$\sigma_{\mathrm{RMS}} = \sqrt{\frac{1}{N}\sum_{i}^{N}(R_i - 1)^2}, \tag{6.19}$$

where R is the response $\frac{d_{\mathrm{HVL,pred}}}{d_{\mathrm{HVL,true}}}$ and N is the number of measurements. Additionally, the minimum and maximum responses are included.

HVL material	μ	σ	σ_{RMS}	min.	max.
Al	0.971	0.0636	0.067	0.872	1.058
Al (corr.)	0.973	0.038	0.046	0.893	1.036
Cu	0.972	0.107	0.11	0.803	1.15
Cu (corr.)	0.957	0.064	0.077	0.83	1.081

Table 6.6.: The statistical quantities for the responses of the half-value layer values of figure 6.33 (b) for different filter materials. Included are the mean response μ, the corresponding standard deviation σ, the mean squared error σ_{RMS} in regards to the perfect response of 1 according to equation (6.19), and the minimum and maximum responses.

The table's values show that the means of the responses are slightly underestimated on average. After energy correction, the standard deviation is reduced by about 40% for both filter materials. σ describes the deviation from the mean, σ_{RMS} from the perfect response of 1. The energy correction leads to a reduction of σ_{RMS} of about 3% for both filter materials. All responses lie in the range of $[0.803, 1.15]$ for uncorrected measurements and $[0.83, 1.081]$ for corrected measurements. Since values are underestimated on average, a correction factor can be introduced to create a more symmetric systematic deviation. The uncertainties are then confined within 10% for the HVL of aluminium. These results are comparable to modern quality assurance devices like the RaySafe X2 [80] and the NOMEX Multimeter [81]. Both can determine HVL with a precision below 10% for values of up to about 14 mm aluminium. The results of the Dosepix system are promising but additional measurements are required to thoroughly analyse its capabilities, including higher X-ray tube voltages and different irradiation angles.

Conversion factors from fluence to air kerma and dose equivalents

The conversion factors from fluence to air kerma and dose equivalents represent the harm of an X-ray tube's spectrum to an exposed human. The corresponding dose values are provided by multiplying these factors with the photon fluence Φ. The true and predicted factors for the R-series measurements are depicted in figure 6.34 (a). The x-axis corresponds to the mean energies of the photon spectra. (b) shows

the response, i.e. the fraction of predicted and true conversion factors. The colours indicate the type of the dose-factors. Solid lines correspond to the predictions of original measurements and dashed lines to the energy-corrected measurements. The dash-dotted lines in (a) additionally indicate the true values of the dose conversion factors.

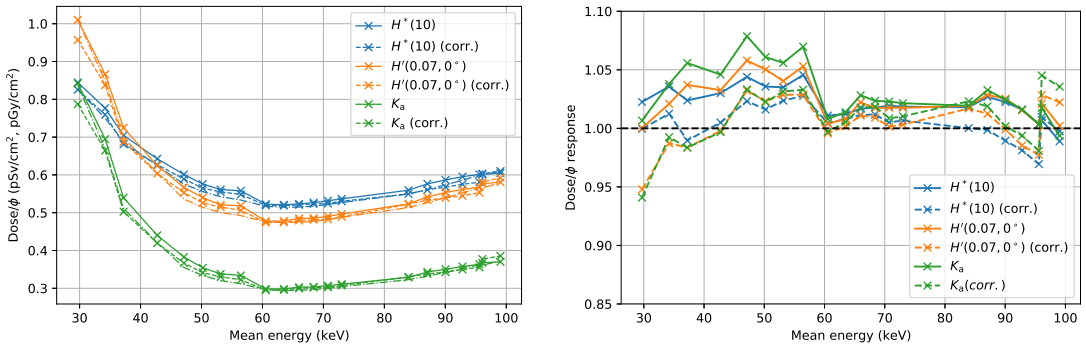

(a) Predicted and true dose conversion factors

(b) Response of predicted and true dose conversion factors

Figure 6.34.: (a) shows the trend of predicted and true dose conversion factors for the R-series measurements. The x-axis corresponds to the mean energies of the X-ray tube spectra. (b) depicts the response, i.e. the fraction of predicted and true doses of (a). The colours represent the dose types according to the legends. Solid lines correspond to the predictions of original measurements, dashed lines to energy corrected measurements. Additionally, a dash-dotted line representing the true values is present in (a).

The responses in (b) resemble the prediction qualities of the network. All dose-types show a similar trend. The responses are the best for mean energies close to about 65 keV. For higher and lower energies, the dose conversion factors are overestimated in the prediction. This issue is explained by the trend of the true dose conversion factors illustrated in figure 6.26. Here, the minima of the curves are also in the region of about 65 keV. If the mean energy deviates due to irregularities in the energy calibration, the dose conversion factor is overestimated. This is also indicated by the statistical quantities of the response curves listed in table 6.7. These include the mean responses μ, the corresponding standard deviations σ, the root mean squared errors in regards to the optimal response of 1, σ_{RMS}, defined by equation (6.19), and the minimum and maximum responses. The prediction slightly overestimates the mean responses for all dose conversion factor types. For dose measurements, underestimations are more dangerous as possible damages due to an exposure to the bearer of a dosemeter are understated. The energy correction does not influence deviation σ much but improves σ_{RMS}. For $H^*(10)$, $H'(0.07)$ and K_{a} the improvements of σ_{RMS} are

Dose type	μ	σ	σ_{RMS}	min.	max.
$H^*(10)$	1.021	0.013	0.025	0.989	1.046
$H^*(10)$ (corr.)	1.004	0.014	0.014	0.969	1.028
$H'(0.07)$	1.024	0.016	0.029	1.000	1.058
$H'(0.07)$ (corr.)	1.004	0.020	0.021	0.948	1.032
K_{a}	1.030	0.022	0.038	0.994	1.079
K_{a} (corr.)	1.009	0.023	0.025	0.941	1.045

Table 6.7.: The statistical quantities of the dose response curves of figure 6.34 (b) for the R-series measurements. Included are the mean responses μ, the corresponding standard deviations σ, and the root mean squared errors in regards to the perfect response of 1, σ_{RMS}. Additionally, the minimum and maximum responses are listed.

44%, 27.6%, and 34.2%. The minimum and maximum deviations for all dose conversion types are within the limits of $[-1.1\%, 7.9\%]$ for uncorrected and $[-5.9\%, 4.5\%]$ for corrected measurements. Under the assumption that photon fluence can be determined with perfect accuracy, the error on the estimated dose corresponds to the error of the dose conversion factors.

6.5 Energy corrected spectrum deconvolution

The energy correction of equation (6.18) is applied to the input data of the deconvolution network to evaluate the R-series measurements. Figure 6.35 illustrates the predicted photon spectra $f_{\mathrm{pred}}(E)$ for an uncorrected (a) and corrected (b) input as dashed lines. The solid lines represent the corresponding simulations $f_{\mathrm{true}}(E)$.

The colours of the lines represent the indices of the R-series spectra according to the colour bar. The bottom plots depict the relative deviation of true spectra $f_{\mathrm{true}}(E)$ and predicted spectra $f_{\mathrm{pred}}(E)$ according to equation (6.9). The agreements of the energy corrected predictions are improved compared to the uncorrected predictions, especially for energies close to the kVp-values of the spectra. Here, the relative deviations of the energy corrected prediction have a positive sign. Small peaks are discernible, indicating slight underestimations of kVp. Their amplitudes are reduced in comparison to the uncorrected predictions. For the rising parts of the spectra, the relative deviation of uncorrected and corrected predictions is similar. The correction shows a small improvement for spectra with lower mean energies.

The median of the relative deviations of figure 6.35 is used to quantify the benefit of the energy correction. The median instead of the mean is chosen as mainly the deviation in the spectra's central regions is concerned, i.e. excluding the rising parts and the values close to the kVp-values. The median relative deviations for corrected and uncorrected predictions are depicted as a function of the R-series spectra's mean

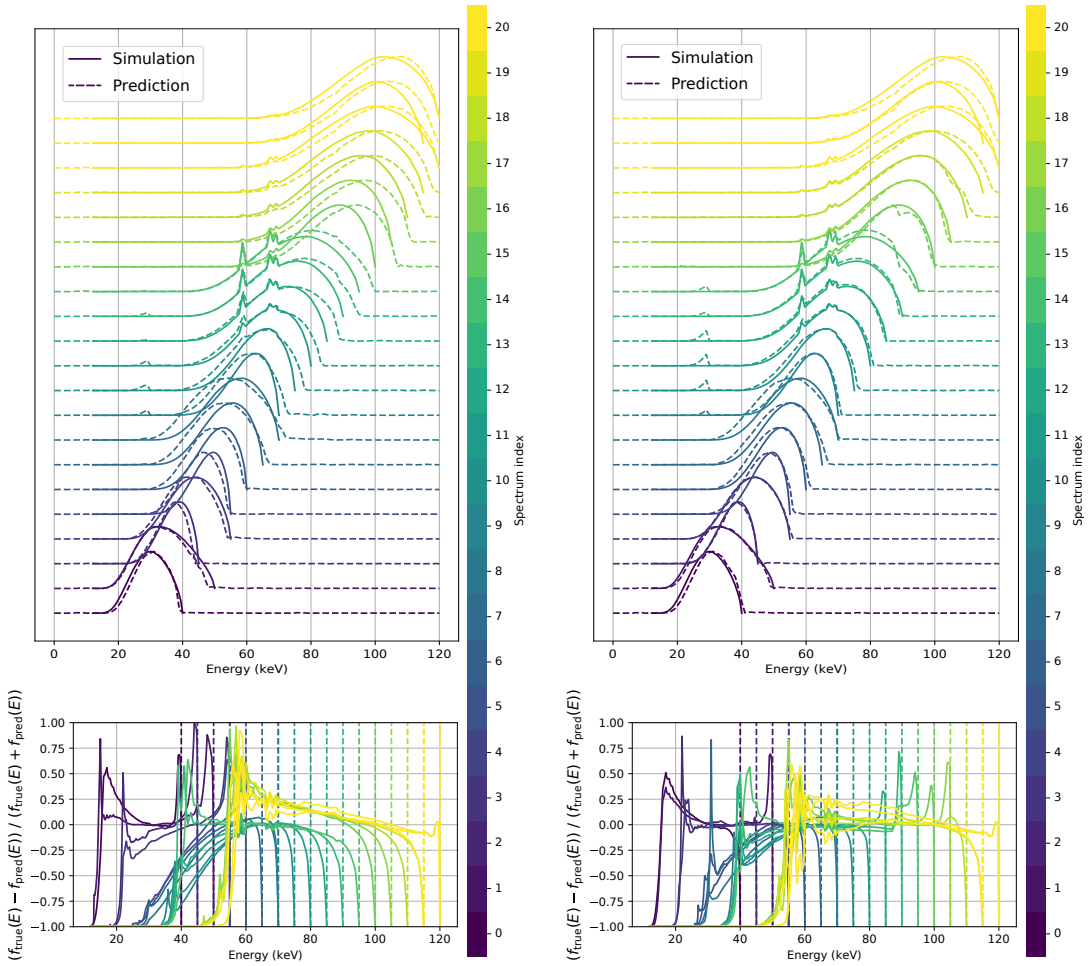

(a) Without energy correction

(b) With energy correction

Figure 6.35.: The predictions of the deconvolution network for R-series measurements. For inputs without energy correction in (a) and with energy correction in (b). The dashed lines represent the predicted photon spectra $f_{\text{pred}}(E)$ and the solid lines the true spectra $f_{\text{true}}(E)$ obtained from simulations. The colour of the curves corresponds to the index of the R-series spectra according to the colour bar. The bottom plot shows the relative deviation of true spectra $f_{\text{true}}(E)$ and predicted spectra $f_{\text{pred}}(E)$ calculated via equation (6.9).

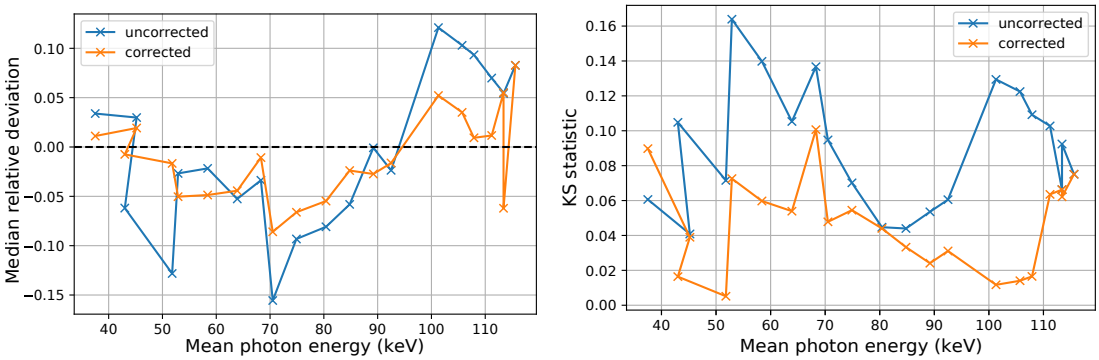

(a) Median relative deviation

(b) Kolmogorov-Smirnov statistic

Figure 6.36.: (a) shows the median of the relative deviations of the curves in the bottom plots of figure 6.36 for uncorrected and corrected predictions. The x-axis corresponds to the mean energies of the R-series spectra. (b) shows the Kolmogorov-Smirnov statistic according to equation (6.10) for the same data as in (a).

energies in figure 6.36 (a). The small peaks in the regions of about 25 keV of the top plots in figure 6.35 are excluded. These are predicted due to Sn-fluorescences of the surroundings in the measurements and would lead to a falsification of the curves of figure 6.36 (a). The median relative deviation shows an improvement for almost all of the R-series spectra.

Additionally, a Kolmogorov-Smirnov test is made to analyse the agreement of simulations and predictions. A description of the test is established in section 6.3.4. The Kolmogorov-Smirnov statistic for the corrected and uncorrected predicted spectra regarding the simulation is depicted in figure 6.36 (b). The null hypothesis that two samples, one from a simulated and one from a predicted spectrum, originate from a common distribution is made. The hypothesis is rejected for a level of $\alpha = 5\%$ if the Kolmogorov-Smirnov statistic exceeds the limit $D_\alpha = 0.175$, calculated via equation (6.11). For all evaluated spectra, the null hypothesis is accepted. Additionally, an improvement of the statistic for almost all R-spectra is present, corresponding to the median relative deviation of figure 6.36 (a). In conclusion, the deconvolution network with energy correction applied can precisely predict photon spectra from measurements.

6.6 Photon fluence estimation

The previous sections described the estimation of the shape of a photon spectrum of an X-ray tube. The corresponding photon fluence is estimated in the following. Using this result to scale the determined shape allows to fully describe the spectrum. The

photon detection efficiencies ε of the Dosepix detectors with different filters installed are known from simulation. The efficiencies describe the fraction of registered events N and photon fluence Φ as a function of energy E, i.e.

$$\varepsilon(E) = \frac{N}{\Phi}(E), \tag{6.20}$$

depicted for the filtered Dosepix detectors in figure 6.15. The photon fluence Φ for N_{tot} registered events can be calculated by using the spectrum $f(E)$ predicted via the deconvolution network and the relation

$$\begin{aligned} \frac{N_{\text{tot}}}{\Phi} &= \frac{\int \mathrm{d}E\, \varepsilon(E) \cdot f(E)}{\int \mathrm{d}E\, f(E)} = \\ \Leftrightarrow \quad \Phi &= N_{\text{tot}} \cdot \frac{\int \mathrm{d}E\, f(E)}{\int \mathrm{d}E\, \varepsilon(E) \cdot f(E)}. \end{aligned} \tag{6.21}$$

Here, the efficiency $\varepsilon(E)$ corresponds to the detector which registered N_{tot} events. Instead, a direct approach with a new convolutional network is made to circumvent possible errors introduced by the deconvolution network. Effectively, this network will then predict a measure proportional to the inverse of the convolution of the photon detection efficiency $\varepsilon(E)$ and a photon spectrum $f(E)$.

There are multiple applications of the predicted photon fluence information. The standard procedure to estimate dose with Dosepix detectors is to calculate a weighted sum of registered events in Dosi-mode and corresponding dose conversion factors. The predictions of the networks require a different approach. The characteristics network predicts the conversion factors from fluence to dose $\frac{D}{\Phi}$. A combination with the predicted fluence Φ allows an estimation of the doses D. Via this method, details about the dose-prediction with Dosepix are revealed, helping to break down the contributions of dose conversion factors $\frac{D}{\Phi}$ and fluence Φ.

Another application of fluence estimation is its combined use with the spectrum deconvolution. The prediction of the initial photon spectrum only returns the shape of the energy distribution, which can then be scaled along the y-axis to represent photon fluence Φ.

6.6.1 Network design

The neural network takes the measured response spectra of three Dosepix detectors as its input. The detector setup depicted in figure 6.9 is used. Instead of predicting the fluence directly, attention about the normalisation of the input and output data is required. The input spectra's distributions should be normalised in the same way, as a bias is introduced otherwise. Each input spectrum is normalised to its sum, denoted by N. Since the input is normalised by N, the corresponding fluence has to be normalised with the same factor so the network will output the normalised fluence $\hat{\Phi} = \frac{\Phi}{N}$. This eliminates the dependence on the number of registered events while

the dependence on the photon spectrum remains. After predicting $\hat{\Phi}$, fluence Φ is obtained by multiplying it with the number of registered events N.

For the estimation of the normalised fluence $\hat{\Phi}$ an independent convolutional neural network is used. Instead of predicting a single value, the normalised fluence for each detector is predicted independently. The output of $\hat{\Phi}$ for each detector allows for agreement studies of measurements and simulations for the differently filtered Dosepix detectors. The three detectors' results are combined in a sum by weighting them with the corresponding relative number of registered events. This decreases the influence of detectors with a large statistical error.

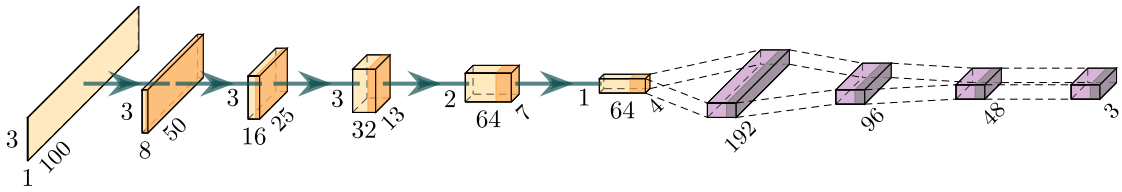

Figure 6.37.: The convolutional neural network for the determination of three normalised fluences, each corresponding to a Dosepix detector. The input consists of the concatenation of the detectors' response spectra corresponding to measurements of an X-ray tube. Yellow blocks represent convolutional layers, and purple blocks dense layers. Dark regions at the ends of the blocks indicate the usage of activation functions. The image is created using [58].

Figure 6.37 depicts the convolutional neural network's design for the prediction of the normalised fluences. The input consisting of three concatenated Dosepix response spectra is followed by five convolutional layers, represented by yellow blocks and using same-padding each. The first three layers have kernel sizes of 3 x 3, to find correlations in the data of the three detectors. This helps to establish internal representations of photon spectra, related to the desired fluence output via equation (6.21). The dimension along the bins is halved from layer to layer by utilising a stride size of 2. Additionally, the filter-size is doubled. The activations of the last two layers are combined along the detector dimension. Afterwards, the layer is flattened, and its dimension is reduced by 4 dense layers, shown in purple, to the final output size of 3. All layers use a ReLU-activation function, except the last one, which uses an absolute function to ensure positive values.

6.6.2 Training and validation data generation

The basis of the training dataset is the same as the ones used for the deconvolution- and characteristics networks before. The input data consists of the three Dosepix response spectra, while the labels comprise the normalised fluences. The initial photon spectra $f(E)$ are used to calculate the corresponding fluences Φ via equation (6.21).

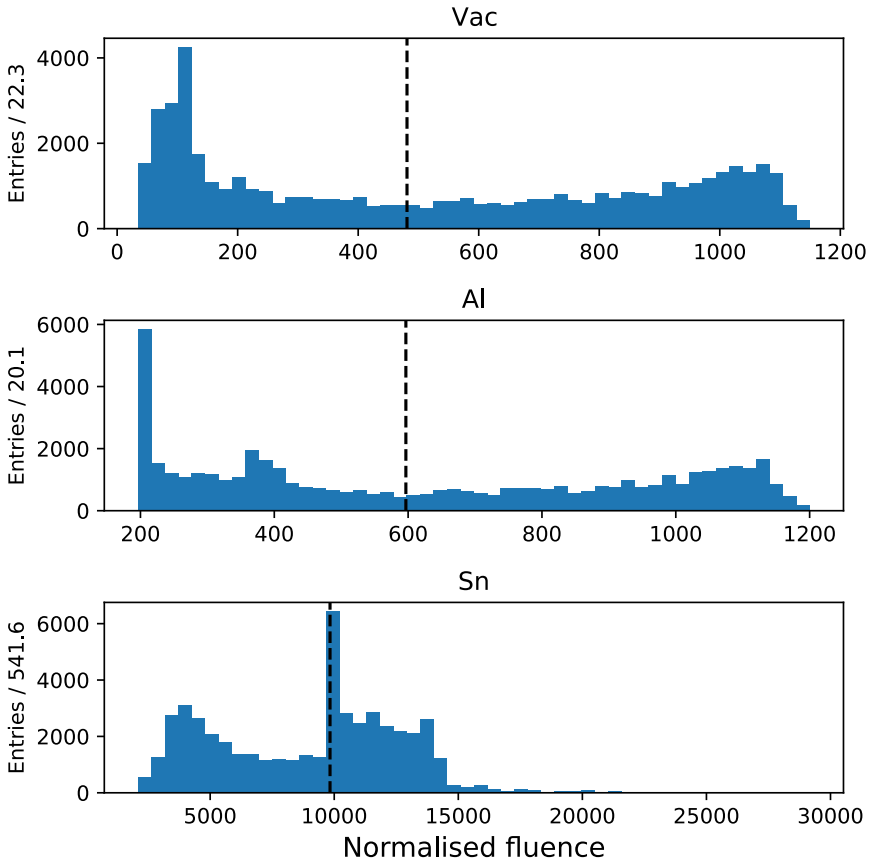

Figure 6.38.: The distributions of the normalised fluences $\hat{\Phi}$ of the label data for 50k samples of the validation dataset. The titles of the plots correspond to the filters of the Dosepix detectors. The dashed lines indicate the mean values of the distributions.

The response spectra are normalised to their number of registered events each. These normalisation factors are applied to the fluence, providing the normalised fluences $\hat{\Phi}$ for each detector representing the label. The distributions of $\hat{\Phi}$ are depicted for 50k samples of the validation dataset in figure 6.38. The titles of the plots correspond to the filters of the Dosepix detectors. Dashed lines represent the mean values of the distributions listed in table 6.8.

The labels are also normalised with the means μ of their distributions to reduce biasing of the network. After prediction, the normalisation factor has to be applied to provide the actual value. The distributions for the *Vac* and *Al* detectors are similar in shape, as the Al filter's attenuation mainly impacts low energy photons. The distributions of figure 6.38 mostly differ for low normalised fluences. The minimum values of the *Al* detector are larger than the ones of the *Vac* detector. This is due to

Dosepix type	μ (1 / cm^2)
Vac	460.67
Al	595.75
Sn	9840.37

Table 6.8.: The mean normalised fluences μ of the distributions of figure 6.38 for the different Dosepix detector types. The types correspond to the filters of the detectors.

the number of registered events N, which is lower, the higher the filter's attenuation. This is evident for the *Sn* detector whose normalised fluences are larger than those of the other detectors, also reflected by the mean μ of the distribution.

6.6.3 Training process

The datasets consist of 800k samples for training and 150k samples for validation. The batch size is set to 1024 samples. A mean squared error $\mathcal{L}_{\text{MSE}}$ is used as loss function. Figure 6.39 depicts L_{MSE} for training and validation of the network for five epochs.

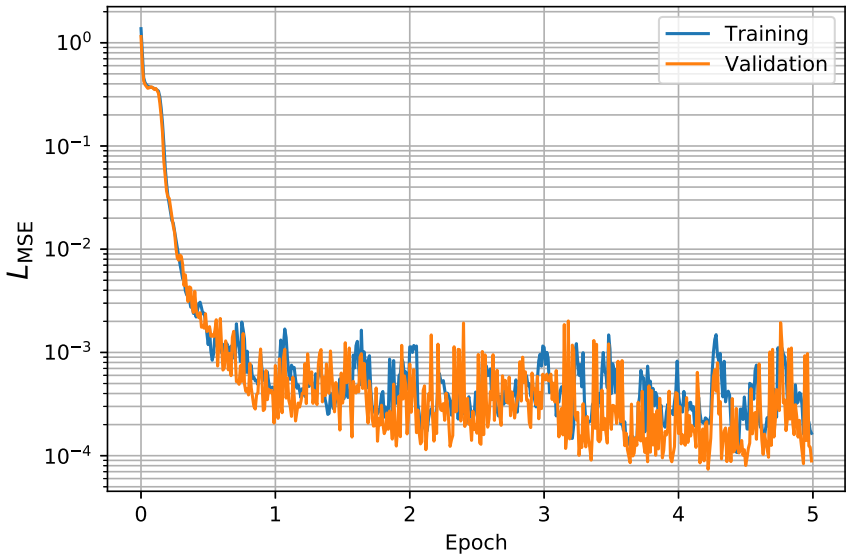

Figure 6.39.: The mean squared error L_{MSE} as a function of epochs for the training and validation of the network to determine normalised fluences $\hat{\Phi}$.

The network converges like expected and shows no signs of overfitting. After the training, the predictions of the network are validated. Figure 6.40 (a) depicts the ratio X of the predicted and true normalised fluences, i.e. $X = \frac{\hat{\Phi}_{\text{pred}}}{\hat{\Phi}_{\text{true}}}$, for the three detectors.

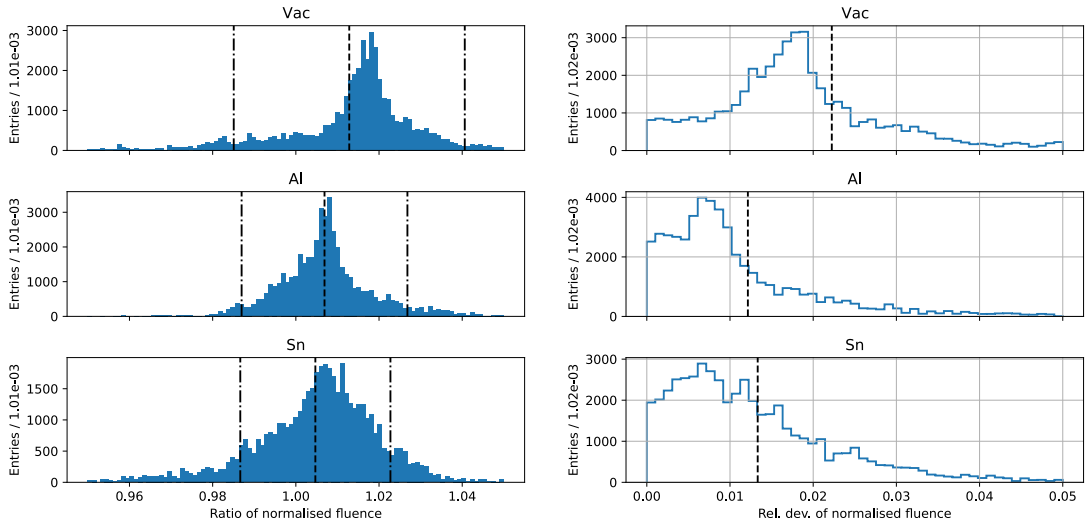

(a) Ratio X of predicted and true values

(b) Relative deviation of predicted and true values

Figure 6.40.: (a) depicts the ratio of predicted and true normalised fluences $X = \frac{\hat{\Phi}_{\text{pred}}}{\hat{\Phi}_{\text{true}}}$ for each detector. (b) shows the relative deviation to the perfect response, $|X - 1|$. The titles of the plots indicate the filters of the detectors. Dashed lines represent the mean values of the distributions, and dash-dotted lines the corresponding standard deviations.

(b) shows the deviation from a perfect response defined as $|X - 1|$. The titles of the plots correspond to the filters of the Dosepix detectors. The dashed lines indicate the mean values of the distributions, the dash-dotted lines in (a) the corresponding standard deviations. The statistical quantities of the distributions are listed in table 6.9. μ and σ correspond to the means and standard deviations in (a). μ_{rel} denotes the means in (b).

Dosepix type	μ	σ	μ_{rel}
Vac	1.014	0.026	0.022
Al	1.007	0.016	0.012
Sn	1.005	0.016	0.013

Table 6.9.: The means μ and standard deviations σ for the distributions of the normalised fluences in figure 6.40 (a). The mean μ_{rel} corresponds to the distributions in (b). The values are denoted for the three Dosepix detectors, indicated by their filters.

The mean values μ reflect that the network slightly overestimates the normalised fluences. Similar to the prediction of the dose conversion factors before, an overes-

timation is considered to be more conservative regarding dose measurements. Here, the risk of undervaluing the harmfulness of irradiation of the bearer of a dosemeter is reduced. The standard deviations σ represent the deviations from the means μ, which are 1.6% and 2.6%. Since the values are not normally distributed, μ_{rel} gives a better representation of the deviation from the perfect response at 1. It shows deviations in a range of 1.2% to 2.2%. The distributions of the relative deviations of figure 6.40 (b) indicate that the responses mostly vary within a range of about 5%. In conclusion, the network is able to predict the fluence normalisation factors for all detectors with high precision.

6.6.4 Results

Since the prediction of the normalised fluences works well for validation data, the network's performance is tested with measurements. The previously introduced R-series spectra are used for this task (see section 6.3.4 for their definition). In the following, no energy correction is applied to the data as there is no significant influence on the network's predicted values.

Actual photon fluences are required to judge the quality of the predictions. These cannot be measured directly, and therefore, another measure is introduced - the air kerma rate. It is acquired via Dosimax Plus, a semiconductor detector for dosimetry applications made by IBA dosimetry [9]. Employing the RQX-sensor, air kerma with uncertainties below 5% according to IEC 61674 [82] are acquired. This detector is placed close to the Dosepix detectors to ensure irradiation with the same photon fluence. The devices must not shield each other from radiation which would falsify the measurements. The prediction via the network provides the normalised fluences $\hat{\Phi}$ for each Dosepix detector. These are multiplied with the number of registered events N per detector to provide the fluence Φ. Fluence Φ is multiplied with the conversion factor of fluence to air kerma $\frac{K_{\mathrm{air}}}{\Phi}$, depicted in figure 6.26, to determine the corresponding air kerma K_{air}. The factor predicted via the characteristics network is used, i.e. the air kerma prediction is independent of any external measures. The Dosepix detectors are irradiated for about 23 s in measurements. The value of K_{air} is divided by this time to obtain the air kerma rate $\dot{K}_{\mathrm{air}}$. It is possible to estimate the irradiation time via Dosepix itself, but the time resolution is limited by the readout time for a frame. Instead, a fixed time is used for the measurements as this increases the precision.

Figure 6.41 shows the predicted dose rates for each Dosepix, denoted by the filters in the legend, and those measured with Dosimax Plus, denoted as „True“, for the R-series measurements. The x-axis corresponds to the mean energies of the initial photon spectra. The predictions for the Dosepix measurements are named and coloured according to the legend. The dashed line is the weighted mean of the detector values,

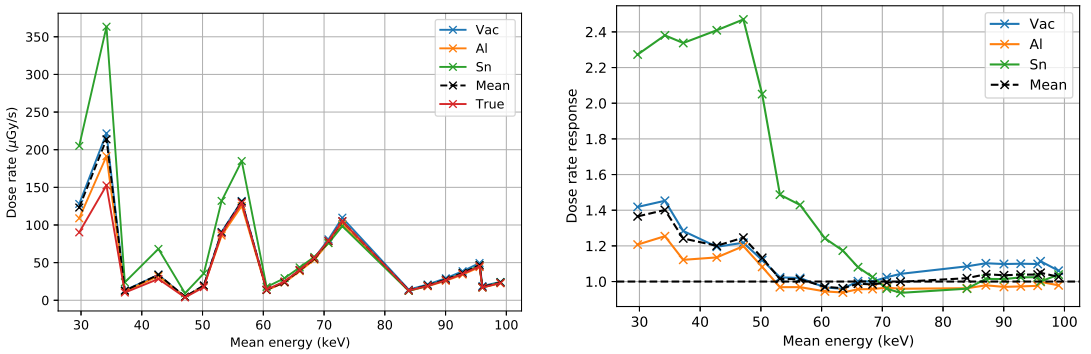

(a) Predicted and true air kerma rates

(b) Responses of predicted and true air kerma rates

Figure 6.41.: (a) depicts air kerma rates predicted via the network for R-series measurements. The x-axis corresponds to the mean energies of the initial photon spectra. The red curve reflects the actual rates measured with Dosimax Plus. The colours of the curves correspond to the filters of the Dosepix detectors according to the legend. The dashed line reflects the weighted mean of the dose rates of the detectors. (b) illustrates the fractions of the predicted and true air kerma rates. The dashed line corresponds to the perfect response of 1.

i.e. the air kerma rate

$$\dot{K}_{\text{air,mean}} = \frac{1}{\Delta t} \cdot \frac{\sum_i N_i \cdot \hat{\Phi}_i}{\sum_i N_i} \cdot \frac{K_{\text{air}}}{\Phi} \tag{6.22}$$

where index $i \in \{\text{Vac}, \text{Al}, \text{Sn}\}$ corresponds to the filters of the Dosepix detectors. Δt is the measurement duration, N_i are the registered events, $\hat{\Phi}_i$ are the predicted normalised fluences and $\frac{K_{\text{air}}}{\Phi}$ is the conversion factor from fluence to air kerma shown in figure 6.26. The responses in figure 6.41 (b) reflect the fractions of the predicted and actual values for the dose rates in (a). The predictions for the *Vac* and *Al* detectors show a good agreement while the *Sn* detector does not. The highest deviations are present for low photon energies for all detectors. If the network was designed to provide a single normalised fluence directly, each detector would have the same influence, which would lead to a large mismatch of predicted and actual values for small mean energies.

Statistical quantities for the responses are listed in table 6.10. μ reflects the mean responses with corresponding standard deviations σ. $\mu_{1/2}$ resembles the median. Additionally, the minimum and maximum responses are stated for the different Dosepix types corresponding to the filters of the detectors. The mean values μ indicate an overestimation of the predicted dose rates on average. The deviations from this mean are reflected by the standard deviations σ and strongly depend on the Dosepix type. The deviation for the *Sn* detector is about 4 to 6 times larger than for the *Vac* and *Al*

Dosepix type	μ	σ	$\mu_{1/2}$	min	max
Vac	1.098	0.131	1.114	0.960	1.453
Al	0.973	0.096	1.024	0.938	1.254
Sn	1.081	0.575	1.444	0.937	2.470
Mean	1.035	0.127	1.084	0.962	1.401

Table 6.10.: Statistical quantities of the air kerma rate responses for the R-series measurements of figure 6.41 (b). μ and σ reflect the means and corresponding standard deviations. $\mu_{1/2}$ represents the median. Also, the minimum and maximum responses are included. The Dosepix type corresponds to the filters of the detectors. The row labelled „*Mean*"denotes the weighted mean of the dose rates of all detectors.

detectors. These discrepancies for the *Sn* detector for low photon energies are mostly due to mismatches of the used filter in simulations and measurements. Even small variations in material density and thickness influence the number of registered events. The weighted mean of the air kerma rates $\dot{K}_{\text{air}}$ of the detectors is used. The corresponding responses lie within a range of $[0.962, 1.401]$. The systematic uncertainty of K_{air} has to be confined within 5% according to IEC 61674 [82]. The measurements with mean photon energies below about 55 keV exceed this limit, while data for the remaining energy range is within limits. The presented responses are calculated under the assumption of perfect Dosimax Plus measurements. However, these also underline uncertainties of $< 5\%$. Measurements with well-defined photon field qualities and simultaneous acquisitions of the corresponding air kerma have to be made to evaluate the Dosepix system's performance fully. An air kerma correction can be performed via the mean photon energy of a predicted spectrum of the deconvolution network using the air kerma response as a function of the mean photon energy of figure 6.41. Additional to air kerma, the doses $H^*(10)$ and $H'(0.07)$ can be calculated which will show similar responses as the conversion factors determined in section 6.4.5 varied only within 6%. The deviations are sufficiently small for dosimetry applications as the responses have to be confined within a range of $[0.71, 1.67]$ according to PTB [83].

In the following, the fluence is examined directly as a measure of the network's prediction performance. The predicted mean fluences are compared to those calculated from Dosimax Plus measurements. Dosimax provides the air kerma rate $\dot{K}_{\text{air}}$ which is transformed to fluence Φ via

$$\Phi = \dot{K}_{\text{air}} \cdot \Delta t \cdot \left(\frac{K_{\text{air}}}{\Phi} \right)^{-1} . \tag{6.23}$$

Here, Δt is the measurement duration and $\frac{K_{\text{air}}}{\Phi}$ the fluence to air kerma conversion factor calculated via the simulated X-ray tube photon spectrum and equation (6.12). Figure 6.42 (a) illustrates the results of the photon fluence predictions. Only the weighted

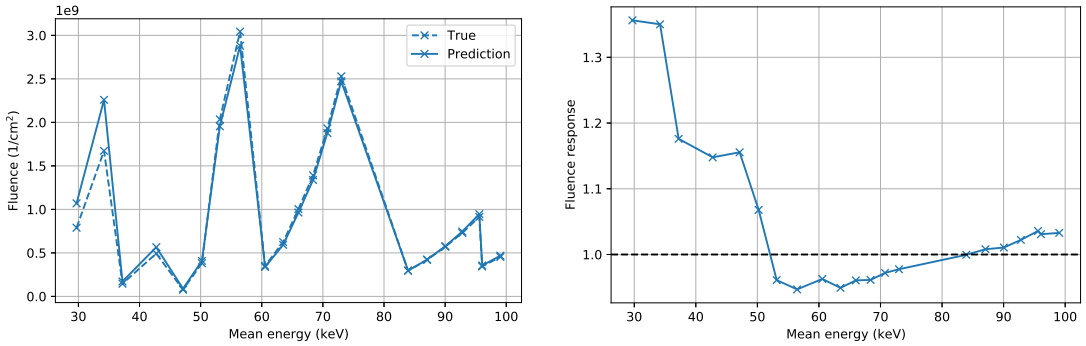

(a) Predicted and true fluences

(b) Response of predicted and true fluences

Figure 6.42.: (a) depicts the predicted and true fluences for the R-series measurements. True values, reflected by a dashed line, correspond to converted air kerma rate measurements of Dosimax Plus. The prediction, as solid line, represents the weighted mean of the predictions of the single Dosepix detectors. (b) resembles the response of predicted and true values in (a). The x-axes of the plots denote the mean energies of the photon spectra.

mean of the detectors is used. The dashed line, labelled „True“, corresponds to the values measured via Dosimax. (b) resembles the responses of the fluences in (a). The x-axes of the plots represent the mean energies of the R-series spectra. The trends of the curves are similar to those of figure 6.41 for the air kerma rates. The agreement of predicted and true values is best for mean photon energies greater 50 keV. The discrepancy increases with decreasing mean energy, leading to an overestimation of the predicted fluence. The statistical quantities of the responses in figure 6.42 (b) are listed in table 6.11.

μ	σ	$\mu_{1/2}$	min	max
1.052	0.118	1.011	0.947	1.356

Table 6.11.: Statistical quantities of the fluence responses of the R-series measurements of figure 6.42 (b). μ and σ are the mean and corresponding standard deviation. $\mu_{1/2}$ represents the median. Also, the minimum and maximum responses are included. Only the weighted mean of all detectors is considered.

The mean and median indicate a tendency of overestimation. All responses lie within a range of $[0.947, 1.356]$. Comparing these responses to the previously determined range for the air kerma rate of $[0.962, 1.401]$ shows that the deviations are similar. The error on the predicted dose almost entirely depends on the precision of the predicted normalised fluence. The results of the characteristics network for the dose

conversion factors only show small deviations from true values. As a consequence, the shapes of the simulated response spectra agree well with reality. The agreement of simulation and prediction of the deconvolution network further approves this. In the trainings of the characteristics and deconvolution networks, the number of registered events is never utilised as the inputs and outputs do not depend on this measure. This is different for the network predicting the normalised fluences. There is an overprediction of registered events, especially for low photon energies, which can be attributed to uncertainties in the simulated responses used in training. This was also observed in section 3.2.6.

The fluences provided from Dosimax Plus measurements are utilised to calculate the photon detection efficiencies ε of the Dosepix detector. They are a measure for the number of registered events N per photon fluence Φ according to equation (6.20). Figure 6.43 (a) depicts these measured efficiencies as solid lines, along with the efficiencies provided from simulations of mono-energetic radiation sources as dashed lines. The sources in measurements are broad spectra, and their mean photon energies are used to indicate the efficiencies. Therefore, their data can only approximately be compared to the simulated efficiencies for monoenergetic sources.

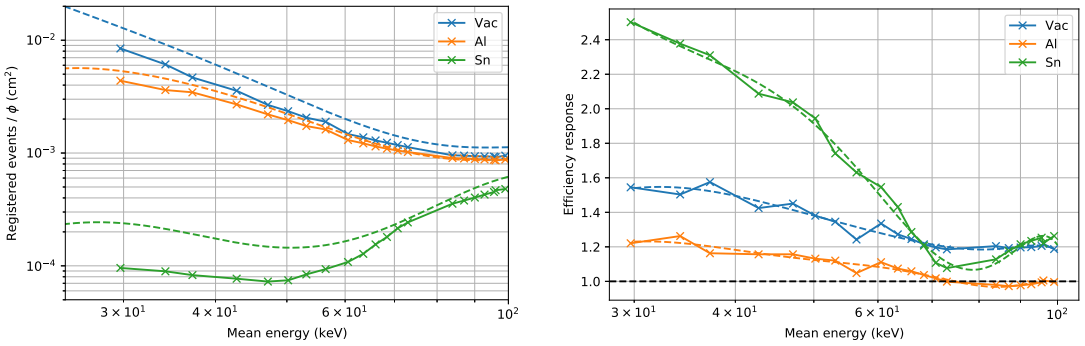

(a) Measured and simulated detector efficiencies

(b) Response of measured and simulated detector efficiencies

Figure 6.43.: (a) depicts the photon detection efficiencies ε according to equation (6.20). Solid lines represent measurements, dashed lines simulations. The colours correspond to the filters of the Dosepix detectors according to the legend. (b) shows the responses of the curves in (a), i.e. the fraction of measured and simulated efficiencies. The x-axes of both plots correspond to the mean energies of the R-series spectra.

Figure 6.43 (b) depicts the response, i.e. the fraction of measured and simulated efficiencies in (a). The dashed line additionally indicates a perfect response of 1. The trend of the measured and simulated efficiencies is similar. There is an offset between the curves that increases with decreasing mean photon energy. The responses for energies greater than 60 keV are almost flat and show a good agreement. There are

discrepancies in the simulation for photons of lower energies. This energy range is challenging to model in the simulation as any material attenuates low energy photons. Slight deviations in thickness of an object lead to large differences in the detectors' registered events. The measurements of figure 6.43 can be utilised to adjust the training data to calibrate the network in regards to fluence prediction. This correction has to be applied in the generation of simulated responses by using modified photon detection efficiencies. A different approach is to use the determined relation of photon fluence and mean photon energy of figure 6.42. Via the mean energy of the predicted photon spectrum $f(E)$, the predicted fluence can be corrected.

6.7 Conclusion

The goal of this chapter was the deconvolution of X-ray tube spectra. Deposited energy spectra measured with a setup consisting of three Dosepix detectors are used to determine a corresponding initial photon spectrum of an X-ray tube. This was achieved by implementing various methods. First, the detectors are operated with shifted bins in Dosi-mode. Using this technique, a dead-time free measurement of deposited energy spectra is possible. However, this approach results in a slightly worse energy resolution in comparison to ToT-mode, which was considered in the simulation. Detector responses for various photon spectra were simulated. They were generated by varying the current and voltage of an X-ray tube and applying filters of different materials and thicknesses. The simulated data were used to train a convolutional neural network. Its task is to determine the photon spectrum from measurements. Simulations of the X-ray tube spectra were compared to the output of the network. Good agreement was achieved for tube voltages of up to about 60 keV. For larger voltages, discrepancies between simulations and predictions were present due to inaccuracies in the energy calibrations of the detectors of the setup. Another neural network predicting characteristics of a photon spectrum was trained. These characteristics include the kVp-value, i.e. the voltage set on the X-ray tube. A function was optimised to perform an energy correction by rescaling the input spectra's deposited energy axis to determine proper kVp-values. This rescale-function was used to correct the inputs of the deconvolution network, which then was able to predict photon spectra in good agreement with the simulation for the used voltage range of 40 keV to 120 keV.

The outputs of the networks to determine the photon spectra's characteristics include the half-value layer, conversion factors from photon fluence to dose equivalents, and photon fluence. The results are promising, especially when using the kVp-corrected input spectra. The deviations of the responses for HVL lie within a range of 10% for aluminium and 20%, those for the conversion factors within 6%. For the determination of photon fluence, discrepancies for lower photon energies are present. The fluence was determined for each detector separately at first. The responses strongly depend on the used filter material of a detector. The values were combined and

weighted with the number of registered events. The determined deviation for the photon fluence response lies within a range of 5% for mean photon energies greater about 55 keV. For lower energies, the deviation increases, revealing a mismatch in the number of registered events for simulation and measurements. As established in chapter 3, this is mainly due to the difficulty to simulate Dosepix responses for low energy photons. The agreement for the conversion factors from fluence to dose is good and mostly depends on the agreement of the shape of the deposited energy spectra. Therefore, it is concluded that the simulation resembles the shape correctly but not the photon fluence for low energies. A method was introduced to determine the photon detection efficiency of Dosepix from measurements. Applying this method, a correction of the efficiency is possible, ultimately leading to a correction of the measured fluence. The performance of the networks in regards to the mean energies of various photon spectra was analysed. The determined responses in combination with the predicted mean energy from the characteristics network can also be used to perform corrections.

In summary, a system of Dosepix detectors is able to determine various characteristics of a photon spectrum. The measurement duration can be short due to the dead-time freeness of the detectors. The characteristics include the photon fluence, half-value layers, and various doses. These results are comparable to established quality assurance systems. Additional measurements and analyses of the Dosepix system are required to prove this further. However, the proposed system's unique feature is its ability to reconstruct the shape of the input spectrum scaled with the corresponding photon fluence. Since the resulting detector setup is small, it is easily applicable in quality assurance of an X-ray tube or to characterise unknown sources.

CHAPTER 7

Dosepix characteristics for high photon flux conditions

Contents

Previous chapters involved the operation of Dosepix in low flux photon fields. It was established that the detector operates well under these conditions. However, there are indications for problems when dealing with high photon flux. Under these circumstances, the detector's event rate reaches levels where pulses in the analogue electronics superimpose, leading to so-called pile-up. Methods are introduced to model this unwanted effect. This requires a thorough understanding of the analogue hardware of Dosepix and a calibration method to describe the behaviour of an individual detector accurately. The model is evaluated via low photon flux measurements and applied to high flux data afterwards. It reveals that the analogue electronics' threshold or baseline voltage is shifting as the detector's event rate increases. This variation is analysed, and a correction method is implemented by changing the threshold level. Increasing the photon flux even further reveals an issue of I_{krum} variation. Its change is analysed and applied in simulations to increase the agreement to measurements. High photon flux capabilities are important for dosimetry with pulsed photon fields and especially for the previously introduced spectroscopy of X-ray tubes. This chapter concerns a description of Dosepix at hardware level. A thorough understanding of the detector's inner workings is established, allowing to judge applicability to measurements. Additionally, the introduced threshold correction allows for measurements with a minimsed distortion of a registered spectrum.

7.1 Analogue circuit and pulse shape model

A mathematical model is required to describe the voltage levels within the analogue electronics of a pixel of a Dosepix detector. Section 2.1.1 provides a brief introduction of these signals. The analogue circuit depicted in figure 7.1 is described in the following. The schematic is based on the design established in [5], which itself is based on the concept for a pixel detector introduced in [84]. Some simplifying changes are applied to the original design. The circuit's polarity is mirrored and works with positive signals which is easier to present and interpret. The leakage current compensation is exchanged with an analogous constant current source of $\frac{I_{\mathrm{krum}}}{2}$. This exchange is reasonable under the assumption that the compensation works correctly at all time. An additional filter section is added to model undershoots of pulses like observed in simulations of Dosepix [5].

The names introduced within the schematic of figure 7.1 are used in the following. The goal is a function which returns an output voltage $U_{\mathrm{out,filt}}$ for an input signal at U_{in} as a function of time. $U_{\mathrm{out,filt}}$ represents the analogue pulse shape signal. It is compared to a threshold voltage U_{THL} to determine the corresponding ToT values. The main parts of the circuit are a charge sensitive amplifier which integrates the current at the input via capacitor C_{f}, a constant current I_{krum} which discharges this capacitor, and a filter section attached to U_{out} which describes the undershoots of the pulse shapes.

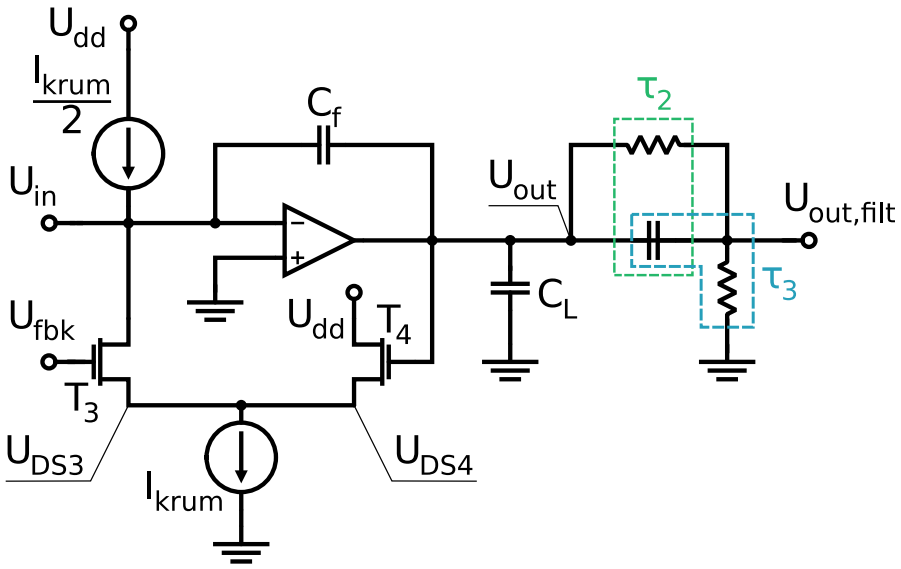

Figure 7.1.: The schematic of a charge sensitive amplifier corresponding to the analogue electronics of Dosepix. All notations correspond to the equations in the text. Close to the output, resistors and capacitors are described by combining their values to time constants τ indicated by the bounding boxes. The circuit is based on [5, 84].

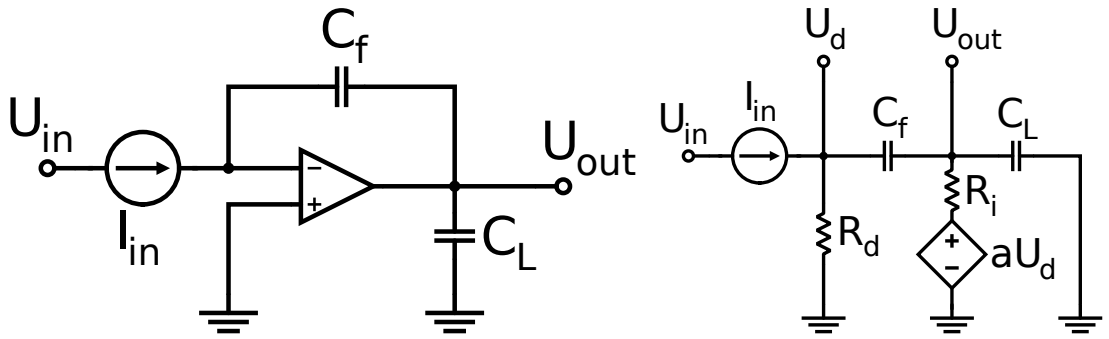

(a) Op-amp section

(b) Op-amp equivalent circuit

Figure 7.2.: (a) represents the op-amp section of the schematic of figure 7.1. (b) shows the corresponding equivalent circuit [85]. A detailed explanation is presented in the text.

Figure 7.2 (a) shows the functioning of the op-amp section of the charge sensitive amplifier. It is described by using the equivalent circuit diagram of figure 7.2 (b) [85]. U_d represents the voltage at the negative input of the op-amp with an input resistance of R_d. The op-amp is assumed to be ideal, which means this resistance is infinite and can be neglected. The internal resistance at the output is named R_i. The op-

amp amplifies the voltage U_d by a factor a, called the gain, indicated by the constant voltage source aU_d. A load capacitance C_L at the output of the op-amp is present. A current I_d is provided by aU_d, described via

$$I_\mathrm{d} = \frac{aU_\mathrm{d}}{R_i}. \tag{7.1}$$

The currents cancel each other at their common knot, corresponding to

$$I_\mathrm{d} = I_\mathrm{in} + I_\mathrm{L} + I_\mathrm{out}. \tag{7.2}$$

Under the assumption that the output is not drawing any current, i.e. that it is buffered from the filter section in-between U_out and $U_\mathrm{out,filt}$, depicted in the schematic of figure 7.1, $I_\mathrm{out} = 0$. The voltage U_f at capacitor C_f is described via two relations. First, it resembles the difference of the potentials of U_d and U_out. Second, C_f is charged or discharged via input current I_in. This results in equation

$$U_\mathrm{f} = U_\mathrm{out} - U_\mathrm{d} = \int \mathrm{d}t \frac{I_\mathrm{in}}{C_\mathrm{f}}. \tag{7.3}$$

Equations (7.2) and (7.3) together with the relation of the current through capacitor C_L, $I_\mathrm{L} = C_\mathrm{L}\frac{\mathrm{d}}{\mathrm{d}t}U_\mathrm{out}$ [86], are combined to yield

$$\begin{aligned} I_\mathrm{d} &= I_\mathrm{in} + I_\mathrm{L} \\ \Leftrightarrow \quad \frac{aU_\mathrm{d}}{R_\mathrm{i}} &= I_\mathrm{in} + C_\mathrm{L}\frac{\mathrm{d}}{\mathrm{d}t}U_\mathrm{out} \\ \Leftrightarrow \quad \frac{a}{R_\mathrm{i}}\left(U_\mathrm{out} - \int \mathrm{d}t\, \frac{I_\mathrm{in}}{C_\mathrm{f}}\right) &= I_\mathrm{in} + C_\mathrm{L}\frac{\mathrm{d}}{\mathrm{d}t}U_\mathrm{out}. \end{aligned} \tag{7.4}$$

The equation is simplified under the assumption of no output capacitance C_L and an infinite gain a to show its function:

$$\begin{aligned} I_\mathrm{in} &= \frac{a}{R_\mathrm{i}}\left(U_\mathrm{out} - \int \mathrm{d}t \frac{I_\mathrm{in}}{C_\mathrm{f}}\right) \\ \Leftrightarrow \quad \frac{R_\mathrm{in}\cdot I_\mathrm{in}}{a} &= U_\mathrm{out} - \int \mathrm{d}t \frac{I_\mathrm{in}}{C_\mathrm{f}} \\ \overset{a\to\infty}{\Leftrightarrow} \quad U_\mathrm{out} &= \frac{1}{C_\mathrm{f}}\int \mathrm{d}t I_\mathrm{in}. \end{aligned}$$

The result corresponds to an integration of the input current I_in via capacitor C_f. Equation (7.4) will still be used in the following. Performing an additional time derivative results in

$$\frac{\mathrm{d}^2 U_\mathrm{out}}{\mathrm{d}t^2} = \frac{a}{C_\mathrm{L}\cdot R_\mathrm{i}}\cdot\frac{\mathrm{d}U_\mathrm{out}}{\mathrm{d}t} - \frac{a}{R_\mathrm{i}\cdot C_\mathrm{L}\cdot C_\mathrm{f}}\cdot I_\mathrm{in} - \frac{1}{C_\mathrm{L}}\cdot\frac{\mathrm{d}I_\mathrm{in}}{\mathrm{d}t}. \tag{7.5}$$

This differential equation describes the output voltage U_{out} as a function of time. It includes constants describing the behaviour of Dosepix and the input current I_{in}, which is analysed in more detail in the following.

An energy deposition within the sensor of Dosepix results in a short charge pulse Q at the input capacitance C_{det} of the analogue electronics. Together with the input resistance R_{det}, this resembles an RC time constant of $\tau_{\text{det}} = R_{\text{det}} C_{\text{det}}$. The input current is described via

$$\begin{aligned} I_{\text{in}} &= \frac{U_{\text{in}}}{R_{\text{det}}} \cdot \exp\left(-\frac{t}{\tau_{\text{det}}}\right) - I = \\ &= \frac{Q}{\tau_{\text{det}}} \cdot \exp\left(-\frac{t}{\tau_{\text{det}}}\right) - I, \end{aligned} \tag{7.6}$$

where the relation for the input voltage $U_{\text{in}} = \frac{Q}{C_{\text{det}}}$ is used. Current I_{in} includes a current I, which opposes the pulse originating from the input charge. It is described by evaluating the knot at the input of the charge sensitive amplifier in figure 7.1 via

$$I = \frac{I_{\text{krum}}}{2} - I_{\text{DS3}} \tag{7.7}$$

and represents the difference of the constant current source of magnitude $\frac{I_{\text{krum}}}{2}$, representing the leakage current compensation, and the drain-source current through MOSFET T_3, I_{DS3}. The assumption that the MOSFET always operates in linear-mode is made, which is valid by adjusting U_{fbk} accordingly. I_{DS3} depends on the state of MOSFET T_4. The drain-source currents of the MOSFETs depend on each other due to the constant current source I_{krum}, resulting in

$$I_{\text{krum}} = I_{\text{DS3}} + I_{\text{DS4}}. \tag{7.8}$$

For the MOSFETs themselves, a simplified model is used in the following. I_{DS3} is described via [87]

$$I_{\text{DS3}} = K \cdot (U_{\text{DS3}} - U_{\text{d}}) \cdot \left((U_{\text{DS3}} - U_{\text{fbk}} - U_{\text{Th}}) - \frac{1}{2} \cdot (U_{\text{DS3}} - U_{\text{d}}) \right), \tag{7.9}$$

where K is a material dependent parameter representing the characteristics of the MOSFET and U_{Th} is the threshold voltage which also depends on the material. The model describes the region the MOSFET operates in. As stated before, the MOSFET will always be in the linear region which is the case if $U_{\text{DS3}} - U_{\text{fbk}} \geq U_{\text{Th}}$ and $U_{\text{DS3}} - U_{\text{fbk}} - U_{\text{Th}} > U_{\text{DS3}}$.

MOSFET T_4 connects to U_{dd} with its drain and to U_{DS3} with its source. Under the assumption that T_3 and T_4 are structurally identical, they share the same values for K and U_{Th}. This leads to the equation for the drain-source current of T_4 [87]

$$I_{\text{DS4}} = K \cdot (U_{\text{DS3}} - U_{\text{dd}}) \cdot \left((U_{\text{DS3}} - U_{\text{out}} - U_{\text{Th}}) - \frac{1}{2} \cdot (U_{\text{DS3}} - U_{\text{dd}}) \right). \tag{7.10}$$

The voltage signal U_{out} at the output of the op-amp, controls the current I_{DS4}. According to equation (7.8), I_{DS3} also varies with U_{out}. Two states of MOSFET T_4 are distinguished in the following. It is „off“ if the gate-source voltage is smaller than the threshold voltage U_{Th}. In this case, no drain-source current is present, i.e. $I_{\text{DS4}} = 0$. If the gate-source voltage is larger than the threshold voltage, the MOSFET is „on“. The off-state is represented by a voltage U_{THL}, which is the solution of $I_{\text{DS4}} = 0$ for U_{DS3}

$$U_{\text{THL}} = -2 \cdot (U_{\text{out}} + U_{\text{Th}}). \tag{7.11}$$

Here, the voltage of U_{dd} is set to 0, which does not change the functioning of the detector model but helps to simplify its description. The state of T_4 is then described as

$$\text{MOSFET } T_4 = \begin{cases} \text{on} & U_{\text{DS3}} \leq U_{\text{THL}} \\ \text{off} & U_{\text{DS3}} > U_{\text{THL}} \end{cases} \tag{7.12}$$

If T_4 is off, there is no drain-source current I_{DS4}, and the current of I_{DS3} equals I_{krum} according to equation (7.8). For current I, discharging capacitor C_{f} according to equation (7.7), this yields $I = \frac{I_{\text{krum}}}{2}$. This leads to the description of I for the different states of MOSFET T_4 of

$$I = \begin{cases} \frac{I_{\text{krum}}}{2} - I_{\text{DS3}} & \text{MOSFET } T_4 \text{ on} \\ \frac{I_{\text{krum}}}{2} & \text{MOSFET } T_4 \text{ off.} \end{cases} \tag{7.13}$$

Using relations (7.8) and (7.10), equation (7.9) is solved for U_{DS3} for the different states of MOSFET T_4

$$U_{\text{DS3}} = \begin{cases} \frac{1}{2} \cdot (-U_{\text{out}} + U_{\text{fbk}} + 2U_{\text{Th}}) - \\ -\frac{1}{2} \cdot \sqrt{(-U_{\text{out}} + U_{\text{fbk}} + 2U_{\text{Th}})^2 + 2 \cdot U_{\text{d}} \cdot (U_{\text{d}} - 2U_{\text{fbk}} - 2U_{\text{Th}})} - & \text{MOSFET on} \\ -\frac{2}{K} \cdot I_{\text{krum}} \\ \\ U_{\text{fbk}} + U_{\text{Th}} - \sqrt{(U_{\text{fbk}} + U_{\text{Th}} - U_{\text{d}})^2 + U_{\text{Th}}^2 + \frac{2}{K} \cdot I_{\text{krum}}} & \text{MOSFET off} \end{cases} \tag{7.14}$$

The equation is used to switch MOSFET T_4 according to equation (7.12).

After the output U_{out} of the op-amp, an additional filter stage to model undershoots in the pulse shapes as observed in simulations is present [5]. This extension is required as the op-amp was assumed to be ideal in the previous descriptions. The filter consists of an RC-differentiatior, resembled by R_3 and C_3, which creates the undershoot. An additional resistor R_2 for pole-zero cancellation is implemented to model the amplitude of the undershoot. R_2 and C_2 are combined to an RC-constant of τ_2, R_3 and

C_2 to τ_3. Under the assumption the output of the filter draws no current, the ansatz consists of equations

$$I_{R_3} = I_{C_2} + I_{R_2}, \tag{7.15}$$

$$U_{R_3} = U_{\text{out,filt}} = U_{\text{out}} - U_2 \tag{7.16}$$

where the indices correspond to the components of the schematic in figure 7.1. Voltage U_2 is shared by R_2 and C_2. Using these equations together with the relation for the voltage across capacitor C_2

$$U_2 = \frac{1}{C_2} \int \mathrm{d}t I_{C_2}, \tag{7.17}$$

finally leads to a differential equation describing the filtered output voltage $U_{\text{out,filt}}$ as a function of U_{out}

$$\frac{\mathrm{d}U_{\text{out,filt}}}{\mathrm{d}t} = \frac{\mathrm{d}U_{\text{out}}}{\mathrm{d}t} + \frac{U_{\text{out}}}{\tau_2} - U_{\text{out,filt}} \cdot \left(\frac{1}{\tau_3} - \frac{1}{\tau_2} \right). \tag{7.18}$$

The simulation of the corresponding analogue voltage signal for a charge deposition Q in the sensor of Dosepix is desired. This charge is related to the deposited energy of an ionising electron from an interaction with a photon via

$$Q = E \cdot \frac{e}{3.62\,\text{eV}}, \tag{7.19}$$

with e the elementary charge and 3.62 eV the average energy required to create an electron-hole pair for silicon [11].

The solutions of the equations are calculated numerically by employing a Runge-Kutta fourth-order algorithm. For more information about the algorithm, see for example [88]. The solutions of differential equations are performed for fixed time steps Δt_s. The relations are evaluated in a loop, where the current time t corresponds to $t = \Delta t_s \cdot n$, for an iteration n. At the beginning of the loop, output voltages U_{out} and $U_{\text{out,volt}}$ are 0 and MOSFET T_4 is on. In the iteration, input current I_{in} is evaluated via equation (7.6). The differential equation of second order (7.5) is solved for U_{out}. Using the result, $U_{\text{out,filt}}$ is evaluated via (7.18). Finally, equation (7.14) is evaluated to yield U_{DS3}. Equation (7.12) tells if the state of MOSFET T_4 has to be switched. Afterwards, a new iteration is started utilising the previously calculated values. During the calculation of the output voltage, a comparison to a threshold voltage U_{THL} is made. Everytime $U_{\text{out,filt}}$ exceeds and undercuts the threshold, the time difference between the intersections is provided as ToT in units of 10 ns.

In the following, the elaborated model of the analogue electronics of Dosepix is used to describe measurements. An optimisation of the various parameters of the model to data is performed.

7.2 Pulse shape model optimisation to calibration data

For normal operation of a Dosepix detector, i.e. under the irradiation with low photon flux, a detector can be described via its calibration curve alone (see chapter 4 for more information). There seldomly is a need to specifically know the exact shape of the signals of the analogue electronics of the detector. However, for large fluxes, pile-up occurs, which can only be explained via a description of the analogue electronics. The previously introduced mathematical model of Dosepix is used in the following. A detector is described by adjusting the parameters of the model. It is established from energy calibrations that every detector and every pixel of a detector behave slightly different. Therefore, the model parameters have to be optimised for each detector separately to do a proper simulation of the analogue signals. Each pixel has to be treated on its own if high precision is required. Since every optimisation requires high computational effort and time, only the average of all pixels is considered. If the equalisation (see section 2.1.1 for more details) of a detector was performed properly, this approximation is sufficient as the calibration curves of the pixels are similar then. The solid lines in 7.3 show the mean calibration curves for different values of I_{krum} for the same detector. Here, the value of I_{krum} is stated in units of DAC, where 1 DAC equals 0.2 nA.

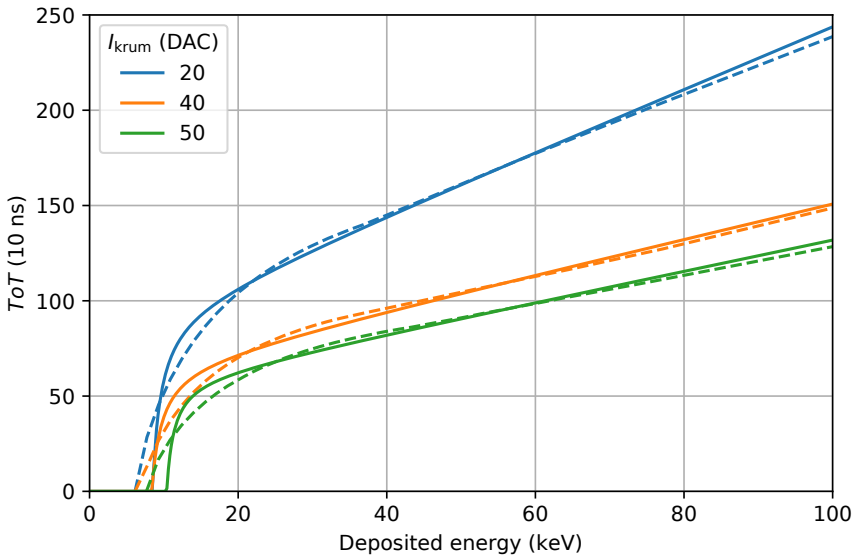

Figure 7.3.: The mean energy calibration curves, i.e. the average of the calibration curves of all pixels of the same Dosepix detector for different settings of I_{krum}. The solid lines correspond to the data provided by the calibration network of chapter 4, while the dashed lines are the results of optimising the pulse model to the solid lines.

The analogue pulse shape model depends on 12 parameters. It takes the deposited energies of events and their times of occurrence as its input and returns an array of corresponding ToT values. To determine a calibration curve, deposited energies are varied within a range of $[0, 75]$ keV for a step size of 1.5 keV, and additionally for energies of $\{100, 200, 300, 400\}$ keV. Lower energies are analysed in more detail to better represent the knee's shape in the calibration curve. Only a few supporting points are evaluated for higher energies since the curve's trend is approximately linear within this regime. Pile-up is prevented by calculating single events.

A Nelder-Mead algorithm [43] is used to minimise the mean squared distance between the calibration curve provided by the calibration network (see chapter 4 for more details) and the curve of the pulse shape model. The start parameters of the model are listed in table 7.1. I_{krum} is not listed and instead set to the value used during calibration measurements. The current is specified in units of nA for the model. To keep the parameters as uncorrelated as possible while providing enough degrees of freedom to properly describe the data, the following values are kept constant: C_{f}, a, U_{fbk}, and U_{Th}. The parameters are chosen heuristically and according to [5].

C_{f}	τ_{det}	τ_2	τ_3	U_{fbk}
11.11 fF	150 ns	40 µs	67 µs	0

K	U_{THL}	U_{Th}	a	C_{l}	R_{i}
200 nA/V	30 mV	0 V	−214	10 nF	30 Ω

Table 7.1.: The start and constant parameters for the optimisation of the calibration curves of the pulse shape model to the curves determined via the calibration network. The value of I_{krum} is set to the value used during measurements.

I_{krum} (DAC)	I_{krum} (nA)	K (nA/V)	U_{THL}(mV)	τ_{det} (ns)	τ_2 (µs)	τ_3 (ns)	C_{l} (nF)	R_{i} (Ω)
20	3.947	139.298	21.738	50.637	20.3	424.317	11.902	7.078
40	4.698	134.647	24.866	28.741	3.903	223.234	18.813	5.167
50	6.578	148.094	28.056	26.267	5.37	391.609	13.617	5.685

Table 7.2.: The parameters of the pulse shape model optimised to the calibration curves in figure 7.3 for different values of I_{krum}. The first column corresponds to I_{krum} set in hardware during detector calibration, whereas the second column reflects the values from optimisation.

The first column of table 7.2, describes I_{krum} in units of DAC and corresponds to the values set during the calibration measurements. The remaining columns represent the values returned from the optimisation. Some of the parameters vary more than others

under the variation of I_{krum}. The deviation is expected to be small, considering some parameters describe a constant part of the detector's hardware. A possible variation of constant parameters is compensated by the optimised parameters. Also, the used model is only an approximation of the true analogue electronics, which is sufficient as long as the pulse shapes are described properly. Especially for the set and fitted values of I_{krum} there is a mismatch. A detailed explanation for this discrepancy is given in section 7.8.2. When I_{krum} is refered to in the following, it always corresponds to the set value.

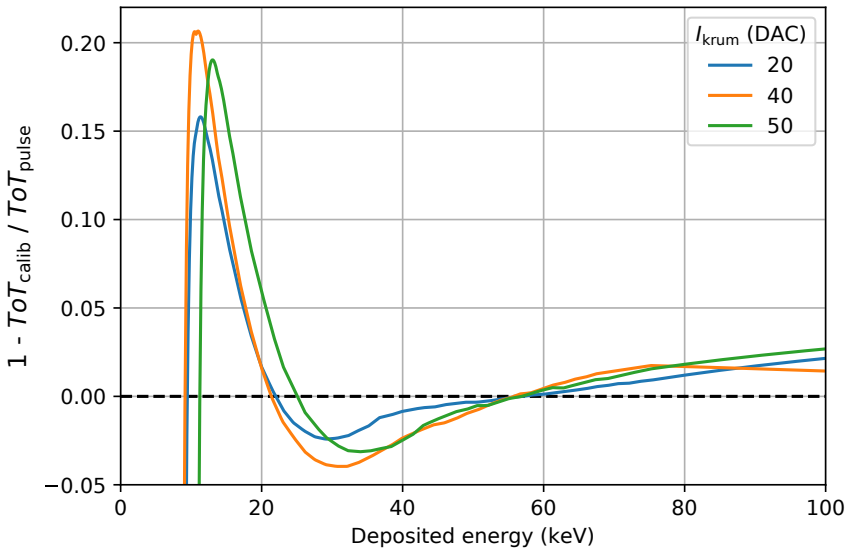

Figure 7.4.: Relative deviation of the calibration curves provided by the calibration network ToT_{calib}, and the curves from the optimisation of the pulse shape model ToT_{pulse}, as a function of deposited energy according to equation (7.20).

The calibration curves of the optimised parameters of the pulse shape model are depicted as dashed lines in figure 7.3. There are discrepancies to the curves from the calibration network, indicated by the solid lines. While the linear parts seem to agree well, the knees of the curves have slightly different shapes. For the pulse shape model, the knee is softer in comparison to the curves of the calibration network. The function describing the calibration curves is only an approximation as was established from measurements with test pulses in section 4.1.4. The pulse shape model shows similar discrepancies as the test pulse measurements before. These dependencies are depicted in figure 7.4 which shows the relative deviation of

$$1 - \frac{ToT_{\text{calib}}}{ToT_{\text{pulse}}}, \tag{7.20}$$

where ToT_{calib} are the values of the network calibration and ToT_{pulse} the values from the optimisation of the pulse shape model. This further proves that the commonly used calibration function does not properly describe the conversion from deposited energy to ToT and that it should only be used as an approximation. Despite the high deviation for low deposited energies, the function's precision is still sufficient for most applications, e.g. dosimetry. Higher accuracy is required for pile-up simulation, especially in the low energy region. Most deposited energy spectra have a bias towards low energy entries, mostly consisting of charge sharing and Compton scattering events. Many of these events are not registered by the detector since they are below the detection threshold in measurements for low fluence conditions. However, simulations show that these events exist and generate a pulse in the analogue electronics of Dosepix. In pile-up simulation, this is important when many low energy events occur within a short time as their piled-up signal may be large enough to surpass the detection threshold.

7.3 Pulse shape model interpolation

The model, together with the optimised parameters, is used to generate the analogue signals of a pixel of Dosepix for a series of deposited energies and corresponding times. Figure 7.5 shows an exemplary output signal, where the detector was used with $I_{\text{krum}} = 20\,\text{DAC}$. The events consist of deposited energies which increase in the range of $[5, 100]\,\text{keV}$ with a step size of $5\,\text{keV}$. The times of occurrence of the events are evenly distributed within a range of $[0, 100]\,\mu\text{s}$. The time in the plot is denoted in units of ToT where $1\,\text{ToT} = 10\,\text{ns}$. The y-axis corresponds to the voltage at the analogue electronics' output $U_{\text{out,filt}}$. In hardware, this voltage is compared to the threshold voltage U_{THL} to determine the ToT-values corresponding to the pulse widths. The time difference between the events is large enough to show no pile-up. The figure reflects that the amplitudes of the pulses increase almost linearly with deposited energy. Additionally, the negative amplitudes of the undershoots increase.

A detailed view of an exemplary pulse shape is depicted in figure 7.6. Here, $I_{\text{krum}} = 20\,\text{DAC}$ and a deposited energy of $50\,\text{keV}$ is used. The shape of a pulse's rising edge is almost independent of deposited energy, while the falling edge is not. It consists of a linear decrease beginning at the time of the maximum. It changes to a more subtle non-linear decrease once a certain voltage is undercut and MOSFET T_4 is in on-state. This part of the pulse shape is essential to be modelled correctly since an approximation with a linear decrease will result in a wrong shape of the knee in the energy calibration function.

A calculation of the pulse shapes, as shown in the example of figure 7.5, requires a high computational effort and, as a consequence, a long computation time. The model's differential equations need to be integrated for small time steps to achieve a high precision of the output voltage. For pile-up simulation, many events are required to get a ToT spectrum of high statistics. Computation time is reduced by pre-

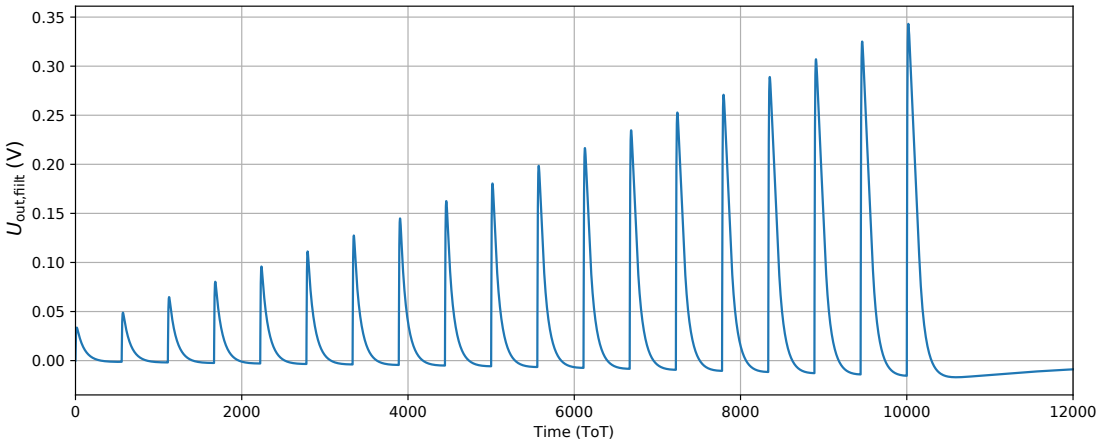

Figure 7.5.: The simulation of the output signal U_{out} of the analogue electronics of a Dosepix detector for $I_{\text{krum}} = 20\,\text{DAC}$. The deposited energies are linearly increased from 5 keV to 100 keV. The times of occurence are set uniformly within a duration of 100 µs.

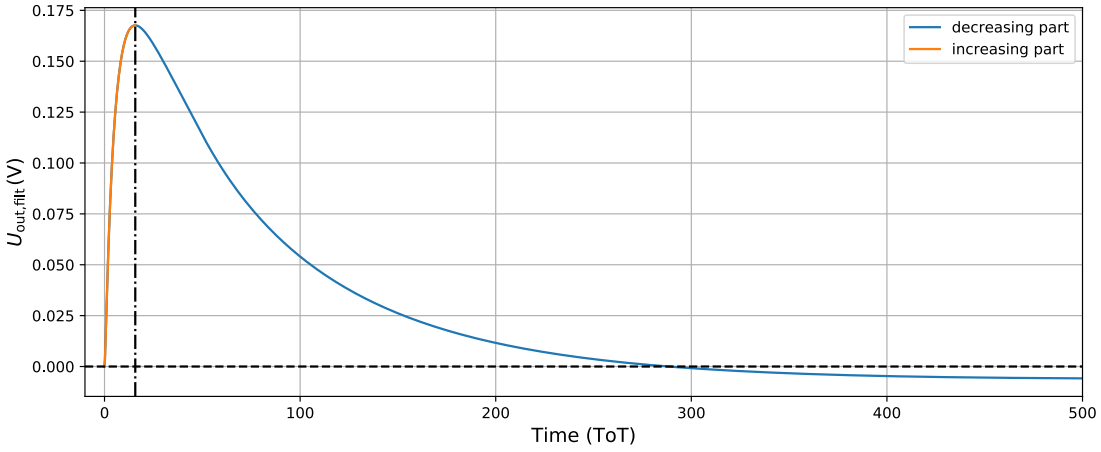

Figure 7.6.: Pulse shape for a Dosepix detector with $I_{\text{krum}} = 20\,\text{DAC}$ for a deposited energy of 50 keV. Different colours indicate the rising and falling edges of the shape according to the legend. The dash-dotted line indicates the time at which the curve reaches its maximum. The dashed line represents the baseline level.

calculating the analogue pulse shapes. When executing the simulation, the shapes then only need to be looked up. Since deposited energy is a continuous input variable, only the pulse shapes for specific energies are calculated. Figure 7.7 shows these energies as a function of the deposited energy index, which consecutively numbers the generated pulses.

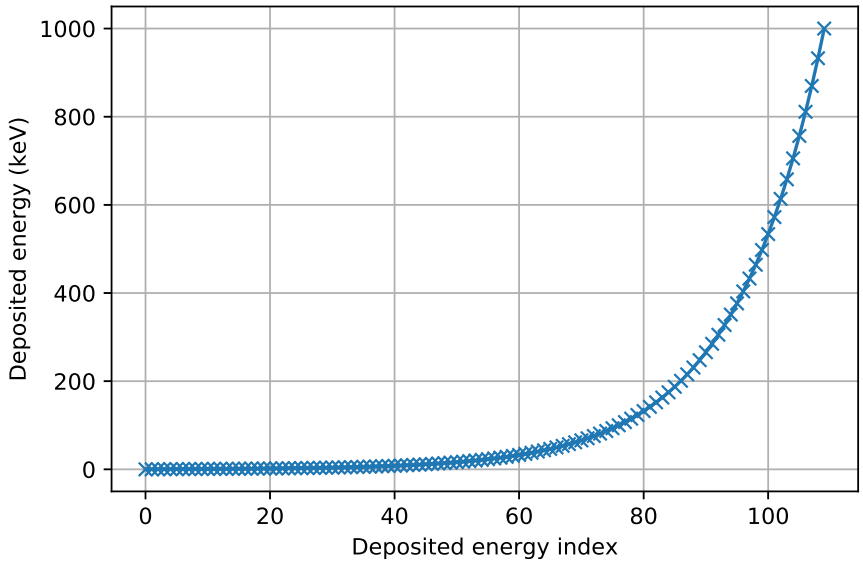

Figure 7.7.: The distribution of deposited energies for the generation of support pulse shapes which are interpolated afterwards. The first 10 energies are distributed uniformly and the remaining 100 energies on a logarithmic scale.

The first 10 deposited energies are distributed uniformly within a range of $[0, 10]$ keV. Another 100 energies are distributed on a logarithmic scale within $[1, 1000]$ keV. This distribution is based on the deposited energy spectra commonly measured via a Dosepix detector. For these spectra, low deposited energies have a high probability of occurring due to effects like charge sharing and Compton scattering. The probability of a photon interacting via photoelectric absorption with the sensor material decreases with increasing energies. However, high values are important since they can occur in the case of pile-up. The time steps of the pulse calculation are chosen to be within a uniform range of $[0, 300]$ µs for 300k points, i.e. a resolution of 1 ns or 0.1 ToT. The smaller the step size, the better the approximation of the model solution. However, computation time also scales with the number of steps. The calculated pulse shapes are depicted in figure 7.8 for a single Dosepix with different settings of I_{krum} indicated by the titles of the plots. The density plots show the amplitude of signal $U_{\mathrm{out,filt}}$ as a function of the time since the event's occurrence Δt_{occ}, and the deposited energy E. Finally, the curves are linearly interpolated to return a function $f(\Delta t_{\mathrm{occ}}, E)$.

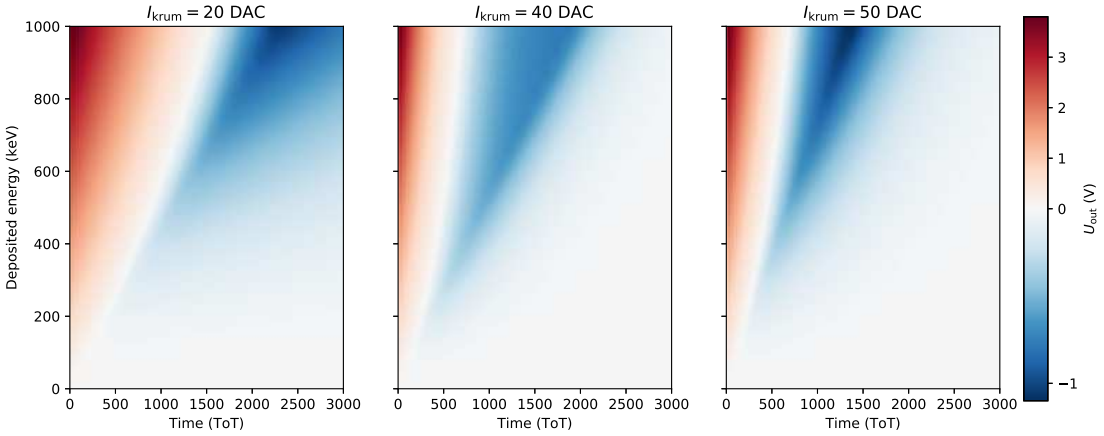

Figure 7.8.: Interpolated pulse shapes for a Dosepix detector for different settings of I_{krum} indicated by the titles of the plots. The levels of the pulses are represented according to the colour bar, i.e. $U_{out,filt}$ as a function of time since occurrence Δt_{occ} and deposited energy E. Negative values of $U_{out,filt}$ represent an undershoot of a pulse.

For the simulation of the output signal of the analogue electronics via the interpolated pulse shapes, some requirements have to be fulfilled. It has to be known if the currently evaluated time corresponds to the increasing or decreasing part of a pulse shape to speed up the signal simulation. Therefore, each shape is split at its maximum voltage U_{max}, which takes place at a time Δt_{max} like previously depicted in figure 7.6 indicated by the dash-dotted line. This time's trend as a function of deposited energy is shown in figure 7.9. The settings of I_{krum} are indicated by the colours according to the legend. The peak time decreases linearly for deposited energies up to about 40 keV. In this region, MOSFET T_4 is permanently on. While the amplitude increases with energy, the pulse's peak will narrow down and slightly shift to lower times. For larger deposited energies, MOSFET T_4 stays on at first but switches off once a certain output voltage is reached. The time of the peak increases approximately logarithmically with increasing energy. The curves of figure 7.9 are linearly interpolated to resemble a function $f_{max}(E)$ for each value of I_{krum}.

Another important feature of the analogue pulses is the peak amplitude as a function of deposited energy, illustrated in figure 7.10. Three curves, for different settings of I_{krum} according to the legend, are depicted. All curves show a linear trend and are hardly visually separable since they are almost independent of I_{krum} as the current mostly affects the decreasing part of a pulse. The curves are interpolated with their axes inverted, resulting in functions $f_{amp}(y)$ which return the deposited energy of a pulse E for a peak voltage level y.

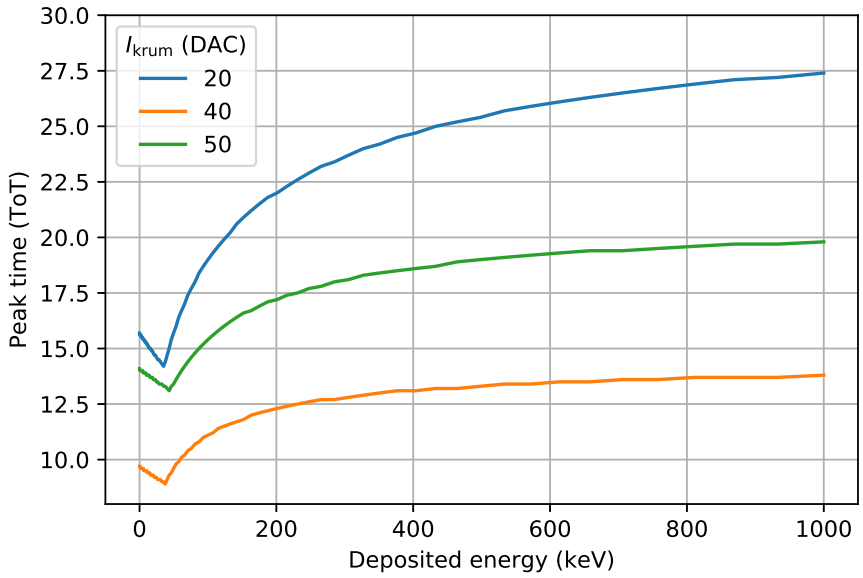

Figure 7.9.: Peak times Δt_{max} the maximum amplitudes of the pulses are reached as a function of deposited energy E. The colours correspond to the settings of I_{krum} according to the legend.

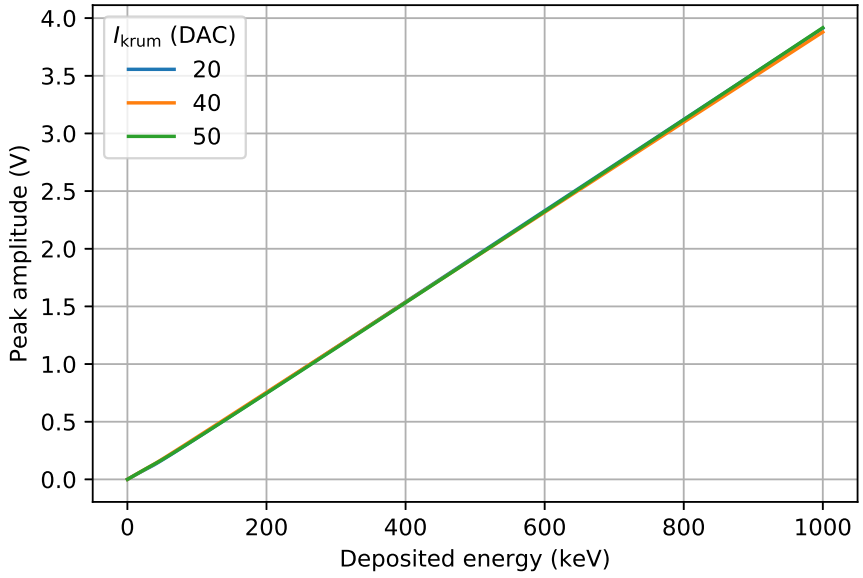

Figure 7.10.: The amplitudes of the analogue pulses as a function of deposited energy. Three curves for different values of I_{krum} according to the legend are depicted.

In summary, three interpolation functions are defined

- $f(\Delta t_{\mathrm{occ}}, E)$ for the shape of the analogue pulses
- $f_{\mathrm{max}}(E)$ for the time the pulses reach their maximum
- $f_{\mathrm{amp}}(y)$ the deposited energy E for an amplitude y of a pulse

These functions are combined to efficiently calculate the ToT values corresponding to a series of deposited energies $\tilde{E}$ occurring at times $\tilde{t}$. Figure 7.11 depicts a flow chart of the algorithm used to determine the ToT values. It consists of three major parts indicated by the lightly coloured backgrounds and the numbers in their top-left corners. The functioning of the blocks is described in the following. Block 1 is executed at the start of the algorithm. Here, some variables are initialised to 0. Their function is described in the following:

- E_{rm}: if another pulse occurs during the rising edge of a first one, the remaining deposited energy corresponding to the height of the first pulse is stored. See block 3 for a detailed description of the calculation of E_{rm}
- x_{tot}: the current time of the simulation
- y_{tot}: the current height of the output signal at time x_{tot}
- F_{THL}: a flag stating if the analogue signal has previously exceeded the threshold level U_{THL}

After initialisation, the main loop of the algorithm is started. It uses an index i, which is compared to the total number of events N_{events} in each iteration. If i is greater than N_{events}, the algorithm finishes. Index i is additionally used to get information about the current event. It has a deposited energy of E which is the sum of the ith entry from the energy array $\tilde{E}$ and the remaining energy E_{rm}. The requirement of E_{rm} is explained in the following. If a pulse has not reached its maximum yet, and another event occurs, the first pulse's rising cannot simply be stopped to continue with a second pulse as this would lead to an underestimation of the amplitude of the final pulse. Instead, the charge at the input of the analogue electronics has to be considered. Its value is decreasing while the analogue pulse rises. If a second event occurs, a new charge is added to the remaining charge of the first event. This corresponds to a sum of the first event's remaining energy and the succeeding events' energy. One extreme example is two events taking place almost immediately, i.e. with only a small time difference between them. The events can be considered a single event with an energy corresponding to the sum of the initial events. For the current event of the loop, the peak of the corresponding pulse is at a time $t_{\mathrm{max}} = f_{\mathrm{max}}(E)$ in regards to the time of occurrence of the event. Additionally, the time difference to the succeeding event is determined by taking the difference $\Delta t = \tilde{t}[i+1] - \tilde{t}[i]$, where $\tilde{t}$ is the array that contains the times of occurrence of the events.

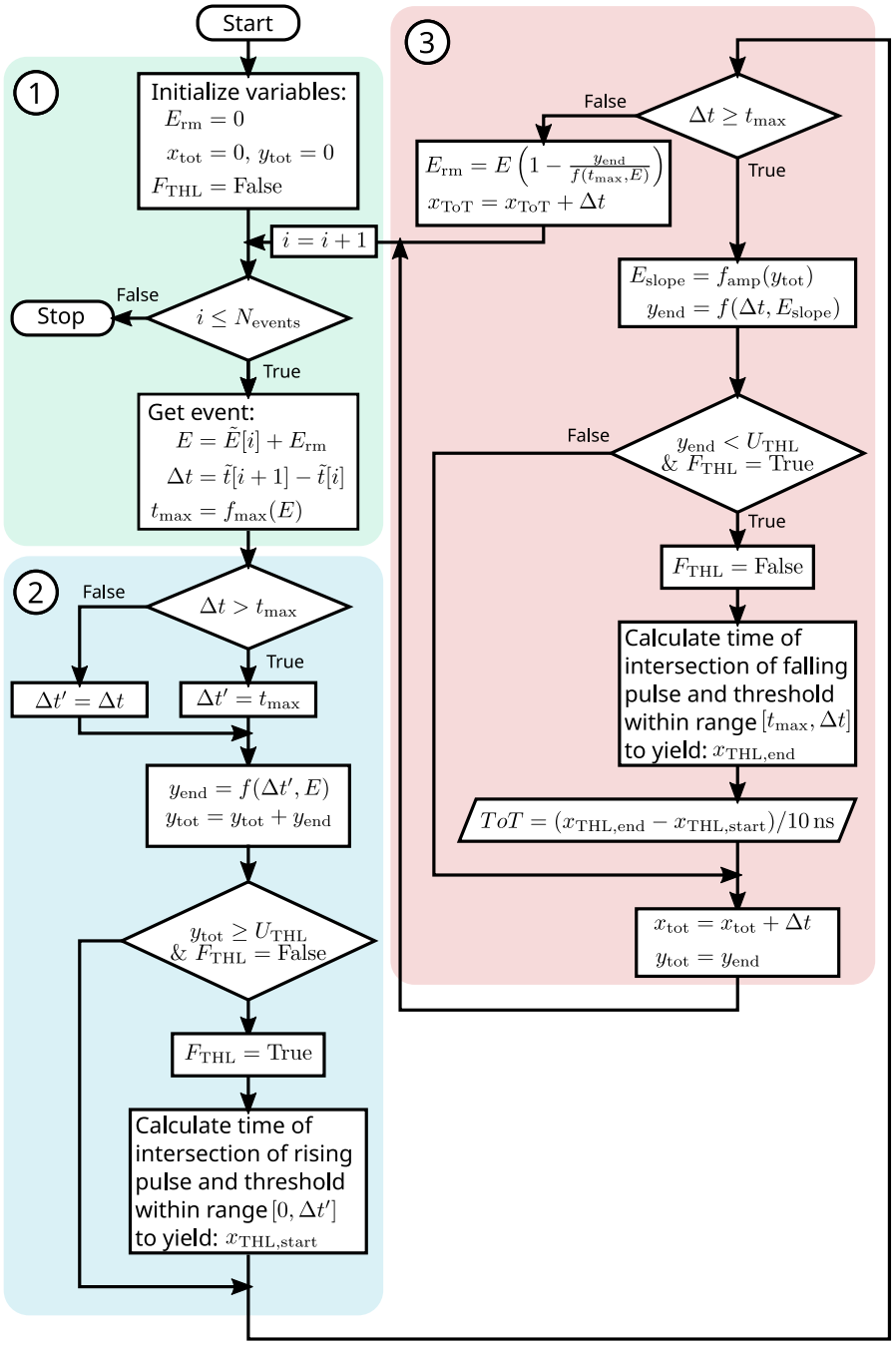

Figure 7.11.: Flow chart for the algorithm to calculate ToT-values from a series of events consisting of deposited energies $\tilde{E}$ occurring at times $\tilde{t}$. The program is divided into three major blocks. The first one initialises important variables, starts the main loop over all events and gets the current event. Block 2 handles the rising edge of the analogue pulse of the event. Block 3 is about the decreasing edge and provides the ToT-value if the pulse exceeded and undercut the threshold U_{THL}.

After initialisation, the rising edge of the currently processed analogue pulse is considered in block 2. If the time difference to the next event is larger than the peak time, i.e. $\Delta t > t_{\text{max}}$, a time difference $\Delta t'$ is set to t_{max}. Otherwise, $\Delta t'$ is set to Δt when the next pulse takes place on the rising edge of the current one. The endpoint of the pulse for time t' is determined via $y_{\text{end}} = f(\Delta t', E)$. Its value is added to the current output level of the analogue signal y_{tot}. If this voltage exceeds the threshold U_{THL}, flag F_{THL} is set. In hardware, this is when the ToT-register begins to count clock signals. In simulation, the exact time of the intersection of the rising edge of the analogue pulse and U_{THL} has to be determined. Here, only the range of $[0, \Delta t']$ is of interest where all times are specified regarding the time of occurrence of the event. Instead of evaluating many points of the interpolated pulse signal or searching for a numerical solution, a more efficient approach is required. First, a fast scan of the intersection within the desired range for 10 uniformly distributed times $\tilde{x}_{\text{THL}}$ is made. The signal levels of the pulse are evaluated via $\tilde{y}_{\text{THL}} = f(\tilde{x}_{\text{THL}}, E) + y_{\text{tot}}$. The two times minimising the distance $|\tilde{y}_{\text{THL}} - U_{\text{THL}}|$ are searched. These are indicated by indices i_{min} and j_{min}, which are set so $\tilde{y}_{\text{THL}}[i_{\text{min}}]$ is larger than U_{THL} and $\tilde{y}_{\text{THL}}[j_{\text{min}}]$ is lower than it. The corresponding times $\tilde{x}_{\text{THL}}[i_{\text{min}}]$ and $\tilde{x}_{\text{THL}}[j_{\text{min}}]$ then define the range the intersection of the rising pulse edge and the threshold U_{THL} is determined. The shape of the pulse is considered to be linear within this new region, resulting in equation

$$\begin{aligned} U_{\text{THL}} &= \frac{\tilde{y}_{\text{THL}}[i_{\text{min}}] - \tilde{y}_{\text{THL}}[j_{\text{min}}]}{\tilde{x}_{\text{THL}}[i_{\text{min}}] - \tilde{x}_{\text{THL}}[j_{\text{min}}]} \cdot (x_{\text{THL,start}} - (\tilde{x}[j_{\text{min}}] + x_{\text{tot}})) + y[j_{\text{min}}] \\ \Leftrightarrow \quad x_{\text{THL,start}} &= x_{\text{tot}} + x[j_{\text{min}}] + (U_{\text{THL}} - y[j_{\text{min}}]) \cdot \frac{\tilde{x}_{\text{THL}}[i_{\text{min}}] - \tilde{x}_{\text{THL}}[j_{\text{min}}]}{\tilde{y}_{\text{THL}}[i_{\text{min}}] - \tilde{y}_{\text{THL}}[j_{\text{min}}]}, \end{aligned}$$

where x_{tot} is the current time of the pulse shape simulation and $x_{\text{THL,start}}$ the time since start the ToT-register begins to count clock ticks.

The third block of the algorithm handles the falling edge of the current pulse. The condition $\Delta t \geq t_{\text{max}}$ checks if there is a falling edge. If this condition is false, the next pulse takes place on the rising edge of the current one. Then, the remaining energy is calculated via

$$E_{\text{rm}} = E \cdot \left(1 - \frac{y_{\text{end}}}{f(t_{\text{max}}, E)}\right).$$

The function approximates the rising pulse via a linear function and compares the current level at y_{end} with the peak level of $f(t_{\text{max}}, E)$. E_{rm} is set according to their fraction. For example, if the pulse is at baseline level, i.e. $y_{\text{end}} = 0$, the remaining energy is the deposited energy, i.e. $E_{\text{rm}} = E$. Afterwards, the next iteration of the main loop is executed.

If the next event takes place on the falling edge of the current event, i.e. for $\Delta t \geq t_{\text{max}}$, the algorithm proceeds in block 3. The energy E_{slope} is determined by evaluating

the function $f_{\mathrm{amp}}(y_{\mathrm{tot}})$ which provides the energy corresponding to the current amplitude of the peak of the analogue signal y_{tot}. E_{slope} differs from E if there is pile-up for the previous event. The endpoint of the pulse of energy E_{slope} is determined via $y_{\mathrm{end}} = f(\Delta t, E_{\mathrm{slope}})$. The value is compared with the threshold level of U_{THL}. If $y_{\mathrm{end}} < U_{\mathrm{THL}}$ and flag F_{THL} was set previously, an intersection of the signal and the threshold takes place for the falling edge. The necessity of F_{THL} is explained in the following. There is a possibility that the signals of the pulses are always lower than U_{THL}, which is the case for events of low deposited energies. All falling edges of these pulses fulfil the condition $y_{\mathrm{end}} < U_{\mathrm{THL}}$. The flag F_{THL} ensures that the signal exceeded and undercut the threshold level. The intersection of the signal and U_{THL} is calculated analogously to the previous description for the rising edge of the pulse. Only the time range of $[t_{\mathrm{max}}, \Delta t]$ is of interest. Instead of narrowing down this range only once, the process is repeated multiple times until $|\min(y_{\mathrm{THL}}[i_{\mathrm{min}}], y_{\mathrm{THL}}[j_{\mathrm{min}}]) - U_{\mathrm{THL}}| < 1 \cdot 10^{-4}\,\mathrm{mV}$. The time of the intersection is denoted as $x_{\mathrm{THL,end}}$, which corresponds to the time the counting of clock ticks for the ToT-register is stopped. Finally, the algorithm provides the ToT-value corresponding to the duration the pulse exceeded the threshold via

$$ToT = \frac{x_{\mathrm{THL,end}} - x_{\mathrm{THL,start}}}{10\,\mathrm{ns}},$$

where the relation $1\,\mathrm{ToT} = 10\,\mathrm{ns}$ is used. Afterwards, the current time and signal level of the simulation is updated by adding the time difference Δt to x_{tot}. This completes the processing of a single event, and the next iteration of the main loop is started.

The benefit of the interpolation algorithm is its speed in comparison to the direct solution of the differential equations of the model. Intersections with the threshold are only calculated if necessary, which is checked by evaluating only a single point of the analogue signal. To finally find the times of intersections, only a few interpolation evaluations are required while keeping the precision of the ToT determination high.

The algorithm can be adjusted to provide the exact shape of the output signal, shown in figure 7.12. Each curve consists of events whose times of occurrence are uniformly distributed within a range of $[0, 5000]$ ToT. The deposited energy per event is sampled from a uniform distribution within a range of $[0, 100]$ keV. The number of events increases from top to bottom, i.e. $\{10, 30, 70, 100\}$. Dashed lines indicate the baseline level of the analogue electronics. The dash-dotted lines represent the threshold level of U_{THL}. The $U_{\mathrm{out,filt}}$-axes of the plots do not share the same scale, i.e. the higher the number of events is set, the higher the amplitudes of the pulses are. For 10 events, the output signal corresponds to a measurement with low photon flux. There is enough time for a pulse to reach the baseline level, or at least to come close to it before the next event takes place. Every peak exceeding and undercutting the threshold provides a ToT-value. Almost every event can be attributed with a corresponding duration in ToT. For an increasing number of events, like depicted in the second plot, this is no longer the case. Pile-up takes place, and pulses begin to

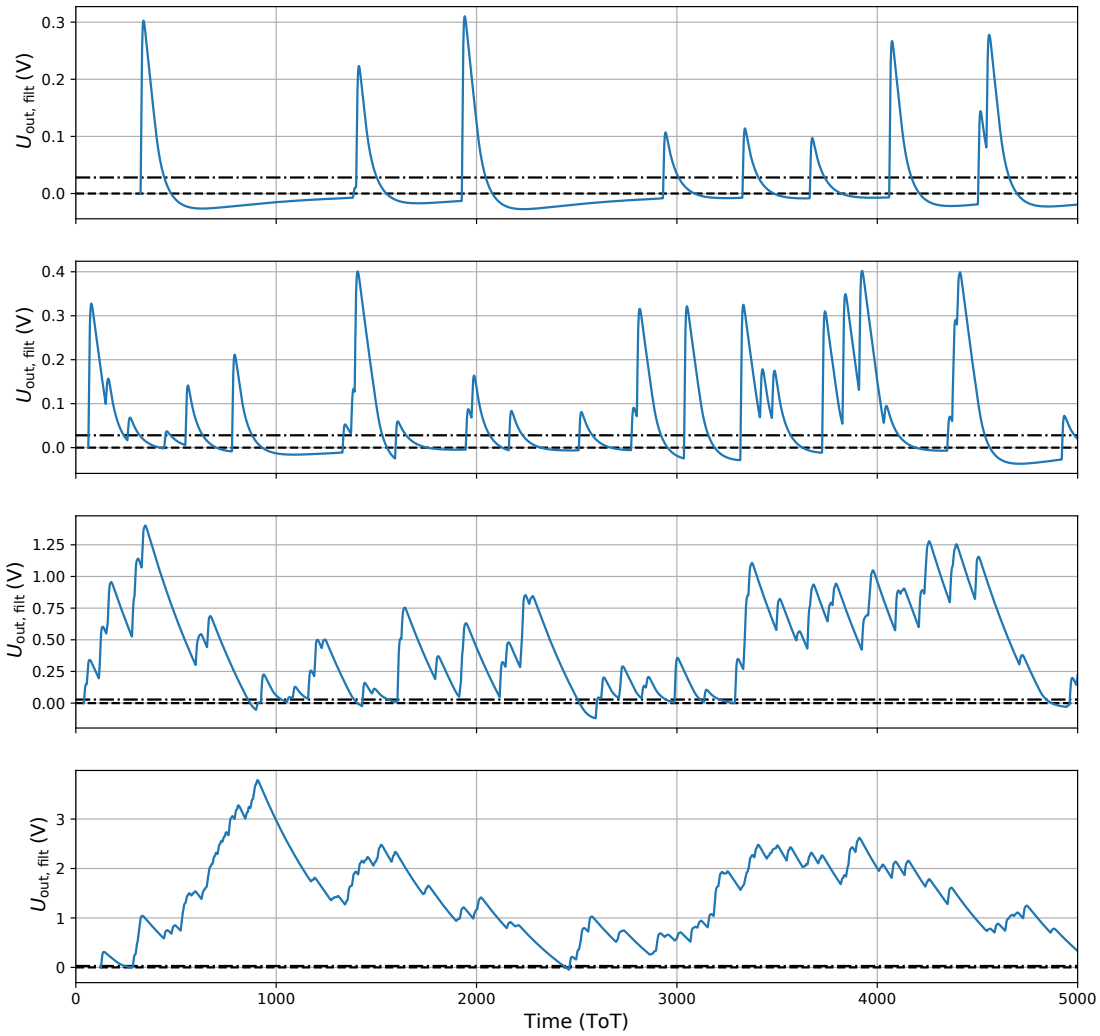

Figure 7.12.: The output signal $U_{\text{out,filt}}$ of the simulation of a Dosepix detector for $I_{\text{krum}} = 20\,\text{DAC}$. The times of occurrence of the events are uniformly distributed within a range of $[0, 5000]$ ToT and deposited energies within $[0, 100]$ keV. The number of events increases from top to bottom: $\{10, 30, 70, 100\}$. Dashed lines indicate the baseline level, and dash-dotted lines the threshold of U_{THL}.

superimpose. Mostly, a second pulse takes place at the decreasing edge of a first one. The time the signal exceeds the threshold is increased, leading to a lower number of ToT-events with higher values. When increasing the flux even further, like in the third and fourth plot, pulses begin to pile-up on the rising edges. This results in higher output voltages $U_{\text{out,filt}}$ and a lower number of ToT-events. The fourth plot shows 100 events. Here, the probability for the signal to reach the baseline level or to come close to it is low. When the fluence is increased even further, the detector will not measure any ToT-events since the signal cannot undercut the threshold anymore. The charge-sensitive-amplifier of the analogue electronics will stay completely satisfied during this operation and renders the detector useless. All Dosepix detector simulations are made via the introduced algorithm using interpolated data in the following.

7.4 Analogue pulse characteristics

In this section, insights about the simulation of the analogue pulses and their characteristics are presented. Figure 7.13 shows the shapes of pulses as a function of ToT for different deposited energies according to the colour bar. The curves are depicted for three settings of I_{krum} according to the titles of the plots.

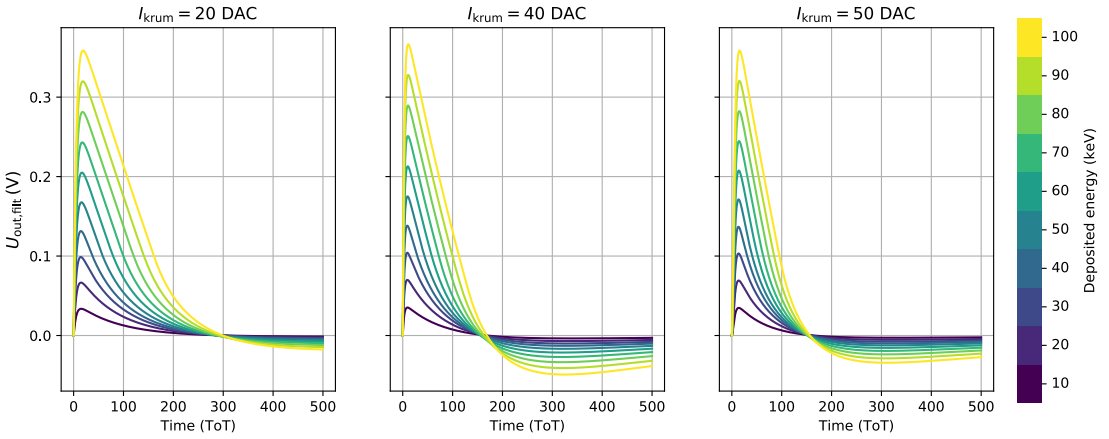

Figure 7.13.: The output voltage $U_{\text{out,filt}}$ of the simulated analogue pulses as a function of ToT for various deposited energies indicated by the colour bar. Three settings of I_{krum}, represented by the titles of the plots, are depicted.

Only times up to 500 ToT are depicted, neglecting the undershoot which takes a long time to reach the baseline level of $U_{\text{out,filt}} = 0$ again. The amplitudes of the pulses only slightly depend on the setting of I_{krum}. This parameter mostly affects the slope of the falling edges and, consequently, the intersection with the threshold level. The amplitudes linearly depend on deposited energy. The higher this energy, the larger the negative amplitude of the undershoot. While the constant current of I_{krum} is used to decrease the capacitor's charge in the charge sensitive amplifier of the

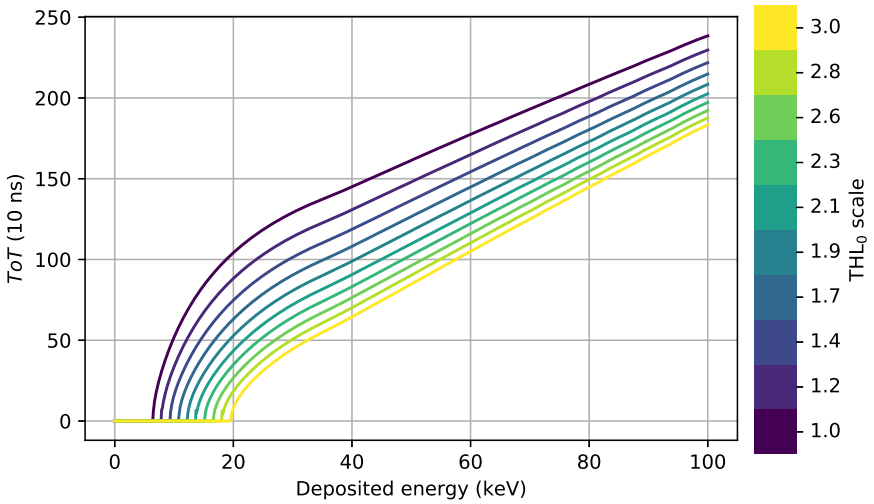

Figure 7.14.: The calibration curves from a simulation with the pulse shape model for a Dosepix detector with $I_{\text{krum}} = 20\,\text{DAC}$. The threshold determined from the fit to the measured calibration curves is denoted as THL_0. The colours of the curves correspond to the scaling of THL_0 according to the colour bar.

electronics, the output voltage does not directly correspond to it. If the charge is high, the trend is linear as a function of time. But if the output voltage undercuts a certain threshold, MOSFET T_4 is switched on leading to a dampening of the output voltage close to the baseline. This results in an intersection with the baseline at times almost independent of deposited energy. Nevertheless, the curves represent the deposited energy via their width, determined via threshold voltage U_{THL}. With increasing I_{krum}, the slope of the falling edge increases and also the time of the baseline intersection is reduced, leading to smaller ToT-values.

The optimised parameters of the pulse shape model describe the Dosepix detector's hardware. Some of these parameters can be adjusted in hardware, e.g. the threshold voltage U_{THL}. Its standard value, which was determined from the fit to the calibration functions, is now denoted THL_0. Figure 7.14 represents the calibration curves determined from the simulation of pulse shapes for the Dosepix detector with $I_{\text{krum}} = 20\,\text{DAC}$. The color bar represents the threshold level as a scaled version of the initial threshold THL_0. Increasing the threshold leads to a shift of the calibration curve towards lower values of ToT. The pulse shapes of figure 7.13 explain this observation. When U_{THL} is high, the parts of the pulses which are greater than the threshold are approximately triangular. The rising edge is neglected since the rise time is short in comparison to the falling edge. Since the amplitude of the peaks depends linearly on the deposited energy and the slope of the falling edge remains constant, the provided ToT-values also increase linearly with energy. For low values of the threshold, the

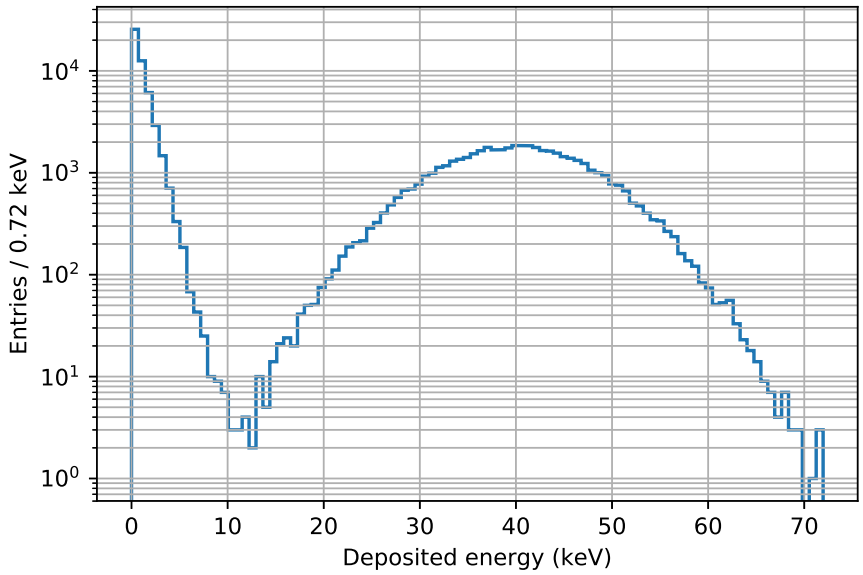

Figure 7.15.: Exemplary deposited energy spectrum representing the input events for the simulation of the analogue signal of a Dosepix detector.

pulse shapes are damped. In the calibration curves, this results in the shape of the knee. The closer the threshold is to the baseline, the larger the radius of the knee. The shapes of the calibration curves correspond to the curves of figure 4.17 (a), where the threshold was varied for measurements evaluated with the calibration network.

The simulation of the analogue signal is now used with a large number of events. The exemplary deposited energy spectrum in figure 7.15 is used. It consists of two main contributions. For low deposited energies, a background is modelled with an exponential distribution for N_{exp} events. The higher deposited energies are normally distributed with a mean of 20 keV and a standard deviation of 4 keV for N_{norm} events. Since this is only an example, the distributions do not directly correspond to any measurements but are similar in shape to the deposited energies of a filtered X-ray tube spectrum. The times of occurrence of the events are distributed uniformly, which corresponds to an exponential distribution of the time differences between two subsequent events. For practical reasons, it is easier to use the exponential distribution

$$f(x, \lambda) = \lambda \exp\left(-\lambda \cdot x\right), \tag{7.21}$$

as its parameter λ directly corresponds to the event rate of the deposited energies. To finally determine the times of occurrence of the events, the cumulative sum of the time differences is calculated. 10 uniformly distributed event rates per pixel within a range of $\lambda = [3 \cdot 10^4, 1.5 \cdot 10^6]\,\text{s}^{-1}$ are evaluated. A fixed exposure of 0.05 s is chosen. The number of simulated events then corresponds to $N = \lambda \cdot 0.05\,\text{s}$. Only a single pixel is simulated.

The deposited energies of the previously defined spectrum and their times of occurrence are used as input of the analogue electronics simulation. It returns the ToT-values of simulated pulses, which are then transformed to deposited energies via the calibration curves introduced in section 7.2 and combined into a histogram.

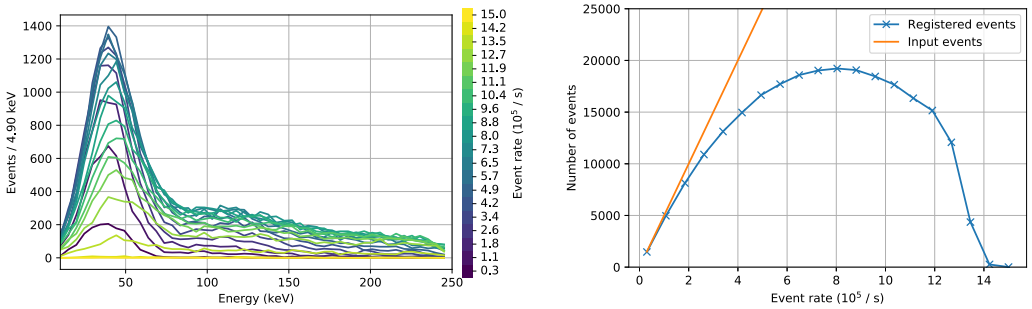

(a) Deposited energy spectra

(b) Registered events

Figure 7.16.: (a) depicts the simulated deposited energy spectra for the input spectrum in figure 7.15. The event rate is varied linearly according to the colour bar. (b) shows the total number of registered events as a function of the event rate via the blue curve. The orange curve represents the number of input events to the simulation.

The histograms for the different event rates are depicted in figure 7.16 (a). The colors of the curves represent the event rate per pixel according to the color bar. The deposited energies are binned within an energy range of $[10, 250]$ keV for 50 bins. (b) depicts the total number of registered events in (a) as a function of the event rate. The blue curve corresponds to the simulation results and the orange to the number of events for a perfect, pile-up free detector. For low event rates, the input energy spectrum and the output spectrum are similar in shape, indicating the proper working of the simulation. Ideally, they should be identical since the probability of pile-up is still very low and the number of registered events is almost identical to the number of input events. However, there is a small offset because only deposited energies higher than the threshold are registered in simulation. When increasing the event rate, pulses begin to superimpose, leading to ToT-values that correspond to deposited energies larger than physically possible. The energy spectra begin to be biased towards higher energies while their peak amplitudes are no longer increasing linearly. Once an event rate per pixel of about $8 \cdot 10^5 \frac{1}{\mathrm{s}}$ is reached, the number of registered events decreases, resembled by a shrinking amplitude of the peak in the spectrum. Events are binned for energies up to 250 keV in figure 7.16 (a). If the event rate succeeds a certain threshold, here about $14 \cdot 10^5 \, \frac{1}{\mathrm{s}}$, the analogue signal is not able to undercut the threshold level, and the detector does not measure any ToT-values.

This first example shows the expectation of how a spectrum changes with an increasing event rate. This is no proof for the correct working of the simulation as it still

has to be evaluated with measurements. These are presented in later sections within this chapter. The pile-up of individual pulses as a function of their times of occurrence is described in the following.

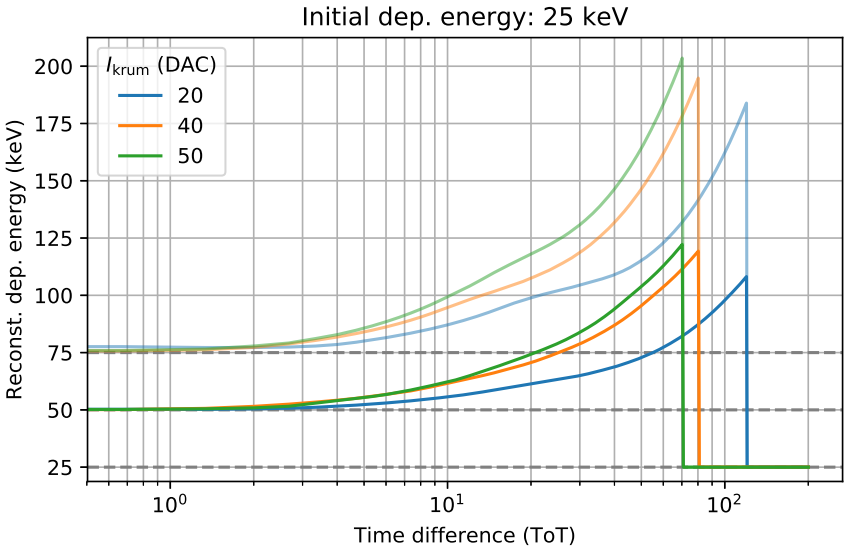

Figure 7.17.: The reconstructed deposited energy for the pile-up of analogue pulses with a deposited energy of 25 keV. Dark-coloured curves represent the pile-up of two events, light-coloured curves of three events. Only the energy of the first registered event is considered. The colours correspond to the settings of I_{krum} according to the legend. Dashed lines represent the reconstructed deposited energy for the case that all events occur simultaneously.

It is shown for an exemplary energy of 25 keV in figure 7.17. The dark-coloured curves represent the pile-up of two events and the light-coloured curves the pile-up of three events. The times of occurrence between the pulses are varied according to the x-axis. The deposited energies and their times are used as input to the analogue electronics simulation, which then provides the corresponding ToT-value. The result is finally converted to deposited energy. Three curves for different settings of I_{krum} according to the legend are depicted. Dashed lines indicate reconstructed energies when the events occured simultaneously. If the time difference between the input events is exactly 0, they can be interpreted as a single event with an energy of the sum of the individual events. Succeeding pulses take place during the rising edges of their previous events for increasing time differences. Since the rise time is fast, the reconstructed deposited energy varies only slightly compared to coincident events. Once the time difference exceeds the rise time of the peak of a pulse, the reconstructed deposited energy starts to increase steeper as a function of time difference. The rise time is almost independent of I_{krum}. This is not the case for the reconstructed energy,

as the effect of pile-up is larger the higher the current is. At a certain time difference between events, the first pulse is able to undercut the threshold. The vertical cutoffs in the plot indicate these times. Here, the reconstructed energy suddenly drops to 25 keV as only the energy of the first pulse is considered. The robustness of the detector regarding pile-up increases with I_{krum}. This is because the duration of a pulse gets shorter, and the probability for a second pulse to take place on the falling edge of the first pulse decreases.

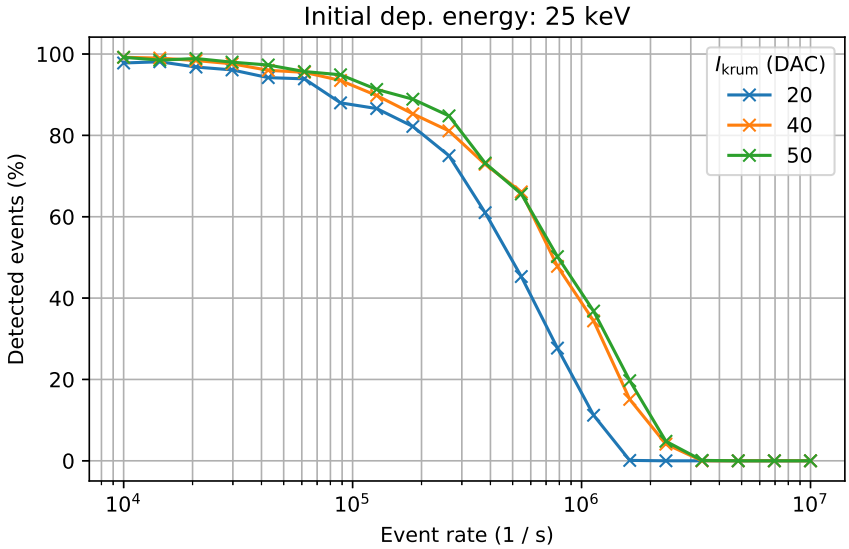

Figure 7.18.: The percentage of registered events in regards to the number of input events as a function of event rate per pixel. The curves represent the settings of I_{krum} according to the legend.

This can also be observed in figure 7.18 which shows the percentage of registered events for a mono-energetic input spectrum of 25 keV as a function of event rate per pixel. The colours represent the different settings of I_{krum} according to the legend. For low rates, the number of registered and input events is almost the same. The number of registered events decreases with an increasing event rate. The detector with the lowest I_{krum} cannot reach rates as high as for higher settings of the current. For large time differences, shown in figure 7.17, the reconstructed deposited energies reach values greater than 100 keV which is over 4 times larger than the initial energy. In this case, the reconstructed energies of the first pulse always stays the same. The second pulse exceeds and undercuts the threshold, resulting in the output of a ToT-value. Figure 7.19 depicts these as a function of the time difference in ToT. The second pulse starts at about the threshold level, leading to reconstructed deposited energies larger than the initial energy. With increasing time difference, the starting point begins to shift closer to the baseline level, resulting in an event with identical reconstructed

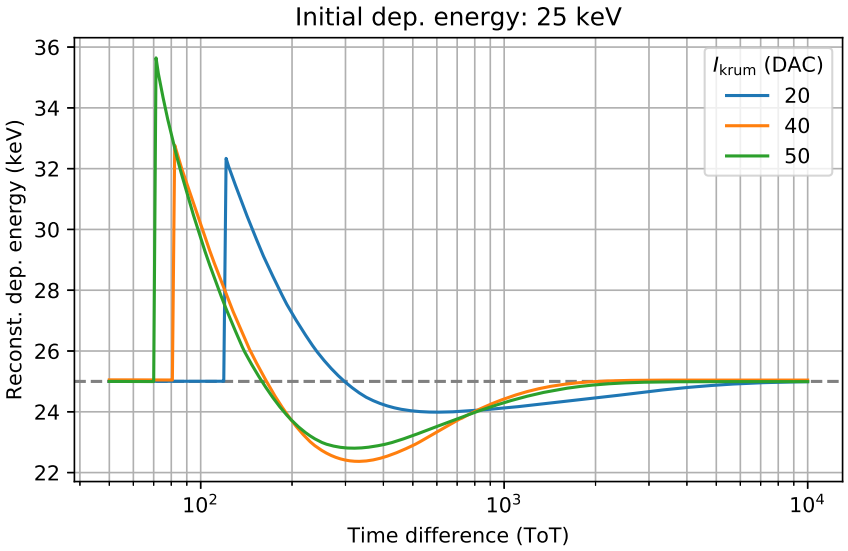

Figure 7.19.: The reconstructed deposited energy for the pile-up of two analogue pulses with deposited energies of 25 keV. Only the energy of the last event is considered. The colours correspond to the settings of I_{krum} according to the legend. The dashed line additionally represents the deposited energy of a single pulse.

and initial energy. This case is represented by the intersection of the curves with the dashed line. For even larger time differences, the second pulse begins on the first pulse's undershoot, leading to an underestimation of the reconstructed energy. The curves reach their minima when the starting point is at the minimum of the first pulse's undershoot. Reconstructed energy begins to increase until the first peak has reached the baseline level again.

The analysis of the reconstruction of deposited energies as a function of the time difference between two events shows that the correct simulation of the analogue signal is a necessity to precisely model pile-up effects. It reflects that the actual and reconstructed deposited energies differ, depending on the time between events and, as a consequence, the event rate.

7.5 Low photon flux evaluation measurements

An evaluation with low photon flux measurements is made to approve the simulation of the analogue electronics. The R-series spectra of section 6.3.4 are utilised. The python package xpecgen [21] is used to generate the initial photon spectra. I_{krum} is set to 50 DAC for all detectors. The setup corresponds to the one defined in section 6.2. All three detectors have plastic caps attached, which protect from physical damages.

Additionally, two of the detectors employ flat metal filters. The Al filter has a thickness of 2 mm, the Sn filter of 1 mm. The detectors are named according to their filters in the following. The detector without filter is denoted as *Vac*. The corresponding deposited energy spectra are generated via the initial photon spectra for all detectors separately via the method introduced in section 6.3.2. Their events are used as input to the analogue electronics simulation, which returns the response spectra for R0 to R19 depicted as solid lines in figure 7.20. Measurements of these spectra are reflected as dashed lines. Here, as introduced in section 6.4.5, the energy correction is applied to measurements. All spectra are normalised to the maximum of the *Vac*-histogram for energies greater than 20 keV.

The plots show that measurements and simulations generally agree well. The shapes of the spectra are reflected accurately, with peak positions at the correct deposited energies. However, there are discrepancies for the amplitudes, especially for low deposited energies. These can mostly be attributed to the detector response simulation analysed in section 6.6 and not to the analogue electronics simulation. Since the shape of the spectra and the cutoff at high energies are modelled correctly, the pulse shape simulation is considered accurate.

7.6 X-ray tube spectra for high photon flux measurements

The behaviour of Dosepix for high photon fluxes is investigated in the following sections. The highest flux is achieved with no filter applied to the X-ray tube and a high setting of the tube's voltage and current. However, all photon spectra look very similar since the low-energy part of the bremsstrahlung spectrum only slightly depends on the tube voltage (see section 2.3 for more details). Different kinds of filters are used for the X-ray tube to get spectra with greater variation in their distributions. These are denoted as WO- and S-series spectra in the following and are listed in table 7.3. The main filter consists of aluminium, as this material only slighty attenuates the photon flux while still influencing the spectrum's shape.

The initial photon spectra are generated via xpegcen [21] and are depicted in figure 7.21 (a). The corresponding deposited energy spectra of the *Vac* detector are shown in (b). The defined initial photon spectra are used in the following sections, which regard measurements made with the Dosepix detector for high flux conditions.

7.7 Threshold variation issue

The previous simulations are expanded by increasing the fluence of the photon field. Pile-up is expected to take place now. Therefore, it shows how the detector works under these conditions and how well the analogue electronics simulation agrees to measurements. In the following, an undesired variation of the threshold is observed.

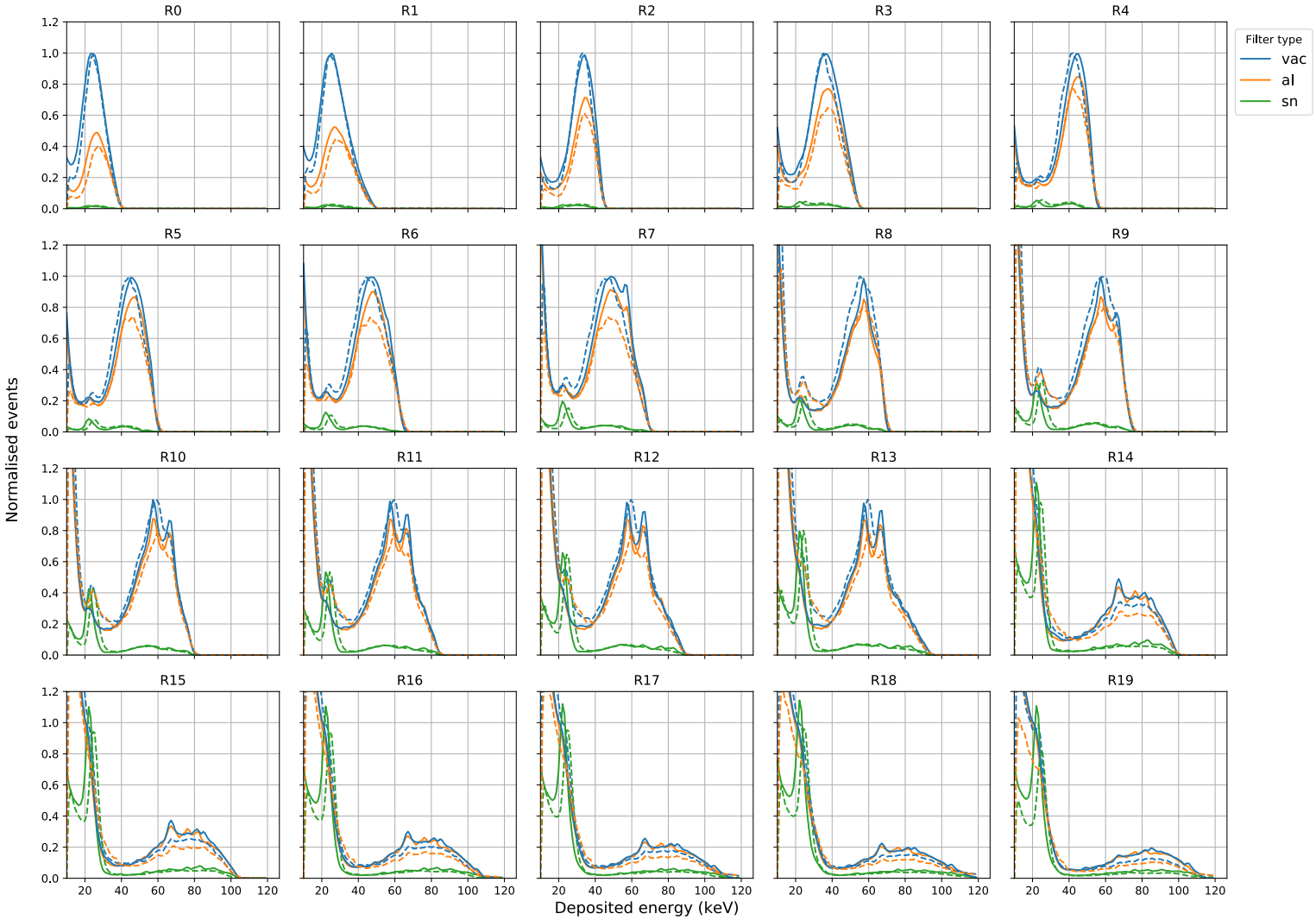

Figure 7.20.: Simulations and measurements of R-series spectra (see section 6.3.4 for their definition). A setup of three Dosepix detectors with filters according to the legend is used. Simulated initial photon spectra are used as input to the analogue electronics simulation to determine the solid curves. The dashed lines reflect the responses of the detectors from measurements. All spectra are normalised to the maximum of the *Vac*-histograms for energies greater than 20 keV.

Code	kVp	Al (mm)	Cu (mm)	Sn (mm)	mean energy (keV)
WO40	40	1.5	0	0	26.98
WO60	60	4	0.2	0	43.95
WO80	80	4	0.2	0	54.59
WO100	100	4	0.2	0	60.6
WO120	120	4	0.2	0	64.91
S60	60	1.5	0	0.06	35.79
SP60	60	6.5	0	0.06	43.04

Table 7.3.: The filter thicknesses and tube voltages for the X-ray tube spectra utilised for measurements of high photon flux conditions. Al, Cu, and Sn are used as filter materials. Additionally, the mean photon energy of each spectrum is listed.

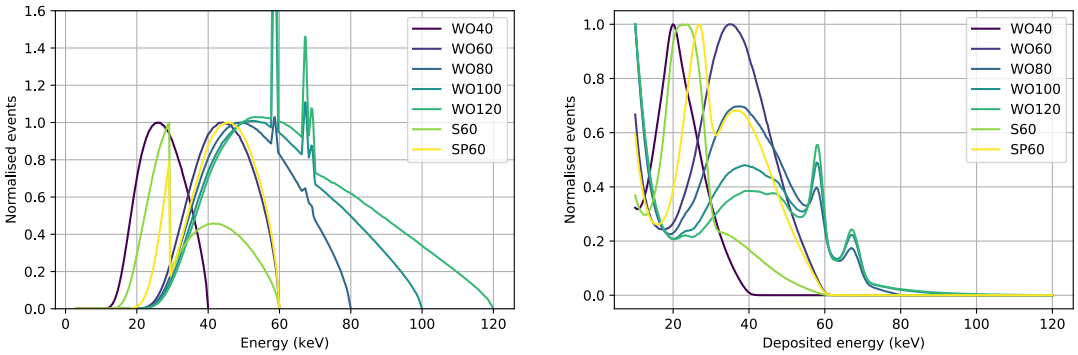

(a) Initial photon spectra

(b) Deposited energy spectra

Figure 7.21.: (a) shows the initial photon spectra for X-ray tube voltages and filters as specified in table 7.3. (b) depicts the corresponding simulated deposited energy spectra for the *Vac* detector. Each curve, in (a) and (b), is normalised to its maximum, excluding the characteristic peaks.

Measures to prevent the issue are introduced and evaluated by comparing measurements and simulation.

7.7.1 Measurements and description of the issue

The behaviour of Dosepix for different settings of I_{krum} is investigated. The detector stays at a fixed position close to the focal spot of the X-ray tube. Only the protective plastic cap is installed. For a selected X-ray tube spectrum with filters installed according to the previous section, the tube voltage setting stays fixed in-between measurements. This ensures that the shape of the photon spectrum remains while the flux

is varied linearly by adjusting I_{XRT}. All measurements are performed with shifted bins in Dosi-mode as described in section 6.1. A split parameter of $s = 4$ is utilised. This allows for fast measurements of the deposited energy spectra without dead-time. However, event statistics are reduced by a factor of 4 due to the applied splitting. Irradiation times are kept short to prevent an overflow of the histogram bins of the Dosepix detector. A value of $\Delta t_{\mathrm{XRT}} = 500\,\mathrm{ms}$ is used for all measurements. This is the safest and easiest method of overflow protection. Another measure is to increase the read-out time of the hardware. However, this requires an optimisation of the hardware and its firmware. Also, there is no guarantee that no overflow takes place for very high photon fluxes nevertheless.

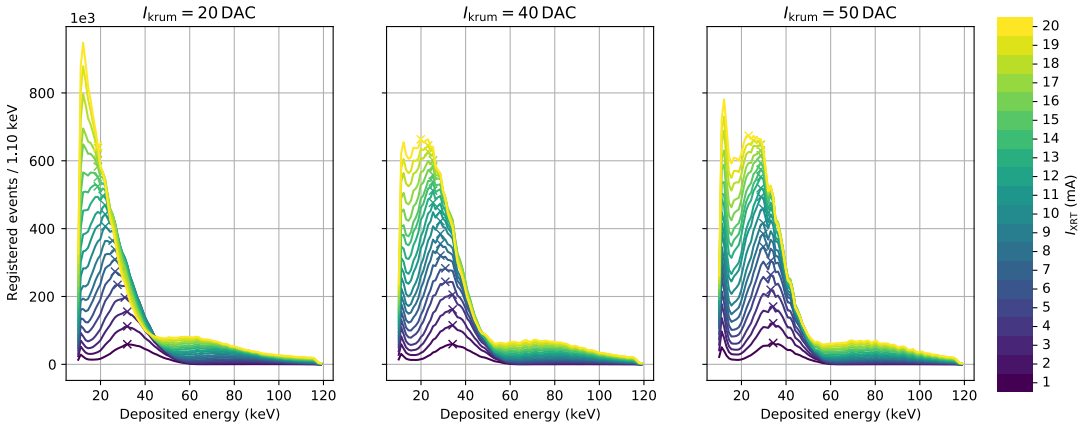

Figure 7.22.: Measurements of a WO60 photon spectrum with a single Dosepix detector for different settings of I_{krum} according to the titles of the plots. The colours of the curves correspond to the tube current I_{XRT} indicated by the colour bar.

Figure 7.22 depicts deposited energy spectra for measurements of a WO60 X-ray tube spectrum, filtered according to table 7.3. The colour of the curves corresponds to the value of the tube current I_{XRT} indicated by the colour bar. The titles of the plots denote the setting of I_{krum}. Due to the measurement with shifted bins in Dosi-mode, all spectra are contained within a region of $[10, 120]$ keV. Additionally, measurements of the air-kerma rate $\dot{K}_{\mathrm{air}}$ are made via Dosimax Plus, a semiconductor detector for dosimetry applications created by IBA dosimetry [9]. Dosepix is exchanged with this detector, and measurements for different I_{XRT} are performed. This results in a linear relation of $\dot{K}_{\mathrm{air}}$ and I_{XRT} described via

$$\dot{K}_{\mathrm{air}} = k \cdot I_{\mathrm{XRT}} \tag{7.22}$$

and $k = (0.3753 \pm 0.0006)\,\frac{\mathrm{mGy}}{\mathrm{mA}}$ for the used setup. All results are presented in regards to I_{XRT} in the following, but can easily be converted to $\dot{K}_{\mathrm{air}}$ via factor k.

For low values of I_{XRT}, the detector registers a deposited energy spectrum whose shape is independent of I_{krum}. The shape corresponds to the spectrum of the simulation in figure 7.21 (b). Increasing the current of the X-ray tube I_{XRT} leads to a linear increase of events within the detector's sensor as indicated by a growing peak amplitude. Pile-up events begin to become discernible in the spectra. These have energies greater than 60 keV which physically is not possible as the highest photon energy is limited by the X-ray tube voltage of 60 kV. The pile-up regime of deposited energies increases towards larger energies while also the number of registered events increases. The colours of the curves correspond to the settings of I_{krum} according to the legend.

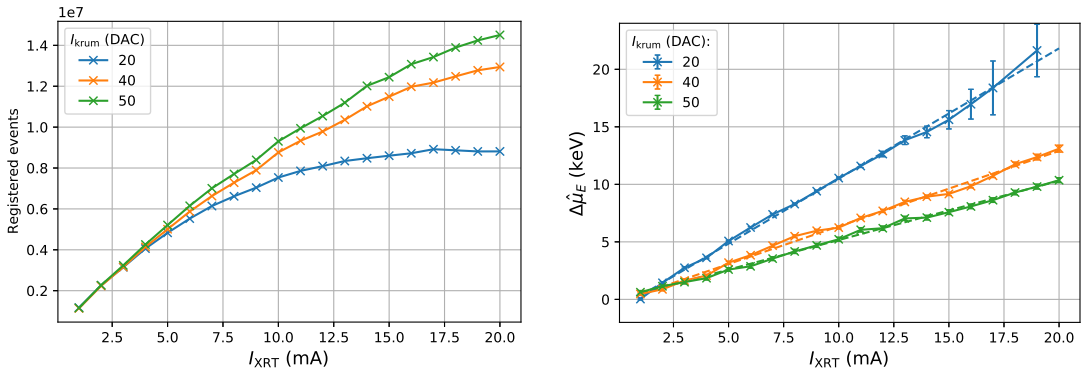

(a) Number of registered events

(b) Peak energy shift $\Delta\hat{\mu}_E$

Figure 7.23.: (a) shows the registered events for the measurements of a WO60 spectrum. (b) depicts the peak energy shift $\Delta\hat{\mu}_E$ in regards to a low photon flux measurement. The peak energies are determined from a fit with function (3.4) to the curves of figure 7.22. The error bars correspond to the fit errors of the peak positions. The dashed lines are linear functions optimised to the curves. Both plots show data as a function of the X-ray tube current I_{XRT}. The colours of the curves correspond to the setting of I_{krum} according to the legends.

The total number of registered events as a function of X-ray tube current I_{XRT} is reflected by the curves in figure 7.23 (a). While the number of photons increases linearly as a function of I_{XRT}, the number of registered events does not. Multiple events are registered as single events due to pile-up as shown for the example in section 7.4. The higher the value of I_{krum}, the more robust the detector is against pile-up and, as a consequence, the higher the number of registered events.

There is an issue in the measurements which is not present in the simulation of the analogue electronics. With increasing I_{XRT}, and therefore, photon flux, the curves in figure 7.22 start to shift towards lower deposited energies. For the simulation, the peak position remains almost independent of the tube current. The measured energy shift $\Delta\hat{\mu}_E$ of the peak energy in regards to the peak energy for low photon flux as a

function of the tube current is depicted in figure 7.23 (b). Here, the peak positions are estimated by a fit to the curves of figure 7.22 via equation (3.4). The error bars correspond to the fit errors. The dashed lines indicate the linear relation between the peak shift and the X-ray tube current. Like for the number of registered events before, for a higher setting of I_{krum} the detector is more robust for high photon flux conditions.

The measurements indicate that the analogue electronics simulation does not fully describe the hardware of the Dosepix detector. The measured deposited energies are determined by converting *ToT* via the corresponding calibration function. *ToT*, as its name *Time over Threshold* indicates, is a measure for the duration of an analogue pulse. The shift of peaks in the deposited energy spectrum is attributed to an underestimation of ToT. Under the assumption of analogue signals keeping their shape, the observed issue is explained by a decreasing baseline voltage or an increasing threshold level U_{THL}. Both effects are exchangeable, and a variation of their level by the same amount but with an opposite sign returns identical results. As the baseline level for a Dosepix detector cannot be varied easily in hardware, a focus on the threshold is put in the following.

7.7.2 Threshold correction

To correct the observed energy shift of the registered spectra, the relation between this shift and the threshold setting must be determined. Various measurements with an X-ray tube are performed with the voltage set to 40 kV, and only the internal filter of the output window of 1.5 mm aluminium present. In general, any X-ray source can be used. The requirement is a dominant peak within the deposited energy spectrum. Multiple measurements under a variation of the threshold voltage are made. Afterwards, the peak positions in the deposited energy spectra are estimated via a fit with equation (3.4). The measured deposited energy spectra are depicted in figure 7.24. In measurements, the Dosepix detector is positioned far away from the focal spot of the X-ray tube. This keeps the photon flux low and reduces pile-up. In between measurements, the value of the threshold is varied by ΔTHL. This change is added to the threshold value determined in the detector's equalisation, i.e. THL_0. The value is set in hardware in digital units, represented by DAC. The values of the threshold variation ΔTHL are indicated by the colour bar. The figure shows three plots, each corresponding to a different setting of I_{krum} denoted by the titles. The dashed lines represent the optimised fit functions that provide the mean deposited energies of the peaks. The differences of the measured peak energies to the peak energy for a measurement with the original threshold of THL_0, i.e. $\Delta\mathrm{THL} = 0$, are denoted as $\Delta\hat{\mu}_E$. The curves of the figure show that reconstructed deposited energies are shifting towards lower energies for increasing ΔTHL, independent of I_{krum}. Figure 7.25 depicts the correlation of $\Delta\hat{\mu}_E$ and the threshold shift ΔTHL. Three curves, one for each setting of I_{krum} as denoted by the legend, are shown. An approximately linear relation is

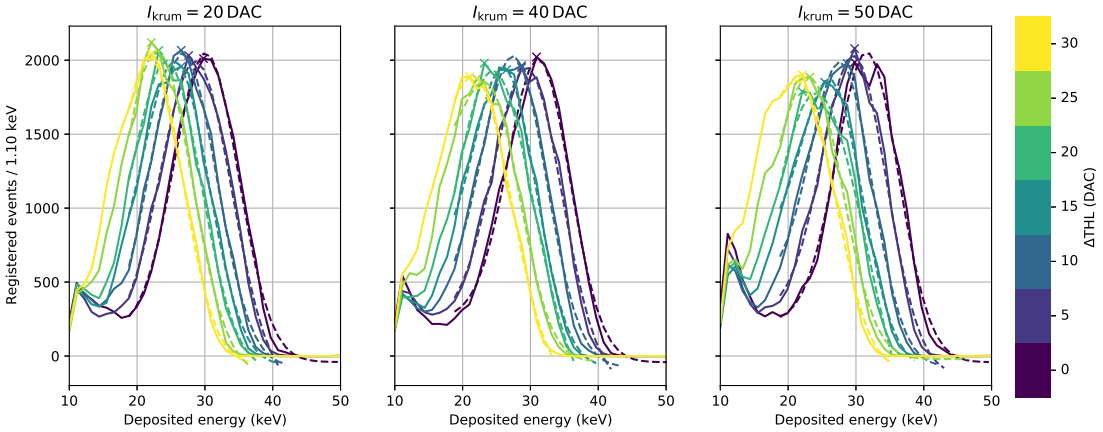

Figure 7.24.: The measurements of an X-ray tube spectrum filtered with 1.5 mm aluminium. The tube voltage is set to 40 keV. The Dosepix detector is used with different settings of I_{krum} according to the titles of the plots. The colours of the curves correspond to the threshold level change ΔTHL indicated by the colour bar.

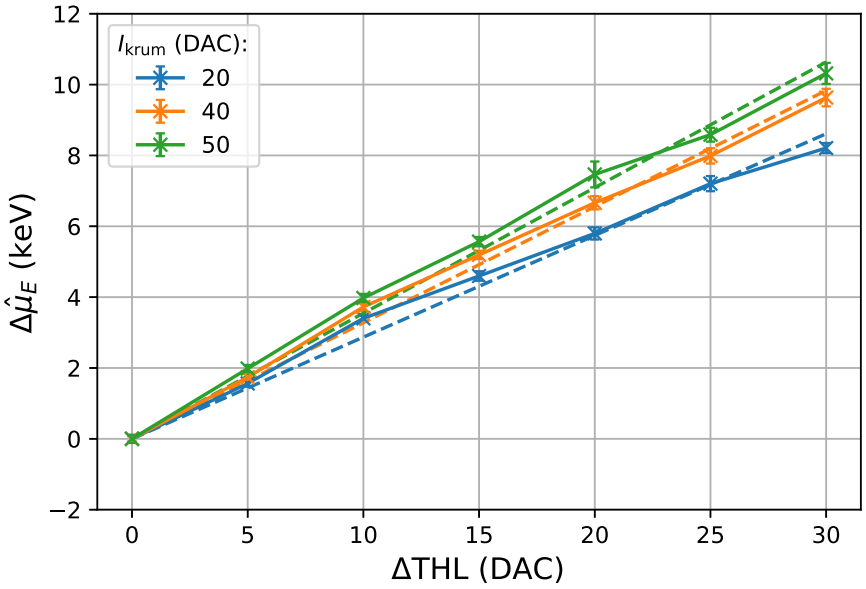

Figure 7.25.: Energy shift $\Delta\hat{\mu}_E$ as a function of THL shift ΔTHL. The colours of the curves correspond to the setting of I_{krum} indicated by the legend. Dashed lines represent the correlation of the parameters according to equation (7.23).

discernible. The slopes of the curves increase with increasing I_{krum}. The conversion from energy shift $\Delta\hat{\mu}_E$ to threshold shift ΔTHL is of interest for later applications. A measured shift in energy can directly be transformed into a corresponding threshold shift. This allows correcting the THL to perform a second measurement. The relation of $\Delta\hat{\mu}_E$ and ΔTHL is defined as

$$\Delta\text{THL}(\Delta\hat{\mu}_E) = w \cdot \Delta\hat{\mu}_E. \tag{7.23}$$

The parameters w are optimised via a fit to the curves of figure 7.25. The values of w and their fit errors δw are listed in table 7.4.

I_{krum}	$w\ \left(\frac{\text{DAC}}{\text{keV}}\right)$	$\delta w\ \left(\frac{\text{DAC}}{\text{keV}}\right)$
20	3.48	0.08
40	3.05	0.05
50	2.82	0.05

Table 7.4.: Optimised fit parameters of equation (7.23) for the datasets of figure 7.25. These depict the correlation of the shift in deposited energy $\Delta\hat{\mu}_E$ as a function of the threshold shift ΔTHL for different values of I_{krum}. w corresponds to the inverse of the slopes in the figure, while δw is the associated error from the fit.

The determined correction function for the threshold level can then be applied to measurements. Previously, WO60 spectra were covered. The uncorrected deposited energy spectra are depicted in figure 7.22. Figure 7.23 (b) shows the corresponding energy shift of the peak $\Delta\hat{\mu}_E$ as a function of the X-ray tube current I_{XRT}. Via linear functions, depicted as dashed lines, the trend of the curves is described by two parameters, i.e.

$$\Delta\hat{\mu}_E(I_{\text{XRT}}) = m_{\text{sh}} \cdot I_{\text{XRT}} + t_{\text{sh}}. \tag{7.24}$$

The offset t is required since the measured shift in deposited energy is regarding the measurement for low flux. It does not necessarily correspond to the lowest possible setting of the tube current I_{XRT} of 1 mA. Instead, an additional measurement with a high distance to the X-ray tube is required for the reference peak energy. The optimised parameters of equation (7.24) are listed in table 7.5 for different values of I_{krum}.

Equations (7.24) and (7.23) are combined to

$$\Delta\text{THL}(I_{\text{XRT}}) = w \cdot (m \cdot I_{\text{XRT}} + t)\,. \tag{7.25}$$

This relation determines the threshold correction ΔTHL for a given tube current I_{XRT}. The setup has to be identical for all measurements as the X-ray tube current I_{XRT} directly represents the photon flux at the position of the detector. Even slight variations

I_{krum}	$m_{\mathrm{sh}}\ \left(\frac{\mathrm{keV}}{\mathrm{mA}}\right)$	$t_{\mathrm{sh}}\ (\mathrm{keV})$
20	1.132 ± 0.015	-0.82 ± 0.17
40	0.655 ± 0.010	-0.20 ± 0.12
50	0.515 ± 0.006	0.01 ± 0.08

Table 7.5.: The optimised parameters of linear equation (7.24) to describe the curves in figure 7.23 (b). They represent the deposited energy shift of the peaks $\Delta\hat{\mu}_E$, as a function of the X-ray tube current I_{XRT} for measurements of a WO60 spectrum. Results for different settings of I_{krum} are listed.

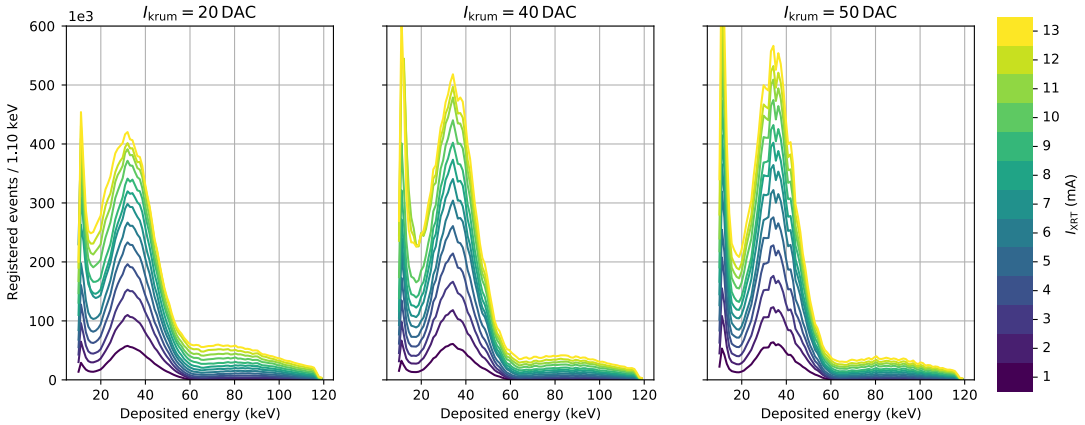

Figure 7.26.: Measurements of a WO60 spectrum with a Dosepix detector for different settings of I_{krum} according to the titles of the plots. For all measurements, the threshold correction of equation (7.25) is applied. The colours of the curves correspond to the tube current I_{XRT} according to the colour bar.

in the position lead to a large error in the threshold correction, and consequently, a wrong correction of the peak energy.

Figure 7.26 depicts the threshold corrected measurements of the WO60 spectrum. For these measurements, the X-ray tube current I_{XRT} is varied in a range of $[1, 13]$ mA in steps of 1 mA. The corresponding air kerma rate $\dot{K}_{\mathrm{air}}$ is calculated via equation (7.22) and $k = (0.3753 \pm 0.0006)\,\frac{\mathrm{mGy}}{\mathrm{mA}}$. For each setting of I_{XRT}, the threshold is corrected according to equation (7.25) and a measurement is made. The shape of the dominant peak, corresponding to the deposited energy spectrum measured for low photon flux conditions, is almost independent of I_{XRT} and I_{krum}. The peak position stays stable while the amplitude increases with increasing I_{XRT} and, therefore, photon flux. Figure 7.27 (a) depicts the total number of registered events as a function of X-ray tube current I_{XRT} for different values of I_{krum}. The trends are approximately linear and only slightly depend on I_{krum}. This is related to the small range of I_{XRT}. A devia-

tion for high values of the current is indicated as the presence of pile-up events starts to increase. Due to the binning of the registered deposited energies, the measurement of energies larger than 120 keV is impossible, which contributes to an underestimation of registered events. Events undercut the energy threshold and are not registered as an energy shift takes place in uncorrected measurements. If the threshold is corrected, these events are preserved, resulting in a steeper slope of registered events as a function of I_{XRT} depicted in figure 7.27 in comparison to figure 7.23 with no correction. The curves in figure 7.26 additionally reflect the probability for pile-up to occur. Deposited energies larger than 60 keV are physically not possible due to the tube voltage of 60 kV. Therefore, this energy region only consists of pile-up events. The amplitude of this region depends on the value of I_{krum}. For higher values, the duration of the analogue pulse shapes is reduced, and the detector is more robust against pile-up. This is reflected by the decreased number of events in the pile-up region. The number of events with deposited energies below 60 keV, for which pile-up is not as dominant, shows larger amplitudes for higher I_{krum}.

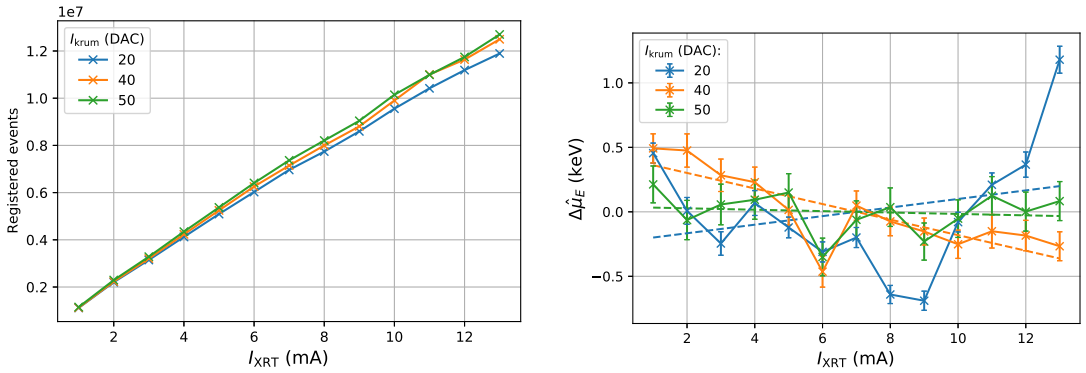

(a) Number of registered events

(b) Peak energy shift $\Delta\hat{\mu}_E$

Figure 7.27.: (a) shows the number of registered events, (b) the peak energy shift $\Delta\hat{\mu}_E$ in regards to a low photon flux measurement as a function of the X-ray tube current I_{XRT} for the WO60 spectrum with applied threshold correction. The peak energies are determined from a fit with equation (3.4) to the curves of figure 7.26. The error bars correspond to the fit errors of the peak positions. The dashed lines are linear functions optimised to the curves. The colours of the curves represents the setting of I_{krum} according to the legends.

Figure 7.27 (b) shows the shift of the peaks as a function of the X-ray tube current and, therefore, photon flux for the threshold corrected WO60 measurements. The different colours of the curves correspond to the settings of I_{krum} according to the legend. All curves are almost flat and show a maximum deviation of about 1 keV. The dashed lines indicate the linear trend of the data via fit. The slopes are small,

and the lines are centred about an energy shift of about 0. Therefore, the threshold correction is successful and can put Dosepix in a state where a correct measurement of the analogue signal is possible. The pile-up effects on these signals are still present as they are not affected by the correction. The threshold correction is made using the X-ray tube current as a reference. A method that is independent of the used setup and its settings is introduced in the following.

7.7.3 Threshold correction via leakage current

A requirement for the threshold correction is that uncorrected and corrected measurements are performed with the same setup. For real applications, this is impractical since all measurements have to be made twice, and many steps are involved to determine the threshold correction. Previously, the current of the X-ray tube represented the photon flux for a setup. Therefore, a measure to replace I_{XRT}, which is independent of the setup, is required. The leakage current I_{leak} of the detector's sensor is used as it includes the combined information of the photon flux and the initial photon spectrum and does not suffer from effects like pile-up. The previously described shift of either the baseline or threshold level of the analogue electronics is probably induced or influenced by a high leakage current. Therefore, a method to find a relation between the measures is required. Calibration measurements with the WO60 spectrum are performed. The Dosepix detector is placed close to the focal point of the X-ray tube. It ensures a high photon flux and, as a consequence, high leakage current I_{leak}.

Figure 7.28 (a) shows the measurement of the leakage current for the WO60 spectrum for different values of the X-ray tube current I_{XRT} as a function of time. The measurements are performed with the Fluke 8845A digital multimeter [89]. The current of the X-ray tube is varied within a range of $[1, 10]\,\mathrm{mA}$ in steps of $1\,\mathrm{mA}$. For each measurement, the X-ray tube was active for about $30\,\mathrm{s}$ to increase the number of acquired data points, resulting in the blue curve of figure 7.28 (a). Between the broad peaks, additional small sharp peaks are discernible. These originate from irradiations with the X-ray tube, which is active for a short time when the setting of the tube current is changed. The blue curve is smoothed via a low-pass filter to reduce the influence of noise. An auxiliary linear function, illustrated by the orange curve, is defined to intersect with each of the green curve's broad peaks twice. The red cross-markers indicate the points of the blue curve closest to the intersections. Via these points, the peak regions are determined. Within these regions, the mean and the corresponding standard error are calculated. These quantities represent the measurements of I_{leak} with increased statistics and are depicted as a function of the X-ray tube current I_{XRT} in figure 7.28 (b). A linear trend is described via

$$I_{\mathrm{leak}}(I_{\mathrm{XRT}}) = m_{\mathrm{leak}} \cdot I_{\mathrm{XRT}} + t_{\mathrm{leak}}. \tag{7.26}$$

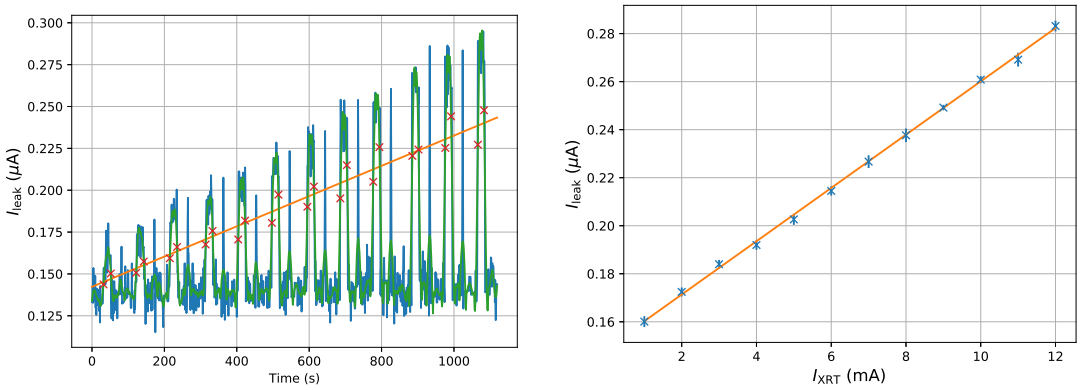

(a) Leakage current as a function of time

(b) Leakage current as a function of tube current I_{XRT}

Figure 7.28.: (a) shows the measurement of the leakage current I_{leak} of the sensor of Dosepix with the Fluke 8845A digital multimeter [89] under the irradiation of a WO60 spectrum. The X-ray tube current I_{XRT} is varied according to the x-axis of the plot in (b). The blue curve in (a) represents the leakage current's raw measurements, while the green curve represents a low-pass filtered version of the data. An orange line is introduced to find the intersection points with the filtered data to determine the different peak ranges. The points of the blue dataset closest to these intersections are indicated with red markers. (b) shows the mean and standard error of the mean for the leakage current values of the determined peak regions in (a) as a function of the X-ray tube current I_{XRT}. The standard error of the mean is reflected by error bars. The data trend is described via a fit with equation (7.26), indicated by the orange curve.

The optimised parameters and their errors from the fit are listed in table 7.6. Their values are represented by the orange curve in the figure. Measurements show that the parameters are approximately independent of the value of I_{krum}.

m_{leak} $\left(\frac{\mu A}{mA}\right)$	t_{leak} (μA)
0.0111 ± 0.0001	0.1492 ± 0.0008

Table 7.6.: Optimised parameters of equation 7.26 which describes the linear relation of the leakage current I_{leak} as a function of the X-ray tube current I_{XRT} for measurements with WO60 spectra.

The leakage current measurements correspond to the previously made measurements shown in figure 7.22 for the determination of the peak energy shift $\Delta\hat{\mu}_E$ as a

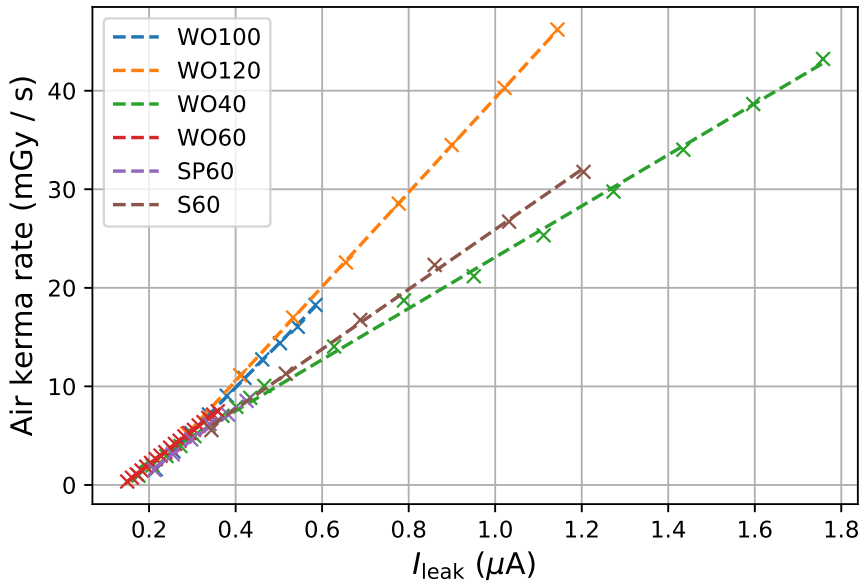

Figure 7.29.: The air kerma rate, measured via Dosimax Plus, as a function of the leakage current I_{leak} of Dosepix for the photon spectra of table 7.3. The dashed lines represent linear fits to the data.

function of X-ray tube current I_{XRT}. The used setup is identical, and therefore, the X-ray tube current represents the same photon flux. Therefore, equations (7.25) and (7.26) are combined to provide a relation between the threshold shift and the leakage current, i.e.

$$\Delta\mathrm{THL}(I_{leak}) = w \cdot \left(\frac{m}{m_{leak}} \cdot (I_{leak} - t_{leak}) + t \right). \tag{7.27}$$

This function is generally applicable to all initial photon spectra using the previously determined parameters from the calibrations via WO60 measurements. This method only requires the acquisition of the leakage current I_{leak} to correct the threshold and is used in measurements if not specified otherwise.

Since the leakage current influences the THL shift, the relation between I_{leak} and the air kerma rate $\dot{K}_{air}$, depicted in figure 7.29, is analysed to determine a description important for practical applications. Measurements of the settings and filters of the X-ray tube according to table 7.3 are executed. The leakage current of Dosepix is recorded via the digital multimeter and the air kerma rate at the position of Dosepix via Dosimax Plus. Linear trends of the curves are described by a fit with equation

$$\dot{K}_{air} = m_{leak2K} \cdot I_{leak} + t_{leak2K}. \tag{7.28}$$

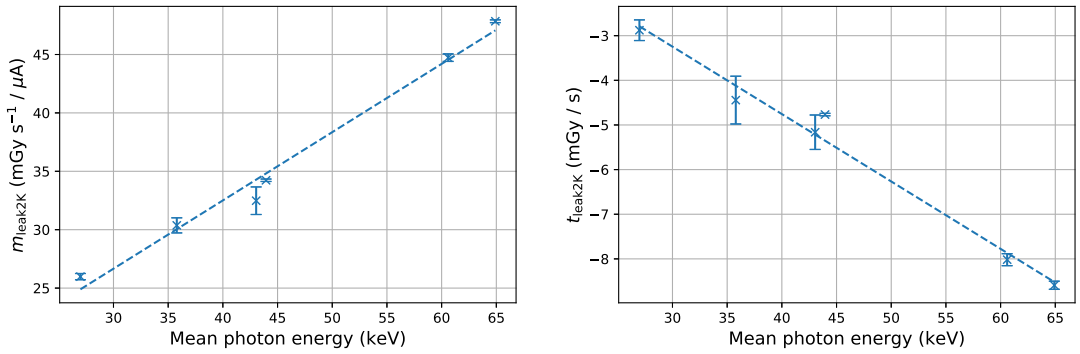

(a) Slope m_{leak2K}

(b) Intercept t_{leak2K}

Figure 7.30.: Slopes m_{leak2K} (a) and intercepts t_{leak2K} (b) of the curves in figure 7.29 as a function of mean photon energy $\overline{E}$. The values are determined from fits via equation equation (7.28). The error bars represent the corresponding fit errors and the dashed lines the linear trends of the data.

Parameter index	s (keV^{-1})	o
m_{leak2K} $\left(\left(\frac{\text{mGy}}{\text{s}}\right) \cdot \mu\text{A}^{-1}\right)$	0.58 ± 0.04	9.1 ± 1.7
t_{leak2K} $\left(\frac{\text{mGy}}{\text{s}}\right)$	-0.151 ± 0.011	1.3 ± 0.5

Table 7.7.: Slope s and intercepts o of the linear relation to describe the parameters m_{leak2K} and t_{leak2K} of equation (7.28) as a function of mean photon energy $\overline{E}$. The names in the first column are used as indices for the parameters of the columns. The unit of a parameter is the product of the units specified for the corresponding row and column.

Figure 7.30 shows the parameters m_{leak2K} (a) and t_{leak2K} (b) of equation (7.28) as functions of the mean photon energies $\overline{E}$ of the X-ray tube spectra. The linear trends of the parameters are described by the slopes s and intercepts o in table 7.7. The rows represent the parameters for the conversion of leakage current to air kerma rate, the rows the corresponding linear relation of these parameters to the mean photon energy $\overline{E}$. The units of o and s are determined by taking the product of the units in the corresponding row and column. A combination of the previously determined linear relations results in

$$\dot{K}_{\text{air}}(I_{\text{leak}}, \overline{E}) = (s_{m_{\text{leak2K}}} \cdot \overline{E} + o_{m_{\text{leak2K}}}) \cdot I_{\text{leak}} + (s_{t_{\text{leak2K}}} \cdot \overline{E} + o_{t_{\text{leak2K}}}), \tag{7.29}$$

which directly describes the air kerma rate $\dot{K}_{\text{air}}$ as a function of the leakage current I_{leak} and mean photon energy $\overline{E}$. Figure 7.31 shows the conversions from I_{leak} to air kerma rate $\dot{K}_{\text{air}}$ (a) and vice versa (b). The relations reflect that for a constant air

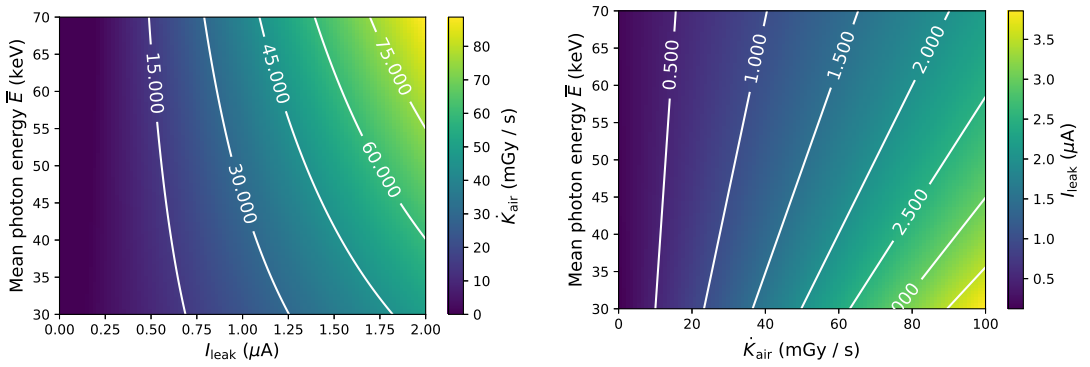

(a) I_{leak} to $\dot{K}_{air}$ (b) $\dot{K}_{air}$ to I_{leak}

Figure 7.31.: The conversions from leakage current I_{leak} to air kerma rate $\dot{K}_{air}$ (a) and vice versa (b) as a function of mean photon energy $\overline{E}$. Equation (7.29) is used with the parameters of table 7.7. The results of the conversions are resembled by the color bars.

kerma rate, the corresponding leakage current increases with decreasing mean photon energy. This is due to the increasing number of events in the sensor of Dosepix as the probability for the photoelectric effect increases. This result is important for dosimetry as for a constant air kerma rate, the stability of Dosepix is decreased for measurements of low photon energies.

7.7.4 Agreement of measurements and simulation

The agreement of threshold corrected measurements and simulations is analysed in the following. First, WO60 spectra are considered. The simulation requires the corresponding deposited energy spectrum for low photon flux and an event rate to distribute the events in the time domain. The rate is varied to optimise the simulated deposited energy spectra to measurements. The measurements are indexed using the X-ray tube current I_{XRT}. The event rate per pixel $\dot{N}$ in the simulation is assumed to depend linearly on this current, i.e. it is described via

$$\dot{N} = w_N \cdot I_{XRT}. \tag{7.30}$$

w_N is varied instead of varying $\dot{N}$ directly. In each iteration of the optimisation, the fitness of simulation and measurement is evaluated via loss $\mathcal{L}$

$$\mathcal{L} = \sum_{i=1}^{n_{krum}} \sum_{j=1}^{n_{XRT}} \mathcal{L}_{max,ij} + \mathcal{L}_{sum,ij} + \mathcal{L}_{curve,ij}. \tag{7.31}$$

Two nested sums are made. Index i iterates over the different settings of I_{krum} which uses values of $\{20, 40, 50\}$ DAC. Therefore, $n_{krum} = 3$. Index j considers the values

of the X-ray tube current I_{XRT} during measurements. n_{XRT} reflects the total number of measurements. The sums comprise three constituents, each attributing to different features of the spectra. In the following description, indices i and j are neglected for simplicity. $\mathcal{L}_{\mathrm{max}}$ considers the position of the maxima within the spectra. It is calculated via

$$\mathcal{L}_{\mathrm{max}} = \left| \frac{\hat{E}_{\mathrm{sim}}}{\hat{E}_{\mathrm{meas}}} - 1 \right| . \tag{7.32}$$

$\mathcal{L}_{\mathrm{max}}$ resembles the relative deviation of the mode of the measured spectrum $\hat{E}_{\mathrm{meas}}$, and the simulated spectrum $\hat{E}_{\mathrm{sim}}$. Only the modes for deposited energies greater than 20 keV are considered to neglect the high number of registered events for low energies, dominated by charge sharing and Compton events.

The loss $\mathcal{L}_{\mathrm{sum}}$ considers the total number of registered events. It is calculated via

$$\mathcal{L}_{\mathrm{sum}} = \left| \frac{N_{\mathrm{sim}}}{N_{\mathrm{meas}}} - 1 \right| , \tag{7.33}$$

i.e. by taking the relative deviation of registered events in measurement N_{meas}, and simulation N_{sim}.

Loss $\mathcal{L}_{\mathrm{curve}}$ represents the deviation of the curves of measured and simulated spectra. It is calculated via

$$\mathcal{L}_{\mathrm{curve}} = \sqrt{\sum_{k=1}^{k=n_E} \left(\frac{f_{\mathrm{sim}}(E_k)}{f_{\mathrm{meas}}(E_k)} - 1 \right)^2} , \tag{7.34}$$

which contains the sum of the deposited energy bins E_k in the spectra ranging from 10 keV to 120 keV. n_E resembles the total number of bins. The number of registered events for energy E_k of a spectrum f is represented via $f(E_k)$. $\mathcal{L}_{\mathrm{curve}}$ describes the relative deviation of the measured spectrum f_{meas} and the simulated spectrum f_{sim}.

The total loss $\mathcal{L}$ of equation (7.31) is used to optimise parameter w_N of equation (7.30) which describes the linearity between the X-ray tube current I_{XRT} and the event rate $\dot{N}$ per pixel. Since the setup is not changed in-between measurements, the parameter w_N is the same for all recorded data and therefore, loss $\mathcal{L}$ considers the whole dataset. A Nelder-Mead optimisation [43] provides a value of $w_N = 1.995 \cdot 10^4 \, \frac{1}{\mathrm{s \cdot mA}}$. However, this result is only valid for the current measurements and the utilised setup conditions. It resembles a constraint that establishes a fixed relation between the event rate and the true photon flux. The measured and simulated deposited energy spectra for WO60 photon spectra are compared to validate the quality of the pile-up simulation. The detector responses are shown in figure 7.32. The plots on the left-hand side represent measurements, the plots on the right-hand side simulations. The rows reflect different settings of I_{krum} according to the titles. The colours of the curves indicate the used values of the X-ray tube current I_{XRT} according to the colour bars. All spectra of a plot are normalised to the sum of the spectrum with the lowest setting of I_{krum}. The

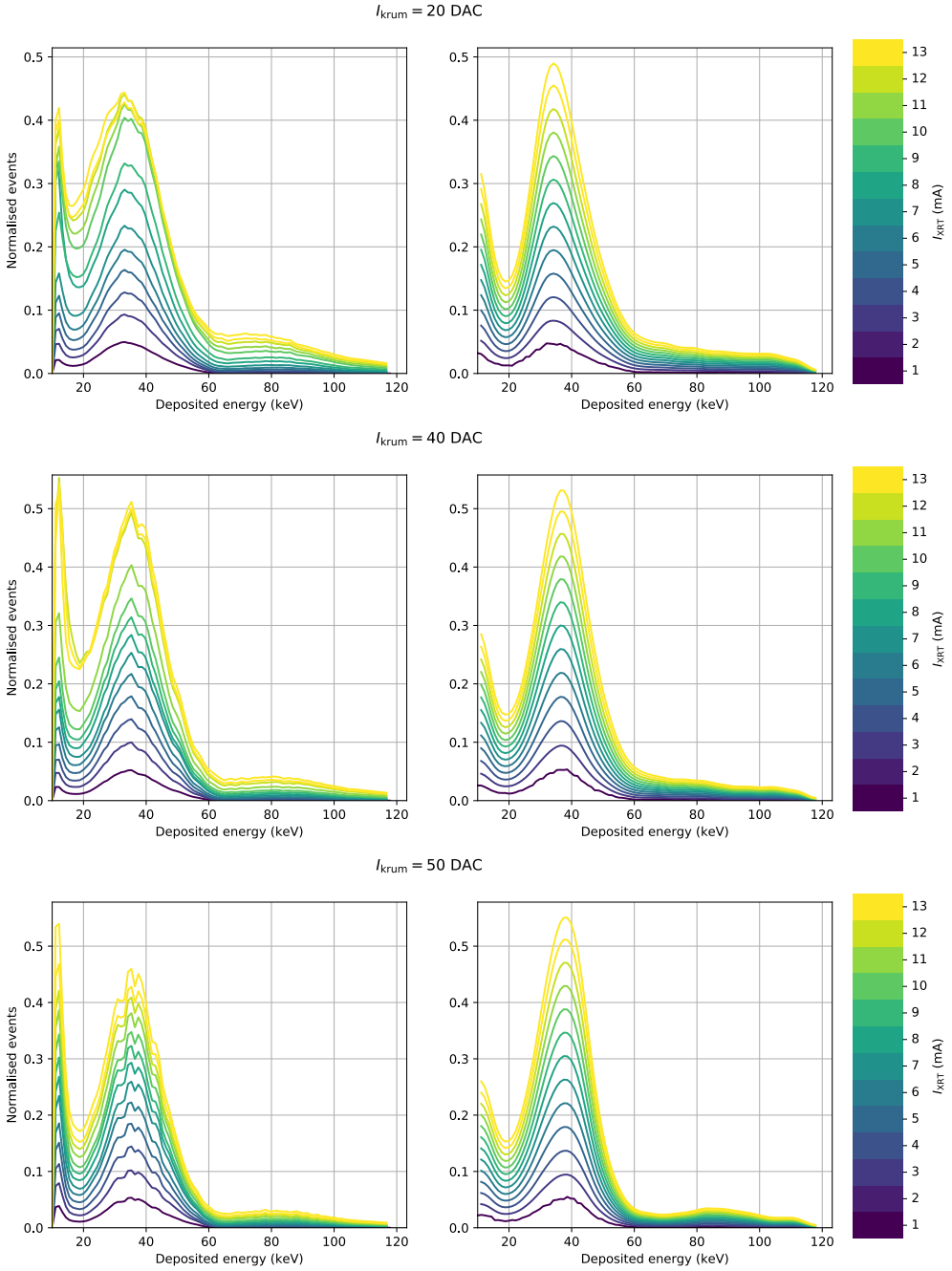

Figure 7.32.: The left-hand side shows measurements, and the right-hand side simulations of WO60 deposited energy spectra. Threshold correction is applied for the measurements. The rows of the plots correspond to the settings of I_{krum} according to the titles. The colours of the curves represent different currents I_{XRT} of the X-ray tube according to the colour bar. All spectra of a plot are normalised to the sum of the spectrum with the lowest setting of I_{XRT}. The used bin width is arbitrary.

number of bins on the deposited energy axis is arbitrary.

The shapes of the deposited energy spectra are compared in the following. Simulations and measurements agree well for low tube currents, independent of the used I_{krum}. The probability for pile-up is low, and deposited energy is measured as expected. With increasing photon flux, pile-up increases and energies greater than physically possible, i.e. 60 keV, are registered. The amplitudes of the dominant peak and the low energy domain, close to the threshold energy, increase while their shapes remain almost the same. Simulations and measurements generally agree well within the region of the dominant peak. However, for $I_{\mathrm{krum}} = 50\,\mathrm{DAC}$, the deviation of the amplitude, especially for the highest value of I_{XRT}, is largest. This issue is investigated via a comparison to measurements for different I_{krum}. For a current of 40 DAC, higher amplitudes are registered than for 50 DAC. However, for a higher value of I_{krum}, the detector is more robust to pile-up and should therefore show a higher amplitude in comparison.

The peaks close to the minimum detectable energy indicate a discrepancy for the threshold. The number of events in simulation is underestimated compared to measurements for all settings of I_{krum}. The dent at about 20 keV is located at approximately the same energy for all spectra. Its height is almost independent of I_{krum} in simulation but varies strongly in measurements, which indicates different thresholds for different I_{krum}. The threshold issue is related to the settings of the detector. The detector is calibrated separately for each setting of I_{krum}. The average of the calibration curves of all pixels is used, leading to only an estimation of the correct energy threshold. When the pile-up model is fitted to these curves, small deviations regarding the threshold may additionally be introduced.

Deposited energies greater than 60 keV only include pile-up events. The region's amplitude increases with increasing tube current and, therefore, photon flux and event rate. The higher I_{krum}, the more robust the detector is to pile-up, and the lower the growth of the peak as a function of photon flux. The amplitudes for simulations and measurements are similar in comparison. However, there are some deviations regarding the shapes of the spectra in this region. The agreement of $I_{\mathrm{krum}} = 50\,\mathrm{DAC}$ is best. Simulation and data show a broad peak at about 85 keV. Its shape is mainly defined by the sum of two deposited events from the dominant peak. An additional shift towards higher energies exists as pile-up has a higher probability of occurring the higher the first event's energy. The peak is discernible for all settings of I_{krum} in measurements. For simulation, the peak is broader in comparison and increasingly broadens with increasing photon flux. This discrepancy can be attributed to deviations of the energy resolution of the deposited energies. Another error source is the simulation of response spectra of Dospix resembling the input to the analogue electronics simulation. Here, the number of charge sharing and low energy Compton scattering events does not entirely agree with measurements. These events have a high contribution to the spectra. Pile-up then leads to a broadening of the deposited energy spectrum. Evalu-

ating the spectra's agreement for energies below the threshold is impossible, and only assumptions about the detector's behaviour can be made.

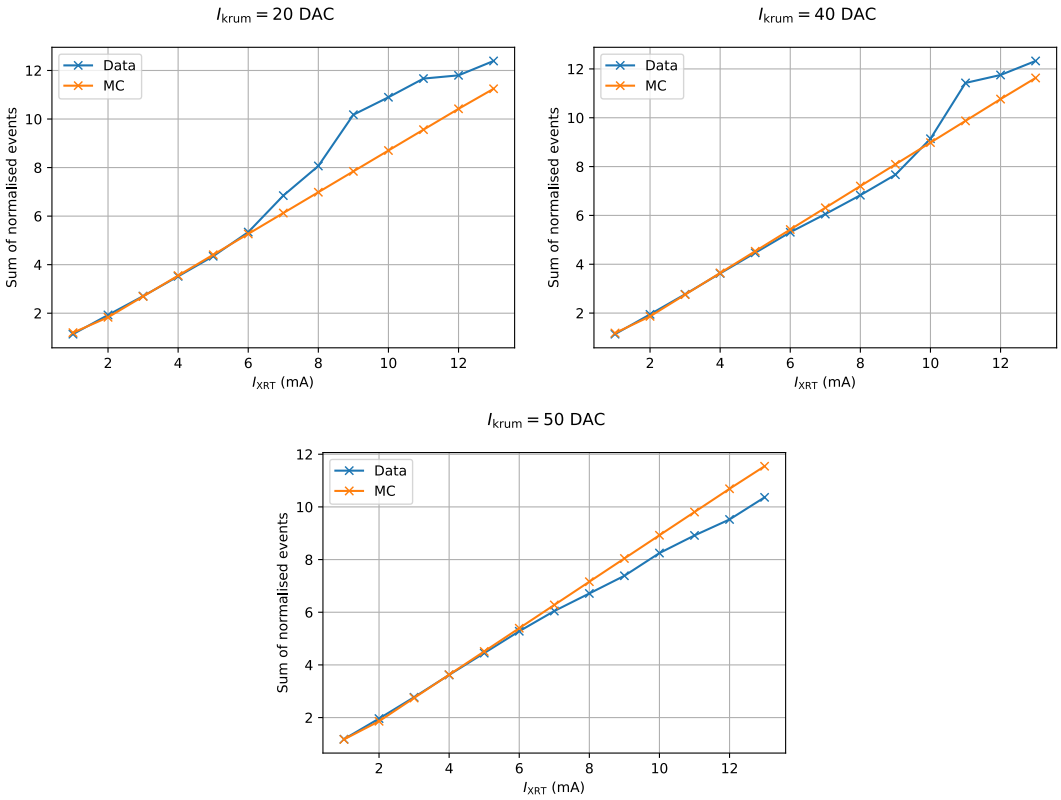

Figure 7.33.: Sum of the normalised spectra shown in figure 7.32 as a function of X-ray tube current I_{XRT} for MC simulations and measurements according to the legends. The plots represent different settings of I_{krum} resembled by the titles.

Figure 7.33 depicts the sum of the spectra of figure 7.32 as a function of the X-ray tube current I_{XRT} for MC simulations and measurements according to the legends. Each plot represents a different setting of I_{krum}, indicated by the title. The simulation predicts a linear relation between I_{XRT} and the corresponding spectra's integrals. There are noticeable deviations in data, indicating that the assumed linearity of the tube current and the photon flux in measurements is not perfect. This discrepancy cannot be attributed to pile-up. For a low setting of I_{krum} and high values of I_{XRT}, the integral overestimates the expected trend. Instead, an underestimation is expected if pile-up is considered.

Another test for the agreement of simulations and measurements of figure 7.32 is made via a two-sample Kolmogorov-Smirnov test. The null hypothesis is stated that two samples, one from the simulated spectrum and one from the measured spectrum,

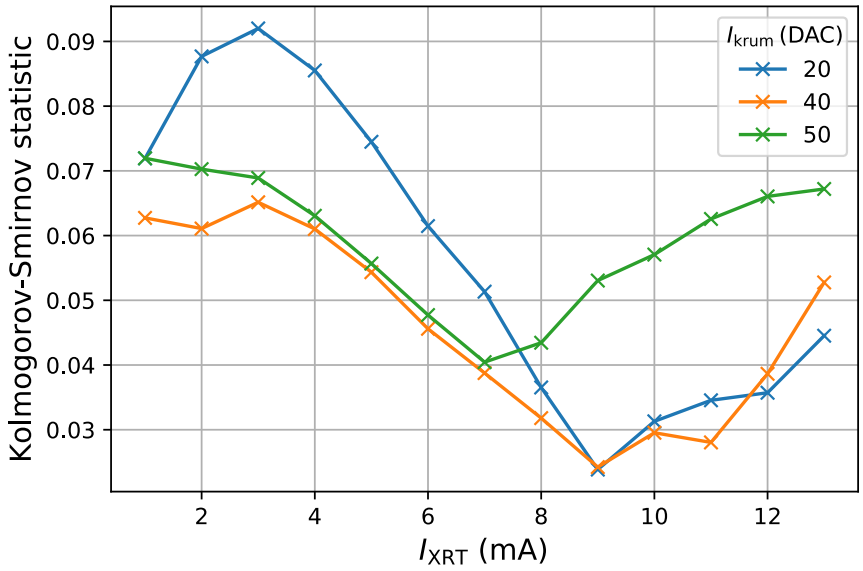

Figure 7.34.: Kolmogorov-Smirnov statistic calculated via equation (6.10) for the simulations and threshold corrected measurements of the WO60 spectra of figure 7.32. The colours of the curves represent different values of I_{krum} according to the legend.

are from a common distribution. The Kolmogorov-Smirnov statistic D is calculated according to equation (6.10) and described in more detail in section 6.3.4. The test is made for deposited energies $\geq 20\,\text{keV}$ to neglect the inaccuracies of the threshold energy. Figure 7.34 shows the determined values as a function of I_{XRT}. A rejection level for the null-hypothesis of $\alpha = 5\%$ is used. A rejection is made if D is greater than the limit $D_\alpha = 0.205$, calculated according to equation (6.11). Therefore, the null hypothesis is accepted for all spectra. This test only regards the shape of the spectra and not their scale. However, the scale was previously tested by analysing the number of registered counts of the spectra.

In conclusion, the simulation generally describes the measurements well. Multiple error sources make a perfect simulation impossible as the analogue pulse model and the measurement setup are complex. The assumption of a linear relation between X-ray tube current and photon flux underlies deviations within the measurements. Therefore, only an approximative description via the simulation is feasible. The achieved precision is considered sufficient as a qualitative representation of the characteristics of Dosepix is in focus.

7.8 I_{krum} variation issue

Previously, only the WO60 spectrum was analysed. Measurements with air kerma rates up to about $5\,\frac{\mathrm{mGy}}{\mathrm{s}}$ were performed. In the following, the S60 spectrum according to table 7.3 is examined. A threshold correction is applied. Simultaneously, photon flux, and as a consequence, the event rate are increased. An air kerma rate of about $12\,\frac{\mathrm{mGy}}{\mathrm{s}}$ for the highest setting of the X-ray tube current I_{XRT} is used. A new issue regarding dominant peaks of deposited energy spectra changing their position with increasing photon flux is observed in measurements. The issue and measures to describe the effect in simulation are discussed in the following.

7.8.1 Measurements and description of the issue

The left-hand side of figure 7.35 depicts the deposited energy spectra from threshold corrected measurements with the detector for a setting of $I_{\mathrm{krum}} = 20\,\mathrm{DAC}$ for S60 spectra. The plot on the right-hand side shows the corresponding simulations where the relation between tube current and event rate per pixel is optimised as described in the previous section. All spectra are normalised to the integral of the spectrum for the lowest setting of I_{XRT} and deposited energies $\geq 20\,\mathrm{keV}$. Parameter w_N of equation (7.30) is determined to $1.096 \cdot 10^5\,\frac{1}{\mathrm{s \cdot mA}}$. The equation is used to convert the X-ray tube current to the corresponding event rate. Figure 7.36 shows the sum of the spectra as a function of I_{XRT} with a good agreement of MC simulations and measurements.

Discrepancies are discernible in the deposited energy spectra of figure 7.35. Within the region the spectra's integrals are linear to the tube current, i.e. up to about $I_{\mathrm{XRT}} = 5\,\mathrm{mA}$, the shapes of the spectra agree well. The dominant peak remains stable and changes its amplitude as photon flux increases. The spectra's integrals decrease for higher currents of I_{XRT}, which is resembled by a decreasing amplitude of the dominant peak. This behaviour is present in measurements and simulation. For measurements, the peak position additionally shifts towards higher deposited energies, and the peaks broaden. This behaviour is not resembled by the simulation, with peaks approximately keeping their positions even at high photon fluxes.

The discrepancies of measurements and simulations indicate an issue of the electronics of Dosepix, extending the previous assumptions about the detector's functioning. Two issues come into question to be accountable for the discrepancy. First, the applied threshold correction might overcompensate if the photon flux is too high. The correction shifts deposited energies towards higher values while a baseline or threshold shift in the analogue electronics moves energies towards lower values. When correctly calibrated, these shifts compensate each other. If the threshold shift saturated for high event rates, overcompensation would occur, and spectra would shift towards higher energies. However, no broadening like observed in the measurements would occur.

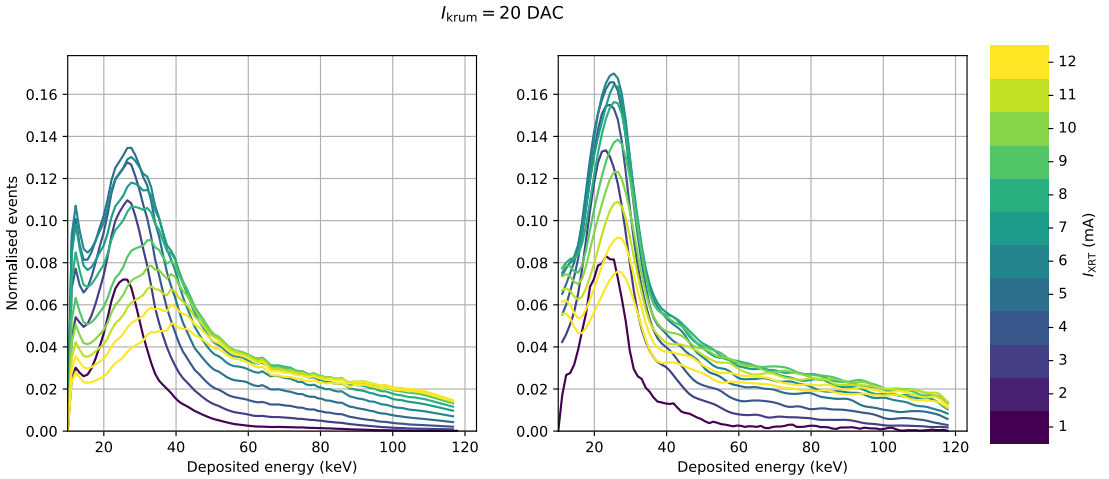

Figure 7.35.: The left-hand side shows threshold corrected measurements, the right-hand side simulations of S60 spectra. The setting of I_{krum} is 20 DAC. The colours of the curves correspond to the settings of the X-ray tube current I_{XRT} according to the colour bar. All spectra are normalised to the integral of the measurement spectrum with the lowest setting of I_{XRT} for deposited energies $\geq$ 20 keV. The binning on the x-axis is arbitrary.

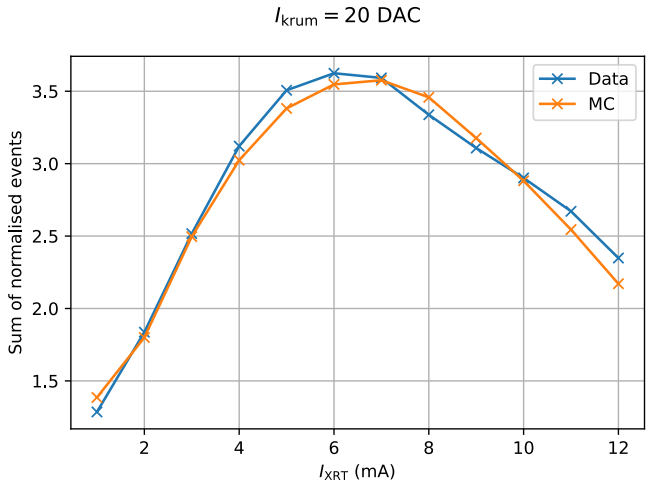

Figure 7.36.: Integrals of the curves of figure 7.35 for the S60 response spectra for MC simulations and measurements according to the legend. The integrals are depicted as a function of the X-ray tube current of the measurements.

Another explanation for the observed discrepancies is a change of I_{krum}. If the detector works perfectly, the value of the current remains constant. If possibly due to the high number of events in the sensor and as a consequence, increased leakage current,

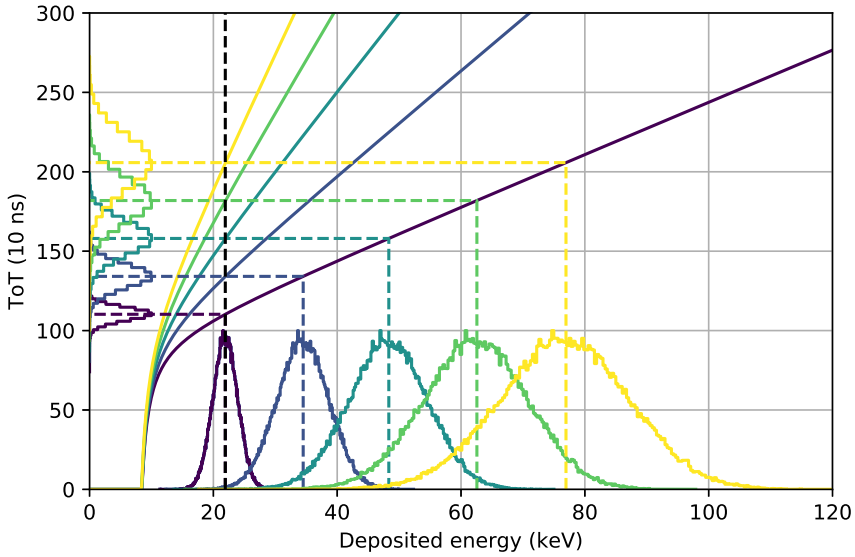

Figure 7.37.: The sketch shows how changes of I_{krum} lead to a distortion of the registered deposited energy spectrum of Dosepix. The dark-blue curve corresponds to high values of I_{krum} while the gradient towards yellow corresponds to a linearly decreasing I_{krum}. A detailed explanation of the observed effect of a shifted deposited energy is given in the text.

I_{krum} effectively decreases, the effects like described in the following occur. The explanation is based on figure 7.37. The calibration curves from deposited energy to ToT are artificial and represent a Dosepix detector for different settings of I_{krum}. The values of I_{krum} are arbitrary but vary linearly. A normally distributed ToT-spectrum on the y-axis is converted to the corresponding deposited energy spectrum on the x-axis. The dashed lines indicate the positions of the means of the spectra. The assumption that I_{krum} reduces with increasing event rate is made, reflected by an increasing slope of the conversion function, represented by a colour gradient from dark blue to yellow. The deposited energy spectrum for low flux, in dark-blue, is converted via the different conversion functions to determine the corresponding ToT-spectra. These spectra reflect what the detector registers. Since only the conversion function for low photon flux is used to convert ToT into deposited energy, the spectra along the y-axis are determined. The deposited spectra's mean values show that an almost linear shift towards higher energies takes place when I_{krum} is reduced. Simultaneously, the peaks broaden, resembling the observations made in measurements.

7.8.2 Dosepix calibration and simulation for a large I_{krum}-range

There is an indication that I_{krum} varies with increasing event rate of Dosepix. The detector is recalibrated for a large I_{krum} range to describe this effect in simulations. The calibration is performed utilising the deep learning approach of chapter 4 for which measurements of low statistics are sufficient. This allows to vary I_{krum} from 10 DAC to 50 DAC in steps of 2 DAC with measurement durations of about 10 minutes per step. Again, only large pixels are considered. The resulting calibration curves are depicted in figure 7.38.

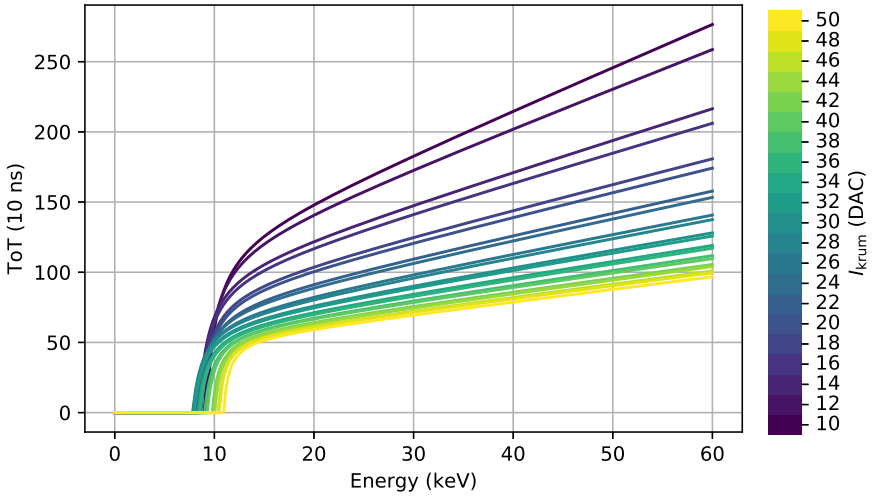

Figure 7.38.: Calibration curves for the conversion of deposited energy to ToT for the used Dosepix detector. The colours of the curves correspond to different settings of I_{krum} according to the colour bar.

The pulse shape model is optimised for each calibration curve according to the method introduced in section 7.2. The relative change of the determined model parameters as a function of I_{krum} are depicted in figure 7.39. Each curve represents a parameter according to the legend. The change is represented by the ratio in regards to the model parameters for $I_{krum} = 10$ DAC as listed in table 7.8.

I_{krum} (DAC)	I_{krum} (nA)	K (nA/V)	U_{THL}(mV)	τ (ns)	τ_2 (µs)	τ_3 (ns)	C_l (nF)	R_i (Ω)
10	2.102	105.729	22.122	67.634	30.369	253.426	11.83	8.712

Table 7.8.: Parameters of the pulse shape model optimised to the calibration curves in figure 7.38 for $I_{krum} = 10$ DAC. The first column corresponds to I_{krum} set in hardware during detector calibration, whereas the second column corresponds to the optimised value.

As described in section 7.2, some of the parameters of the model are assumed to be constant. Variations are observed because free parameters compensate inaccuracies of constant parameters. Also, an undefined behaviour of Dosepix under a variation of I_{krum} is possible. However, all parameters only change slightly and not by magnitudes. The variation lies within a range of about 0.4 to 1.9.

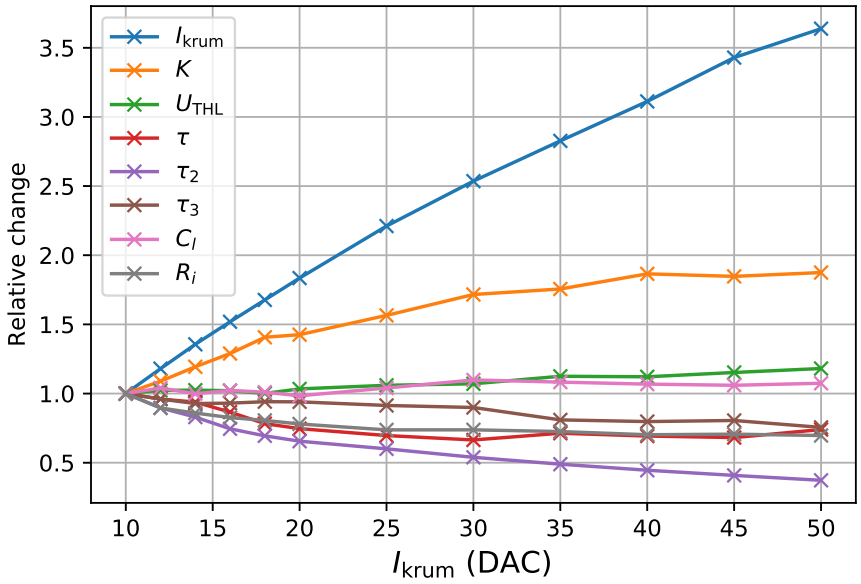

Figure 7.39.: The variation of the optimised pulse shape model parameters as a function of the set I_{krum}. All curves are normalised to the values for $I_{\text{krum}} = 10\,\text{DAC}$.

The value of I_{krum} provided from optimisation to the pulse shape model, called $I_{\text{krum,pulse}}$, is an exception. $I_{\text{krum,pulse}}$ is analysed separately since it is expected to vary linearly with the set value of I_{krum}, called $I_{\text{krum,set}}$. Figure 7.40 shows the correlation of optimised and set values via the blue curve. All values are represented in units of nA, utilising the conversion of $1\,\text{DAC} = 0.2\,\text{nA}$. The dashed line illustrates the relation $I_{\text{krum,set}} = I_{\text{krum,pulse}}$ which resembles the expectation. A large deviation is discernible, which is further investigated in the following. The calibration curves are utilised to describe the value of I_{krum} directly. The output voltage $U_{\text{out,filt}}$ of a pulse in the analogue electronics is reduced by a constant current of $-\frac{I_{\text{krum}}}{2}$ within a duration of Δt, described by equations 7.6 and 7.7. The time difference Δt is approximately proportional to the registered ToT-value. A pulse's voltage amplitude is proportional to the deposited energy.

Therefore, the relation $\frac{\Delta E}{\Delta ToT} \propto I_{\text{krum}}$ holds. This applies to the falling edge of a pulse shape but also to the linear parts of the calibration functions in figure 7.39. The fractions $\frac{\Delta E}{\Delta ToT}$ are calculated as a function of the set $I_{\text{krum,set}}$. Assuming the relation

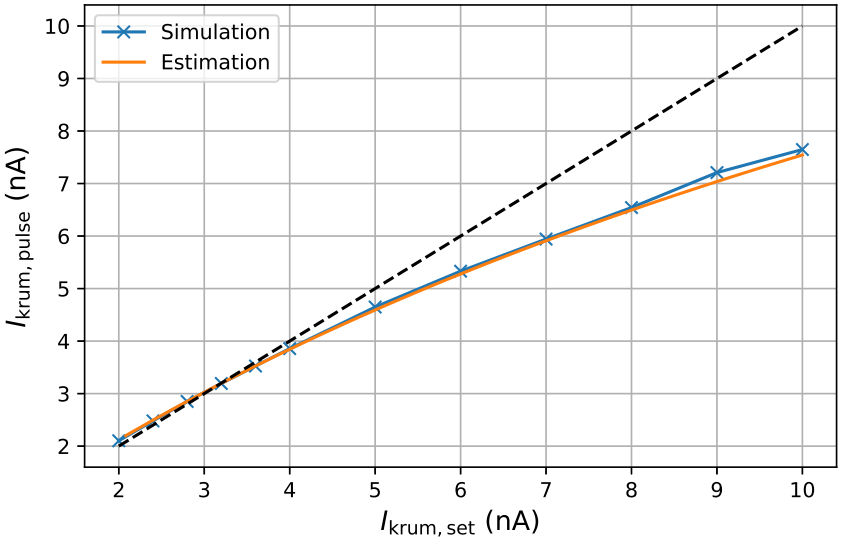

Figure 7.40.: Value $I_{krum,pulse}$ determined from fit to the pulse shape model in blue, and via an estimation from the calibration curves in orange as a function of $I_{krum,set}$. The dashed line represents the relation $I_{krum,set} = I_{krum,pulse}$.

$I_{krum,set} = I_{krum,pulse}$ holds for small values, the calculated fractions are normalised in regards to $I_{krum,set} = 2\,nA$. The resulting curve is illustrated in figure 7.40 in orange. The curve matches well with the blue one, corresponding to the simulation results. In conclusion, the effective value of I_{krum} is lower than the set one for values greater than about 4 nA. In the following, when refering to I_{krum} the set value in units of DAC is used. The optimised models of Dosepix for different values of I_{krum} can now be used in the pulse-shape simulation to implement the observed pulse shifting in measurements.

7.8.3 I_{krum} correction

Previously, when fitting the simulation to measurements, only the event rate per pixel was varied. Now, additionally, the change of I_{krum} is considered. Due to this additional dimension, the calculation time for the optimisation increases a lot. The process is sped up by precalculating the response spectra as a function of I_{krum} and event rate $\dot{N}$ and by linearly interpolating the results. This provides a function that is easily evaluated and compared to measurements by calculating the loss $\mathcal{L}$ via equation (7.31).

Figure 7.41 shows the integrals of the response spectra as a function of I_{krum} and event rate $\dot{N}$. Only simulated supporting points are shown. In between these points, a linear interpolation is executed. The number of registered events increases with increasing I_{krum}. Simultaneously, it increases with the event rate up to a certain rate.

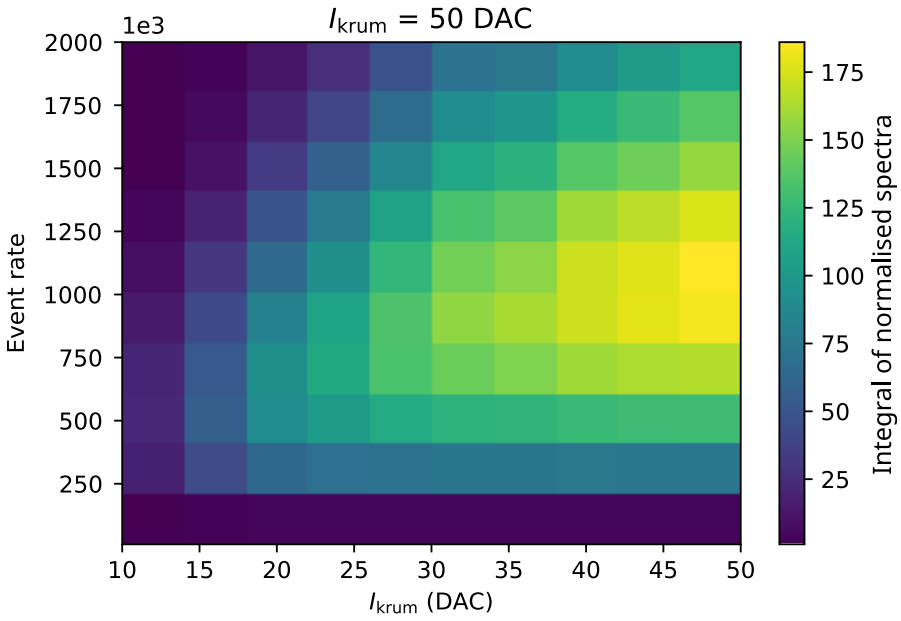

Figure 7.41.: The number of registered events for deposited energy spectra as a function of I_{krum} and event rate. The integrals are normalised to the integral with the lowest number of events.

Once too many events per second are present at the input of the analogue electronics, response spectra are dominated by pile-up, and the number of registered events decreases. When response spectra are sampled from the interpolated function, the conversion from ToT to deposited energy is always performed via the conversion function of the initial setting of I_{krum}. This corresponds to the method used in measurements. It would be preferable to correct I_{krum} during measurements, but would require a high effort to calibrate. Simultaneously, I_{krum} had to be changed, which would introduce dead-time and requires a measure to estimate the current event rate. Therefore, the simulation in regards to the measurements is adapted instead.

When optimising the simulation to measurements, the previous assumption of a linear relation between I_{krum} and the event rate registered by the detector holds. Additionally, the assumption of I_{krum} remaining constant until a certain event rate is exceeded is made. After this excess, I_{krum} decreases linearly with the event rate, represented via I_{XRT}. This effect is applied to the true current of I_{krum} in units of nA. A conversion from true to set I_{krum} is achieved via the relation of figure 7.40. In summary, the behaviour of I_{krum} is resembled by the function

$$I_{krum}(I_{XRT}) = \begin{cases} I_{krum,0} & \text{if } I_{krum} > I_{krum,0} \\ I_{XRT} \cdot m_{krum} + t_{krum} & \text{else} \end{cases}, \tag{7.35}$$

where $I_{krum,0}$ represents the start value of I_{krum}, i.e. the value the detector was calibrated with. The linear trend of the current is described via parameters m_{krum} and

t_{krum}. The threshold value for the tube current at which the decline begins corresponds to

$$I_{\mathrm{XRT,krum}} = \frac{I_{\mathrm{krum},0} - t_{\mathrm{krum}}}{m_{\mathrm{krum}}}. \tag{7.36}$$

Taking threshold- and I_{krum}-correction into account, the simulation's precalculated response spectra are fitted to measurements of S60 spectra. Three measurements, each for a different setting of the initial I_{krum}, are performed. These measurements are considered independent, i.e. parameters are not shared between the datasets. A loss like defined in equation (7.31) is used but the sum over I_{krum} is neglected. The measurements and optimised simulations are depicted in figure 7.43. The determined parameters for equation (7.30), describing the conversion from X-ray tube current I_{XRT} to event rate, and for equation (7.35), describing the trend of I_{XRT} as a function of the tube current, are listed in table 7.9.

I_{krum} (DAC)	w_N $(1/(\mathrm{s}\cdot\mathrm{mA}))$	m_{krum} $(\frac{\mathrm{nA}}{\mathrm{mA}})$	t_{krum} (nA)
20	$9.2 \cdot 10^4$	$-4.892 \cdot 10^{-2}$	3.793
40	$8.165 \cdot 10^4$	$-3.486 \cdot 10^{-2}$	6.351
50	$7.54 \cdot 10^4$	$-4.02 \cdot 10^{-2}$	7.366

Table 7.9.: Optimised parameters for the fit of simulation to measurements of S60 spectra. w_N describes the relation between X-ray tube current I_{XRT} and the event rate according to equation (7.30). Parameters m_{krum} and t_{krum} belong to equation (7.35) which describes the change of I_{krum} as a function of I_{XRT}.

The corresponding functions of the optimised parameters are depicted in figure 7.42. The event rate as a function of the tube current I_{XRT} is depicted in (a). The slopes for all initial settings of $I_{\mathrm{krum},0}$ are similar. Small variations are possible due to the inaccuracy of the threshold, i.e. the minimum deposited energy a detector can register. It is because different calibrations are used for different values of $I_{\mathrm{krum},0}$. The higher the photon flux, which depends linearly on I_{XRT}, the higher the deviation of the event rate if the thresholds differ.

Figure 7.42 (b) shows I_{krum} as a function of I_{XRT}. The y-axis reflects the values corresponding to the set values of Dosepix, while the variation of I_{krum} is performed on the true values of the current. All curves show a decrease of I_{krum} with increasing photon flux or I_{XRT}. This trend is discernible for the lowest setting of the tube current for which the values of I_{krum} is already lower than the initial setting $I_{\mathrm{krum},0}$. The slopes of the curves for different $I_{\mathrm{krum},0}$ are approximately the same.

The measured deposited energy spectra and the optimised simulations are depicted in figure 7.43. The different rows correspond to different settings of I_{krum} according to the titles. The left plot column shows the measurements, the right column the simulations. Different colours represent the settings of the X-ray tube current according

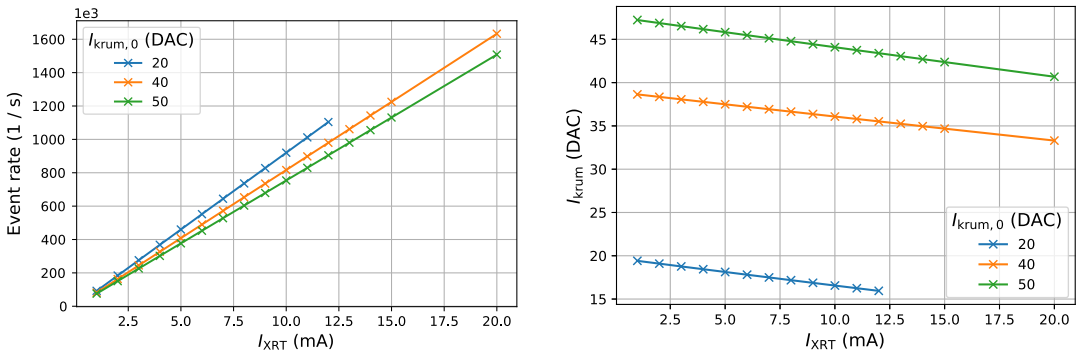

(a) Event rate vs. I_{XRT}

(b) I_{krum} vs. I_{XRT}

Figure 7.42.: Event rate (a) and effective I_{krum} (b) as a function of X-ray tube current I_{XRT}. The depicted values are the results from the optimisation of the pulse shape simulation to S60 measurements, shown in the left-hand column of figure 7.43. Three curves are depicted per plot where each corresponds to a different setting of the initial $I_{krum,0}$ as indicated by the legend.

to the colour bars. For $I_{krum} = 20\,\mathrm{DAC}$, the maximum value of I_{XRT} is 12 mA, while for the other plots it is 20 mA. For lower settings of I_{krum}, the detector is not as stable and cannot measure proper energy spectra once the photon flux is too high. The agreement of all spectra for low deposited energies shows deviations. This is again attributed to variations of the set and actual energy thresholds of the detector. For all settings of I_{krum}, the amplitudes of the spectra as a function of I_{XRT} agrees well for simulations and measurements. Also, the peaks now shift in simulation the way they do in measurements. However, while the curves show the correct height, the primary peak's width is slightly underestimated. This deviation is larger for smaller values of the initial I_{krum}. This is possibly due to inaccuracies of the conversion function from ToT to deposited energy and an underestimation of the energy resolution of the Dosepix detector. Due to the complexity of the model, there are various error sources for this observation. One major contribution is an inaccuracy introduced when fitting the pulse shape model to the calibration curve.

Figure 7.44 depicts the number of registered events for the spectra of figure 7.43 as a function of X-ray tube current. The plots correspond to different values of the initial I_{krum} indicated by the titles. The curves are normalised to the measurement with the lowest I_{XRT} each. For all settings of I_{krum}, simulations and measurements show a linearly increasing number of events for increasing X-ray tube current at first. The trend saturates until a maximum is reached, at which the number of registered events decreases again. The decrease takes place once pile-up starts to dominate, and multiple events at the analogue electronics input are detected as single events. The

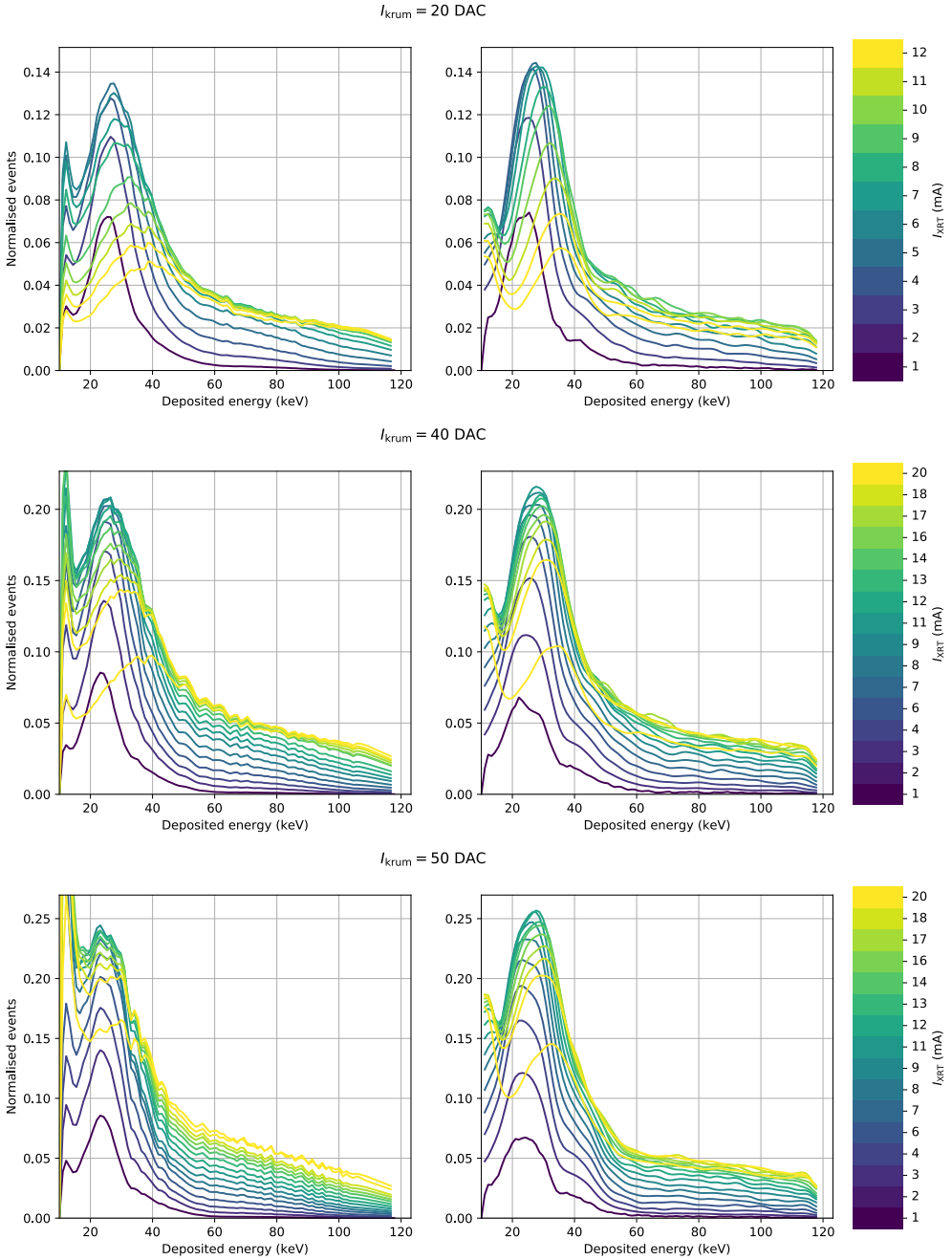

Figure 7.43.: The left-hand side shows measurements, the right-hand side simulations of S60 spectra. Threshold correction is applied for the measurements. I_{krum} correction is performed for simulations. The rows of the plots correspond to the settings of I_{krum} according to the titles. The colours of the curves represent different currents I_{XRT} of the X-ray tube according to the colour bar. All spectra are normalised to the sum of the spectrum with the lowest setting of I_{XRT} for deposited energies $\geq 20\,\text{keV}$. The used bin width is arbitrary.

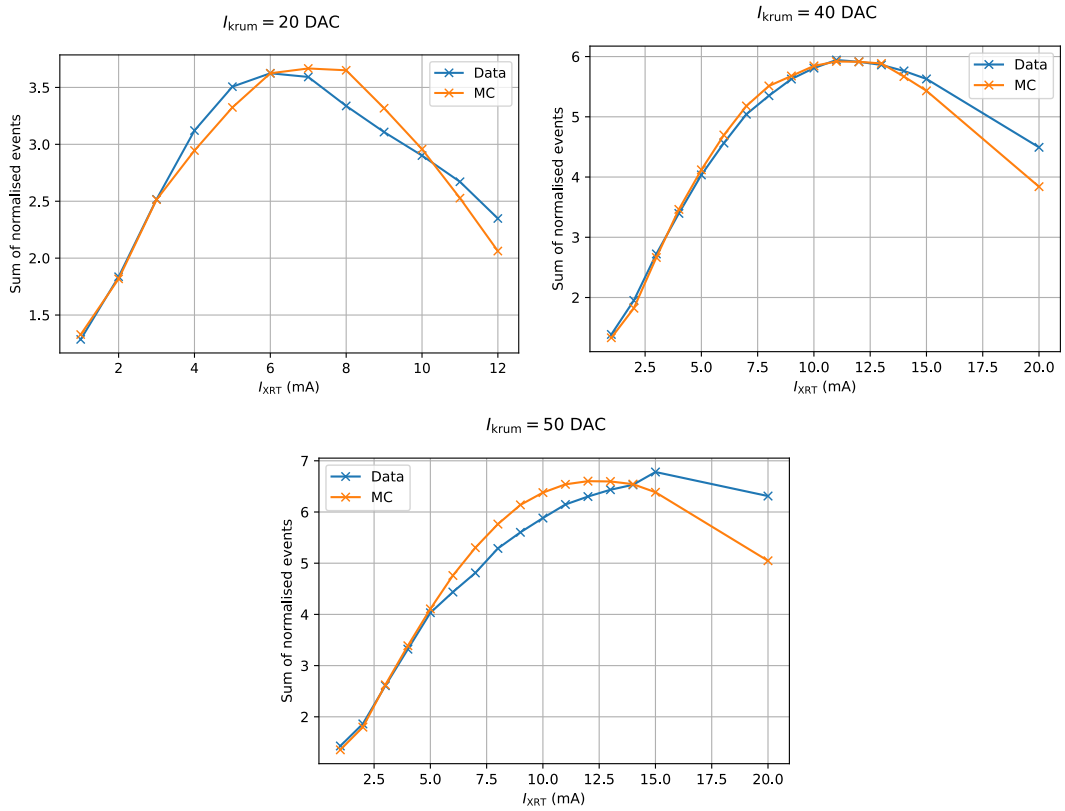

Figure 7.44.: Integrals of the normalised S60 spectra of figure 7.43 as a function of X-ray tube current I_{XRT}. Each plot depicts the data for different settings of I_{krum} according to the titles.

agreement of MC and measurements is good for the linear increase of the different curves. The falling trend is only reflected qualitatively.

The agreement of the shapes of the spectra is additionally evaluated via a Kolmogorov-Smirnov test. The two-sample Kolmogorov-Smirnov statistic D is calculated according to equation (6.10) and illustrated in figure 7.45. The null-hypothesis of two samples being from a common distribution under a rejection level of $\alpha = 5\%$ is neglected if D is greater than $D_\alpha = 0.205$ according to equation 6.11. The figure shows that the null hypothesis is accepted independent of I_{krum}.

In conclusion, by implementing the threshold correction in measurements and the I_{krum} correction in simulation, a good agreement is achieved. This provides information about the behaviour of Dosepix for high flux conditions. An investigation of how the effective I_{krum} changes as a function of dose rate is presented in the following.

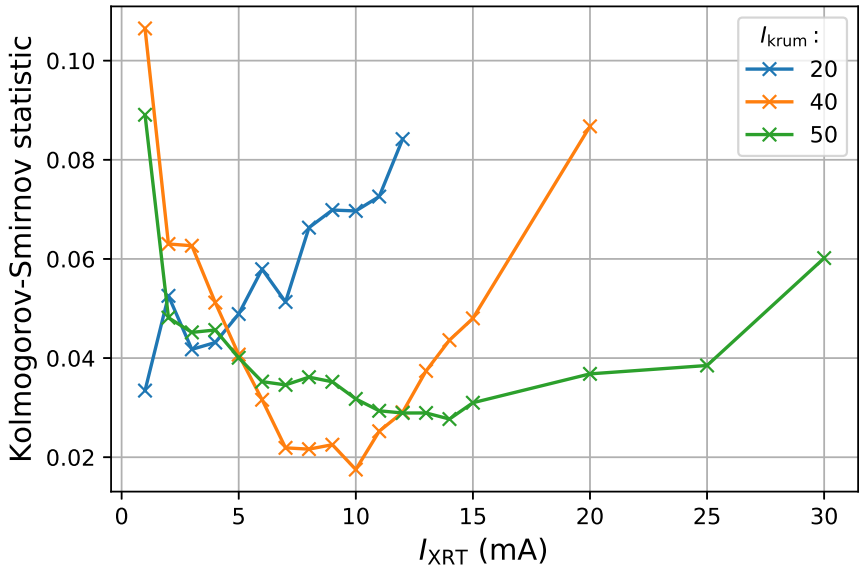

Figure 7.45.: Kolmogorov-Smirnov statistic calculated via equation (6.10) for the simulations with I_{krum} variation and threshold corrected measurements of S60 spectra of figure 7.32. The colours of the curves represent different values of I_{krum} according to the legend.

7.8.4 Effective I_{krum} for dose rate variation

The last section shows that the set and effective value of I_{krum} differ for high photon flux conditions. A further investigation of the correlation of these measures is made. The initial value of $I_{\text{krum},0}$ is set to 50 DAC. The shift of the dominant peak in the deposited energy spectra is determined as a function of the air kerma rate. This is shown for a measurement of the WO40 spectrum. The corresponding deposited energy spectra are depicted in figure 7.46. All curves are normalised to the maximum of the spectrum for the lowest dose rate in (a) and to their maxima in (b). The colours represent the air kerma rates according to the colour bars, which are measured via Dosimax Plus of IBA dosimetry [9].

The variation of the peak positions is determined by finding the maxima of each curve. First, the position is estimated by searching for the maximum value. A region of a width of 20 keV about the estimated position is selected and a Gaussian function is fitted to the data. The determined peak values as a function of air kerma rate are depicted in figure 7.47 (a). Fit errors are reflected by error bars, but are too small to be discernible. The true error is higher since it depends on the calibration of the Dosepix detector. The errors are considered to lie within a range of 1 keV. If the air kerma rate is high, the deposited energy spectra's distortion is too high to find a peak position. The distortion of the spectra is represented by figure 7.46 (b), where each curve is

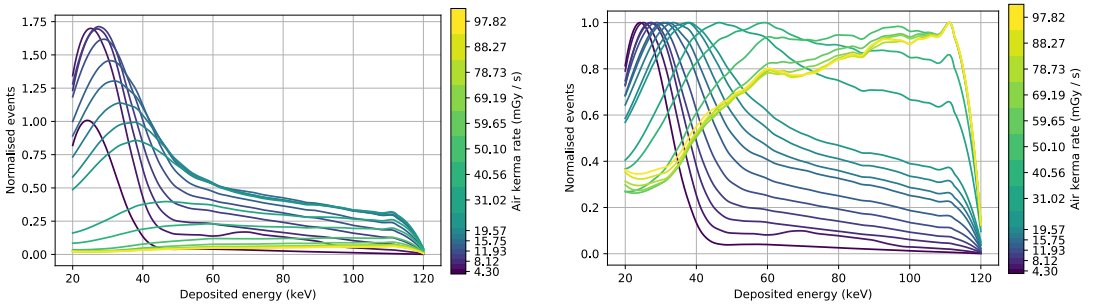

(a) WO40 (normalised to low air kerma rate) (b) WO40 (independently normalised)

Figure 7.46.: Measurements of deposited energy spectra for a W40 spectrum. The air kerma rate is varied according to the colour bar. All spectra are normalised to the maximum of the curve for the lowest dose rate in (a). The spectra are normalised to their maximum each in (b).

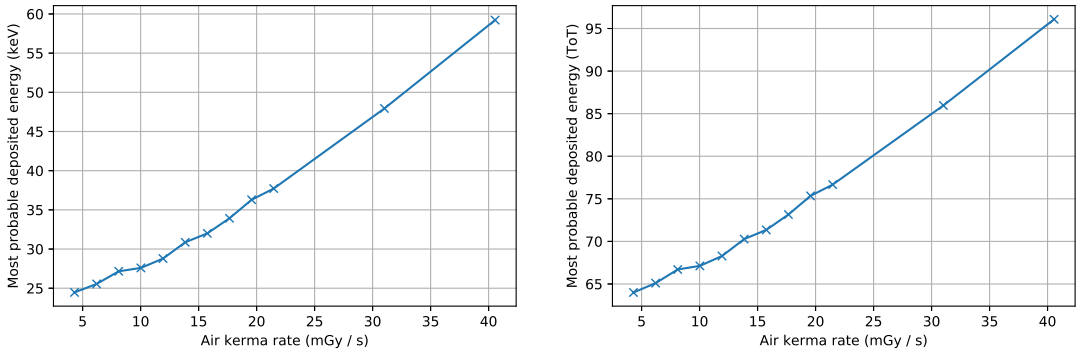

(a) In units of keV (b) In units of ToT

Figure 7.47.: Positions of the maxima of the measured deposited energy spectra of a WO40 spectrum, illustrated in figure 7.46. The values are specified in units of keV in (a) and are converted to ToT using the calibration function shown in figure 7.38 for $I_{\mathrm{krum}} = 50\,\mathrm{DAC}$ in (b). Different photon fluxes were used during measurements. These are reflected by the air kerma rate, denoted on the x-axes of the plots. The modes of the deposited energy spectra are determined by fitting a Gaussian function to the peaks. The fit error from is reflected via error bars but is too small to be discernible in the plot.

normalised to its maximum. This limits the data in figure 7.47 to rates of $40.56\,\frac{\mathrm{mGy}}{\mathrm{s}}$. Once the air kerma rate exceeds a certain level, all spectra show a similar shape. It indicates that I_{krum} does not change anymore and saturates. The original peak shift

takes place within the ToT spectra. These are then converted to deposited energy via the calibration function of the initial $I_{\mathrm{krum},0}$, leading to the spectra of figure 7.46. This process is inverted and the calibration function shown figure 7.38 for $I_{\mathrm{krum}} = 50\,\mathrm{DAC}$ is used to provide the ToT values of the previously determined peak values, resulting in the curve depicted in figure 7.47 (b). For the lowest air kerma rate, no peak shifting and therefore no change of I_{krum} is present. The corresponding ToT value is used as reference in the following. The peak in ToT shifts due to a change of I_{krum}, resulting in different effective calibration curves in figure 7.38. For the reference ToT-value, the intersections with these calibration curves are determined.

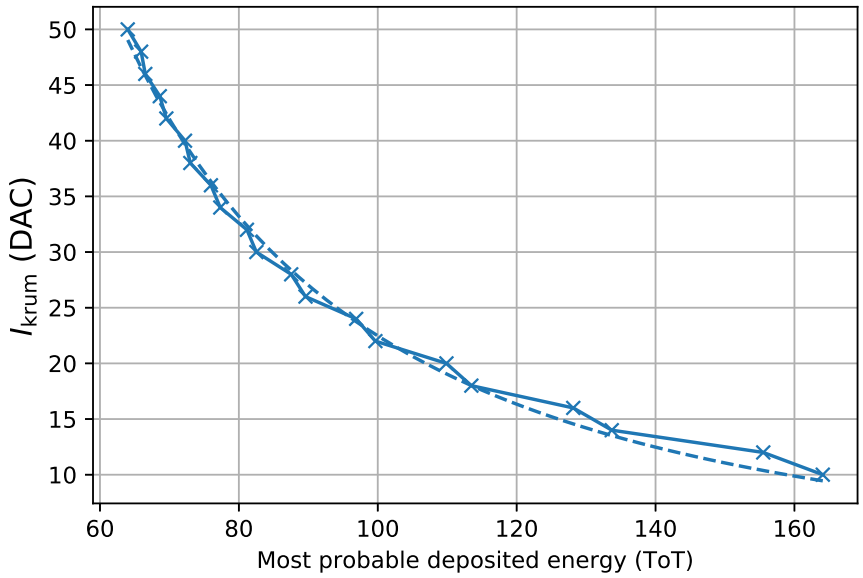

Figure 7.48.: Effective I_{krum} as a function of the peak position in ToT, P_{ToT}, for the measurements of WO40 spectra. The data is fitted via equation (7.37) and represented by the dashed curve.

This results in the blue curve of figure 7.48 which shows the effective I_{krum} as a function of the peak position in ToT, P_{ToT}. The trend of the curve is described via

$$I_{\mathrm{krum}} = \exp\left(\log(P_{\mathrm{ToT}}) \cdot a + b\right), \tag{7.37}$$

with the parameters $a = 97.62 \pm 0.04$ and $b = 57.53 \pm 0.17$, indicated by the dashed curve in the plot. Units are neglected, but P_{ToT} has to be provided in ToT, and I_{krum} in DAC. The optimised function is used to determine the effective values of I_{krum} for the different peak positions of figure 7.47 (b). This conversion results in the data of figure 7.49 which reveals the relation of the effective I_{krum} to the air kerma rate $\dot{K}_{\mathrm{air}}$. This curve is only valid for the investigated WO40 spectrum. Since the trend of the

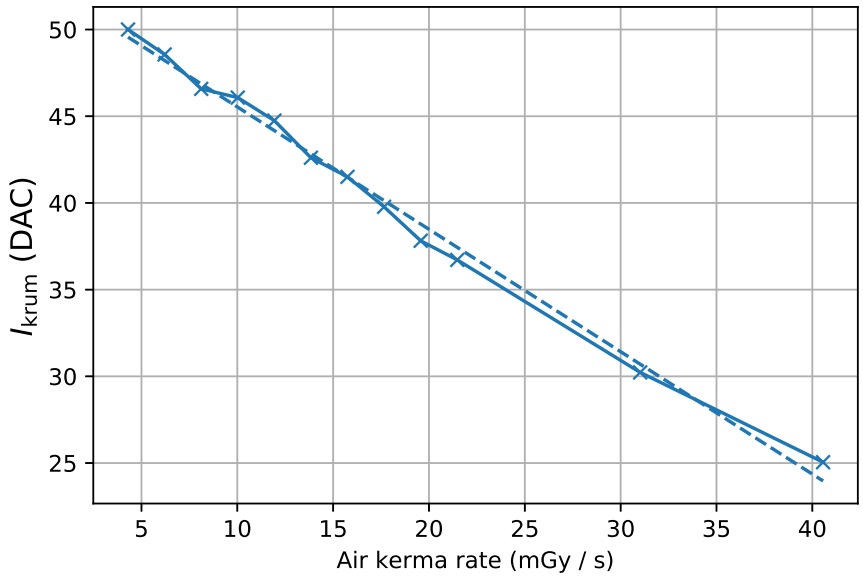

Figure 7.49.: Effective I_{krum} as a function of the air kerma rate $\dot{K}_{air}$ for WO40 photon spectra. The solid curve represents the values from measurements and the dashed curve a linear fit to the data.

Code	$m \left(\left(\frac{\text{mGy}}{\text{s}} \right)^{-1} \cdot \text{DAC} \right)$	t (DAC)
WO40	-0.706 ± 0.018	3.7 ± 0.4
WO60	-0.589 ± 0.028	11.43 ± 0.29
WO100	-0.285 ± 0.022	20.3 ± 1.0
WO120	-0.240 ± 0.012	21.9 ± 2.1

Table 7.10.: Optimised parameters of linear equation (7.38), describing the relation of I_{krum} and air kerma rate $\dot{K}_{air}$. Depicted are the values corresponding to the photon spectra of the first column. The errors of the parameters are determined from the fit.

relation is linear, it is described via

$$I_{krum} = (\dot{K}_{air} \cdot m + t) + 50\,\text{DAC}, \tag{7.38}$$

where I_{krum} is restricted to values $\leq 50\,\text{DAC}$. The described procedure is repeated for multiple photon spectra. Here, WO60, WO100, and WO120 are defined according to table 7.3. For each spectrum, the parameters of equation (7.38) are optimised. Their values are listed in table 7.10. The relation of I_{krum} to air kerma rate is linear, independent of the used photon spectrum. Therefore, the effective I_{krum} also depends linearly

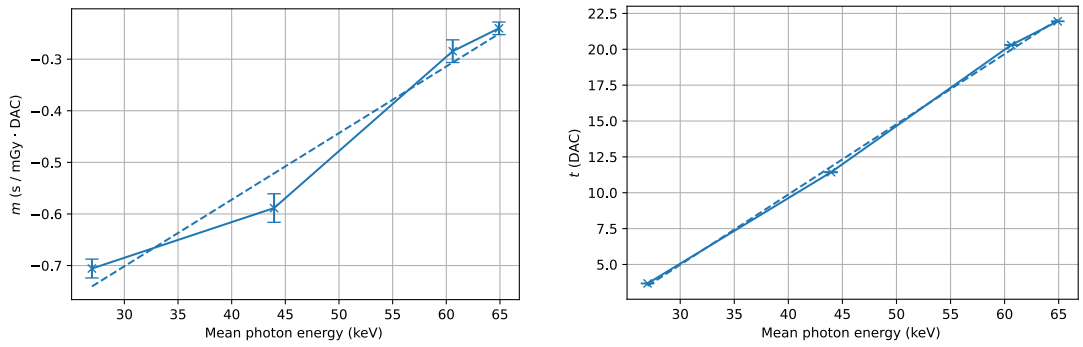

(a) Parameter m

(b) Parameter t

Figure 7.50.: Parameters m and t of equation (7.38) to describe the effective I_{krum} as a function of air kerma rate $\dot{K}_{\text{air}}$. The parameters are determined for different photon spectra whose mean energies are specified on the x-axis. Error bars represent the errors from the fit.

on the leakage current as it is proportional to the air kerma rate for a spectrum as established in equation 7.29.

Figure 7.50 depicts the optimised slopes m (a) and offsets t (b) of equation 7.38 as a function of the mean photon energies of the utilised spectra, listed in table 7.3. Linear trends are discernible in each plot which are described via linear functions. The slope is now called s and the intercept o. Additionally, the parameters receive an index which represents the parameter they are describing. For example, m is described via s_m and o_m. The optimised values of the parameters are listed in table 7.11. The rows represent the parameters for converting air kerma rate to effective I_{krum}. The columns describe the linear relation between these parameters and mean photon energy. The unit of a value is the product of the units specified for the parameter names in the corresponding row and column of the table.

Parameter index	s (keV^{-1})	o
m $\left(\left(\frac{\text{mGy}}{\text{s}}\right)^{-1} \cdot \text{DAC}\right)$	0.0129 ± 0.0019	-1.09 ± 0.10
t (DAC)	0.490 ± 0.013	-9.7 ± 0.7

Table 7.11.: Slope s and offset o of the linear relations to describe the parameters m and t of equation (7.37) as a function of mean photon energy. The names in the first column are used as indices for the parameters of the remaining columns. The unit of a parameter is the product of the units specified for the corresponding row and the column.

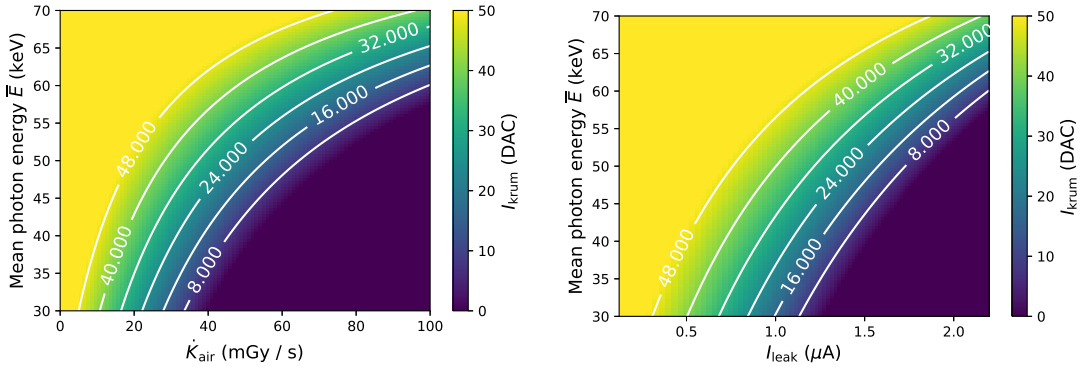

(a) $\dot{K}_{air}$ to I_{krum}

(b) I_{leak} to I_{krum}

Figure 7.51.: The conversions from air kerma rate $\dot{K}_{air}$ to I_{krum} (a) and leakage current I_{leak} to I_{krum} (b) as a function of mean photon energy $\overline{E}$. Equation (7.39) is used with the parameters of table 7.11. The results of the conversions are resembled by the color bars.

Combining the previous results, a formula representing the effective I_{krum} as a function of mean photon energy $\overline{E}$ and air kerma rate is described via

$$I_{krum}(\dot{K}_{air}, \overline{E}) = \left((s_m \cdot \overline{E} + o_m) \cdot \dot{K}_{air} + (s_t \cdot \overline{E} + o_t)\right) + 50\,\mathrm{DAC}, \tag{7.39}$$

where the value of I_{krum} is restricted to $\leq 50\,\mathrm{DAC}$. Figure 7.51 shows the corresponding conversions from air kerma rate $\dot{K}_{air}$ to I_{krum} (a) and vice versa (b), using equation (7.29). The relations reflect that I_{krum} stays stable as long as the air kerma rate and the leakage current are small. The lower the mean photon energy $\overline{E}$, the less stable I_{krum} becomes. Equation (7.39) in combination with previous results allows to simulate the threshold corrected detector responses for arbitrary photon spectra.

7.9 Event rate response

Previously, the simulation was optimised to measurements by determining a correlation between the X-ray tube current and the event rate at the input of the Dosepix detector. Additionally, the air kerma rate was measured with Dosimax to validate these results. In the following, a method to determine the event rate of Dosepix from these measurements are introduced.

Additional steps are required to determine the event rate from the air kerma rate $\dot{K}_{air}$. First, the used photon spectra are convolved with the air kerma to fluence factors $\frac{K_{air}}{\Phi}$, described in section 6.4.2, to calculate conversion factors for each spectrum. By dividing the air kerma rate $\dot{K}_{air}$ of Dosimax with the previously determined factors $\frac{K_{air}}{\Phi}$, the photon flux $\dot{\Phi}$ is determined. This flux is multiplied by the photon detection

efficiency ε of Dosepix, describing the number of registered events per fluence Φ, to estimate the event rate. $\varepsilon(E)$ as a function of photon energy E is depicted in figure 6.15. The curve for *Vac* is considered since no additional filter is used for the Dosepix detector. The photon spectrum is convolved with $\varepsilon(E)$ to get a single efficiency value ε representing the spectrum. In summary, the following formula describes the calculation of event rate $\dot{N}$ from air kerma rate $\dot{K}_{\text{air}}$

$$\dot{N} = \dot{K}_{\text{air}} \cdot \left(\frac{K_{\text{air}}}{\Phi} \right)^{-1} \cdot \varepsilon. \tag{7.40}$$

The calculation of $\dot{N}$ is performed for all photon spectra of table 7.3. Since measurements are performed for different X-ray tube currents, and therefore, photon fluxes, their relationship is described via equation (7.30) and parameter w_N. The same parameter is determined by optimising the pulse shape model to the measurements.

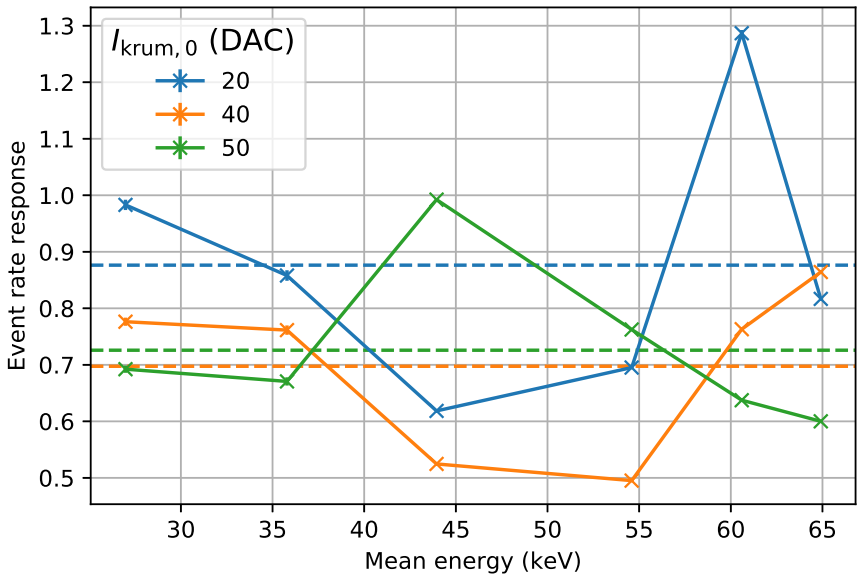

Figure 7.52.: Event rate response as a function of the photon spectra's mean energy listed in table 7.3. The responses reflect the fraction of event rates from pulse-shape simulations optimised to detector measurements and rates from air kerma measurements. Three curves are presented, each corresponding to a different initial value of $I_{\text{krum},0}$.

The result is depicted in figure 7.52 which shows the response, i.e. the fraction of simulated and measured w_N. The x-axis corresponds to the mean energies of the initial photon spectra according to table 7.3. Three curves are depicted in the figure, each representing a different initial value of $I_{\text{krum},0}$. The mean and standard deviations of the event rate responses are additionally listed in table 7.12. The simulation underestimates the event rate on average, independent of I_{krum}. Nevertheless, the responses

$I_{\mathrm{krum},0}$ (DAC)	μ	σ
20	0.88	0.22
40	0.7	0.14
50	0.73	0.13

Table 7.12.: Mean and standard deviations of the curves of figure 7.52. These resemble the event rate responses of optimised simulations and measurements for different initial values of $I_{\mathrm{krum},0}$.

are close to the perfect response of 1. The event rate reconstructed via simulation and determined directly from measurements lie within the same range, i.e. they do not differ in their magnitudes. For $I_{\mathrm{krum},0} = 20\,\mathrm{DAC}$, the performance in regards to the average response is best. However, the corresponding standard deviation is the largest. There is no trend discernible for the different settings of $I_{\mathrm{krum},0}$. The observed deviations of the responses can mostly be attributed to a mismatch between the pulse shape model and the measurements. Also, irregularities due to the measurements of the air kerma rate via Dosimax Plus exist. The device has to be placed at the same position as Dosepix to measure correctly. Therefore, measurements are performed via Dosepix and Dosimax switching place. Even small inevitable deviations in the position lead to large errors as the photon field directly in front of the X-ray tube is not homogeneous in regards of photon flux. Measurements with a high power X-ray tube are required in the future. This allows to place the detectors in the far field and ensures a more position independent photon flux. The presented results of this section validate the pulse shape simulation further, which can sufficiently predict the event rate using only information from measured deposited energy spectra. The simulation is able to describe the behaviour of Dosepix even for high photon flux conditions.

7.10 Conclusion

This chapter's goal was the investigation of the behaviour of Dosepix for high photon flux conditions. A model to describe the shapes of the analogue signals of the detector's electronics was established, and its parameters were optimised to measurements. This allowed a comparison of expectations and measurements. It became apparent that the detector does not work as intended once the number of registered events is high. Registered deposited energy spectra are shifted towards lower energies and are additionally distorted. It was deduced that this is an issue of a shifting threshold level or a change of the analogue signal's baseline. Changing the threshold as a function of air kerma rate or leakage current fixed this problem. Spectra did no longer shift, and pile-up events in the spectrum became visible. Further increasing the event rate with threshold correction applied showed that dominant peaks within the spectra are shifting towards higher energies while they should remain according

to the expectations and the simulation. It was shown that this issue is related to a reduction of the effective value of I_{krum}. Implementing this assumption in simulation lead to spectra comparable to measurements. The analyses showed that attention is required if Dosepix is used in high photon flux photon fields. This might be the case for scientific applications or in dosimetry. Knowledge about the behaviour of Dosepix is essential for the X-ray spectroscopy introduced in chapter 6. If distorted spectra are used to predict photon spectra with the developed network, the output will not reflect the expectation. The analogue electronics simulation might be used to extend the deconvolution capabilities to predict photon spectra of high flux in future works. Additionally, if the measurement of the leakage current is possible, a threshold correction can be applied. However, this can never get rid of pile-up events. The documentation of the behaviour of Dosepix under high photon flux conditions is relevant for future analyses. The most important relations are the threshold shift as a function of leakage current of equation 7.27, the air kerma rate as a function of the leakage current and mean photon energy of equation 7.29, and the effective I_{krum} as a function of the air-kerma rate and mean photon energy of equation 7.39. The parameters of these relations have to be determined for a Dosepix detector via measurements. The introduced descriptions of Dosepix can either be used to perform corrections for measurements or avoid situations where the detector will not work as intended. Since the found issues are possible related to the detector's hardware design, the documentation might help fixing issues in future revisions of Dosepix.

CHAPTER 8

Summary and outlook

Dosepix is a detector with the ability to count photons and resolve their energies. Due to its pixelation, it is able to work under high photon flux conditions. These features allow the measurement and characterisation of X-ray sources. In this thesis, Dosepix was used in various tasks, including dosimetry and spectroscopy. The detector and its readout hardware were implemented in a simulation. The geometry was extended to match measurement setups depending on the application. For example, phantoms are included, and metal filters are applied to the Dosepix detectors in dosimetry applications. The simulation was evaluated by comparing it to measurements of X-ray sources. A good agreement was achieved, and a detector's energy resolution was determined in the process. The ability of Dosepix to estimate dosimetric quantities was evaluated. Mono-energetic sources emitting photons on a phantom with a setup of multiple Dosepix detectors were simulated. The responses of the detectors were utilised to optimise conversion coefficients from registered events to dose. These coefficients were improved via measurements to achieve good responses for personal dose equivalents. Great performance is achieved for $H_\mathrm{p}(10)$ for photon energies of 12 keV to about 1250 keV. The capabilities are limited to energies above about 25 keV for $H_\mathrm{p}(0.07)$ as deviations for irradiation angles of up to 60° are present for lower energies. The deposited energies and, consequently, the reconstructed doses depend on temperature. A calibration procedure of this dependency was established to correct measurements.

Dosepix registers deposited energies in units of ToT. The determined values depend on the used detector and its settings. A convolutional neural network was developed to perform an energy calibration of a detector, which matches ToT to corresponding deposited energies. It improved the classic calibration method by reducing the required measurements and the measurement duration while providing comparable accuracy. The network's performance was evaluated by applying it to measurements performed with different detector settings. The resulting deposited energy spectra satisfied the expectations well.

Dosimetry setups involving Dosepix usually employ three detectors with different filters attached. The number of required detectors was reduced by optimising PMMA filters for a detector in simulation. The energy range was limited to maximum energies of 250 keV to satisfy requirements for medical applications. The estimation of personal dose equivalents $H_\mathrm{p}(3)$ and $H_\mathrm{p}(0.07)$ is easily possible, i.e. the dose response only slightly depends on the thickness and shape of the filter. The requirements for $H_\mathrm{p}(10)$ are more strict. The optimised filter has a thickness of 7 mm at its centre, increasing towards the edges to almost 2 cm. The determined filters allow estimating dose with single Dosepix detectors. These results concern simulations only. $H_\mathrm{p}(10)$ is estimated correctly for energies greater than about 14 keV for irradiation angles of up to 60°. If no filter is used, $H_\mathrm{p}(0.07)$ can be determined for energies above 15 keV. If the filter optimised for $H_\mathrm{p}(10)$ is used to measure $H_\mathrm{p}(0.07)$, the energy range is reduced to values greater than about 20 keV. For $H_\mathrm{p}(3)$, proper dose estimation for up to 250 keV and 90° irradiation angle is possible with a 1 mm thick PMMA filter. However, photon energies below about 15 keV limit the capabilities to about 70° irradiation. These results are promising and need to be evaluated in future analyses. The determined filters have to be manufactured, and measurements for different irradiation angles have to be made.

A setup of three Dosepix detectors was used for spectroscopy and quality assurance tests of an X-ray tube. Multiple convolutional neural networks were developed to reconstruct the initial photon spectrum and its characteristics, which include the kVp-value, the half-value layers for materials of aluminium and copper, the conversion factors from fluence to dose equicalents $H^*(10)$, $H'(0.07, 0°)$ and air kerma, and the photon fluence. A method to improve the energy calibration of the detectors via predicted kVp-values was introduced. The initial photon spectra for various X-ray tube measurements with voltages from 40 keV to 120 keV were correctly reconstructed by the corresponding network. The deviations of the predicted half-value layer values are within about 10% for aluminium and 20% for copper. The deviations for conversion factors from fluence to dose and air kerma are within about 6%, photon fluences within about 5% for mean initial photon energies above 55 keV. The deviation increases with decreasing energy. The separate prediction of photon fluence and fluence to dose factors allows analysing the mismatches in dose reconstruction for the simulation and measurements. The reconstructed shapes of the spectra agree well with measurements, while the fluence does not. The photon detection efficiency was determined and compared for simulations and measurements. Future analyses can correct simulations with the observed deviations. The predicted photon fluence was analysed as a function of mean photon energy. These mean energies are available from the predictions of the measured photon spectra and can be used to correct the fluence and conversion factors from fluence to air kerma and dose equivalents. In conclusion, the proposed Dosepix system can reconstruct the shape of an X-ray tube spectrum correctly scaled with its photon fluence.

The last chapter presents an in-depth investigation of the behaviour of Dosepix for high photon flux conditions. A model describing the signals of a pixel's analogue electronics as a function of time was established. It was used to explain effects like pile-up and variations in voltage levels. A change of the effective threshold level and I_{krum} for high photon flux, and consequently, high event-rates per pixel, was determined by comparing measurements and simulations. A correction of the threshold was introduced and the I_{krum} variation was implemented in simulation. It was shown that the stability of the detector increases with the set I_{krum}. The investigation of the Dosepix hardware allows judging which applications are suitable for the hardware. Measurements can be explained, and possible deviations can partly be corrected. This is important for applications with high photon fluxes like in pulsed photon fields, or the introduced X-ray spectroscopy.

A thorough understanding of the detector was established in various simulations in this thesis. Combinations of simulations and measurements were made to improve the detector's performance. The behaviour of the detector for different conditions of temperature and photon flux was investigated and methods to correct deviations were developed. Systems consisting of one or multiple Dosepix detectors show promising characteristics. Dosimetry is possible for conditions of high photon flux and pulsed radiation fields. A single detector with a special filter is able to reconstruct personal dose equivalents for a photon energy range limited to medical applications. A system of three detectors can estimate important measures for the quality assurance of X-ray tubes. Simultaneously, the corresponding energy spectra scaled with their photon fluences can be reconstructed. There are still engineering efforts required to build reliable devices for the presented applications. Additionally, official tests have to be performed to satisfy legal requirements. In conclusion, the analyses and developed methods in this thesis show the excellent capabilities of Dosepix regarding dosimetry and X-ray spectroscopy.

Appendix

Bin edge b_i	*Vac* (keV)	*Al* (keV)	*Sn* (keV)
1	12	12	32
2	18	17	37
3	21	31	47
4	24.5	40	57.5
5	33.5	45.5	68.5
6	43	50.5	80
7	53.5	60.5	91.5
8	66.5	68	104
9	81.5	91	117
10	97	102.5	131
11	113	133	145
12	131.5	148	163.5
13	151.5	163	183.5
14	173	196	207.5
15	200.5	220	234.5
16	236	257	269.5

Table A.1.: The settings of the 16 bin edges b_i for the pixels of the Dosepix detectors operated in Dosi-mode for personal dose measurements with three Dosepix detectors. The detector types correspond to the filter in front of the detectors.

Index i	$b_{i,\mathrm{vac}}$ (keV)	$H_\mathrm{p}(10)$ (μSv)	$b_{i,\mathrm{al}}$ (keV)	$H_\mathrm{p}(10)$ (μSv)	$b_{i,\mathrm{sn}}$ (keV)	$H_\mathrm{p}(10)$ (μSv)
1	12.0	$2.357658 \cdot 10^{-3}$	12.0	$7.240882 \cdot 10^{-3}$	32.0	$1.617864 \cdot 10^{-3}$
2	18.0	$8.907795 \cdot 10^{-4}$	17.0	$4.763841 \cdot 10^{-3}$	37.0	$1.563656 \cdot 10^{-4}$
3	21.0	$1.662654 \cdot 10^{-3}$	31.0	$3.184529 \cdot 10^{-3}$	47.0	$4.973117 \cdot 10^{-6}$
4	24.5	$1.554367 \cdot 10^{-3}$	40.0	$3.987113 \cdot 10^{-3}$	57.5	$4.700597 \cdot 10^{-5}$
5	33.5	$1.133144 \cdot 10^{-3}$	45.5	$2.934285 \cdot 10^{-3}$	68.5	$1.967456 \cdot 10^{-5}$
6	43.0	$7.846520 \cdot 10^{-4}$	50.5	$1.990079 \cdot 10^{-3}$	80.0	$2.839299 \cdot 10^{-4}$
7	53.5	$5.266790 \cdot 10^{-4}$	60.5	$1.929429 \cdot 10^{-3}$	91.5	$7.490655 \cdot 10^{-4}$
8	66.5	$4.519280 \cdot 10^{-4}$	68.0	$1.038565 \cdot 10^{-3}$	104.0	$1.159700 \cdot 10^{-3}$
9	81.5	$1.439059 \cdot 10^{-4}$	91.0	$4.230756 \cdot 10^{-4}$	117.0	$1.238558 \cdot 10^{-3}$
10	97.0	$1.353906 \cdot 10^{-4}$	102.5	$3.363124 \cdot 10^{-4}$	131.0	$1.718868 \cdot 10^{-3}$
11	113.0	$1.067828 \cdot 10^{-4}$	133.0	$2.596788 \cdot 10^{-4}$	145.0	$1.822988 \cdot 10^{-3}$
12	131.5	$6.934383 \cdot 10^{-5}$	148.0	$2.331480 \cdot 10^{-4}$	163.5	$1.744768 \cdot 10^{-3}$
13	151.5	$7.143382 \cdot 10^{-5}$	163.0	$1.776723 \cdot 10^{-4}$	183.5	$1.120562 \cdot 10^{-3}$
14	173.0	$5.856134 \cdot 10^{-5}$	196.0	$1.340748 \cdot 10^{-4}$	207.5	$9.319820 \cdot 10^{-4}$
15	200.5	$4.374679 \cdot 10^{-5}$	220.0	$4.465636 \cdot 10^{-5}$	234.5	$6.662891 \cdot 10^{-4}$
16	236.0	$2.723558 \cdot 10^{-5}$	257.0	$1.149641 \cdot 10^{-4}$	269.5	$7.274129 \cdot 10^{-4}$
Index i	$b_{i,\mathrm{vac}}$ (keV)	$H_\mathrm{p}(0.07)$ (μSv)	$b_{i,\mathrm{al}}$ (keV)	$H_\mathrm{p}(0.07)$ (μSv)	$b_{i,\mathrm{sn}}$ (keV)	$H_\mathrm{p}(0.07)$ (μSv)
1	12.0	$3.088486 \cdot 10^{-3}$	12.0	$7.170944 \cdot 10^{-3}$	32.0	$1.602022 \cdot 10^{-3}$
2	18.0	$1.073909 \cdot 10^{-3}$	17.0	$4.728131 \cdot 10^{-3}$	37.0	$1.572710 \cdot 10^{-4}$
3	21.0	$1.635528 \cdot 10^{-3}$	31.0	$3.142512 \cdot 10^{-3}$	47.0	$1.794128 \cdot 10^{-4}$
4	24.5	$1.726725 \cdot 10^{-3}$	40.0	$3.854301 \cdot 10^{-3}$	57.5	$8.349316 \cdot 10^{-4}$
5	33.5	$1.099189 \cdot 10^{-3}$	45.5	$2.879429 \cdot 10^{-3}$	68.5	$1.955054 \cdot 10^{-5}$
6	43.0	$7.421748 \cdot 10^{-4}$	50.5	$1.929578 \cdot 10^{-3}$	80.0	$1.140007 \cdot 10^{-3}$
7	53.5	$3.818445 \cdot 10^{-4}$	60.5	$1.506984 \cdot 10^{-3}$	91.5	$8.810495 \cdot 10^{-4}$
8	66.5	$3.519238 \cdot 10^{-4}$	68.0	$7.186354 \cdot 10^{-4}$	104.0	$1.891423 \cdot 10^{-3}$
9	81.5	$2.041210 \cdot 10^{-4}$	91.0	$3.089212 \cdot 10^{-4}$	117.0	$1.155497 \cdot 10^{-3}$
10	97.0	$1.305996 \cdot 10^{-4}$	102.5	$3.152165 \cdot 10^{-4}$	131.0	$1.481798 \cdot 10^{-3}$
11	113.0	$1.034846 \cdot 10^{-4}$	133.0	$2.180950 \cdot 10^{-4}$	145.0	$1.572473 \cdot 10^{-3}$
12	131.5	$8.688862 \cdot 10^{-5}$	148.0	$1.954615 \cdot 10^{-4}$	163.5	$1.217154 \cdot 10^{-3}$
13	151.5	$7.960937 \cdot 10^{-5}$	163.0	$1.441288 \cdot 10^{-4}$	183.5	$1.065752 \cdot 10^{-3}$
14	173.0	$8.607817 \cdot 10^{-5}$	196.0	$9.647649 \cdot 10^{-5}$	207.5	$7.566397 \cdot 10^{-4}$
15	200.5	$5.272322 \cdot 10^{-5}$	220.0	$5.124426 \cdot 10^{-5}$	234.5	$5.342495 \cdot 10^{-4}$
16	236.0	$1.129851 \cdot 10^{-4}$	257.0	$3.327415 \cdot 10^{-5}$	269.5	$9.936894 \cdot 10^{-4}$

Table A.2.: Conversion coefficients from registered events to personal dose equivalents $H_\mathrm{p}(10)$ and $H_\mathrm{p}(0.07)$ for the large pixels. Three detectors with filters according to the titles of the columns are used. The coefficients are optimised to simulations.

Index i	$b_{i,\mathrm{vac}}$ (keV)	$H_\mathrm{p}(10)$ (μSv)	$b_{i,\mathrm{al}}$ (keV)	$H_\mathrm{p}(10)$ (μSv)	$b_{i,\mathrm{sn}}$ (keV)	$H_\mathrm{p}(10)$ (μSv)
1	12.0	$2.347818 \cdot 10^{-3}$	12.0	$7.201501 \cdot 10^{-3}$	32.0	$1.611552 \cdot 10^{-3}$
2	18.0	$8.873950 \cdot 10^{-4}$	17.0	$4.713101 \cdot 10^{-3}$	37.0	$1.569421 \cdot 10^{-4}$
3	21.0	$1.640917 \cdot 10^{-3}$	31.0	$3.143366 \cdot 10^{-3}$	47.0	$7.714020 \cdot 10^{-6}$
4	24.5	$1.529496 \cdot 10^{-3}$	40.0	$3.873080 \cdot 10^{-3}$	57.5	$5.010433 \cdot 10^{-5}$
5	33.5	$1.107704 \cdot 10^{-3}$	45.5	$2.880199 \cdot 10^{-3}$	68.5	$2.352335 \cdot 10^{-5}$
6	43.0	$7.783327 \cdot 10^{-4}$	50.5	$1.941486 \cdot 10^{-3}$	80.0	$2.840215 \cdot 10^{-4}$
7	53.5	$5.167214 \cdot 10^{-4}$	60.5	$1.954507 \cdot 10^{-3}$	91.5	$7.354124 \cdot 10^{-4}$
8	66.5	$4.475018 \cdot 10^{-4}$	68.0	$9.756122 \cdot 10^{-4}$	104.0	$1.129944 \cdot 10^{-3}$
9	81.5	$1.876281 \cdot 10^{-4}$	91.0	$4.361833 \cdot 10^{-4}$	117.0	$1.201577 \cdot 10^{-3}$
10	97.0	$1.650902 \cdot 10^{-4}$	102.5	$3.331790 \cdot 10^{-4}$	131.0	$1.638655 \cdot 10^{-3}$
11	113.0	$1.102451 \cdot 10^{-4}$	133.0	$2.468026 \cdot 10^{-4}$	145.0	$1.731869 \cdot 10^{-3}$
12	131.5	$5.765619 \cdot 10^{-5}$	148.0	$2.073348 \cdot 10^{-4}$	163.5	$1.621696 \cdot 10^{-3}$
13	151.5	$5.618669 \cdot 10^{-5}$	163.0	$1.400955 \cdot 10^{-4}$	183.5	$1.053530 \cdot 10^{-3}$
14	173.0	$3.581167 \cdot 10^{-5}$	196.0	$1.228816 \cdot 10^{-4}$	207.5	$8.671618 \cdot 10^{-4}$
15	200.5	$2.225799 \cdot 10^{-5}$	220.0	$4.106909 \cdot 10^{-5}$	234.5	$6.234710 \cdot 10^{-4}$
16	236.0	$9.540547 \cdot 10^{-6}$	257.0	$1.112875 \cdot 10^{-4}$	269.5	$6.836181 \cdot 10^{-4}$
Index i	$b_{i,\mathrm{vac}}$ (keV)	$H_\mathrm{p}(0.07)$ (μSv)	$b_{i,\mathrm{al}}$ (keV)	$H_\mathrm{p}(0.07)$ (μSv)	$b_{i,\mathrm{sn}}$ (keV)	$H_\mathrm{p}(0.07)$ (μSv)
1	12.0	$2.404496 \cdot 10^{-3}$	12.0	$7.521881 \cdot 10^{-3}$	32.0	$1.628362 \cdot 10^{-3}$
2	18.0	$1.145302 \cdot 10^{-3}$	17.0	$4.873064 \cdot 10^{-3}$	37.0	$2.073654 \cdot 10^{-4}$
3	21.0	$1.934394 \cdot 10^{-3}$	31.0	$3.299762 \cdot 10^{-3}$	47.0	$6.881782 \cdot 10^{-6}$
4	24.5	$1.908948 \cdot 10^{-3}$	40.0	$4.075397 \cdot 10^{-3}$	57.5	$4.688494 \cdot 10^{-5}$
5	33.5	$1.223553 \cdot 10^{-3}$	45.5	$3.786515 \cdot 10^{-3}$	68.5	$1.959346 \cdot 10^{-5}$
6	43.0	$8.010219 \cdot 10^{-4}$	50.5	$1.980557 \cdot 10^{-3}$	80.0	$2.822985 \cdot 10^{-4}$
7	53.5	$5.021174 \cdot 10^{-4}$	60.5	$1.797912 \cdot 10^{-3}$	91.5	$7.519457 \cdot 10^{-4}$
8	66.5	$3.705274 \cdot 10^{-4}$	68.0	$9.367800 \cdot 10^{-4}$	104.0	$1.156275 \cdot 10^{-3}$
9	81.5	$1.062122 \cdot 10^{-4}$	91.0	$2.870639 \cdot 10^{-4}$	117.0	$1.210538 \cdot 10^{-3}$
10	97.0	$1.186709 \cdot 10^{-4}$	102.5	$3.220055 \cdot 10^{-4}$	131.0	$1.646975 \cdot 10^{-3}$
11	113.0	$7.717966 \cdot 10^{-5}$	133.0	$2.116799 \cdot 10^{-4}$	145.0	$1.714097 \cdot 10^{-3}$
12	131.5	$5.908508 \cdot 10^{-5}$	148.0	$2.024268 \cdot 10^{-4}$	163.5	$1.565714 \cdot 10^{-3}$
13	151.5	$8.239023 \cdot 10^{-5}$	163.0	$1.462855 \cdot 10^{-4}$	183.5	$9.779804 \cdot 10^{-4}$
14	173.0	$7.010934 \cdot 10^{-5}$	196.0	$1.078412 \cdot 10^{-4}$	207.5	$8.173455 \cdot 10^{-4}$
15	200.5	$3.675085 \cdot 10^{-5}$	220.0	$2.112100 \cdot 10^{-5}$	234.5	$5.801192 \cdot 10^{-4}$
16	236.0	$1.366170 \cdot 10^{-4}$	257.0	$7.059564 \cdot 10^{-5}$	269.5	$6.617378 \cdot 10^{-4}$

Table A.3.: Conversion coefficients from registered events to personal dose equivalents $H_\mathrm{p}(10)$ and $H_\mathrm{p}(0.07)$ for the large pixels. Three detectors with filters according to the titles of the columns are used. The coefficients are optimised to simulations and measurements.

Index i	$b_{i,\mathrm{vac}}$ (keV)	$H_\mathrm{p}(10)$ (μSv)	$b_{i,\mathrm{al}}$ (keV)	$H_\mathrm{p}(10)$ (μSv)	$b_{i,\mathrm{sn}}$ (keV)	$H_\mathrm{p}(10)$ (μSv)
1	12.0	$3.081193 \cdot 10^{-3}$	12.0	$7.634933 \cdot 10^{-4}$	32.0	$1.542459 \cdot 10^{-1}$
2	18.0	$1.029104 \cdot 10^{-3}$	17.0	$1.063987 \cdot 10^{-2}$	37.0	$3.256100 \cdot 10^{-1}$
3	21.0	$8.664213 \cdot 10^{-4}$	31.0	$6.638154 \cdot 10^{-2}$	47.0	$1.916155 \cdot 10^{-4}$
4	24.5	$1.216447 \cdot 10^{-1}$	40.0	$4.044160 \cdot 10^{-1}$	57.5	$1.078658 \cdot 10^{-2}$
5	33.5	$4.974304 \cdot 10^{-2}$	45.5	$6.540822 \cdot 10^{-2}$	68.5	$1.568718 \cdot 10^{-2}$
6	43.0	$1.434765 \cdot 10^{-2}$	50.5	$1.207149 \cdot 10^{-2}$	80.0	$2.004276 \cdot 10^{-1}$
7	53.5	$1.665622 \cdot 10^{-2}$	60.5	$1.219502 \cdot 10^{-2}$	91.5	$5.012874 \cdot 10^{-3}$
8	66.5	$1.799169 \cdot 10^{-2}$	68.0	$1.383287 \cdot 10^{-2}$	104.0	$9.006958 \cdot 10^{-2}$
9	81.5	$6.893234 \cdot 10^{-3}$	91.0	$5.192911 \cdot 10^{-3}$	117.0	$1.369100 \cdot 10^{-1}$
10	97.0	$7.709490 \cdot 10^{-3}$	102.5	$4.462174 \cdot 10^{-3}$	131.0	$6.474950 \cdot 10^{-2}$
11	113.0	$5.294466 \cdot 10^{-3}$	133.0	$4.392574 \cdot 10^{-5}$	145.0	$2.611863 \cdot 10^{-2}$
12	131.5	$1.678381 \cdot 10^{-3}$	148.0	$7.287129 \cdot 10^{-3}$	163.5	$4.890299 \cdot 10^{-2}$
13	151.5	$1.136649 \cdot 10^{-3}$	163.0	$6.570815 \cdot 10^{-4}$	183.5	$5.768260 \cdot 10^{-2}$
14	173.0	$8.885501 \cdot 10^{-4}$	196.0	$1.106937 \cdot 10^{-2}$	207.5	$2.690431 \cdot 10^{-2}$
15	200.5	$1.563319 \cdot 10^{-3}$	220.0	$5.981774 \cdot 10^{-3}$	234.5	$2.908943 \cdot 10^{-2}$
16	236.0	$3.877391 \cdot 10^{-4}$	257.0	$1.868861 \cdot 10^{-2}$	269.5	$3.804913 \cdot 10^{-2}$
Index i	$b_{i,\mathrm{vac}}$ (keV)	$H_\mathrm{p}(0.07)$ (μSv)	$b_{i,\mathrm{al}}$ (keV)	$H_\mathrm{p}(0.07)$ (μSv)	$b_{i,\mathrm{sn}}$ (keV)	$H_\mathrm{p}(0.07)$ (μSv)
1	12.0	$2.813259 \cdot 10^{-3}$	12.0	$3.965329 \cdot 10^{-4}$	32.0	$4.121180 \cdot 10^{-1}$
2	18.0	$2.109096 \cdot 10^{-2}$	17.0	$3.870762 \cdot 10^{-1}$	37.0	$6.911998 \cdot 10^{-2}$
3	21.0	$7.817146 \cdot 10^{-2}$	31.0	$8.698655 \cdot 10^{-2}$	47.0	$1.513645 \cdot 10^{-7}$
4	24.5	$2.041481 \cdot 10^{-1}$	40.0	$3.579460 \cdot 10^{-1}$	57.5	$3.015531 \cdot 10^{-3}$
5	33.5	$4.043206 \cdot 10^{-2}$	45.5	$5.693344 \cdot 10^{-2}$	68.5	$2.694999 \cdot 10^{-2}$
6	43.0	$4.363517 \cdot 10^{-5}$	50.5	$1.636800 \cdot 10^{-3}$	80.0	$2.279560 \cdot 10^{-1}$
7	53.5	$1.099514 \cdot 10^{-2}$	60.5	$9.099082 \cdot 10^{-3}$	91.5	$5.484591 \cdot 10^{-3}$
8	66.5	$1.507740 \cdot 10^{-2}$	68.0	$8.597374 \cdot 10^{-3}$	104.0	$9.802037 \cdot 10^{-2}$
9	81.5	$6.383407 \cdot 10^{-3}$	91.0	$4.798141 \cdot 10^{-3}$	117.0	$1.399485 \cdot 10^{-1}$
10	97.0	$8.039044 \cdot 10^{-3}$	102.5	$3.455513 \cdot 10^{-3}$	131.0	$6.276094 \cdot 10^{-2}$
11	113.0	$3.553145 \cdot 10^{-3}$	133.0	$6.843451 \cdot 10^{-6}$	145.0	$2.744972 \cdot 10^{-2}$
12	131.5	$2.656516 \cdot 10^{-3}$	148.0	$3.390430 \cdot 10^{-3}$	163.5	$4.016804 \cdot 10^{-2}$
13	151.5	$7.700755 \cdot 10^{-5}$	163.0	$1.651352 \cdot 10^{-3}$	183.5	$4.613418 \cdot 10^{-2}$
14	173.0	$1.132734 \cdot 10^{-3}$	196.0	$1.193533 \cdot 10^{-2}$	207.5	$3.084131 \cdot 10^{-2}$
15	200.5	$2.322267 \cdot 10^{-3}$	220.0	$4.991225 \cdot 10^{-3}$	234.5	$2.865201 \cdot 10^{-2}$
16	236.0	$1.588093 \cdot 10^{-2}$	257.0	$1.157184 \cdot 10^{-2}$	269.5	$3.303557 \cdot 10^{-2}$

Table A.4.: Conversion coefficients from registered events to personal dose equivalents $H_\mathrm{p}(10)$ and $H_\mathrm{p}(0.07)$ for the small pixels. Three detectors with filters according to the titles of the columns are used. The coefficients are optimised so small and large pixels return the same dose.

index i \ $H_p(10)$	$p_{Vac,i}$	$p_{Al,i}$	$p_{Sn,i}$
0	$1.261 \cdot 10^{-4}$	$-1.903 \cdot 10^{-5}$	$1.013 \cdot 10^{-3}$
1	$-1.266 \cdot 10^{-5}$	$5.589 \cdot 10^{-6}$	$-6.753 \cdot 10^{-5}$
2	$2.524 \cdot 10^{-7}$		$4.175 \cdot 10^{-6}$
3	$-5.205 \cdot 10^{-10}$		
index i \ $H_p(0.07)$	$p_{Vac,i}$	$p_{Al,i}$	$p_{Sn,i}$
0	$4.478 \cdot 10^{-4}$	$2.515 \cdot 10^{-4}$	$-1.729 \cdot 10^{-3}$
1	$-3.545 \cdot 10^{-5}$	$-3.699 \cdot 10^{-6}$	$1.921 \cdot 10^{-5}$
2	$8.456 \cdot 10^{-7}$		$-1.555 \cdot 10^{-7}$
3	$-5.519 \cdot 10^{-9}$		

Table A.5.: Parameters of the polynomial functions of equation 3.23 to determine the dose conversion coefficients k_f from number of registered events of detector d to personal dose equivalents $H_p(10)$ and $H_p(0.07)$ for large pixels. Three detectors with filters according to the titles of the columns are used.

Index i	b_i (keV)	$H_p(3)$ (μSv)	b_i (keV)	$H_p(10)$ (μSv)	b_i (keV)	$H_p(0.07)$ (μSv)
1	10.3	$5.719011 \cdot 10^{-5}$	10.9	$5.137635 \cdot 10^{-5}$	10.4	$1.367654 \cdot 10^{-4}$
2	23.7	$1.153996 \cdot 10^{-4}$	21.1	$1.074317 \cdot 10^{-4}$	13.6	$8.954601 \cdot 10^{-5}$
3	31.1	$1.521188 \cdot 10^{-4}$	32.8	$1.995339 \cdot 10^{-4}$	36.4	$2.425032 \cdot 10^{-4}$
4	42.8	$3.117573 \cdot 10^{-4}$	42.0	$3.593896 \cdot 10^{-4}$	43.0	$3.508682 \cdot 10^{-4}$
5	59.0	$7.191542 \cdot 10^{-4}$	55.4	$7.606446 \cdot 10^{-4}$	60.6	$8.179112 \cdot 10^{-4}$
6	67.0	$1.026151 \cdot 10^{-3}$	66.4	$1.311798 \cdot 10^{-3}$	67.5	$9.843243 \cdot 10^{-4}$
7	81.2	$1.964862 \cdot 10^{-3}$	76.3	$2.565951 \cdot 10^{-3}$	77.8	$1.827342 \cdot 10^{-3}$
8	87.5	$2.978802 \cdot 10^{-3}$	92.3	$3.973984 \cdot 10^{-3}$	88.5	$3.366962 \cdot 10^{-3}$
9	99.7	$5.091333 \cdot 10^{-3}$	100.8	$6.720498 \cdot 10^{-3}$	102.9	$5.723458 \cdot 10^{-3}$
10	113.6	$7.884823 \cdot 10^{-3}$	110.4	$6.731689 \cdot 10^{-3}$	112.4	$7.785916 \cdot 10^{-3}$
11	125.9	$1.158600 \cdot 10^{-2}$	125.3	$1.871787 \cdot 10^{-2}$	122.0	$1.113358 \cdot 10^{-2}$
12	135.0	$1.820201 \cdot 10^{-2}$	132.1	$2.243045 \cdot 10^{-2}$	134.1	$2.071226 \cdot 10^{-2}$
13	145.2	$6.739717 \cdot 10^{-2}$	144.7	$1.886649 \cdot 10^{-2}$	145.7	$3.734784 \cdot 10^{-2}$
14	151.6	$4.051697 \cdot 10^{-2}$	156.2	$5.883628 \cdot 10^{-2}$	158.7	$6.219769 \cdot 10^{-2}$
15	170.0	$1.155193 \cdot 10^{-1}$	164.1	$5.453947 \cdot 10^{-2}$	171.0	$1.146146 \cdot 10^{-1}$
16	177.2	$4.971313 \cdot 10^{-2}$	178.6	$4.665729 \cdot 10^{-2}$	182.3	$3.446552 \cdot 10^{-2}$

Table A.6.: Optimised bin edges b_i and corresponding dose conversion coefficients in Dosi-mode of a single Dosepix to measure personal dose equivalents for the dose types in the table. The optimisation is performed to simulations concerning a perpendicular irradiation. The used PMMA-filter thicknesses are 1 mm ($H_p(3)$), 7 mm ($H_p(10)$) and 1 mm ($H_p(0.07)$).

Index i	b_i (keV)	start (μSv)	optimised (μSv)	reoptimised (μSv)
1	10.9	$5.137635 \cdot 10^{-5}$	$3.928969 \cdot 10^{-5}$	$5.758158 \cdot 10^{-5}$
2	21.1	$1.074317 \cdot 10^{-4}$	$1.056197 \cdot 10^{-4}$	$1.052979 \cdot 10^{-4}$
3	32.8	$1.995339 \cdot 10^{-4}$	$1.619587 \cdot 10^{-4}$	$2.002986 \cdot 10^{-4}$
4	42.0	$3.593896 \cdot 10^{-4}$	$3.950673 \cdot 10^{-4}$	$3.472902 \cdot 10^{-4}$
5	55.4	$7.606446 \cdot 10^{-4}$	$7.387778 \cdot 10^{-4}$	$7.535444 \cdot 10^{-4}$
6	66.4	$1.311798 \cdot 10^{-3}$	$1.041895 \cdot 10^{-3}$	$1.205817 \cdot 10^{-3}$
7	76.3	$2.565951 \cdot 10^{-3}$	$3.789193 \cdot 10^{-3}$	$2.363017 \cdot 10^{-3}$
8	92.3	$3.973984 \cdot 10^{-3}$	$3.204862 \cdot 10^{-3}$	$3.754616 \cdot 10^{-3}$
9	100.8	$6.720498 \cdot 10^{-3}$	$5.534426 \cdot 10^{-3}$	$5.004779 \cdot 10^{-3}$
10	110.4	$6.731689 \cdot 10^{-3}$	$9.442898 \cdot 10^{-3}$	$8.689978 \cdot 10^{-3}$
11	125.3	$1.871787 \cdot 10^{-2}$	$1.264691 \cdot 10^{-2}$	$1.808955 \cdot 10^{-2}$
12	132.1	$2.243045 \cdot 10^{-2}$	$2.199891 \cdot 10^{-2}$	$1.914253 \cdot 10^{-2}$
13	144.7	$1.886649 \cdot 10^{-2}$	$2.247542 \cdot 10^{-2}$	$3.296169 \cdot 10^{-2}$
14	156.2	$5.883628 \cdot 10^{-2}$	$3.631710 \cdot 10^{-2}$	$3.446430 \cdot 10^{-2}$
15	164.1	$5.453947 \cdot 10^{-2}$	$5.814281 \cdot 10^{-2}$	$5.069877 \cdot 10^{-2}$
16	178.6	$4.665729 \cdot 10^{-2}$	$7.444124 \cdot 10^{-2}$	$7.978522 \cdot 10^{-2}$

Table A.7.: Optimised bin edges b_i and corresponding dose conversion coefficients used in Dosi-mode of a single Dosepix to measure $H_\mathrm{p}(10)$. Dose conversion coefficients for the flat filter („start“), the optimised filter („optimised“), and the optimised filter for a full Allpix^2 simulation („reoptimised“) are listed.

Index i	b_i (keV)	w/ filter (μSv)	w/o filter (μSv)
1	10.9	$1.474300 \cdot 10^{-4}$	$8.265184 \cdot 10^{-5}$
2	21.1	$1.068900 \cdot 10^{-4}$	$1.009617 \cdot 10^{-4}$
3	32.8	$1.837400 \cdot 10^{-4}$	$1.825798 \cdot 10^{-4}$
4	42.0	$3.077800 \cdot 10^{-4}$	$3.150821 \cdot 10^{-4}$
5	55.4	$6.330100 \cdot 10^{-4}$	$6.456518 \cdot 10^{-4}$
6	66.4	$9.726400 \cdot 10^{-4}$	$1.027120 \cdot 10^{-3}$
7	76.3	$2.007060 \cdot 10^{-3}$	$1.985942 \cdot 10^{-3}$
8	92.3	$3.296730 \cdot 10^{-3}$	$3.626496 \cdot 10^{-3}$
9	100.8	$4.537680 \cdot 10^{-3}$	$6.234615 \cdot 10^{-3}$
10	110.4	$8.001250 \cdot 10^{-3}$	$7.433225 \cdot 10^{-3}$
11	125.3	$1.650087 \cdot 10^{-2}$	$1.091989 \cdot 10^{-2}$
12	132.1	$1.754262 \cdot 10^{-2}$	$2.056396 \cdot 10^{-2}$
13	144.7	$3.059072 \cdot 10^{-2}$	$3.063546 \cdot 10^{-2}$
14	156.2	$3.566193 \cdot 10^{-2}$	$3.477422 \cdot 10^{-2}$
15	164.1	$4.776410 \cdot 10^{-2}$	$5.179360 \cdot 10^{-2}$
16	178.6	$8.526246 \cdot 10^{-2}$	$7.008044 \cdot 10^{-2}$

Table A.8.: Optimised bin edges b_i and corresponding dose conversion coefficients used in Dosi-mode of a single Dosepix to measure $H_\mathrm{p}(0.07)$. Dose conversion coefficients for the detector without filter and for the $H_\mathrm{p}(10)$ optimised PMMA filter are listed.

Bibliography

[1] BfS, Bundesamt für Strahlenschutz, "Grenzwerte für beruflich exponierte Personen", [Online]. Available: https://www.bfs.de/DE/themen/ion/strahlenschutz/beruf/grenzwerte/grenzwerte.html.

[2] O. Hupe, H. Zutz, and J. Klammer, "Radiation protection dosimetry in pulsed radiation fields", [Online]. Available: https://www.irpa.net/members/TS2f.3.pdf.

[3] I. Clairand, J.-M. Bordy, J. Daures, *et al.*, "Active personal dosemeters in interventional radiology: tests in laboratory conditions and in hospitals", *Radiation Protection Dosimetry*, vol. 144, no. 1-4, pp. 453–458, Dec. 2010, ISSN: 0144-8420. DOI: 10.1093/rpd/ncq556. eprint: https://academic.oup.com/rpd/article-pdf/144/1-4/453/4583829/ncq556.pdf. [Online]. Available: https://doi.org/10.1093/rpd/ncq556.

[4] EURADOS, European Radiation Dosimetry Group e.V., "EURADOS Report 2012-02: Optimization of Radiation Protection of Medical Staff", 2012. [Online]. Available: https://eurados.sckcen.be/-/media/Files/Eurados/documents/EURADOS_Report_201202.pdf?la=en&hash=06DAE419D9DE476193197192640860015D1D9143E.

[5] W. Wong, "A hybrid pixel detector asic with energy binning for real-time, spectroscopic dose measurements", Ph.D. dissertation, Mid Sweden University, Department of Information Technology and Media, 2012, p. 238, ISBN: 978-91-87103-20-9.

[6] *European Organization for Nuclear Research (CERN)*. [Online]. Available: https://home.cern/.

[7] W. Wong, G. Anton, R. Ballabriga, *et al.*, "A pixel detector asic for dosimetry using time-over-threshold energy measurements", *Radiation Measurements*, vol. 46, no. 12, pp. 1619–1623, 2011, Proceedings of the 16th Solid State Dosimetry Conference , September 19-24 , Sydney , Australia, ISSN: 1350-4487. DOI: https://doi.org/10.1016/j.radmeas.2011.06.061. [Online]. Available: http://www.sciencedirect.com/science/article/pii/S1350448711003209.

[8] *Erlangen Centre for Astroparticle Physics (ECAP)*. [Online]. Available: https://ecap.nat.fau.de/.

[9] *IBA dosimetry*. [Online]. Available: https://www.iba-dosimetry.com/.

[10] T. Gabor, "Simulationen und Experimente zur Anwendung eines neuartigen spektroskopischen Pixeldetektors in der Personendosimetrie", Diplomarbeit, Friedrich-Alexander-Universität Erlangen-Nürnberg (FAU), 2012.

[11] F. E. Emery and T. A. Rabson, "Average energy expended per ionized electron-hole pair in silicon and germanium as a function of temperature", *Phys. Rev.*, vol. 140, A2089–A2093, 6A 1965. DOI: 10.1103/PhysRev.140.A2089. [Online]. Available: https://link.aps.org/doi/10.1103/PhysRev.140.A2089.

[12] H. Berg, *Random walks in biology*. Princeton, N.J: Princeton University Press, 1993, ISBN: 9780691000640.

[13] J. Durst, "Modellierung und Simulation physikalischer eigenschaften photonenzählender Röntgenpixeldetektoren für die Bildgebung", Ph.D. dissertation, Friedrich-Alexander-Universität Erlangen-Nürnberg (FAU), 2008.

[14] A. Krzyżanowska, G. W. Deptuch, P. Maj, P. Gryboś, and R. Szczygieł, "Characterization of the photon counting chase jr., chip built in a 40-nm cmos process with a charge sharing correction algorithm using a collimated X-Ray beam", *IEEE Transactions on Nuclear Science*, vol. 64, no. 9, pp. 2561–2568, 2017. DOI: 10.1109/TNS.2017.2734821.

[15] J. H. Hubbell and S. M. Seltzer, "X-ray mass attenuation coefficients", 2004. [Online]. Available: https://physics.nist.gov/PhysRefData/XrayMassCoef/chap2.html.

[16] W. Schlegel, C. P. Karger, and O. Jäkel, *Medizinische Physik*. Springer Berlin Heidelberg, 2018. DOI: 10.1007/978-3-662-54801-1. [Online]. Available: https://doi.org/10.1007/978-3-662-54801-1.

[17] S. Seltzer, "XCOM-photon cross sections database, NIST standard reference database 8", en, 1987. DOI: 10.18434/T48G6X. [Online]. Available: http://www.nist.gov/pml/data/xcom/index.cfm.

[18] H. Krieger, *Grundlagen der Strahlungsphysik und des Strahlenschutzes*. Vieweg Teubner Verlag, 2012. DOI: 10.1007/978-3-8348-2238-3. [Online]. Available: https://doi.org/10.1007/978-3-8348-2238-3.

[19] F. E. Zink, "X-ray tubes.", *RadioGraphics*, vol. 17, no. 5, pp. 1259–1268, Sep. 1997. DOI: 10.1148/radiographics.17.5.9308113. [Online]. Available: https://doi.org/10.1148/radiographics.17.5.9308113.

[20] Siemens Healthineers, "X-ray tubes & x-ray tube assemblies", [Online]. Available: https://www.oem-products.siemens-healthineers.com/x-ray-tube.

[21] G. Hernández and F. Fernández, "Xpecgen: A program to calculate x-ray spectra generated in tungsten anodes", *The Journal of Open Source Software*, vol. 1, no. 7, p. 62, 2016. DOI: 10.21105/joss.00062. [Online]. Available: https://doi.org/10.21105/joss.00062.

[22] NIST - National Institute of Standards and Technology, "X-ray transition energy database", [Online]. Available: https://physics.nist.gov/PhysRefData/XrayTrans/Html/search.html.

[23] M. Winter, "The periodic table of the elements", *The University of Sheffield and WebElements Ltd, UK*, [Online]. Available: https://www.webelements.com/.

[24] Lenntech B.V., "Chemical properties of tin", [Online]. Available: https://www.lenntech.com/periodic/elements/sn.htm.

[25] W. C. Roesch, *scattering to complete diffusion of high energy electrons, Proceedings of the Fourth Symposium on Microdosimetry, Commission of the European Communities EUR 5122*. Rad. Research 15 (1958), Luxembourg, 1973.

[26] D. R. White, J. Booz, R. V. Griffith, J. J. Spokas, and I. J. Wilson, "Report 44", *Journal of the International Commission on Radiation Units and Measurements*, vol. os23, no. 1, NP–NP, 2016, ISSN: 1473-6691. DOI: 10.1093/jicru/os23.1.Report44. eprint: https://academic.oup.com/jicru/article-pdf/os23/1/NP/9587047/jicruos23-NP.pdf. [Online]. Available: https://doi.org/10.1093/jicru/os23.1.Report44.

[27] ICRP, "The 2007 recommendations of the international commission on radiological protection, ICRP publication 103", 2007. [Online]. Available: https://www.icrp.org/publication.asp?id=ICRP%20Publication%20103.

[28] F. Chollet *et al.*, "Keras", 2015.

[29] Martın Abadi, Ashish Agarwal, Paul Barham, *et al.*, "TensorFlow: Large-scale machine learning on heterogeneous systems", 2015, Software available from tensorflow.org. [Online]. Available: http://tensorflow.org/.

[30] M. A. Nielsen, *Neural Networks and Deep Learning*. Determination Press, 2015. [Online]. Available: http://neuralnetworksanddeeplearning.com.

[31] C. M. Bishop, *Neural Networks for Pattern Recognition*. Oxford University Press, Inc., 1995, ISBN: 0198538642.

[32] F. Bre, J. Gimenez, and V. Fachinotti, "Prediction of wind pressure coefficients on building surfaces using artificial neural networks", *Energy and Buildings*, vol. 158, Nov. 2017. DOI: 10.1016/j.enbuild.2017.11.045.

[33] D. P. Kingma and J. Ba, *Adam: A method for stochastic optimization*, 2017. arXiv: 1412.6980 [cs.LG].

[34] A. Krizhevsky, I. Sutskever, and G. E. Hinton, "Imagenet classification with deep convolutional neural networks", in, 2012. [Online]. Available: http://papers.nips.cc/paper/4824-imagenet-classification-with-deep-convolutional-neural-networks.pdf.

[35] I. Goodfellow, Y. Bengio, and A. Courville, *Deep Learning*. MIT Press, 2016, http://www.deeplearningbook.org.

[36] V. Dumoulin and F. Visin, *A guide to convolution arithmetic for deep learning*, 2018. arXiv: 1603.07285 [stat.ML].

[37] S. Spannagel, K. Wolters, D. Hynds, *et al.*, "Allpix^2: A Modular Simulation Framework for Silicon Detectors", *Nucl. Instrum. Meth.*, vol. A901, pp. 164–172, 2018. DOI: 10.1016/j.nima.2018.06.020. arXiv: 1806.05813 [physics.ins-det].

[38] S. Agostinelli *et al.*, "GEANT4: A Simulation toolkit", *Nucl. Instrum. Meth. A*, vol. 506, pp. 250–303, 2003. DOI: 10.1016/S0168-9002(03)01368-8.

[39] A. Zang, G. Anton, R. Ballabriga, *et al.*, "The dosepix detector — an energy-resolving photon-counting pixel detector for spectrometric measurements", *Journal of Instrumentation*, vol. 10, no. 4, 2015. DOI: doi:10.1088/1748-0221/10/04/C04015.

[40] National Electrical Mfr Association, "NEMA LI 1-1998 (R2011) industrial laminated thermosetting products", 2012. [Online]. Available: https://www.nema.org/standards/view/industrial-laminated-thermosetting-products.

[41] IAEA - Nuclear Data Section, "Live chart of nuclides", [Online]. Available: https://www-nds.iaea.org/relnsd/vcharthtml/VChartHTML.html.

[42] A. Savitzky and M. J. E. Golay, "Smoothing and differentiation of data by simplified least squares procedures.", *Analytical Chemistry*, vol. 36, no. 8, pp. 1627–1639, 1964. DOI: 10.1021/ac60214a047. eprint: https://doi.org/10.1021/ac60214a047. [Online]. Available: https://doi.org/10.1021/ac60214a047.

[43] J. A. Nelder and R. Mead, "A Simplex Method for Function Minimization", *The Computer Journal*, vol. 7, no. 4, pp. 308–313, Jan. 1965, ISSN: 0010-4620. DOI: 10.1093/comjnl/7.4.308. eprint: https://academic.oup.com/comjnl/article-pdf/7/4/308/1013182/7-4-308.pdf. [Online]. Available: https://doi.org/10.1093/comjnl/7.4.308.

[44] M. Böhnel, "Evaluierung und Entwicklung von Röntgendetektoren für die Dosimetrie", Ph.D. dissertation, Friedrich-Alexander-Universität Erlangen-Nürnberg (FAU), 2012.

[45] International Organization for Standardization, "ISO 4037-1: Radiological protection — X and gamma reference radiation for calibrating dosemeters and dose-rate meters and for determining their response as a function of photon energy — Part 1: Radiation characteristics and production methods", Geneva, CH, Standard, 2019.

[46] International Organization for Standardization, "ISO4037-3: Radiological protection — X and gamma reference radiation for calibrating dosemeters and doserate meters and for determining their response as a function of photon energy — Part 3: Calibration of area and personal dosemeters and the measurement of their response as a function of energy and angle of incidence", Geneva, CH, Standard, 2019.

[47] Andeggs, *3D spherical coordinates*, 2019. [Online]. Available: https://commons.wikimedia.org/wiki/File:3D_Spherical.svg.

[48] T. Michel, M. Böhnel, J. Durst, P. Sievers, and G. Anton, "Low energy dosimetry with photon counting pixel detectors such as medipix", *Nuclear Science, IEEE Transactions on*, vol. 56, pp. 417–423, May 2009. DOI: 10.1109/TNS.2009.2015229.

[49] Friedrich-Alexander-Universität Erlangen-Nürnberg (FAU), G. Anton, M. Böhnel, *et al.*, "Anordnungen und Verfahren zur Bestimmung von Dosismessgrößen und zur Ermittlung von Energieinformation einfallender Strahlung aus Photonen oder geladenen Teilchen mit zählenden Detektoreinheiten (DE102006006411A1)", 2007. [Online]. Available: https://patents.google.com/patent/DE102006006411A1/un.

[50] T. Michel, G. Anton, M. Böhnel, *et al.*, "A fundamental method to determine the signal-to-noise ratio (SNR) and detective quantum efficiency (DQE) for a photon counting pixel detector", *Nuclear Instruments and Methods in Physics Research Section A: Accelerators, Spectrometers, Detectors and Associated Equipment*, vol. 568, no. 2, pp. 799–802, 2006, ISSN: 0168-9002. DOI: https://doi.org/10.1016/j.nima.2006.08.115. [Online]. Available: http://www.sciencedirect.com/science/article/pii/S0168900206015580.

[51] *Physikalisch-Technische Bundesanstalt (PTB)*. [Online]. Available: www.ptb.de.

[52] D. Haag, "Active personal dosimetry with the hybrid pixelated DOSEPIX detector", Master's thesis, Friedrich-Alexander-Universität Erlangen-Nürnberg (FAU), 2018.

[53] Physikalisch-Technische Bundesanstalt (PTB), "PTB-Anforderungen PTB-A 23.2 "Strahlenschutzmessgeräte; Personendosimeter zur Messung der Tiefen- und Oberflächen-Personendosis". Ausgabe November 2013", de, 2015. DOI: 10.7795/510.20151109M. [Online]. Available: https://oar.ptb.de/resources/show/10.7795/510.20151109M.

[54] F. Beißer, "Temperature dependence of the hybrid pixel detector Dosepix with respect to I_{Krum} variation", Bachelor's thesis, Friedrich-Alexander-Universität Erlangen-Nürnberg (FAU), 2019.

[55] D. Haag, S. Schmidt, P. Hufschmidt, *et al.*, "Personal dosimetry in continuous photon radiation fields with the dosepix detector", *IEEE Transactions on Nuclear Science*, 2021. DOI: 10.1109/TNS.2021.3068832.

[56] I. Ritter, G. Anton, R. B. Sune, *et al.*, "Characterization of the dosepix detector with XRF and analog testpulses", *Journal of Instrumentation*, vol. 9, no. 05, pp. C05069–C05069, 2014. DOI: 10.1088/1748-0221/9/05/c05069. [Online]. Available: https://doi.org/10.1088%2F1748-0221%2F9%2F05%2Fc05069.

[57] J. Jakubek, "Precise energy calibration of pixel detector working in time-over-threshold mode", *Nuclear Instruments and Methods in Physics Research Section A: Accelerators, Spectrometers, Detectors and Associated Equipment*, vol. 633, S262–S266, 2011, 11th International Workshop on Radiation Imaging Detectors (IWORID), ISSN: 0168-9002. DOI: https://doi.org/10.1016/j.nima.2010.06.183. [Online]. Available: http://www.sciencedirect.com/science/article/pii/S0168900210013732.

[58] H. Iqbal, *HarisIqbal88/PlotNeuralNet v1.0.0*, version v1.0.0, 2018. DOI: 10.5281/zenodo.2526396. [Online]. Available: https://doi.org/10.5281/zenodo.2526396.

[59] Canon Electron Tubes & Devices Co., Ltd., *Medical X-ray tubes*. [Online]. Available: https://etd.canon/en/product/category/xray/medical.html.

[60] Euratom, "Council Directive 2013/59/Euratom of 5 December 2013 laying down basic safety standards for protection against the dangers arising from exposure to ionising radiation, and repealing Directives 89/618/Euratom, 90/641/Euratom, 96/29/Euratom, 97/43/Euratom and 2003/122/Euratom", 2013. [Online]. Available: https://eur-lex.europa.eu/legal-content/EN/TXT/?uri=CELEX%3A02013L0059-20140117.

[61] Belgian Nuclear Research Centre, "ORAMED (Optimization of radiation protection of medical staff)", 2008. [Online]. Available: https://www.oramed-fp7.eu/en.

[62] Friedrich-Alexander-Universität Erlangen-Nürnberg (FAU), T. Michel, S. Schmidt, *et al.*, "Device for detecting a radiation dose impinging on an eye lens (de102020206247a1)", (patent pending), 2020. [Online]. Available: https://patents.google.com/patent/DE102020206247A1/en?oq=DE102020206247A1.

[63] Inductiveload, *A diagram of the cylinder, or top hat, function*, 2007. [Online]. Available: https://commons.wikimedia.org/wiki/File:Cylinder_Function.svg.

[64] M. Hohenwarter, M. Borcherds, G. Ancsin, *et al.* (2021). "GeoGebra 6.0.507.0", [Online]. Available: http://www.geogebra.org.

[65] N. Dodgson, "Variation and extrema of human interpupillary distance", vol. 5291, 2004, pp. 36–46, ISBN: 0819451940. DOI: 10.1117/12.529999.

[66] polymerdatabase.com, "Poly(methyl methacrylate)", 2020. [Online]. Available: https://polymerdatabase.com/polymers/polymethylmethacrylate.html.

[67] Physikalisch-Technische Bundesanstalt (PTB), "Ergänzung der PTB-Anforderungen PTB-A 23.2 "Strahlenschutzmessgeräte; Personendosimeter zur Messung der Tiefen- und Oberflächen-Personendosis". Ausgabe November 2013", de, 2018. DOI: 10.7795/510.20181129A. [Online]. Available: https://oar.ptb.de/resources/show/10.7795/510.20181129A.

[68] F.-A. Fortin, F.-M. De Rainville, M.-A. Gardner, M. Parizeau, and C. Gagné, "DEAP: Evolutionary algorithms made easy", *Journal of Machine Learning Research*, vol. 13, pp. 2171–2175, 2012.

[69] A. H. Barr, "Superquadrics and angle-preserving transformations", vol. 1, no. 1, pp. 11–23, 1981, ISSN: 0272-1716 (print), 1558-1756 (electronic). [Online]. Available: http://ieeexplore.ieee.org/xpl/RecentIssue.jsp?punumber=38.

[70] Scratchapixel, 2016. [Online]. Available: https://www.scratchapixel.com/lessons/advanced-rendering/rendering-distance-fields.

[71] T. Veldhuizen. (1998). "The Wiener Filter", [Online]. Available: https://homepages.inf.ed.ac.uk/rbf/CVonline/LOCAL_COPIES/VELDHUIZEN/node15.html.

[72] T. Michel, P. T. Talla, M. Firsching, *et al.*, "Reconstruction of X-ray spectra with the energy sensitive photon counting detector Medipix2", *Nuclear Instruments and Methods in Physics Research Section A: Accelerators, Spectrometers, Detectors and Associated Equipment*, vol. 598, no. 2, pp. 510–514, 2009, ISSN: 0168-9002. DOI: https://doi.org/10.1016/j.nima.2008.09.049. [Online]. Available: http://www.sciencedirect.com/science/article/pii/S0168900208014757.

[73] P. Sievers, T. Weber, T. Michel, *et al.*, "Bayesian deconvolution as a method for the spectroscopy of X-rays with highly pixelated photon counting detectors", *Journal of Instrumentation*, vol. 7, no. 03, P03003–P03003, 2012. DOI: 10.1088/1748-0221/7/03/p03003. [Online]. Available: https://doi.org/10.1088/1748-0221/7/03/p03003.

[74] G. Hernández and F. Fernández, "A model of tungsten anode x-ray spectra", *Medical Physics*, vol. 43, no. 8Part1, pp. 4655–4664, 2016. DOI: 10.1118/1.4955120. [Online]. Available: https://doi.org/10.1118/1.4955120.

[75] L. Sachs, *Angewandte Statistik Methodensammlung mit R*. Springer, 2006, ISBN: 9783540321613.

[76] D. Haag, *Filter combinations of R-qualities*, Private Communication, 2020.

[77] ICRU, "Report 57", *Journal of the International Commission on Radiation Units and Measurements*, vol. os29, no. 2, NP–NP, 2016, ISSN: 1473-6691. DOI: 10.1093/jicru/os29.2.Report57. eprint: https://academic.oup.com/jicru/article-pdf/os29/2/NP/9587428/jicruos29-NP.pdf. [Online]. Available: https://doi.org/10.1093/jicru/os29.2.Report57.

[78] U.S. Food & Drug Administration, "Performance standards for ionizing radiation emitting products", [Online]. Available: https://www.ecfr.gov/cgi-bin/text-idx?SID=5d32a4692b7341340102cbbe69ad9765&mc=true&node=se21.8.1020_130&rgn=div8.

[79] International Electrotechnical Comission, "Medical electrical equipment - dosimetric instruments used for non-invasive measurement of X-ray tube voltage in diagnostic radiology", vol. IEC 61676:2002, 2002.

[80] FLUKE Biomedical, "Raysafe X2 X-ray measurement system", [Online]. Available: https://www.flukebiomedical.com/products/radiation-measurement/x-ray-qa-instruments/raysafe-x2-x-ray-measurement-system.

[81] PTW-Freiburg, *NOMEX Multimeter*. [Online]. Available: https://www.ptwdosimetry.com/en/products/nomex-multimeter/.

[82] International Electrotechnical Comission, "Medical electrical equipment - dosimeters with ionization chambers and/or semiconductor detectors as used in X-ray diagnostic imaging", vol. IEC 61674:2012, 2012.

[83] Physikalisch-Technische Bundesanstalt (PTB), "PTB-Anforderungen PTB-A 23.3 "Strahlenschutzmessgeräte; Ortsdosimeter zur Messung der Umgebungs- und Richtungs-Äquivalentdosis und der Umgebungs- und Richtungs-Äquivalentdosisleistung". Ausgabe November 2013", de, 2018. DOI: 10.7795/510.20181129B. [Online]. Available: https://oar.ptb.de/resources/show/10.7795/510.20181129B.

[84] F. Krummenacher, "Pixel detectors with local intelligence: An IC designer point of view", *Nuclear Instruments and Methods in Physics Research Section A: Accelerators, Spectrometers, Detectors and Associated Equipment*, vol. 305, no. 3, pp. 527–532, 1991, ISSN: 0168-9002. DOI: https://doi.org/10.1016/0168-9002(91)90152-G. [Online]. Available: https://www.sciencedirect.com/science/article/pii/016890029190152G.

[85] P. Ganguly, *Principles of electronics*. New Delhi: PHI Learning, 2015, ISBN: 812035124X.

[86] R. Dorf and J. Svoboda, *Introduction to Electric Circuits*. Wiley, 2001, ISBN: 9780471386896. [Online]. Available: https://books.google.de/books?id=l-weAQAAIAAJ.

[87] U. Tietze, *Halbleiter-Schaltungstechnik*. Berlin, Germany: Springer Vieweg, 2019, ISBN: 978-3-662-48553-8.

[88] W. H. Press, S. A. Teukolsky, W. T. Vetterling, and B. P. Flannery, *Numerical Recipes 3rd Edition: The Art of Scientific Computing*, 3rd ed. USA: Cambridge University Press, 2007, ISBN: 0521880688.

[89] F. Corporation, *Fluke 8845A 6.5 digit precision multimeter*. [Online]. Available: https://www.fluke.com/en-us/product/precision-measurement/bench-instruments/fluke-8845a-8846a.

Acknowledgements / Danksagungen

A huge thanks to everyone who supported me throughout this process of this thesis:

Ein großes Dankeschön an all diejenigen, die mich während der Zeit, in der diese Arbeit entstanden ist, unterstützt haben:

Dr. Thilo Michel, für seine ausgezeichnete Betreuung und Hilfestellungen in allen Lebenslagen. Sein unerschöpflicher Ideenreichtum sorgt dafür, dass es immer etwas Interessantes zu tun gibt. Die Kombination mit seinem Optimismus stellt sicher, dass es immer vorangeht, auch wenn die Lage noch so festgefahren erscheint.

Prof. Dr. Gisela Anton, für die jahrelange tolle Leitung des Lehrstuhls und die ausgezeichnete akademische Begleitung am ECAP.

Franziska Eberle, die sich immer die Zeit genommen hat, sich mit meinen Ideen zu befassen, auch wenn sie noch so wild waren. Die aber auch sonst stets mit Rat und Tat zur Verfügung stand und mehr kann, als sie denkt.

Dennis Haag, meinen Sitznachbarn, der immer da ist, wenn man ihn braucht. Sei es, wenn man vergessen hat, in welcher ISO-Richtlinie etwas steht oder wie man am besten seine Messungen durchführt. Auch ist er stets für die eine oder andere kontroverse Diskussion bereit, sodass es nie langweilig wurde.

Patrick Hufschmidt, der Mann von schräg gegenüber, für die gemeinsame Zeit der Erforschung des Dosepix-Detektors und die hitzigen politischen Debatten im Büro.

Jutta Dziwis und **Sabine Link**, für die freundliche Unterstützung bei der Bewältigung diverser bürokratischer Aufgaben.

Tobias Ziegler, für die vielen unterhaltsamen Stunden im Büro und das regelmäßige Fensterbankgärtnern. Für die Hilfsbereitschaft bei allen möglichen Problemstellungen und für das Teilen deiner Probleme, was meinem Verständnis von Deep Learning sehr geholfen hat.

Franziska Eberle, Dennis Haag, Patrick Hufschmidt und **Tobias Ziegler** für das Korrekturlesen dieser Arbeit. Ihr habt mir sehr dabei geholfen, diesen rohen Klotz in etwas halbwegs Ansehnliches zu verwandeln. Einen herzlichen Dank dafür!

Die restliche Besatzung der Büros 208 **und** 209, die sowohl fachlich als auch menschlich immer eine große Hilfe und Freude waren. Ich hatte viel Spaß bei Andi

Zmijas Zuggeschichten, Pizzaabenden mit Federico Bontempo, DJ-Sessions mit teilweise fragwürdiger Musikwahl von Johanne Link, philosophischen Diskussionen mit Michael Wagenpfeil und Gartengesprächen mit Naomi Vogel, die mich auch immer ertragen musste, wenn mir einmal langweilig war.

Das Team des RRZE (Regionales Rechenzentrum Erlangen), für ihren super Service und die vielen Stunden, die ich auf ihren HPC-Systemen rechnen durfte, was die Simulationen in dieser Arbeit überhaupt erst möglich gemacht hat.

Meiner Familie, für ihre langjährige Unterstützung und das gegenseitige Aushalten.